SCUOLA DI DOTTORATO
UNIVERSITÀ DEGLI STUDI DI MILANO-BICOCCA

Dipartimento di / Department of

Medicine and Surgery

Dottorato di Ricerca in / PhD program **Translational and Molecular Medicine (Dimet)**
Ciclo / Cycle **38°**

Curriculum in (se presente / if it is) .....

Atomic Force Microscopy as a Translational Tool: Quantitative Nanomechanical Profiling of Cells and Biological Tissues.

Cognome / Surname **Campanile** Nome / Name **Riccardo**

Matricola / Registration number **825974**

Tutore / Tutor: **Francesco Mantegazza**

Cotutore / Co-tutor: **Valeria Cassina**
(se presente / if there is one)

Supervisor: .....
(se presente / if there is one)

Coordinatore / Coordinator: **Francesco Mantegazza**

ANNO ACCADEMICO / ACADEMIC YEAR 2024/2025

To my family,
and to everyone who shared this journey with me.

Abstract

Understanding how biological systems behave mechanically at the nanoscale is essential to link structure, function, and pathology. This thesis explores the potential of Atomic Force Microscopy (AFM) as a versatile and quantitative tool to investigate the mechanical properties of living cells and tissues, aiming to bridge nanoscale physics with biomedical relevance. AFM allows the measurement of forces in the pico- to nanoNewton range allowing also imaging with nanometric resolution, providing unique insight into how mechanical properties are reflecting physiological or pathological states.

Through the combination of imaging, force spectroscopy, and microrheology, in this thesis, AFM was employed to quantify elasticity, adhesion, and viscoelasticity in a variety of biological samples. These complementary modalities revealed how mechanical cues at the nanoscale can serve as sensitive biomarkers of cellular state and function. Mechanical alterations were measured in both soft connective tissues and hematological cells, highlighting how diseases or pharmacological treatments reshape the underlying biomechanical architecture.

A major focus of this work was the development and refinement of advanced AFM protocols designed to overcome traditional experimental limitations in studying soft and not-adherent round cells. The implementation of wedged cantilever and stepwise confinement techniques enabled controlled, uniaxial compression and dynamic monitoring of individual cell mechanics—approaches that significantly improved the reproducibility and physiological relevance of AFM-based measurements. These methods allowed the extraction of time-dependent viscoelastic parameters, revealing the active remodeling processes underlying cellular adaptation to mechanical stress.

Applying these optimized methods, AFM-based nanomechanical profiling was

used to investigate how mechanical parameters correlate with biological phenomena. For instance, in tissues such as the meniscus, AFM detected stiffness gradients and nanoscale heterogeneity associated with extracellular matrix remodeling during degeneration. In hematological malignancies, AFM identified distinct nanomechanical signatures in leukemic cells, sensitive to cytoskeletal-targeting drugs. These results demonstrate that mechanical fingerprints can reflect both disease progression and therapeutic modulation.

Altogether, this work positions AFM not merely as a high-resolution imaging tool but as a quantitative biophysical instrument capable of linking nanomechanical signatures to cellular behavior and pathology. By merging physical precision with biological complexity, AFM emerges as a promising candidate for mechanobiological characterization of samples, offering a path toward the integration of mechanical biomarkers into translational research.

Riassunto

Comprendere come i sistemi biologici si comportano meccanicamente su scala nanometrica è fondamentale per collegare la loro struttura, funzione e stato fisiologico. Questa tesi esplora il potenziale della Microscopia a Forza Atomica (Atomic Force Microscopy, AFM) come strumento quantitativo e altamente versatile per studiare le proprietà meccaniche di cellule vive e tessuti, con l'obiettivo di collegare la fisica su scala nanometrica con la rilevanza biomedica. L'AFM consente di misurare forze nell'intervallo dei pico- fino ai nanoNewton e di acquisire immagini con risoluzione nanometrica, offrendo un punto di vista unico su come le proprietà meccaniche riflettano stati fisiologici o patologici.

Attraverso la combinazione di imaging, force spectroscopy e microrheology, in questa tesi l'AFM è stato impiegato per quantificare l'elasticità, l'adesione e la viscoelasticità in un'ampia gamma di campioni biologici. Queste modalità complementari hanno mostrato come i segnali meccanici su scala nanometrica possano agire come biomarcatori sensibili dello stato e della funzione cellulare. Alterazioni delle proprietà meccaniche sono state osservate sia in tessuti connettivi molli sia in cellule ematologiche, evidenziando come patologie o trattamenti farmacologici possano rimodellare l'architettura biomeccanica sottostante.

Un aspetto centrale di questo lavoro di tesi è stato lo sviluppo e l'ottimizzazione di protocolli AFM avanzati, progettati per superare le limitazioni sperimentali tradizionali nello studio di cellule circolanti. L'introduzione di cantilever wedged e di tecniche di stepwise confinement ha reso possibile applicare una compressione uniassiale controllata e monitorare dinamicamente la risposta meccanica di singole cellule. Tali approcci hanno migliorato significativamente la riproducibilità e la rilevanza fisiologica delle misure AFM. Questi metodi hanno inoltre permesso l'estrazione di parametri viscoelastici time-dependent, rivelando i processi di

rimodellamento attivo alla base dell'adattamento cellulare allo stress meccanico.

Applicando questi metodi ottimizzati, la profilazione nanomeccanica basata su AFM è stata utilizzata per esplorare la correlazione tra parametri meccanici e stati biologici. In tessuti come il menisco, l'AFM ha rilevato gradienti di rigidità e eterogeneità su scala nanometrica associati al rimodellamento della matrice extracellulare durante i processi degenerativi. Nelle neoplasie ematologiche, l'AFM ha identificato tratti nanomeccanici distintivi nelle cellule leucemiche, anche in presenza di trattamenti farmacologici mirati al citoscheletro. Questi risultati dimostrano che le fingerprints meccaniche possono riflettere sia la progressione della malattia sia la risposta terapeutica.

Nel complesso, questa tesi propone l'AFM non solo come uno strumento di imaging ad alta risoluzione, ma come un vero e proprio strumento biofisico quantitativo capace di connettere la nanomeccanica al comportamento cellulare e alla patologia. Unendo la precisione della fisica alla complessità della biologia, l'AFM si afferma come un approccio promettente per la caratterizzazione meccanobiologica di cellule e tessuti, aprendo la strada all'integrazione di biomarcatori meccanici nella ricerca traslazionale.

Contents

Part I

State of Art

Chapter 1

Introduction to Atomic Force Microscopy

1.1 Historical development and impact of AFM

The invention of the Atomic Force Microscope (AFM) in 1986 by Binnig, Quate and Gerber represented a watershed moment in nanoscale science and technology [1] (Fig. 1.1). Prior to its development, the principal method for investigating surfaces at the atomic level was the Scanning Tunneling Microscope (STM), which itself had been a revolutionary tool, earning Binnig and Rohrer the Nobel Prize in Physics in 1986 [2]. While the STM enabled imaging of conductive surfaces with atomic resolution, it was intrinsically limited by its dependence on electrical conductivity [3]. This meant that many materials of biological and technological interest, such as polymers, ceramics, and living tissues, remained inaccessible. The AFM was conceived as a solution to this fundamental constraint, and its introduction broadened the scope of scanning probe techniques to virtually any type of surface, regardless of conductivity [4–7].

The earliest demonstrations of AFM focused primarily on imaging solid surfaces in ambient air, revealing nanoscale features with unprecedented clarity [8–10]. However, it soon became clear that the true potential of the instrument lay in its ability to operate in liquids, including physiological buffers, which opened the door to the study of biological samples in their native environments [11–14]. By

the 1990s, AFM was being applied to image DNA, proteins, membranes, and even intact living cells [6, 15, 16]. This capacity to bridge structural and functional biology at the nanoscale, distinguished AFM from electron microscopy, which requires sample fixation and metallization, and from light microscopy, which is limited in resolution by the diffraction barrier.

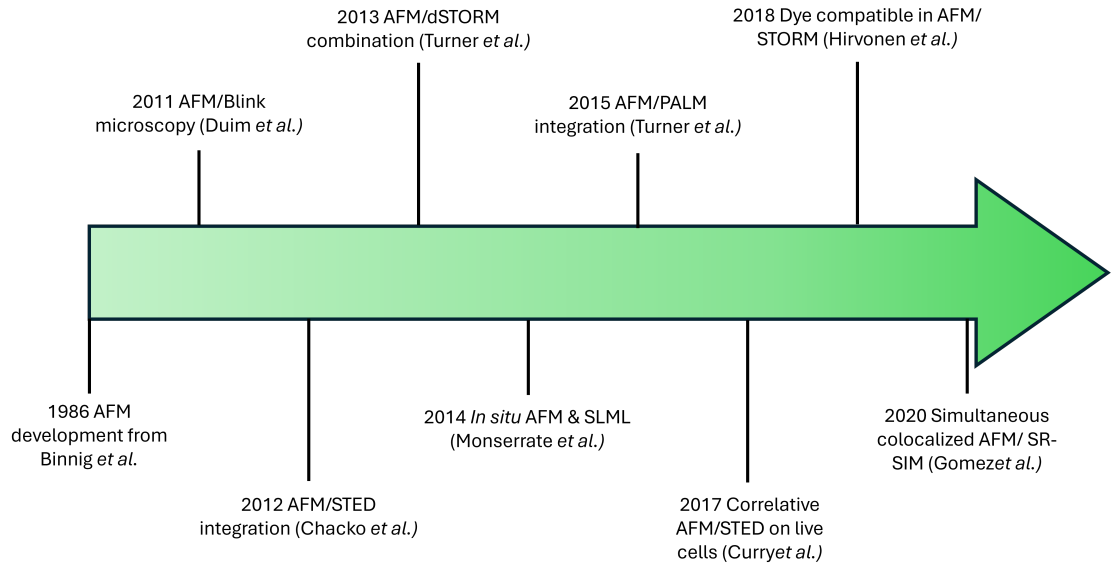

Figure 1.1: **Timeline of AFM innovations over the past decades.** The illustration highlights the most significant developments in AFM implementations focusing primarily on optical advances. These innovations aimed at enabling a more comprehensive characterization of biological samples including both mechanical and optical properties. The timeline was adapted from [17].

Over the last three decades, AFM has evolved from a niche instrument into a versatile and widely adopted platform (Fig. 1.1). Today, AFM is not only used for imaging but also for quantifying mechanical properties, mapping molecular interactions, and probing dynamic processes in real time [18–21]. It has become an indispensable tool in diverse disciplines, including surface chemistry, polymer physics, biomaterials science, and, most significantly for this thesis, mechanobiology [22–26]. The ability of AFM to combine nanometer resolution with pico- to nanoNewton force sensitivity has made it uniquely powerful for addressing fundamental questions in biology and medicine [27].

1.2 Principles of AFM and key elements

1.2.1 AFM setup and working principle

At its core, an AFM consists of a microfabricated cantilever with a sharp probe at its free end, a piezoelectric scanner to precisely move the sample in three dimensions, and an optical detection system that records cantilever deflections [1, 28] (Fig. 1.2 **A, B**). The most common detection scheme involves reflecting a laser beam off the back of the cantilever onto a position-sensitive photodiode [10, 29, 30]. As the tip interacts with the sample surface, the cantilever bends, producing a shift in the position of the reflected beam [16, 30] (Fig. 1.2 **A**). This optical lever method translates the minute bending of the cantilever into a measurable displacement of the laser spot on the detector, allowing the user to estimate cantilever deflection with sub-nanometer precision. Since cantilever bending is directly proportional to the force exerted at the tip-sample surface, this detection scheme enables quantitative force measurements with high sensitivity [31].

The working principle of the AFM relies on monitoring how laser deflections change as the probe approaches, contacts, or retracts from the sample. When operated in imaging modes, the piezoelectric scanner systematically moves the sample in the x–y plane while adjusting the z-axis position to maintain a constant interaction between tip and surface, thereby reconstructing topographic maps with nanometer resolution. In force spectroscopy modes, the approach and retraction of the cantilever relative to the sample provide force–distance curves that contain detailed information on tip–sample interactions. These interactions arise from a combination of physical and chemical forces, including van der Waals, electrostatic, capillary, steric, and hydration contributions in biological systems [12, 16, 32].

The magnitude of the interaction force is obtained using Hooke's law:

$$F = k \cdot \Delta z, \tag{1.1}$$

where F is the force, k is the spring constant of the cantilever, and Δz its deflection. This deceptively simple relationship underscores the central role of accurate cantilever calibration: even small uncertainties in k propagate into proportional errors in the derived force values [33]. For this reason, modern AFM systems pay

considerable attention to cantilever characterization and calibration protocols [15, 33, 34].

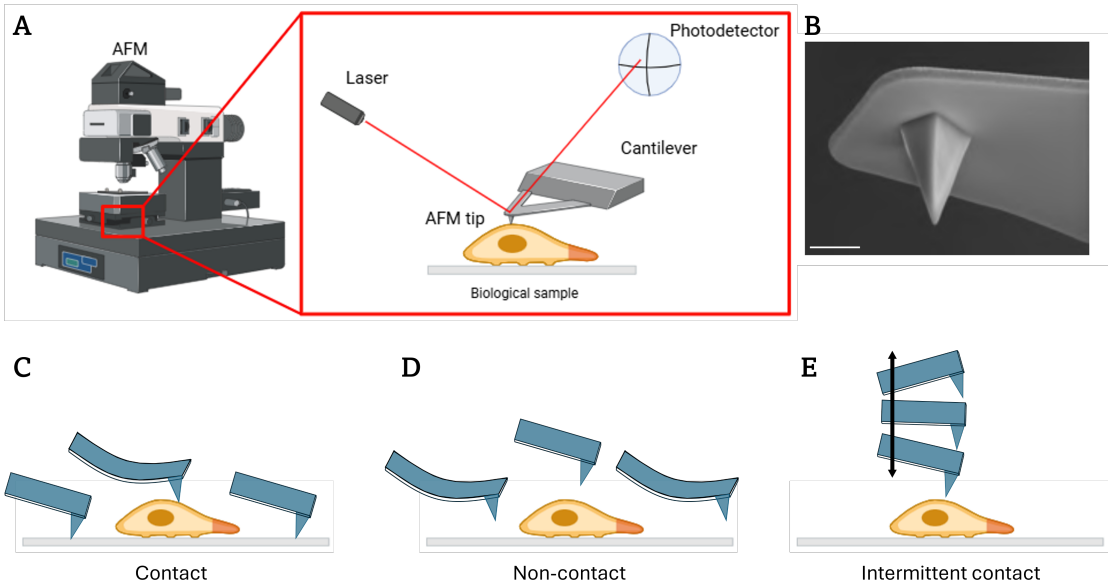

Figure 1.2: **Schematic representation of the AFM setup and imaging acquisition modes.** **(A)** AFM setup with focus on the AFM head, which contains the core components of the instrument. A laser beam is reflected from the back of the cantilever and detected by a quadrant photodiode, allowing measurement of cantilever deflection during tip–sample interactions. The displacement of the laser spot is converted into cantilever deflection, enabling quantitative calculation of the forces applied to the sample via equation (1.1). **(B)** Scanning electron microscopy image of a square-based pyramidal AFM tip mounted at the extremity of the cantilever (Image taken from [35], MLCT-BIO tip). Scale bar of 2 μm. **(C–E)** Schematic illustrations of the main AFM imaging modes: **(C)** contact mode, **(D)** non-contact mode, and **(E)** intermittent-contact (tapping) mode, each optimized for specific sample types and experimental conditions.

1.2.2 Acquisition modes for nanomechanical analysis

AFM is extraordinarily versatile because it can operate in multiple modes, each tailored to different types of information. The three main categories of operation are imaging, force spectroscopy, and microrheology [36].

1.2.2.1 Imaging modes.

Contact mode, the earliest AFM imaging method, involves maintaining continuous contact between tip and surface (Fig. 1.2 **C**). In this configuration, the vertical deflection of the cantilever is kept constant by a feedback loop that adjusts the z-position of the scanner as the tip traces the surface topography. Although this mode provides excellent spatial resolution and direct measurement of repulsive tip–sample forces, the continuous lateral drag exerted during scanning can deform or damage soft samples such as live cells or fragile biomaterials [7, 31]. To address these limitations, non-contact (Fig. 1.2 **D**) and intermittent-contact, or tapping, (Fig. 1.2 **E**) modes were subsequently developed [37, 38]. In non-contact mode, the cantilever is driven to oscillate close to its resonance frequency without the tip physically touching the surface. Weak long-range interactions, such as van der Waals or electrostatic forces, induce small shifts in oscillation amplitude, phase, or frequency, which are then used to reconstruct surface features [36]. This approach minimizes tip wear and sample damage, but is more sensitive to environmental factors, particularly contamination layers and hydration films, which can complicate stable operation in liquid environments [39]. Tapping mode was introduced as a compromise between the robustness of contact imaging and the softness of non-contact operation. Here, the cantilever oscillates with sufficient amplitude to intermittently touch the sample at the bottom of each cycle. The brief tip–sample interactions reduce destructive shear forces while still allowing high-resolution imaging of fine surface details [37]. Because of its ability to preserve biological integrity while maintaining image quality, tapping mode has become the most widely used AFM imaging method in life sciences. The introduction of these advanced modes transformed AFM into a versatile tool for biological research, making it possible to routinely image delicate structures such as live cells, viruses, and protein assemblies under cell culture conditions (Fig. 1.3 **A, B**) [40–45].

1.2.2.2 Force spectroscopy.

In force spectroscopy, the cantilever is repeatedly approached and retracted from the sample while recording force–distance curves that describe the interaction forces as a function of tip–sample separation (Fig. 1.3 **C**) [31]. These curves

contain distinct regions corresponding to the approach, contact, and retraction phases, from which different physical parameters can be extracted. By fitting the contact portion of the curve with appropriate mathematical models, such as the Hertz or Sneddon contact mechanics equations, it is possible to derive quantitative information including indentation depth, adhesion energy, molecular binding forces, and the elastic modulus, commonly expressed as Young's Modulus (YM), of cells and tissues (Fig. 1.3 **C, D**) [22, 46, 47]. Accurate extraction of these quantities requires careful calibration of cantilever mechanical-parameters and proper consideration of tip geometry, as both factors strongly influence the validity of the mechanical model applied [48, 49].

Beyond single-point measurements, force spectroscopy can be extended to spatially resolved acquisitions. By collecting force–distance curves over a grid of positions, AFM generates force–volume maps that provide nanoscale distributions of mechanical and adhesive properties across heterogeneous samples [50, 51] (Fig. 1.3 **A, B**). These maps integrate topographic and mechanical data, enabling researchers to correlate structural features with local variations in stiffness or adhesion. Such an approach is particularly powerful in fields like medicine, biology, and biophysics, where cellular and extracellular matrix mechanics are increasingly recognized as critical regulators of physiology and disease. Indeed, AFM-based detection of nanoscale mechanical alterations has been closely associated with processes such as malignant transformation, tumor progression, and metastatic potential [13, 45–47, 52, 53]

1.2.2.3 Microrheology.

More recently, AFM has been adapted to probe not only elastic but also time-dependent mechanical properties of biological materials by studying viscoelasticity. This is achieved either by applying oscillatory forces to the sample or by monitoring stress relaxation following a controlled indentation [54]. Unlike purely elastic measurements, which are limited to a single modulus, this microrheological approach yields both the storage modulus (G'), reflecting the elastic energy stored and recovered during deformation, and the loss modulus (G''), which quantifies viscous dissipation [55, 56]. Together, G' and G'' provide a comprehensive

description of how cells and tissues respond to dynamic mechanical loading and deformation [57, 58] (Fig. 1.3 **E, F**).

The typical experimental procedure involves first approaching the cantilever toward the sample until a predetermined setpoint corresponding to a maximum force is reached (Fig. 1.3 **E**). This ensures that the probe indents the specimen to a controlled depth. The cantilever position is then held constant during a relaxation phase, allowing the force exerted by the sample to decay over time as viscoelastic rearrangements occur. Following this pause, a small sinusoidal modulation is superimposed on the cantilever position (green section of the plot in Fig. 1.3 **E**). By analyzing the amplitude and phase shift of the resulting force oscillations with appropriate mathematical models, it becomes possible to extract quantitative information on the frequency-dependent viscoelastic properties of the sample (Fig. 1.3 **F**).

This type of analysis is particularly relevant for biological systems, where cells and tissues rarely behave as purely elastic materials [59]. Instead, they exhibit a complex interplay between solid-like and fluid-like responses that reflects the organization of the cytoskeleton, the turnover of molecular cross-links, and the properties of the extracellular matrix [59, 60]. Consequently, AFM-based microrheology has provided crucial insights into cytoskeletal remodeling, extracellular matrix elasticity, and mechanobiological processes underlying pathological conditions. Alterations in viscoelastic behavior, revealed through changes in G' and G'', have been linked to cancer progression, fibrotic diseases, and other disorders that profoundly affect tissue mechanics [46, 57, 60].

1.2.3 Types of AFM probes

The design of the AFM probe determines both the resolution of imaging and the accuracy of force measurements (Fig. 1.4 **A, B**). Sharp tips, often with radii below 10 nm, are indispensable for high-resolution imaging of surfaces and molecular structures [35, 61–63]. For quantitative mechanical characterization, however, sharp tips can be problematic because their small contact area complicates the use of continuum mechanics models [64]. To address this issue, spherical colloidal probes have been developed, in which a micrometer-sized bead is attached to the

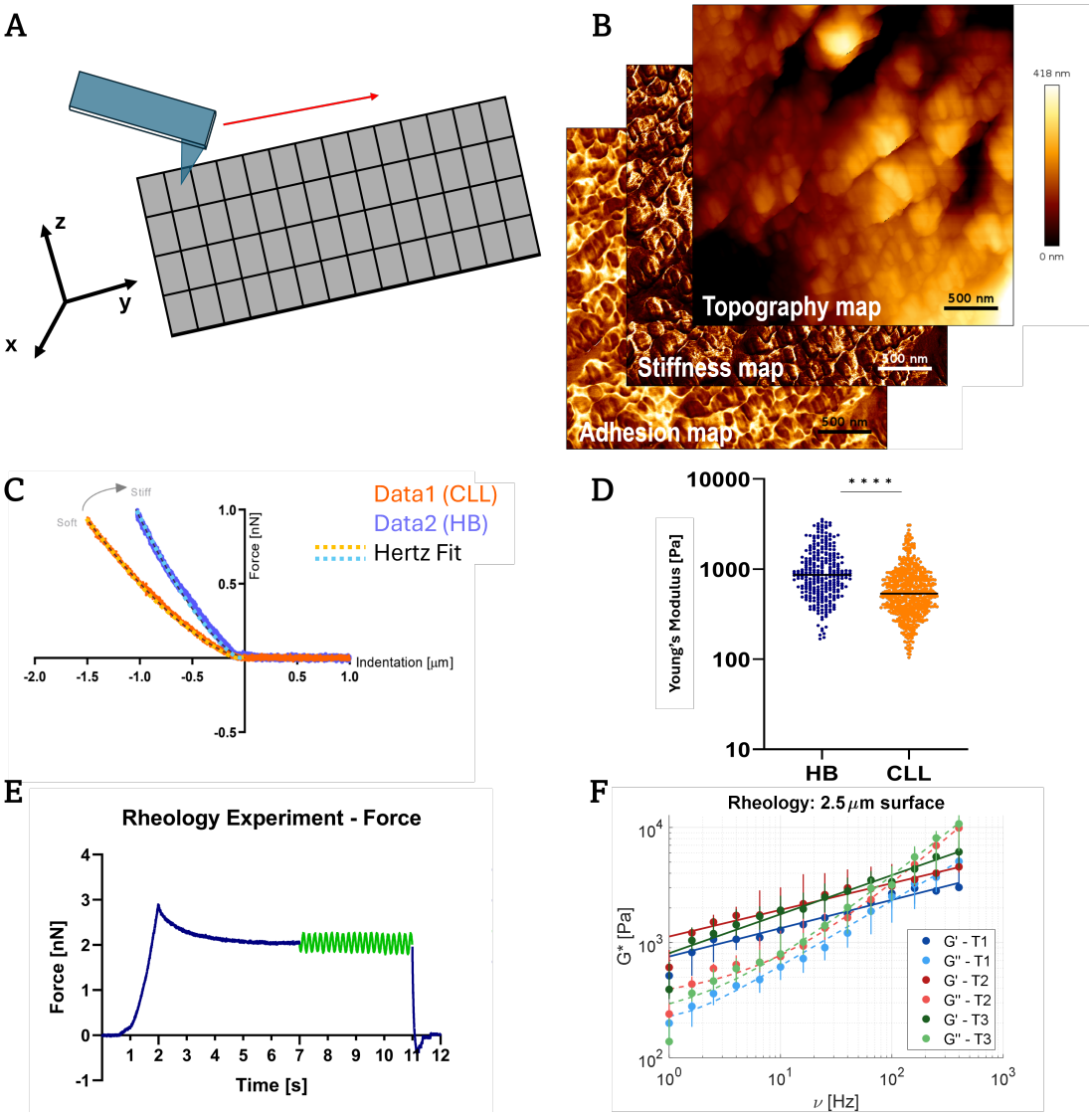

Figure 1.3: **Representation of the possible outputs obtainable from AFM measurements.** **(A, B)** Outputs from AFM imaging experiments performed in tapping mode. **(A)** Schematic representation of the imaging workflow: a grid of points is defined over the sample, and a force spectroscopy measurement is carried out at each position. By analyzing the resulting force curves, it is possible to obtain multiple types of information, including topographical maps, stiffness maps, and adhesion maps of the sample, shown in **(B)**.Images adapted from [45] **C, D** Outputs from force spectroscopy. **(C)** Example of force–distance curves acquired on different samples; the slope of the curves, fitted using appropriate mathematical models, allows the calculation of the YM shown in **(D)**. The steeper the slope of the curve, the higher the stiffness. Images adapted from [22]. **(E, F)** Outputs from microrheology experiments. **(E)** Representative force–time curve from a standard microrheology experiment. The applied sinusoidal modulation is reported in green. **(F)** Storage modulus G' and loss modulus G" as a function of frequency; colors represent datasets fitted with single (solid) or double (dashed) power laws.

cantilever [65] (Fig. 1.4 **A, B**). The well-defined geometry allows straightforward application of Hertzian or JKR contact mechanics, yielding more reliable modulus values for soft samples such as cells and hydrogels [35, 62, 63, 65–67].

Other geometries include cylindrical probes, which are used to simulate needle-like interactions, and wedged cantilevers [68, 69], which provide a flat surface for attaching functional objects such as living cells or to provide unaxially parallel confinement of the sample [67, 68]. The versatility of probe geometries ensures that AFM can be adapted to a wide variety of biological questions [35, 62, 63] (Fig. 1.4 **A, B**).

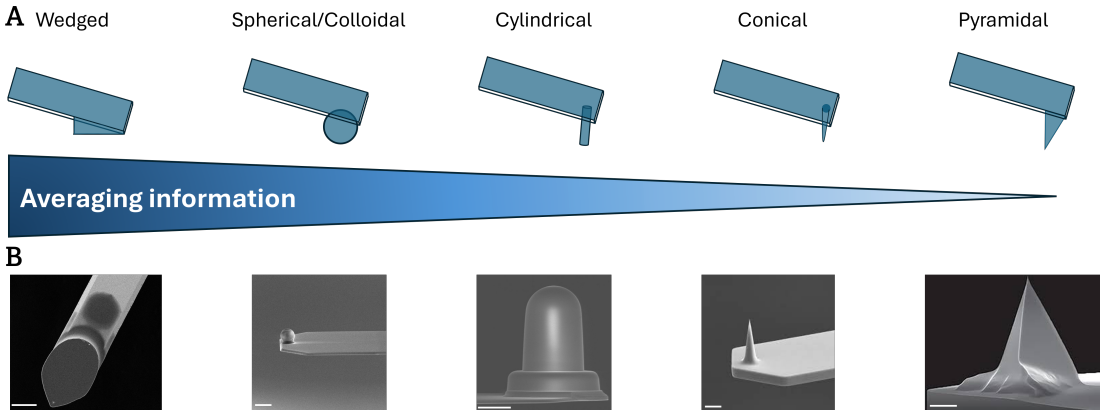

Figure 1.4: **Schematic representation of different AFM tip geometries used for measurements and thermal noise calibration. (A)** Tip geometry influences experimental outcomes: sharper tips provide higher resolution for imaging experiments, whereas larger tip geometries allow greater averaging and more reliable data in force spectroscopy and microrheology experiments. **(B)** SEM images of the different tip geometries: wedged [68], spherical [58], cylindrical [35], conical [62], and sharp [35]. All scale bars represent 5 μm, except for the wedged tip, which is 20 μm. The **(A)** was adapted from [26].

1.2.4 Thermal noise calibration

Accurate force measurement requires reliable determination of the cantilever spring constant [70, 71]. Among the available approaches, the thermal noise method is widely used because it is non-invasive, requires no additional instrumentation, and does not rely on external calibration standards [72, 73]. This procedure, however, begins with the determination of the deflection sensitivity (Fig. 1.4 **A, B, C**).

A force-distance curve is first acquired by pressing the cantilever against a rigid substrate, such as glass or plastic, to establish the proportionality factor between the photodiode signal (in Volts) and the actual cantilever deflection (in nanometers) [68, 72]. Typically, this calibration is performed on a standard glass slide under conditions mimicking the experimental environment, such as in cell culture medium and at controlled temperature, to ensure accurate sensitivity estimation. The slope of the linear contact region of the force–distance curve (Fig. 1.4 **A, B, C**) provides the deflection sensitivity, which is then used to convert the raw voltage signal from the optical lever system into true cantilever displacements [72].

Once the deflection sensitivity has been established, the thermal noise method can be applied. In this approach, the cantilever is treated as a mechanical oscillator undergoing spontaneous Brownian motion due to collisions with surrounding molecules in the fluid or air environment [72]. These thermally driven fluctuations can be described by the dynamics of a damped harmonic oscillator [74, 75]. According to the equipartition theorem, the thermal energy associated with each degree of freedom is related to the mean square deflection of the cantilever:

$$\frac{1}{2}k\langle \Delta z^2 \rangle = \frac{1}{2}k_B T, \tag{1.2}$$

where $\langle \Delta z^2 \rangle$ is the mean square deflection of the cantilever, k_B the Boltzmann constant, and T the absolute temperature. Experimentally, the deflection fluctuations are recorded through the optical lever system and converted into nanometers using the previously determined sensitivity factor. Their power spectral density (thermal noise spectrum) is then obtained by Fourier transformation of the time-dependent signal (Fig. 1.4 **D**) [73]. The thermal noise spectrum displays a characteristic Lorentzian peak at the cantilever fundamental resonance frequency, from which both the resonance frequency and quality factor can be extracted [76]. By fitting the experimental spectrum with the theoretical response of a damped harmonic oscillator, the spring constant k can be accurately calculated (Fig. 1.4 **D**) [72].

This two-step approach, first determining deflection sensitivity and subsequently analyzing thermal fluctuations, provides a direct and self-consistent calibration of AFM cantilevers. The powerfulness of this methods relies in the fact

that it is not dependent on the geometry of the cantilever, making possible to extend it to every probe available. Proper calibration is therefore indispensable, as inaccuracies in k proportionally affect all subsequent force spectroscopy measurements [49].

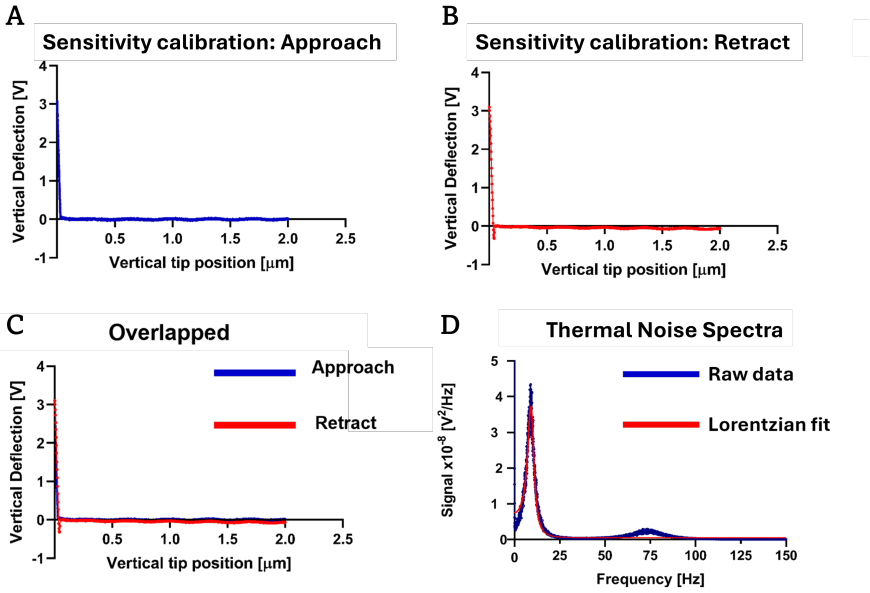

Figure 1.5: **Measurements of deflection sensitivity and and thermal noise calibration.(A, B)** Representative averaged force curves used to determine cantilever deflection sensitivity, showing approach (blue) and retract (red) traces. Linear fitting of the slope provides the sensitivity calibration. **(C)** Overlap of the previous two graphs: the better is the overlap of the two curves, the better is the deflection sensitivity determination. **(D)** Thermal noise spectra, showing raw data (blue) and Lorentzian fit (red). The fit is used to determine the cantilever spring constant via the specified equation (1.2).

1.3 The importance of cell stiffness as biomarker

Cellular stiffness represents a central biophysical parameter that mirrors the structural integrity and, mainly, organization of the cytoskeleton. This property emerges from the coordinated action of actin filaments, microtubules, and intermediate filaments, as well as their dynamic interactions with the extracellular matrix (ECM) [77]. Proper regulation of cell stiffness is indispensable for numerous physiological processes, such as embryonic development [78], immune cell migration [79], and

wound healing [80], where transient fluctuations in mechanical properties accompany tissue remodeling and morphogenetic events [81].

In recent years, the dysregulation of cell mechanics has been increasingly recognized as a hallmark of cancer progression, contributing to invasion, metastatic dissemination, and resistance to therapy [82–85]. A consistent observation across several tumor type, is that malignant cells often display reduced stiffness compared to nonmalignant counterparts when probed at the single-cell level [82]. This mechanical softening is particularly pronounced in highly metastatic cells, whose lower elastic modulus facilitates their migration through dense extracellular barriers and enhances their ability to intravasate into the circulation [86, 87]. Yet, an intriguing paradox emerges when tumor mechanics are examined on a macroscopic scale. For instance, breast tumors are frequently palpated as rigid masses during clinical examination due to a stiffened stromal and ECM environment, such as collagen cross-linking. In contrast, isolated breast cancer cells are often softer than healthy epithelial cells [88, 89]. This apparent contradiction underscores the need to distinguish between cell-intrinsic determinants of mechanics, such as cytoskeletal reorganization, altered adhesion complexes, and pathways controlling actomyosin contractility, and extrinsic influences from the surrounding microenvironment, including ECM composition, stiffness, and interactions with stromal cells.

Beyond oncology, stiffness measurements at the tissue level have proven valuable as diagnostic tools in diverse pathologies. Early disease detection has been enabled by quantifying mechanical alterations in organs such as the liver, where progressive stiffening serves as a biomarker for fibrosis [90], and in vascular tissue, where changes in arterial mechanics can indicate the onset of atherosclerosis [91, 92]. At the cellular scale, deviations in stiffness similarly provide insight into disease progression. In fibrotic disorders, for example, myofibroblasts in idiopathic pulmonary fibrosis become markedly stiffer due to excessive ECM deposition and cytoskeletal remodeling [93]. This coupling of cytoskeletal changes with aberrant ECM production highlights the pathological consequences of increased stiffness and positions cell mechanics as a defining feature not only of cancer but also of non-malignant diseases.

Finally, in the fields of regenerative medicine and tissue engineering, mechani-

cal phenotyping of cells has emerged as a predictive tool for guiding differentiation outcomes. Stiffness signatures of progenitor cells often correlate with lineage commitment, distinguishing, for instance, osteogenic from adipogenic fates [94, 95]. Collectively, these findings demonstrate that cell stiffness serves as a critical readout for understanding basic cell biology and as a translational lever for applications spanning diagnostics, drug development, personalized medicine, and tissue regeneration strategies.

1.4 Cell viscoelasticity

Cellular stiffness, or elasticity, alone cannot capture the complexity of cellular mechanics, as living cells also display time-dependent, viscous responses. In particular, mammalian cells behave as heterogeneous viscoelastic systems whose mechanical properties vary with frequency, since the relaxation of distinct structural components occurs across multiple timescales [96]. Beyond the cytoskeletal and intermediate filament contributions to cellular mechanics, viscoelasticity reflects the ability of cells to deform, recover, and dissipate stress under dynamic environments. This dual capacity enables cells to adapt to complex microenvironments during tissue morphogenesis, repair, and migration [97].

The viscoelastic response arises from the interplay of different cytoskeletal networks and their associated regulators. At short timescales, in the millisecond range, the actin cytoskeleton and its cross-linking proteins dominate the elastic component, providing resistance to deformation [60, 98]. At longer timescales, processes involving the cytoplasm and microtubule organization become more relevant, as they govern relaxation and the ability of cells to withstand larger compressive loads [99, 100]. Through this integration of structural and temporal elements, cells achieve remarkable mechanical adaptability that is critical for diverse biological functions.

This adaptability is particularly evident in dynamic physiological contexts. For instance, metastatic cancer cells exploit enhanced viscous behavior, driven by cytoskeletal remodeling, to navigate confined environments and invade tissues [101, 102]. During wound repair, cells transiently stiffen and stabilize their cytoskeleton to interact with the newly deposited extracellular matrix [103]. Conversely, in

developmental processes, local softening or fluidization permits large-scale tissue remodeling [104, 105]. Such examples highlight how the fine balance between elasticity and viscosity shapes cell behavior, allowing them to sense and respond appropriately to external mechanical cues.

Understanding cell viscoelasticity is thus essential not only for explaining how cells preserve integrity and reorganize under stress but also for advancing biomedical applications. Engineered scaffolds that replicate native viscoelastic properties can promote appropriate cellular responses [106, 107]. Moreover, alterations in viscoelastic parameters are increasingly recognized as hallmarks of disease. Malignant cells, for example, display characteristic stiffness and relaxation profiles that favor tumor progression and dissemination [108]. Consequently, dissecting viscoelastic behavior provides both fundamental insight into cell mechanics and translational opportunities in regenerative medicine, biomaterial design, and cancer diagnostics.

1.5 AFM limits and advanced applications

Despite its power, AFM faces challenges. One major limitation arises when probing small, soft, and weakly adherent cells, such as lymphocytes or round cells, like many stem cells [69]. Under conventional, and commercially available, tip geometries, indentation experiments often induce lateral forces that cause the cell to slide instead of deforming, leading to unreliable data [68, 69, 109]. This specific phenomenon is mainly due to the cantilever tilt angle with respect the microfabricated chip to which is mounted on.

To address this, specialized probe designs have been developed. Wedged probes, which provide a flat surface, enable parallel plate compression of cells [68, 69]. This geometry minimizes sliding and ensures uniform stress distribution. The resulting technique, known as uniaxial parallel plate force spectroscopy, has proven highly effective for round, weakly adherent cells [68, 69].

Another innovation is the stepwise confinement experiment, in which a cell is progressively compressed in discrete steps (Fig. 1.6 **A**) while recording its mechanical response (Fig. 1.6 **B**) [110]. Stepwise confinement mimics physiological scenarios such as passage through narrow tissue spaces, providing valuable insights into cell behavior under mechanical stress [111]. This method reveals nonlinear-

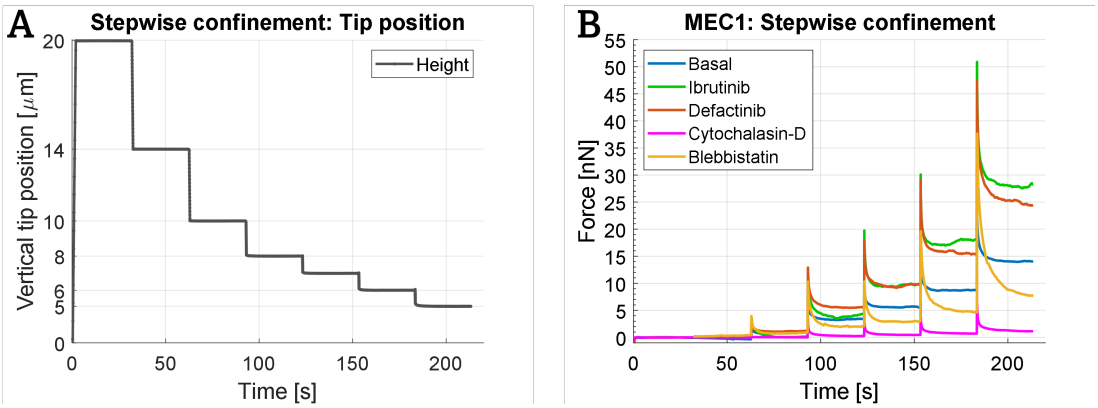

Figure 1.6: (**A**) Representative plot of the vertical position (height) of the AFM wedged tip during a stepwise confinement experiment, showing six sequential compression steps applied to a single cell. (**B**) Representative force spectra showing the mechanical responses of MEC1 cells, a standard leukemic cell lines used for studying human-B leukemia, under different pharmacological treatments corresponding to the AFM-tip trajectory shown in panel (**A**). Each trace reflects the cell force response profile under sequential compression, with color-coded lines indicating specific drug conditions as detailed in the legend. Both figures were adapted from [110]

ities, adaptive cytoskeletal changes, and time-dependent remodeling that cannot be captured by single indentations [112]. In the work presented in this thesis, stepwise confinement experiments were carried out as follow: initially, the AFM tip was retracted from the bottom of the plate until a height of 20 μm above the surface was reached, with a retraction velocity of 10 μm/s and an acquisition frequency of 2048 Hz. Subsequently, six confinement steps were applied sequentially, with step sizes of 6, 4, 2, 1, 1, and 1 μm, respectively (Fig. 1.6 **A**). The approach velocity for each step was set to 10 μm/s. After each confinement step, the tip position (height) was kept constant for 30 seconds, allowing the force to evolve freely as the cell underwent relaxation (Fig. 1.6 **A, B**). During the lowering steps of the AFM tip and the confinement phases, the acquisition frequency was set at 4096 Hz. A z-closed loop control was maintained throughout the experiment. At the end of the sixth confinement step, the tip was retracted from the cell until it reached a height of 50 μm above the bottom of the Petri dish. [110]

Together, these advanced applications demonstrate the adaptability of AFM and highlight the importance of continuous methodological innovation. While lim-

itations remain, the ongoing development of novel probes, hybrid setups, and computational tools ensures that AFM will remain central to nanomechanical studies in biology and medicine.

1.6 Viscoelastic characterization beyond AFM: pros and cons of alternative techniques

Beyond AFM, several complementary techniques are routinely employed to probe the viscoelastic properties of soft matter and biological systems, each offering specific advantages depending on the scale and application of interest. Bulk rheometry provides robust and standardized measurements of viscoelastic moduli over a wide range of frequencies and deformations, making it particularly suitable for characterizing hydrogels, biofluids, and tissue-mimicking materials [113, 114]. However, its macroscopic nature limits spatial resolution and precludes the investigation of local mechanical heterogeneities that are often critical in biological tissues [113].

On the other hand, optical tweezers enable highly precise force application and fast temporal probing at the single-particle or molecular level, offering exceptional sensitivity for studying intracellular mechanics and dynamic responses, yet they are constrained by limited force ranges, optical accessibility, and the need for transparent samples or exogenous probes [115, 116].

Lastly, acoustic and ultrasound-based imaging techniques, including elastography, offer the significant advantage of non-invasive, real-time mechanical mapping over large tissue volumes and are already integrated into clinical workflows [117, 118]. Nevertheless, their spatial resolution remains orders of magnitude lower than that of AFM, restricting their ability to resolve nanoscale mechanical features.

In this landscape, AFM occupies a unique position by combining high spatial resolution, quantitative force control, and applicability to living cells and tissues, while remaining complementary rather than competitive with these established methodologies.

1.7 Aim of the thesis

The aim of this PhD thesis is to exploit the versatility of Atomic Force Microscopy as a quantitative and multiparametric instrument for exploring the mechanical properties of biological systems at nanoscale level, with the ultimate goal of correlating biophysical parameters with physiological or pathological cellular states. By integrating physics and biomedicine, this work aims to consolidate AFM as a bridge between nanomechanics and translational medicine, capable of providing mechanical biomarkers that reflect and characterize disease progression and/or therapeutic response. To this scope, AFM was employed in its various operational modes (imaging, force spectroscopy, and microrheology) to obtain complementary information on topography, elasticity, adhesion, and viscoelasticity of living cells and tissues under cell culture conditions. Moreover, a substantial methodological effort was dedicated to optimizing AFM-based mechanical protocols for soft and not-adherent biological samples, like round cells. In particular, the development and implementation of wedged-cantilever and stepwise confinement approaches addressed key experimental limitations, enabling uniaxial compression and dynamic analysis of single cell mechanical responses. Through this combination of methodological innovation and biological application, the thesis aims to advance AFM from a descriptive tool to a standardized and translational method for nanomechanical phenotyping in biomedicine.

Part II

Paper collection

Collection of Papers:

1. #Bracchi, M., **Campanile, R.**, Crippa, M., Mauri, M., Cassina, V., Mantegazza, F., Nicotra, F., Waldner, J., Zatti, G., Bigoni, M., #Turati, M., #Russo, L. (2025). ***Meniscal Extracellular Matrix Remodeling Caused by Injuries and Degeneration.*** *Engineering.* (Status: Addressing referees' comments).

2. #Pellegrino L., Savorana, G., Valeria, C., **Campanile, R.**, Centola, M., Belgiovine, C., Vinci, V., Klinger, M., D'Imprima, E., Mantegazza, F., Secchi, E., #Rusconi, R. (2025). ***Reduction of bacterial colonization on buckling-induced wrinkled surfaces under fluid shear.*** *Nature Communication.* DOI Link. (Status: Published).

3. #Sampietro, M., Cassina, V., Salerno, D., Barbaglio, F., Buglione, E., Marrano, C. A., **Campanile, R.**, Scarfò, L., Biedenweg, D., Fregin, B., Zamai, M., Díaz Torres, A., Labrador Cantarero, V., Ghia, P., Otto, O., Mantegazza, F., #Caiolfa, V., #Scielzo, C. (2023). ***The Nanomechanical Properties of CLL Cells Are Linked to the Actin Cytoskeleton and Are a Potential Target of BTK Inhibitors.*** *HemaSphere*, 7(8):p e931. DOI link. (Status: Published).

4. #Brevi, A., #Lorenzoni, M., Caputo, S., Yamada, Y., Grioni, M., Cogrossi, L., Vidal, L. M., Cassina, V., Cipria, D., Venegoni, C., Zordan, P., Matafora, V., Tascini, A. S., Tenace, N. P., **Campanile, R.**, Cucchiara, V., Pinna, V., Jachetti, E., Galli, R., Bachi, A., Colecchia, M., Briganti, A., Freschi, M., Mantegazza, F., Lombardo, A., Demichelis, F., Beltran, H., #Alfano, M., #Bellone, M. (2025). ***Intercepting Yes-associated protein 1 in prostate cancer blocks neuroendocrine progression.*** *Cancer Research.* (Status: Addressing Referees' Comments).

5. #Piazzoni, M., Borghi, I., Cadamuro, F., Dalfino, S., **Campanile, R.**, Nizzolo, S., Cassina, V., Tallia, F. J., Jones, J. R., Mantegazza, F., Bertini, S., Moroni, L., #Nicotra, F., #Russo, L. (2025). ***Endothelial cells angiogenesis in sulfated glycosaminoglycan (GAG) hydrogels enhanced***

by bioactive glass released ions. *Advanced Functional Materials*. DOI Link. (Status: Published).

6. #**Campanile, R.**, Helenius J., Scielzo, C., Scarfò, L., Salerno, D., Bossi, M., Falappi, M., Saponara, A., Müller, D. J., Mantegazza F., #Cassina, V. (2025). ***Production of AFM wedged cantilevers for stress-relaxation experiments: Uniaxial loading of soft, spherical cells.*** *Methods*, 236: 1-9. DOI Link. (Status: Published)

7. #**Campanile, R.**, Helenius, J., Scielzo, C., Salerno, D., Müller, D. J., Mantegazza, F., #Cassina, V. (2026). ***Stepwise Confinement Unveils HS1 Contribution to the Mechanical Phenotype of CLL Cells.*** (Status: Work in Progress, Ready to Be Submitted).

Meniscal extracellular matrix remodelling caused by injuries and degeneration

Maddalena Bracchi[1], Riccardo Campanile[1], Marco Crippa[1-3], Mario Mauri[1], Valeria Cassina[1], Francesco Mantegazza[1], Francesco Nicotra[1], Judith Waldner[1,2], Giovanni Zatti [1,2] , Marco Bigoni[1,3-4], Marco Turati[1-3]*, Laura Russo[1,2]*

[1]School of Medicine and Surgery, Università degli Studi di Milano-Bicocca, Monza, Italy

[2] Orthopedic Department, Fondazione IRCCS San Gerardo dei Tintori, Monza, Italy

[3] Transalpine Center of Pediatric Sports Medicine and Surgery, University of Milano-Bicocca - Hospital Couple Enfant, Monza (Italy), Grenoble, France

[4] Department of Orthopedic Surgery, Policlinico San Pietro, Ponte San Pietro, Italy

Keywords

Meniscus, ECM, collagen, GAGs, knee

Abstract

The characterization of meniscal extracellular matrix (ECM) is fundamental for tissue engineering to design a functional substitute. However, most of the available data come from animal studies. The meniscus has a complex ECM, characterized by a specific orientation of collagen fibres related to its function. In this work, both paediatric and adult meniscal tissues were examined from morphological, biochemical and mechanical perspectives to identify the characteristics of physiological tissue and changes caused by injuries and degeneration. Additionally, a comparison was performed between menisci from patients with normal and valgus knees to observe the ECM remodelling due to biomechanics changes. The obtained results were then compared to data available in literature to identify similarities and differences between humans with various ages and animals.

Introduction

The extracellular matrix (ECM) is a non-cellular complex polymer network that mirrors the biochemical and mechanical properties of a tissue and undergoes continuous remodelling, especially during pathological conditions [1]. In tissue engineering, a meniscal scaffold should mimic the biomolecular features and composition of the native tissue to achieve a functional substitute. Therefore, the characterization of physiological and pathological meniscal tissue is fundamental to correctly determine the biochemical and mechanical changes during ECM remodelling, which is crucial for designing an effective replacement for regenerative medicine applications [2], [3].

Meniscal tears are among the most common intra- articular injuries of the knee and can lead to significant pain and functional impairment [4]. The medial and lateral menisci are fibrocartilaginous structures located within the knee joint, between the femoral condyles and the tibial plateau. Their primary functions include load distribution, facilitation of joint rotation, and stabilization of translational movements [5]. By increasing the contact surface area between the femur and tibia, the menisci play a crucial role in evenly distributing the load transmitted from the femur, thereby reducing stress on the articular cartilage [6]. These mechanical properties are given by their cellular, biochemical and structural composition [7]: their extracellular matrix (ECM) is highly hydrated (70-80% water); in the remaining portion, collagen (50-75%), which is responsible of tensile strength, glycosaminoglycans (GAGs, 15-30%), DNA (2%), adhesion glycoproteins (<1%) and elastin (<1%) are found [8], [9]. These data might vary depending on age, injuries and other pathological conditions [10], [11], but only limited data are available on human tissues due to the fact that most of the knowledge on menisci comes from animal experiments [11]. The distribution of collagen fibers in the meniscus is highly anisotropic, and three distinct layers can be distinguished: a superficial fibril network which covers femur and tibia articulating surfaces, a lamellar layer radially oriented and a central zone with circumferential fibres [12], [13]. Taking the triangular-shaped cross section of the meniscus, three zones can be distinguished from the outside to the inside:

- Red-Red zone (R-R): vascularized, mainly type I collagen, higher mechanical properties and with fibroblast-like cells;
- Red-White zone (R-W): partially vascularized, with intermediate properties;
- White-White zone (W-W): non- vascularized (nutrition depends on synovial fluid diffusion), mainly type II collagen, smoother and with chondrocyte-like cells [5], [14].

From the biomechanical point of view, human and animal meniscal tissues have been characterized in several studies. The ovine model is considered the most similar to human tissue in terms of stiffness, compression and residual force, but also vascularity and collagen structure [15], [16] . However, Sweigart et al. compared the biomechanical properties of canine, bovine, baboon, porcine, lapine and human menisci, and concluded that animal models are not entirely representative of human meniscus [17]. Histological studies were also performed on human and animal menisci to determine the ECM composition (Table 1). Notably, Sandmann et al. emphasized that no animal model fully replicates the histological and structural characteristics of the human [16].

Table 1 Histological studies found in literature on human and animal meniscal ECM

Meniscal tissue	**Masson Trichrome**	**Alcian Blue**	**Safranin - Fast Green**	**Van Gieson Trichrome**	**Haematoxilin - Eosin**	**References**
Human		x	x		x	[11], [15], [16], [18]
Bovine	x		x		x	[16], [19]
Ovine			x		x	[15], [16]
Pig	x	x	x		x	[16], [20]
Horse		x	x	x	x	[21]

Rabbit			x		x	[15], [22]

Meniscal tissue has a very limited healing capacity due to its poor vascularization. Despite this, injuries are quite common and can be classified as either traumatic or degenerative. Traumatic lesions occur in patients with previously healthy joints when excessive forces are applied to the articulation; in contrast, degenerative lesions are frequently associated with aging and the presence or onset of osteoarthritic disease [23], [24]. During the degenerative process of the knee, macroscopic and microscopic variations in the ECM can be observed [7]. Understanding these changes is crucial for the development of meniscal substitutes in regenerative medicine, where the physiological characteristics of native tissue must be mimicked. In this study, histological, morphological and biomechanical properties of menisci from paediatric and adult patients with different pathologies were investigated to discover the variations between physiological and pathological tissues. Additionally, a comparison was made between normal and valgus knees to evaluate differences in the behaviour of medial and lateral menisci.

Materials and methods

Samples collection

Human menisci were obtained from patients undergoing arthroscopic meniscectomy, occasionally in conjunction with Anterior Cruciate Ligament reconstruction, or total knee arthroplasty at the Orthopaedic and Traumatology Unit of IRCCS San Gerardo dei Tintori Hospital, Monza. The material collected was discarded tissue, which would have been disposed of at the end of the surgical procedures. Arthroscopic en bloc meniscectomy technique was performed only in patients with a significant traumatic meniscal lesion (e.g., peripheric bucket- handle tears) who refused to be treated with meniscal repair for personal and specific reasons (e.g., impossibility to follow an adequate follow-up and rehabilitation protocol). All patients were informed about the study protocol and provided written informed consent for the use of their tissue samples.

Inclusion criteria:

- Paediatric or adult patients with meniscal injuries treated with arthroscopic meniscectomy surgery (performed using the en bloc technique).
- Paediatric or adult patients with anterior cruciate ligament injury requiring reconstructive surgery and concomitant meniscal injury necessitating meniscectomy
- Adult patients with severe gonarthrosis requiring total knee arthroplasty surgery

Exclusion criteria:

- Meniscal tears treated by arthroscopic meniscectomy using shavers instead of the en bloc technique.
- Small meniscal tears where obtaining an adequate sample for analysis was not possible.
- Meniscal lesions where it was not possible to definitively determine the originating portion of the meniscus.
- Presence of arthritis or chronic inflammatory diseases.
- History of intra-articular drug injections.

After removal, the meniscal pieces were immediately placed in sterile tubes containing 10 mL of 0.9% NaCl physiological solution, stored in a container with ice and transferred to the laboratory. There, the samples were washed twice with 0.9% NaCl physiological solution and then stored at -80°C until further use.

Histological analysis

Samples stored at -80°C were gradually defrosted by transferring them to -20°C [25]; after 24 h, they were washed with 0.9% NaCl physiological solution, fixed in 10% formalin for 1 hour and washed twice more with 0.9% NaCl physiological solution. The meniscal pieces were then embedded in tissue freezing medium, frozen for 1 hour and sectioned with a cryostat (Leica CM 1520, Cornegliano Laudense, Lodi, Italy) to obtain 5 μm thick coronal sections.

The slices were mounted on microscope slides (VWR® SuperFrost® Plus, Milano, Italy) and stained with Haematoxylin-Eosin (Bio-Optica, Milano, Italy) and Van Gieson (Bio-Optica, Milano, Italy) to evaluate the cell distribution and to have a general overview of tissue organization, Masson's trichrome (Bio-Optica, Milano, Italy) to observe the collagen content and distribution, Alcian blue pH 2.5 (Bio-Optica, Milano, Italy) for the proteoglycans distribution and mucoid degeneration and Safranin – Fast green (Thermo Scientific) to highlight the accumulation of acidophil molecular complexes (proteoglycans and glycosaminoglycans). In Table 2 the characteristics of each stain and the corresponding ECM colours observed after staining are summarized.

Table 2 Summary of stain characteristics and resulting ECM colours according to manufacturer datasheets

Staining	**Stained ECM components**	**Colours**
Haematoxylin-Eosin	Cytoplasm, collagen, ECM Nuclei	Red Blue
Van Gieson	Collagen fibres Nuclei	Red Black
Masson's trichrome	Collagen Cytoplasm	Blue Red
Alcian blue pH 2.5	Acidic GAGs Mucins	Blue Purple
Safranin – Fast green	Proteoglycans, cartilage Ligamentous tissue, ECM	Red Green

The slides were then observed at 10X magnification to compare different patients and 20X magnification to see the differences between Red-Red and White-White zones with an inverted microscope (Zeiss Axio Observer / Cell Observer) and analysed with Zeiss Zen lite. The staining

quantification was performed using Fiji ImageJ with the colour deconvolution plugin, and the percentage of each coloration was determined using Equation 1.

$$Stain\ percentage = \frac{Pixels_{stain}}{Total\ Pixels_{sample}} * 100$$

Equation 1 formula used for stains quantification, where $Pixels_{stain}$ represents the number of the pixels coloured with the respective stain, and Total $Pixels_{sample}$ corresponds to the number of pixels in the meniscal sample before colour deconvolution.

For Masson Trichrome, Alcian Blue pH 2.5, and Haematoxylin-Eosin, pre-inserted vectors were utilized for quantification. However, for Safranin-Fast green and Van Gieson, values were extracted from the regions of interest (ROI) in the images and kept consistent for each stain. A 100% stacked column graph was then generated for each staining using Origin(Pro), Version 2022 (OriginLab Corporation, Northampton, MA, USA).

Scanning electron microscopy (SEM)

The morphology of paediatric and adult meniscal tissue was observed with SEM analysis. The collected meniscal tissue was washed three times with demineralized water, frozen at -80°C for 48 hours and freeze-dried with Vacuum Freeze Dryer (Boyikang Laboratory Instruments Inc, Beijing, China) for 24 hours at T = -50°C and pressure below 15 Pa. Then, they were put on aluminium supports and covered with a gold coating to make them conductive.

Finally, samples were observed with SEM (Zeiss Gemini 500 GrbH scanning electron microscope, Jena, Germany) at 300X and 1000X magnifications and the collected images were analysed with an image analysis software (Fiji ImageJ). A comparison between the Red-Red zone and White-White zone from paediatric and adult patients was performed.

Quantitative imaging (QI) mode AFM measurements

The nanoscale surface morphology and mechanical properties of dried meniscal tissue were evaluated using Quantitative Imaging (QI) mode on a NanoWizard 4XP Atomic Force Microscope (AFM, JPK Instruments, Bruker). In this mode, a complete force–distance curve is recorded at each pixel, allowing for high-resolution mapping of both topography and mechanical characteristics (Young's Modulus, YM) while minimizing lateral forces during scanning.

Sample slices were prepared as previously described; however, in this case, 30 µm-thick coronal sections were obtained. These sections were rinsed with deionized water to remove residual debris and then left to air dry at room temperature. Once fully dried, they were mounted on the AFM stage for analysis. Measurements were carried out in air using a RTESP (Bruker, AFM probes) cantilever with a nominal spring constant of 30 N/m. Nevertheless, the spring constant was estimated by contact-free calibration methods before each experiment [26], [27]. Indentation was performed with a maximum applied force of 60 nN and the approach/retract velocity was set to 120 µm/s.

Force–distance curves were acquired across a scanned area of 2.5x2.5 μm^2 with 512x512 points and they were used to extract quantitative tissue stiffness by fitting them with Hertz-Sneddon model [28].

The Mann–Whitney test, a non-parametric test for independent samples, was used to compare differences between two groups. This test does not assume normal distribution and is appropriate for ordinal or non-normally distributed continuous data. All analyses were performed using GraphPad Prism (GraphPad Software, San Diego, CA, USA). Statistical significance was defined as $p < 0.05$.

Compression test

The global mechanical properties of meniscal tissue were evaluated by compression test using a Texture Analyzer (Stable Micro Systems, Godalming, United Kingdom) equipped with a 2 mm cylindrical probe. Meniscal cross-sections, 2.5 mm thick, were prepared with a scalpel and hydrated in PBS pH 7.4 at room temperature for 3 h. Compression was performed until 40% deformation with pre- and post-test speeds of 10 mm/min, a test speed of 0.5 mm/min, and a trigger force of 0.05 N. Stress–strain curves were obtained in triplicate for each sample, and R–R and W–W zones were

analysed to calculate YM. Statistical analysis was conducted in OriginPro 2022b using one-way ANOVA, followed by Tukey's post-hoc test for multiple comparisons, with $p < 0.05$ considered statistically significant.

Results

Samples collection

A total of eight patients were included in this study: two of them belong to the paediatric group (age < 18 years), the other six to the adult group (age ≥ 18 years). The mean age in the paediatric group was 14.5 ± 0.5 years and 65.2 ± 14.2 years in the adult group; the characteristics of the population examined in this study are shown in the table below.

Table 3 Index of patients used for meniscal tissue characterization, ACL indicates Anterior Cruciate Ligament, TKA indicates Total Knee Arthroplasty

Patient	Age	Sex	Knee	Portion	Alignment	Intraoperative findings
P1	14	Male	Left	Lateral	Normal	Traumatic lateral meniscal tear associated with a complete ACL tear
P2	15	Male	Left	Medial	Normal	Isolated traumatic medial meniscal tear
P3	25	Male	Left	Lateral	Normal	Traumatic lateral meniscal tear associated with a complete ACL tear
P4	48	Female	Right	Medial	Normal	Isolated traumatic meniscal injury

P5	77	Female	Right	Lateral	Normal	Macroscopic good quality of lateral meniscus in patient treated with TKA for osteoarthritis
P6	82	Female	Left	Medial + Lateral	Valgus	Macroscopic good quality of lateral and medial meniscus in patient treated with TKA for osteoarthritis
P7	56	Female	Right	Medial + Lateral	Valgus	Macroscopic good quality of medial and lateral meniscus in patient treated with TKA for osteoarthritis. in a valgus knee
P8	63	Female	Left	Medial + Lateral	Normal	Macroscopic good quality of medial and lateral meniscus in patient treated with TKA for osteoarthritis

Histological analysis

The results of histological analysis on meniscal tissue of patients are shown in Figure 1. Due to the high heterogeneity of meniscal tissue, the central region of the meniscus was selected for characterization. In the first column, Masson's Trichrome staining highlighted a ligament-like outer zone, predominantly composed of collagen fibers, which appear blue. In contrast, the inner zone exhibited a more cartilage-like structure, rich in negatively charged proteoglycans, stained red with Safranin-Fast Green (second column, Figure 1). GAGs were uniformly distributed throughout the

section, appearing blue with Alcian Blue (third column). Overall, cellularity was low: elongated fibroblast-like cells were observed in the R-R zone, whereas rounded chondrocyte-like cells became more frequent toward the W-W zone, with the outer region showing slightly higher cell density. Cellularity was visualized using Haematoxylin-Eosin and Van Gieson stains, presented in the fourth and fifth columns, respectively.

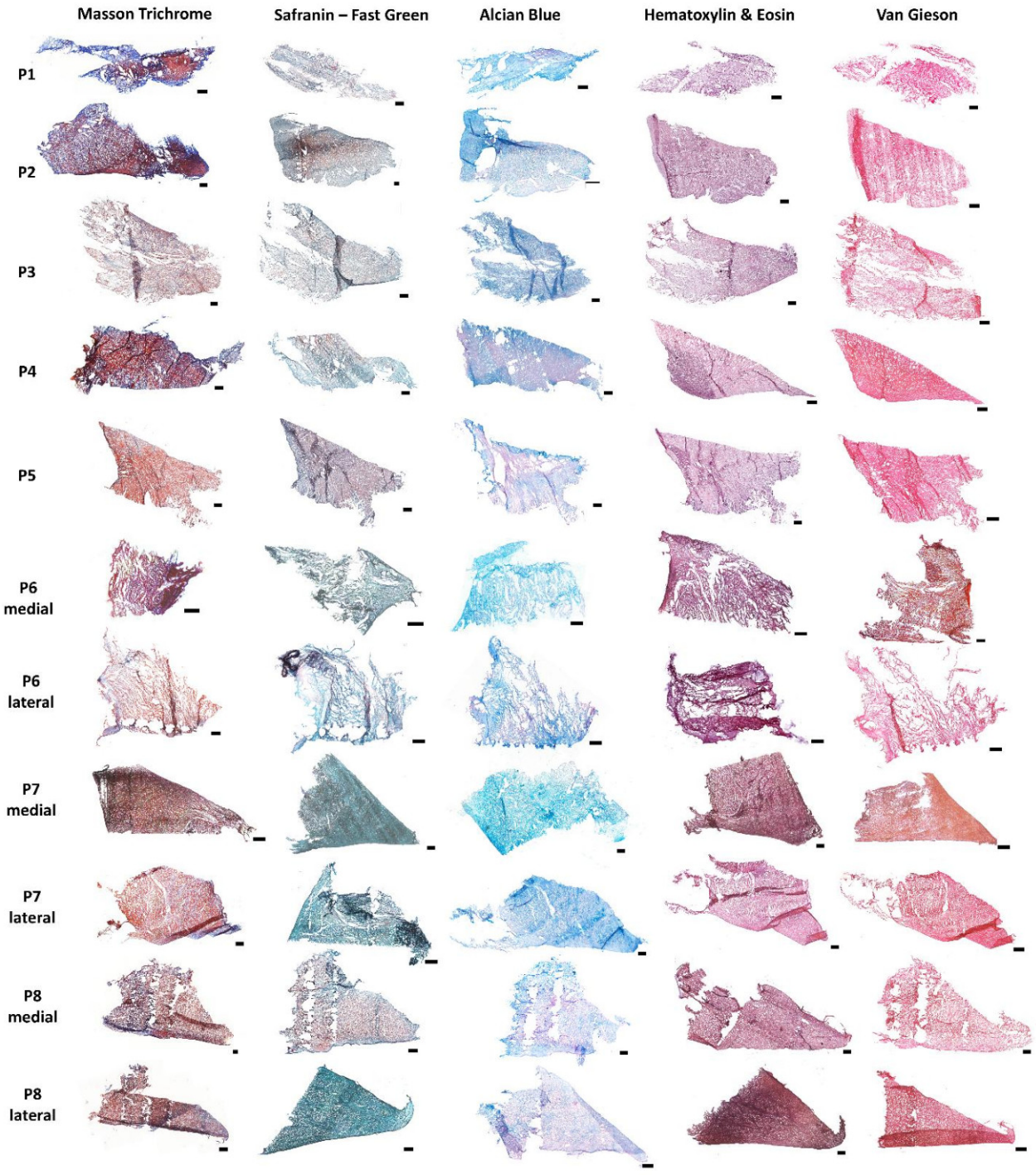

Figure 1 Histological characterization performed on 5µm slices of meniscal tissue from P1-P8 patients, 10X magnification, scale bar: 500µm

In Figure 2, stain percentages and respective percentage stacked column graphs are pictured. These percentages were calculated using the colour deconvolution function on stained images. In Masson's trichrome, the red stain represents the cytoplasm of cells, while the blue stain indicates collagen

content (Figure 2A). Higher collagen percentages were observed in P1, P2, and P4, with values of 64%, 60%, and 60%, respectively, whereas the lowest levels were found in P5 and P7 lateral (26% and 24%). In Safranin–Fast Green, purple indicates proteoglycan content, and green represents the fibrous ECM (Figure 2B). Proteoglycans were more abundant in P2 and P5 (50% and 70%), although their percentage was reduced in P4, P6 lateral, P7 lateral and P8 lateral, with values of 27%, 23%, 28% and 26%, respectively. In Alcian Blue, blue denotes GAGs content, while purple highlights mucins (Figure 2C). In this case, GAGs were more present in P1, P2, P6 medial, P6 lateral and P7 lateral (93%, 79%, 84%, 80% and 79%), although in P4 and P5 mucins were more abundant (64% and 67%). In Haematoxylin–Eosin, blue marks the cell nuclei, red represents both the cytoplasm and protein structures (Figure 2D). All patients exhibited low cellularity, with values ranging from 10% to 17%. Lastly, in Van Gieson, black indicates cell nuclei, while red marks the cytoplasm and fibres (Figure 2E). Similarly, the presence of cell nuclei was reduced, with values ranging from 2% to 14%. Greater variability was observed in this case, with the lowest values in P5 and P7 medial, and the highest in P2. At this point, two comparisons were performed: P1-P5 samples were used to compare

physiological-paediatric and pathological-adult tissues, P6-P8 to investigate the differences between medial and lateral menisci in conditions of normal and valgus knee.

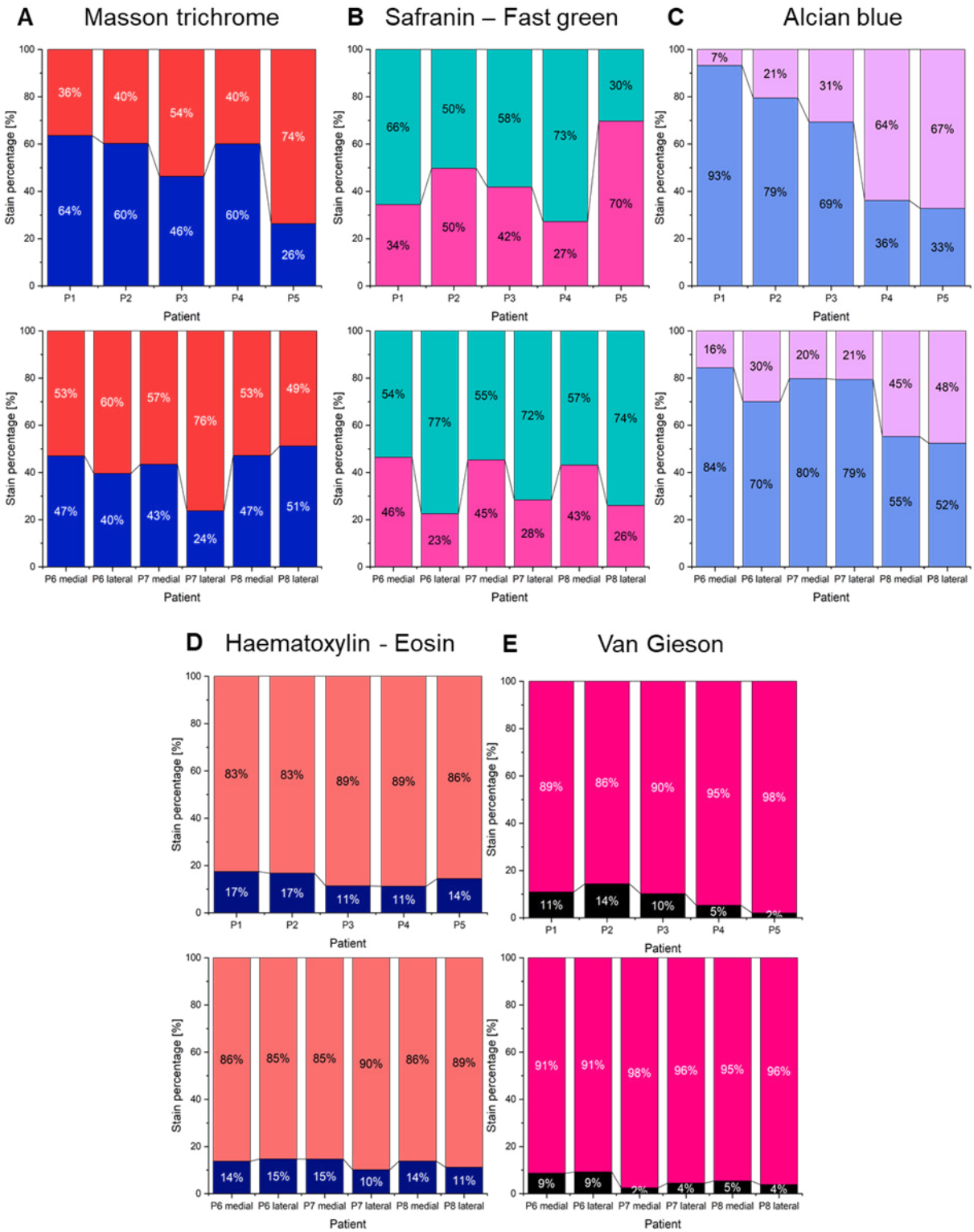

Figure 2 Percentage stacked column graphs were generated from staining quantification. Specifically: (A) blue represents collagen content stained with Masson, and red represents cytoplasmic content; (B) pink indicates positive Safranin staining, and green shows the Fast green counterstain; (C) blue represents GAG content stained with Alcian Blue, and purple corresponds to mucin stain; (D) blue indicates nuclei stained with Haematoxylin, and pink represents Eosin counterstain; (E) black represents nuclei, and red indicates collagen stained with Van Gieson

Comparison between paediatric and adult tissues

In adult patients, collagen and GAG content was noticeably reduced, while mucin levels increased, reflecting tissue degeneration, particularly in P5. In contrast, the two paediatric patients showed similar percentages of collagen and GAGs (Figures S1 and S3, Supplementary Material). Proteoglycan distribution varied widely among all patients (Figure S2, Supplementary Material). Notably, in P1 and P2, proteoglycans were concentrated in the inner zone and were less abundant in the outer region, whereas in adults, their distribution appeared more random (Figure S2, Supplementary Material). Cell distribution was consistent across all samples, with elongated cells in the outer zone and rounded cells in the inner zone (Figures S4 and S5, Supplementary Material). Overall, although cellularity was relatively low, a slight decline in cell numbers was observed with advancing meniscal degeneration.

Comparison between lateral and medial menisci in normal and valgus knee

In P8, the lateral meniscus showed a slightly higher collagen content compared to the medial meniscus. A similar trend was observed in P6 lateral and P7 medial menisci, which exhibited less damage than their lateral counterparts (Figure S6, Supplementary Material). Regarding GAG distribution, no significant differences were found between the medial and lateral menisci of P7 and P8. In contrast, P6 showed lower GAG content and higher mucin levels in the lateral meniscus (Figure S8, Supplementary Material). Proteoglycan content was consistently lower in lateral menisci

compared to medial ones, regardless of knee alignment (Figure S7, Supplementary Material). In normal knees, the medial meniscus is more subjected to damage due to its higher congruency and attachment to the medial collateral ligament. In valgus knees, altered stress distribution increases loading on the lateral meniscus, making it more susceptible to degeneration. Overall, cellularity was similar across all samples.

Morphological analysis

Morphological characterization of meniscal tissue was conducted to examine its key structural features and identify changes associated with pathology. Given the high heterogeneity of this tissue, the central region was selected for analysis. Initial observations at low magnification allowed assessment of the overall collagen fibre orientation. The collagen architecture within the meniscus is illustrated in Figure 3: at the edges in contact with the femoral and tibial articulating surfaces, fibres are radially oriented, whereas the central region exhibits a porous structure formed by sections of circumferential fibres. This architectural pattern is observed in both paediatric and adult tissues.

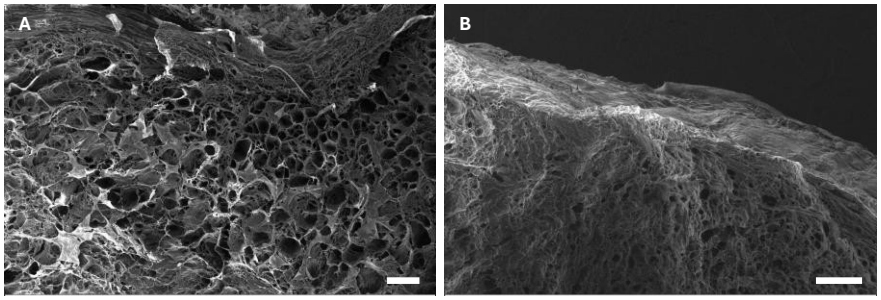

Figure 3 SEM images of P1 (A) and P5 (B) sections, scale bar: 200µm

Menisci were then examined at higher magnifications to investigate structural differences associated with various pathologies and injuries. Comparing pediatric and adult tissues (Figure 4), P1 and P2 displayed regular pores with thinner, smoother fibers, and similar porosity in the R-R and W-W zones. With increasing age, pores became less regular and fibers thicker and more wrinkled, reflecting the accumulation of fibrotic tissue, particularly in the W–W zone, which appeared less porous.

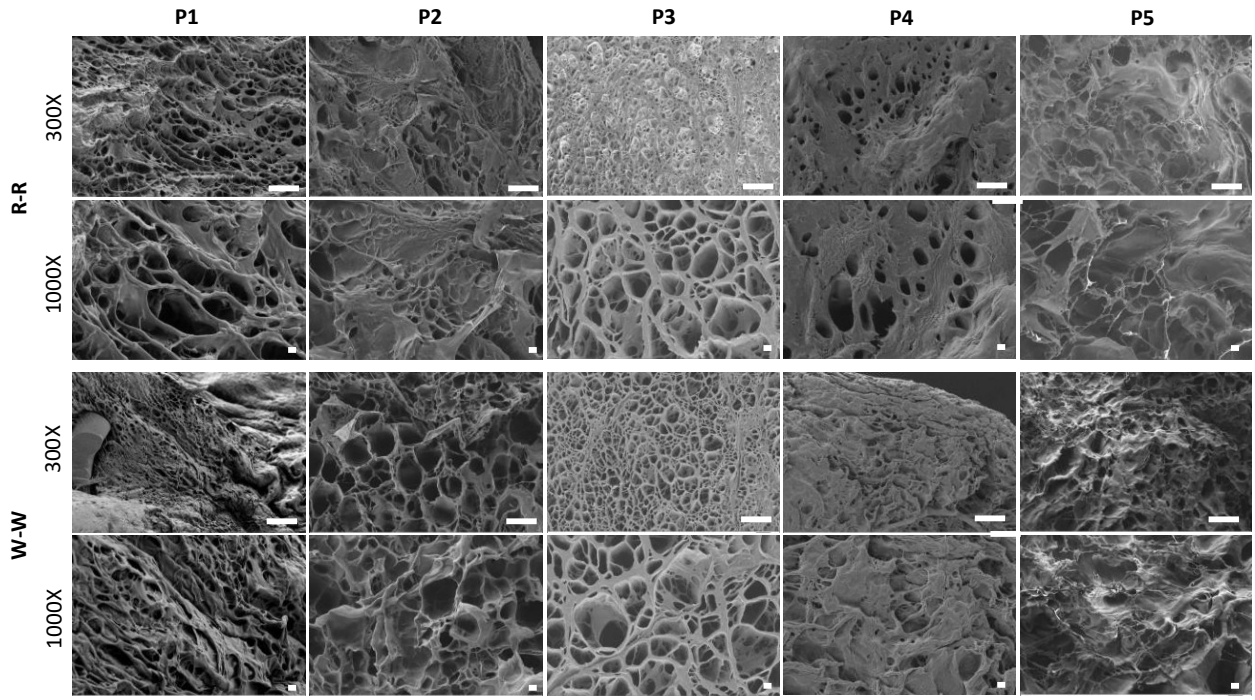

Figure 4 SEM images of R-R and W-W zones of P1-P5 at 300X and 1000X magnifications. Scale bars: 100µm (300X) and 10µm (1000X)

A second comparison was performed between patients with normal and valgus knee configurations, with results shown in Figure 5. Overall porosity was similar across all samples: the R-R zone appeared more porous than the W-W zone, which exhibited a more irregular collagen fibre distribution. In the R-R zone, collagen fibres in P6 lateral, P7 lateral, and P8 medial were more frayed compared to P6 medial, P7 medial, and P8 lateral, where fibres appeared less damaged.

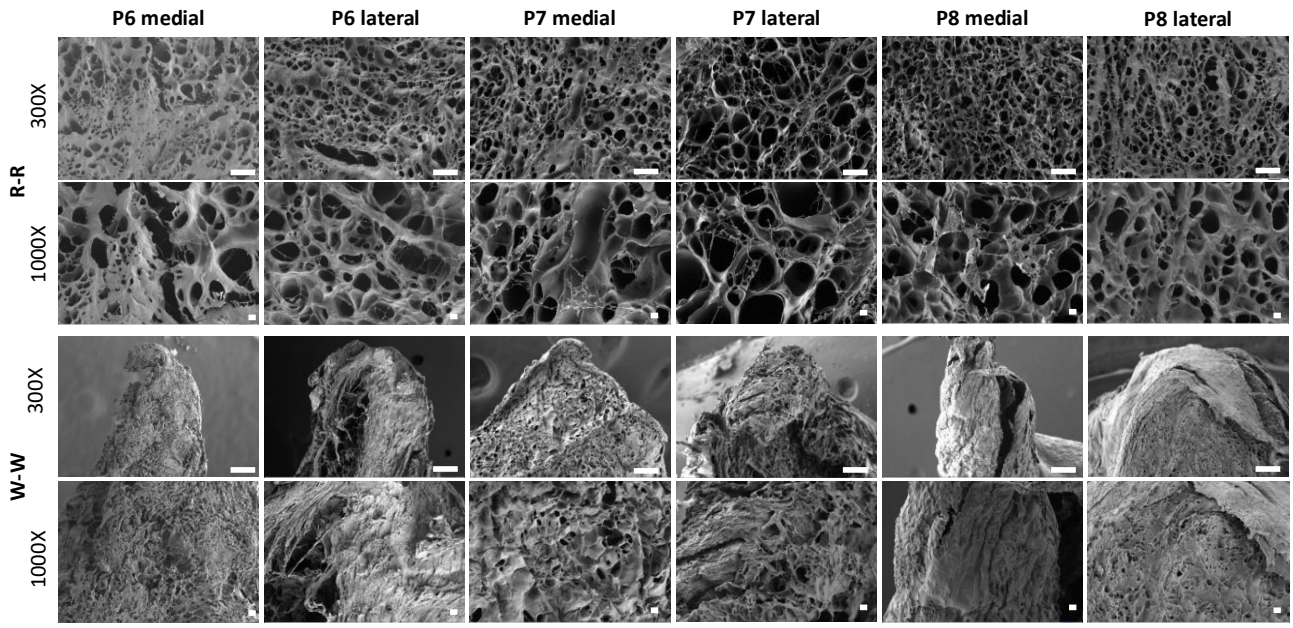

Figure 5 SEM images of R-R and W-W zones of P6-P8 at 300X and 1000X magnifications. Scale bars: 100µm (300X) and 10µm (1000X)

Quantitative imaging (QI) mode AFM measurements

The surface morphology and mechanical properties of meniscal tissues from patients P6, P7, and P8 were assessed using QI mode AFM. Only patients with both medial and lateral menisci available were included, as the goal was to evaluate morphological and mechanical changes associated with valgus knee alignment compared to normal knees. The resulting maps of YM and contact point (cp), together with Alcian Blue-stained and SEM images, are presented below. YM maps provide nanoscale insights into tissue organization through stiffness variations, while cp maps reveal localized surface morphology.

At the microscale, the medial meniscus from patient P6 (Figure 6) displayed a porous matrix, particularly in the R-R zone, which contained larger pores. GAGs were predominant in this region, whereas mucins were more abundant in the inner zone (Figure 6, Alcian Blue images). At the nanoscale, AFM revealed an amorphous structure in the outer region of the ECM, while the inner region appeared more porous; stiffness, however, was relatively homogeneous (Figure 6, cp and YM maps).

A similar external architecture was observed in the lateral meniscus of P6 (Figure 7). In contrast, the W-W zone exhibited greater heterogeneity, featuring a mixture of fibrillar and amorphous regions (Figure 7, cp and YM maps). The fibrillar structures, approximately 50–70 μm in diameter, likely contributed to tissue aggregation, although regions with increased agglomeration were also noted. This dual composition was also observed in the SEM images, where both organized fibrils and less structured areas were clearly visible. The proportions of GAGs and mucins were comparable in both the R-R and W-W zones (Figure 7 Alcian blue images); however, the ECM appeared more porous externally, while in the W-W zone was more compact and fibrous (Figure 7 SEM images). In the medial meniscus of patient P7, a porous architecture was microscopically observed in both R-R and W–W zones, which also had a similar GAGs and mucins distribution (Figure 8 Alcian blue images). In particular, mucins were less abundant compared to P6 lateral, with a distribution pattern more closely resembling that of the P6 medial meniscus. At the nanoscale level, most of the tissue exhibited a well-oriented and fibrillar organization (Figure 8 cp and YM images). Amorphous regions were confined to the W–W zone, and were also visible in SEM images, particularly between some pores. The lateral meniscus of P7 revealed a primarily amorphous and less organized nanostructure, with evident agglomerates and a heterogeneous stiffness (Figure 9 cp and YM images). Microscopically, the morphology closely resembled that of the medial counterpart, exhibiting larger pores in the R-R zone and a more compact structure in the W-W region (Figure 9 SEM images). The external portion showed a GAG distribution similar to the previous sample, although mucins were barely present in the inner region (Figure 9 Alcian blue images). The medial meniscus of patient P8 demonstrated the greatest heterogeneity within the W–W zone. SEM analysis highlighted a complex and irregular matrix, which was also found nanoscopically in AFM imaging. These images revealed an intricate composition featuring fibrillar, porous, and amorphous regions (Figure 10 cp and YM images). Greater structural regularity was observed in the outer zone, which resembled that of previous samples: porous at the microscopic level and amorphous at the nanoscale. The matrix contained an abundant number of mucins both internally and externally, although GAGs appeared to be more

concentrated in the W-W zone (Figure 10 Alcian blue images). In the lateral meniscus of P8, distinct differences between the outer and inner portions were also noted. Macroscopically, the outer region appeared porous and well-organized, while the inner region was fibrous and more compact (Figure 11 SEM images). The distribution of GAGs was similar to that observed in P6 lateral, with mucins abundantly present in both internal and external regions (Figure 11 Alcian blue images). AFM analysis revealed subtle variations in nanostructure, with fibrillar elements present in the R–R zone, and a more porous and less organized composition deeper within the tissue (Figure 11 cp and YM images).

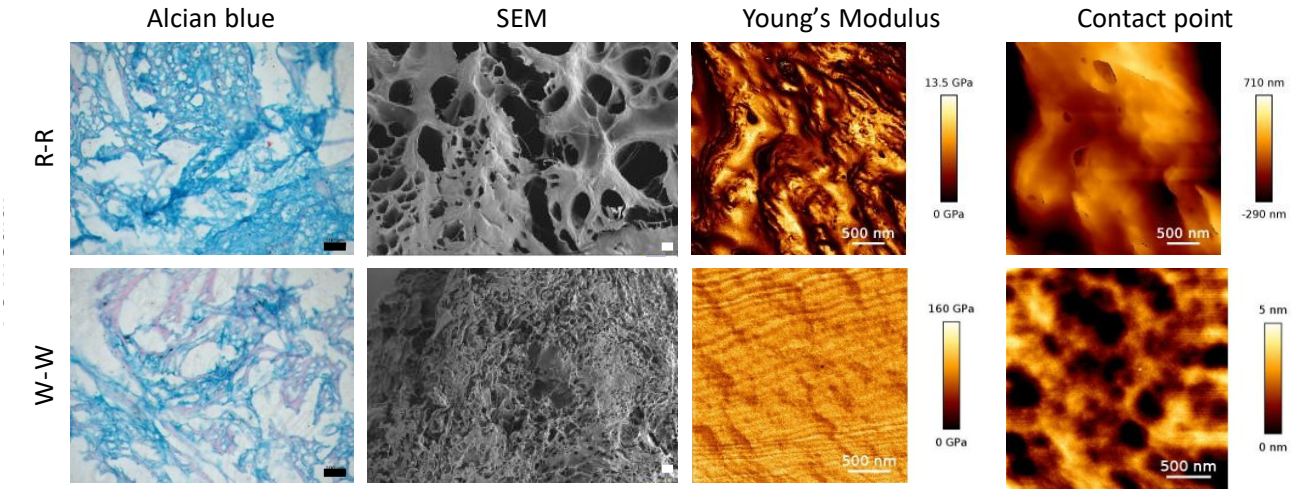

Figure 6 Alcian blue staining, SEM and AFM images of YM and contact point acquired on P6 medial meniscal tissue. Scale bars: 100 µm for Alcian blue images, 10 µm for SEM images, 500 nm for cp and YM images

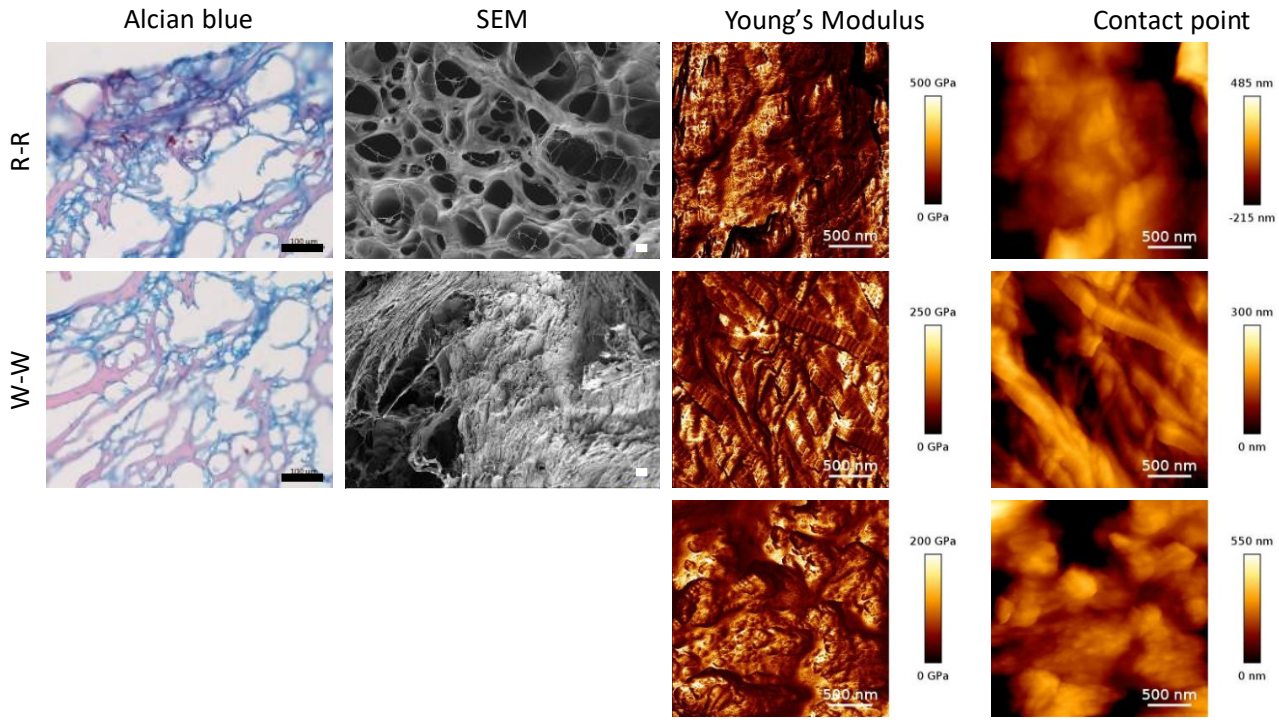

Figure 7 Alcian blue staining, SEM and AFM images of YM and contact point acquired on P6 lateral meniscal tissue. For W-W zone, two images were acquired due to the heterogeneous compostion of the ECM in this portion. Scale bars: 100 µm for Alcian blue images, 10 µm for SEM images, 500 nm for cp and YM images

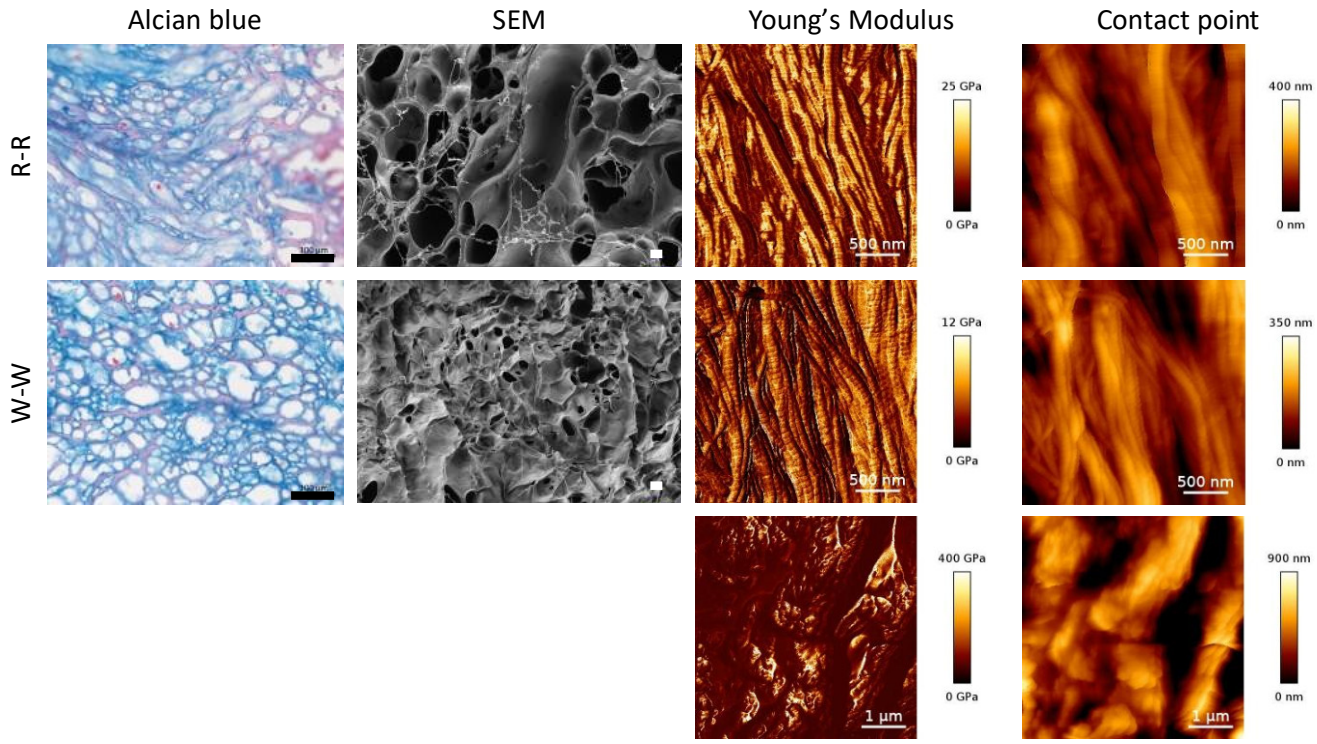

Figure 8 Alcian blue staining, SEM and AFM images of YM and contact point acquired on P7 medial meniscal tissue. For W-W zone, two images were acquired due to the heterogeneous compostion of the ECM in this portion. Scale bars: 100 µm for Alcian blue images, 10 µm for SEM images, 500 nm for cp and YM images

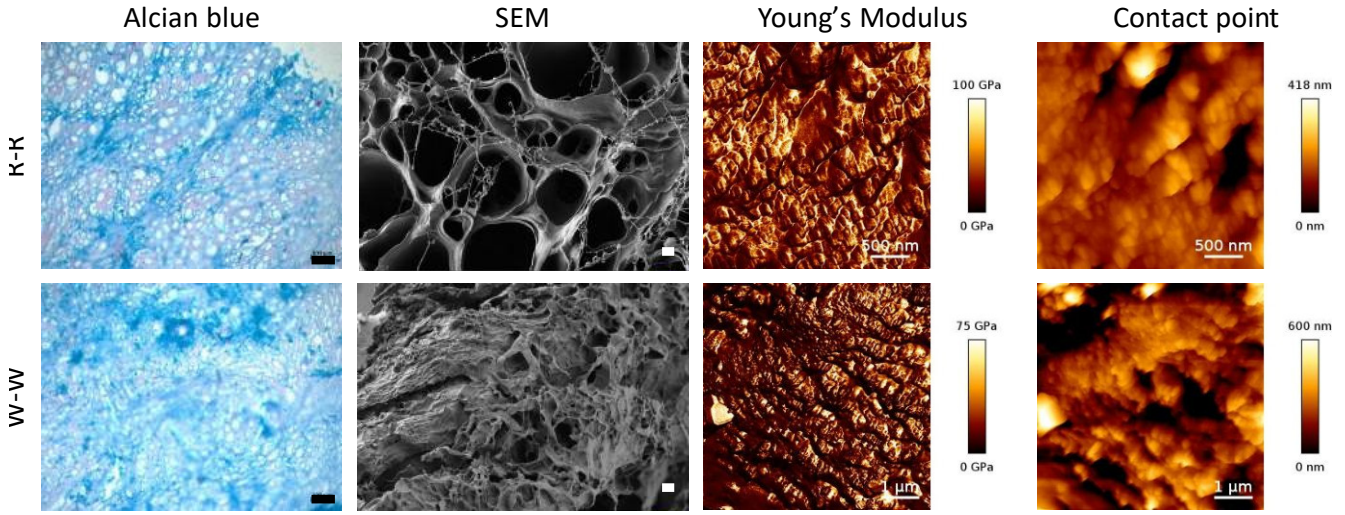

Figure 9 Alcian blue staining, SEM and AFM images of YM and contact point acquired on P7 lateral meniscal tissue. Scale bars: 100 µm for Alcian blue images, 10 µm for SEM images, 500 nm for cp and YM images

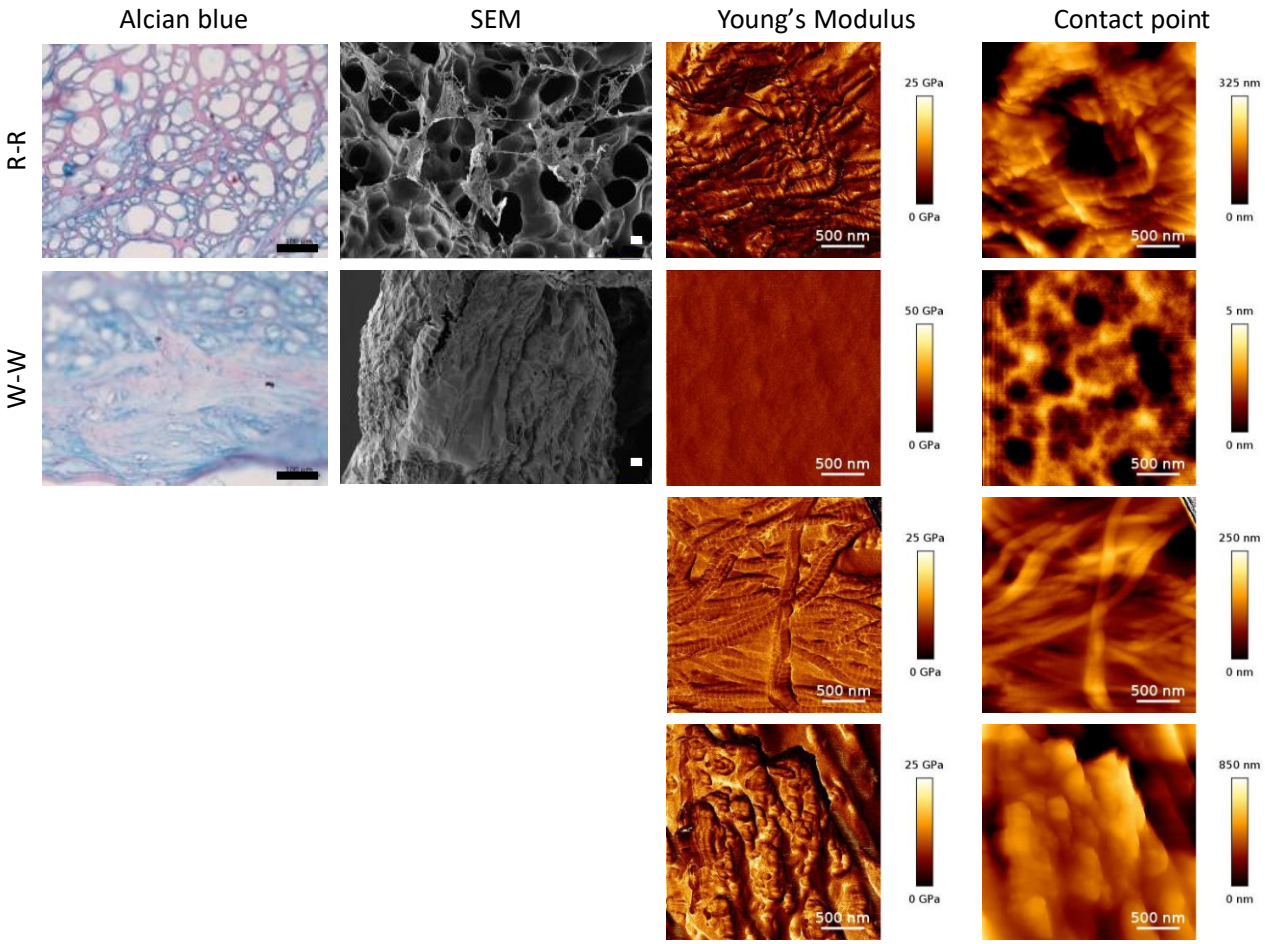

Figure 10 Alcian blue staining, SEM and AFM images of YM and contact point acquired on P8 medial meniscal tissue. For W-W zone, three images were acquired due to the heterogeneous compostion of the ECM in this portion. Scale bars: 100 µm for Alcian blue images, 10 µm for SEM images, 500 nm for cp and YM images

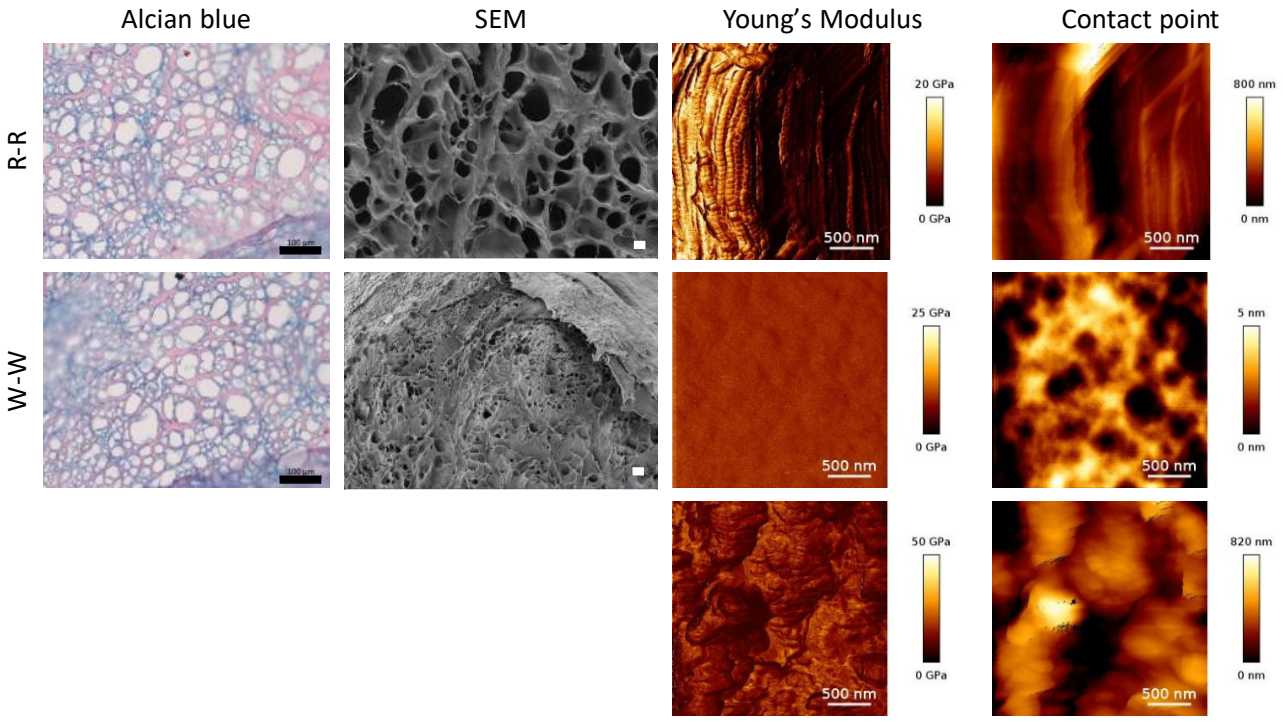

Figure 11 Alcian blue staining, SEM and AFM images of YM and contact point acquired on P8 lateral meniscal tissue. For W-W zone, two images were acquired due to the heterogeneous compostion of the ECM in this portion. Scale bars: 100 µm for Alcian blue images, 10 µm for SEM images, 500 nm for cp and YM images

In Figure 12 the median values of YM obtained in R-R and W-W zones of meniscal tissue are shown. It is important to note that these YM values reflect nanoscale measurements, representing the stiffness of specific structural features or tissue organizations, such as localized fibrotic regions or characteristic collagen fibril orientations. The global compressive properties of meniscal tissue are described in the following paragraph. In P6, statistically significant differences in nanoscale stiffness were observed between lateral and medial menisci and between the R-R and W-W zones. Specifically, YM measured at the nanoscale was higher in the R-R portion of the lateral meniscus and lower in the corresponding medial region, suggesting more localized degeneration on the medial side. In contrast, nanoscale YM values in the W-W zones were comparable between lateral and medial menisci. In P7 and P8, no statistically significant zonal differences were detected, indicating a more globally distributed degeneration pattern. In P7, nanoscale YM of the R-R zone remained slightly higher in

the lateral side compared to the medial one, while a reduction was also visible in the W-W portions. The largest decrease was found between the R-R zones of P6 and P7. Conversely, in the medial side of P7, nanoscale YM increased relative to P6, suggesting that aging combined with valgus alignment may have promoted degeneration localized mainly in the medial R-R region. In P8, this trend became more pronounced: lateral nanoscale YM values were lower than medial ones, particularly in the lateral R-R zone, reflecting more severe degeneration. Medial values remained comparable to P7, consistent with their similar age and valgus alignment. A global comparison of nanoscale YM across different formulations is shown in Figure S11 Supplementary Material.

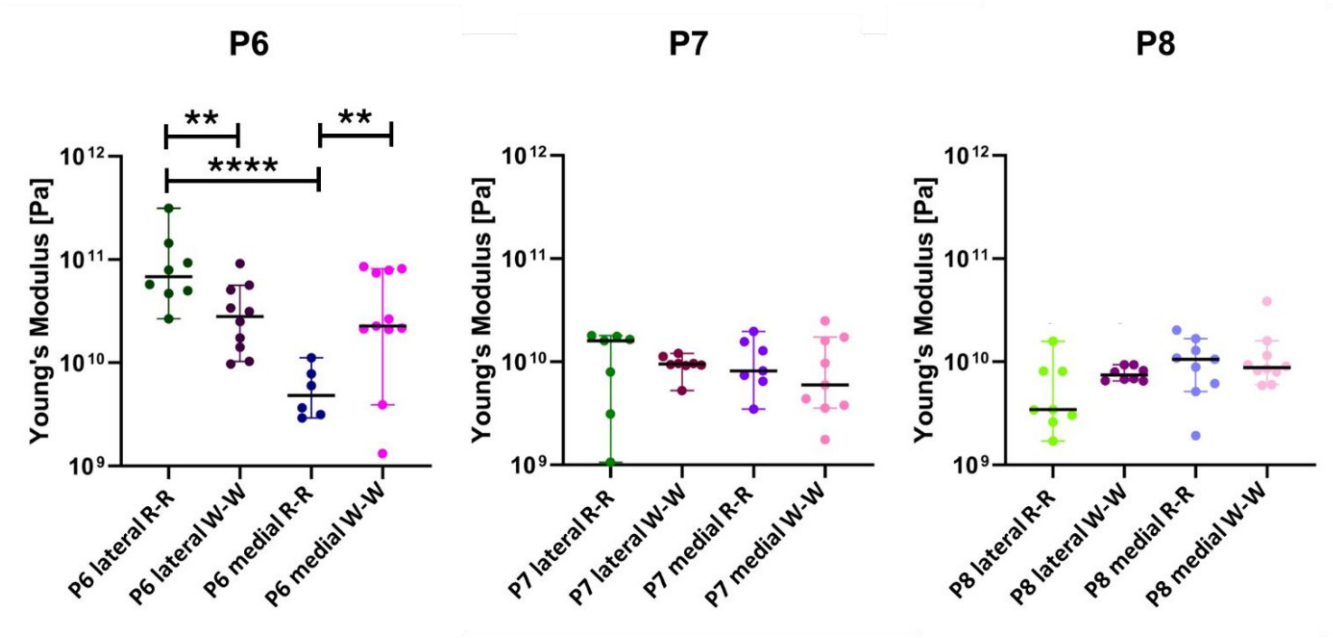

Figure 12 median values of YM obtained in medial, lateral, internal end external portions of P6, P7 and P8. Statistical analysis was performed with Mann-Whitney test and significative differences were shown with "", where ** indicates $p < 0.05$, *** $p < 0.005$ and **** $p < 0.0005$*

Compression test

To assess global mechanical properties, meniscal tissue from patients P6, P7, and P8 underwent compression test up to 40% deformation, from which YM was determined in the elastic region of the stress–strain curves (Figure 13A). All curves displayed an initial toe region, characterized by a nonlinear stress-strain response with progressively increasing slope. This behaviour, typical of

biological tissues, reflects the gradual realignment of wavy collagen fibres. Once the collagen fibrils became fully straightened, the elastic region began, where stress and strain showed a linear relationship and the slope corresponded to the YM [29]. In P6 and P7, the slope was similar in the lateral menisci and in the medial R-R zones, whereas the medial W-W zones exhibited slopes of greater magnitude. In contrast, in P8 the slopes were comparable across both W-W and R-R portions. It is important to note that at 40% strain none of the samples reached the yield point, indicating that they remained within the elastic region.

YM values were calculated for each region in each sample, and statistical differences were evaluated using ANOVA with multiple comparisons (Figure 13B and Table S1 Supplementary Material). Overall, YM was consistently higher in the W-W portions, consistent with collagen fibre orientation. In the R-R zones, collagen fibres are primarily aligned circumferentially, exposing their cross-sections under compression; these fibrils are optimized for tensile rather than compressive loading and therefore result in a less compact and more porous structure. Conversely, in the W-W zones, fibres exhibit a more random orientation, generating a denser matrix, as also confirmed by previous SEM observations, and yielding higher YM values. In agreement with previous results, P6 and P7 showed a marked decrease in YM in the lateral W-W zones, indicating localized deformation. Both patients exhibited valgus knee alignment, which increases loading on the lateral meniscus. This region is anatomically less stabilized by ligaments than the medial side, making it more susceptible to degeneration. Previous observations revealed a reduction in collagen fibres in these samples, which was not seen in the lateral W-W zone of P8. Since collagen fibres provide mechanical strength to the meniscal ECM, their loss due to degeneration results in decreased mechanical properties. When comparing medial W-W zones, P7 and P8 exhibited similar YM values, whereas P6 displayed lower values. Given that P6 was the oldest patient, while P7 and P8 were of similar age, the reduction in YM in P6 likely reflects age-related degenerative changes. A similar trend was observed between P6 and P7: the younger patient had higher YM in the lateral W-W zone, implying that although valgus configuration is the main driver of reduction, aging likely amplifies the effect.

Differences were observed between YM values measured by AFM and those obtained from compression tests. This is consistent with the fact that compression testing reflects the macroscopic mechanical properties of the tissue, whereas AFM captures the YM of nanoscale structures, which exhibit high heterogeneity due to the anisotropic nature of meniscal tissue. This heterogeneity arises from variations in collagen fibre orientation, as revealed by SEM, and differences in chemical composition between physiological and pathological regions, as shown by histological analysis.

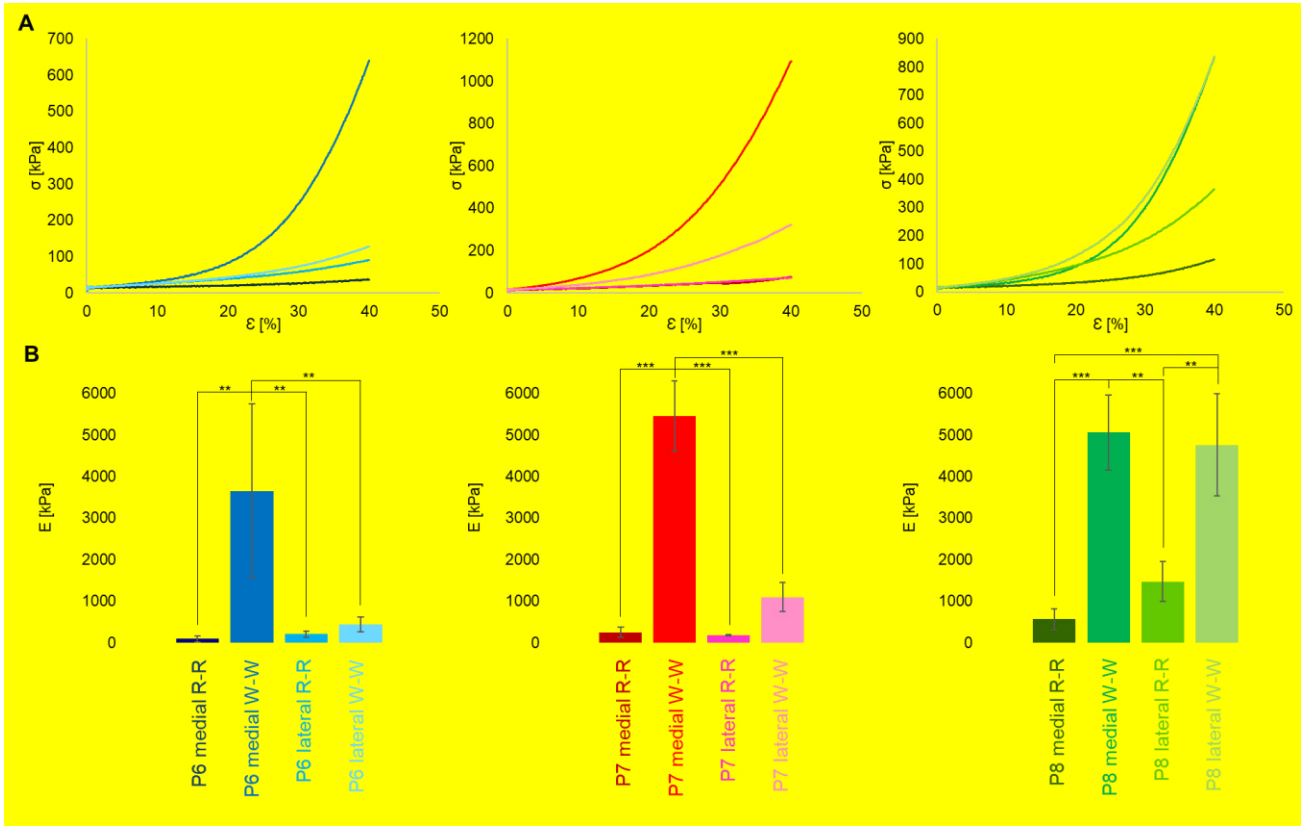

Figure 13 stress-strain curves (A) and barplot with YM values obtained after compression test on meniscal tissue (B), where data are expressed as mean ± SD. Tukey's post-hoc test for multiple comparisons was performed to compare different samples, and significative differences were indicated as"" for 0.05<p ≤0.01, "**" for 0.01<p ≤0.001 and "***" for p>0.001*

Discussion

The menisci are essential in both tibiofemoral compartments for load distribution and shock absorption [18]. Different studies were performed to characterize meniscal ECM of different species

from histological, morphological and biomechanical point of views, and several works compare them with human tissue (Table 4). In Sandmann et al., human meniscal tissue was compared with bovine, ovine, and porcine menisci from biomechanical and biochemical point of views to investigate species differences and identify the most physiologically similar tissue [16]. It is important to note that differences between human and animal ECM arise not only from variations in meniscal size but also from differences in knee flexion and extension during walking [15], [16]. Moreover, both intra- and interspecies differences in meniscal tissue characteristics are well documented, as degeneration leads to macroscopic and microscopic alterations in the tissue [17]. The aim of this work was to evaluate the properties of meniscal ECM in human patients of different ages and with various pathologies, in order to study the changes associated with disease. Paediatric patients were also included, since their meniscal tissue, originating from traumatic rather than degenerative lesions, can be considered physiological. A comparison was also performed between lateral and medial menisci from normal and valgus knee to detect the ECM variations induced by this pathological state, in which knee joint is angled out and away from the body's mid-line [30].

Histological characterization

To study the histology of meniscal tissue, different stains were used: Haematoxylin-Eosin and Van Gieson Trichrome to evaluate the cellularity and Masson Trichrome, Alcian Blue and Safranin-Fast Green for the extracellular matrix characterization. In terms of cell morphology, two cell types are found in analysed samples: fusiform fibroblast-like cells in the fibrocartilaginous region subjected to tensile loads and spherical chondrocyte-like cells in the inner part, subjected to compressive loads [15], [31], [32]. Overall, the number of cells is limited, but a slight decrease in the cell population occurs during meniscal degeneration. Several studies on human meniscal tissue described a reduction in cell density, associated by mucoid degeneration and a loss of collagen fibre organization in pathological tissues, as well as age increases [11], [33], [34]. Concerning the ECM characterization, the content of collagen fibres stained with Masson Trichrome decreases in relation to the degeneration

of the tissue (Figure S1 Supplementary material). This result is consistent with Sun et al. study, where a decrease in collagen content in osteoarthritic patients using Picrosirius Red, a staining method analogous to Masson's trichrome for collagen detection [35]. Safranin O staining was performed with a Fast green counterstain to detect negatively charged proteoglycans, as it stoichiometrically binds to the anionic glycosaminoglycan component of proteoglycans [36], [37]. In paediatric patients, proteoglycans are mainly localized in the inner zone. However, in adults, their distribution appears more variable: some samples show proteoglycans spread throughout the entire section, while others exhibit a reduced percentage (Figure S2 Supplementary material). These results align with previous works found in literature. For instance, in a Sun et al. study a comparison between normal and osteoarthritic menisci was done using Safranin O staining and an increase of proteoglycans was observed [38]. Similarly, Videman et al. reported a comparable result after inducing osteoarthritis through limb immobilization in rabbits [39]. However, Djurasovic et al. found a decrease in proteoglycan content following osteoarthrosis induction via limb immobilization in mature beagles [40]. Additionally, other studies have reported a reduction in proteoglycans in human osteoarthritic cartilage, highlighting the need for further research to better understand this phenomenon [41], [42], [43]. Alcian Blue was performed to detect sulphated GAGs, which are about 80% of total GAGs: paediatric samples showed a very intense stain compared to pathological samples, in which mucins increased (Figure S3 Supplementary material). Ribitsch et al. studied meniscal tissues from horses of different ages and concluded that GAG content and distribution are age dependent. In young horses, GAGs were generally more evenly distributed, while in older horses, the menisci exhibited distinct areas of positive or negative GAG presence [21]. Lopez-Franco et al. investigated proteoglycans changes in human menisci and found a decrease in the matrix of osteoarthritic patients: consistently with other studies, GAGs synthesis is reduced during degeneration [11], [44]. These results are consistent with Herwig et al. studies, in which alterations in water, collagen and GAGs content were observed in various degrees of degeneration [9]. Under the same physiological and biomechanical conditions, a decrease in collagen, GAGs, and ligamentous tissue, along with an increase in mucins,

can be observed in the medial meniscus (Figure S6, S7 and S8 Supplementary material): this result aligns with the fact that the medial compartment is more congruent than the lateral compartment, making it more susceptible to increased compression and more frequent meniscal tears [24], [45]. In the case of a valgus knee, greater degeneration is observed in the ECM of the lateral meniscus. This is attributed to alterations in the joint biomechanics, leading to increased damage and erosion on the lateral side [46], [47].

Morphological characterization

Morphologically, in all the samples, three different layers were observed: a thin fibrillar network on the femoral and tibial surfaces, a radially oriented lamellar layer and a central portion with circumferential fibres. In Petersen et al., the randomly oriented fibrillar layer was estimated to have a diameter of 35 nm, while the collagen fibrils beneath it measured 120 nm in diameter, forming a superficial fibrillar layer approximately 150–200 μm thick. The thickness of this layer decreases to 20–30 μm towards the inner circumference [13].

Table 4 Characteristics of meniscal tissue in human and animals

Source	**Results**	**References**
Human paediatric	Collagen predominant in the outer zone, GAGs in the inner zone, low cellularity. Ligamentous-like structure in the external part, cartilaginous-like in the internal one. Collagen fibres are physiologically oriented and no damaged.	This study
Human adult	Collagen and GAGs decrease when age increases, mucins and fibrotic tissue increase. Low cellularity. Collagen fibres are more irregular and thicker. At nanoscale level, great heterogeneity of the tissue, varying from porous to fibrillar and amorphous aspect.	This study

Human	In pathological meniscal tissue, matrix degeneration and different biochemical properties are observed.	[15], [16], [33]
Bovine	Fibres organization and thickness increase with age due to higher loading.	[19]
Ovine	Is the most like the human meniscus from viscoelastic and biological point of views. Collagen pattern is consistent with human tissue.	[15], [16]
Pig	GAGs distribution is different, but collagen fibre's structure is like human meniscus.	[16], [20]
Horse	GAGs content and distribution is age-dependant, like in human meniscal tissue.	[21]
Rabbit	Different biomechanics to human meniscal tissue, cellularity and vascularization are higher. Collagen pattern is consistent with human tissue.	[15], [16]

Differences were observed in the rabbit meniscal ECM, where the lamellar layer was not detected, highlighting the importance of having significative data on humans [15]. In degenerative conditions, thicker and irregular collagen fibres can be observed, potentially indicating fibrotic tissue, especially in the medial meniscus. Similarly, this structure is more common in the lateral meniscus of a valgus knee. Nanoscale imaging using QI-mode AFM confirmed the heterogeneous composition of the ECM, ranging from porous to fibrillar and amorphous structures, thus highlighting the intrinsic anisotropy of the tissue. Similar fibrils with a comparable diameter were observed in previous works on murine and porcine meniscal tissues [48], [49]. When comparing different biomechanical configurations, patient with valgus alignment combined with aging exhibited drastically reduced localized stiffness in the R-R zone of the medial meniscus, suggesting signs of degeneration. Statistically significant differences in stiffness among the various meniscal zones were observed in this group, indicating a clear distinction between regions. Conversely, in younger patients, which both

had normal and valgus alignment, localized YM of the R-R and W-W zones of both medial and lateral menisci did not show statistically significant differences. This reduced contrast between zones may be attributed to more generalized tissue degeneration, less localized within the medial meniscus R-R zone. This interpretation is supported by the markedly decreased stiffness values observed in the R-R zones of the lateral meniscus in these patients. Additionally, the W-W zones demonstrated localized stiffness more comparable to those of the normal knee. In Kwok et al, nanomechanical profiles of meniscal tissues from healthy young, aged and osteoarthritic patients were evaluated using AFM. Healthy aged tissue showed similar differential elasticity among inner and outer zones, with higher YM externally, instead degenerated osteoarthritic tissue showed more similar stiffness in R-R and W-W zones [50]. From the biochemical point of view, all samples presented mucoid degeneration, which seemed to be more evident in lateral menisci, which is also associated to loss of collagen fibre organization. These results align with a previous study in which Alcian Blue and Safranin O staining were quantified to analyse human meniscal tissues from patients of varying ages and pathological conditions, aiming to identify ECM changes associated with age and disease. That study reported a decrease in cell density and an increase in mucoid degeneration, which correlated with a loss of collagen fibre organization as pathology progressed. Moreover, pathological samples exhibited heterogeneous proteoglycan distribution, with regions of intense staining alongside areas lacking any signal. These observations are consistent with the data obtained in the present work [33].

Mechanical characterization

Global compressive properties of meniscal cross-sections were also assessed, revealing lower YM in the R-R zones, consistent with the predominance of circumferential collagen fibres in this region, which primarily function under tension. In the W-W zones, patients with valgus knee alignment showed a marked reduction in YM in the lateral compartment, indicating greater degeneration in this region due to altered biomechanical loading; this was associated with a decrease in collagen content, as confirmed by histological analysis. Additionally, a gradual decline in YM with age was observed

in the W-W zones of medial menisci, suggesting that aging is a contributing factor to tissue degeneration. In Fischenich et al., the mechanical properties of human menisci at different stages of osteoarthritic damage were examined. Their results indicated that tensile YM remained unchanged across all degenerative grades, while compressive YM was already affected in the early stages of gross degeneration and continued to decline with disease progression, consistent with our observations [51]. Assessing compressive YM in patients is therefore clinically relevant, as it may serve as a valuable indicator to guide surgical decisions, such as whether to resect or suture a meniscal tear [52]. This underscores the importance of our study, in which we also linked pathological biochemical alterations to changes in compressive YM.

Limits and perspectives

This study is subject to several limitations. One could be the small sample size, which included only eight patients, making it difficult to draw generalizable conclusions. To our knowledge, this research represents the first attempt to characterize the "meniscal ECM" in skeletally immature subjects [53]. Although a significant increase in meniscal procedures in children has been documented, the difficulties in increasing the number of samples are evident. In fact, in our routine clinical practice, most patients programmed for meniscal pathologies are treated with meniscal repair and suture surgery [54]. Additionally, no previous studies have specifically examined the correlation between physical properties of the meniscal ECM, such as stiffness, and the tissue morphology and histological composition in both healthy and pathological menisci. This study evaluated the impact of various pathologies, including valgus knee alignment and arthritis, on tissue morphology, stiffness, and composition, as well as the interrelationships among these factors. Moreover, the fact that this is a single-centre study may further limit generalizability, as all data were collected from a single hospital, potentially restricting its applicability to broader clinical settings. Variability in the sampling technique is another limitation, differences in surgical methods (e.g., en bloc meniscectomy) and the exclusion of smaller meniscal tears could introduce selection bias by including only specific types of

lesions. Furthermore, the exclusive use of discarded tissue from surgery may not fully represent the entire meniscus or its different zones comprehensively. For this reason, future directions include expanding the study to additional meniscal samples from various lesion types and anatomical regions to gain a deeper understanding of ECM degeneration processes and to obtain more generalizable results. However, the results observed in both paediatric and adult pathological meniscal tissues are consistent with findings reported in a previous study [33], supporting the reliability of the data. Specifically, the structural and biochemical alterations described in the literature were also identified in this work. Notably, no prior data were available comparing valgus knee alignment to physiological conditions. This study is particularly significant as it is the first to examine the correlation between morphology, histological composition, and stiffness in meniscal tissue across patients of varying ages and with different pathologies. The results obtained may be significant not only for improving the medical diagnosis of meniscal pathologies but also for developing more personalized treatments, given that each meniscal condition presents unique ECM differences in both stiffness and composition. Furthermore, this work can be useful in regenerative medicine, as the design of a functional scaffold must replicate both the mechanical and biochemical properties of native tissue.

Acknowledgments

Supported by a grant from Italian Ministry for Universities and Research (MUR), Dipartimenti di Eccellenza 2023-2027 (l. 232/2016, art. 1, commi 314–337). Financial support from: Iniziativa “PNC0000003 - “ANTHEM: AdvaNced Technologies for Human-centrEd Medicine”. CUP BICOCCA B53C2200667000; Ministero della Salute, RF-2021-12371959 Tackling immunomodulatory properties of stromal cells to improve therapeutic strategies in lung cancer. MUR PRIN 2022, 2022MY7AZT Dynamic multifunctional hydrogels for glioblastoma therapy (DINGO).

References

[1] A. Aazmi *et al.*, “Biofabrication methods for reconstructing extracellular matrix mimetics,” *Bioact Mater*, vol. 31, pp. 475–496, Jan. 2024, doi: 10.1016/j.bioactmat.2023.08.018.

[2] J. Nicolas, S. Magli, L. Rabbachin, S. Sampaolesi, F. Nicotra, and L. Russo, “3D Extracellular Matrix Mimics: Fundamental Concepts and Role of Materials Chemistry to Influence Stem Cell Fate,” *Biomacromolecules*, vol. 21, no. 6, pp. 1968–1994, Jun. 2020, doi: 10.1021/acs.biomac.0c00045.

[3] S. Zhu *et al.*, “Microstructure Analysis and Reconstruction of a Meniscus,” *Orthop Surg*, vol. 13, no. 1, pp. 306–313, Feb. 2021, doi: 10.1111/os.12899.

[4] E. Luvsannyam, M. S. Jain, A. R. Leitao, N. Maikawa, and A. E. Leitao, “Meniscus Tear: Pathology, Incidence, and Management,” *Cureus*, May 2022, doi: 10.7759/cureus.25121.

[5] E. A. Makris, P. Hadidi, and K. A. Athanasiou, “The knee meniscus: Structure-function, pathophysiology, current repair techniques, and prospects for regeneration,” Oct. 2011. doi: 10.1016/j.biomaterials.2011.06.037.

[6] P. E. Gelber, B. Barenius, and S. Perelli, “Role of Alignment and Osteotomy in Meniscal Injuries,” Jan. 01, 2020, *W.B. Saunders*. doi: 10.1016/j.csm.2019.08.006.

[7] M. López-Franco and E. Gómez-Barrena, “Cellular and molecular meniscal changes in the degenerative knee: A review,” 2018, *Springer*. doi: 10.1186/s40634-018-0126-8.

[8] C. S. Proctor, M. B. Schmidt, R. R. Whipple, M. A. Kelly, and V. C. Mow, “Material Properties of the Normal Medial Bovine Meniscus.”

[9] J. Herwig, E. Egner, and E. Buddecke, “Chemical changes of human knee joint menisci in various stages of degeneration,” 1984.

[10] C. A. Mcdevitt and R. J. Webber, “The Ultrastructure and Biochemistry of Meniscal Cartilage.” [Online]. Available: http://journals.lww.com/clinorthop

[11] M. López-Franco *et al.*, “Meniscal degeneration in human knee osteoarthritis: in situ hybridization and immunohistochemistry study,” *Arch Orthop Trauma Surg*, vol. 136, no. 2, pp. 175–183, Feb. 2016, doi: 10.1007/s00402-015-2378-4.

[12] F. Flandry and G. Hommel, “Normal Anatomy and Biomechanics of the Knee,” 2011. [Online]. Available: www.sportsmedarthro.com

[13] W. Petersen and B. Tillmann, “Collagenous fibril texture of the human knee joint menisci,” *Anat Embryol (Berl)*, vol. 197, no. 4, pp. 317–324, Mar. 1998, doi: 10.1007/s004290050141.

[14] E. Stocco, A. Porzionato, E. De Rose, S. Barbon, R. De Caro, and V. Macchi, “Meniscus regeneration by 3D printing technologies: Current advances and future perspectives,” Jan. 01, 2022, *SAGE Publications Ltd*. doi: 10.1177/20417314211065860.

[15] A. Chevrier, M. Nelea, M. B. Hurtig, C. D. Hoemann, and M. D. Buschmann, “Meniscus structure in human, sheep, and rabbit for animal models of meniscus repair,” *Journal of Orthopaedic Research*, vol. 27, no. 9, pp. 1197–1203, Sep. 2009, doi: 10.1002/jor.20869.

[16] G. H. Sandmann *et al.*, “Biomechanical comparison of menisci from different species and artificial constructs,” *BMC Musculoskelet Disord*, vol. 14, 2013, doi: 10.1186/1471-2474-14-324.

[17] M. A. Sweigart *et al.*, “Intraspecies and Interspecies Comparison of the Compressive Properties of the Medial Meniscus,” 2004.

[18] C. Pauli *et al.*, “MAcroscopic And Histopathologic Analysis Of Human Knee Menisci In Aging And Osteoarthritis,” *Osteoarthritis Cartilage*, vol. 19, no. 9, pp. 1132–1141, Sep. 2011, doi: 10.1016/j.joca.2011.05.008.

[19] S. Bansal *et al.*, “Structure, function, and defect tolerance with maturation of the radial tie fiber network in the knee meniscus,” *Journal of Orthopaedic Research*, vol. 38, no. 12, pp. 2709–2720, Dec. 2020, doi: 10.1002/jor.24697.

[20] Y. He *et al.*, “Preparation and Characterization of an Optimized Meniscal Extracellular Matrix Scaffold for Meniscus Transplantation,” *Front Bioeng Biotechnol*, vol. 8, Jul. 2020, doi: 10.3389/fbioe.2020.00779.

[21] I. Ribitsch *et al.*, “Structure—Function relationships of equine menisci,” *PLoS One*, vol. 13, no. 3, Mar. 2018, doi: 10.1371/journal.pone.0194052.

[22] K. Nakagawa *et al.*, “Histological Analysis of the Wrapping Treatment for Meniscal Horizontal Tears in Rabbits,” *Cartilage*, vol. 13, no. 2_suppl, pp. 1551S-1561S, Dec. 2021, doi: 10.1177/1947603519870838.

[23] P. E. Greis, D. D. Bardana, M. C. Holmstrom, and R. T. Burks, “Meniscal injury: I. Basic science and evaluation.,” 2002. doi: 10.5435/00124635-200205000-00003.

[24] M. Englund, A. Guermazi, and L. S. Lohmander, “The Meniscus in Knee Osteoarthritis,” Aug. 2009. doi: 10.1016/j.rdc.2009.08.004.

[25] BD Biosciences, “Preparation and Staining of Frozen Tissue Sections.”

[26] M. J. Higgins *et al.*, “Noninvasive determination of optical lever sensitivity in atomic force microscopy,” *Review of Scientific Instruments*, vol. 77, no. 1, Jan. 2006, doi: 10.1063/1.2162455.

[27] H. Schillers *et al.*, “Standardized Nanomechanical Atomic Force Microscopy Procedure (SNAP) for Measuring Soft and Biological Samples,” *Sci Rep*, vol. 7, no. 1, p. 5117, Jul. 2017, doi: 10.1038/s41598-017-05383-0.

[28] D. Wu, P. Isaksson, S. J. Ferguson, and C. Persson, “Young’s modulus of trabecular bone at the tissue level: A review,” *Acta Biomater*, vol. 78, pp. 1–12, Sep. 2018, doi: 10.1016/j.actbio.2018.08.001.

[29] R. K. and S. Saarakkal, “Biomechanics and Modeling of Skeletal Soft Tissues,” in *Theoretical Biomechanics*, InTech, 2011. doi: 10.5772/19975.

[30] P. Ahsan, Md. S. Ezaz, I. Jahan, N. S. Asma, and M. Anjoom, “Total Knee Replacement in a Young Patient with Valgus Knee Osteoarthritis: A Case Report,” *J Orthop Case Rep*, vol. 14, no. 1, pp. 48–53, 2024, doi: 10.13107/jocr.2024.v14.i01.4144.

[31] F. N. Ghadially, I. Thomas, N. Yong, and J.-M. A. Lalonde, “Ultrastructure of rabbit semilunar cartilages,” 1978.

[32] M.-P. Hellio *et al.*, “The cells of the rabbit meniscus : their arrangement, interrelationship, morphological variations and cytoarchitecture,” 2001.

[33] C. Pauli *et al.*, “MAcroscopic And Histopathologic Analysis Of Human Knee Menisci In Aging And Osteoarthritis,” *Osteoarthritis Cartilage*, vol. 19, no. 9, pp. 1132–1141, Sep. 2011, doi: 10.1016/j.joca.2011.05.008.

[34] M. Albersheim *et al.*, “Cell Count and Cell Density Decrease as Age Increases in Cadaveric Pediatric Medial Menisci,” *Arthrosc Sports Med Rehabil*, vol. 5, no. 6, Dec. 2023, doi: 10.1016/j.asmr.2023.100795.

[35] V. MARCOS-GARCÉS, M. HARVAT, P. MOLINA AGUILAR, A. FERRÁNDEZ IZQUIERDO, and A. RUIZ-SAURÍ, “Comparative measurement of collagen bundle orientation by Fourier analysis and semiquantitative evaluation: reliability and agreement in Masson’s trichrome, Picrosirius red and confocal microscopy techniques,” *J Microsc*, vol. 267, no. 2, pp. 130–142, Aug. 2017, doi: 10.1111/jmi.12553.

[36] A. Alibegović, R. Blagus, and I. Z. Martinez, “Safranin O without fast green is the best staining method for testing the degradation of macromolecules in a cartilage extracellular matrix for the determination of the postmortem interval,” *Forensic Sci Med Pathol*, vol. 16, no. 2, pp. 252–258, Jun. 2020, doi: 10.1007/s12024-019-00208-0.

[37] K. M. Kjosness, P. L. Reno, and M. A. Serrat, “Modified Periodic <scp>Acid-Schiff</scp> (<scp>PAS</scp>) Is an Alternative to Safranin O for Discriminating Bone–Cartilage Interfaces,” *JBMR Plus*, vol. 7, no. 6, Jun. 2023, doi: 10.1002/jbm4.10742.

[38] Y. Sun *et al.*, “Histological examination of collagen and proteoglycan changes in osteoarthritic menisci.,” *Open Rheumatol J*, vol. 6, pp. 24–32, 2012, doi: 10.2174/1874312901206010024.

[39] T. Videman, I. Eronen, C. Friman, and A. Langenskiöld, “Glycosaminoglycan Metabolism of the Medial Meniscus, the Medial Collateral Ligament and the Hip Joint Capsule in Experimental Osteoarthritis Caused by Immobilization of the Rabbit Knee,” *Acta Orthop Scand*, vol. 50, no. 4, pp. 465–470, Jan. 1979, doi: 10.3109/17453677908989791.

[40] M. Djurasovic, J. W. Aldridge, R. Grumbles, M. P. Rosenwasser, D. Howell, and A. Ratcliffe, “Knee Joint Immobilization Decreases Aggrecan Gene Expression in the Meniscus,” *Am J Sports Med*, vol. 26, no. 3, pp. 460–466, May 1998, doi: 10.1177/03635465980260032101.

[41] S. Saarakkala, P. Julkunen, P. Kiviranta, J. Mäkitalo, J. S. Jurvelin, and R. K. Korhonen, “Depth-wise progression of osteoarthritis in human articular cartilage: investigation of composition, structure and biomechanics,” *Osteoarthritis Cartilage*, vol. 18, no. 1, pp. 73–81, Jan. 2010, doi: 10.1016/j.joca.2009.08.003.

[42] A. Lahm *et al.*, “Changes in content and synthesis of collagen types and proteoglycans in osteoarthritis of the knee joint and comparison of quantitative analysis with Photoshop-based image analysis,” *Arch Orthop Trauma Surg*, vol. 130, no. 4, pp. 557–564, Apr. 2010, doi: 10.1007/s00402-009-0981-y.

[43] G. R. Squires, S. Okouneff, M. Ionescu, and A. R. Poole, “The pathobiology of focal lesion development in aging human articular cartilage and molecular matrix changes characteristic of osteoarthritis,” *Arthritis Rheum*, vol. 48, no. 5, pp. 1261–1270, May 2003, doi: 10.1002/art.10976.

[44] J. A. ’Buckwalter, H. J. ’Mankin, and A. J. ’Grodzinsky, “Articular cartilage and osteoarthrits,” *Instr Course Lect 2005*, vol. 54, pp. 465–480, 2005.

[45] S. D. Masouros, I. D. McDermott, A. A. Amis, and A. M. J. Bull, “Biomechanics of the meniscus-meniscal ligament construct of the knee,” *Knee Surgery, Sports Traumatology, Arthroscopy*, vol. 16, no. 12, pp. 1121–1132, Dec. 2008, doi: 10.1007/s00167-008-0616-9.

[46] P. E. Gelber, B. Barenius, and S. Perelli, “Role of Alignment and Osteotomy in Meniscal Injuries,” *Clin Sports Med*, vol. 39, no. 1, pp. 211–221, Jan. 2020, doi: 10.1016/j.csm.2019.08.006.

[47] D. Nikolopoulos, I. Michos, G. Safos, and P. Safos, “Current surgical strategies for total arthroplasty in valgus knee,” *World J Orthop*, vol. 6, no. 6, p. 469, 2015, doi: 10.5312/wjo.v6.i6.469.

[48] Q. Li *et al.*, “Biomechanical properties of murine meniscus surface via AFM-based nanoindentation,” *J Biomech*, vol. 48, no. 8, pp. 1364–1370, Jun. 2015, doi: 10.1016/j.jbiomech.2015.02.064.

[49] J. Sanchez-Adams, R. E. Wilusz, and F. Guilak, “Atomic force microscopy reveals regional variations in the micromechanical properties of the pericellular and extracellular matrices of the meniscus,” *Journal of Orthopaedic Research*, vol. 31, no. 8, pp. 1218–1225, Aug. 2013, doi: 10.1002/jor.22362.

[50] J. Kwok, S. Grogan, B. Meckes, F. Arce, R. Lal, and D. D’Lima, “Atomic force microscopy reveals age-dependent changes in nanomechanical properties of the extracellular matrix of native human menisci: implications for joint degeneration and osteoarthritis,” *Nanomedicine*, vol. 10, no. 8, pp. 1777–1785, Nov. 2014, doi: 10.1016/j.nano.2014.06.010.

[51] K. M. Fischenich, J. Lewis, K. A. Kindsfater, T. S. Bailey, and T. L. Haut Donahue, “Effects of degeneration on the compressive and tensile properties of human meniscus,” *J Biomech*, vol. 48, no. 8, pp. 1407–1411, Jun. 2015, doi: 10.1016/j.jbiomech.2015.02.042.

[52] B. Rasheed *et al.*, “Intraoperative identification of patient-specific elastic modulus of the meniscus during arthroscopy,” *Comput Methods Programs Biomed*, vol. 254, p. 108269, Sep. 2024, doi: 10.1016/j.cmpb.2024.108269.

[53] M. Turati *et al.*, “An increase in paediatric arthroscopy in Europe: Experience of the EPOS Sport Study Group,” *J Child Orthop*, vol. 19, no. 1, pp. 64–74, Feb. 2025, doi: 10.1177/18632521241302997.

[54] M. Hampton, F. Ali, N. Nicolaou, and A. Ajuied, “The management of isolated meniscal tears in skeletally immature children. An international expert consensus,” *Knee Surgery, Sports Traumatology, Arthroscopy*, Oct. 2024, doi: 10.1002/ksa.12493.

Meniscal extracellular matrix remodelling caused by injuries and degeneration

Maddalena Bracchi[1], Riccardo Campanile[1], Marco Crippa[1-3], Mario Mauri[1], Valeria Cassina[1], Francesco Mantegazza[1], Francesco Nicotra[1], Judith Waldner[1,2], Giovanni Zatti [1,2] , Marco Bigoni[1,3-4], Marco Turati[1-3]*, Laura Russo[1,2]*

[1]School of Medicine and Surgery, Università degli Studi di Milano-Bicocca, Monza, Italy

[2] Orthopedic Department, Fondazione IRCCS San Gerardo dei Tintori, Monza, Italy

[3] Transalpine Center of Pediatric Sports Medicine and Surgery, University of Milano-Bicocca - Hospital Couple Enfant, Monza (Italy), Grenoble, France

[4] Department of Orthopedic Surgery, Policlinico San Pietro, Ponte San Pietro, Italy

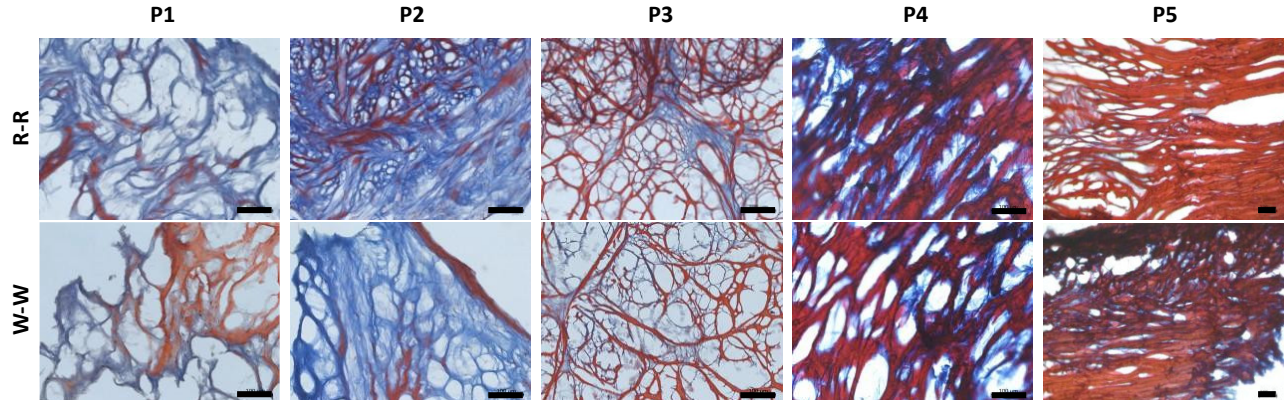

Figure S1 20X magnification of Masson Trichrome on P1-P5, scale bar 100µm

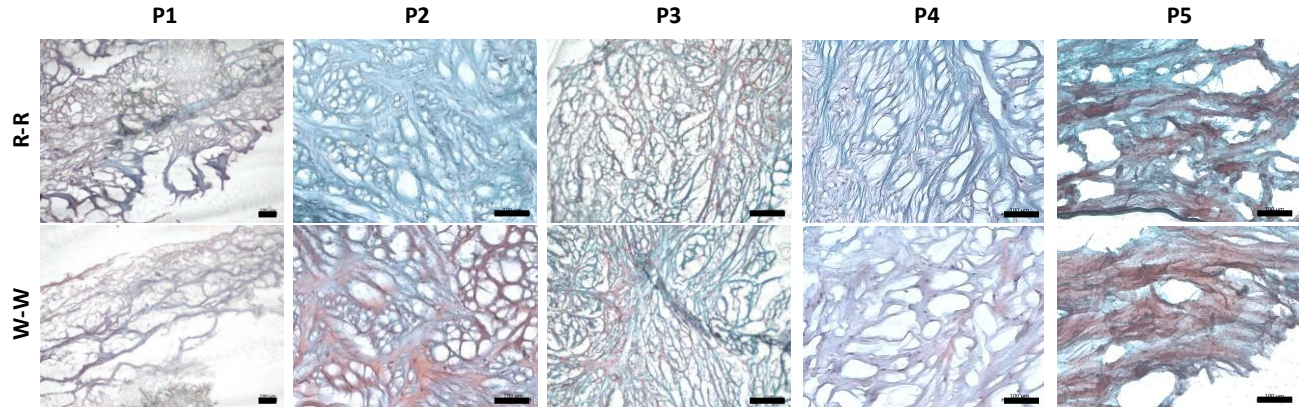

Figure S2 20X magnification of Safranin-Fast Green on P1-P5, scale bar 100µm

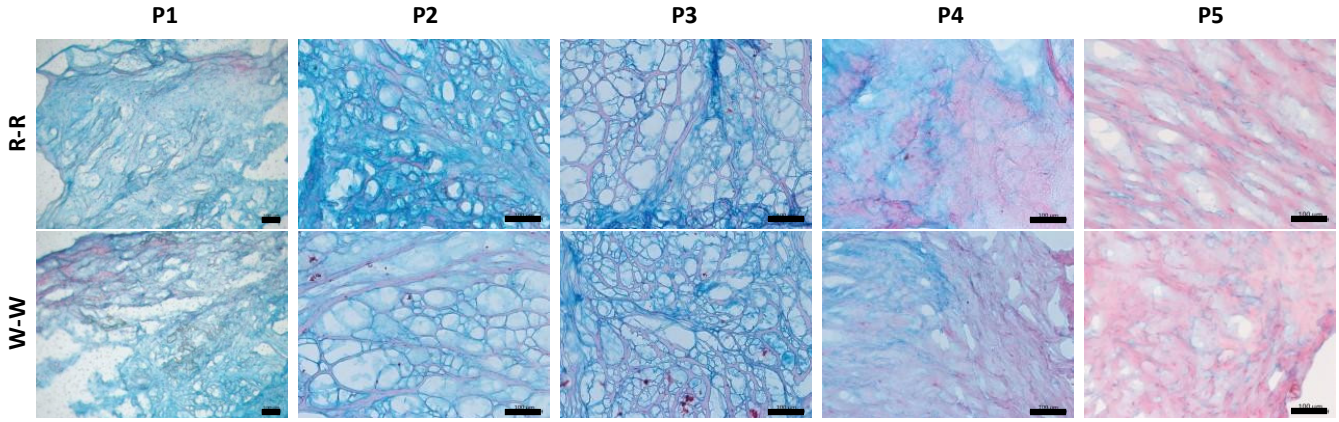

Figure S3 20X magnification of Alcian Blue on P1-P5, scale bar 100µm

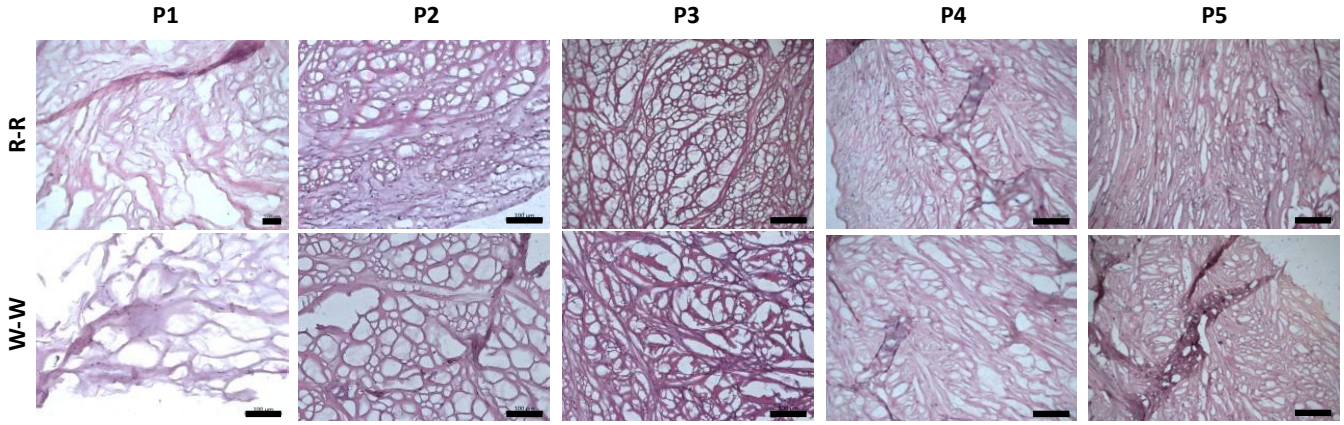

Figure S4 20X magnification of Haematoxilin-Eosin on P1-P5, scale bar 100µm

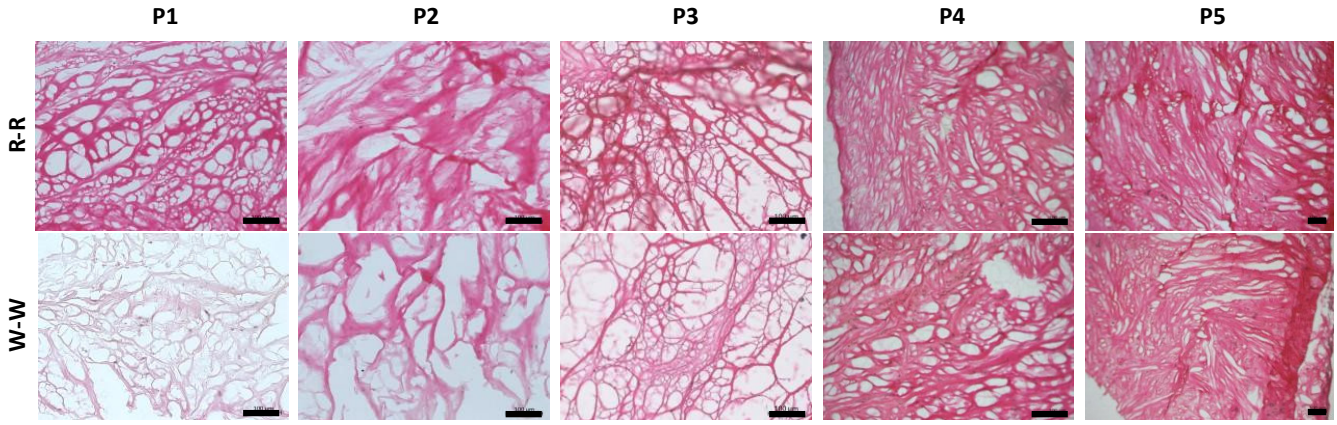

Figure S5 20X magnification of Van Gieson on P1-P5, scale bar 100µm

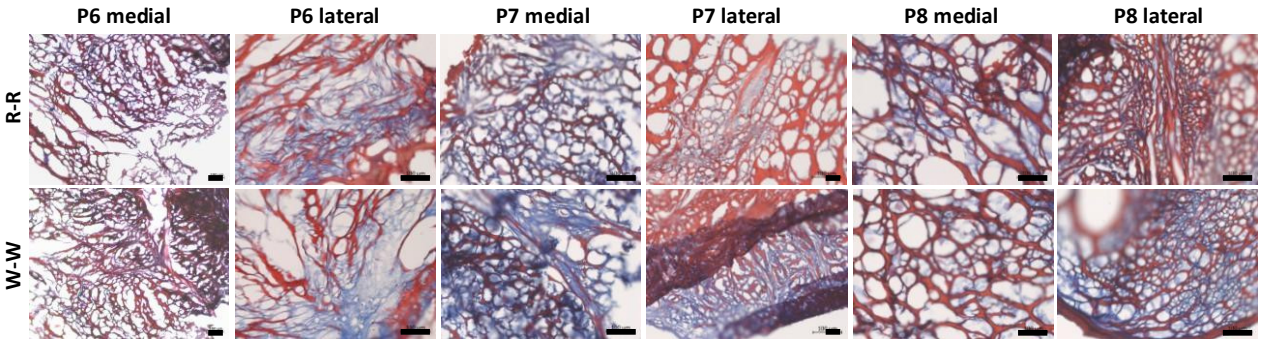

Figure S6 20X magnification of Masson Trichrome on P6-P8, scale bar 100µm

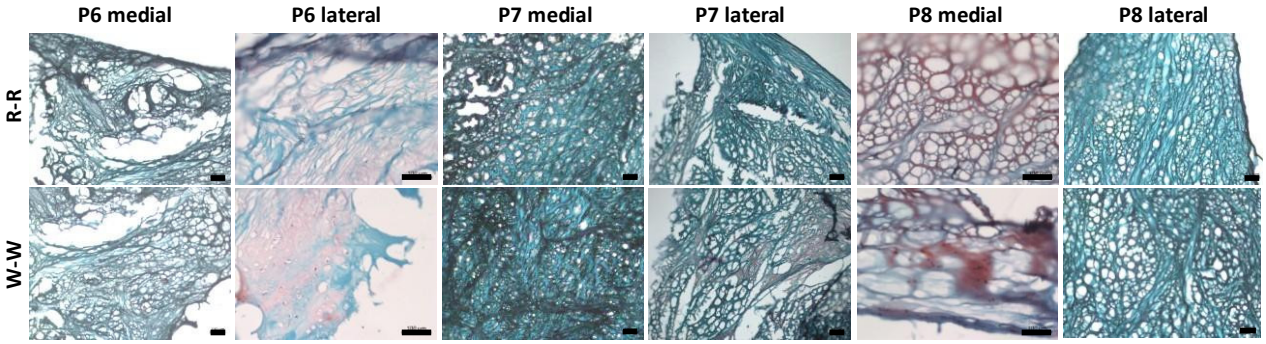

Figure S7 20X magnification of Safranin-Fast Green on P6-P8, scale bar 100µm

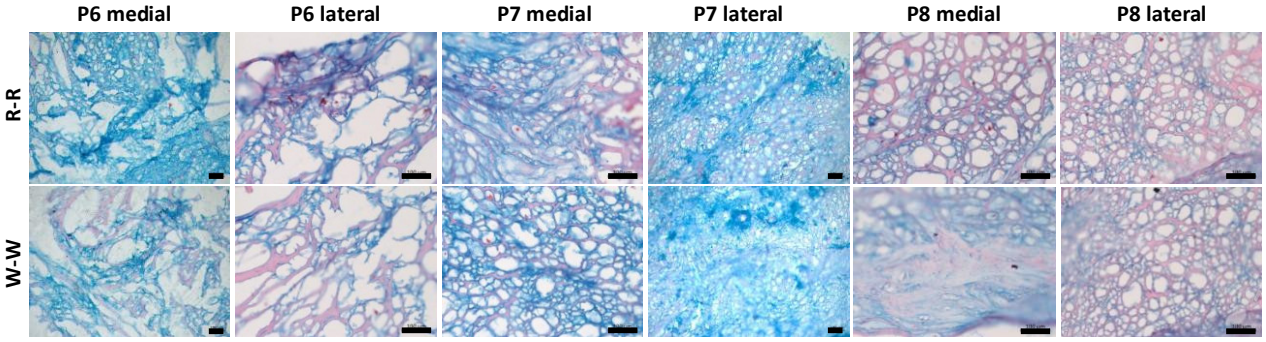

Figure S8 20X magnification of Alcian Blue on P6-P8, scale bar 100µm

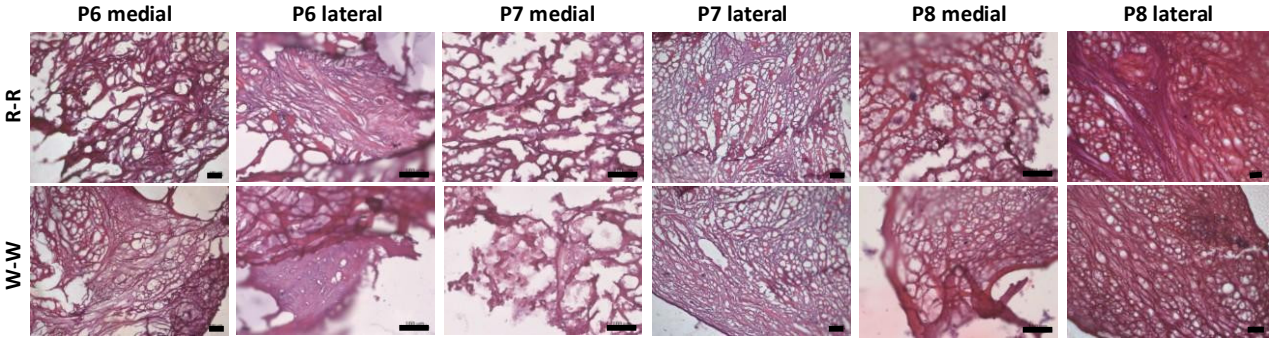

Figure S9 20X magnification of Haematoxilin-Eosin on P6-P8, scale bar 100µm

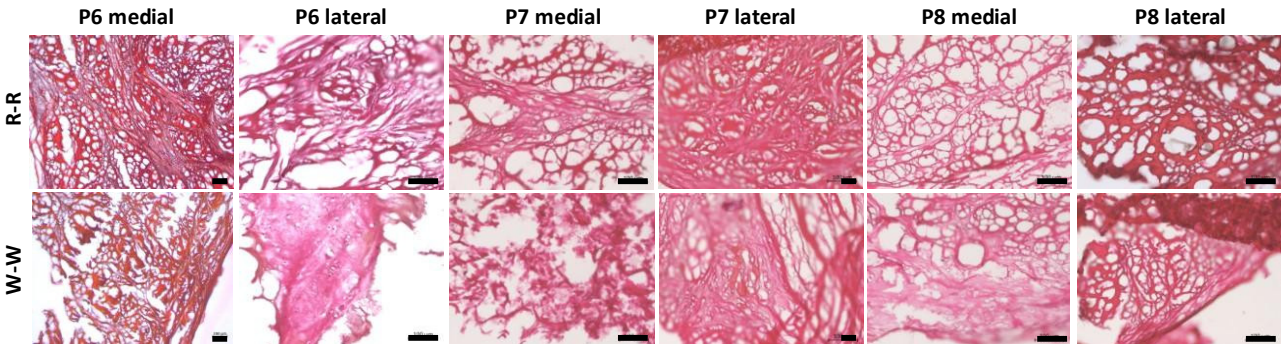

Figure S10 20X magnification of Van Gieson on P6-P8, scale bar 100µm

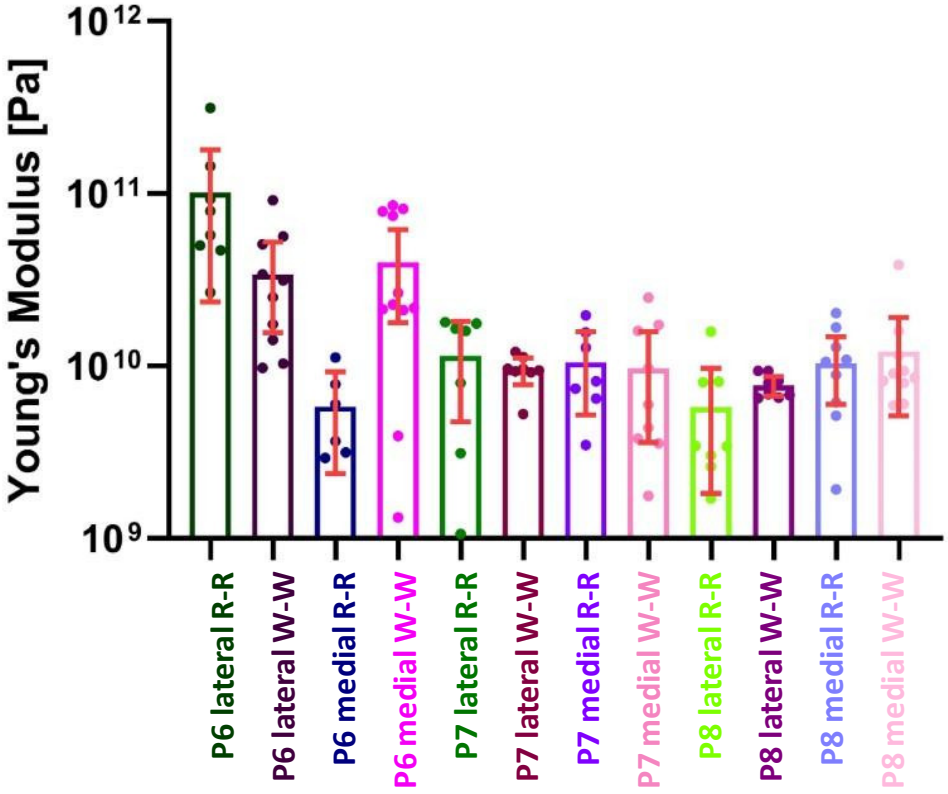

Figure S11 YM of medial, lateral, internal and external portions of P6, P7 and P8 meniscal tissue

Table S.1 ANOVA and multiple comparisons results

	Mean	**Groups**		
P7 medial W-W	5462.02	A		
P8 medial W-W	5057.16	A		

P8 lateral W-W	4761.59	A		
P6 medial W-W	3651.89	A	B	
P8 lateral R-R	1471.43		B	C
P7 lateral W-W	1098.82			C
P8 medial R-R	564.70			C
P6 lateral W-W	441.84			C
P7 medial R-R	253.05			C
P6 lateral R-R	207.15			C
P7 lateral R-R	182.26			C
P6 medial R-R	93.02			C

Nature Communications

https://doi.org/10.1038/s41467-025-68078-5

Article in Press

Reduction of bacterial colonization on buckling-induced wrinkled surfaces under fluid shear

Received: 18 May 2025

Accepted: 16 December 2025

Cite this article as: Pellegrino, L., Savorana, G., Cassina, V. *et al.* Reduction of bacterial colonization on buckling-induced wrinkled surfaces under fluid shear. *Nat Commun* (2025). https://doi.org/10.1038/s41467-025-68078-5

Luca Pellegrino, Giovanni Savorana, Valeria Cassina, Riccardo Campanile, Martin Centola, Cristina Belgiovine, Valeriano Vinci, Marco Klinger, Sigolène Lecuyer, Edoardo D'Imprima, Francesco Mantegazza, Eleonora Secchi & Roberto Rusconi

Reduction of bacterial colonization on buckling-induced wrinkled surfaces under fluid shear

Luca Pellegrino[1,2*], Giovanni Savorana[3], Valeria Cassina[4], Riccardo Campanile[4], Martin Centola[2,5], Cristina Belgiovine[6], Valeriano Vinci[1,2], Marco Klinger[2,7], Sigolène Lecuyer[8], Edoardo D'Imprima[2,5], Francesco Mantegazza[4], Eleonora Secchi[3], Roberto Rusconi[1,2*]

[1]Department of Biomedical Sciences, Humanitas University, 20072 Pieve Emanuele, Italy.
[2]IRCCS Humanitas Research Hospital, 20089 Rozzano, Italy.
[3]Institute of Environmental Engineering, ETH Zürich, 8093 Zürich, Switzerland.
[4]School of Medicine and Surgery, NANOMIB Nanomedicine Center, University of Milano-Bicocca, 20854 Vedano al Lambro, Italy.
[5]Correlative Light and Electron Microscopy Core, Humanitas University, 20072 Pieve Emanuele, Italy.
[6]Department of Biology and Biotechnology, University of Pavia, 27100 Pavia, Italy.
[7]Department of Medical Biotechnologies and Translational Medicine, University of Milan, 20133 Milan, Italy.
[8]Laboratoire de Physique (LPENSL UMR 5672), CNRS, ENS de Lyon, 69342 Lyon Cedex 07, France.

*Corresponding author(s). E-mail(s):
luca.pellegrino@humanitasresearch.it; roberto.rusconi@hunimed.eu;

Abstract

Microbial colonization and biofilm formation drive infection persistence and the spread of antimicrobial resistance, particularly under flow conditions typical of medical and natural environments. Here, we combine spontaneously buckled

wrinkled topographies with microfluidic platforms to investigate the adhesion of *Pseudomonas aeruginosa* and *Staphylococcus aureus* across shear rates of 0.4–200 s^{-1}. Wrinkled surfaces with tunable wavelengths (0.5–20 μm) are fabricated and characterized using optical, atomic force, and scanning electron microscopy. Sinusoidal wrinkles with a 2 μm wavelength reduce bacterial colonization by over 70% when oriented perpendicular to flow, while folded wrinkles of 5 μm achieve more than 90% reduction across broader shear regimes and suppress biofilm formation by over 85% relative to flat controls. These topographies retain antifouling performance under pulsatile flow. This work demonstrates a scalable, chemical-free strategy for passive biofilm control through geometric surface design, enabling durable antimicrobial materials for biomedical and industrial applications.

Introduction

Material surface properties critically influence bacterial adhesion through direct physicochemical interactions – such as roughness and surface energy – as well as indirect interactions mediated by adsorbed molecules or preconditioning films [1, 2]. Following irreversible attachment to a substrate, bacteria often develop matrix-encased colonies known as biofilms. Biofilms protect bacteria from immune responses and antibiotics, making them highly resilient and a leading cause of persistent infections [3].

The effects of nano- and microscale surface topography on bacterial attachment and subsequent biofilm formation have been explored through various mechanisms [4–8]. Nanoscale features can modulate surface energy, cell membrane deformation, and interfacial chemical gradients, mimicking the bactericidal properties of natural nanopatterns found on cicada and dragonfly wings [9–11]. In contrast, microscale structures (above 1 μm) primarily affect surface hydrodynamics, microbial entrapment, and surface conditioning [2, 12–14]. Topographies comparable in scale to bacterial dimensions ($\approx$ 1 to 3 μm) can direct spatial organization and proliferation by modulating key parameters such as periodicity, amplitude, and curvature. Specific geometries that reduce the available fouling area [15], limit adhesive contact points [16], or alter local curvature [17] can physically confine bacteria, restricting motility and intercellular connections [2, 18, 19] and thereby disrupting biofilm formation.

Natural biological tissues provide inspiration for such design strategies. Many interfaces – from cerebral cortices to skin and gut epithelia – exhibit wrinkled or folded morphologies arising from mechanical instabilities in layered systems [20, 21]. These topographies influence not only mechanical behavior but also biological interactions, shaping how cells, fluids, and microbes engage with surfaces. Reproducing and controlling these morphologies synthetically enables fundamental studies of bacterial adhesion and biofilm dynamics, as well as the design of functional surfaces for medical and industrial use [3]. Hydrodynamic conditions further complicate these interactions. In flowing environments, shear stress strongly affects bacterial attachment and colonization [22, 23]. The interplay between fluid dynamics and surface topography is complex, as local flow rates and mechanical stresses are governed by the geometry and spatial

arrangement of surface features [23, 24]. Although previous studies have investigated bacterial responses to either surface topography or hydrodynamic shear independently, their combined and dynamic effects remain poorly understood.

In this work, we investigate the coupled influence of surface-induced mechanical confinement and shear-induced local stress variations on bacterial colonization. We engineer buckling-induced wrinkled and folded topographies with controlled geometries and integrate them into microfluidic channels. Using *Pseudomonas aeruginosa* and *Staphylococcus aureus* – two clinically relevant pathogens associated with device-related infections – we demonstrate how wrinkling instabilities can be harnessed to mitigate bacterial adhesion and biofilm formation in biomedical and industrial contexts.

Results

Wrinkled patterns within microfluidic channels

Wrinkled patterns can be generated in multilayered structures subjected to mechanical deformation and plasma oxidation. Specifically, in a bilayer system consisting of a semi-infinite soft substrate of elastic modulus E_s and a thin, stiff top layer of elastic modulus E_f, spontaneous buckling instabilities arise under compression once a critical strain (ϵ_c) is exceeded. The resulting buckling regime depends on both the magnitude and direction of the applied strain (ϵ). For moderate strains (up to $\sim$20%), a sinusoidal wrinkling mode emerges, characterized by a wavelength (λ) and amplitude (A) dictated by the mechanical mismatch between the bilayer components (Methods), with an aspect ratio of A/λ ranging from 0.1 to 0.2. At higher compressions ($\sim$40%), purely sinusoidal wrinkles transition into folds, ridges, creases, or even delaminated buckling, depending on the bending energy of the film, the viscoelastic properties of the substrate, and the interfacial energies [25]. Building upon prior studies of wrinkling mechanics [15, 26–33], we engineered patterned surfaces with prescribed wavelengths and topographies, constructing a phase diagram of the explored wrinkling instabilities (Fig. 1a).

We focused on two distinct pattern modes: sinusoidal wrinkling (w_s) with periodicities (λ) of 0.5 μm and 2 μm, and doubling/folding (w_f) patterns with λ of 5 μm and 20 μm (Fig. 1a). These patterns were generated through plasma oxidation of silicone polymers [30, 31]. The formation of sinusoidal wrinkled surfaces was controlled by adjusting the stiffness of the polydimethylsiloxane (PDMS) bilayer, while, to induce folding, a lower modulus mismatch between the bilayer components was required. This was accomplished using Ecoflex ($E_s \approx 100$ kPa) as the foundation material, which enabled a purely folding instability under 50% compressive strain [25, 34]. Details of the fabrication process are provided in the Methods section. To preserve the mechanical properties of the bilayer materials and the integrity of the wrinkled patterns, we eliminated the glassy layer formed during PDMS and Ecoflex surface vitrification using a replication strategy. This involved silanization with octadecyltrichlorosilane (OTS), followed by PDMS molding. Because a single silanization-replication step inverts the

surface topography, we performed a double replication to restore the original concavity. The first replica was gently plasma-oxidized, passivated in ethanol vapor to remove unreacted PDMS monomers, and then molded with fresh PDMS.

The w_s and w_f patterned surfaces were integrated into a custom-designed microfluidic device, hereafter referred to as the 'microfluidic wrinkling' device (Fig. 1b). These patterned surfaces formed the bottom of a microfluidic channels with a rectangular cross-section of 800 μm x 70 μm (width $\times$ height) and oriented in two configurations, namely according to the flow direction ($w_{s\parallel}, w_{f\parallel}$) and perpendicular to the flow direction ($w_{s\perp}, w_{f\perp}$). Multiple channels were assembled on a microscope glass slide to enable direct visualization. We used this setup to investigate the colonization of wrinkled surfaces by pathogenic bacteria, employing phase-contrast and fluorescence imaging on an inverted microscope (Methods) and atomic force microscopy (AFM) for high-resolution surface and bacteria characterization (Fig. 1c).

To investigate the impact of surface topography on fluid flow, we performed numerical simulations of rod-shaped bacteria attached to sinusoidal w_s and folding w_f surfaces (Methods). Wrinkled profiles significantly alter the local shear field, generating stress concentration points at the hilltops where the calculated shear rate is 2–3 times higher than that of a flat surface (Fig. 2a). When a bacterium settles in the valley regions, corresponding to the periodic minima of the sinusoid (Fig. 2b, left), the contact area is maximized while the experienced flow velocity and shear stress are minimized, creating favorable conditions for attachment. In contrast, a bacterium positioned at the hilltops, perpendicular to the pattern direction, has limited contact area, primarily at its poles (Fig. 2b, right), and experiences shear stress hotspots. Notably, these stress enhancements were more pronounced for sinusoidal patterns oriented perpendicular rather than parallel to the flow, as the fluid directly interacts with the polar region of the cell. On $w_{f\perp}$ surfaces with $\lambda = 5$ μm and $A/\lambda = 0.4$, the folding geometry further modifies the shear rate distribution, producing hotspots up to 4 times higher than on flat surfaces (Fig. 2c). For the same geometry but with larger wavelengths ($\lambda = 20$ μm) and lower aspect ratio ($A/\lambda = 0.2$), the pattern length scales exceed bacterial dimensions, creating larger low-shear regions (Fig. 2d). Comparing velocity streamlines for $w_{f\perp}$ surfaces with $A/\lambda = 0.4$ (Fig. 2e, left) and $w_{s\perp}$ surfaces with $A/\lambda = 0.25$ (Fig. 2e, right), recirculation zones were observed only for the former folding pattern.

Our simulations demonstrate that surface topography critically shapes local hydrodynamic conditions by redistributing shear stresses at the cell–fluid interface. On sinusoidal features, ridge crests concentrate shear due to curvature-induced flow acceleration, whereas valleys act as stagnation zones with reduced velocity gradients. This is consistent with prior theoretical studies showing that curvature generates stress concentration points and alters near-wall shear layers [35]. Folding geometries with $\lambda = 5$ μm and $A/\lambda = 0.4$ further amplify these effects: they not only elevate local shear by up to fourfold compared to flat surfaces but also induce localized recirculation zones. Such recirculation may act to further inhibit bacterial settlement [2, 19], thereby reinforcing the antifouling potential of these topographies.

Effect of fluid shear on the attachment of *Pseudomonas aeruginosa* on wrinkled surfaces

Building on insights from our numerical simulations of bacterial attachment to patterned surfaces, we conducted experimental investigations using the microfluidic wrinkling device. A suspension of GFP-labeled *P. aeruginosa* PA14 cells (OD_{600} = 0.2) was introduced at an average shear rate of $\dot{\gamma} = 80\ s^{-1}$, a value comparable to that encountered in catheters and stents [3, 22]. The surfaces under study included a flat control (F), $w_{s\parallel}$, and $w_{s\perp}$, with a wavelength of 2 μm. Fluorescence and phase-contrast imaging (Supplementary Information, Fig. S1) were used to analyze the behavior of PA14 on these surfaces over a 4-hour period. On flat surfaces, *P. aeruginosa* formed individual colonies that expanded and proliferated randomly across the surface. In contrast, bacterial colonization was reduced on both $w_{s\parallel}$ and $w_{s\perp}$ surfaces.

We then examined bacterial surface coverage on the sinusoidal 2 μm wrinkled surface across a range of shear rates (0.4 to 200 s^{-1}) that mimic physiological conditions [3, 22, 36]. To quantify bacterial colonization within the first 4 hours of exposure to flowing bacterial suspensions, we calculated the surface coverage (S_c), defined as the percentage of surface area covered by bacterial cells, as well as the normalized surface coverage (S_c/S_F), where S_F denotes the coverage on flat control surfaces at the corresponding time point. Our analysis revealed that the normalized surface coverage on both $w_{s\parallel}$ and $w_{s\perp}$ surfaces decreased with increasing shear rates (Fig. 3a-b).

To assess the effect of flow direction relative to the surface pattern, we analyzed bacterial orientation on F, $w_{s\parallel}$, and $w_{s\perp}$ surfaces at the 2-hour mark using a computed probability distribution function (PDF) (Fig. 3c). Fluorescence images were segmented into discrete sections, and fast Fourier transform (FFT) techniques were applied to determine bacterial orientation relative to both the wrinkles and the imposed flow direction. By combining individual FFTs, we obtained an overall PDF, which provided insights into the angular distribution of PA14 cells. On flat surfaces, the PDF spanned the full angular range, with a slight polarization at zero radians, indicating weak alignment along the flow direction due to fluid shear, an effect already observed for microscale, elongated particles [37]. In contrast, surface patterning significantly affected orientation. On $w_{s\parallel}$ surfaces, bacteria exhibited a pronounced alignment where flow and pattern direction were parallel. On $w_{s\perp}$ surfaces, where wrinkles opposed the flow, bacterial orientation was evenly distributed between the pattern direction ($\pm\ \pi/2$ radians) and the flow direction (zero radians). These effects were evident in the FFT insets of Fig. 3c, which showed an isotropic circular distribution on flat surfaces (top), an elongated ellipse aligned with both flow and pattern directions on $w_{s\parallel}$ (center), and a cross-shaped distribution resulting from the competing influences of flow and surface patterning on $w_{s\perp}$ (bottom). Furthermore, AFM imaging revealed distinct bacterial organization across the different surfaces (Supplementary Information, Fig. S2). After the experiment, the microfluidic winkling chip was filled with 4% paraformaldehyde to fix bacterial cells before being opened for AFM imaging. The measured bacterial cell length of 2.5-3 μm on the F control was consistent with existing literature [15]. However, on wrinkled surfaces, PA14 cells preferentially settled in pattern valleys, where their length was reduced to $\sim$2 μm, likely due to physical constraints [15].

Analyzing the surface coverage S_c on both w_s surfaces compared to a flat surface at the 3-hour time point, we observed three distinct regimes in response to varying shear rates (Fig. 3d). At low shear rates (0.4 s^{-1}), wrinkled surfaces exhibited slightly higher bacterial coverage than flat surfaces, a phenomenon we termed *low-shear adhesion*. In this regime, bacteria tend to occupy the entire available surface without hindrance from shear forces. The orientation of the pattern has minimal influence on colonization, as motile PA14 cells can adhere to both $w_{s\parallel}$ and $w_{s\perp}$ surfaces without significant differences. However, at shear rates exceeding $\sim$1 s^{-1}, a transition occurs. Flat surfaces exhibited increased bacterial coverage with rising shear rates, consistent with prior reports showing that motile bacteria become trapped in high-shear regions of Poiseuille flow, which enhances encounter frequency and promotes surface colonization [22]. In contrast, on both $w_{s\parallel}$ and $w_{s\perp}$ wrinkled surfaces, bacterial coverage decreased as shear rate increased. This *shear-decreased adhesion* behavior occurs because, despite the modest increase in surface area ($\sim$10%, Methods) and the near-wall accumulation driven by shear trapping, bacterial colonization is confined primarily to the low-shear valleys of the sinusoidal pattern. These valleys represent approximately 60–70% of the total surface area relative to an equivalent flat substrate, owing to their slightly broader and deeper geometry compared to the ridge crests. This estimate was obtained from line-integral analysis of the sinusoidal profile and validated by AFM cross-sectional imaging [15].In contrast, adhesion at the peaks is reduced by elevated local wall shear stress and by limited effective contact with the surface. Consequently, motile bacteria must reorient through tumbling or twitching to achieve stable attachment; failure to do so leads to detachment by fluid flow, an effect that becomes more pronounced at higher shear rates. Detachment is further amplified on $w_{s\perp}$ surfaces, where the misalignment between flow direction and surface pattern enhances removal, as schematically shown in Fig. 3d. Together, these findings demonstrate that the interplay between surface topography and shear forces critically shapes bacterial adhesion, with wrinkled surfaces selectively suppressing colonization under elevated shear rates.

Impact of surface wrinkling on the attachment of non-motile *Pseudomonas aeruginosa* mutants

To examine the role of motility in bacterial surface coverage on wrinkled surfaces, we compared the behavior of the wild-type PA14 strain with a non-motile mutant lacking the flagellar motor, PA14 $\Delta motABCD$ (Fig. 4a-b). The shear-induced adhesion on the flat substrate observed for the wild-type strain was notably less pronounced in the mutant (Fig. 4c; Supplementary Information, Fig. S3), consistent with expectations for non-motile microswimmers [22]. Unlike the wild-type strain, the mutant initially exhibited an increase in surface coverage on both wrinkled surfaces, followed by a gradual decline, indicating detachment across all tested shear rates. The transition point from attachment to detachment varied with shear rate, occurring earlier at higher shear rates. Analyzing the normalized surface coverage relative to an equivalent flat surface (S_c/S_F) as a function of shear rate for both strains and surface types revealed a significant reduction in coverage for the mutant, particularly on $w_\perp$ surfaces (Fig. 4c).

Similar to passive particles, non-motile bacteria attach to surfaces only when their transporting streamline brings them into sufficient contact. Moreover, their attachment is weaker than that observed in wild-type strains, leading to shear-induced detachment at earlier time points. When bacteria encounter an unfavorable orientation relative to the surface pattern, motility allows them to reposition and achieve more favorable attachment conditions to resist fluid shear. However, the non-motile PA14 $\Delta motABCD$ strain lacks this ability, causing bacterial cells to behave as passive rods [37]. As a result, attachment under these conditions depends on the frequency of successful positioning events, and the absence of repositioning, combined with early detachment in high shear environments, explains the lower coverage observed on both $w_{s\parallel}$ and $w_{s\perp}$ surfaces. This underscores the critical role of bacterial motility in adapting to dynamic environments, directly influencing attachment outcomes under mechanical constraints and fluid shear forces.

Influence of buckling regimes on *Pseudomonas aeruginosa* surface colonization

The colonization of *P. aeruginosa* on wrinkled surfaces is dictated by the interplay between surface topography and fluid flow. As shown in Fig. 1a, different pattern morphologies arise depending on the mechanical strain applied to the bilayer during fabrication. Specifically, w_s surfaces exhibit sinusoidal wrinkling, while w_f surfaces fall within the transitional regime between period doubling and folding. By definition, sinusoidal wrinkles are symmetric, with equal hilltop and valley areas. In contrast, folding patterns introduce asymmetry, with increased amplitude resulting from the progressive contact and merging of adjacent wrinkles. This post-buckling evolution transforms sinusoidal wrinkles into a new morphology characterized by deeper and narrower valleys, producing high-aspect-ratio structures. The formation of folds in Ecoflex bilayers results in larger wavelengths under identical plasma oxidation conditions compared to PDMS due to the lower modulus mismatch. In contrast, PDMS-plasma bilayers exhibit sinusoidal wrinkling because the higher modulus mismatch makes folding less energetically favorable. To quantify these morphological differences, we analyzed the curvature of the patterns using linear integration of 1D profiles extracted from AFM measurements (Supplementary information, Fig. S4). Symmetric sinusoidal patterns exhibit comparable minimum (κ_{min}) and maximum curvature (κ_{max}) curvature values, whereas folding leads to steeper inflection points, deeper valleys, and an overall increase in pattern amplitude. We hypothesized that the reduced accessible valley areas in folding patterns could constrain bacterial attachment to hilltop regions, where cells were more exposed to fluid shear and, as a result, more susceptible to detachment.

We performed microfluidic experiments on wrinkled surfaces with wavelengths of 5 μm and 20 μm, as well as on smaller sinusoidal patterns with a wavelength of 0.5 μm, to assess their effect on microbial colonization. Our results showed that the 5 μm pattern led to a further reduction in surface colonization – up to 99% compared to a flat surface (Supplementary Table 1) – relative to the 2 μm pattern at a shear rate of 80 s^{-1}. In contrast, higher surface coverage was observed on 0.5 μm and 20 μm patterns (Fig. 5a-b). Moreover, surface coverage data plotted as a function of the pattern aspect ratio (A/λ) display that surfaces with aspect ratios greater than 0.25

effectively delayed colonization (Fig. 5c). Pattern aspect ratios were quantified using cross-sectional scanning electron microscopy (SEM) images obtained through focused ion beam (FIB) milling (Fig. 5d; Supplementary Information, Fig. S5). The folding pattern with $\lambda = 5$ μm and an aspect ratio of 0.4 proved to be the most effective geometry in limiting bacterial colonization.

Our findings are summarized schematically in Fig. 5e, where 1D cross-sectional profiles were extracted from AFM analysis. On 0.5 μm w_s surfaces, the measured $A/\lambda = 0.05$ was insufficient to significantly influence bacterial adhesion. A similar trend was observed for shallower 20 μm folding patterns ($A/\lambda = 0.2$), where extensive 'flat-like' hilltop regions provided sufficient surface area for bacterial colonization. Although 2 μm w_s surfaces also effectively reduced PA14 coverage, the 5 μm w_f pattern emerged as the optimal compromise, combining a higher aspect ratio that effectively confined PA14 cells with an enhanced capacity for their removal by fluid flow. This effect was evident not only at 80 s^{-1}, consistent with the simulations shown in Fig. 2, but also across a broader range of shear rates (4–200 s^{-1}), as detailed in Supplementary Information (Fig. S6). For this pattern, orientation perpendicular to the flow direction further impaired surface coverage, including at lower flow rates and earlier colonization times. Overall, these results are consistent with our numerical simulations, which demonstrated that the combination of elevated shear at ridge crests and localized recirculation zones in valleys establishes hydrodynamic conditions that are unfavorable for stable bacterial attachment.

Role of buckling-induced surfaces in *Pseudomonas aeruginosa* colonization by type IV pili mutants

From our observations, the combination of sinusoidal ($w_{s\perp}$) and folding ($w_{f\perp}$) patterns with $0.25 < A/\lambda < 0.4$, together with fluid shear, was highly effective in reducing wild-type PA14 colonization. *Pseudomonas aeruginosa* is well known to rely on type IV pili (T4P) for adhesion, surface sensing, twitching motility, and biofilm initiation [38–41]. Understanding the role of T4P in surface colonization is therefore critical for explaining how surface topography and fluid shear shape bacterial attachment. While the effect of shear stress on pili-depleted PA14 on glass and flat surfaces has been previously investigated [42], we sought to build on these findings by examining the contribution of surface topography and pili-dependent adhesion mechanisms. To this end, we tested our $w_{s\perp}$ and $w_{f\perp}$ patterns using the PA14 Δ*pilB* mutant.

The *pilB* gene encodes the extension ATPase required for producing dynamic type IV pili, which mediate initial attachment, mechanical sensing, and twitching motility. These functions promote bacterial accumulation in sheltered microenvironments and trigger downstream signaling pathways (e.g., cAMP and c-di-GMP) that drive biofilm initiation. In our experiments (Fig. 6a–b), PA14Δ*pilB* exhibited the same qualitative response to increasing shear and surface topography as the wild-type strain: surface coverage decreased with increasing shear, and surfaces with $A/\lambda = 0.4$ (5 μm folding wavelength) strongly limited colonization (Fig. 6c). However, compared with the wild-type, the Δ*pilB* strain consistently displayed lower coverage values across all conditions, indicating that T4P-mediated adhesion enhances the ability of *P. aeruginosa*

to exploit low-shear valleys and resist detachment at high-shear ridges. This underscores the critical role of T4P in mediating the combined effects of surface topography and fluid shear on bacterial colonization.

Reduction of *Staphylococcus aureus* surface colonization on wrinkled substrates

To evaluate the potential of buckling-induced wrinkled substrates in reducing bacterial colonization across different bacterial species, we tested their effect on *Staphylococcus aureus*, a Gram-positive pathogen, under fluid flow conditions. In contrast to *P. aeruginosa* PA14, a Gram-negative, motile, and ellipsoidal bacterium, *S. aureus* is non-motile, spheroidal, and typically measures between 1 and 1.5 μm in diameter. We selected the GFP-labeled *S. aureus* Newman strain [43], a clinically relevant human pathogen associated with strong virulence [44] and frequently implicated in nosocomial infections [45], bacteremia [46], endocarditis [47], and sepsis [48]. Furthermore, *S. aureus*, along with other Staphylococcus species, is a major contributor to periprosthetic joint infections, often leading to sepsis and implant failure in acute cases[49].

We first examined the effect of shear rate on 5 μm w_f surfaces (Fig. 7a) to assess whether the previously observed reduction in bacterial colonization also applied to *S. aureus*. Surface coverage analysis (Fig. 7b) confirmed that the shear-induced reduction in adhesion by the patterned surfaces persisted for this pathogenic strain, despite *S. aureus* displaying a higher overall surface coverage percentage ($S_c(\%)$) compared to *P. aeruginosa* PA14. Notably, while *S. aureus* exhibited stronger adhesion, the reduction in colonization on wrinkled surfaces remained substantial (close to 90%, Supplementary Table 1). To further investigate the impact of surface geometry, we evaluated bacterial attachment across the four different w_s and w_f surface wavelengths and analyzed coverage as a function of the pattern aspect ratio (Fig. 7c-d). Again, patterns with wavelengths of 2 μm and, more effectively, 5 μm significantly reduced bacterial colonization, supporting the idea of a synergistic pattern-decreased adhesion mechanism, further illustrated by the optical microscopy images (Fig. 7e). As observed with PA14 strains, these patterns hinder the establishment of stable adhesion sites. In contrast, the spherical morphology of *S. aureus* made adhesion insensitive to pattern orientation relative to fluid flow, as confirmed by the surface coverage data (Fig. 7b–d).

Effect of pulsatile flow on bacterial colonization on flat and wrinkled surfaces

To further analyze how patterned surfaces influence the attachment and removal of *P. aeruginosa* and *S. aureus* under physiologically relevant conditions, we performed additional experiments using a pulsatile flow regime representative of catheter and stent environments. Specifically, we tested $w_{f\perp}$ folding surfaces with $\lambda = 5$ μm. The syringe pump was programmed to alternate between $Q_{\min} = 0$ μl/min and $Q_{\max} = 4$ μl/min with a cycle period of $T = 10$ s, corresponding to a frequency of 0.1 Hz, which aligns with the bandwidth recommended for urodynamic measurements to capture physiological variations in urine flow [50]. The experiments were run for 900 cycles

(2.5 h), yielding an average flow rate of $\bar{Q} = 2$ μl/min, corresponding to an average shear rate of $\bar{\dot{\gamma}} = 80$ s^{-1} (Fig. 8a).

From the analysis of segmented microscopy images (Fig. 8b), we observed that both *S. aureus* and *P. aeruginosa* cells preferentially accumulated during the static phase ($Q_{\min}$). Upon transition to peak flow ($Q_{\max}$), exposure to shear rates of approximately $\dot{\gamma}_{\max} = 160$ s^{-1} induced rapid detachment events, a pattern consistently observed across successive pulsatile cycles (Fig. 8b). Overall, pulsatile flow on wrinkled surfaces led to an even stronger reduction in surface colonization than continuous-flow conditions at the same mean shear rate, and to significantly lower colonization than flat surfaces under pulsatile flow (Fig. 8c–d). These dynamics resemble a 'fill-and-flush' mechanism, where transient colonization occurs during quiescent intervals but is efficiently cleared during high-shear phases, with the folded surface geometry significantly amplifying this effect. Together, these findings highlight an additional dimension in the interplay between hydrodynamics and surface topography and further support the potential of wrinkled surfaces to mitigate colonization under conditions that more closely mimic those in medical devices.

Effect of pattern morphology and shear rate on biofilm formation

Our results demonstrate that w_s and w_f surface patterns in microfluidic wrinkling significantly reduce early-stage bacterial colonization for up to 4 hours under a wide range of fluid flow and shear conditions. To further assess the potential application of these surfaces in biomedical devices, we performed a 24-hour biofilm formation experiment comparing 5 μm w_f patterns, oriented perpendicular to the flow direction, to flat surfaces (Fig. 9). Propidium Iodide (PI), added at a final concentration of 1 μg/mL, was used to detect extracellular DNA (eDNA) associated with biofilm formation [51, 52]. A shear rate of 200 s^{-1}, representative of conditions found in urinary catheters [3], was applied during the experiment. We used a bacterial suspension with an optical density (OD) of 0.005, which corresponds to approximately 10^5 cells/mL, a relatively high concentration that represents an evident state of bacterial contamination and is relevant for clinical applications. On flat surfaces (F), PA14 WT formed large colonies at 12 hours, which continued to expand through 24 hours (Fig. 9a). In contrast, *S. aureus* Newman formed bigger colonies at 12 hours, highlighted by the strong binding of PI, eventually covering the entire surface by 24 hours (Fig. 9b). On $w_\perp$ surfaces, no biofilm formation was observed for PA14 WT, although colonies did form by 24 hours. For *S. aureus*, the valley regions of the $w_\perp$ surfaces were occupied, but full colony formation was not observed. These results highlight a significant reduction – i.e., more than 80% for both strains after 24 hours (Supplementary Table 2) – in biofilm formation, demonstrating the potential of wrinkled surface patterns in reducing bacterial colonization in medical device applications, even under a high level of bacterial contamination.

Discussion

Our study demonstrates that microfluidic wrinkled surface patterns with wavelengths of 2 μm–5 μm, generated through buckling instabilities, significantly reduce bacterial adhesion and biofilm formation under flow conditions. By evaluating *Pseudomonas aeruginosa* and *Staphylococcus aureus*, we found that these patterns effectively hinder bacterial colonization, even at high initial concentrations representative of clinical contamination. The reduction in surface coverage exceeded 90% under shear flow, underscoring the strong anti-adhesive properties of these substrates.

Biomedical devices and implants, particularly those subjected to fluid flow, such as urinary catheters and biliary stents, are highly susceptible to deterioration and fouling due to microbial colonization [3, 23, 53]. Catheters, which are widely used in hospitals for minimally invasive procedures – including urinary retention relief, blood sampling, nutrient transport, and dialysis – pose a significant risk of local or systemic infections as a result of bacterial attachment and biofilm formation [54, 55]. Conventional approaches to prevent device-related infections primarily rely on periodic antibiotic flushing or the locking technique, in which an antibiotic solution is retained within the device for a specified duration [56]. However, the widespread use of antibiotics in such settings has contributed to the emergence of multidrug-resistant (MDR) strains, limiting the effectiveness of these strategies [57]. In contrast, the implementation of wrinkled surface patterns offers an antibiotic-free approach to reduce bacterial colonization.

Our findings suggest that these microstructured surfaces can be seamlessly integrated into medical devices to significantly mitigate bacterial adhesion. These patterns could be generated through the buckling of laminated silicone tubes or replicated from 3D-printed negative masters, making them a scalable and cost-effective solution. By reducing initial bacterial attachment and biofilm formation, these surface modifications have the potential to extend device longevity, lower infection rates, and ultimately decrease the clinical reliance on antibiotics, thus addressing both medical and antimicrobial resistance challenges. Importantly, our results are most relevant to small-scale devices such as catheters and stents, where flow remains laminar but shear rates can still be significant due to the narrow radii of the conduits. Under these conditions, antifouling behavior emerges only when surface pattern dimensions are comparable to bacterial size, whereas larger wavelengths (e.g., 20 µm) lose this effect and instead promote colonization (Supplementary Information, Fig. S7). This distinction highlights the difference from shark riblet structures, which rely on larger scales, complex denticle geometries, and vortex dynamics in turbulent regimes to achieve antifouling performance [58].

To investigate the coupling between fluid flow and surface topography in bacterial colonization, we leveraged microfluidic technology. The integration of multiple patterned surfaces within a single microfluidic chip was crucial for enabling direct, side-by-side comparisons under identical experimental conditions. This approach ensured that bacterial attachment and biofilm formation were evaluated simultaneously on different surfaces, using the same bacterial suspension and controlled ambient parameters, eliminating variations that could arise from batch-to-batch differences [22]. Beyond its biomedical relevance, fluid flow is a defining feature of microbial habitats,

influencing colonization dynamics across a wide range of natural and artificial settings. The ability to control bacterial adhesion and biofilm formation through surface engineering has potential benefits in industries such as food processing, water filtration, and marine engineering. For instance, mitigating bacterial fouling on ship hulls could improve fuel efficiency and reduce maintenance costs. By providing a controlled platform to dissect the interplay between flow conditions and surface properties, our study highlights the broader potential of microfluidic wrinkled surfaces in microbial control strategies across multiple disciplines.

In addition to their role as anti-adhesive substrates, these microstructured surfaces provide a powerful platform for investigating the fundamental interactions between microbes and surface topography. By tuning the pattern geometry, such surfaces can be designed not only to influence bacterial attachment but also to affect bacterial motility, by altering, for instance, movement behaviors such as twitching [59] or swarming [60], and even modulating growth rates. Moreover, these patterned surfaces offer a unique opportunity to explore how eukaryotic cells, particularly immune cells, respond to complex topographies [61]. While immune cell behavior is known to be highly sensitive to microenvironmental cues, the role of surface topography in modulating immune responses remains poorly understood. Recent studies suggest that specific topographical features can promote chronic inflammation, yet the underlying mechanisms remain elusive [62]. The buckling-induced fabrication method employed in this study presents a distinct advantage by allowing the controlled evaluation of cellular responses to surface topography without altering the underlying material properties. This approach ensures that observed effects arise purely from topographical influences, making it an invaluable tool for studying microbe-surface and immune cell-surface interactions in both fundamental and applied biomedical research.

Overall, this work demonstrates that bacterial adhesion and early colonization are governed not by surface topography or shear alone, but by their combined and dynamic interaction. By introducing controlled wrinkling geometries into microfluidic channels, we revealed bacterial behaviors that cannot be explained by single-factor studies, providing a mechanistic basis for how flow and topography act together. Importantly, our additional experiments under pulsatile flow show that these interactions are also influenced by temporal variations in shear, indicating that time-dependent hydrodynamic cues can further regulate bacterial attachment. Taken together, these results move the field beyond static views of surface effects and point toward design principles that integrate both spatial and temporal control of flow and topography for biofilm management in biomedical, industrial, and environmental settings.

Methods

Patterned surfaces fabrication

Patterned surfaces were fabricated using plasma oxidation of polydimethylsiloxane (PDMS, Sylgard 184 kit, Dow Corning) and Ecoflex (Ecoflex 00-31 Near Clear, Smooth-On). The bilayer structure was generated through uniaxial stretch using a custom-built mechanical actuator, followed by plasma oxidation of a PDMS or Ecoflex substrate. Upon release of the applied strain beyond a critical threshold ϵ_c, a sinusoidal

buckling instability was induced, characterized by a wavelength λ and amplitude A, as described by

$$\epsilon_c = \frac{1}{4}\left(\frac{3\bar{E}_s}{\bar{E}_f}\right)^{\frac{2}{3}} \tag{1}$$

$$\lambda = 2\pi h\left(\frac{\bar{E}_f}{3\bar{E}_s}\right)^{\frac{1}{3}} \tag{2}$$

$$A = h\left(\frac{\epsilon}{\epsilon_c} - 1\right)^{\frac{1}{2}} \tag{3}$$

where h is the thickness of the oxidized stiff skin, while $\bar{E}_f$ and $\bar{E}_s$ represent the plane strain modulus and the substrate modulus, respectively. λ is defined as the peak-to-peak distance of the sinusoidal profile, and A as the half of the profile height. By adjusting the applied strain and the plasma treatment parameters (exposure time and power), different geometries can be fabricated. Specifically, 0.5 μm w_s sinusoidal surfaces where obtained by stretching a 2 mm-thick PDMS coupon at $\epsilon = 20\%$ and plasma treating it for 30 minutes in a MHz plasma chamber (Harrick). The 2 μm w_s sinusoidal surfaces were fabricated using the same strain conditions but with a 5-minute exposure in a kHz plasma chamber (Diener Femto). The 5 μm w_f surfaces were produced by stretching a 2 mm-thick Ecoflex coupon to 80% strain and exposing it to plasma oxidation for 2 minutes in the MHz plasma chamber. 20 μm w_f surfaces were obtained by stretching a 2 mm-thick Ecoflex coupon to 50% strain and applying 15 minutes of plasma oxidation in the MHz plasma chamber. Pattern characterization was carried out using phase-contrast optical microscopy, SEM, and AFM. Wavelengths in the range of 2 μm to 20 μm were measured by phase-contrast optical microscopy at 40X and 60X magnification and confirmed by AFM. For each sample, at least 20 measurements were collected across different regions and averaged. AFM was further used to obtain full topographical maps, enabling precise quantification of pattern amplitude and validation of the optical wavelength measurements. SEM provided large-area visualization of the surface morphology as well as cross-sectional imaging of the patterns.

Microfluidic assays

For all the experiments, we fabricated a microfluidic chip consisting of six parallel straight channels (Fig. 1a) in PDMS, molded from a silicon master wafer. The chip was assembled by plasma bonding the flat and wrinkled surfaces to the PDMS channels. A syringe pump (Harvard Apparatus) was used to perfuse the channels, allowing simultaneous experiments at five different shear rates. For each experiment, syringes were loaded with fresh Tryptone Broth (TB) or Columbia Broth (CB), depending on the bacterial strain. Syringe volumes ranged from 1 to 5 mL, depending on the flow rate. The bacterial inoculum was prepared by measuring the optical density at 600 nm (OD_{600}) and adjusting it to the desired concentration, optimized from previous calibration experiments in microfluidic channels. Specifically, an inoculum of $OD_{600} = 0.2$ ($\sim 10^8$ cells) was used for colonization experiments, while $OD_{600} = 0.005$ was used for biofilm formation assays.

Bacterial cultures

The bacterial strains used in this study were *Pseudomonas aeruginosa* wild-type (PA14 WT), the motility-deficient mutant PA14Δ*motABCD* (O'Toole strain 2128, 2127), the pili-deficient mutant PA14Δ*pilB* (Kolter collection number ZK3351), and *Staphylococcus aureus* Newman strain tagged with GFP (NCTC 10833). Bacterial suspensions were prepared by inoculating colonies from agar plates into 3 mL of Terrific Broth (TB, 14 g L^{-1} tryptone) for *P. aeruginosa* strains and Columbia Broth (CB, BD DIFCO, 30 g L^{-1}) for *S. aureus*. Cultures were incubated at 37°C for 4 hours. Following incubation, suspensions were diluted with fresh medium to the desidered concentration. Fluorescent labeling of PA14 WT was performed using a CellTracker^{TM} Green (Thermo Fisher Scientific) at a final concentration of 3 mM. Cells were incubated at room temperature for 15 minutes, centrifuged at 2683 RCF to remove the excess dye, and resuspended in fresh medium to the final concentration.

Image acquisition and analysis

Bacterial spatial distribution under flow was analyzed using fluorescence and phase-contrast microscopy (20X and 40X magnification) on an inverted microscope (Leica DMi8, LAS X 3.10.0.28982, MetaMorph 7.10.1.161) equipped with an automated stage and temperature-controlled incubator. Images were acquired every five minutes in three different regions of the microfluidic channels, with at least three replicate experiments. Image processing and segmentation were performed using Fiji (ImageJ 1.54p [63]) and Ilastik (Ilastik 1.4.0.post1), a machine learning-based segmentation toolkit [64]. High-resolution imaging of bacterial cells was conducted using atomic force microscopy (AFM, Nanowizard IV XP, JPK Instruments, Germany) in tapping mode under ambient conditions. Scans were performed over a 50 μm by 50 μm region at 0.5 Hz. Bacterial orientation analysis was performed by dividing fluorescence microscopy images into grids and applying a local fast FFT to each subimage/tile separately. The individual FFTs were then averaged to obtain the angular probability density function (PDF) of bacterial alignment relative to the flow direction. Statistical analyses were performed on datasets comprising at least $N = 500$ individual cells per frame. For each experimental condition, three frames were acquired per microfluidic channel, and three independent channels were analyzed as technical replicates. Each experiment was repeated on three separate days to provide biological replicates.

Sample preparation for SEM imaging

Bacterial fixation was performed by flowing a 4% paraformaldehyde (PFA) solution through the microfluidic channels, followed by a 15-minute incubation at room temperature. After fixation, channels were flushed with deionized (DI) water and dried. For imaging, circular patches of PDMS and Ecoflex were obtained using a 8 mm biopsy punch. These discs were mounted on standard SEM stubs (Zeiss, 12.5 mm diameter) using carbon conductive tape (PELCO/Ted Pella). In some cases, samples were cut into thinner strips using a razor blade and mounted on SEM stubs with conductive carbon tape. To ensure stable attachment and improve electrical grounding, a small drop of conductive silver paint (L200N, Agar Scientific) was applied. A thin conductive

chromium layer was sputter-coated onto the samples using a Quorum Q150T ES Plus sputter coater equipped with a 57 mm Cr target (Quorum Technologies). Sputtering parameters were set to 120 mA for 20 seconds, with a tooling factor of 2.30. Samples with bacteria underwent the same metallization procedure following PFA fixation.

FIB-SEM imaging and milling

Samples were imaged using a Zeiss Crossbeam 550 FIB-SEM microscope (Carl Zeiss AG, Jena, Germany). SEM imaging was performed at an accelerating voltage of 5 kV using the secondary electron detector. The working distance was set to 5.1 mm, corresponding to the eucentric height of the FIB beam. To maximize contrast, images were acquired in line averaging mode, with each line sampled 10 times. The scan speed was set to 5, resulting in an acquisition time of approximately 3.5 minutes per image at a resolution of 4096 × 3072 pixels. Overview images were taken at magnifications of 65× (pixel spacing: 429.4 nm), and 250× (pixel spacing: 116.5 nm). Higher-magnification images were acquired using dedicated magnification depending on the wavelength of the pattern. Gallium ion FIB milling was performed at 30 kV in bidirectional scanning mode using SmartFIB, with cycle mode set to loop. The milling current was empirically determined to achieve a clean cut without damaging the sample. The track and pixel spacing were set to 50%, and the ion dose was maintained at 200 $mC\ cm^{-2}$. Tilt compensation was applied during image acquisition to ensure accurate measurement of the ridge depths.

CFD simulations

We characterized the flow field inside the microchannels with wrinkled walls at different wavelengths and geometries by performing 3D numerical simulations with COMSOL Multiphysics 6.0 (COMSOL AB, Stockholm, Sweden). The hydrodynamic problem was solved using the Laminar Flow interface of the CFD module, implementing the incompressible form of the Navier–Stokes and continuity equations. To optimize computational efficiency, we set a vertical symmetry plane at the centerline of the channel and solved the equations for only one-half of the geometry. By exploiting the periodicity of the patterned surfaces, we applied periodic boundary conditions and simulated only a short portion of channel in the direction of flow, assigning the inlet and outlet as source and destination surfaces, respectively. The pressure difference $\Delta p = p_{src} - p_{dst}$ between source and destination surfaces was set to match the experimental average velocity U inside the channel. Δp was calculated during the simulations as the pressure value satisfying the additional global equation $U - u_{in}^{av} = 0$, where $u_{in}^{av} = 0$ is the average velocity value of the numerical solution at the inlet. For patterns perpendicular to the flow direction, we used a periodic box with length $L = 10\lambda$ in the direction of flow. For patterns aligned to the direction of flow, we set $L = \lambda$. In both configurations, the mesh was swept along the pattern direction and consisted of approximately $1.5 \cdot 10^5$ elements. To analyze the flow field near surface-attached bacterial cells, we incorporated 3D objects representing individual bacteria within the simulated microchannel. Each bacterium was modeled as a cylinder with hemispherical caps, with radius $R = 0.5\ \mu m$ and a total length $L = 3\ \mu m$. Simulations were performed with single cells in

three different positions on the wrinkled walls: in a minimum, in a maximum, and in an intermediate position. In the intermediate position, the cell is touching the surface at a distance $\lambda/4$ from a maximum. To avoid artifacts due to symmetry constraints, we modeled cells across the symmetry plane whenever possible, ensuring that only half of the bacterium was explicitly simulated while the other half was mirrored. When this was not feasible, we placed cells sufficiently far from the symmetry plane to minimize flow perturbations caused by their mirrored images. A finer mesh was used around the bacterial cells to improve accuracy, leading to a total of approximately $5 \cdot 10^6$ elements.

Data Availability. Additional data supporting this study are available in the Supplementary Information. A Source Data file containing all data displayed in the figures and reported in the tables is provided with this paper and is accessible at 10.5281/zenodo.17303681. Any remaining data underlying this study are available from the corresponding author upon request.

References

[1] Krajewski, S. *et al.* Bacterial interactions with proteins and cells relevant to the development of life-threatening endocarditis studied by use of a quartz-crystal microbalance. *Analytical and Bioanalytical Chemistry* **406**, 3395–3406 (2014).

[2] Cheng, Y., Feng, G. & Moraru, C. I. Micro-and nanotopography sensitive bacterial attachment mechanisms: a review. *Frontiers in microbiology* **10**, 191 (2019).

[3] Caldara, M., Belgiovine, C., Secchi, E. & Rusconi, R. Environmental, microbiological, and immunological features of bacterial biofilms associated with implanted medical devices. *Clinical Microbiology Reviews* **35**, e00221–20 (2022).

[4] Hsu, L. C., Fang, J., Borca-Tasciuc, D. A., Worobo, R. W. & Moraru, C. I. Effect of micro-and nanoscale topography on the adhesion of bacterial cells to solid surfaces. *Applied and Environmental Microbiology* **79**, 2703–2712 (2013).

[5] Tripathy, A., Sen, P., Su, B. & Briscoe, W. H. Natural and bioinspired nanostructured bactericidal surfaces. *Advances in colloid and interface science* **248**, 85–104 (2017).

[6] Skoog, S. A., Kumar, G., Narayan, R. J. & Goering, P. L. Biological responses to immobilized microscale and nanoscale surface topographies. *Pharmacology & Therapeutics* **182**, 33–55 (2018).

[7] Luan, Y. *et al.* Bacterial interactions with nanostructured surfaces. *Current opinion in colloid & interface science* **38**, 170–189 (2018).

[8] Lee, S. W., Phillips, K. S., Gu, H., Kazemzadeh-Narbat, M. & Ren, D. How microbes read the map: Effects of implant topography on bacterial adhesion and

biofilm formation. *Biomaterials* 120595 (2020).

[9] Ivanova, E. P. *et al.* Impact of nanoscale roughness of titanium thin film surfaces on bacterial retention. *Langmuir* **26**, 1973–1982 (2010).

[10] Mainwaring, D. E. *et al.* The nature of inherent bactericidal activity: insights from the nanotopology of three species of dragonfly. *Nanoscale* **8**, 6527–6534 (2016).

[11] Elbourne, A., Crawford, R. J. & Ivanova, E. P. Nano-structured antimicrobial surfaces: From nature to synthetic analogues. *Journal of Colloid and Interface Science* **508**, 603–616 (2017).

[12] Tuson, H. H. & Weibel, D. B. Bacteria–surface interactions. *Soft Matter* **9**, 4368–4380 (2013).

[13] Vasudevan, R., Kennedy, A. J., Merritt, M., Crocker, F. H. & Baney, R. H. Microscale patterned surfaces reduce bacterial fouling-microscopic and theoretical analysis. *Colloids and Surfaces B: Biointerfaces* **117**, 225–232 (2014).

[14] Hong, S.-H. *et al.* Surface waves control bacterial attachment and formation of biofilms in thin layers. *Science Advances* **6**, eaaz9386 (2020).

[15] Pellegrino, L., Kriem, L. S., Robles, E. S. & Cabral, J. T. Microbial response to micrometer-scale multiaxial wrinkled surfaces. *ACS Applied Materials & Interfaces* **14**, 31463–31473 (2022).

[16] Hizal, F. *et al.* Impact of 3d hierarchical nanostructures on the antibacterial efficacy of a bacteria-triggered self-defensive antibiotic coating. *ACS applied materials & interfaces* **7**, 20304–20313 (2015).

[17] Chang, Y.-R., Weeks, E. R. & Ducker, W. A. Surface topography hinders bacterial surface motility. *ACS Applied Materials & Interfaces* **10**, 9225–9234 (2018).

[18] Mok, R., Dunkel, J. & Kantsler, V. Geometric control of bacterial surface accumulation. *Physical Review E* **99**, 052607 (2019).

[19] Zheng, S. *et al.* Implication of surface properties, bacterial motility, and hydrodynamic conditions on bacterial surface sensing and their initial adhesion. *Frontiers in Bioengineering and Biotechnology* **9**, 643722 (2021).

[20] Surapaneni, V. A. *et al.* Groovy and gnarly: Surface wrinkles as a multifunctional motif for terrestrial and marine environments. *Integrative and Comparative Biology* **62**, 749–761 (2022).

[21] Demenego, G. *et al.* Neurodevelopmental origins of structural and psychomotor defects in cxcr4-linked primary immunodeficiency. *Neuron* **113**, 2636 – 2655.e9 (2025).

[22] Rusconi, R., Guasto, J. S. & Stocker, R. Bacterial transport suppressed by fluid shear. *Nature physics* **10**, 212–217 (2014).

[23] Secchi, E. *et al.* The effect of flow on swimming bacteria controls the initial colonization of curved surfaces. *Nature communications* **11**, 2851 (2020).

[24] Lee, Y. K., Won, Y.-J., Yoo, J. H., Ahn, K. H. & Lee, C.-H. Flow analysis and fouling on the patterned membrane surface. *Journal of membrane science* **427**, 320–325 (2013).

[25] Wang, Q. & Zhao, X. A three-dimensional phase diagram of growth-induced surface instabilities. *Scientific reports* **5**, 8887 (2015).

[26] Allen, J. The classification of cross-stratified units. with notes on their origin. *Sedimentology* **2**, 93–114 (1963).

[27] Efimenko, K. *et al.* Nested self-similar wrinkling patterns in skins. *Nature Materials* **4**, 293–297 (2005).

[28] Genzer, J. & Groenewold, J. Soft matter with hard skin: From skin wrinkles to templating and material characterization. *Soft Matter* **2**, 310–323 (2006).

[29] Bayley, F. A., Liao, J. L., Stavrinou, P. N., Chiche, A. & Cabral, J. T. Wavefront kinetics of plasma oxidation of polydimethylsiloxane: limits for sub-μm wrinkling. *Soft Matter* **10**, 1155–1166 (2014).

[30] Nania, M., Foglia, F., Matar, O. K. & Cabral, J. T. Sub-100 nm wrinkling of polydimethylsiloxane by double frontal oxidation. *Nanoscale* **9**, 2030–2037 (2017).

[31] Pellegrino, L., Khodaparast, S. & Cabral, J. T. Orthogonal wave superposition of wrinkled, plasma-oxidised, polydimethylsiloxane surfaces. *Soft Matter* **16**, 595–603 (2020).

[32] Pellegrino, L., Tan, A. & Cabral, J. T. Ripple patterns spontaneously emerge through sequential wrinkling interference in polymer bilayers. *Physical Review Letters* **128**, 058001 (2022).

[33] Nakazawa, K. *et al.* A human septin octamer complex sensitive to membrane curvature drives membrane deformation with a specific mesh-like organization. *Journal of Cell Science* **136**, jcs260813 (2023).

[34] Li, B., Cao, Y.-P., Feng, X.-Q. & Gao, H. Mechanics of morphological instabilities and surface wrinkling in soft materials: a review. *Soft Matter* **8**, 5728–5745 (2012).

[35] Stroock, A. D. *et al.* Chaotic mixer for microchannels. *Science* **295**, 647–651 (2002).

[36] Pyke, K. E., Dwyer, E. M. & Tschakovsky, M. E. Impact of controlling shear rate on flow-mediated dilation responses in the brachial artery of humans. *Journal of applied physiology* **97**, 499–508 (2004).

[37] Zöttl, A. *et al.* Dynamics of individual Brownian rods in a microchannel flow. *Soft Matter* **15**, 5810–5814 (2019).

[38] Shen, Y., Siryaporn, A., Lecuyer, S., Gitai, Z. & Stone, H. A. Flow directs surface-attached bacteria to twitch upstream. *Biophysical Journal* **103**, 146 – 151 (2012).

[39] Leighton, T. L., Buensuceso, R. N., Howell, P. L. & Burrows, L. L. Biogenesis of p seudomonas aeruginosa type iv pili and regulation of their function. *Environmental microbiology* **17**, 4148–4163 (2015).

[40] Duvernoy, M.-C. *et al.* Asymmetric adhesion of rod-shaped bacteria controls microcolony morphogenesis. *Nature communications* **9**, 1120 (2018).

[41] Roberge, N. A. & Burrows, L. L. Building permits—control of type iv pilus assembly by pilb and its cofactors. *Journal of Bacteriology* **206**, e00359–24 (2024).

[42] Lecuyer, S. *et al.* Shear stress increases the residence time of adhesion of pseudomonas aeruginosa. *Biophysical journal* **100**, 341–350 (2011).

[43] Parente, R. *et al.* A Multilayered Imaging and Microfluidics Approach for Evaluating the Effect of Fibrinolysis in Staphylococcus aureus Biofilm Formation. *Pathogens* **12**, 1141 (2023).

[44] Baba, T., Bae, T., Schneewind, O., Takeuchi, F. & Hiramatsu, K. Genome sequence of staphylococcus aureus strain newman and comparative analysis of staphylococcal genomes: polymorphism and evolution of two major pathogenicity islands. *Journal of bacteriology* **190**, 300–310 (2008).

[45] Forson, A. M., van der Mei, H. C. & Sjollema, J. Impact of solid surface hydrophobicity and micrococcal nuclease production on staphylococcus aureus newman biofilms. *Scientific Reports* **10**, 12093 (2020).

[46] Parsons, J. B., Westgeest, A. C., Conlon, B. P. & Fowler Jr, V. G. Persistent methicillin-resistant staphylococcus aureus bacteremia: host, pathogen, and treatment. *Antibiotics* **12**, 455 (2023).

[47] Liesenborghs, L., Verhamme, P. & Vanassche, T. Staphylococcus aureus, master manipulator of the human hemostatic system. *Journal of Thrombosis and Haemostasis* **16**, 441–454 (2018).

[48] McAdow, M. *et al.* Preventing staphylococcus aureus sepsis through the inhibition of its agglutination in blood. *PLoS pathogens* **7**, e1002307 (2011).

[49] Belgiovine, C. *et al.* Interaction of bacteria, immune cells, and surface topography in periprosthetic joint infections. *International Journal of Molecular Sciences* **24**, 9028 (2023).

[50] Gammie, A. *et al.* International continence society guidelines on urodynamic equipment performance. *Neurourology and Urodynamics* **33**, 370 – 379 (2014).

[51] Secchi, E. *et al.* The structural role of bacterial edna in the formation of biofilm streamers. *Proceedings of the National Academy of Sciences of the United States of America* **119** (2022).

[52] Savorana, G., Słomka, J., Stocker, R., Rusconi, R. & Secchi, E. A microfluidic platform for characterizing the structure and rheology of biofilm streamers. *Soft Matter* **18**, 3878 – 3890 (2022).

[53] Lee, S. W., Phillips, K. S., Gu, H., Kazemzadeh-Narbat, M. & Ren, D. How microbes read the map: Effects of implant topography on bacterial adhesion and biofilm formation. *Biomaterials* **268**, 120595 (2021).

[54] Nicolle, L. E. Catheter associated urinary tract infections. *Antimicrobial resistance and infection control* **3**, 1–8 (2014).

[55] Werneburg, G. T. Catheter-associated urinary tract infections: current challenges and future prospects. *Research and reports in urology* 109–133 (2022).

[56] Marschall, J., Carpenter, C. R., Fowler, S. & Trautner, B. W. Antibiotic prophylaxis for urinary tract infections after removal of urinary catheter: meta-analysis. *Bmj* **346** (2013).

[57] Holmes, A. H. *et al.* Understanding the mechanisms and drivers of antimicrobial resistance. *The Lancet* **387**, 176–187 (2016).

[58] Dean, B. & Bhushan, B. Shark-skin surfaces for fluid-drag reduction in turbulent flow: A review. *Philosophical Transactions of the Royal Society A: Mathematical, Physical and Engineering Sciences* **368**, 4775 – 4806 (2010).

[59] Gomez, S. *et al.* Substrate stiffness impacts early biofilm formation by modulating Pseudomonas aeruginosa twitching motility. *eLife* **12**, e81112 (2023).

[60] Ariel, G. *et al.* Swarming bacteria migrate by Lévy Walk. *Nature Communications* **6**, 8396 (2015).

[61] Lauta, F. C., Pellegrino, L. & Rusconi, R. Macrophages on the wrinkle: Exploring microscale interactions with substrate topography. *Biophysics Reviews* **5** (2024).

[62] Vinci, V. *et al.* Breast implant surface topography triggers a chronic-like inflammatory response. *Life Science Alliance* **7** (2024).

[63] Schneider, C. A., Rasband, W. S. & Eliceiri, K. W. Nih image to imagej: 25 years of image analysis. *Nature Methods* **9**, 671–675 (2012).

[64] Berg, S. *et al.* ilastik: interactive machine learning for (bio)image analysis. *Nature Methods* **16**, 1226–1232 (2019).

Acknowledgments. This work was supported by EU funding within the Italian Ministry of Universities and Research (MUR) PNRR Extended Partnership initiative on Emerging Infectious Diseases (Project no. PE00000007, INF-ACT) to R.R., EU HORIZON-TMA-MSCA-PF-EF Investigating microbial colonization and removal on dynamic patterned surfaces (Grant no. 101110029, MOBILE) to L.P., and by a grant from Italian Ministry of Universities and Research (MUR), Dipartimenti di Eccellenza 2023-2027 (I.232/2016, art. 1, commi 314-337) to V.C., R.C., and F.M.. E.D.I. and M.C. are grateful to Humanitas University Office of Information Technology for the computing resources maintenance. V.C., R.C., and F.M. gratefully acknowledge the support of the ISIS@MACH ITALIA Research Infrastructure, the hub of ISIS Neutron and Muon Source (UK), [MUR official registry U. 0008642.28-05-2020 – 16th April 2020]. IM@IT is listed in the Italian Ministry of University and Research's Piano Nazionale delle Infrastrutture di Ricerca (PNIR 2021-2027) "in the broader notion of ISIS", and ISIS Facility and IM@IT are jointly listed in high priority RI's (see Table 6 page 30, note 38, PNIR in 2021-2027).

Author Contributions. L.P. and R.R. conceived and designed the project. L.P. conducted the microfluidic experiments and performed data analysis. L.P., G.S., and E.S. carried out numerical simulations and interpreted the results. L.P., V.C., R.C., and F.M. performed and analyzed AFM measurements. M.C. and E.D.I. conducted and analyzed SEM measurements. S.L. and C.B. contributed to data analysis and interpretation. V.V., M.K., and R.R. acquired funding and supervised the research. L.P. and R.R. wrote the original draft, and all authors contributed to reviewing and editing the manuscript.

Competing Interests. The authors have no conflicts of interest to declare.

Figure Legends

Figure 1

Tunable patterned surfaces are fabricated via spontaneous buckling and integrated into a microfluidic device. a Phase diagram illustrating the mechanical instability modes in soft bilayers, computing the mismatch in mechanical properties as the ratio of the elastic modulus of the foundation material E_s over the elastic modulus of the thin film layer E_f. Representative 3D atomic force microscopy (AFM) projections show experimental sinusoidal wrinkling (w_s) and period-doubling/folding modes (w_f) observed in our plasma-oxidized silicone elastomeric substrates. **b** Schematic of the microfluidic wrinkled device. The upper section consists of six straight polydimethylsiloxane (PDMS) channels, each with a cross-section of 70 μm x 800 μm (height x width). The lower section features a PDMS substrate with a flat (unpatterned, F) surface and two sinusoidal wrinkling patterns w_s: one aligned parallel to the

flow direction ($w_{s\parallel}$) and one perpendicular to it ($w_{s\perp}$). **c** AFM images showing representative 3D projections of adhered *Pseudomonas aeruginosa* on a flat surface (F) and on a sinusoidal w_s pattern within the microfluidic wrinkling device. Scale bar, 5 μm.

Figure 2

Numerical simulations reveal how wrinkled topographies and attached bacteria generate shear gradients that influence surface colonization. a Rod-shaped bacterium attached to a flat surface (F), with orientation perpendicular (left) and parallel (right) to the flow, under a defined shear rate of $\dot{\gamma} = 80\ s^{-1}$. **b** Sinusoidal wrinkled surface $\lambda = 2$ μm and $A/\lambda = 0.25$, oriented perpendicularly to the flow direction ($w_{s\perp}$). **c** Folding surface with $\lambda = 5$ μm and $A/\lambda = 0.4$, oriented perpendicularly to the flow direction ($w_{f\perp}$). **d** Folding surface with $\lambda = 20$ μm and $A/\lambda = 0.2$, oriented perpendicularly to the flow direction ($w_{f\perp}$). Two attachment configurations were considered: hilltop attachment and valley attachment. Bacteria were modeled as cylinders with hemispherical caps (radius $R = 0.5$ μm, total length $L = 3$ μm). **e** Shear rate streamlines for a $w_{f\perp}$ surface ($A/\lambda = 0.4$), showing the occurrence of recirculation zones in the valley region (left), and for a $w_{s\perp}$ surface ($A/\lambda = 0.25$, right). Data are reported as normalized 'excess shear rate' ($\dot{\gamma}_{w_s}/\dot{\gamma}_F$).

Figure 3

Shear flow and pattern orientation modulate *Pseudomonas aeruginosa* PA14 adhesion on wrinkled surfaces. a-b Temporal evolution of the surface coverage S_c (insets) of wild-type *P. aeruginosa* PA14 on 2 μm wrinkled surfaces, $w_{s\parallel}$ (**a**) and $w_{s\perp}$ (**b**), normalized by the coverage of a flat (F) surface S_c/S_F across different shear rates. **c** Probability distribution functions of bacterial orientation obtained from the fluorescent images shown in Fig. S1**a** for the F, $ws_{\parallel}$, and $ws_{\perp}$ after 2 hours of continuous flow. Insets display the fast Fourier transform of the distribution. Scale bar is 0.02 μm^{-1}. Created in BioRender. Rusconi, R. (2025) https://BioRender.com/ihbaq87 **d** Comparison of surface coverage on $w_{s\parallel}$ (circle) and $w_{s\perp}$ patterns (squares) at different shear rates with a flat surface (diamonds) at the 3-hour time point. Insets represent schematic representations of the *shear-induced adhesion* phenomenon observed on flat surfaces and the *shear-decreased adhesion* behavior observed on wrinkled substrates. Created in BioRender. Rusconi, R. (2025) https://BioRender.com/7g5edk6. For **a**–**b** and **d**, data represent the mean ± SEM from at least $N = 500$ cells per frame, three frames per channel, and three technical channels per condition, with three independent biological replicates. Source data are provided as a Source Data file.

Figure 4

Motility influences the adhesion response of *Pseudomonas aeruginosa* to shear on wrinkled surfaces. a-b Normalized surface coverage S_c/S_F of the non-motile PA14 Δ*motABCD* on $w_{s\parallel}$ (left) and $w_{s\perp}$ (right) surfaces at different time points and shear rates. **c** Surface coverage S_c/S_F as a function of shear rate, comparing the PA14 Δ*motABCD* mutant and wild-type (WT) PA14 on on $w_{s\parallel}$ (circles) and $w_{s\perp}$ (squares) surfaces. **d** Schematic depicting the attachment and detachment behavior

of WT (orange) and Δ*motABCD* mutant (purple) strains on $w_{s\perp}$ surfaces. Created in BioRender. Rusconi, R. (2025) https://BioRender.com/2ckm3h6. For **a**–**c**, data represent the mean ± SEM from at least $N = 500$ cells per frame, three frames per channel, and three technical channels per condition, with three independent biological replicates. Source data are provided as a Source Data file.

Figure 5

Surface wavelength and aspect ratio determine *Pseudomonas aeruginosa* PA14 adhesion on wrinkled and folded surfaces. a Normalized surface coverage (S_c/S_f) of *P. aeruginosa* PA14 cells, relative to an equivalent flat surface, at a shear rate of 80 s^{-1}. For $w_{s\parallel}$, $w_{f\parallel}$ (circles), $w_{s\perp}$, and $w_{f\perp}$ surfaces (squares), bacterial coverage decreases as λ increases up to 5 μm, followed by an increase at $\lambda = 20$ μm. **b** Optical microscopy images showing the attachment of PA14 wild-type cells on $w_{s\perp}$ and $w_{f\perp}$ surfaces with λ values of 0.5 μm, 2 μm, 5 μm, and 20 μm at a shear rate of 80 s^{-1}. **c** Normalized surface coverage (S_c/S_f) of PA14 cells, relative to an equivalent flat surface, at a shear rate of 80 s^{-1}. Coverage is plotted for $w_{s\parallel}$, $w_{f\parallel}$ (circles), $w_{s\perp}$, and $w_{f\perp}$ surfaces (squares) as a function of pattern aspect ratio (A/λ). For surfaces with aspect ratios above 0.25, including 2 μm w_s and 5 μm w_f patterns, a decrease in bacterial adhesion is observed. **d** Scanning electron microscopy (SEM) images of 2 μm w_s and 5 μm w_f surfaces. Focused ion beam (FIB) milling cuts show surface cross-sectional profiles without PA14 cells (left) and with adhered PA14 cells (right). **e** Schematic representation of PA14 cells adhered to sinusoidal and folding profiles based on AFM measurements. Significant decreased adhesion is observed for patterns with A/λ values above 0.25. For **a**, data represent the mean ± SEM from at least $N = 500$ cells per frame, three frames per channel, and three technical channels per condition, with three independent biological replicates. Source data are provided as a Source Data file.

Figure 6

Wrinkled and folded substrates reduce surface colonization of type IV pili–defective *Pseudomonas aeruginosa* PA14 under shear flow. a-b Normalized surface coverage (S_c/S_F) of PA14 Δ*pilB* on sinusoidal $w_{s\perp}$ (**a**, left) and folding $w_{f\perp}$ (**b**, right) surfaces at different time points and shear rates. **c** Surface coverage at 3 h as a function of shear rate for $w_{s\perp}$ (circles) and $w_{f\perp}$ (squares) surfaces. For **a**–**c**, data represent the mean ± SEM from at least $N = 500$ cells per frame, three frames per channel, and three technical channels per condition, with three independent biological replicates. Source data are provided as a Source Data file.

Figure 7

Shear flow and pattern geometry regulate *Staphylococcus aureus* surface colonization on folded substrates. a Fluorescence and phase-contrast overlaid optical microscopy images of *Staphylococcus aureus* Newman on 5 μm patterned $w_{f\perp}$ surfaces at different shear rates. **b** *S. aureus* Newman surface coverage (S_c) as a function of imposed shear stress on 5 μm patterned surfaces, comparing $w_{f\perp}$ (squares)

and $w_{f\parallel}$ (circles) orientations with F surfaces (triangles) at 3 hours. **c** *S. aureus* Newman surface coverage (S_c) as a function of pattern wavelength at 3 hours and a shear stress of 80 s^{-1} for parallel $w_{\parallel}$ (circles) and perpendicular $w_{\perp}$ orientations (squares). **d** *S. aureus* Newman surface coverage (S_c) as a function of pattern aspect ratio (A/λ) at 3 hours and a shear stress of 80 s^{-1} for parallel $w_{\parallel}$ (circles) and perpendicular $w_{\perp}$ orientations (squares). **e** Fluorescence and phase-contrast overlaid optical microscopy images of *S. aureus* Newman on $w_{f\perp}$ surfaces with different pattern wavelengths at 3 hours. For **b**–**d**, data represent the mean ± SEM from at least $N = 500$ cells per frame, three frames per channel, and three technical channels per condition, with three independent biological replicates. Source data are provided as a Source Data file.

Figure 8

Pulsatile flow shapes *Pseudomonas aeruginosa* and *Staphylococcus aureus* attachment on folded surfaces. a Schematic of the pulsatile flow cycle. The syringe pump alternated between $Q_{max} = 4$ μl/min ($\dot{\gamma} = 160$ s^{-1}) and $Q_{min} = 0$ μl/min with a cycle period of $T = 10$ s. **b** Segmented images of *S. aureus* Newman at different phases of the pulsatile cycle, showing bacterial accumulation at Q_{min} and detachment at Q_{max}. Scale bar, 5 μm. **c** Surface coverage $S_c(\%)$ of PA14 under pulsatile (purple) continuous (pink) flow for flat surfaces (squares) and 5 μm w_f surfaces (circles). Inset: normalized surface coverage S_c/S_f. **d** Surface coverage $S_c(\%)$ of *S. aureus* Newman under pulsatile (green) and continuous (blue) flow for flat surfaces (squares) and 5 μm w_f surfaces (circles). Inset: normalized surface coverage S_c/S_F. For **c**–**d**, data represent the mean ± SEM from at least $N = 500$ cells per frame, three frames per channel, and three technical channels per condition, with three independent biological replicates.

Figure 9

Folded surface topography suppresses biofilm formation under high shear. a-b Optical microscopy images showing biofilm formation of **a** *P. aeruginosa* PA14 WT and **b** *S. aureus* Newman on flat (F, first and third column) and 5 μm $w_{f\perp}$ surfaces (second and fourth column) under a shear rate of 200 s^{-1} at 12 h (first line) and 24 h (second line). Biofilm formation was tracked by labeling the bacterial suspension with propidium iodide (PI, red signal), which binds extracellular DNA produced by bacteria at different stages of biofilm formation. Scale bar, 10 μm.

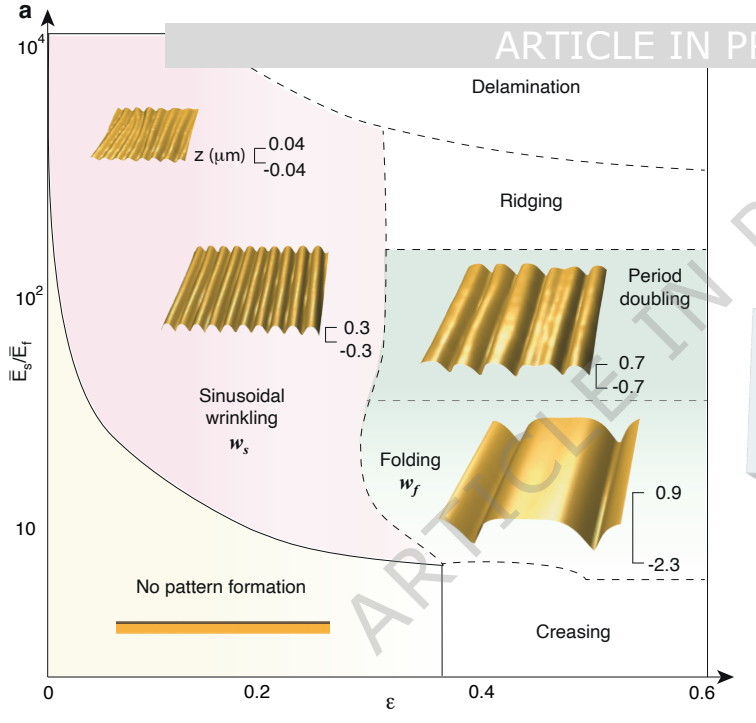

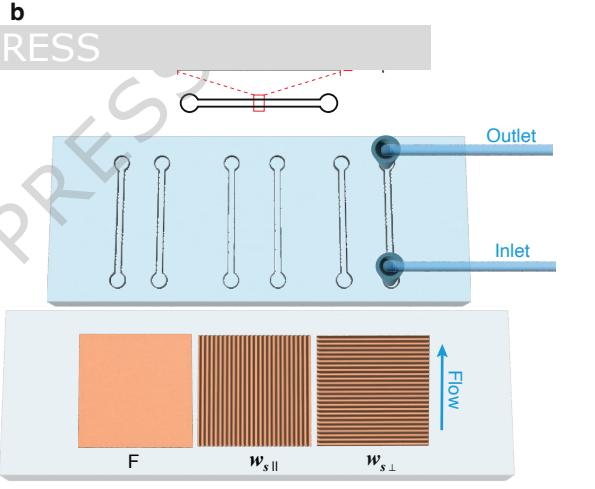

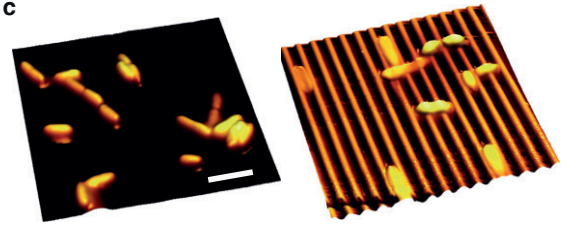

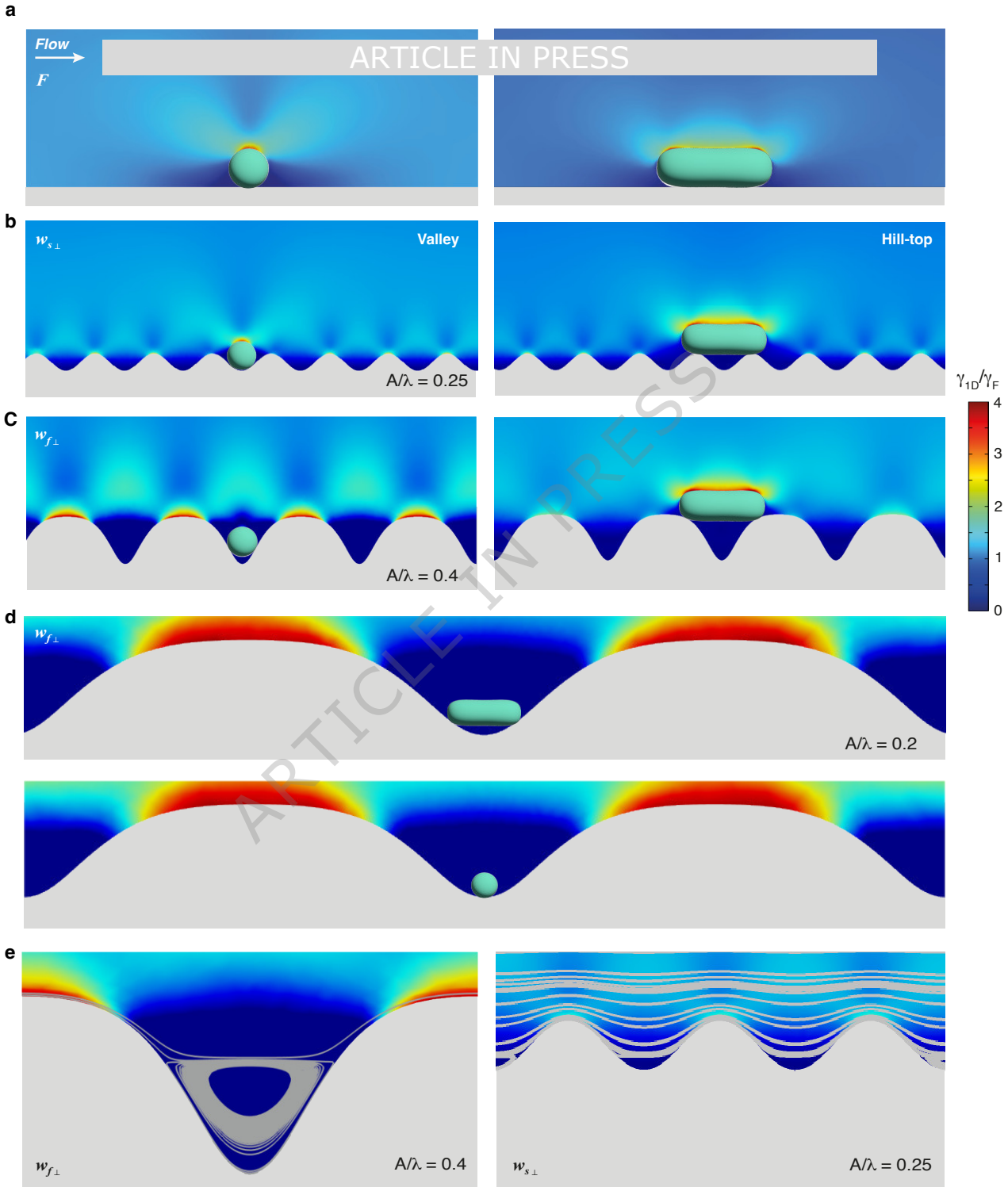

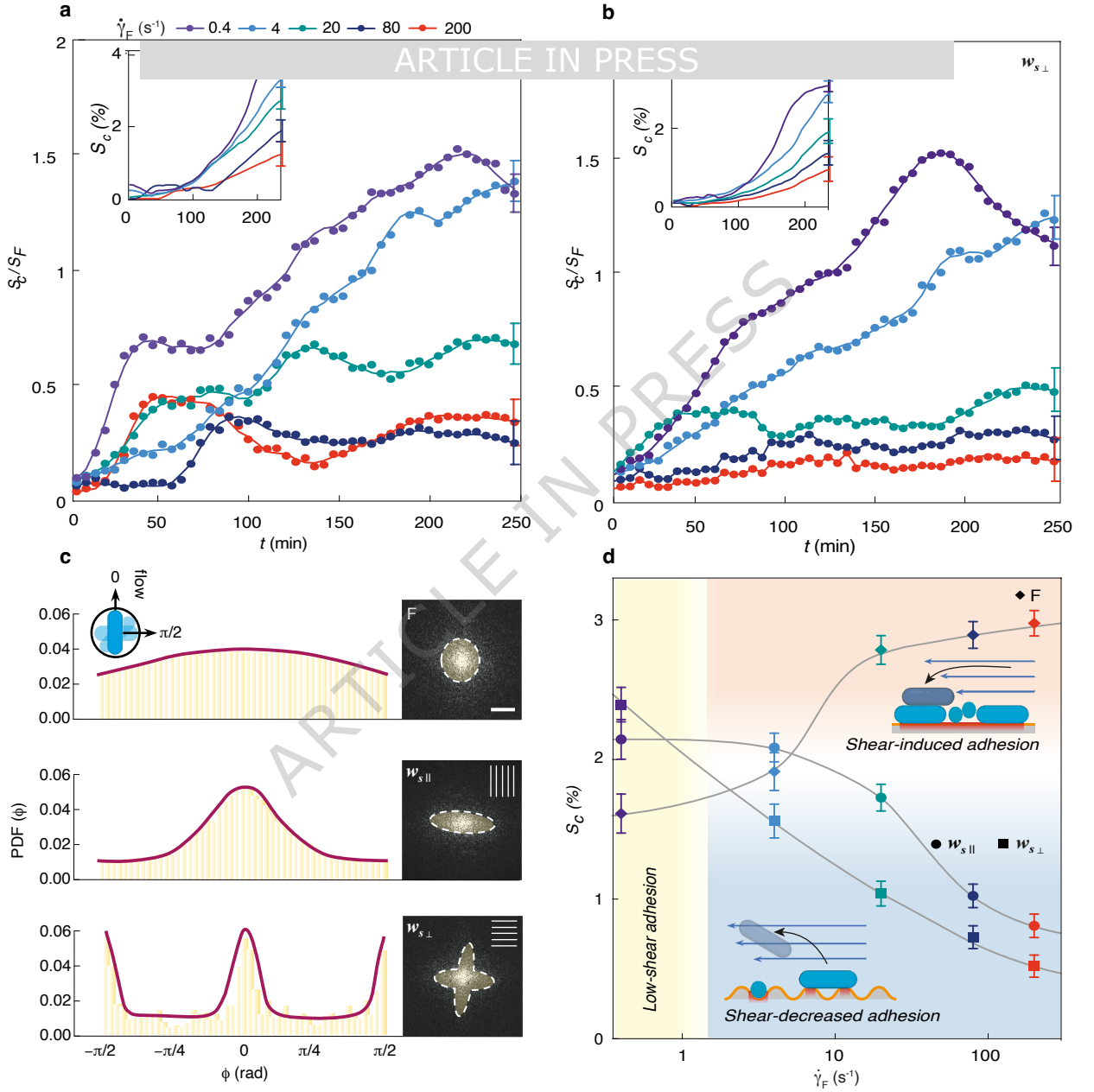

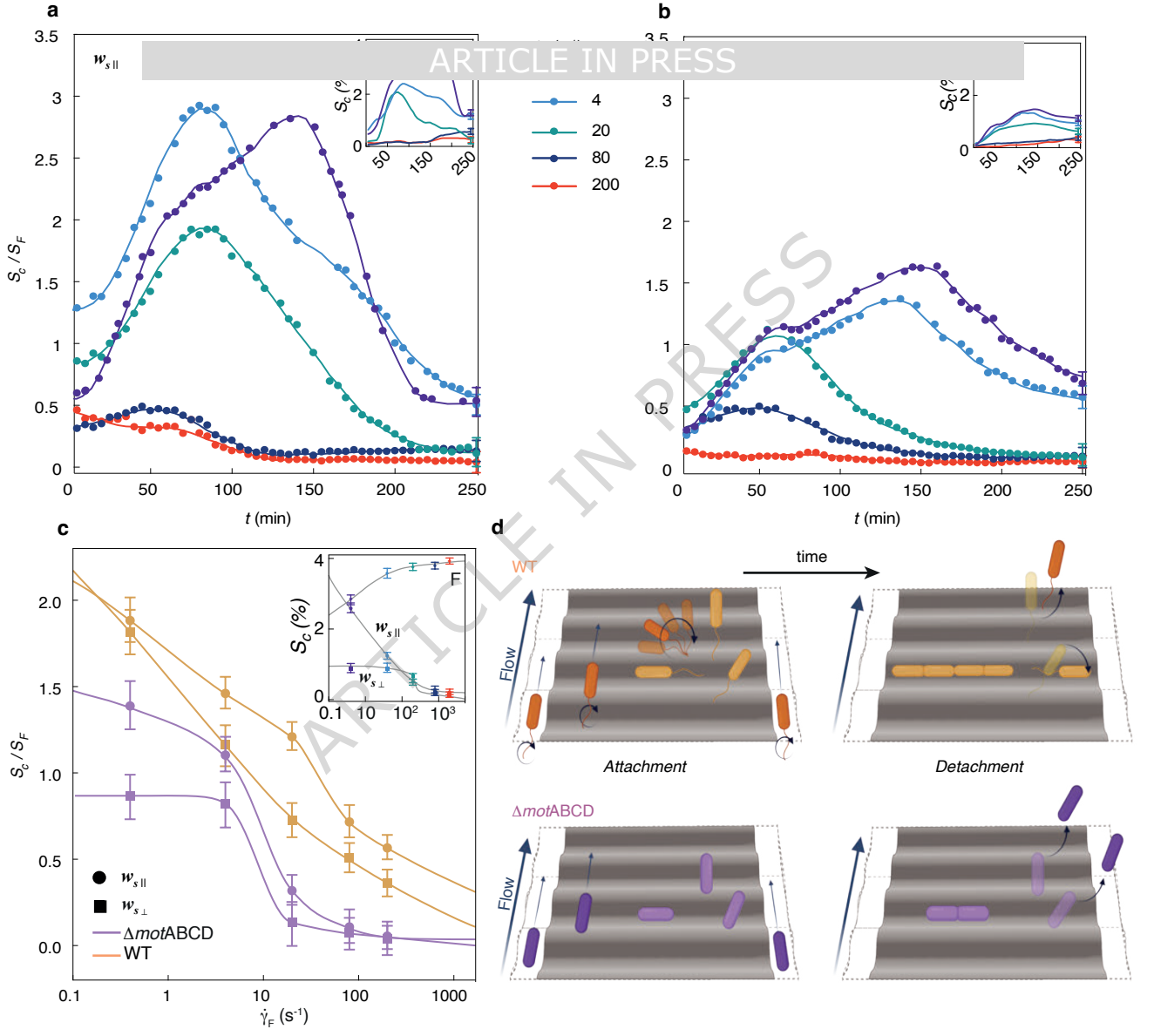

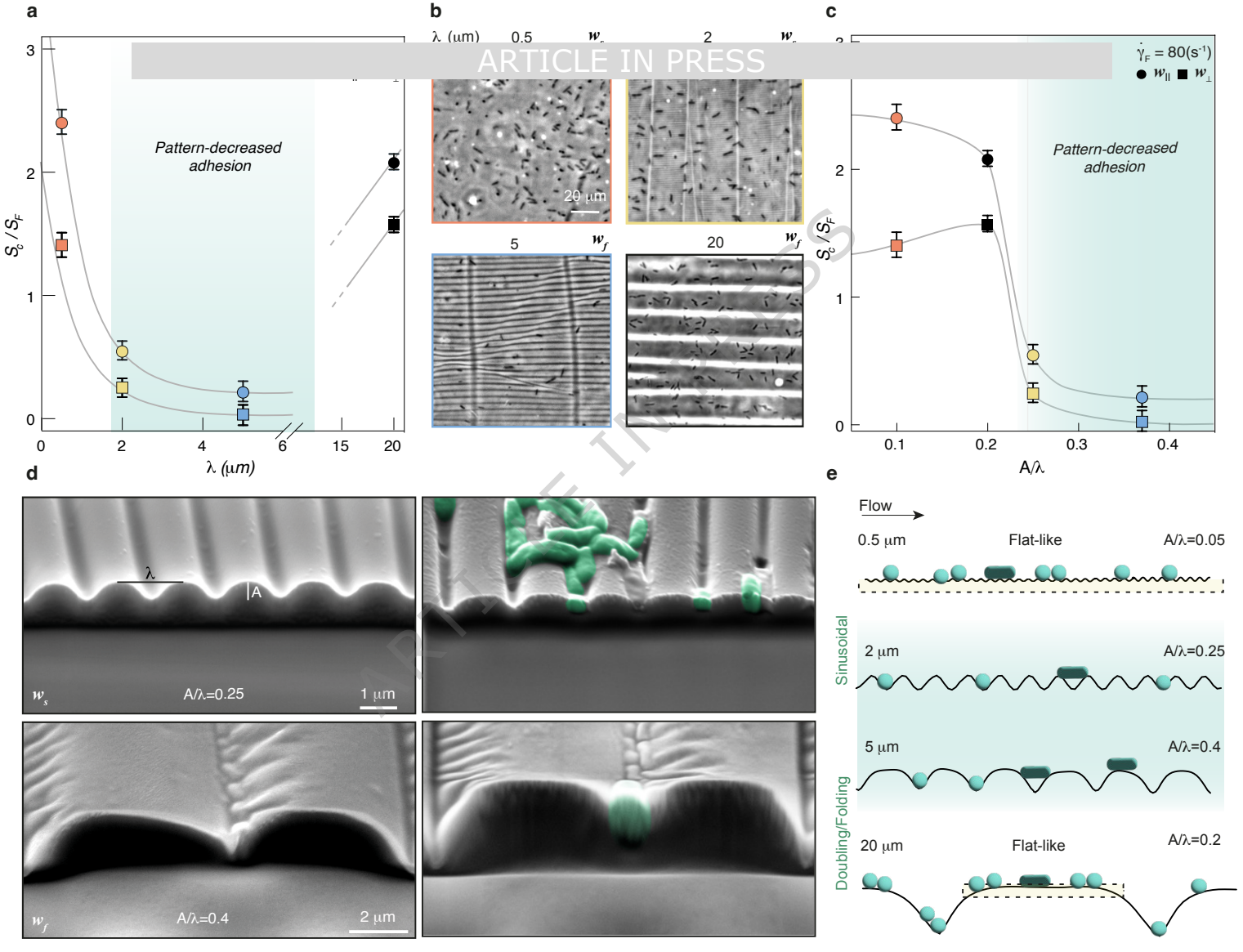

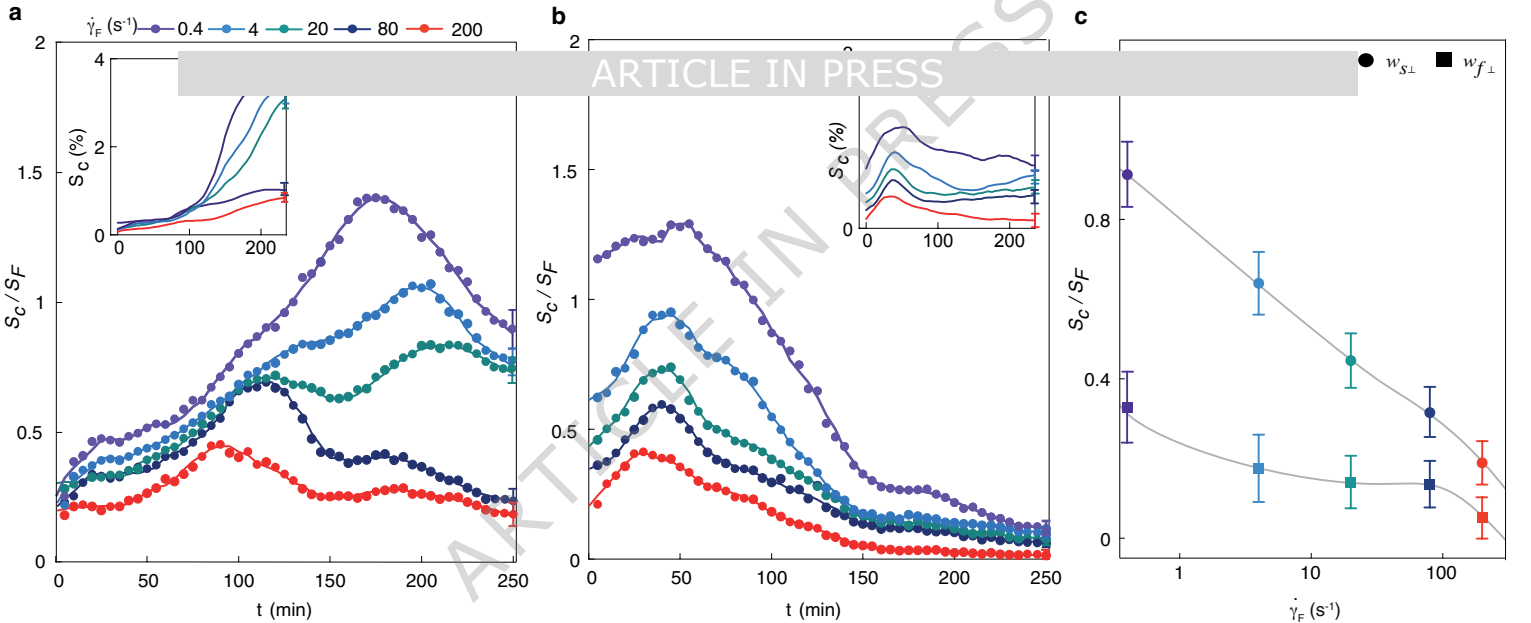

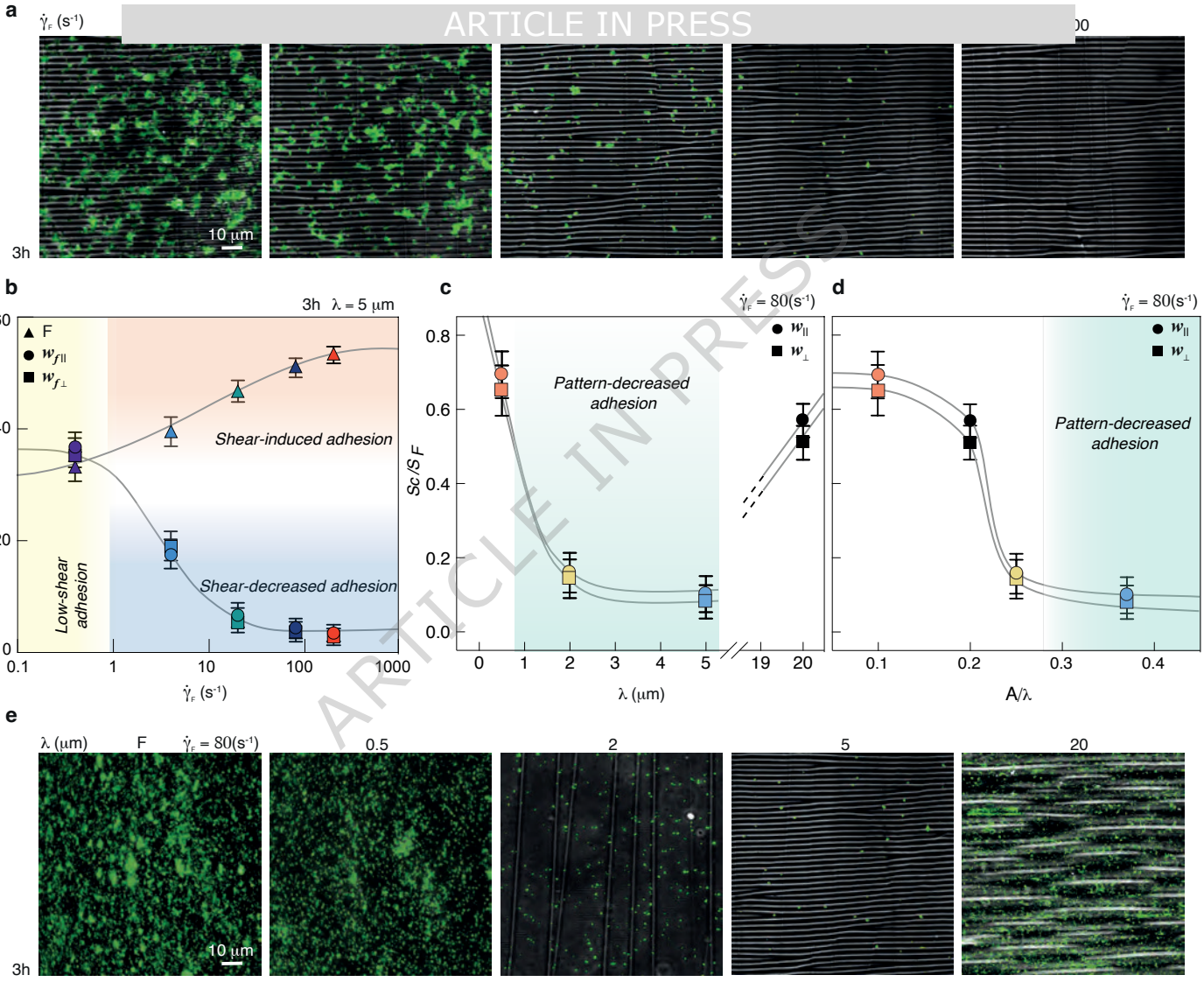

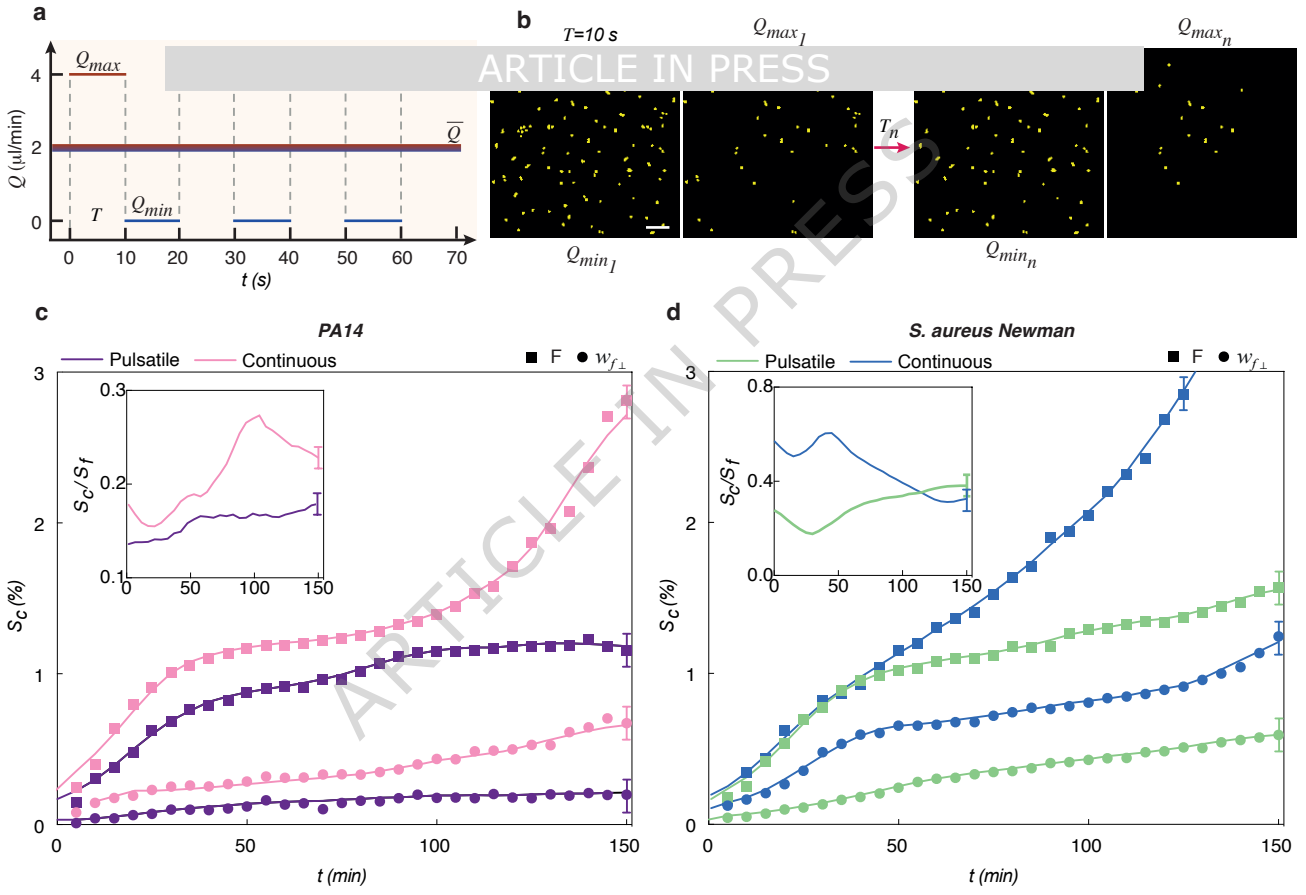

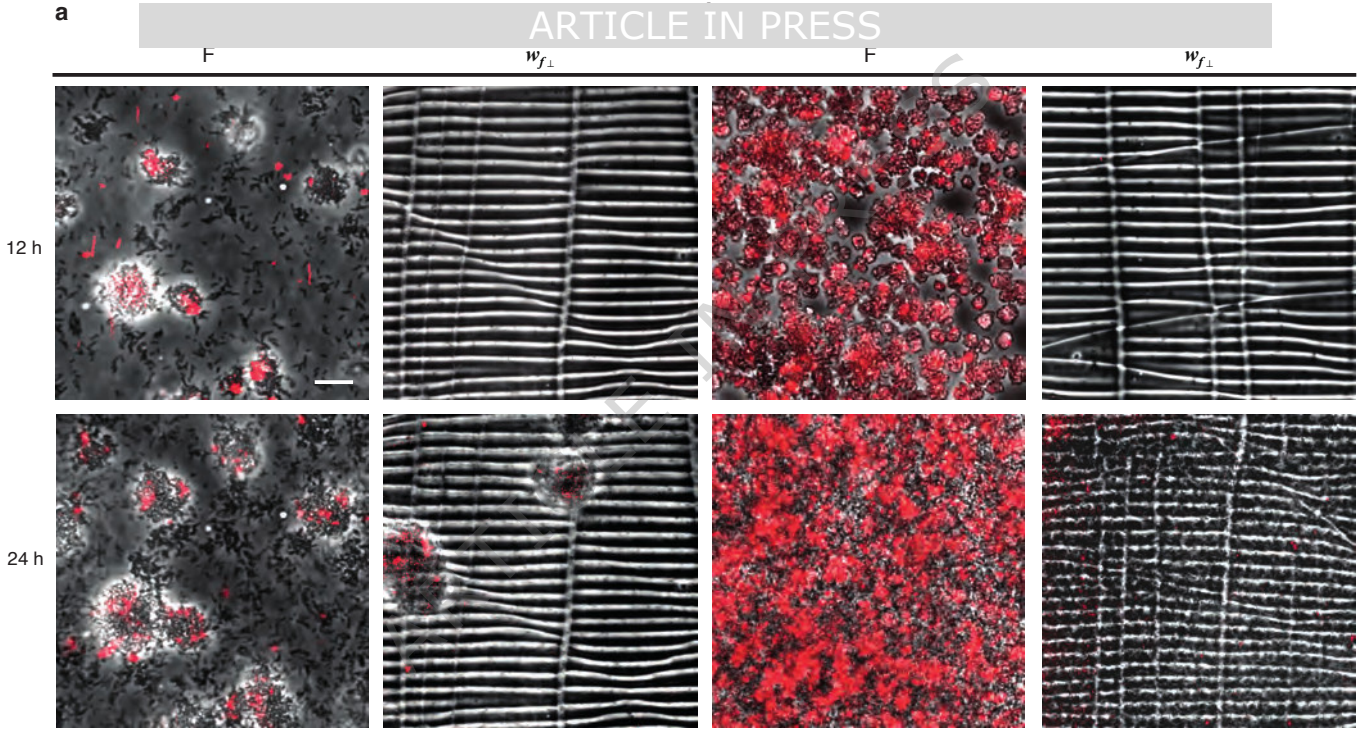

Supplementary Information: Reduction of bacterial colonization on buckling-induced wrinkled surfaces under fluid shear

Luca Pellegrino, Giovanni Savorana, Valeria Cassina, Riccardo Campanile, Martin Centola, Cristina Belgiovine, Valeriano Vinci, Marco Klinger, Sigolène Lecuyer, Edoardo D'Imprima, Francesco Mantegazza, Eleonora Secchi, and Roberto Rusconi

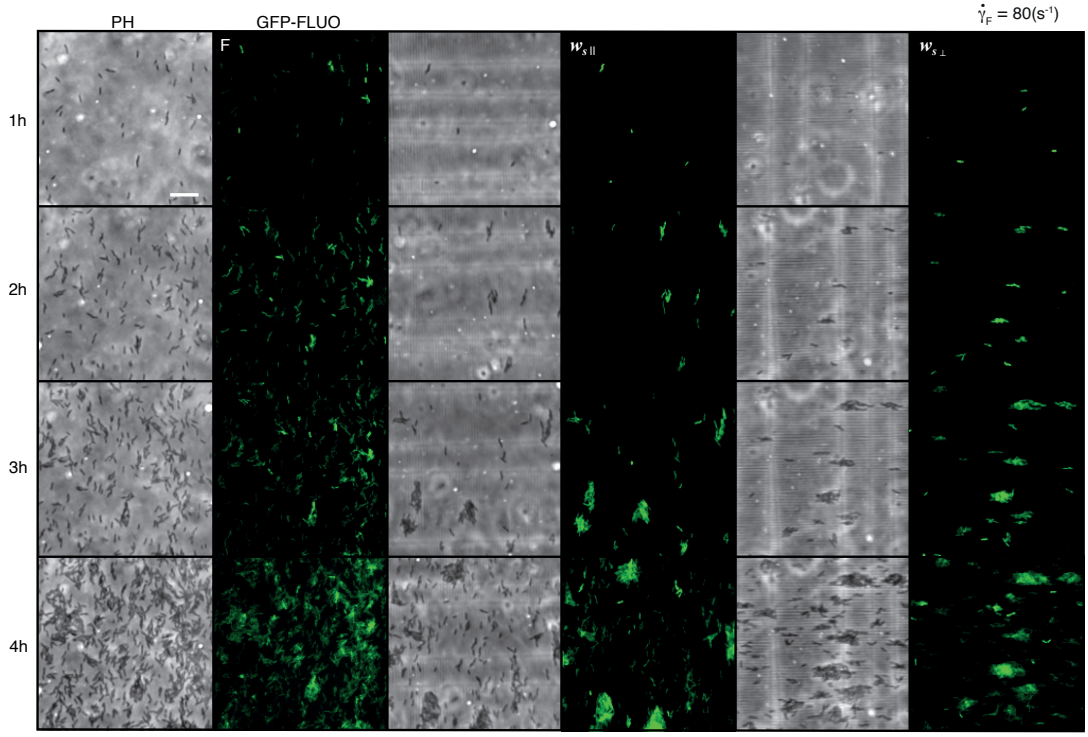

FIG. S1. Pattern orientation affects early surface colonization by *Pseudomonas aeruginosa* PA14 under shear. Optical microscopy characterization of wild-type PA14 attachment on F, $\lambda = 2$ μm $ws_{\parallel}$ surfaces and $ws_{\perp}$ at different time points, at a shear rate $\dot{\gamma} = 80$ s^{-1}. Optical images display phase contrast (PH) and green fluorescent (GFP-FLUO) channels to highlight, respectively, the wrinkling pattern and the bacteria. Scale bar, 50 μm.

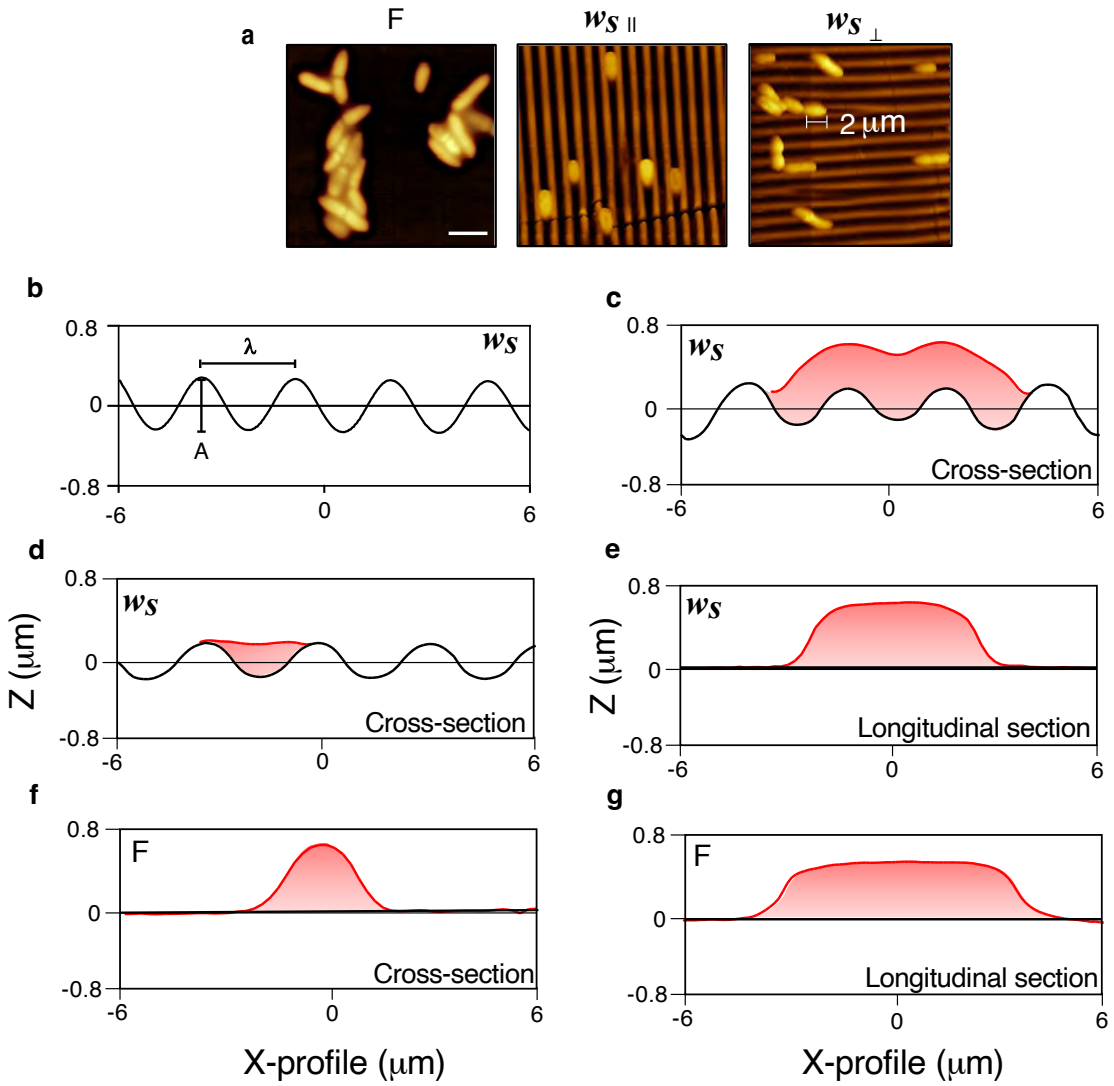

FIG. S2. Sinusoidal wrinkles confine *Pseudomonas aeruginosa* PA14 cells. a AFM imaging of PA14 WT cells attached on F, $ws_{\parallel}$, and $ws_{\perp}$ surfaces. 1D-profiles extracted from AFM imaging of **b** cross-section profile of a sinusoidal wrinkling surface w_s with characteristic λ= 2 μm and A= 0.3 μm. **c** Cross-section of a PA14 WT cell adhered against the pattern direction. **d** Cross-section of a PA14 cell adhered in a valley portion of the sinusoidal profile. **e** Longitudinal section of **d**. Bacterial profiles on sinusoidal surfaces are compared to cells adhering on F surfaces in **f**-**g**.

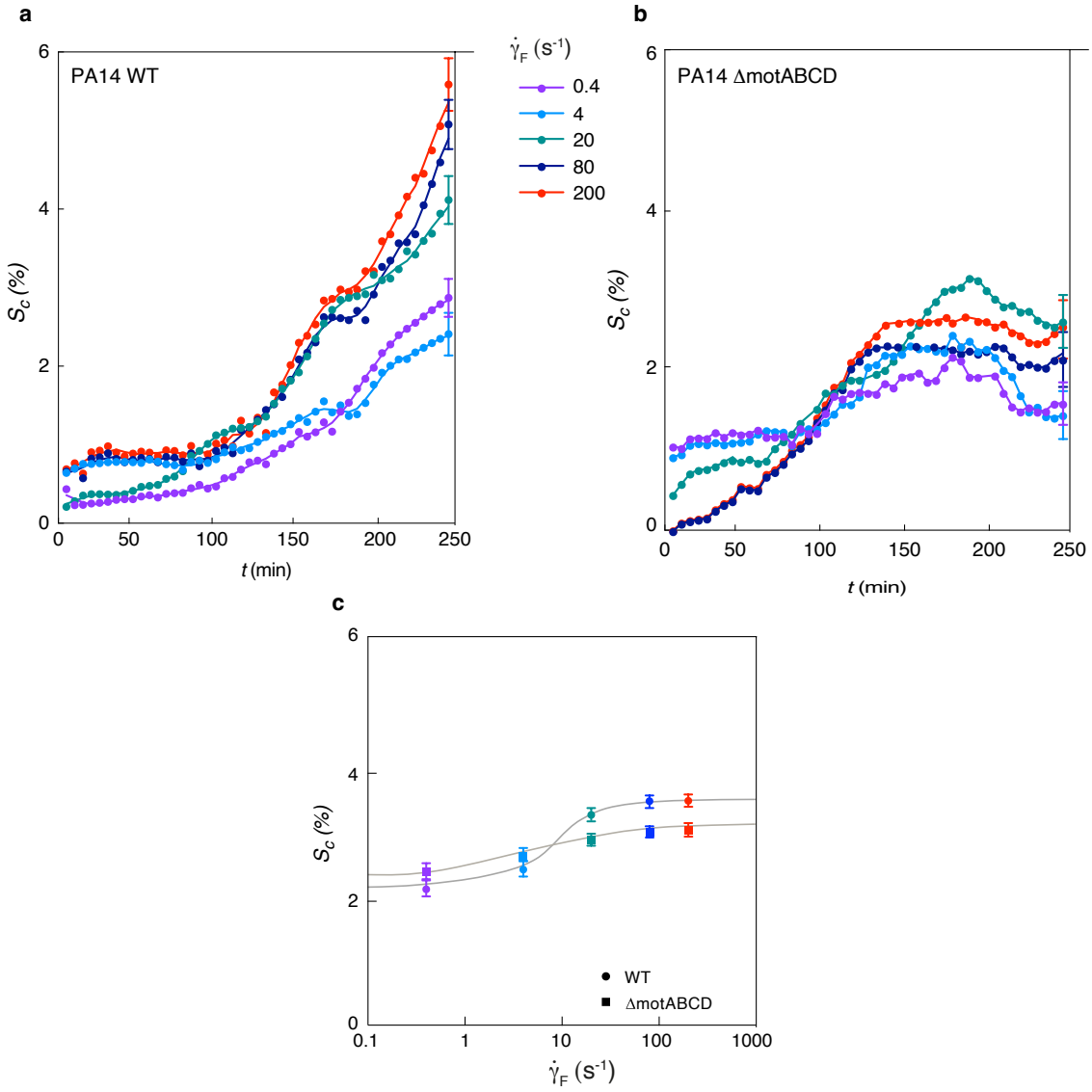

FIG. S3. Shear increases colonization of flat substrates by motile *Pseudomonas aeruginosa* PA14. Surface coverage analysis of **a** motile PA14 WT and **b** non-motile PA14Δ*motABCD* strains on F surfaces up to 4 hours, at different shear rates. **c** Surface coverage at 3h for PA14 WT and PA14Δ*motABCD*. For **a-c**, data represent the mean ± SEM from at least $N = 500$ cells per frame, three frames per channel, and three technical channels per condition, with three independent biological replicates. Source data are provided as a Source Data file.

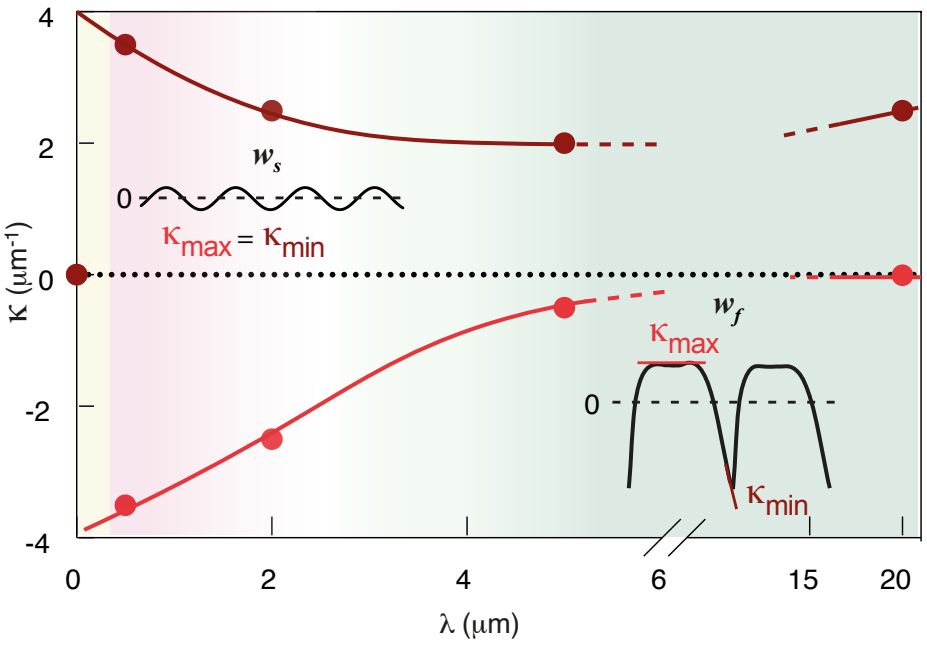

FIG. S4. Curvature analysis of sinusoidal and folded surface patterns. One-dimensional maximum (κ_{max}) and minimum (κ_{min}) curvatures as functions of λ, derived from AFM line profiles of the surfaces.

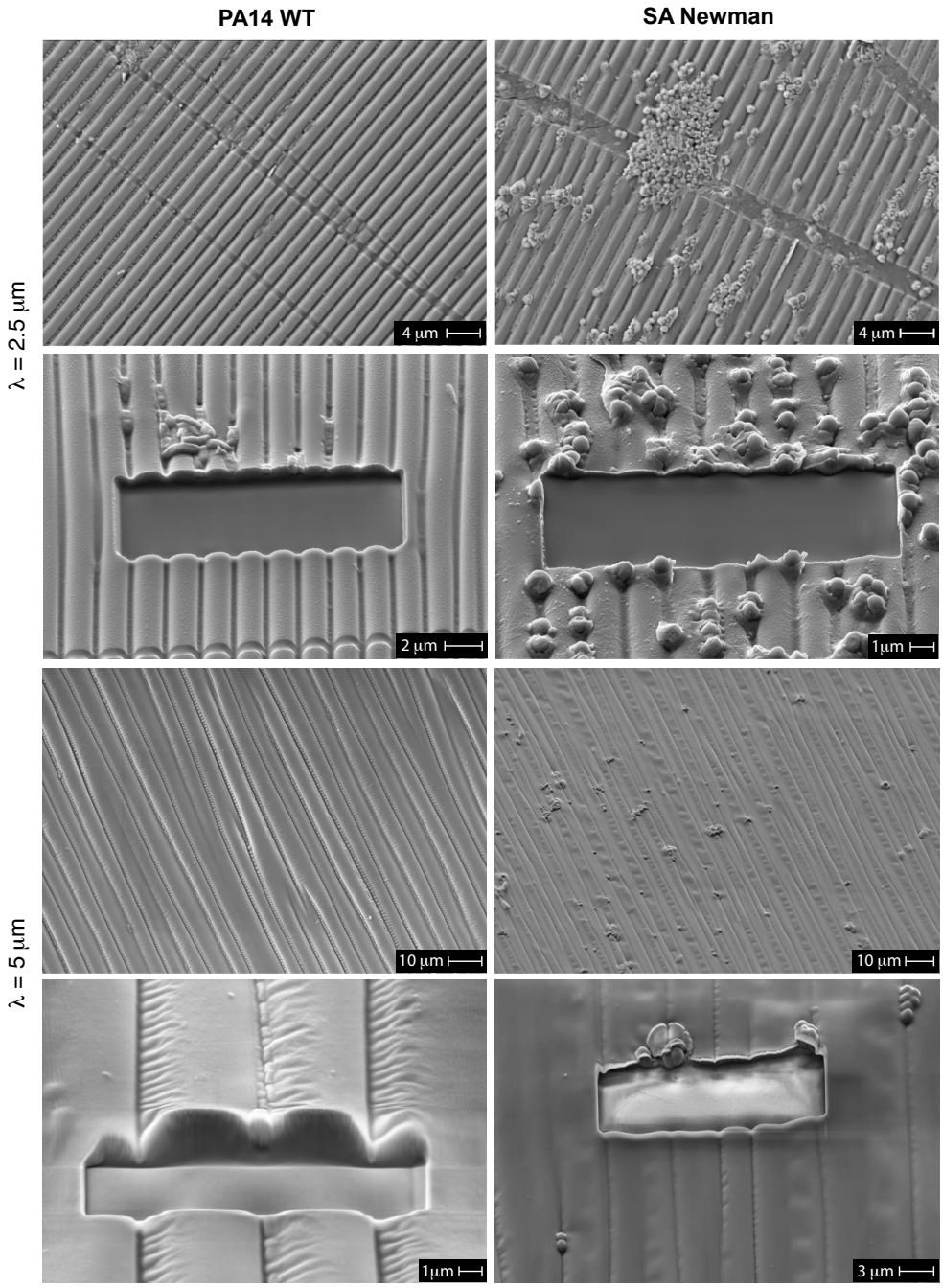

FIG. S5. FIB-SEM characterization of pattern features and microbial confinement in folded and wrinkled substrates. SEM images at different magnifications and FIB cross-sectional cuts of PA14 WT and SA Newman strains on 2 μm $w_{s\perp}$ and 5 μm $w_{f\perp}$ surfaces.

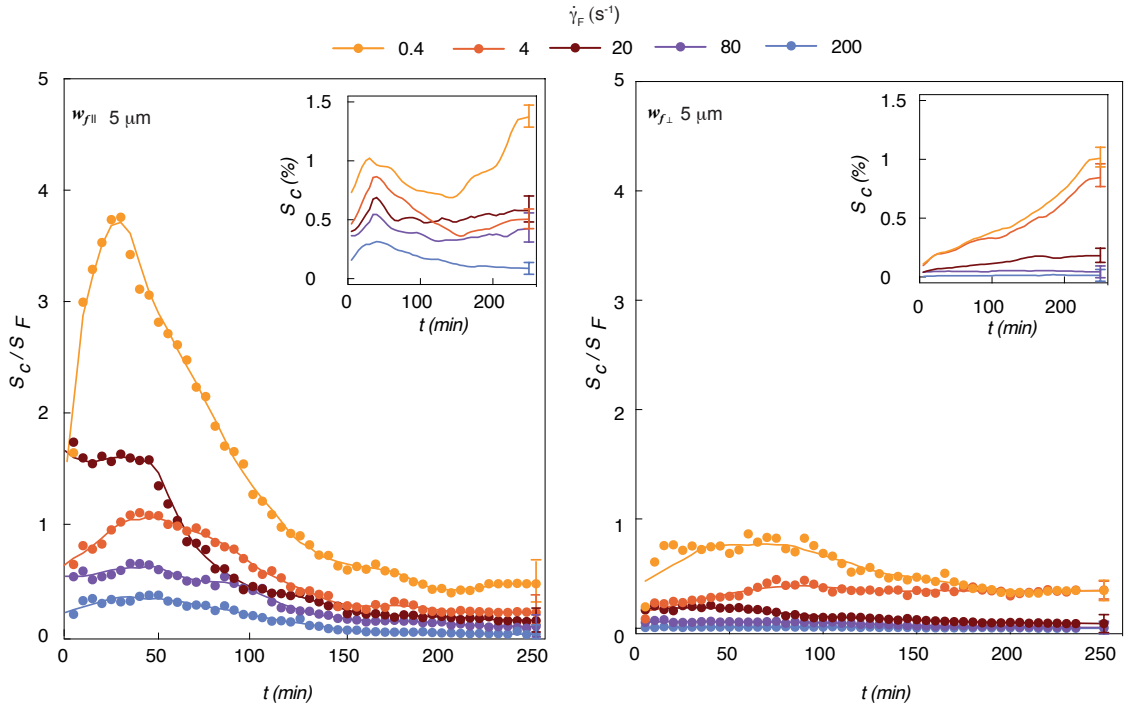

FIG. S6. Effect of folded substrate orientation on initial surface colonization by PA14 WT. Surface coverage analysis of PA14 WT strains on 5 μm $w_{f\parallel}$ (left) and 5 μm $w_{f\perp}$ (right) surfaces up to 4 hours, at different shear rates. Data represent the mean ± SEM from at least $N = 500$ cells per frame, three frames per channel, and three technical channels per condition, with three independent biological replicates. Source data are provided as a Source Data file.

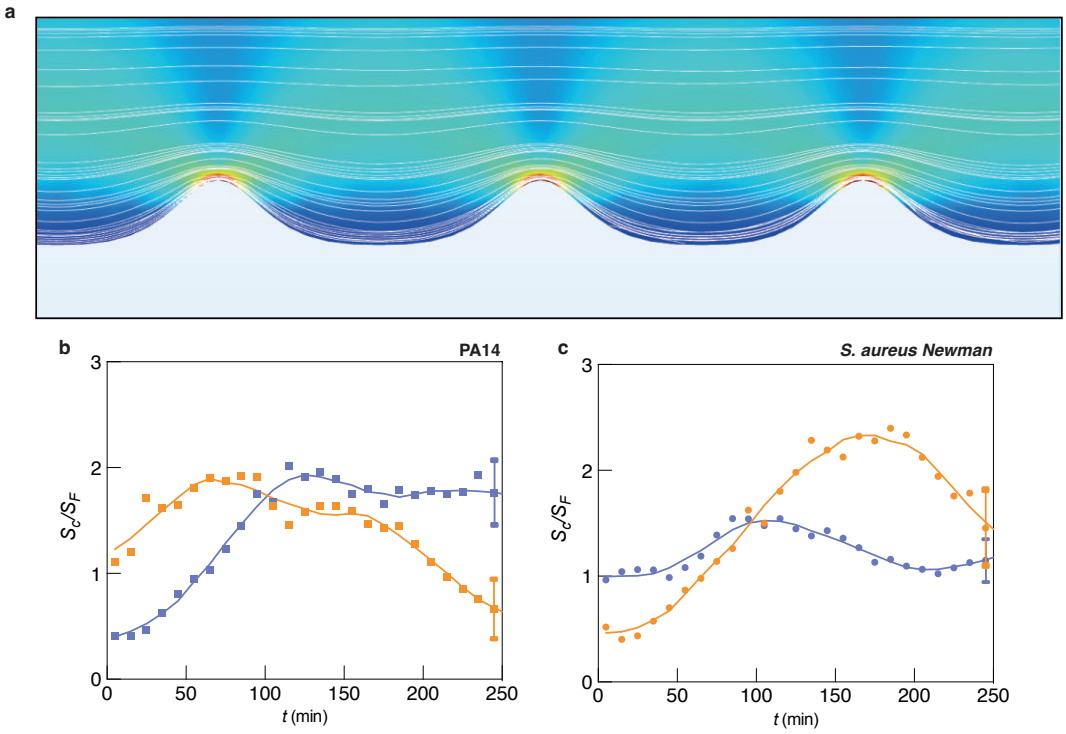

FIG. S7. Riblet-like patterns do not alter surface colonization compared to flat substrates. a Numerical simulation of a riblet-like pattern obtained from the negative replica of the 20 μm w_f surfaces (A/λ = 0.25). **b** Normalized surface coverage of PA14 on a riblet-like pattern (orange squares) compared to a 20 μm w_f surface (blue squares). **c** Normalized surface coverage of *S. aureus* Newman on a riblet-like pattern (orange circles) compared to a 20 μm w_f surface (blue circles). For **b-c**, data represent the mean ± SEM from at least $N = 500$ cells per frame, three frames per channel, and three technical channels per condition, with three independent biological replicates. Source data are provided as a Source Data file.

TABLE I. Reduction in bacterial surface coverage relative to a flat surface (%). Percentage coverage reductions for the different bacterial strains described in the main manuscript, PA14, PA14ΔmotABCD and SA Newmann on patterned surfaces $w_{\parallel}$ and $w_{\perp}$ bearing different wavelengths λ (μm) and exposed to different shear rates $\dot{\gamma}$ (s^{-1}). Reduced coverages are calculated comparing the actual coverage at 3 hours on $w_{\parallel}$ and $w_{\perp}$ surfaces S_c to the one relative to an equivalent F surface S_f and expressed as 1-(S_c/S_f)*100. Source data are provided as a Source Data file.

		PA14 WT		**PA14Δmot**		**SA Newman**	
λ (μm)	$\dot{\gamma}$ (s^{-1})	$w_{\parallel}$	$w_{\perp}$	$w_{\parallel}$	$w_{\perp}$	$w_{\parallel}$	$w_{\perp}$
0.5	80	-12.5± 2.2	-14.9± 3.4			51.3 ± 8.1	51.4± 5.3
	0.4	-45.6 ± 11.4	-50.4± 2.1	-27.9 ± 5.5	2.5 ± 2.1		
	4	-35.6± 10.1	-8.4 ± 7.4	9.4 ± 2.3	10.1± 5.3		
2	20	41.7 ± 3.2	64.2± 3.9	64.3 ± 3.3	85.3 ± 1.7		
	80	69.1 ± 1.7	72.4 ± 3.3	87.7 ± 1.1	91.3 ± 0.8	84.2 ± 1.5	85.8 ± 1.8
	200	66.4 ± 1.3	82.9 ± 1.3	94.5 ± 0.4	96.2 ± 0.4		
	0.4	47.9 ± 4.1	63.4 ± 1.7			26.1 ± 1.5	28.9 ± 1.5
	4	70.4 ± 1.5	62.2 ± 1.3			47.1 ± 1.1	49.1 ± 1.2
5	20	81.1 ± 1.6	94.1 ± 0.6			89.2 ± 1.6	92.6 ± 1.2
	80	86.8 ± 0.4	98.2 ± 0.3			89.9 ± 1.2	93.6 ± 1.1
	200	96.5 ± 0.1	99.4 ± 0.3			93.8 ± 1.1	96.1± 0.5
20	80	-10.9± 0.6	-5.2± 3.3			28.9 ± 1.5	26.1± 1.5

TABLE II. Reduction of biofilm coverage on folded surfaces under high shear. Percentage biofilm coverage reduction for PA14 WT and SA Newman on 5 μm $w_{f\perp}$ surfaces at a shear rate of $\dot{\gamma}$ =200 (s^{-1}) at 12 h and 24 h. Reduced coverage has been calculated comparing the integrated intensity of the propidium iodide (PI), red fluorescent stain marking the extracellular DNA and indicative of biofilm formation, for $w_{f\perp}$ surfaces and compared to the integrated intensity registered on equivalent F surfaces.

	Reduced biofilm formation (%)	
time (h)	PA14 WT 5 μm $w_{f\perp}$	SA Newman 5 μm $w_{f\perp}$
12	75.7 ± 2.5	86.5 ± 1.5
24	80.3 ± 1.4	83.1 ± 1.9

HemaSphere

EHA EUROPEAN HEMATOLOGY ASSOCIATION

Article
Open Access

The Nanomechanical Properties of CLL Cells Are Linked to the Actin Cytoskeleton and Are a Potential Target of BTK Inhibitors

Marta Sampietro[1,2,3], Valeria Cassina[1], Domenico Salerno[1], Federica Barbaglio[2], Enrico Buglione[1], Claudia Adriana Marrano[1], Riccardo Campanile[1], Lydia Scarfò[4,5,6], Doreen Biedenweg[7], Bob Fregin[8,9,10], Moreno Zamai[3], Alfonsa Díaz Torres[3], Veronica Labrador Cantarero[3], Paolo Ghia[4,5,6], Oliver Otto[8,9,10], Francesco Mantegazza[1], Valeria R. Caiolfa[3,11,*], Cristina Scielzo[2,*]

GRAPHICAL ABSTRACT

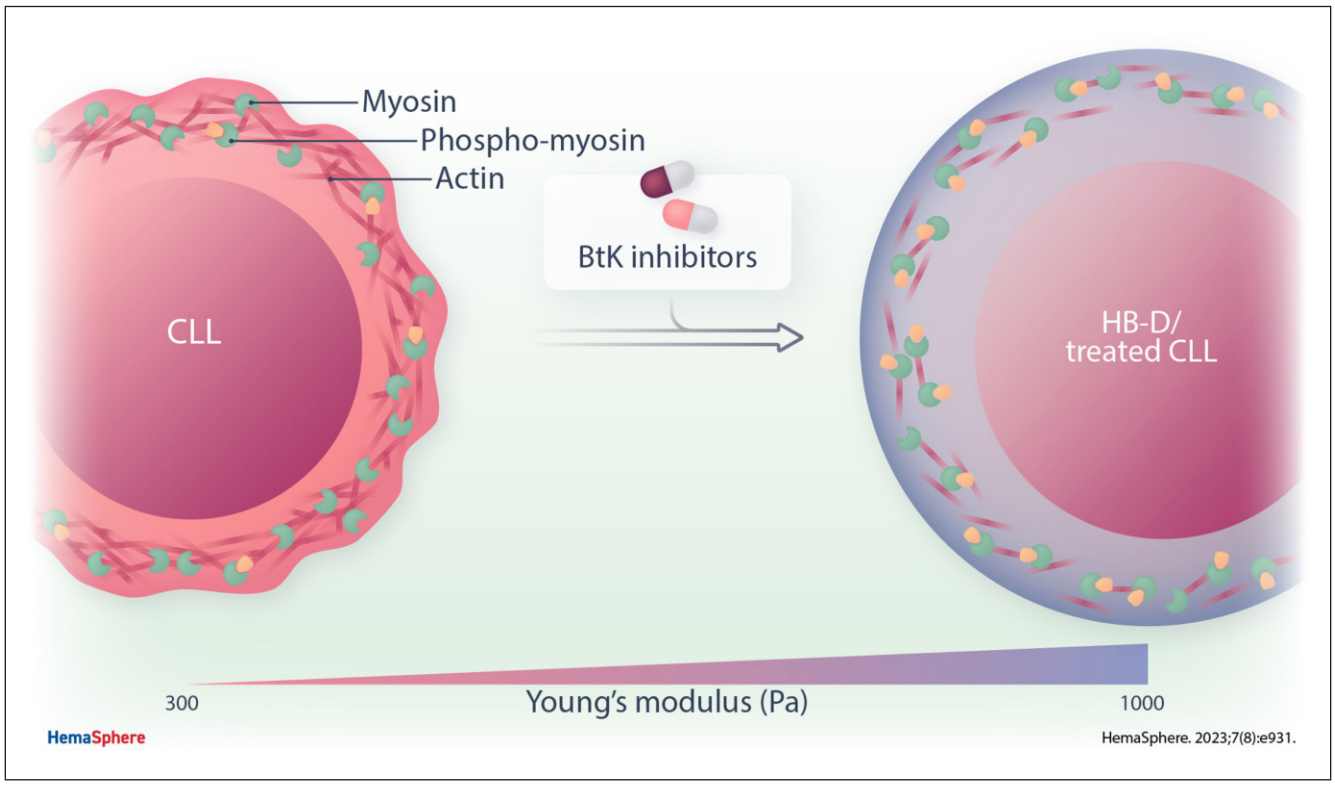

HemaSphere

EHA EUROPEAN HEMATOLOGY ASSOCIATION

Article
Open Access

The Nanomechanical Properties of CLL Cells Are Linked to the Actin Cytoskeleton and Are a Potential Target of BTK Inhibitors

Marta Sampietro[1,2,3], Valeria Cassina[1], Domenico Salerno[1], Federica Barbaglio[2], Enrico Buglione[1], Claudia Adriana Marrano[1], Riccardo Campanile[1], Lydia Scarfò[4,5,6], Doreen Biedenweg[7], Bob Fregin[8,9,10], Moreno Zamai[3], Alfonsa Díaz Torres[3], Veronica Labrador Cantarero[3], Paolo Ghia[4,5,6], Oliver Otto[8,9,10], Francesco Mantegazza[1], Valeria R. Caiolfa[3,11,*], Cristina Scielzo[2,*]

Correspondence: Cristina Scielzo (scielzo.cristina@hsr.it); Valeria Cassina (valeria.cassina@unimib.it).

ABSTRACT

Chronic lymphocytic leukemia (CLL) is an incurable disease characterized by an intense trafficking of the leukemic cells between the peripheral blood and lymphoid tissues. It is known that the ability of lymphocytes to recirculate strongly depends on their capability to rapidly rearrange their cytoskeleton and adapt to external cues; however, little is known about the differences occurring between CLL and healthy B cells during these processes. To investigate this point, we applied a single-cell optical (super resolution microscopy) and nanomechanical approaches (atomic force microscopy, real-time deformability cytometry) to both CLL and healthy B lymphocytes and compared their behavior. We demonstrated that CLL cells have a specific actomyosin complex organization and altered mechanical properties in comparison to their healthy counterpart. To evaluate the clinical relevance of our findings, we treated the cells in vitro with the Bruton's tyrosine kinase inhibitors and we found for the first time that the drug restores the CLL cells mechanical properties to a healthy phenotype and activates the actomyosin complex. We further validated these results in vivo on CLL cells isolated from patients undergoing ibrutinib treatment. Our results suggest that CLL cells' mechanical properties are linked to their actin cytoskeleton organization and might be involved in novel mechanisms of drug resistance, thus becoming a new potential therapeutic target aiming at the normalization of the mechanical fingerprints of the leukemic cells.

INTRODUCTION

Chronic lymphocytic leukemia (CLL) is the most common leukemia in the Western world and it is characterized by progressive accumulation of mature monoclonal CD5$^+$ B lymphocytes in the peripheral blood (PB), bone marrow (BM), and secondary lymphoid organs.[1] The traffic of CLL cells[2] between the PB and lymphoid organs is thought to be an active process involving a dynamic cytoskeletal remodelling[3] that contributes to disease maintenance and progression, creating niches where CLL cells can survive and proliferate.[4] These mechanisms represent a portion of a more complex scenario outlining a dynamic and heterogeneous disease,[5] a complexity that may underlie the fact that CLL still remains incurable. Deeper understanding of CLL and the B-cell receptor (BCR) signaling pathway has resulted in the development of new therapeutic approaches that have remarkably improved patient outcomes.[6] Among them, new target therapies (ie, kinase and BCL2 inhibitors)[6,7] are progressively replacing chemoimmunotherapy. In particular, the Bruton's tyrosine kinase (BTK) inhibitors[8] such as ibrutinib,[9,10] are an effective therapy leading to sustained responses, although patients may become resistant and relapse.[11] Ibrutinib promotes CLL cells mobilization from the tissues to the PB[12] where they lose the

[1]School of Medicine and Surgery, BioNanoMedicine Center NANOMIB, Università di Milano-Bicocca, Vedano al Lambro, Italy
[2]Unit of Malignant B cells biology and 3D modelling, Division of Experimental Oncology, IRCCS Ospedale San Raffaele, Milan, Italy
[3]Unit of Microscopy and Dynamic Imaging, Centro Nacional de Investigaciones Cardiovasculares (CNIC), Madrid, Spain
[4]Unit B Cell Neoplasia, Division of Experimental Oncology, IRCCS Ospedale San Raffaele, Milan, Italy
[5]Università Vita-Salute San Raffaele, Milan, Italy
[6]Strategic Research Program on CLL, Division of Experimental Oncology, IRCCS Ospedale San Raffaele, Milan, Italy
[7]Klinik für Innere Medizin B, Universitätsmedizin Greifswald, Fleischmannstr, Germany
[8]Deutsches Zentrum für Herz-Kreislauf-Forschung e.V., Standort Greifswald, Universitätsmedizin Greifswald, Fleischmannstr, Germany
[9]Zentrum für Innovationskompetenz: Humorale Immunreaktionen bei kardiovaskulären Erkrankungen, Universität Greifswald, Fleischmannstr, Germany
[10]Institute of Physics, Universität Greifswald, Felix-Hausdorff-Strasse, Germany
[11]Experimental Imaging Center, IRCCS Ospedale San Raffaele, Milan, Italy
*VRC and CS share last authorship and have contributed equally to this work.
Supplemental digital content is available for this article.

HemaSphere (2023) 7:8(e931).
http://dx.doi.org/10.1097/HS9.0000000000000931.
Received: December 29, 2022 / Accepted: June 15, 2023

protective effect exerted by the microenvironment and eventually undergo apoptosis. However, what really occurs in the tissues, and which are the processes regulating CLL cells dynamics and resistance to the therapy remains to be elucidated also due to methodological limitations.[4] An important aspect currently unexplored in CLL is how leukemic cells are able to adapt and remodel themselves and their microenvironments, once exposed to physical forces (ie, shear stress and compression).[13–16] In particular, cells are able to sense[17,18] these forces through mechanoreceptors and respond to them by exerting reciprocal cytoskeletal (ie, actomyosin complex) dependent generated forces, through a process termed mechanoreciprocity.[19] Loss of mechanoreciprocity has shown to promote cancer progression in solid tumors[20,21]; however, just a few reports studied how the cytoskeleton and cell-intrinsic mechanical properties might affect hematological cancer development, progression, and response to therapies.[22,23] In the present work, we combined different techniques to gather information at the single-cell level on cytoskeleton organization and the mechanical properties of primary B lymphocytes isolated, from patients with CLL and healthy donors (HD-B). We compared the actomyosin complex architecture by super resolution microscopy (stimulated emission depletion microscopy [STED][24]), cellular swelling by osmotic shock,[25] cell elasticity by atomic force microscopy in force spectroscopy mode (AFM-FS),[26–28] and real-time deformability cytometry (RT-DC),[29,30] identifying a significant different mechanical behavior of CLL cells in comparison to HD-B.

Furthermore, AFM-FS was employed to investigate the effect of ibrutinib on the mechanical properties of B cells. Importantly, we observed that in vitro and in vivo ibrutinib administration restores the mechanical properties of CLL cells toward the phenotype of HD-B lymphocytes until the onset of drug resistance and activates the actomyosin complex. All these data suggest that the mechanical fingerprint of CLL cells is linked to the actin cytoskeleton and is strongly associated with their malignant behavior and that the benefits of ibrutinib administration may also include the restoration of cell stiffness to physiological levels.

MATERIALS AND METHODS

Patients

Patients with CLL were diagnosed according to the updated National Cancer Institute Working Group guidelines.[31] PB samples were obtained after informed consent from patients who were either (1) untreated or off treatment for at least 6 months or (2) under ibrutinib treatment. The study was approved by the Ospedale San Raffaele ethics committee under the protocol VIVI-CLL entitled: "In vivo and in vitro characterization on CLL." Clinical and biological characteristics of CLL patients used for the experiments are reported in the Supplemental material (Table 1).

Stimulated emission depletion microscopy

We used a gated STED-3X-WLL SP8 microscope (Leica Microsystems, Wetzlar, Germany) and a HC Pl Apo CS2 100×/1.40 oil objective for all experiments. The microscope was equipped with 592-nm and 660-nm depletion lasers, and the excitation was provided by a pulsed white laser. The acquisition software was LAS X 3.5.6.21594 (Leica Microsystems, Wetzlar, Germany). Cells were stained with anti-myosin-Alexa-532 Ab and/or anti-actin-Alexa-568 Ab. STED images were acquired under X,Y depletion at 660 nm, deconvolved (Huygens software, Scientific Volume Imaging BV, Hilversum, The Netherlands) and analyzed by ImageJ/Fiji software (Image.net).[32] For details see Supplemental methods section and previous protocol optimization.[24]

Swelling experiment

Cells were seeded on polyornithine (1:10) precoated µ-Slide 8 Well (Ibidi, Gräfelfing, Germany) in 100 µL of PBS to maintain a low level of soluble in the culture. Time-lapse bright-field sequences were recorded using a spinning disk confocal-base Zeiss microscope (Zeiss, Cell Observer SD, Oberkochen, Germany). In some cases, we stained the nuclear chromatin with Hoechst 33342 solution, 1:2000 for <10 minutes and washed the sample before microscopy. Time-lapse sequences were acquired for 30 minutes at a rate of 1 frame/s. After the first 50 seconds, we injected 450 µL of MilliQ water in the medium using a submillimeter tube (500 µm in diameter). Cells were immediately swelling. Adaptive focus was used for following the volume increase. Time-lapse image sequences were segmented using an ad hoc software developed in MATLAB software (MathWorks inc, Natick, MA). The starting point is the 16-bit tiff images generated from the microscope system which, following a procedure based on the H-Maxima transformation algorithm, are segmented to identify the area of the different cells. The cell radius is considered as half of the major axis of each individual area.

Atomic force microscopy in force spectroscopy mode

For AFM-FS measurement, primary cells were plated on adapted 34 mm petri dish (TPP, 93040, Trasadingen, Switzerland) coated o/n with poly-L-ornithine solution 0.01% (Merck, Darmstadt, Germany) in Roswell Park Memorial Institute medium supplemented with 10% fetal bovine serum for 2 hours in standard incubator with a concentration of 2×10^5 cells/plate. After careful removal of medium, cells were washed twice with PBS. Measures were carried out in PBS supplemented with Ca^{2+} and Mg^{2+} (Thermo Fisher Scientific, Waltham, MA). AFM-FS measurements were performed with a Nanowizard II (JPK Instruments, Berlin, Germany) equipped with a square-based pyramid probe (MLCT-BIO, cantilever E, 0.1 N/m nominal spring constant).[33–35] All measures were carried out at room temperature in PBS Ca^{2+} Mg^{2+}. The calibration of each cantilever spring constant was performed by thermal noise method[36,37] both in air and in PBS just before the measurements on every petri dish. Force-indentation curves were acquired with a maximum applied force of 1 nN, a 4 µm ramp length and a constant speed of 2 µm/s on a grid of 1×1 µm^2 with 4×4 points. The force-distance curves were corrected for the bending of the cantilever to obtain the force-indentation curves. The evaluation of cellular elastic properties, described quantitatively through the Young's Modulus (YM), was obtained by force-indentation curves analysis with the Hertz-Sneddon model, taking into account the shape of the tip[38,39] (see Supplemental Digital Content). Each force-indentation curve was fitted by JPK data processing software (JPK Instruments, Berlin, Germany) up to about 500 nm of indentation depth. To prevent significant changes in morphology or viability of living cells, each petri dish was measured within 2 hours. After measurements, a cell count with Trypan Blue (Merck, C8273, Darmstadt, Germany) was performed and compared with a control petri dish kept in the incubator in the standard seeding medium. No significant difference in the death count was detected.

Real-time deformability cytometry

Cell mechanical measurements have been carried out using an AcCellerator system (Zellmechanik Dresden, Germany) with a fluorescence module. Suspended cells were driven through a microfluidic chip with a 300-µm long constriction of 20×20 µm^2 cross-section where they were deformed by shear and normal stresses.[29,30] Frozen samples from both patients and healthy donors were centrifuged for 5 minutes at 1500 rpm and resuspended in CellCarrierB ($PBS^{-/-}$ without Ca^{2+}/Mg^{2+} and supplemented with 0.6% [w/v] methyl cellulose) to a final concentration of 5×10^5 cell/mL. Measurements

were performed at a total constant flow rate of 0.08 µL/s. A total of about 10,000 cells per sample were captured. Analysis of cell shape was made with ShapeOut software version 0.9.6 (Zellmechanik Dresden, Germany) using an area ratio of 1.05 (ratio between raw area and area within contour) to ensure that cell contour represented the cell periphery.

Drug treatment for AMF-FS measurements

For treatment for AFM-FS measurement, Cytochalasin D (Sigma, C8273, Albuquerque, New Mexico) was added directly to PBS, incubated for 10 minutes, and then maintained in the plate during the measurement. Similar protocol was used for treatment with IgM (Southern biotech, 9023-01, Birmingham); 10 µL/mL of IgM was added directly to PBS and maintained in the medium during all measurements. The experiment lasted no longer than 2 hours to avoid saturation of the BCR signal. Ibrutinib (Selleckchem, S2680, Planegg, Germany) and acalabrutinib (Selleckchem, S8116, Planegg, Germany) were administered at concentrations of 1 µM or 10 µM[40] to cells in suspension. After 4 hours incubation, the unbound drugs were washed out by centrifuging the cell suspension. Cells were then seeded on polyornithine precoated dishes (1:10) for 2 hours to obtain stable adhesion, as described above for AFM-FS experiments in the absence of the drug.

Statistical analysis

Statistical analyses were performed with Graphpad (San Diego, CA) and Matlab (MathWorks inc, Natick, MA) software applying Mann-Whitney *U* test, considering statistically significant a value of $P < 0.05$ (*), and consequently $P < 0.005$ (**) and $P < 0.0005$ (***).

RESULTS

Nanoscale cytoskeleton architecture of CLL cells

The nanoscale architecture of the actin cytoskeleton in primary healthy and leukemic B cells has never been explored so far. We applied single-cell STED super resolution microscopy optimized as previously published.[24] We isolated primary B cells from PB of patients with CLL (n = 8; Table 1) and from HD-B donors (n = 3). Primary cells were plated on precoated polyornithine coverslips and stained for actin to visualize long and short actin filaments.[41] For single-cell analysis, 3 optical sections were imaged at the top, equatorial, and bottom regions (Figure 1A), to compare, under identical acquisition conditions, actin density, filament length and branching in representative cell areas. Quantification was pursued by single optical section—single-cell analysis (Suppl. Figure S1). Actin filaments in CLL and HD-B cells are organized in a compact meshwork-like structure (Figure 1A). At the top regions, actin density in CLL cells was higher than in HD-B cells ($P < 0.0001$), while we did not observe significant differences at the bottom regions (Figure 1B). At the equatorial regions, actin appeared more packed and intense in CLL cells, depicting a thicker area in the cytosol (Suppl. Figure S2), and resulting in a higher density as compared with HD-B cells ($P < 0.0001$; Figure 1B). Next, we analyzed 2 structural elements of the actin-meshwork, filament length, and number of branching (Figure 1C; Suppl. Figure S3). It is known that filaments portions longer than 300 nm readily buckle under compressive forces involving the actomyosin complex,[42] for this reason, we limited our analysis to the cell top and bottom regions where single filaments were detectable and we considered only filaments longer than 260 nm, also consistent with our experimental resolution (Suppl. Figure S4). Despite similar actin densities, significant differences were found at the bottom regions (Figure 1C; bottom panel), where CLL cells showed longer ($P = 0.002$) and more branched filaments ($P < 0.0001$) than normal HD-B cells. At the top regions where actin density was higher in CLL cells (Figure 1B), we observed only a moderate increase of branching ($P = 0.04$) but no longer filaments (Figure 1C; upper panel). The diversity of the actin organization captured by our analysis on 3 optical sections was confirmed with whole-cell reconstructions as shown in the representative 3D-STED stack (Suppl. Videos S1 and S2). To evaluate the contractile force generators in the cellular cortex,[43,44] we further determined the local density of the nonmuscular myosin IIA, known motor and cross-linker protein (Suppl. Figure S1). HD-B (n = 2) and CLL (n = 6) cells were stained for myosin and STED images were acquired at the top, equatorial, and bottom regions of single cells (Figure 1D). In contrast to actin filaments, myosin shows punctuate and diffuse patterns. In CLL cells, myosin density at the top regions was significantly higher than at the bottom regions (Figure 1E; top region *P* value = 0.02; bottom region *P* value = 0.06). At the equatorial regions, a significant increase of myosin in HD-B compared with CLL cells regions was observed ($P = 0.03$). We performed an in-silico analysis (Blueprint Consortium) on the expression levels of the myosin regulatory light chain 2 *(MLC2)* and myosin heavy chain, nonmuscle IIa (*MYH9*), comparing primary CLLs and HD-Bs. In-silico analysis confirmed that CLL cells overexpress these genes, in line with our STED results (Suppl. Figure S5), and consistently suggesting an altered cytoskeleton organization in CLL cells.

The actomyosin complex is altered in CLL cells

Actin and myosin work as actomyosin complex to regulate cell contraction and cellular tension.[42–46] We further analyzed the colocalization of actin and myosin in both primary HD-B and CLL cells (HD-B donors n = 2; CLL patients n = 6) to further study how the spatial arrangement of myosin motors at the cortex affects cortical tension and the possible involvement of this complex in CLL pathogenesis. Actin-myosin colocalization was analyzed in 2D-STED images of bottom and equatorial regions obtaining the percentage of colocalization of actin and myosin by Manders' coefficient[47] (Figure 2A and 2B), (Methods and Suppl. Figures S6 and S7). Actin density at the bottom regions did not change (Figure 1B), while we detected an increase of myosin density (Figure 1E) in CLL. Despite that, in those regions, actomyosin colocalization was found significantly reduced in CLL cells (Figure 2A; right panel; $P < 0.0001$). Moreover, although actin was denser at the cell equators (Figure 1A) in CLL, actin and myosin colocalization was higher in HD-B cells (Figure 2B; right panel; $P < 0.0001$). Noticeably, the loss of actomyosin colocalization was evident despite the intrapopulation heterogeneity (Figure 2). Considering myosin colocalization with actin as a sign of activation and contractility, our results suggest a remarkable cytoskeleton alteration in CLL, affecting the actomyosin complex (Figure 2C), possibly underlying a decreased cellular contractility and tension[42] that may be responsible for altered mechanical responses.

Different cytoskeletal architecture in CLL cells correlate with specific mechanical response

To further investigate cellular tension in response to external stimuli in HD-B and CLL cells, we performed a swelling experiment, measuring single-cell area in the presence of an osmotic pressure over time.[25,48–50] As for STED imaging, cells were set in adhesion on precoated polyornithine in multi-well (HD-B donors n = 3; CLL patients n = 4). After water addition, cells swelled progressively, and their volume increased noticeably in the first 10 minutes (Suppl. Video S3; Figure 3A). The cellular radius over time was used to track hypoosmotic swelling (see Methods and Suppl. Figures S8 and S9) up to equilibrium. The cellular radius at equilibrium was calculated as the asymptotic fitting value (R_{fin}) of an exponentially increasing function. The increase of the radius, expressed as R_{fin}/R_{in} (where R_{in} represents the initial value of the radius) was undoubtedly more pronounced in CLL cells as obtained by the global fitting of the pooled kinetics (Figure 3B;

Table 1

Clinical and Biological Parameters of the Patients With CLL Used in the Experiments (n = 46)

Pt number	Rai	Binet	CD38 Result	IGHV Homology	IGHV Homology Outcome	FISH	Clinical course	Application
1	1	A	NA	NA	NA	Not done	Stable	AFM
2	0	A	12.3	100	uCLL	del13q14.3 (90.6%, homozygous 27.8%, heterozygous 62.8%)	Progressive	AFM (ibrutinb), RT-DC
3	0	A	12.4	94.04	mCLL	del13q14.3 (20%), del13q34 (16.5%)	Stable	AFM, RT-DC, STED (Ibrutinib)
4	1	A	0.68	95.49	mCLL	del13q14.3 (29%), del13q34 (17.4%)	Stable	AFM, RT-DC
5	0	A	5.2	92.28/96.18	mCLL	Not done	Stable	AFM
6	1	A	57.2	93.75	mCLL	Not done	Stable	AFM
7	0	A	19.1	95.14	mCLL	Not done	Stable	AFM, RT-DC
8	0	A	0.1	93.33	mCLL	Normal	Stable	AFM
9	0	A	0	96.26	mCLL	del13q14.3 (90%)	Stable	AFM
10	0	A	15.90	98.30	uCLL	normal	Progressive	AFM (ibrutinb)
11	1	A	2	95.53	mCLL	del17p13.1 (12%), +12 (80%)	Progressive	AFM (ibrutinb)
12	0	A	0	90.97	mCLL	Not done	Stable	AFM
13	0	A	0.1	100	uCLL	Normal	Stable	AFM, STED (Ibrutinib)
14	0	A	5	100	uCLL	Normal	Progressive	AFM, RT-DC
15	NA	NA	NA	91.67	mCLL	NA	Stable	AFM
16	1	NA	1	93.15	mCLL	del13q14.3 (92.8%)	Progressive	AFM
17	0	A	41.5	100	mCLL	del(11q) 84%, del(13q14.3) 97%	Progressive	AFM–BM
18	0	A	36.4	100	uCLL	del(13q14) 87.8%	Progressive	AFM–BM
19	0	A	3	88.9	mCLL	NA	Progressive	RT-DC
20	0	A	0.1	97.98	mCLL	Not done	Stable	RT-DC
21	0	A	2.42	92.36	mCLL	NA	Stable	RT-DC
22	0	A	4.6	100	uCLL	del(13q14) 8%	Progressive	RT-DC
23	NA	NA	NA	91.67	mCLL	del(17p) 12%	Progressive	RT-DC, STED
24	0	A	0.4	91.32	mCLL	NA	Stable	RT-DC, WB
25	0	A	0.58	93.4	mCLL	NA	Stable	STED, AFM (acalabrutinib)
26	0	A	0.4	93.75	mCLL	Normal	Stable	STED
27	0	A	0.8	96.53	mCLL	del(13q) 80%	Stable	STED
28	0	A	0.6	87.02	mCLL	NA	Stable	STED
29	0	A	0	88.54	mCLL	NA	Stable	Swelling
30	1	A	1.3	100	uCLL	NA	Stable	Swelling
31	0	A	NA	92.63	mCLL	NA	Stable	Swelling
32	1	A	0.8	96.2	mCLL	NA	Stable	Swelling
33	0	A	16.32	100	uCLL	del(17p)	Progressive	AFM (ibrutinb)
34	0	A	0.16	3.94375	mCLL	del13q14.3 (10%), del13q34 (8.4%), del11q22 (8.4%), del17p13 (11.2%)	Stable	AFM (IgM)
35	0	A	0.3	93.8	mCLL	del13q14.3 (75.5%), del13q34 (10%)	Stable	AFM (IgM)
36	0	A	0.1	92.71	mCLL	NA	Stable	WB
37	1	A	0	96.18	mCLL	del17p (11%), del13q14.3 (18%) e del13q34 (9%)	Progressive	WB
38	1	A	0.1	91.23	mCLL	NA	Stable	WB
39	2	B	9	100	uCLL	Trisomy 12 (65.5%)	Progressive	WB
40	1	A	0	95,09	mCLL	NA	Stable	WB, AFM (acalabrutinib)
41	0	A	18.7	99.66	uCLL	Trisomy 12 (75%)	Stable	STED (Ibrutinib)
42	1	A	NA	NA	NA	NA	Progressive	AFM-Lynph node
43	1	A	1.4	100	uCLL	Trisomy 12 (71.7%)	Progressive	AFM-Lynph node
44	NA	NA	NA	NA	NA	NA	Progressive	AFM-Lynph node
45	0	A	3.33	100	uCLL	del17p (91%) and del 13q14.3 (23.5%)	Progressive	AFM (acalabrutinib)
46	0	A	0.16	91.41	mCLL	Normal	Stable	STED

CLL = chronic lymphocytic leukemia; mCLL = mutated=good prognosis; NA = not available; uCLL = unmutated=good prognosis.

$P < 0.0001$; Suppl. Figure S9). The same conclusion was reached by fitting each individual cell kinetics first, and then averaging the R_{fin}/R_{in} values (Figure 3B). Thus, regardless the analytical method and despite swelling kinetics were characterized by heterogeneous distributions of characteristic times (τ) (Suppl. Figure S10). Results were in line with the different cytoskeleton organization in normal and patient-derived cells. The results suggest that a divergent response of the cells to tension and, ultimately, their altered mechanical properties might be a consequence of such a modified actomyosin complex in CLL cells.[44] Considering that actin and myosin largely dominate the mechanical properties of cells and have an impact on cellular elasticity,[51,52] we measured single-cell cortical stiffness by AFM-FS (Figure 3C).[53] All measurements were performed with cells in adhesion and no changes in cell viability were observed (Suppl. Figure S11). We recorded force-indentation curves that describe the relationship between the applied force and the cell deformation (Figure 3D). We calculated the YM values by fitting the approaching force-indentation curve at <500 nm indentation depth, which can be referred to as cortical stiffness.[53] The analysis of HD-B and CLL cells (from HD-B donors n = 9; CLL patients n = 22) indicated that CLL cells have a systematically lower cortical stiffness than HD-B cells ($P < 0.0001$; Figure 3E;

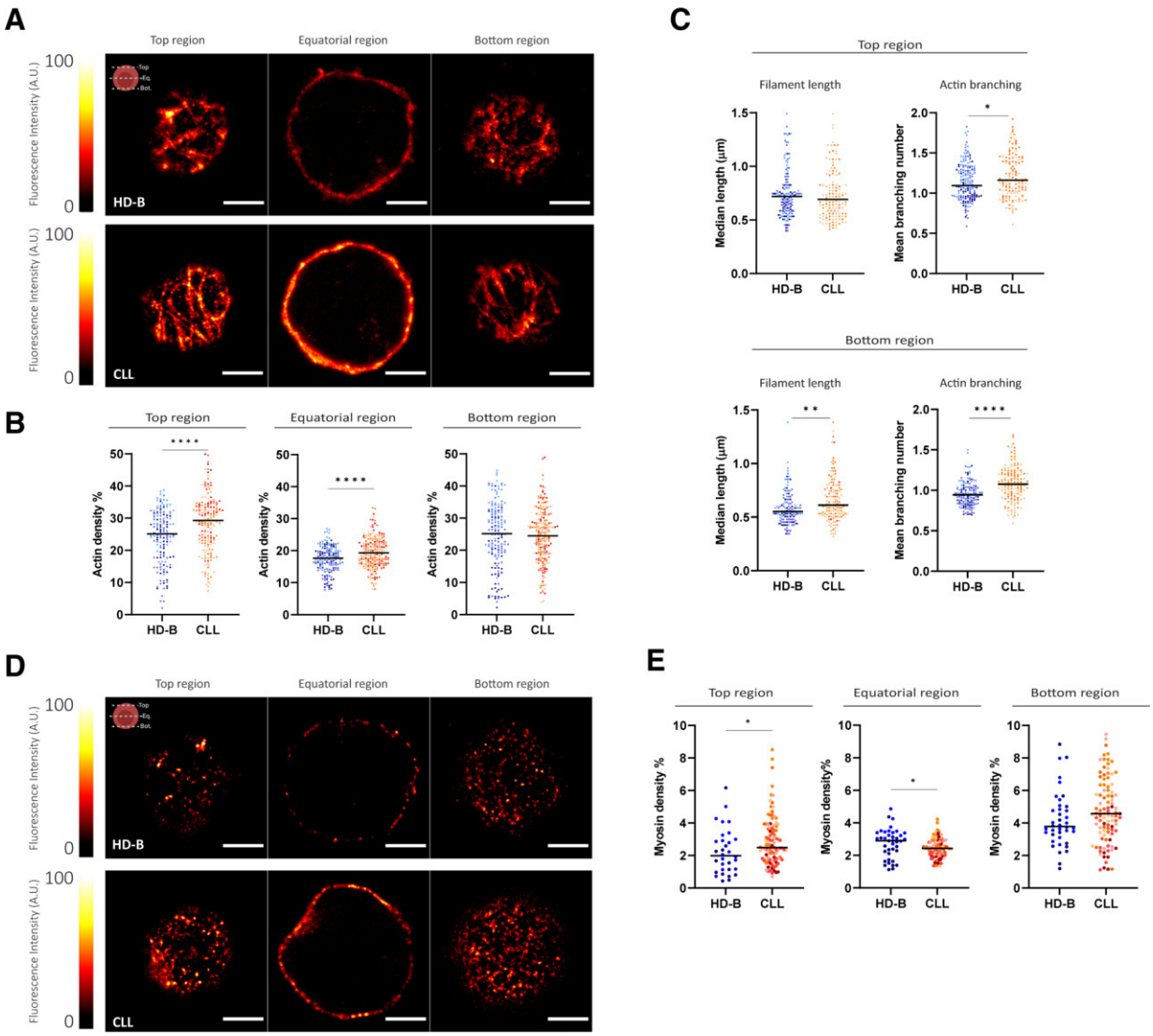

Figure 1. Single-cell analysis by STED super resolution microscopy for actin. (A) Representative images of anti-actin–Alexa-568 immunostained HD-B and CLLs cells acquired under identical experimental conditions at the three selected cellular regions. Scale bar = 2 µm. (B) Scatter plots of actin density expressed as percentage of the fluorescence intensity counts over the ROI total area intensity, obtained for the three explored cellular regions (see Materials and Methods). Cells derived from the same healthy donor (HD-B) or patient (CLL) are identified by color-code. Horizontal bars: median values. Top region: HD-B median 25.1%, and CLL median 29.3%; $P < 0.0001$. n = 147 HD-B cells from 3 donors and n = 181 CLL cells from 8 patients. Equatorial region: HD-B median 17.6%, and CLL median 19.3%, $P < 0.0001$. n = 158 HD-B cells from 3 donors and n = 213 CLL cells from 8 patients. Bottom region: HD-B median 24.7%, and CLL median 24.8%; $P = 0.76$, n = 159 HD-B cells from 3 donors and n = 156 CLL cells from 8 patients. (C) Actin morphology evaluated as length and branching of filaments at the top and bottom regions. In the scatter plots of actin filament length, we show the median filament length per cell. Top region: HD-B median 0.72 µm, and CLL median 0.69 µm, $P = 0.34$. n = 152 HD-B cells from 3 donors and n = 134 CLL cells from 5 patients. Bottom region: HD-B median 0.55 µm, and CLL median 0.61 µm, $P = 0.002$. n= 128 HD-B cells from 3 donors and n = 134 CLL cells from 5 patients. The filament branching plots illustrate the mean number of actin branching per filament and per cell. Top region: HD-B mean 1.10, and CLL median 1.16; $P = 0.04$. n = 164 HD-B cells from 3 donors and n = 139 CLL cells from 5 patients. Bottom region: HD-B mean 0.94, and CLL median 1.08; $P < 0.0001$. n = 142 HD-B cells from 3 donors and n = 146 CLL cells from 5 patients. (D) Representative STED images of anti-myosin-Alexa-532 immunostained HD-B and CLLs cells acquired under identical experimental conditions at the 3 selected optical regions. Scale bar = 2 µm. (E) Scatter plots of myosin density expressed as percentage of the fluorescence intensity counts over the ROI total area intensity as obtained for the three explored cellular regions (see Materials and Methods). Cells are color-coded according to each healthy donor (HD-B) or patient (CLL) from which they were obtained. Top region: HD-B median 2.0%, and CLL median 2.5%; $P = 0.02$; 32 HD-B cells from 2 donors and 101 CLL cells from 6 patients. Equatorial region: HD-B median 2.9%, and CLL median 2.4%; $P = 0.03$; 40 HD-B cells from 2 donors and 98 CLL cells from 6 patients. Bottom region: HD-B median 3.78%, and CLL median 4.57%; $P = 0.06$; 40 HD-B cells from 2 donors and 100 CLL cells from 6 patients. All graphical schemes were made with Biorender. CLL = chronic lymphocytic leukemia; HD = healthy donors; STED = stimulated emission depletion microscopy.

Suppl. Figures S12 and S13). We further investigated whether there was a correlation between cortical stiffness and patients' prognostic factors (Table 1). We examined the distributions of the cell cortical stiffness after segmenting patients according to the *IGHV* gene mutational status (*IGHV*<98%=mutated=good prognosis [mCLL, n = 16] and *IGHV*≥98%=unmutated=bad prognosis [uCLL, n = 5]).[54] The results reported in Suppl. Figure S14A indicate a correlation between cell stiffness and *IGHV* mutational status, being uCLL cells significantly softer than the mCLL population ($P = 0.04$). In contrast, we did not observe any correlation with the disease progression (Suppl. Figure S14B).

Considering the intrinsic plasticity of lymphocytes and their ability to traffic and home in different anatomical compartments,[55–57] we further assessed their mechanical properties

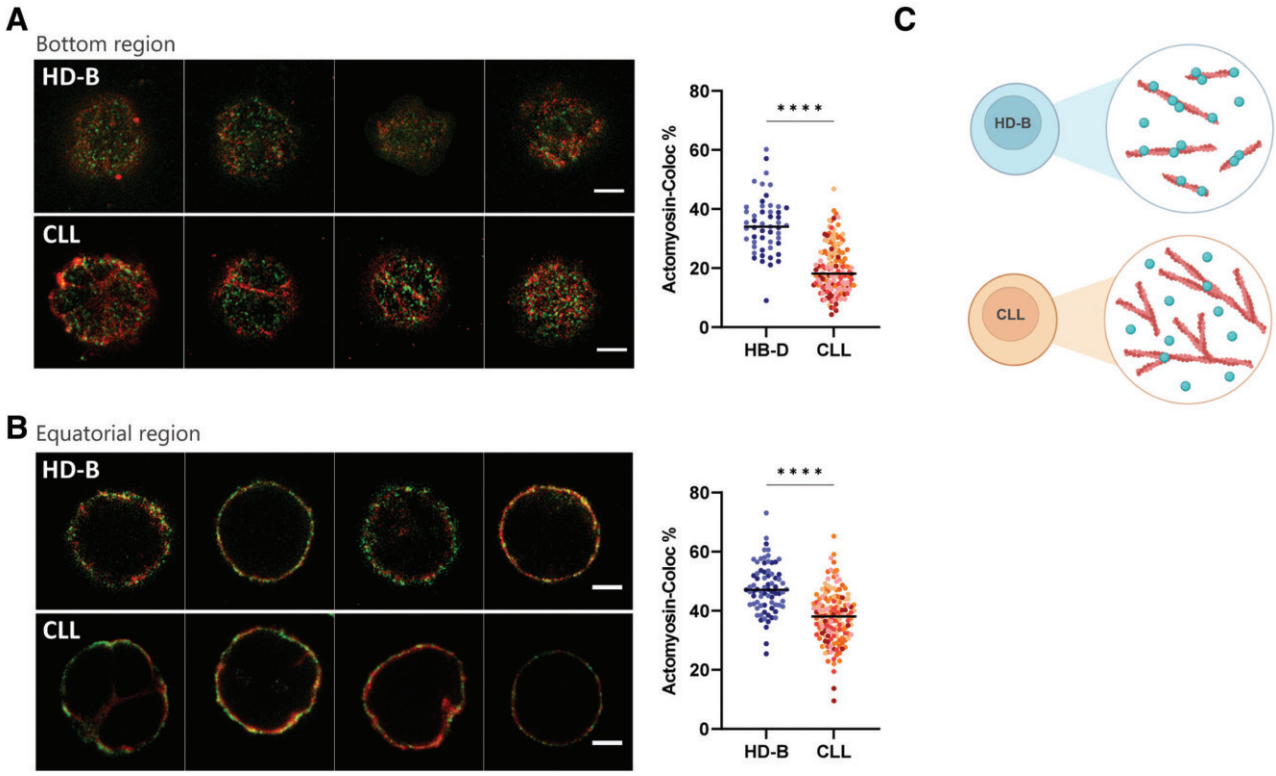

Figure 2. Single-cell actomyosin colocalization by STED super resolution microscopy. (A, left) Representative images of costained anti-myosin-Alexa-532 (green) and anti-actin-Alexa-568 (red) HD-B and CLL cells acquired under identical experimental conditions at the bottom region. Scale bar = 2 µm. (A, right) Quantification of the colocalization of myosin and actin by Manders' coefficient expressed as percentage of colocalized actin pixels on myosin pixels. HD-B median 34.0%, and CLL median 18.2%; $P < 0.0001$; 51 HD-B cells from 2 donors and 150 CLL cells from 6 patients. (B; left) Representative images of costained anti-myosin-Alexa-532 (green) and anti-actin-Alexa-568 (red) representative HD-B and CLL cells acquired under identical experimental conditions at the equatorial region. Scale bar = 2 µm. (B; right) Quantification of colocalization of ActoMyosion with Manders' coefficient expressed as percentage of colocalized myosin pixels on actin pixels. HD-B median 47.1% and CLL median 38.10%; $P < 0.0001$; 75 HD-B cells from 2 donors and 147 CLL cells from 6 patients. (C) Graphical representation made by Biorender of the actomyosin complex organization, where the blue dots represent myosin and the red fibrils represent actin. CLL = chronic lymphocytic leukemia; HD = healthy donors; STED = stimulated emission depletion microscopy.

under a different noncontact environmental constraint. We performed RT-DC measurements, which allows us to determine the elasticity of cells in suspension by shape analysis (Figure 3F).[29] Each measurement summarizes the deformation and size of thousands of cells (Figure 3G). We then derived the median deformation for each experiment (Figure 3H), demonstrating that CLL cells deform less than HD-B ($P = 0.003$; HD-B donors n = 12; CLL patients n = 13). In parallel, a numerical model was used to calculate the elasticity value expressed as the YM (see Methods), where we noted a systematic softer behavior of HD-B cells compared with their leukemic counterparts ($P = 0.0001$). As for AFM-FS analysis, we segmented the patients according to the *IGHV* gene mutational status and diseased progression. We found that progressive CLL are significantly softer than stable CLL cases ($P = 0.007$; Suppl. Figure S15). Interestingly, we observed that CLL cells exhibit a wider intrinsically size heterogeneity with respect to HD-Bs; however, no relevant difference in the median area was noticed (Figure 3H).[58] Moreover, we found a significant correlation between CLL cells area and the mutational status of the *IGHV* genes: uCLL (n = 3 patients) are smaller than mCLL (n = 8 patients) ($P < 0.0001$; Suppl. Figure S15), while YM value measured by AFM did not depend on cell size, showing a negligible Pearson correlation coefficient (data not shown). All together, these results confirm the differences between healthy and leukemic B cells and suggest that CLL mechanical adaptation properties are very dependent on the specific environmental cues as shown in suspension (circulation-like) for RT-DC and in adhesion (tissue-like) for AFM.

CLL cells mechanical response can be tuned in vitro

We further tested to which extent the mechanical properties of the cells could be modulated in vitro by specific stimuli. We verified that in none of the experiments, cellular viability was altered at the selected drug concentration (Suppl. Figure S16). First, we used mycotoxin cytochalasin D[59,60] as a conventional stimulus known to prevent actin monomer polymerization,[61,62] thus decreasing cell elasticity. Its effect was appreciable on HD-B cells, which displayed a significant decrease in cortical stiffness ($P < 0.0001$) (Suppl. Figure S17). On the contrary, the drug had no evident effect on CLL cells (Suppl. Figure S17), suggesting that their intrinsically low cortical stiffness could not be further modulated. These results prove that we can detect drug-mediated effects on lymphocytes' cortical stiffness by AFM-FS and prompted us to further investigate this aspect using a clinically relevant drug. We analyzed whether the kinase inhibitor ibrutinib[9,10] could have an impact on the mechanical properties of CLL cells. We incubated cells with ibrutinib for 4 hours at a final concentration of 1 µM and 10 µM[40] and we did not observe any differences in the effect of the 2 concentrations (Suppl. Figure S18). Incubation with ibrutinib induced an increase of cortical stiffness in CLL cells (Figure 4A; $P < 0.0001$ and Suppl. Figure S19) to almost physiological level but did not significantly alter the response of HD-B cells ($P = 0.1$; HD-B donors n = 2; CLL patients n = 5). To confirm the direct involvement of BTK inhibition, we tested a more specific inhibitor namely acalabrutinib[8] on 3 additional patients with CLL and we confirmed the increase in stiffness

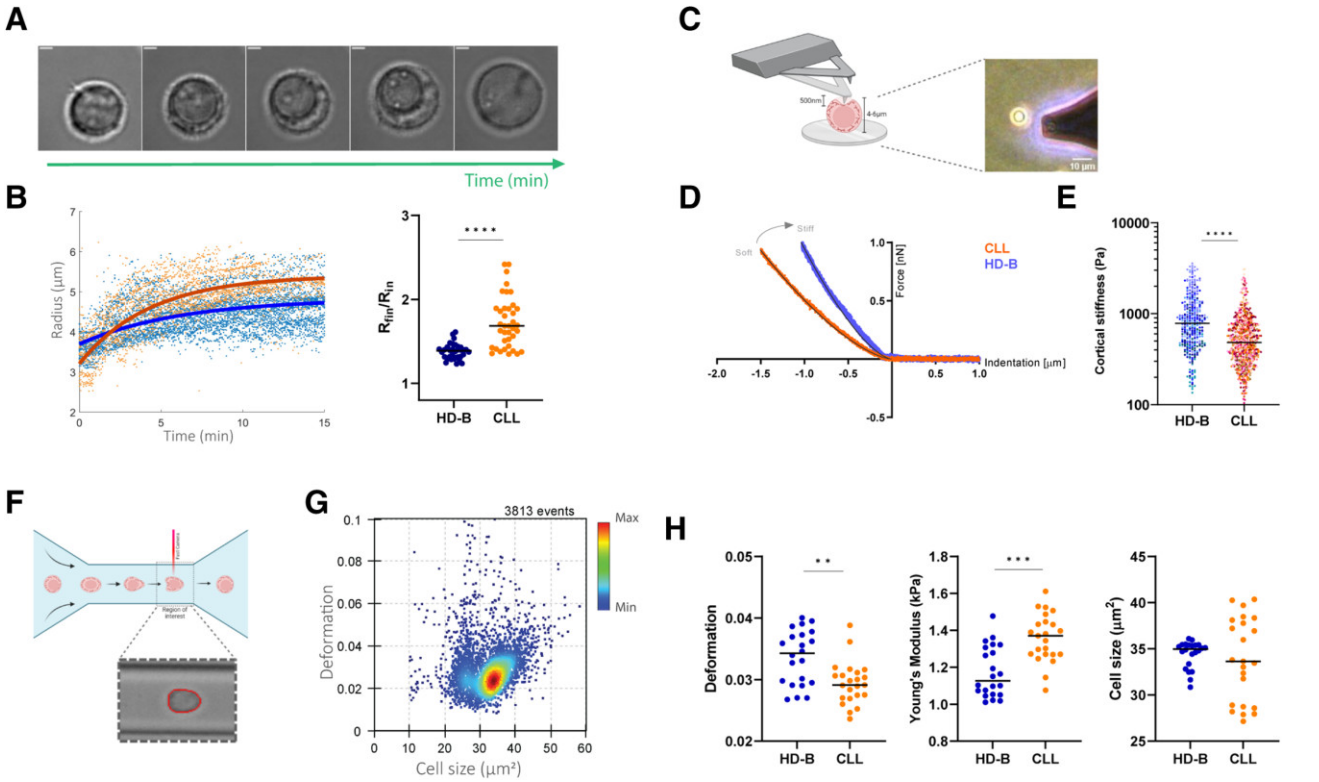

Figure 3. Nanomechanical analysis of CLL and HD-B cells. (A) Bright-field images of a representative 20 min time-lapse record of a single cell swelling as a consequence of osmotic shock. Scale bar = 5 µm. (B) Swelling kinetics of individual cells. (B; left) The continuous blue and red lines show global fitted curves on the total pool of HD-B and CLL cells respectively. The fit function is $([R_{fin}-R_{in}] \times [1-\exp[-t/\tau]] + R_{in})$, where R_{in} and R_{fin} are the initial and final radius of the cell, t is the time and the τ is the swelling characteristic time. (B; right) Scatter plot of the swelling ratio (R_{fin}/R_{in}), HD-B median 1.39 and CLL median 1.68; $P < 0.0001$. 37 HD-B cells from 3 donors and CLL cells 39 from 4 patients. (C, left) Schematic representation (BioRender.com) of the AFM-FS basic principle, showing a cantilever pressing on a B cell at the cortical level. (C, right) The image shows a real snapshot of the AFM cantilever tip approaching a cell. Scale bar = 10 µm. (D) Representative force-indentation curves from an AFM experiment in the force spectroscopy mode for HD-B (blue dots) and CLL (orange dots) cells. Black lines are the fitting curves according to the Hertz-Sneddon model (see Methods for details). (E) Scatter plot of the cortical stiffness expressed as Young's Modulus (Pa) of HD-B and CLL cells. HD-B median 785.1 Pa and CLL median 484.0 Pa; $P < 0.0001$; 345 HD-B cells from 9 donors and 765 CLL cells from 22 patients. Cells are color-coded according to each healthy donor (HD-B) or patient (CLL) from which they were obtained. (F) Biorender scheme of RT-DC, showing a cell passing through a microfluidic channel. Inset exemplifies bright-field image of a cell within region-of-interest, where deformation is obtained from red contour. (G) Representative scatter plot of cell deformation versus cell size (cross-sectional area) for n = 3813 HD-B cells analyzed by RT-DC. The color-code indicates a linear density scale. (H) Deformation, YM and cell size for HD-B from 7 donors and CLL from 6 patients. For deformation and YM each dot represents the median value of each individual experiment, with overall HD-B deformation median 0.034 and CLL median 0.029; $P = 0.003$ as well as overall HD-B Young's Modulus median 1.13 kPa and CLL median 1.37 kPa; $P < 0.0001$. For cell size analysis each dot represents the mean cell size of each individual measurement with overall HD-B mean cell size 35.0 µm² and CLL mean 33.6 µm²; $P = 0.9$. Measurements have been performed at a flow rate of 0.08 µL/s and statistical analysis has been done using linear mixed models. AFM-FS = atomic force microscopy in force spectroscopy; CLL = chronic lymphocytic leukemia; HD = healthy donors; RT-DC = real-time deformability cytometry; STED = stimulated emission depletion microscopy.

($P < 0.0001$; Figure 4A). The possible involvement of the BCR receptor activation in this context was tested by stimulating CLL and HD-B cells with anti-IgM. We did not observe any changes of the cortical stiffness values (Suppl. Figure S20; HD-B $P = 0.3$; CLL $P = 0.6$) indicating that the BCR activation is not directly affecting B cell cellular stiffness. In addition, by western blot, we quantified the activation of p-myosin following ibrutinib treatment (Figure 4B) in order to evaluate the potential involvement of the actomyosin complex in the mechanism of action of ibrutinib in 5 CLL patients. We observed that ibrutinib can upregulate at variable levels myosin phosphorylation in vitro (Figure 4B, right panel; Suppl. Figure S21) in CLL cells, suggesting a drug modulation effect on the actomyosin complex. Therefore, we studied the cellular colocalization of the 2 proteins by 2-color 2D-STED microscopy before and after treatment with ibrutinib. We focused this analysis on the cell bottom where we did not see a significant difference between healthy B cell and CLL cells when we studied the 2 proteins individually (Figure 1). In this section, myosin and actin densities were unchanged as compared with the healthy counterparts but their colocalization decreases dramatically in CLL (Figure 2B). Interestingly, we observed a significant recovery of actin and myosin colocalization in these bottom cell sections ($P < 0.0001$) upon treatment with ibrutinib (Figure 4C). As comparison we also imaged the actomyosin complex at the cell equators, where we previously detected less difference in terms of myosin (Figure 1E), and we did not observe a significant change in the complex organization after ibrutinib treatment (Figure 4D). All together, these results suggest an effect of the drugs on both actomyosin complex and cortical stiffness (Figure 4E).

CLL cells mechanical properties are reverted to normal phenotype by ibrutinib in vivo

In view of the above results, we asked whether the mechano-response observed in CLL cells in vitro might have a clinical relevance in patients under treatment. We evaluated by AFM-FS the cortical stiffness of single CLL cells isolated from PB of 4 patients before and during ibrutinib treatment (4, 8, 9,

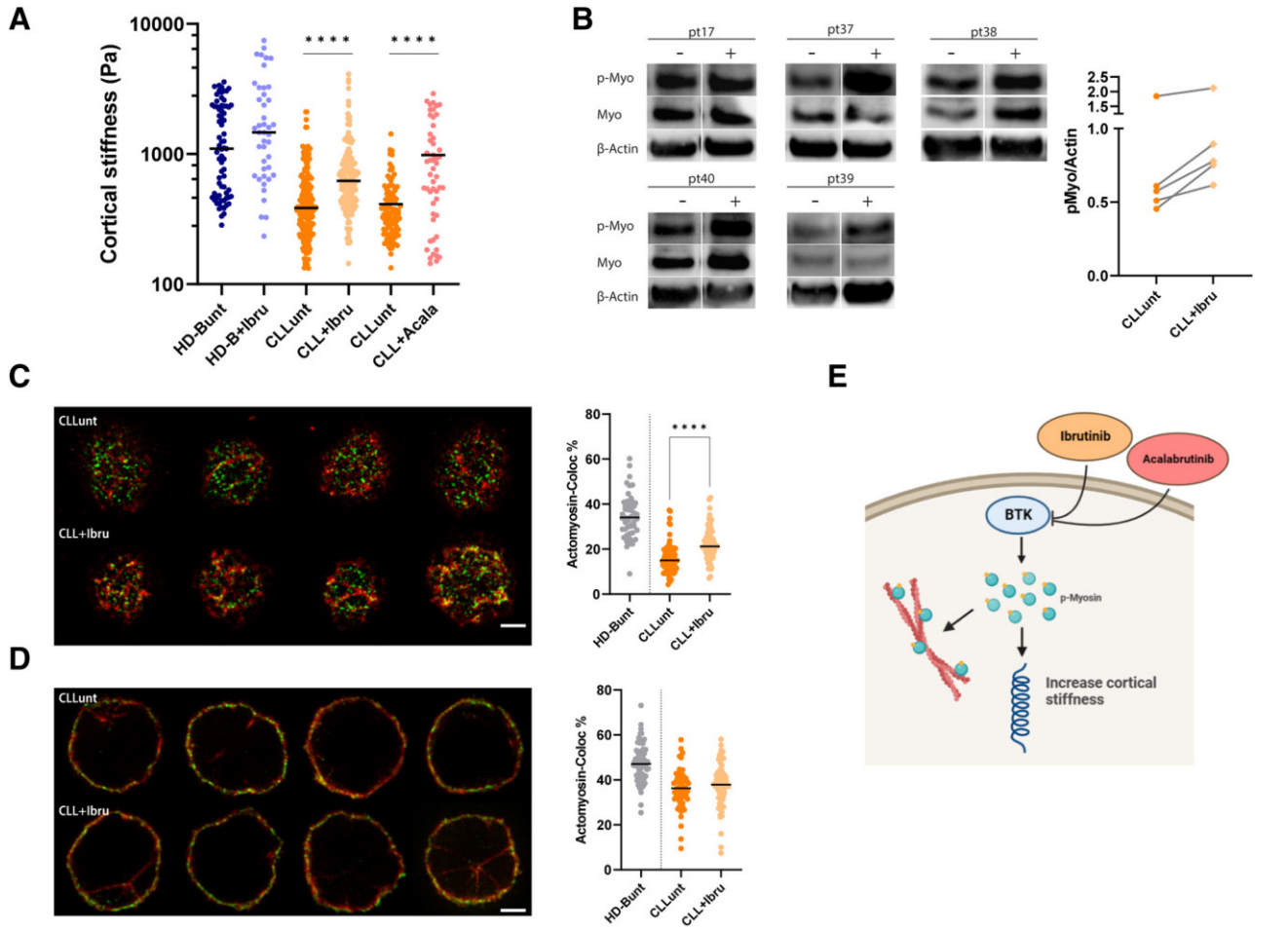

Figure 4. Drug modulation of CLL cells mechano-response in vitro. (A) Scatter plot of the cortical stiffness measured by AFM-FS of primary HD-B and CLL cells before (unt = untreated) and after drugs treatment (+Ibru= ibrutinib treatment; +Acala= acalabrutinib treatment). HD-Bunt median 1100 Pa, HD-B+Ibru median 1465 Pa; $P = 0.1$. 71 HD-Bunt cells and 44 HD-B+Ibru cells from 2 donors. CLLunt median 385 Pa and CLL+Ibru median 622 Pa; $P < 0.0001$; 211 CLLunt cells and 144 CLL+Ibru cells from 5 patients. CLLunt median 352.3 Pa, CLL+Acala 733.9 Pa; $P < 0.0001$. CLLunt 52 and CLL+Acala 102 from 3 patients. (B, left) WB analysis of cell lysates of CLL cells before (CLLunt) and after 4 h treatment with 10 μM Ibrutinib (CLL+Ibru) (n = 5). Bands represent respectively phospho myosin, total myosin, and β-actin. (B, right) Western Blot quantification of p-myosin increases upon treatment with ibrutinib in single patients. P-myosin increase was normalized as the ratio between p-myosin protein and actin (housekeeping gene). (C, left) Representative images of costained anti-myosin-Alexa-532 (green) and anti-actin-Alexa-568 (red) of CLLunt and CLL+Ibru upon treatment with 1 μM ibrutinib. Cells were acquired under identical experimental conditions at the bottom region. Scale bar = 2 μm. (C, right) Quantification of the colocalization of myosin and actin by Manders' coefficient expressed as percentage of colocalized actin pixels on myosin pixels. HD-B as a reference in gray and CLLunt median 15% and CLL+Ibru 21%; $P < 0.0001$. 80 CLLunt and 69 CLL+Ibru from 3 patients. (D, left) Representative images of costained anti-myosin-Alexa-532 (green) and anti-actin-Alexa-568 (red) of CLLunt and CLL+Ibru upon treatment with 1 μM ibrutinib. Cells were acquired under identical experimental conditions at the equatorial region. Scale bar = 2 μm. (D, right) Quantification of the colocalization of myosin and actin by Manders' coefficient expressed as percentage of colocalized actin pixels on myosin pixels. HD-B as a reference in gray and CLLunt median 36% and CLL+Ibru 38%; $P = 0.3$. 63CLLunt and 61 CLL+Ibru from 3 patients. (E) Schematic representation (BioRender.com) of the pathway involved in CLL cell's mechanical properties modulation. Ibrutinib inhibition of the BTK induces an increase of myosin phosphorylation (blue and yellow spot), which is directly involved in the modulation of cellular mechanical properties. AFM-FS = atomic force microscopy in force spectroscopy; BTK = Bruton's tyrosine kinase; CLL = chronic lymphocytic leukemia; HD = healthy donors; WB = Western Blot.

and 22 weeks, respectively). As shown in Figure 5A and Suppl. Figures S22 and S23, CLL cells isolated from patients under treatment showed a significant recovery of physiological cortical stiffness ($P < 0.0001$), mirroring what we observed in vitro, and confirming the rescue of circulating cells to a healthy phenotype during treatment. To prove that the mechanical modulation toward a healthy phenotype during treatment with ibrutinib is lost once the patients become resistant to therapy, we checked the cortical stiffness value of an ibrutinib-resistant patient. We measured, by AFM-FS, the cortical stiffness of single CLL cells isolated from PB of a patient at 3 different stages of the disease, CLL cells were collected: (1) at basal level before starting ibrutinib treatment; (2) during the first-line treatment while showing a clinical response to ibrutinib; (3) during treatment at the time of the onset of the resistance, before a second-line treatment. We confirmed an increase of the cortical stiffness during ibrutinib treatment, and interestingly we observed a trend of decreasing stiffness in CLL cells becoming resistant to ibrutinib, suggesting a reversal to the initial leukemic phenotype (Figure 5B). This observation prompted us to analyze CLL cells in the tissues where they could possibly behave differently based on the different environmental cues (CLL PB n = 19; CLL from Lymph node [LN] = 3; and BM n = 2). As shown in Figure 5C, tissue-resident CLL showed cortical stiffness values higher than those of circulating CLL cells (LN: $P < 0.0001$; BM: $P = 0.008$). The data suggest that the differences observed in the mechanical properties and mechano-response of CLLs as response to ibrutinib might also depend on the tissue localization of the lymphocytes and on their plastic properties.

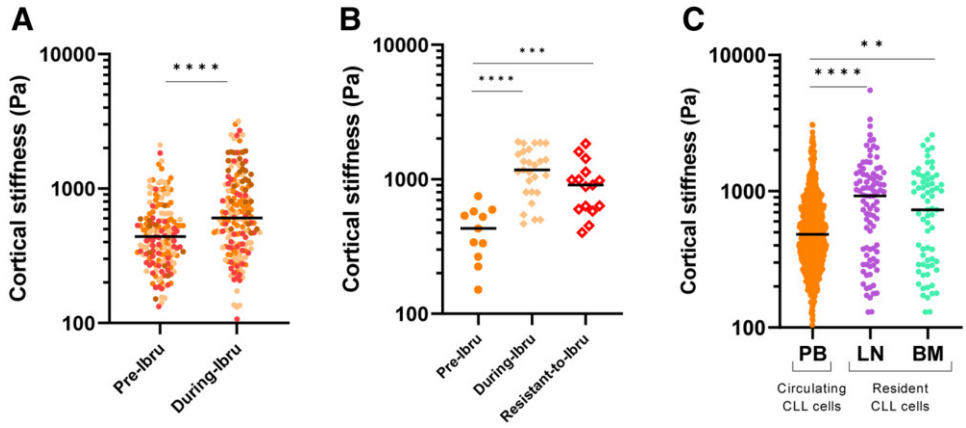

Figure 5. Cortical stiffness measurement by AFM-FS of cells from patients with CLL under ibrutinib therapy. (A) Scatter plot of the cortical stiffness of a pull of CLL cells from patients under treatment with ibrutinib at 4, 8, 9 and 22 weeks. Pretreatment (before starting the treatment) median 440 Pa, and during ibrutinib treatment median 600 Pa, $P < 0.0001$. 159 basal cells and 170 under ibrutinib treatment cells from 4 patients. Cells are color-coded according to each patient (CLL) from which they were obtained. (B) Scatter plot of the cortical stiffness of a patient at 3 time point during the course of the disease: Pretreatment (before starting the treatment), during ibrutinib treatment and resistant to ibrutinib (ones the patient relapse during the therapy). Basal median 430 Pa, Ibrutinib median 1175 Pa and resistant median 910 Pa. Basal vs Ibrutinib $P < 0.0001$, basal vs resistant $P = 0.0002$, and Ibrutinib vs resistant $P = 0.06$. 11 Basal cells, 22 cells under Ibrutinib treatment, and 15 cells resistant from 1 patient. (C) Scatter plot of the cortical stiffness of circulating CLL cells from PB and resident CLL cells from LNs and BM of patients. Circulating CLL median 484 Pa and resident CLL from LN median 926 Pa; $P < 0.0001$. CLL from BM median 731 Pa; $P = 0.008$. Circulating 765 CLL cells from 22 patients, LN 93 from 3 patients and BM 68 CLL cells from 2 patients. AFM-FS = atomic force microscopy in force spectroscopy; BM = bone marrow; CLL = chronic lymphocytic leukemia; LNs = lymph nodes; PB = peripheral blood.

DISCUSSION

We here report the first study linking the actomyosin nanoarchitecture to the mechanical properties of primary CLL cells in comparison to healthy B cells at single-cell level.[22,63] The driving hypothesis was that CLL cells frequently rearrange their cytoskeleton to favor continuous cell entry and egress from the tissue where they are exposed to the most disparate physical forces[15,64] and they can modify their response to mechanical cues, and this potentially differs from HD-B cells.[65] The implication of the cytoskeleton in the dynamic behavior of CLL cells was already observed in the past showing that CLL cells have impaired,[66] and aberrant cytoskeleton rearrangement and activation.[56,67] Moreover, the presence of the so-called smudge cells in the blood smear of the patients underlines a fragility of CLL cells that can be directly attributed to the cytoskeleton. The actin network links the extracellular environment with the inner of the cells and it is able to convert extracellular mechanical stimulation into a biological response, in fact the cytoskeleton is one of the major complexes involved in cellular mechanics.[68] Mechanobiology has been a neglected aspect in CLL pathophysiology so far, although it can be very relevant especially for migrating cells as lymphocytes. This observation, together with the alterations that we found in the actomyosin complex by super resolution microscopy, prompted our investigation on the study of CLL mechanical phenotype by using complementary approaches. We here demonstrated that CLL cells have a cortical stiffness lower than HD-B cells. This result appears to disagree with the findings reported by Zheng et al,[22] that obtained for CLL cells a YM value higher than for healthy cells. However, Zheng et al considered lymphocytes as a whole population, while we restricted our analysis only to B lymphocyte subpopulations. It is not unexpected to find specific mechanical properties for a cellular subgroup that might remain hidden in a mixed cohort. Keeping this in mind, we selected a heterogeneous cohort of CLL patients, both mutated and unmutated subgroups to assess whether our findings are generally true for the whole CLL cell population. Interestingly, although we have detected a clear difference between CLL and HD-B cells, we were able to observe that mCLL are stiffer than uCLL, thus more similar to their healthy counterparts. This suggests that cell softening could be part of the worsening of the disease. In line, by discriminating CLL samples based on the mutational status of the *IGHV* gene, by RT-DC we observed a correlation of the mutational status with the cellular size: mCLL were bigger than uCLL, confirming the less aggressive phenotype behavior more similar to that of HD-B cells. This observation also suggests that the size and the stiffness may reflect the functional differences in the type of antigenic interaction through the BCR; however, we could not find any significant variation in stiffness following BCR stimulation. RT-DC that allows the investigation of the mechanical properties of CLL cells in nonadhesive environments confirmed the noticeable differences between CLL and HD-B cells, highlighting the complementary readouts of our approaches. Along this line, swelling experiments showed that adhered CLL cells are more prone to modify their shape/deformation than HD-B cells, as for AFM-FS, proving that the environmental conditions (adhesion or suspension, tissue or circulation) can be determinant to define a specific mechano-response. This aspect is also clinically relevant considering that the primary action of ibrutinib (a first-line treatment for CLL) is to induce CLL cells mobilization from the tissues into the PB,[12] with a poorly defined mechanism.

Previous reported AFM-FS analysis on 2 other types of leukemia cells[23] showed that chemotherapy treatments renormalize the stiffness of the malignant cells. Accordingly, we hypothesized a possible involvement of ibrutinib in modulating the mechanical properties of CLL cells. Indeed, we were able to demonstrate the following in response to ibrutinib: (1) overall, HD-B cells exhibit an unaltered mechanical phenotype; (2) after exposure to drugs, leukemic cells recover the physiological range of cortical stiffness of HD-Bs; and (3) CLL cells show a partial recovery of actin and myosin colocalization and activation of the actomyosin complex. In addition, we proved the reproducibility of these observations also in vivo, in patients under ibrutinib treatment.

One of the possible mechanisms underlying our observations might be the ibrutinib inhibitory effect on lipid metabolism in CLL as proposed by recently published evidence.[69] Moreover, Lei et al[53] showed that depletion of membrane cholesterol induces an increase of stiffness of cancer cells. Therefore, ibrutinib might modify the cell membrane tension and elasticity

through a mechanism that is worthy of further studies. These observations might also hint a role of ibrutinib in restoring the mechanoreciprocity of leukemic cells in the tissue microenvironment. To support this hypothesis, we undertook the first study of the mechanical properties of tissue-resident CLL cells isolated from the distinct BM and LN niches. Interestingly, a persistent stiffening of resident versus circulating cells was observed, indicating a possible involvement of ibrutinib in modulating the life cycle of CLL cells,[70] by impairing the re-entry of CLL cells into tissues during drug treatment. This singular feature, then, might impact on a mechanism of resistance to ibrutinib,[11] limiting CLL cells mobilization from the tissues where they possibly lurk during therapy. This hypothesis finds preliminary evidence on the results obtained on cells from a single CLL patient at the time of the ibrutinib resistance onset, for which the cellular mechanical properties reverted to those measured before the response to therapy.

Overall, our findings suggest that the pathological alteration of the intrinsic mechanical phenotype could be a possible mechanism of CLL cells retention within the tissue during progression and could be reverted by effective therapies. Detailed studies aimed at dissecting the relation between the mechanical properties of CLL cells and the involved signaling pathways are warranted in the future to define new potential therapeutic targets and strategies, aiming at the normalization of the mechanical fingerprints of the leukemic cells.

ACKNOWLEDGMENTS

This study makes use of data generated by the Blueprint Consortium. A full list of the investigators who contributed to the generation of the data is available from https://www.blueprint-epigenome.eu. We thank Pamela Ranghetti, Eleonora Perotta, and Luca Russo for technical suggestions. We gratefully acknowledge Igor Sokolov for the helpful discussion.

AUTHOR CONTRIBUTIONS

MS, VC, EB, FB, ADT, DB, CS, and RC performed the experiments. MS, EB, VC, DS, MZ, VLC, DB, OO, FM, CS, and RC analyzed the data. VC, VRC, MZ, PG, OO, FM, and CS supervised the activity. MS, EB, VC, CAM, FM, CS, and VRC wrote the article. LS and PG provided patients' and clinical information. MS, EB, VC, DS, CAM, LS, PG, OO, VRC, MZ, FM, and CS revised the article.

DATA AVAILABILITY

All data generated and analyzed during this study are included in this article and its supplemental digital content files.

DISCLOSURES

OO is the cofounder of Zellmechanik Dresden commercialising real-time deformability cytometry. PG is a HemaSphere editor. All the other authors have no conflicts of interest to disclose.

SOURCES OF FUNDING

CS project is supported by Associazione Italiana per la Ricerca sul Cancro AIRC under IG 2018 - ID 21332 project. OO gratefully acknowledges financial support from the German Federal Ministry of Education and Research (ZIK grant to OO under grant agreement no. 03Z22CN11) as well as from the German Center for Cardiovascular Research (Postdoc start-up grant to OO under grant agreement no. 81X3400107). CAM acknowledges financial support from the Italian Ministry of University and Research (MIUR) Department of Excellence project PREMIA (PREcision MedIcine Approach: bringing biomarker research to clinics). STED microscopy was conducted at the Microscopy & Dynamic Imaging Unit, CNIC, ICTS-ReDib, co-funded by MCIN/AEI/10.13039/501100011033, and FEDER "*Una manera de hacer Europa*" (#ICTS-2018-04-CNIC-16). The CNIC is supported by the Ministerio de Ciencia e Innovación and the Pro CNIC Foundation and is a Severo Ochoa Center of Excellence (CEX2020-001041-S). Schemes in figures 1, 2, 3 and 4 have been generated with BioRender.com. Funding for the project was provided by the European Union's Seventh Framework Programme (FP7/2007-2013) under grant agreement no 282510 – BLUEPRINT.

REFERENCES

1. Davids MS, Burger JA. Cell trafficking in chronic lymphocytic leukemia matthew. *J Hematol*. 2012;100:130–134.
2. Redondo-Muñoz J, García-Pardo A, Teixidó J. Molecular players in hematologic tumor cell trafficking. *Front Immunol*. 2019;10:156.
3. Scielzo C, Ten Hacken E, Bertilaccio MTS, et al. How the microenvironment shapes chronic lymphocytic leukemia: the cytoskeleton connection. *Leuk Lymphoma*. 2010;51:1371–1374.
4. Scielzo C, Ghia P. Modeling the leukemia microenviroment in vitro. *Front Oncol*. 2020;10:607608.
5. Robbe P, Ridout KE, Vavoulis DV, et al. Whole-genome sequencing of chronic lymphocytic leukemia identifies subgroups with distinct biological and clinical features. *Nat Genet*. 2022;54:1675–1689.
6. Schiattone L, Ghia P, Scarfò L. The evolving treatment landscape of chronic lymphocytic leukemia. *Curr Opin Oncol*. 2019;31:568–573.
7. Freise KJ, Jones AK, Eckert D, et al. Impact of venetoclax exposure on clinical efficacy and safety in patients with relapsed or refractory chronic lymphocytic leukemia. *Clin Pharmacokinet*. 2017;56:515–523.
8. Ahn IE, Brown JR. Targeting Bruton's Tyrosine Kinase in CLL. *Front Immunol*. 2021;12:687458.
9. O'Brien S, Jones JA, Coutre SE, et al. Ibrutinib for patients with relapsed or refractory chronic lymphocytic leukaemia with 17p deletion (RESONATE-17): a phase 2, open-label, multicentre study. *Lancet Oncol*. 2016;17:1409–1418.
10. Deeks ED. Ibrutinib: a review in chronic lymphocytic leukaemia. *Drugs*. 2017;77:225–236.
11. Skanland SS, Mato AR. Overcoming resistance to targeted therapies in chronic lymphocytic leukemia. *Blood Adv*. 2021;5:334–343.
12. Herman SEM, Gordon AL, Hertlein E, et al. Bruton tyrosine kinase represents a promising therapeutic target for treatment of chronic lymphocytic leukemia and is effectively targeted by PCI-32765. *Blood*. 2011;117:6287–6296.
13. Haga M, Yamashita A, Paszkowiak J, et al. Oscillatory shear stress increases smooth muscle cell proliferation and Akt phosphorylation. *J Vasc Surg*. 2003;37:1277–1284.
14. Butcher DT, Alliston T, Weaver VM. A tense situation: forcing tumour progression. *Nat Rev Cancer*. 2009;9:108–122.
15. Huse M. Mechanical forces in the immune system. *Nat Rev Immunol*. 2017;17:679–690.
16. Du H, Bartleson JM, Butenko S, et al. Tuning immunity through tissue mechanotransduction. *Nat Rev Immunol*. 2022;23:174–188.
17. Lim CG, Jang J, Kim C. Cellular machinery for sensing mechanical force. *BMB Rep*. 2018;51:623–629.
18. Polacheck WJ, Chen CS. Measuring cell-generated forces: a guide to the available tools. *Nat Methods*. 2016;13:415–423.
19. Van Helvert S, Storm C, Friedl P. Mechanoreciprocity in cell migration. *Nat Cell Biol*. 2018;20:8–20.
20. Plodinec M, Loparic M, Monnier CA, et al. The nanomechanical signature of breast cancer. *Nat Nanotechnol*. 2012;7:757–765.
21. Byun S, Son S, Amodei D, et al. Characterizing deformability and surface friction of cancer cells. *Proc Natl Acad Sci U S A*. 2013;110:7580–7585.
22. Zheng Y, Wen J, Nguyen J, et al. Decreased deformability of lymphocytes in chronic lymphocytic leukemia. *Sci Rep*. 2015;5:1–5.
23. Lam WA, Rosenbluth MJ, Fletcher DA. Chemotherapy exposure increases leukemia cell stiffness. *Blood*. 2007;109:3505–3508.
24. Sampietro M, Zamai M, Díaz Torres A, et al. 3D-STED super-resolution microscopy reveals distinct nanoscale organization of the hematopoietic cell-specific lyn substrate-1 (HS1) in normal and leukemic B cells. *Front Cell Dev Biol*. 2021;9:1–11.
25. Božič B, Zemljič Jokhadar S, Kristanc L, et al. Cell volume changes and membrane ruptures induced by hypotonic electrolyte and sugar solutions. *Front Physiol*. 2020;11:582781.
26. Wu PH, Aroush DRB, Asnacios A, et al. A comparison of methods to assess cell mechanical properties. *Nat Methods*. 2018;15:491–498.
27. Thomas G, Burnham NA, Camesano TA, et al. Measuring the mechanical properties of living cells using atomic force microscopy. *J Vis Exp*. 2013:50497. doi:10.3791/50497.
28. Lee Y, Koay EJ, Zhang W, et al. Human equilibrative nucleoside transporter-1 knockdown tunes cellular mechanics through epithelial-mesenchymal transition in pancreatic cancer cells. *PLoS One*. 2014;9:e107973.

29. Otto O, Rosendahl P, Mietke A, et al. Real-time deformability cytometry: on-the-fly cell mechanical phenotyping. *Nat Methods*. 2015;12:199–202, 4 p following 202.
30. Mietke A, Otto O, Girardo S, et al. Extracting cell stiffness from real-time deformability cytometry: theory and experiment. *Biophys J*. 2015;109:2023–2036.
31. Hallek M, Cheson BD, Catovsky D, et al. Guidelines for the diagnosis and treatment of chronic lymphocytic leukemia: a report from the International Workshop on Chronic Lymphocytic Leukemia updating the National Cancer Institute-Working Group 1996 guidelines. *Blood*. 2008;111:5446–5456.
32. Schindelin J, Arganda-Carreras I, Frise E, et al. Fiji: an open-source platform for biological-image analysis. *Nat Methods*. 2012;9:676–682.
33. Di Stefano V, Torsello B, Bianchi C, et al. Major action of endogenous lysyl oxidase in clear cell renal cell carcinoma progression and collagen stiffness revealed by primary cell cultures. *Am J Pathol*. 2016;186:2473–2485.
34. Torsello B, De Marco S, Bombelli S, et al. The 1ALCTL and 1BLCTL isoforms of Arg/Abl2 induce fibroblast activation and extra cellular matrix remodelling differently. *Biol Open*. 2019;8:bio038554.
35. Marini M, Zeynali A, Collini M, et al. Proteinaceous microstructure in a capillary: a study of non-linear bending dynamics. *Lab Chip*. 2022;22:4917–4932.
36. Hutter JL, Bechhoefer J. Calibration of atomic-force microscope tips. *Rev Sci Instrum*. 1998;64:1868.
37. Sneddon IN. The relation between load and penetration in the axisymmetric boussinesq problem for a punch of arbitrary profile. *Int J Eng Sci*. 1965;3:47–57.
38. Dokukin ME, Sokolov I. On the measurements of rigidity modulus of soft materials in nanoindentation experiments at small depth. *Macromolecules*. 2012;45:4277–4288.
39. Butt HJ, Cappella B, Kappl M. Force measurements with the atomic force microscope: Technique, interpretation and applications. *Surf Sci Rep*. 2005;59:1–152.
40. Barbaglio F, Belloni D, Scarfò L, et al. Three-dimensional co-culture model of chronic lymphocytic leukemia bone marrow microenvironment predicts patient-specific response to mobilizing agents. *Haematologica*. 2021;106:2334–2344.
41. Melak M, Plessner M, Grosse R. Correction: actin visualization at a glance [J. Cell Sci., 130, 3, (2017), 525-530]doi: 10.1242/jcs.189068. *J Cell Sci*. 2017;130:1688–1688.
42. Koenderink GH, Paluch EK. Architecture shapes contractility in actomyosin networks. *Curr Opin Cell Biol*. 2018;50:79–85.
43. An Truong Quang B, Peters R, Cassani D, et al. Extent of myosin penetration within the actin cortex regulates cell surface mechanics. *Nat Commun*. 2021;12:6511.
44. Salbreux G, Charras G, Paluch E. Actin cortex mechanics and cellular morphogenesis. *Trends Cell Biol*. 2012;22:536–545.
45. Guhathakurta P, Prochniewicz E, Thomas DD. Actin-myosin interaction: structure, function and drug discovery. *Int J Mol Sci* . 2018;19:2628.
46. Kim JM, Jo YJ, Jung JW, et al. A mechanogenetic role for the actomyosin complex in branching morphogenesis of epithelial organs. *Development*. 2021;148:dev190785.
47. Manders EMM, Verbeek FJ, Aten JA. Measurment of co-localization of object in dual-colour confocal images. *J Microsc*. 1992;169:35–382.
48. Fischer-Friedrich E, Hyman AA, Jülicher F, et al. Quantification of surface tension and internal pressure generated by single mitotic cells. *Sci Rep*. 2014;4:6213.
49. Urbanska M, Muñoz HE, Shaw Bagnall J, et al. A comparison of microfluidic methods for high-throughput cell deformability measurements. *Nat Methods*. 2020;17:587–593.
50. Guz N, Dokukin M, Kalaparthi V, et al. If cell mechanics can be described by elastic modulus: study of different models and probes used in indentation experiments. *Biophys J*. 2014;107:564–575.
51. Tseng Y, Kole TP, Lee JSH, et al. How actin crosslinking and bundling proteins cooperate to generate an enhanced cell mechanical response. *Biochem Biophys Res Commun*. 2005;334:183–192.
52. Francis ML, Ricketts SN, Farhadi L, et al. Non-monotonic dependence of stiffness on actin crosslinking in cytoskeleton composites. *Soft Mat*. 2019;15:9056–9065.
53. Lei K, Kurum A, Kaynak M, et al. Cancer-cell stiffening via cholesterol depletion enhances adoptive T-cell immunotherapy. *Nat Biomed Eng*. 2021;5:1411–1425.
54. Condoluci A, Di Bergamo LT, Langerbeins P, et al. International prognostic score for asymptomatic early-stage chronic lymphocytic leukemia. *Blood*. 2020;135:1859–1869.
55. de Gorter DJJ, Beuling EA, Kersseboom R, et al. Bruton's Tyrosine Kinase and Phospholipase Cγ2 mediate chemokine-controlled B cell migration and homing. *Immunity*. 2007;26:93–104.
56. Scielzo C, Bertilaccio MTS, Simonetti G, et al. HS1 has a central role in the trafficking and homing of leukemic B cells. *Blood*. 2010;116:3537–3546.
57. Apoorva F, Loiben AM, Shah SB, et al. How biophysical forces regulate human B cell lymphomas. *CellReports*. 2018;23:499–511.
58. Schuh A, Becq J, Humphray S, et al. Monitoring chronic lymphocytic leukemia progression by whole genome sequencing reveals heterogeneous clonal evolution patterns. *Blood*. 2012;120:4191–4196.
59. Schliwa M. Action of cytochalasin D on cytoskeletal networks. *J Cell Biol*. 1982;92:79–91.
60. Wakatsuki T, Schwab B, Thompson NC, et al. Effects of cytochalasin D and latrunculin B on mechanical properties of cells. *J Cell Sci*. 2001;114:1025–1036.
61. Elson EL, Pasternak C, Daily B, et al. Cross-linking surface immunoglobulin increases the stiffness of lymphocytes. *Mol Immunol*. 1984;21:1253–1257.
62. Wang N, Butler JP, Ingber DE. Mechanotransduction across the cell surface and through the cytoskeleton. *Science*. 1993;260:1124–1127.
63. Li M, Liu L, Xiao X, et al. Viscoelastic properties measurement of human lymphocytes by atomic force microscopy based on magnetic beads cell isolation. *IEEE Trans Nanobioscience*. 2016;15:398–411.
64. Shin HY, Fukuda S, Schmid-Schönbein GW. Fluid shear stress-mediated mechanotransduction in circulating leukocytes and its defect in microvascular dysfunction. *J Biomech*. 2021;120:110394.
65. Ben-Shmuel A, Joseph N, Sabag B, et al. Lymphocyte mechanotransduction: the regulatory role of cytoskeletal dynamics in signaling cascades and effector functions. *J Leukoc Biol*. 2019;105:1261–1273.
66. Stark R, Liebes L, Shelanski M, et al. Anomalous function of vimentin in chronic lymphocytic leukemia lymphocytes. *Blood*. 1984;63:415–420.
67. Caligaris-Cappio F, Bergui L, Tesio L, et al. Cytoskeleton organization is aberrantly rearranged in the cells of B chronic lymphocytic leukemia and hairy cell leukemia. *Blood*. 1986;67:233–239.
68. Pegoraro AF, Janmey P, Weitz DA. Mechanical properties of the cytoskeleton and cells. *Cold Spring Harb Perspect Biol*. 2017;9:a022038.
69. Rozovski U, Harris DM, Li P, et al. Ibrutinib inhibits free fatty acid metabolism in chronic lymphocytic leukemia. *Leuk Lymphoma*. 2018;59:2686–2691.
70. Chen SS, Chang BY, Chang S, et al. BTK inhibition results in impaired CXCR4 chemokine receptor surface expression, signaling and function in chronic lymphocytic leukemia. *Leuk*. 2015;30:833–843.

Supplementary Information

SUPPLEMENTARY METHODS

Healthy samples

The buffy coats study was approved by the IRCCS Ospedale San Raffaele (OSR) ethics committee under the protocol Leu-Buffy coat entitled: "Characterization of leukocyte subpopulations from buffy coats".

Human primary sample purification

CD19 cells were negatively selected from fresh peripheral blood (PB), bone marrow (BM) and lymph nodes (LN) from patients or healthy donors using the RosetteSep B-lymphocyte enrichment kit (StemCell Technologies, Vancouver, Canada). HD-B cells were further negatively selected using B-lymphocyte enrichment kit (StemCell Technologies, Vancouver, Canada). The purity of all preparations was always higher than 99%, and the cells co-expressed CD19 and CD5 on their surface as assayed by flow cytometry (FC500; Beckman Coulter, Brea, California); preparations were virtually devoid of natural killer cells, T lymphocytes, and monocytes. After purification, cells were immediately frozen for further experiments.

Immunofluorescence Staining

Primary cells were seeded on coated polyornithine (1:5) coverslip (22 × 22-mm high-precision glass, code: 0101050, Paul Marienfeld GmbH & Co. KG, Lauda-Königshofen, Germany) and incubated for 2 h at 37°C and 5% CO_2. For single and double immunostaining, cells were washed with PBS and fixed with PFA 4%, incubated for 15 min in the dark at room temperature, and permeabilized in blocking buffer solution (blocking buffer: 0.1% w/v BSA, 10% v/v FBS in PBS), containing 0.3% v/v Triton-X 100 (Sigma- Aldrich, Merck, Germany), to limit nonspecific antibody binding. Samples were then incubated overnight at 4°C with primary monoclonal anti-mouse beta actin monoclonal (BA3R) antibody (code: MA5-15739, Thermo Fisher Scientific, Waltham, Massachusetts, USA), primary monoclonal myosin light chain 2 Antibody (code: 3672S, Cell Signaling Technology, Danvers, Massachusetts, USA) or both for co-staining, then labeled with an goat-anti-mouse-Alexa568 (code: A-11031, Thermo Fisher Scientific, Waltham, Massachusetts, USA), goat-anti-rabbit-Alexa532 (code: A-11009, Thermo Fisher Scientific, Waltham, Massachusetts, USA) or both, for 2h at RT and in the dark. Samples were then washed with PBS and mounted with ProLong Gold antifade reagents (Invitrogen, Thermo Fisher Scientific, USA). For Ibrutinib treatment, cells were

plated on pre-coated polyornithine 1:5 dishes for 1h in controlled condition. At the end of the incubation, 1uM Ibrutinib (Selleckchem, S2680, Planegg, Germany) was added directly in the dish and incubated for 2h at 37°C and 5% CO_2. Cells were then fixed and permeabilized and double immunostaining was performed following the protocol described above.

STED microscopy

Cells stained for Alexa532 immunolabeled myosin or Alexa568 immunolabeled actin were imaged with X, Y depletion at 660 nm set at 80% laser power, with a gated unidirectional resonant scanning mode at 8,000 Hz. For actin filament analysis, excitation was at 578 nm by a white laser at 15% power. Images were acquired at 48-line and 6-frames average per optical section. For myosin quantification, excitation was at 525 nm by a white laser at 15% power. Images were acquired at 48-line and 9-frames average per optical section. Fluorescence (589 nm - 632 nm) for actin and (531 nm - 562 nm) for myosin was collected using a HyD spectral detector in standard mode and applying a gating of 0.2 and 0.3 ns respectively. A zoom of 3.5 times was applied to optical sections of 1248 x 1248 pixels acquired at the top, equatorial and bottom regions of the cells, with a pixel size of 33 x 33 nm.

To perform colocalization analysis of Alexa532 immunolabeled myosin and Alexa568 immunolabeled actin, samples were acquired with X, Y with depletion at 660 nm and 80% power for actin and 100% power for myosin, with a gated unidirectional scanning mode at 700 Hz. Fluorophores were excited at 583 nm (18% white laser power) and 520 nm (39% white laser power) for actin and myosin respectively. Fluorescence was collected using two HyD spectral detectors in standard mode with a gaiting of 0.3 ns. Spectral detection was set at 530 nm - 546 nm for myosin and 608 nm - 632 nm for actin. A zoom of 2 times was applied to collect optical sections of 3200 x 3200 pixels acquired at the bottom and equatorial sections of cells, with a pixel size of 58 x 58 nm. This setting was chosen among others to maximize the X, Y resolution, minimize photobleaching, avoid crosstalk between the two channels, autofluorescence and reflections, keeping the white laser excitation at the minimum, yet being capable of maintaining the same settings for all cells, which showed variable intensities. Depletion laser power, image format, zoom, and scanning conditions were optimized according to the same principle to obtain minimal photobleaching. The image resolution under all these conditions optimized for our samples was determined by measuring the X, Y PSF with a 23-nm nanobead sample coated with the Alexa568 and Alexa532 (GATTAquant GmbH, Gräfelfing, Germany) (**Fig. S4**).

Image Analysis

All images were analyzed by ImageJ/Fiji software[1]. STED images were post-processed for background subtraction with a rolling ball radius of 30 and deconvolved applying the CLME algorithm to each optical section (Huygens software, Scientific Volume Imaging BV, Hilversum, The Netherlands). Then images were cropped to define single cell ROIs. To determine the actin density, the cellular perimeter was set as reference ROI by thresholding (ImageJ/Fiji, Triangle algorithm). The actin inside the cellular ROI was segmented (ImageJ/Fiji Moment thresholding). We consider the total area as the occupation value of the intensity inside the reference ROI. The same method was used for myosin density analysis (**Fig. S1**). For measuring actin filament, images were post-processed for background subtraction, followed by deconvolution, and contrast enhancement (ImageJ/Fiji, CLAHE function). Actin distribution was then detected by applying the ImageJ/FiJi LoG3 PlugIn[2]. Finally, images were converted into binary masks (ImageJ/Fiji, Phansalkar auto local threshold algorithm, radius of 20) and skeletonized for measuring the length of actin filaments and branches (**Fig. S3**). For statistical analysis filaments shorter than 260 nm were discarded. For actomyosin colocalization, after deconvolution optical sections were single cell cropped to minimize the background around each cell. Colocalization analysis was performed using the JACoP plugin in ImageJ/Fiji[3] applying the Moment thresholding to both channels (**Fig. S6**). We considered the Manders' coefficient 2 (Channel 2: actin on Channel 1: myosin). We also performed the Costes' randomized test[3] to prove the no-randomness of the results.

AFM-FS data analysis

The mechanical properties of a complex system such as a cell were described through several theoretical models returning different values of the mechanical parameters[4,5]. The most common model describing the elastic properties of cells is the Hertz model[6,7,8], corrected by Sneddon considering the tip geometry[9] that affects the contact area. Following this model, the relation between the loading force F, the Young's Modulus E, and the resulting indentation δ for a pyramidal tip is:

$$F = \quad E' \, tan(\alpha) \, \delta^2/\sqrt{2}$$

Where α is the face tip angle and $E' = E/(1-\mu^2)$ is the reduced Young's Modulus that takes into account the cell Poisson ratio μ, usually assumed to be 0.5. As shown in **Fig. 3D**, the acquired data are well described by the Hertz-Sneddon model. It has been observed that this is not always

the case and deviations from the Hertz-Sneddon model have been often reported[10]. We faced this issue with an operational approach by selecting all the curves which were more effectively described by the model and disregarding the others. It is also worth noting that the absolute value of Young's Modulus is difficult to determine. For this reason, no matter what model is applied, it is useful to use a differential approach in which all results are compared to a reference sample. Here we used as reference sample B lymphocytes from healthy donors and cells treated with drugs of known effect.

Tips with different shapes are available on the market for AFM-FS measurements, and recently a lot of authors choose the colloidal probes for the investigation of cell stiffness[11]. In this work, we performed stiffness measurements with pyramidal probes in order to have an easier experimental strategy. Indeed, several attempts to acquire reproducible force-indentation curves on B lymphocytes with colloidal probes (Novascan Technologies, Chicago, USA, on 0.06 N/m cantilevers) or tipless cantilever (Bruker, MLCT-O10, Billerica, Massachusetts, USA) resulted in buckling contact points and sliding cells (data not shown). In addition, the use of pyramidal probes allows us to measure the cellular cortical stiffness, since the small tip and the reduced indentation allows probing the cortex mechanical properties[129].

RT-DC data analysis

RT-DC measures the deformation *D* of a cell, which is defined:

$$D = 1 - C = 1 - 2\frac{\sqrt{\pi A}}{P}$$

where *C* is its circularity, *A* the area and *P* the perimeter. For an ideal circle, $D = 0$, and for any deformation at constant volume $D > 0$ [13]. The analysis is performed in real-time on thousands of cells in a single experimental run and an analytical as well as numerical model enables derivation of the Young's Modulus[14,15].

Viability counts for AFM-FS experiments

To exclude that cell death could affect the experiments, a control petri dish was kept in the incubator in the same conditions of the cells under measure. Cells were counted by trypan blue staining. No significant differences were found in terms of cell viability at the end of the measurement window (maximum 2h, **Fig. S11**). However, beyond this temporal window the viability of both HD-B and CLL cells started to decrease steeply, drastically reducing the number of possible measurements for every patient.

Protein lysis and Western Blot (WB)

Cells were lysed on ice for 15 minutes in RIPA Buffer (Sigma-Aldrich, Burlington, Massachusetts, USA) with fresh protease and phosphatase inhibitors cocktail (Roche, Basel, Switzerland). Cells were then centrifuged at 13.000 rpm for 15 minutes at 4°C, and supernatants were collected and stored at −80°C until further use. Protein content was determined using the BCA protein assay kit (Bio-Rad, Hercules California USA) according to the manufacturer's instructions. The total of protein content of about 5x106 cells was supplemented with NuPage Sample Buffer (4x) and NuPage Sample Reducing Agent (10x) and loaded onto 4–12% sodium dodecyl sulfate-polyacrylamide gradient gels (Invitrogen, Waltham, Massachusetts, USA), then transferred to nitrocellulose membranes (Thermo Scientific, Waltham, Massachusetts, USA). Membranes were blocked for 1.30h in PBS-Tween containing 5% BSA and incubated overnight with the following primary antibodies: Anti-phospho myosin light chain II (cell signaling-3674s-Rabbit 1:1000) and Anti-myosin light chain II (Cell Signaling-3672s- Rabbit 1:1000, Danvers, Massachusetts, USA). Incubation with primary antibodies was followed by species-specific Horseradish Peroxidase (HRP)-conjugated secondary antibodies (anti-Rabbit-A16023-Invitrogen, Waltham, Massachusetts, USA, diluted 1:10000) for 1h. All WB were normalized to anti β-actin HRP conjugated (Cell Signaling, Rabbit, Danvers, Massachusetts, USA, 1:50000). Amersham ECL Western Blotting Analysis System from GE Healthcare was used to visualize immuno-reactive bands. Western blots were acquired using Biorad Chemidoc (Bio Rad, Hercules, California, USA) and quantification of relative protein expression levels was performed using Image Lab Software for PC Version 6.1. Graphs and statistical analysis were performed using GraphPad Prism (San Diego, California, USA, https://www.graphpad.com/scientific-software/prism/).

SUPPLEMENTARY FIGURES

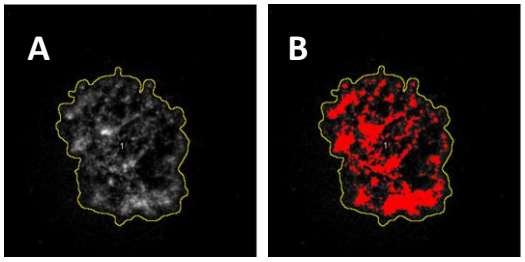

Fig. S1 Example of analysis of actin or myosin density in 2D-STED optical sections.
(A) Images were post-processed for background subtraction, followed by deconvolution, and selection of the cell total area (yellow trace ROI). **(B)** The ImageJ/FiJi threshold Moment algorithm was applied to select the fluorescent fraction inside the cell ROI and obtain the density of myosin in the single cell

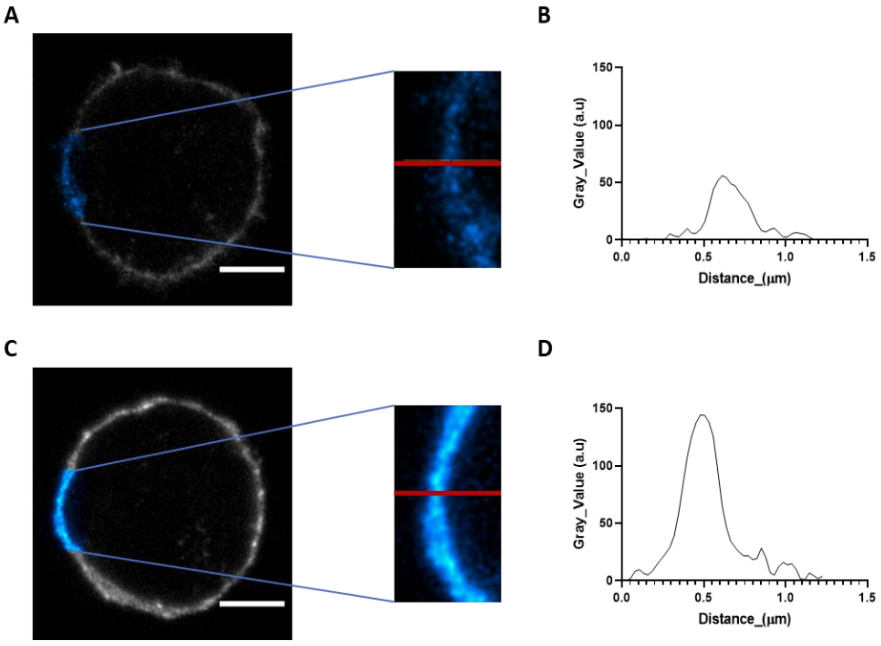

Fig. S2 Example of actin density in 2D-STED equatorial optical section in single cell.
Representative HD-B **(A)** and CLL **(C)** cells and corresponding intensity profiles **(B, D)** drawn by a central line (red) in a zoomed ROI. Scale bar = 2µm.

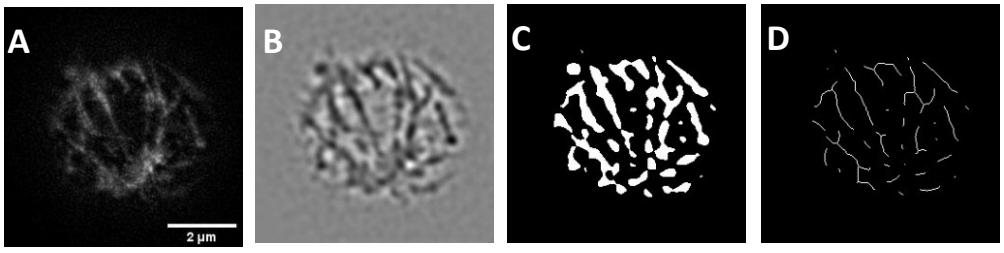

Fig. S3 Steps for actin filament length and branching analysis in 2D-STED optical sections.
(A) Images were post-processed for background subtraction, followed by deconvolution, and contrast

enhancement; **(B)** actin distribution was then detected by applying the ImageJ/FiJi LoG3 PlugIn, **(C)** finally images were converted into binary mask **(D)**, and skeletonized for measuring the length of actin filaments and branches by ImageJ/FiJi.

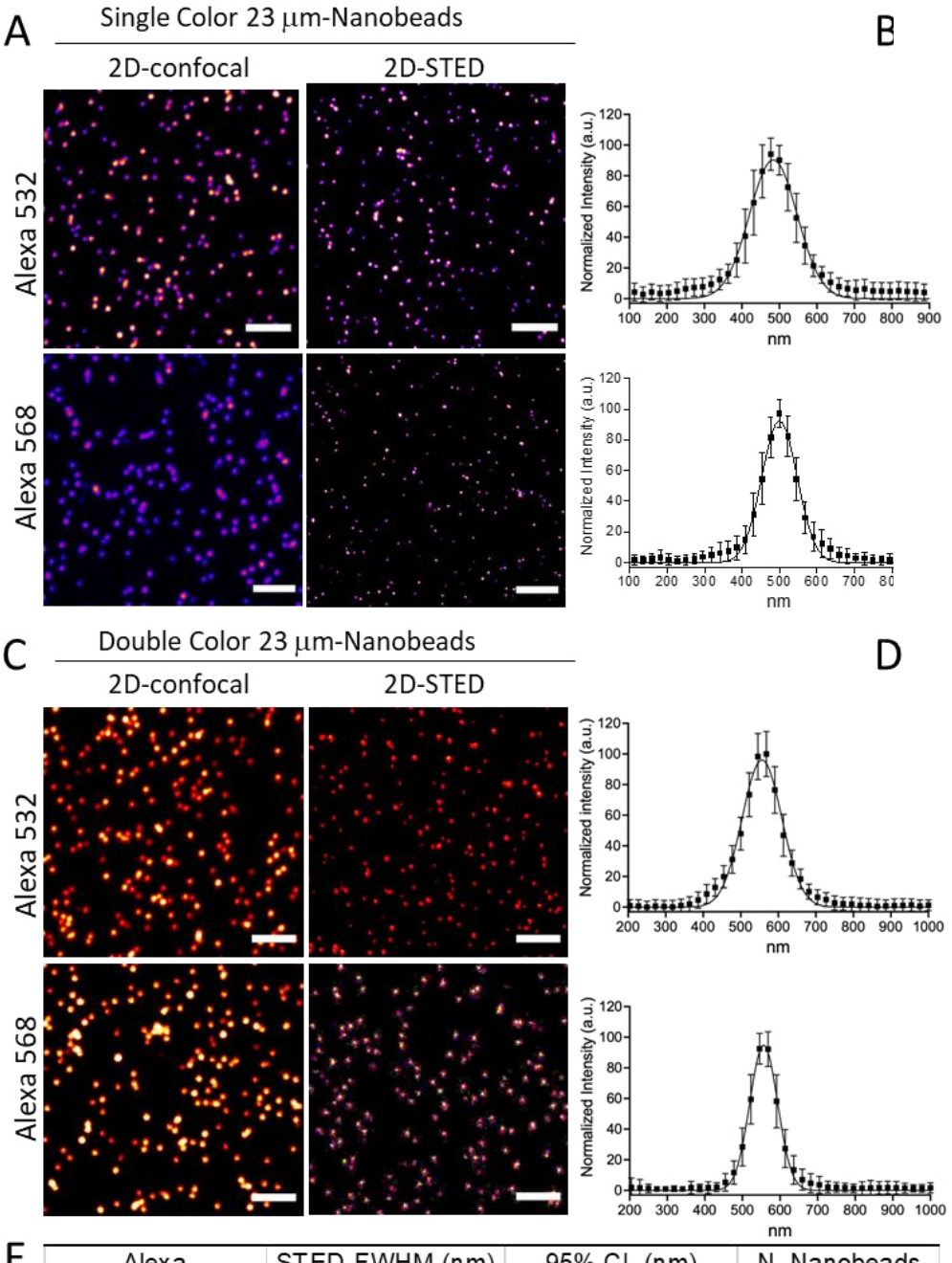

E

Alexa		STED-FWHM (nm)	95% CL (nm)	N. Nanobeads
532	double color	126.7	[124.6 - 128.8]	50
	single color	113.5	[110.4 - 116.6]	25
568	double color	88.6	[87.9 - 90.1]	50
	single color	98.5	[90.5 - 107.4]	25

Fig. S4 Single and Double color 2D-STED optical resolution.
The optical resolution in 2D-STED anti-myosin-Alexa532 and anti-actin-Alexa569 images was determined by measuring the FWHM of fluorescent 23 mm nanobeads depleted at the experimental conditions applied to either to single or double-stained cells with 660 nm STED depletion: Representative confocal and STED images of single color **(A)** and double color **(C)** Alexa-nanobeads. Gaussian fits +/- SD of nanobead normalized fluorescence intensities X,Y-profiles averaged on replicate measurements are shown in **(B)** and **(D)**. FWHM

values obtained for single- and double-stained nanobeads are shown in **(E)**. Scale bar = 2 μm.

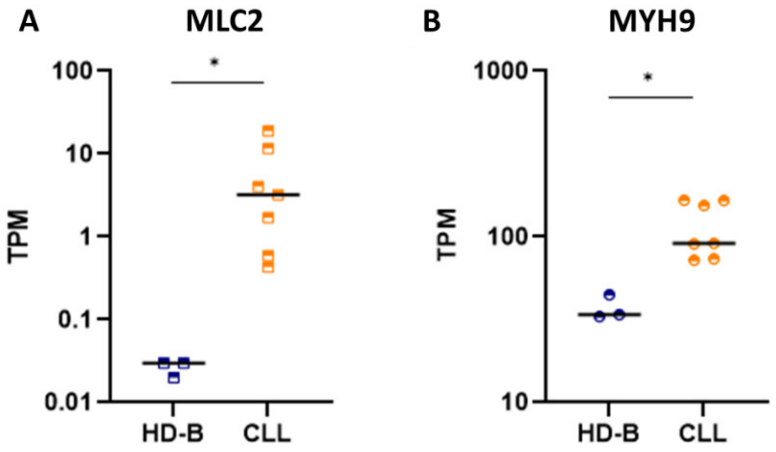

Fig. S5 Myosin expression.
In-silico analysis (Blueprint Consortium) on primary HD-B and CLL cells isolated from peripheral blood of the protein level expressed as Transcripts Per Million (TPM) of **(A)** myosin regulatory light chain 2 (MLC2, p value = 0.016) and **(B)** myosin heavy chain, non-muscle IIa (MYH9, p value = 0.017).

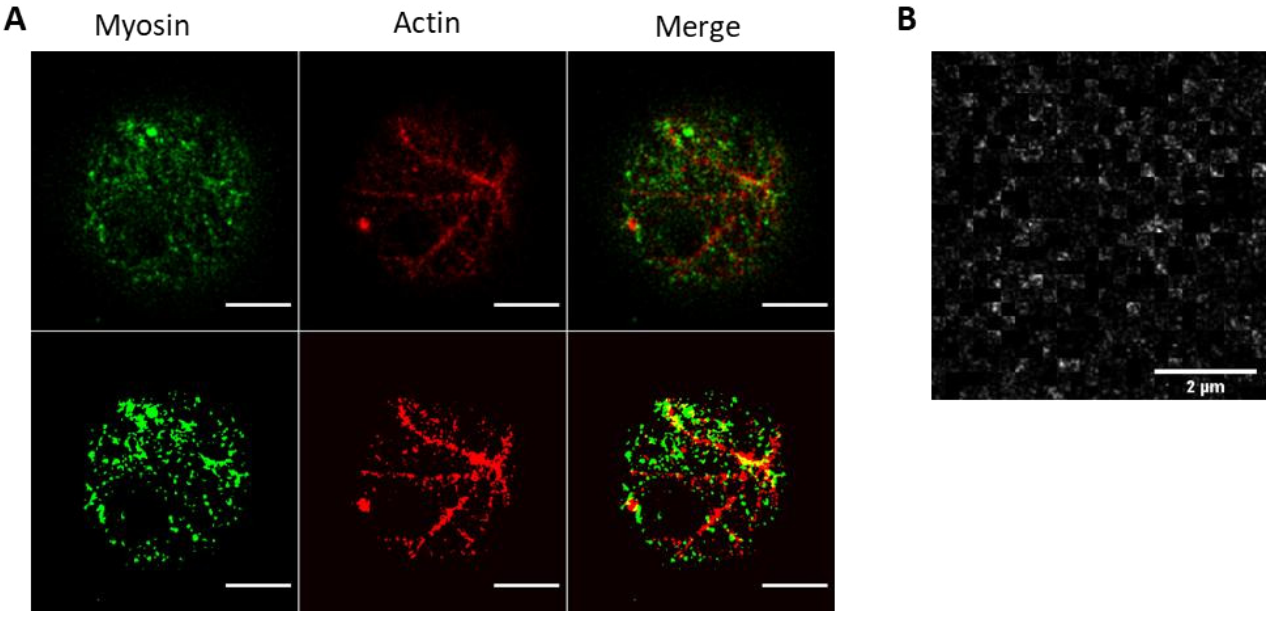

Fig. S6 Representative example of colocalization analysis of double color 2D-STED optical sections.
(A) Anti-myosin-Alexa532, anti-actin-Alexa568 and merged images of bottom regions in a representative CLL cell (top), and the corresponding binary masks obtained after thresholding (bottom) that were used for computing the colocalization score by JACoP plug-In in ImageJ/Fiji **(B)** Costes' Randomization control test. Scale bars = 2µm.

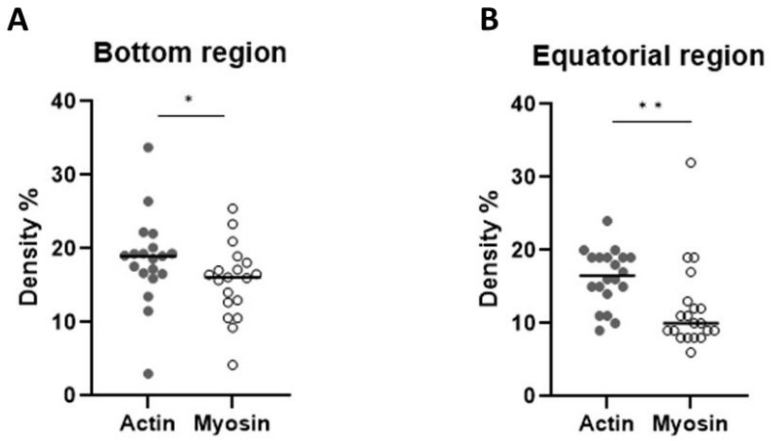

Fig. S7 Actin and myosin densities in co-stained 2D-STED images.
(A) Density % of actin *vs* myosin on bottom cellular sections. Actin median 19.0 (CI 16.6/20.1) and myosin median 16.1 (CI 12.7/18.1) (p value = 0.03). **(B)** Density % of actin *vs* myosin in equatorial cellular sections actin median 16.5 (CI 15.0/19.0) and myosin median 10.0 (CI 9.0/12.0) (p value = 0.001). HD-B are represented in dark gray and CLL are represented in light gray. (19 images were analyzed for both the 2 sections). In each optical section actin density has a higher median compared to myosin.

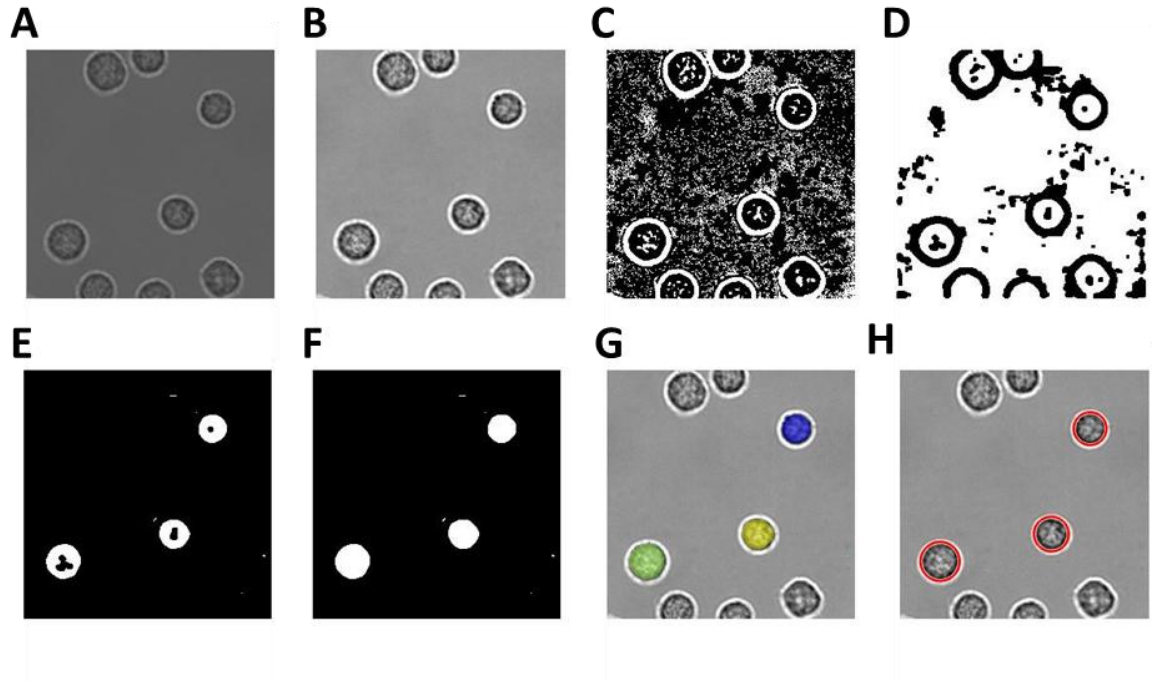

Fig. S8 Cell segmentation procedure for swelling experiments.
(A) Original Image. **(B)** Intensity equalized image. **(C)** H-maxima transformation image. **(D)** Inverted image. **(E)** Cleared border Image. **(F)** Convex transformation image. **(G)** Labeled object superimposed to the equalized image. **(H)** Circles of maxima diameter superimposed to the equalized image.

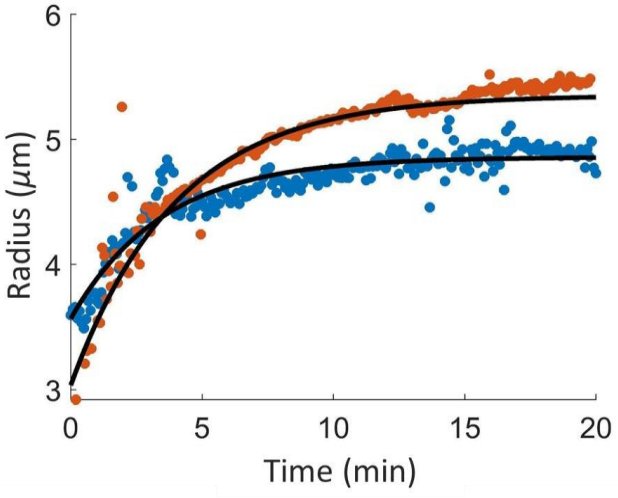

Fig. S9 Example of a time-radius cell growing during hypoosmotic stress response.
Dots are the extracted radius for each timepoint (blue for HD-B cell and orange for CLL cell) using the segmentation procedure described in material and methods, the continuous black lines represent a fit to the data with an exponential increasing function $((R_{fin}-R_{in})*(1-\exp(-t/\tau))+R_{in})$ where t is the time and the free parameters are the final and initial radius R_{fin} and R_{in} and the characteristic growing time τ.

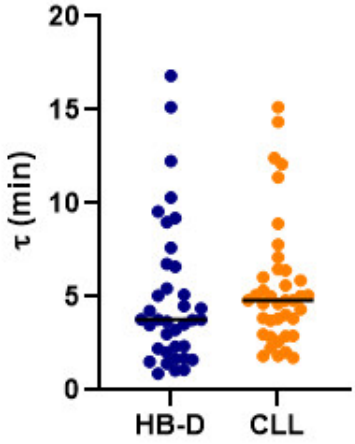

Fig. S10 Distribution of τ values from swelling kinetics, obtained from fitted exponentially increasing functions for HD-B and CLL cells. HD-B median 3.8 min, and CLL median 4.8 min, (p value = 0.1). 37 HD-B cells from 3 donors and 39 CLL cells from 4 patients.

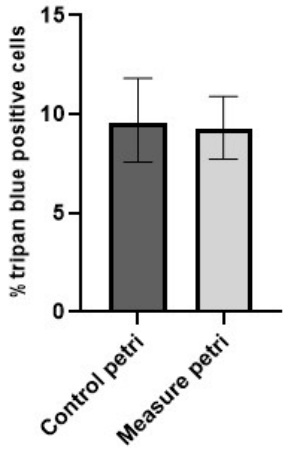

Fig. S11 Control of cell viability during AFM-FS experiments.
Histogram of the percentage of dead cells in adhesion on a poly-L-ornithine coating in PBS (both CLL (n=1) and HD-B (n=1)) for the petri dish before (dark gray) and after (light gray) AFM-FS measurement showing that AFM-FS measurements do not affect cell viability. Control means 9.4 (CI 7.5/11.6) and measured mean 9.1 (CI 7.8/10.7).

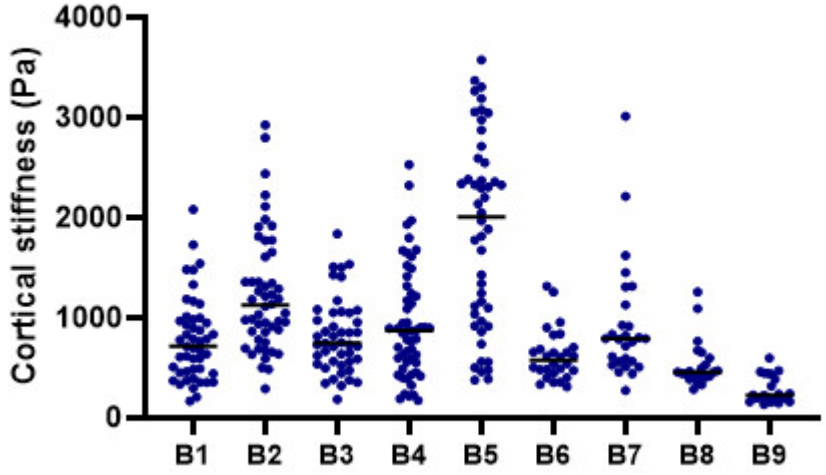

Fig. S12 Distribution of cortical stiffness in cells from single HD-B donors.
In the scatter plot, each dot represents the median cortical stiffness of each single cell measured during the AFM-FS analysis for each HD-B donor (7). The bar shows the median for each single sample. B1 = 47 cells, B2 = 51 cells, B3 = 45 cells, B4 = 54 cells, B5 = 50 cells, B6 = 28 cells, B7 = 27 cells, B8 = 23 cells, B9 = 23 cells.

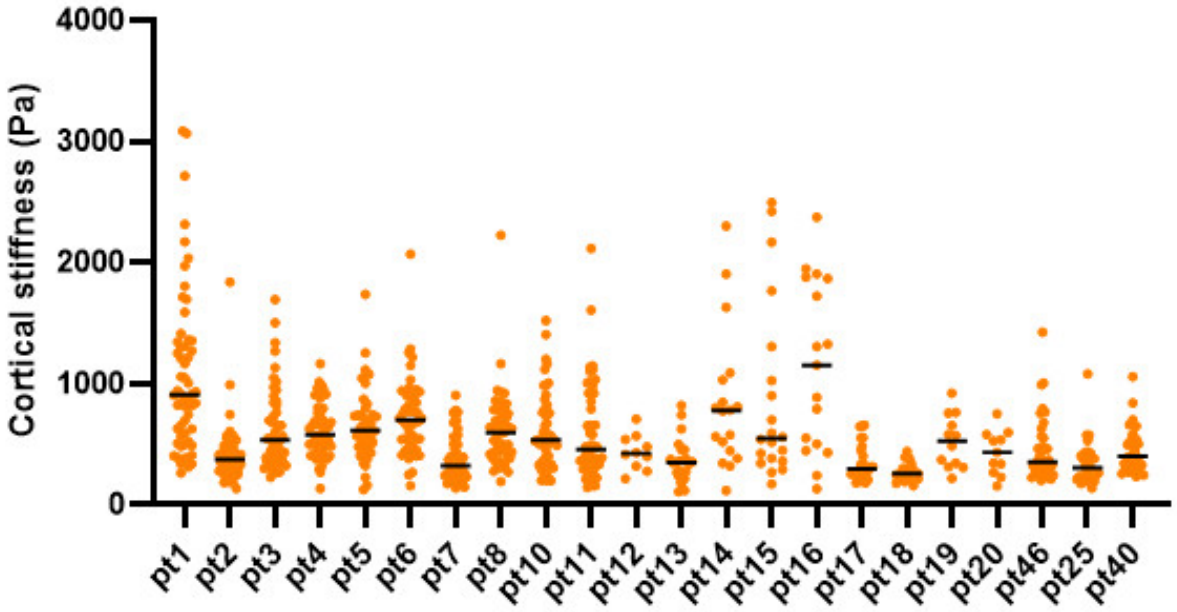

Fig. S13 Distribution of single CLL patients' cortical stiffness.
In the scatter plot each dot corresponds to the median cortical stiffness of each single cell measured during the AFM-FS analysis for each CLL patient (15). The bar shows the median for each single sample. Pt-1 = 58 cells, pt-2 = 45 cells, pt-3 = 50 cells, pt-4 = 52 cells, pt-5 = 42 cells, pt-6 = 53 cells, pt-7 = 52 cells, pt-8 = 52 cells, pt-10 = 51 cells, pt-11 = 52 cells, pt-12 = 10 cells, pt-13 = 24 cells, pt-14 = 18 cells, pt-15 = 20 cells, pt-16 = 17 cells, pt-17 = 26 cells, pt-18 = 18 cells, pt-19 = 12 cells, pt-20 = 11 cells, pt- 46 = 41 cells, pt-25 = 31 cells, pt-40 = 30 cells.

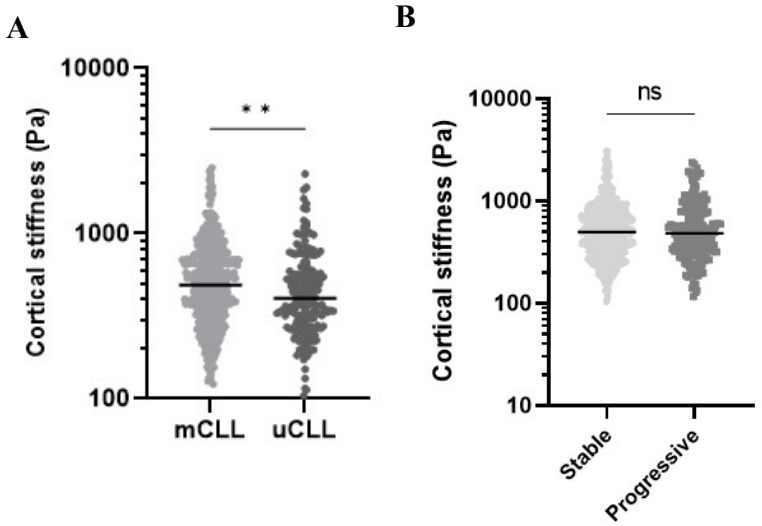

Fig. S14 Cortical stiffness of CLL patients used in for the analysis classified based on clinical and biological prognostic markers (Table I).
(A) Scatter plot of CLL cortical stiffness classified based on the mutational status (patients mCLL n=16, uCLL n=5) of the IGHV chain (p value = 0.04). **(B)** Scatter plot of CLL cortical stiffness based on the clinical course of the disease (p value = 0.7). Patients Stable n=16, progressive n=6.

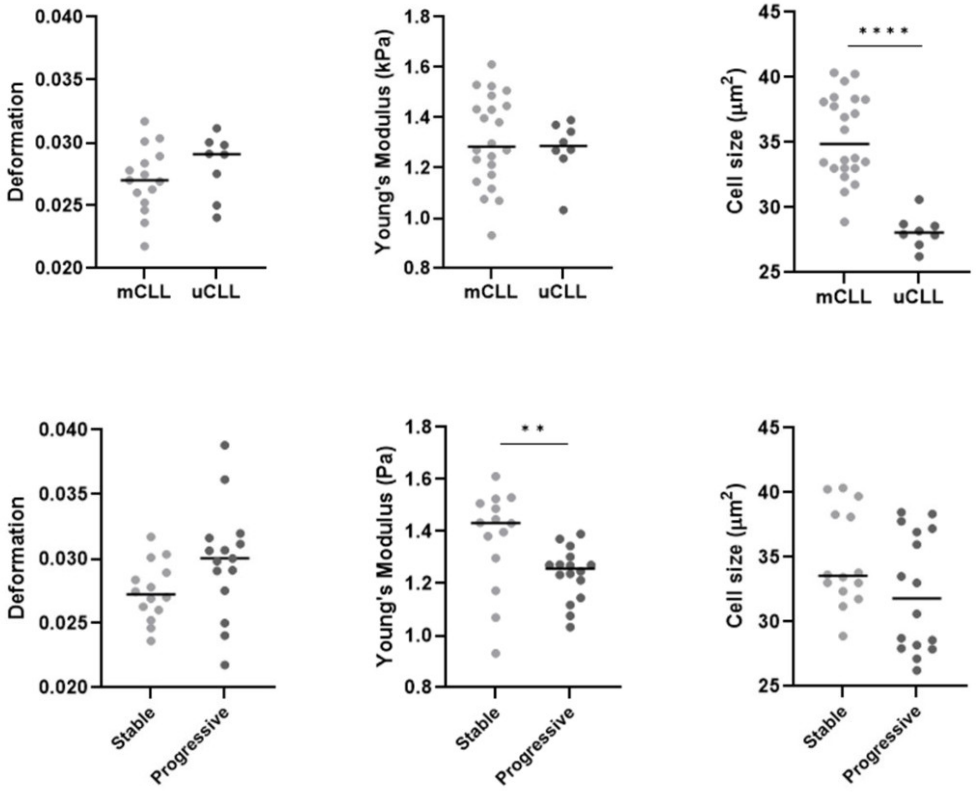

Fig. S15 RT-DC parameters based on diagnostic markers (Table1).
(Upper panel) Scatter plots of cellular deformation (p value = 0.3), Young's Modulus (p value = 0.7) and cellular area (p value < 0.0001) respectively of CLL cells based on the mutational state of the IGHV chain. In light gray mutated patients for the IGHV chain (mCLL= 8), in dark gray unmutated patients for the IGHV chain (uCLL=3). **(Lower panel)** Scatter plots of cellular deformation (p value = 0.06), Young's Modulus (p value = 0.007) and cellular size (p value = 0.09) respectively, of CLL cells classified based on the disease progression (stable=6 in light gray, progressive=5 in dark gray).

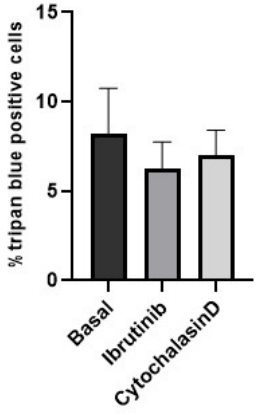

Fig. S16 Cell viability upon treatment with specific stimuli. The histogram shows the percentage of dead cells in untreated samples (basal, black), in samples treated with ibrutinib for 4 hours (dark gray) and in samples treated with cytochalasin D for 2 hours (light gray).

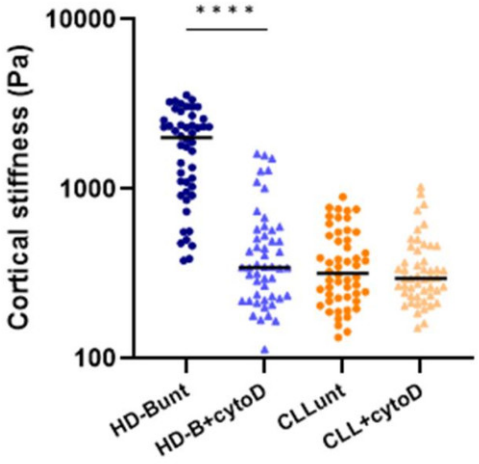

Fig. S17 Cytochalasin D treatment. Distribution of the cortical stiffness obtained by AFM-FS for HD-B and CLL cells before (unt= untreated) and after cytochalasin D treatment (+cytoD), p value < 0.0001.

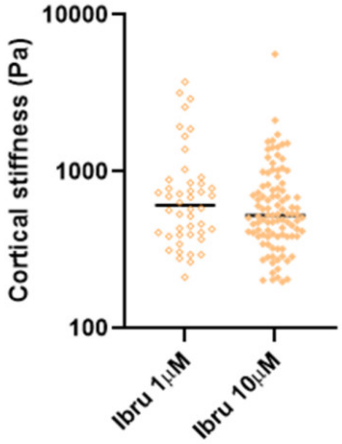

Fig. S18 Ibrutinib treatment at different doses. The cortical stiffness of CLL cells treated *in vitro* with Ibrutinib at 1μM and 10μM at the same incubation time, did not show significant difference (p value = 0.3), CLL patients n=3. Ibrutinib 1μM median 610.1 Pa (CI: 435/754 Pa) and ibrutinib 10μM median 526.7 Pa (CI: 476/591 Pa).

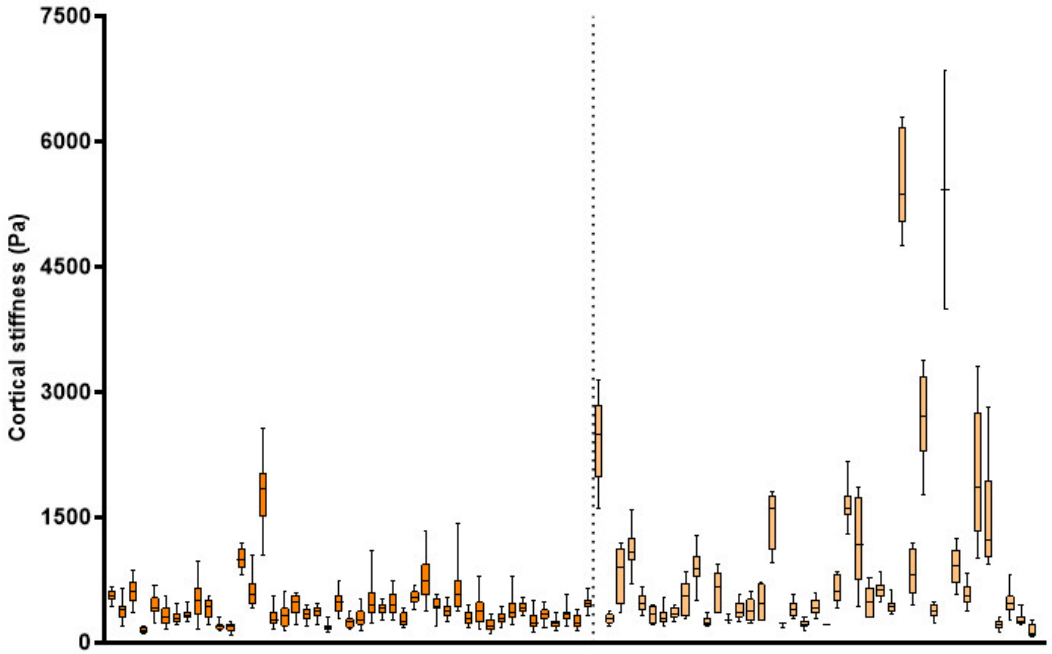

Fig. S19 Representative whisker plot of single cell cortical stiffness obtained by AFM-FS on cells from patients before and after *in vitro* treatment with ibrutinib for 4h. Each box plot represents a single cell, the bar represents the min and max values. Dark orange box plot represents untreated cells, light orange box plot represents treated patients with ibrutinib.

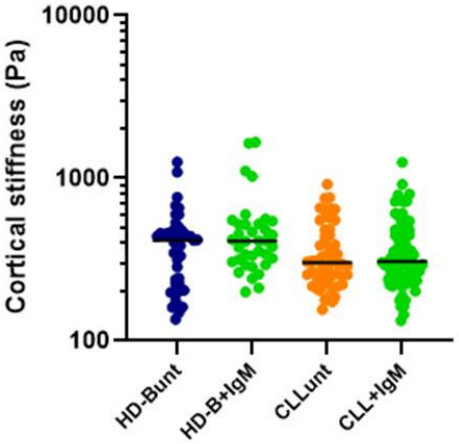

Fig. S20 IgM stimulation. Scatter plot of the cortical stiffness by AFM of primary HD-B and CLL cells before (unt = untreated) and after (+IgM) stimulation with Anti-IgM. HD-Bunt median 416 Pa, (CI 284/450), HD-B+IgM, median 410 Pa (CI 333/480 Pa), p value = 0.3; CLLunt median 303 Pa (CI 261/341 Pa) and CLL+IgM median 307 Pa (CI 289/352 Pa), p value = 0.6. HD-Bunt n= 46 cells, HD-B+IgM n= 36 cells. from 2 donors. CLLunt n = 56 cells, CLL+IgM n= 86 cells, from 3 patients.

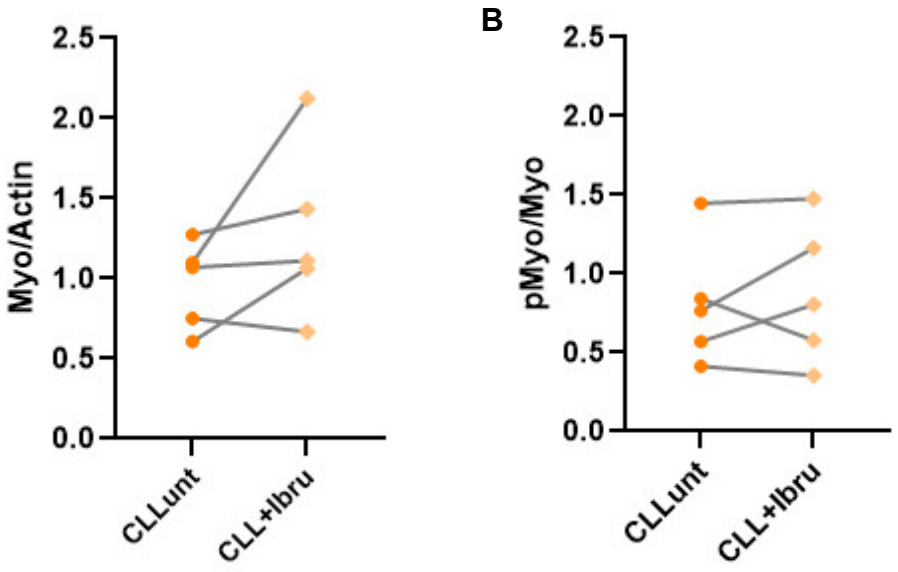

Fig. S21 Western Blot analysis of CLL primary cells following ibrutinib treatment *in vitro*. Data were obtained from WB of primary CLL cells (n=5) before (CLLunt) and after 4h treatment with ibrutinib 10μM (CLL+Ibru). **(A)** Quantification of the myosin increases upon treatment with ibrutinib in single patients. The intensity of the myosin band was normalized as the ratio between myosin total protein and actin (housekeeping gene) bands **(B)** Quantification of the p-myosin increase upon treatment with Ibrutinib in single patients. p-myosin increase was normalized on the total myosin protein.

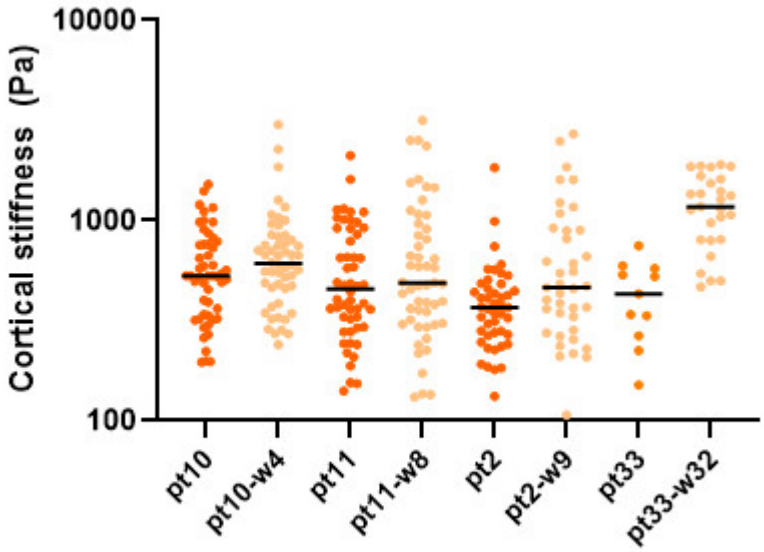

Fig. S22 *In vivo* ibrutinib treatment. Scatter plot showing the cortical stiffness in cells from single patients at the basal status and during treatment. Cells were collected from patient at different treatment times, week 4, 8, 9 and 32 respectively. The percentage of CD19+ CD5+ cells was at least 98% in all the samples analyzed.

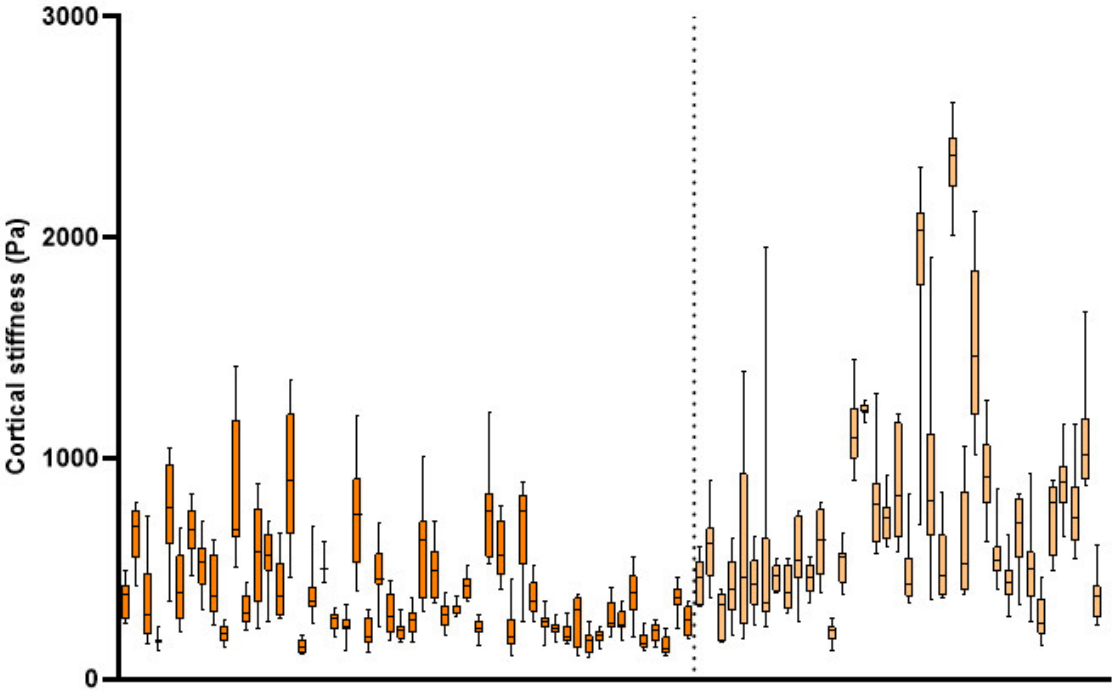

Fig. S23. Representative whisker plot of single cell cortical stiffness. Data obtained by AFM-FS on cells from CLL patients *under ibrutinib clinical treatment*. Each box plot represents a single cell, the bar show the min and max values. Dark orange box plot represents cells of untreated patients, light orange bars represent patients treated with Ibrutinib.

LEGEND VIDEO

Video S1 and S2. STED-3D rendering of CLL cells and HD-B cells stained for Alexa568 immunolabeled actin. For the Z-stack we used a STED-3X-WLL SP8 microscope with a 100x/1.40 oil objective. Samples were acquired with X, Y, Z depletion at 660 nm and at 80% power in gated bidirectional resonant scanning mode at 8,000 Hz scan speed. Excitation was performed at 578 nm by a white laser at 15% power, acquiring 32-line average and 4-frames per optical section. Fluorescence (589 nm - 632 nm) was collected using a HyD spectral detector in standard mode and applying a gating of 0.2, zoom of 3 times, image format of 1248 x 659 x 106 pixels, with a voxel size of 31 nm x 31 nm x 80 nm. Images were deconvoluted with GLME algorithm (Huygens software, Scientific Volume Imaging BV, Hilversum, The Netherlands) and 3D rendering performed by Imaris software (Oxford Instruments).

Video S3. Timelapse acquisition during swelling. *Left panel:* Bright field time-lapse record of a single cell swelling kinetics after hypoosmotic shock. *Right panel:* Segmentation of single cell area during hypoosmotic stress.

BIBLIOGRAPHY

1. Schindelin J, Arganda-Carreras I, Frise E, et al. Fiji: an open-source platform for biological-image analysis. *Nat Methods 2012 97*. 2012;9(7):676-682. doi:10.1038/nmeth.2019
2. Sage D, Neumann FR, Hediger F, Gasser SM, Unser M. Automatic tracking of individual fluorescence particles: Application to the study of chromosome dynamics. *IEEE Trans Image*

Process. 2005;14(9):1372-1383. doi:10.1109/TIP.2005.852787

3. Bolte S, Cordelières FP. A guided tour into subcellular colocalization analysis in light microscopy. *J Microsc*. 2006;224(3):213-232. doi:10.1111/j.1365-2818.2006.01706.x
4. Sokolov I, Dokukin ME, Guz N V. Method for quantitative measurements of the elastic modulus of biological cells in AFM indentation experiments. *Methods*. 2013;60(2):202-213. doi:10.1016/j.ymeth.2013.03.037
5. Dokukin ME, Sokolov I. On the measurements of rigidity modulus of soft materials in nanoindentation experiments at small depth. *Macromolecules*. 2012;45(10):4277-4288. doi:10.1021/ma202600b
6. Lekka M, Pabijan J. Measuring Elastic Properties of Single Cancer Cells by AFM. *Methods Mol Biol*. 2019;1886:315-324. doi:10.1007/978-1-4939-8894-5_18
7. Lekka M, Laidler P, Gil D, Lekki J, Stachura Z, Hrynkiewicz AZ. Elasticity of normal and cancerous human bladder cells studied by scanning force microscopy. *Eur Biophys J*. 1999;28(4):312-316. doi:10.1007/S002490050213
8. Lekka M. Discrimination Between Normal and Cancerous Cells Using AFM. *Bionanoscience*. 2016;6(1):65-80. doi:10.1007/S12668-016-0191-3
9. Sneddon IN. The relation between load and penetration in the axisymmetric boussinesq problem for a punch of arbitrary profile. *Int J Eng Sci*. 1965;3(1):47-57. doi:10.1016/0020-7225(65)90019-4
10. Guz N, Dokukin M, Kalaparthi V, Sokolov I. If cell mechanics can be described by elastic modulus: study of different models and probes used in indentation experiments. *Biophys J*. 2014;107(3):564-575. doi:10.1016/J.BPJ.2014.06.033
11. Iyer S, Gaikwad RM, Subba-Rao V, Woodworth CD, Sokolov I. Atomic force microscopy detects differences in the surface brush of normal and cancerous cells. *Nat Nanotechnol*. 2009;4(6):389-393. doi:10.1038/nnano.2009.77
12. Lei K, Kurum A, Kaynak M, et al. Cancer-cell stiffening via cholesterol depletion enhances adoptive T-cell immunotherapy. *Nat Biomed Eng*. 2021;5(12):1411-1425. doi:10.1038/s41551-021-00826-6
13. Otto O, Rosendahl P, Mietke A, et al. Real-time deformability cytometry: On-the-fly cell mechanical phenotyping. *Nat Methods*. 2015;12(3):199-202. doi:10.1038/nmeth.3281
14. Herbig M, Kräter M, Plak K, Müller P, Guck J, Otto O. Real-Time Deformability Cytometry: Label-Free Functional Characterization of Cells. *Methods Mol Biol*. 2018;1678:347-369. doi:10.1007/978-1-4939-7346-0_15
15. Mokbel M, Mokbel D, Mietke A, et al. Numerical Simulation of Real-Time Deformability Cytometry To Extract Cell Mechanical Properties. ACS Biomater Sci Eng.2017;3:2962-2973. doi:10.1021/acsbiomaterials.6b00558

Intercepting Yes-associated protein 1 in prostate cancer blocks neuroendocrine progression

Arianna Brevi[1,#], Marco Lorenzoni[1,#], Sara Caputo[1], Yasutaka Yamada[2], Matteo Grioni[1], Laura Lucia Cogrossi[1,3], Laura Martinez Vidal[4], Valeria Cassina[5], Deborah Cipria[6], Chiara Venegoni[4], Paola Zordan[1], Vittoria Matafora[7], Anna Sofia Tascini[8], Nazario Pio Tenace[9], Riccardo Campanile[5], Vito Cucchiara[4], Valeria Pinna,[10] Elena Jachetti,[10] Rossella Galli[11], Angela Bachi[7], Maurizio Colecchia[3,9], Alberto Briganti[3,4], Massimo Freschi[9], Francesco Mantegazza[5], Angelo Lombardo[3,6], Francesca Demichelis[12], Himisha Beltran[2], Massimo Alfano[4], Matteo Bellone[1,12]

[1]Cellular Immunology Unit, Division of Immunology, Transplantation and Infectious Diseases, IRCCS Ospedale San Raffaele, Milan, Italy; [2]Department of Medical Oncology, Dana Farber Cancer Institute, Harvard Medical School, Boston, MA, USA; [3]Vita-Salute San Raffaele University, Milan, Italy; [4]Division of Experimental Oncology/Unit of Urology, URI, IRCCS Ospedale San Raffaele, Milan, Italy; [5]School of Medicine and Surgery, BioNanoMedicine Center NANOMIB, Università di Milano-Bicocca, Vedano al Lambro (MB), Italy; [6]San Raffaele Telethon Institute for Gene Therapy, IRCCS Ospedale San Raffaele, Milan, Italy; [7]Proteomics Unit, IFOM-FIRC Institute of Molecular Oncology, Milan, Italy; [8]Center for Omics Sciences, IRCCS Ospedale San Raffaele, Milan, Italy; [9]Unità Operativa Anatomia Patologica, IRCCS Ospedale San Raffaele, Milan, Italy; [10]Molecular Immunology Unit, Department of Experimental Oncology, Fondazione IRCCS Istituto Nazionale dei Tumori di Milano, Milan, Italy; [11]Division of Neuroscience, IRCCS Ospedale San Raffaele, Milan, Italy; [12]Cellular, Computational and Integrative Biology (CIBIO), University of Trento, Trento, Italy; [12]Lead Contact.

[#]These authors equally contributed to the work.

Current address for Arianna Brevi: Division of Gastroenterology, University of California San Diego, La Jolla, CA; and current address for Sara Caputo: L-Nutra Italia SRL, Milan, Italy.

Running title: α2-YAP axis in neuroendocrine prostate cancer

Correspondence: Matteo Bellone, MD, IRCCS Ospedale San Raffaele, DIBIT 1, Via Olgettina 58, 20132, Milan, Italy. E-mail: bellone.matteo@hsr.it; Arianna Brevi, PhD, E-mail: abrevi@health.ucsd.edu

Conflict of interest: The authors declare no potential conflicts of interest.

Words in the main text: 4334

Words in the Abstract: 247

Figures: 7

Supplementary figures: 11

Supplementary tables: 3

STATEMENT OF SIGNIFICANCE

Novel interactions between poorly differentiated neuroendocrine and exocrine prostate cancer cells and the surrounding extracellular matrix, especially in the absence of androgens, promote NEPC and metastasis through the α2-YAP axis.

ABSTRACT

The emergence of the neuroendocrine phenotype in patients affected by castration resistant prostate cancer (CRPC) associates with poor prognosis. We hypothesized that castration-induced death of fully differentiated, androgen-sensitive PC cells foster novel interactions among rare androgen-independent, less differentiated cancer cells and the extracellular matrix (ECM), eventually promoting the development of neuroendocrine PC (NEPC).

Here, we investigated physical and molecular interactions between mouse less differentiated PC cells with exocrine (PAC) or neuroendocrine features (PNE), which recapitulated pre-existing human CRPC-like cells, and decellularized prostate ECM. Analyses were conducted by flow cytometry, polarized light, electron and atomic force microscopy, immunofluorescence, mass spectrometry and transcriptomics. Pharmacologic inhibition and gene knockout confirmed the relevance of the identified molecular pathways in primary mouse models and in patient's derived CRPC organoids.

We found that without androgens, PAC cells and PC-derived ECM promoted *in vitro* invasiveness of PNE cells by inducing integrin α2 upregulation and Yes-associated protein 1 (YAP) activation. Inhibition of RANK/RANKL and NF-κB prevented α2 upregulation in PNE cells, indicating a cell-to-cell and cell-to-matrix contact-driven process. Integrin α2β1 and YAP inhibition also reduced PNE invasiveness. Microenvironment-conditioned PNE cells showed a YAP-dependent metastatic behavior *in vivo*, and YAP inhibition suppressed the development of NEPC and metastasis in castration-naïve mice and CRPC-NE in transgenic adenocarcinoma of the mouse prostate mice. Importantly, YAP inhibitors also restrained the growth of human CRPC organoids.

Our findings unveil unprecedented mechanisms of NEPC development and implicate the integrin α2-YAP axis as a therapeutic target in PC patients receiving androgen-deprivation therapy.

KEYWORDS

neuroendocrine prostate cancer, castration resistance, extracellular matrix, integrin, Yes-associated protein 1, transgenic adenocarcinoma of the mouse prostate.

INTRODUCTION

Neuroendocrine prostate cancer (NEPC) accounts for less than 2% of *de novo* prostate tumors (1). Nevertheless, small areas of PC with neuroendocrine features are found in > 30% prostate biopsies and primary surgical specimens, and up to 20% of castration-resistant PC (CRPC) patients progress to neuroendocrine CRPC (CRPC-NE) (2), which is highly metastatic (3). As male hormones [i.e. testosterone and dihydrotestosterone (DHT)] promote growth and proliferation of prostate cells, androgen deprivation therapy (ADT) is the mainstay for patients affected by advanced disease. Yet, ADT is ineffective in CRPC patients, whose median overall survival is 7-24 months (1). Understanding the causes of progression to NEPC is required to design more effective therapies.

According to the consensus, CRPC-NE arises by trans-differentiation of castration-refractory adenocarcinoma cells (4). However, *de novo* NEPC and CRPC-NE are very similar at DNA and RNA levels (5). Rare pre-existing CRPC-like cells also exist in untreated primary PC, some of which display neuroendocrine features (6). All together, these observations suggest that lineage plasticity is an early event in PC and becomes clinically evident in most cases after ADT. In support of this hypothesis, loss of *TP53* and *RB1* in human PC cells establishes a state of lineage plasticity that, under the pressure of ADT, induces cancer cells to transition to the neuroendocrine lineage (7,8). The mechanisms by which androgens inhibit the expansion of rare NEPC precursors remain to be fully elucidated.

Remodeling of the extracellular matrix (ECM) into a rigid and linearized pattern promotes tumor cell migration and metastasis (9), and support lineage plasticity and stemness (10). Integrins mediate adhesion to the ECM, and regulate survival, proliferation, migration, and fate of both normal and transformed cells. Integrin α2β1 is expressed in PC cells, and promotes metastasis upon engagement with collagen within the ECM (11). Despite this, the contribution of tumor-conditioned ECM to NEPC development and progression remains largely unexplored.

The Hippo pathway inactivates Yes-associated protein 1 (YAP) (12). YAP regulates tissue size during development by inducing cell cycle, survival, and invasion genes (13), and thus can favor cancer

progression. The interaction between integrin α2β1 and the ECM activates YAP, eventually favoring cell proliferation and migration (12). YAP also regulates its own activity by inducing AMOT and AMOTL1, which sequester YAP in the cytoplasm and activate Hippo kinases (12). YAP expression is higher in adenocarcinomas than in the normal prostate epithelium (14), and further increases with tumor, node and metastasis staging (15). Conversely, full-blown NEPC is YAP negative and lacks expression of integrin/ECM/adhesion genes (15,16). Consequently, the role of YAP and the ECM in NEPC progression has been overlooked.

Based on these premises, we hypothesized that the loss of more differentiated, androgen-sensitive PC cells following castration provides the opportunity for novel interactions between surviving androgen-independent, less differentiated PC cells, and between these cells and the ECM, thereby supporting NEPC aggressiveness. Using well-defined lines of poorly-differentiated mouse PC cells with exocrine or neuroendocrine features (17) and decellularized ECM (18), we conducted an in-depth investigation of the interactions between androgen-independent neuroendocrine and exocrine PC cells, and the ECM in the contexts of androgen-sufficiency and ablation.

MATERIALS AND METHODS

Mice, cell lines and reagents. Heterozygous transgenic adenocarcinoma of the mouse prostate (TRAMP) mice on the C57BL/6 background (19) were generated by crossing wild-type (WT) males with heterozygous females as described previously (20). Mice were typed for Tag expression by PCR, as described in www.jax.org. NOD.Cg-PrkdcSCIDIl2rgtm1Wjl/SzJ (NSG) mice (Charles River) and TRAMP mice were housed in a specific pathogen-free animal facility at San Raffaele Institute, Milan, Italy. Animals were treated in accordance with the European Community guidelines and with the approval of the Institutional Ethical Committee (IACUC 707). PAC and PNE cell lines were generated as described previously (17). TRAMP-C2 cells (ATCC CRL-2731™, RRID:CVCL_3615), were obtained from one TRAMP adenocarcinoma (21) and were purchased from ATCC. RM-1 cells (RRID:CVCL_B459, ras/Myc adenocarcinoma on a C57BL/6 background (22) were a kind gift of Dr. Elena Jachetti (Istituto Nazionale dei Tumori, Milan, Italy). Cells were routinely tested for *Mycoplasma* every 3 months by PCR using specific primers (Fw: ACTCCTACGGGAGGCAGCAGTA; Rv: TGCACCATCTGTCACTCTGTTAACCTC).

Generation of knockout cell lines. We used a multi-sgRNA approach to knock out YAP1, ITGA2 or TNFRSF11A (RANK) in PNE. Briefly, two or three gRNAs targeting the first exon of each gene were designed and synthetized by IDT (Integrated DNA Technologies). These gRNAs were used in combination to excise a defined genomic fragment, facilitating gene disruption through deletion. The following sgRNA targeting sequences were used to target:

Yap1: GAGGCACGTTGGCCGTCTTG, ACCAGGTCGTGCACGTCCGC, GTCCCGGCCGGAGACACGGA;

Itga2: ACCCAAGATGGGACCGGGAC, CGGCTGCTAATGCTAGTTCA;

Tnfrsf11a: TGCTCGTTCCACTGCAGGTA, CCATGGCCCCGCGCGCCCGG, CAGAGCGCCAGCAGCGGCGC.

PNE cells were Nucleofected using the Amaxa™ 4D-Nucleofector™ Protocol DS-150 in SF solution (LONZA) with a mix of 1μg Cas9 mRNA and 1μg of each sgRNA. CRISPR gene editing was

assessed 5–6 days after nucleofection. Cells were lysed to extract genomic DNA with QuickExtract DNA Extraction Solution (Biosearch technologies) and 700-800 bp genomic regions, covering the cut sites, were amplified with GoTaq Hot Start Polymerase (PROMEGA) according to manufacturer's instructions. The resulting amplicons were used to verify excision of the targeted genomic region by size shift. Primer sequences: AACTCAATGGACCAGTTCAACC and GCTCCTCGCAACTTTTTAGTTT to amplify YAP1, GTCCACATAGATGCAGAGCAGA and CCCTGGCTCTTCTTCTGAGTTA to amplify ITGA2.

Cell cultures. PAC and PNE cells were cultured in serum-free medium (NeuroCULT, STEMCELL Technologies, Cat# 05751) in the presence of 20 ng/ml EGF (STEMCELL Technologies, Cat# 78006.1) and 10 ng/ml FGFb (STEMCELL Technologies, Cat# 78003.1). Cells were split every 3–4 days. Briefly, prostaspheres were dissociated mechanically by gentle pipetting (100×) of the pellet and the single-cell suspension was seeded (1×10^5 cells/ml) in a T25 flask (Corning). TRAMP-C2 cells and RM-1 cells were cultured in Dulbecco's modified Eagle's medium (DMEM; Corning, Cat# 10-013-CV) supplemented with 10% fetal bovine serum (FBS; Invitrogen). PC-3 cells (ATCC CRL-1435™, RRID:CVCL_0035) were cultured in RPMI (Corning, Cat# 15-040-CV) supplemented with 10% FBS.

Flow cytometry. Single-cell suspensions were labelled for 15 min at 4°C with anti-mouse fluorochrome-conjugated monoclonal antibodies specific for the following: α2 integrin (1:200, clone: HMα2, BD Bioscience Cat# 558295, RRID:AB_398658), CD44 (1:200, clone: IM7, BD Bioscience Cat# 560780, RRID:AB_1937316), CD166 (1:200, clone: eBioALC48, eBioscience, Cat# 12-1661-81, RRID:AB_823126), CD133 (1:200, clone: 315-2c11, BioLegend, Cat# 141208, RRID:AB_10896756), β1 integrin (1:200, clone: Ha2/5, BD Bioscience, Cat# 555005, RRID:AB_395639), Sca-1 (1:200, clone: D7, Biolegend, Cat# 108143, RRID:AB_2629684), RANK (1:50, clone: REA961, Miltenyi Biotec, Cat# 130-116-067, RRID:AB_2727323), RANKL (1:50, clone: REA 1026, Miltenyi Biotec, Cat# 130-117-297, RRID:AB_2727911). For intranuclear detection of YAP1, cells were fixed and permeabilized with the eBioscience™ Foxp3/Transcription

Factor Staining Buffer kit (Thermo Fisher Scientific, Cat# 00-5523-00) according to manufacturer's instructions, and stained with anti-YAP1 antibody (1:50, clone: D8H1X; Cell Signaling Technology, Cat# 14074, RRID:AB_2650491) for 30 min at RT. After washing, cells were incubated for 30 min at RT with Alexa Fluor® 488-conjugated anti-rabbit IgG (H+L), F(ab')2 Fragment antibody (1:500; Cell Signaling Technology, Cat# 4412, RRID:AB_1904025). Labeled cells were acquired using a BD FACS Canto™ (BD, RRID:SCR_018055) or CytoFLEX LX (Beckman Coulter, RRID:SCR_025067). Dead cells were excluded by 7-AAD (1:100, BD Bioscience, Cat# 559925) or Zombie fixable viability dye (1:400, BioLegend, Cat# 423102) staining. Data were analyzed with FlowJo software (RRID:SCR_008520). The MFI was calculated by gating the whole population of interest.

Co-culture experiments. CMTMR (ThermoFisher Scientific, Cat# C2927)-labeled PNE cells were seeded alone or in the presence of CFSE (ThermoFisher Scientific, Cat# C34554)-labeled PAC or TRAMP-C2 or RM-1 cells at the indicated PNE:other cell ratio (1:1 unless specified otherwise). Cells (2.5×10^4 total cells in 200 µl serum-free NeuroCULT medium) were cultured in 96-well polystyrene round-bottom plates (Sigma-Aldrich) at 37°C. After 4 days, cells were harvested, prostaspheres were dissociated mechanically, and cells were incubated with dye-conjugated monoclonal antibody (see Flow cytometry section) for 15 min 4°C. Dead cells were excluded by 7-AAD staining. Cells were acquired using FACS Canto™.

For co-culture in the presence of DHT, cells were prepared as described above and treated with or without DHT (1 µg/ml, Sigma-Aldrich, Cat# 10300). Cells were also cultured in the presence of 10 ng/ml OPG (Peprotech, Cat# 450-14) or 250 µM sulfasalazine (Selleckchem, Cat# S1576) or 1µM SC75741 (SC75, Selleckchem, Cat# S7273). Alternatively, CMTMR-labeled PNE cells were cultured in the presence of PAC or PNE conditioned medium with fresh serum-free NeuroCULT medium (1:1). Briefly, 0.5×10^6 cells were cultured in 5 ml serum-free medium. After 4 days, the cells were recovered, and the supernatant was isolated by centrifugation at 1000 rpm for 10 min and stored at -20°C. For the coculture assay with Transwell, PAC cells (2.5×10^4 cells in 100 µl serum-free

NeuroCULT medium) were seeded in the upper chamber of a Transwell insert containing a porous membrane (0.4 μm pore size, Merck, Cat# CLS3413) and PNE cells (2.5×10^4 cells in 100 μl serum-free NeuroCULT medium) were seeded in the lower chamber. After 4 days PNE cells were recovered, stained and acquired using a FACS Canto™. Technical triplicates were included for each condition.

***In vitro* invasion assay.** To evaluate invasive ability, PNE cells were cultured either alone or in the presence of PAC cells as described above. After 4 days in co-culture, cells were analyzed by flow cytometry for upregulation of α2 integrin and PNE cells were seeded either alone or with PAC cells in 200μl of serum-free NeuroCULT medium in the upper chamber of a Transwell insert containing a porous (8 μm) membrane (Merck, Cat# CLS3422) previously coated with 50 μl of 0.2% collagen I (Serva, Cat# 47254). Subsequently, 800 μl serum-free NeuroCULT medium, with or without 500 μM of TC-I 15 (α2 integrin inhibitor, Tocris, Cat# 4527), or 0,5μM of CA-3 (YAP inhibitor, Selleckchem, Cat# S8661), or 1μM of PF573228 (PF57, FAK inhibitor, Selleckchem, Cat# S2013), or 1μM of Dasatinib (src inhibitor, Merck, Cat# SML2589) added to the lower chamber. Cells were incubated at 37°C for 16 h before the cells in each compartment were harvested and relative counts were acquired using a FACS Canto™. Briefly, cells in the upper chamber were recovered without pipetting to avoid disrupting the collagen coating. The residual cells were then removed from the upper side of the membrane with a cotton swab and the collagen gel was digested by the addition of 300 μl collagenase ABD solution (Roche) for 5 min at 37°C. Dead cells were excluded by 7-AAD staining. Technical triplicates were performed for each condition.

CA-3 treatment of TRAMP mice. Heterozygous TRAMP male mice (aged 14 weeks) were anesthetized with Avertin (0.6 mg/g, i.p., Sigma-Aldrich) according to procedures approved by the Institutional Ethical Committee prior to surgical castration. After 2 weeks, when the wound was healed, mice were randomized and treated intraperitoneally (i.p.; 3× per week) with 1 mg/kg CA-3 (Selleckchem) or vehicle (PBS) for the entire duration of the experiment. Mice were monitored for NEPC by palpation (3× per week) and sacrificed by CO_2 asphyxiation when tumor became palpable

or if animals developed signs of distress (e.g., 20% weight loss) according to approved protocol. The prostate and metastatic organs were removed and fixed for 24 h in formalin and embedded in paraffin for further H&E or IHC analysis. All tumors and metastases were confirmed by trained pathologist.

***In vivo* metastatic models.** PNE cells (either WT or KO for YAP1) were diluted 1:1 in Matrigel™ High Concentration (Corning, Cat# 356231) and 200 µl of the admixture containing 2×10^6 cells was injected subcutaneously (s.c.) into male NSG recipients. Mice were monitored (3× per week) and the three dimensions (height, length and width) of the tumor were measured with caliper. Tumor volume was calculated as follows: height/2×length/2×width×3,14×4/3. At tumor appearance, mice were randomized and treated i.p. (3× per week) with 1 mg/kg CA-3 (Selleckchem) or vehicle (PBS). Tumors were surgically resected when they reached 10×10 mm diameter. Mice were sacrificed by CO_2 asphyxiation when LN metastasis became palpable or if animals developed signs of distress according to approved protocol. Male C57BL/6N recipients were injected s.c. with TRAMP-C2 cells (2.5×10^6 in 200 µl DMEM), PC-3 cells (2×10^6 in 200µl PBS) were injected s.c. into NSG males. Mice were treated as described above for PNE tumor-bearing mice.

Mouse organoids. Mouse organoids were derived from either WT prostate or primary NEPC from TRAMP mice following the protocol described in (23). Cells were resuspended in Advanced DMEM (Thermo Fisher Scientific, Cat# 12634010) with L-glutamine (1×, Gibco, Cat# 25030081), 100 U/ml penicillin, 100µg/ml streptomycin (Gibco, Cat# 15140122), B27 (1x, Thermo Fisher Scientific, Cat# 17504001), N2 (1x, Thermo Fischer Scientific, Cat# 17502048), Mouse Recombinant EGF 50ng/ml (Thermo Fischer Scientific, Cat# 315-09), mouse recombinant Noggin 100 ng/ml (Thermo Fischer Scientific, Cat# 120-10C), recombinant mouse R-spondin1 50 ng/ml (Thermo Fischer Scientific, Cat# 120-38), A-83-01 200nM (MedChemExpress, Cat# HY-10432). Medium was supplemented with either DHT 10nM for WT mouse organoids culture or FGF-basic 10ng/ml (Thermo Fischer Scientific, Cat# 100-18B) for NEPC-derived organoids. Cells were finally resuspended in 80% growth factor-reduced Matrigel (Corning, Cat# 356231) and seeded as 40 µl droplets onto each well of a cell culture

plate. The droplets solidified for 30 min into a cell culture incubator at 37 °C and 5% CO_2 before 1 ml of culture media was added to each well. The culture was replenished with fresh media every 2 – 3 days during organoid growth. Organoids were passaged weekly through enzymatic and mechanical disruption before re-plating the cells.

Mouse organoids viability assay. On day 0, 1000 cells/droplet were seeded in triplicate and grown for 3 days. Organoids were then treated with either 0,5 μM or 5μM of CA-3 (Selleckchem) from day 4 to 7. Cultures were imaged with the stereomicroscope at day 5 and 7 and organoids counted to determine growth inhibition. At day 7, organoids were passaged and all the cells re-seeded to measure the frequency of organoids formation after treatment.

Human organoid culture. Human organoids were developed in Puca et al. (24) and cultured as described (25). Cells were resuspended in Advanced DMEM (Thermo Fisher Scientific, Cat# 12634010) with GlutaMAX (1×, Invitrogen, Cat# 35050061), 100 U/ml penicillin, 100μg/ml streptomycin (Gibco, Cat# 15140122), Primocin 100μg/mL (InvivoGen, Cat# ant-pm-05), B27 (Thermo Fisher Scientific, Cat# 17504001), N-Acetylcysteine 1.25mM (Sigma-Aldrich, Cat# A9165), Mouse Recombinant EGF 50ng/ml (Thermo Fisher Scientific, Cat # PMG8041), Human Recombinant FGF-10 20ng/ml (Thermo Fisher Scientific, Cat # 100-26), Recombinant Human FGF-basic 1ng/ml (Thermo Fischer Scientific, Cat# 100-18B), A-83-01 500nM (MedChemExpress, Cat# HY-10432), SB202190 10μM (Sigma-Aldrich, Cat# S7067), Nicotinaminde 10mM (Sigma-Aldrich, Cat# N3376), DHT 1nM, PGE2 1μM (R&D Systems, Cat# 2296), Noggin conditioned media (5%) and R-spondin conditioned media (5%). The final resuspended pellet was admixed to growth factor-reduced Matrigel (Corning, Cat# 356231) in a 1:2 volume ratio. Droplets of 75 μl cell suspension/Matrigel mixture were pipetted onto each well of a cell suspension culture plate (Sarstedt Ltd.). The droplets solidified for 30 min into a cell culture incubator at 37 °C and 5% CO_2 before 3 ml of culture media was added to each well. The culture was replenished with fresh media every 3−4 day during organoid growth. Organoids were passaged weekly.

Human organoid viability assay. On day -1, 3,000 cells/well were seeded in triplicate in 96 well plate. After 24h cells received increasing concentration of CA-3 or Verteporfin (Selleckchem, Cat# S1786) ranging from 0 to 10 μM. At day 6 the cell viability was measured with CellTiter-Glo Cell Viability Assay (Promega, Cat# G7570). Cell viability of PM1078 was measured at day 4 in consideration of cell growth. Both drugs were diluted in DMSO and the control samples received DMSO alone.

RNA extraction and qRT-PCR. RNA was isolated from cells using RNeasy Mini Kit (QIAGEN, Cat# 74134) and 1 μg of RNA was reverse transcribed into cDNA using iScript Advanced cDNA Synthesis Kit (Bio-Rad, Cat# 1725038). qRT-PCR was performed with CFX Opus 96 Real-Time PCR System (Bio-Rad). Relative quantification was calculated by the ΔCt method. *GAPDH* was used as an internal control.

Immunohistochemistry. Tumors and metastasis were fixed in formalin for 24 h and embedded in paraffin. Sections (5 μm) were stained with Mayer's hematoxylin and eosin (BioOptica) and evaluated by an expert pathologist. Contrary to the human disease, TRAMP mice do not develop tumors of mixed adenocarcinoma and neuroendocrine phenotype. For human organoids, IHC was performed on deparaffinized FFPE sections. Slides were incubated with 3% hydrogen peroxide (Thermo Scientific #H312-500) for 10 minutes, rinsed with Tris-buffered saline with 0.1% Tween-20 Detergent (TBST), and incubated in 1.5% blocking buffer (Vector Laboratories) for 1 hr. The following antibodies were used: SYP (1:500, clone: MRQ-40, Millipore, Cat# 336R, RRID:AB_3096182), AR (1:250, polyclonal, Millipore , Cat# 06-680, RRID:AB_310214), NKX3.1 (1:200, clone: D6D2Z, Cell signaling technology, Cat# 92998, RRID:AB_2800197), YAP (1:100, clone: D8H1X, Cell Signaling technology, Cat# 14074, RRID:AB_2650491), TAZ (1:200, polyclonal, Millipore, Cat# HPA007415, RRID:AB_1080602).

Immunofluorescence analysis. For the detection of YAP1 by immunofluorescence staining, PNE cells were cultured alone or with GFP-expressing PAC and seeded on glass slides in an artificial extracellular matrix composed of neutralized collagen I (Serva) and Matrigel™ Growth Factor

reduced (Corning) (3:1) in the presence of 300 µl serum-free NeuroCULT medium. After 4 days, the medium was removed and cells were washed with PBS cells before fixation with 4% PFA for 30 min at RT. Cells were then washed with PBS and permeabilized with 300 µl Block and Perm solution (0.3% Triton, 10% FBS, 1 mg/ml BSA and PBS) for 30 min at RT. After washing with PBS, cells were stained with a primary antibody against YAP1 (1:250, clone: 63.7, Santa Cruz Biotechnology, Cat# sc-101199, RRID:AB_1131430) overnight at 4°C. The cells were then washed and incubated with Alexa Fluor 568 anti-mouse secondary antibody (Thermo Fisher Scientific, Cat# A-11004, RRID:AB_2534072) RT for 2h. Nuclei were stained with DAPI (3 µg/ml) (Thermo Fisher, Cat# 62248) for 10 min. PC3 cells were used as positive control for nuclear YAP localization and processed as indicated above. Sections were examined under a TCS SP2 confocal laser scanning microscope (Leica, RRID:SCR_020231).

Preparation of ECM from murine prostate and co-culture with PAC and PNE cells. Briefly, each prostatic lobe was micro-dissected *ex vivo* from the urogenital apparatus of TRAMP mice (aged 12–13 weeks) and age-matched WT littermates. Decellularized ECMs from each lobe were generated as described previously (18) and cultured with 2.5×10^4 CMTMR-labelled PNE cells or with 1.25×10^4 CMTMR-labelled PNE cells plus 1.25×10^4 CFSE-labelled PAC cells in 200 µl serum-free NeuroCULT medium. After 4 days, cells were recovered by gentle pipetting and the viability and expression of α2 integrin and CD44 were analyzed by flow cytometry. Hemi-matrixes from each pair of prostatic lobes were tested.

Polarized light analysis on prostate samples. Human prostatic tissue slides for analysis were provided by the Pathology Department of IRCCS San Raffaele Hospital. Forty patients diagnosed with prostatic acinar adenocarcinoma, ISUP Grade Group 4 (Gleason Score = 8; n = 20) or 5 (Gleason Score = 9 or 10; n = 20), by expert uropathologists in the same Institution were identified. For each case the most representative H&E slide containing both neoplastic and perilesional tissue was selected. Finally, H&E slides of ISUP Grade Group 4 prostatic adenocarcinoma and (n = 20) H&E

slides of ISUP Grade Group 5 prostatic adenocarcinoma (n = 20) were used for polarized light analysis. The degree of organization of fibrils (anisotropy) was evaluated as recently reported (26). Briefly, collagen birefringence was acquired on the hematoxylin/eosin-stained tissues by using the polarized light in darkfield microscope (Zeiss AxioImager M2M) and virtual images were generated with the use of Axio Vision Imaging software (AxioVision, vers. SE64 Rel.4.9.1). All images were captured using 5X objective (NEOFLUAR 5X- NA 0.15). Anisotropy was measured in multiple stromal areas in each tissue by using the ImageJ software plug-in FibrilTool (27). Anisotropy was expressed as range from 0 to 1, with 0 representing casual orientation of the fibrils, and 1 the maximum of linearization of collagen fibrils.

Atomic force microscopy. Atomic force microscopy in force spectroscopy mode (AFM-FS) was performed at room temperature in PBS with a Nanowizard II (JPK Instruments, Berlin, Germany) equipped with a square-based pyramid probe (MLCT-BIO, cantilever E, 0.1 N/m nominal spring constant) (28). The calibration of each cantilever spring constant was performed by thermal noise method in PBS before the measurements (29). Force-indentation curves were obtained with a maximum applied force of 20 nN, an 8 μm ramp length and a constant speed of 1 μm/s on a grid of 15 × 15 μm^2 with 15 × 15 points. The force-distance curves were corrected for the bending of the cantilever to obtain the force-indentation curves. The evaluation of tissue stiffness, described quantitatively through the Young's Modulus (YM), was obtained by force-indentation curve analysis with the Hertz-Sneddon model, considering the shape of the tip (30). Each force-indentation curve was fitted by JPK data processing software (JPK Instruments, Berlin, Germany) up to about 2 μm of indentation depth.

ECM proteomic analysis. ECMs were weighed, cut into small pieces and dissolved in 100 μL of a buffer containing 5 M urea, 2 M thiourea, 2% CHAPS, 2% Zwittergent and 10 μl/ml protease inhibitors. After shaking (1,400 rpm) at RT for 24 h, the samples were sonicated using a Bioruptor (2 cycles of 30'' on/30'' off) and centrifuged (14,000 rpm) at 4 °C for 15 minutes. The total protein concentration in the supernatant was determined using a Bio-Rad protein assay with BSA as the

345 standard. Samples (25 μg) of total protein from each sample were digested using the Filter Aided
346 Sample Preparation (FASP) protocol. Briefly, using Microcon filters with a 10-kDa cutoff
347 (Millipore), cysteine reduction and alkylation was performed by adding10 mM TCEP (Thermo
348 Scientific) and 40 mM 2-chloroacetamide (Sigma-Aldrich) in urea 8 M Tris100 mM pH 8 for 30 min
349 at RT. After centrifugation at 10,000 rpm for 10 min, the buffer was replaced with ammonium
350 bicarbonate 50 mM and the proteins were digested with trypsin (Trypsin, Sequencing Grade, Roche)
351 (1:50 enzyme:secreted proteins) overnight at 37°C. Peptides were recovered from the bottom of the
352 Microcon filters by centrifugation at 10,000 rpm for 10 min, with two consecutive washes of 50 μl
353 0.5 M NaCl. Eluted peptides were purified on a C18 StageTip. Digested samples (5 μg) were injected
354 onto a quadrupole Orbitrap Q-exactive HF mass spectrometer (Thermo Scientific) and peptides
355 separation was achieved on a linear gradient (95% solvent A (2% ACN, 0.1% formic acid) to 55%
356 solvent B (80% acetonitrile, 0.1% formic acid) over 75 min and from 55% to 100% solvent B over 3
357 min) and at a constant flow rate of 0.25 μl/min on a UHPLC Easy-nLC 1000 (Thermo Scientific).
358 The LC system was connected to a 23-cm (75 μm inner diameter) fused-silica emitter (New
359 Objective, Inc. Woburn, MA, USA) packed in-house with ReproSil-Pur C18-AQ 1.9 μm beads (Dr.
360 Maisch Gmbh, Ammerbuch, Germany) using a high-pressure bomb loader (Proxeon). The mass
361 spectrometer was operated in DDA mode: dynamic exclusion enabled (exclusion duration,15 s); MS1
362 resolution, 70,000; MS1 automatic gain control target, 3×10^6; MS1 maximum fill time, 60 ms; MS2
363 resolution, 17,500; MS2 automatic gain control target, 1×10^5; MS2 maximum fill time, 60 ms; and
364 MS2 normalized collision energy, 25. For each cycle, one full MS1 scan range (300–1650 m/z) was
365 followed by 12 MS2 scans using an isolation window size of 2.0 m/z.
366 **MS analysis and database search.** MS analysis was performed as reported previously (31). Raw
367 MS files were processed with MaxQuant software (1.5.2.8), which enables high peptide identification
368 rates, individualized ppb-range mass accuracies and proteome-wide protein quantification by using
369 the Andromeda search engine. MS/MS peak lists were searched against the UniProtKB Human
370 complete proteome database (uniprot_cp_Mouse_20150401) using trypsin specificity with ≤2 missed

cleavages allowed. Searches were performed selecting alkylation of cysteine by carbamidomethylation as the fixed modification, and oxidation of methionine and N-terminal acetylation as the variable modifications. Mass tolerance was set to 5 ppm and 10 ppm for parent and fragment ions, respectively. A reverse decoy database was generated within Andromeda and the False Discovery Rate (FDR) was set to <0.01 for peptide spectrum matches (PSMs). For identification, at least two identified peptides per protein were required, of which at least one peptide was required to be unique to the protein group. Technical duplicates were included in these experiments.

Quantification and analysis of MS data. Label free from DDA .raw files were analyzed by MaxQuant software for protein quantitation and label-free quantification (LFQ) intensities were used. Statistical analysis was performed using the Perseus software (version 1.5.6.0) included in the MaxQuant package and *t*-tests were performed applying FDR <0.05. The proteins identified by proteomic analysis were matched with the matrisome DB2.0 (revised on 2016) (http://matrisomeproject.mit.edu/proteomics-data-sets/). RAW proteomics data files were deposited together with all peptides and proteins identified and parameters used for the analysis at the ProteomeXchange Consortium via the PRIDE partner repository with the dataset identifier PXD027625.

Transcriptomic analysis. RNA-sequencing data from Beltran et al. were analyzed to identify transcriptomic differences between castration-resistant neuroendocrine prostate cancer (CRPC-NE) and adenocarcinoma (CRPC-Adeno). The gene expression read count matrix provided in the report by Beltran et al. (4) were analyzed using R (v. 3.6.2). The study included 13 CRPC-NE and 34 CRPC-Adeno samples. Only genes with a counts per million (CPM) value >1 in at least 13 samples were retained for the analysis. Differentially expressed genes (DEGs) were identified using the DESeq Bioconductor package. *P*-values were adjusted using an FDR threshold ≤0.05. Heatmaps of all DEGs (FDR < 0.05) and modulated genes enriched in extracellular matrix organization according to GO analysis (GO:0030198) were plotted with the CRAN package pheatmap (v.1.0.12). To identify both up- and down-modulated pathways, we performed enrichment analysis of the genes with adjusted *P*

< 0.05 using the EnrichR package (v.2.1), which provides an R interface to the 'Enrichr' databases and statistics. Enrichment was performed on the GO_Biological_Process_2018, GO_Cellular_Component_2018, GO_Molecular_Function_2018, Reactome_2016, KEGG_2016, WikiPathways_2016, BioCarta_2016, BioPlanet_2019 datasets.

Single-cell RNA sequencing data from Cheng et al. (6), Song et al. (32), and Zaidi et al. (33) were reanalyzed to evaluate the expression of key genes and gene signatures. The genes of interest included *YAP1*, NE markers (*EZH1*, *EZH2*, *SYP*, *NDRG1*), and *ITGA2*. The gene signatures analyzed were CRPCsig51 as defined by Cheng et al. (6), SCL and NE defined in Tang et al. (34), and YAP-TAZ targets defined in Wang et al. (35), as specified in Supplementary Table S1. The analyses were performed across various PC datasets, including PC lineage subtypes in CRPC cells (6), primary treatment-naïve PC (32), and castration-sensitive PC, castration-resistant adenocarcinoma and castration-resistant NEPC prostate tissues (33). Count files for each sample of the Cheng et al. dataset (with ".h5" extension) were obtained from the paper authors and aggregated into a single feature-barcode matrix by cellranger v 6.1.2, using the "cellranger aggr" function. The aggregated count file was imported in R (v.4.0.5) and analyzed with the default Seurat (v. 4.0.5) workflow as described by Cheng et al. Seurat RDS objects, including the analysis of Song et al. and Zaidi et al., were made available by the paper authors and downloaded at the following links: https://github.com/angelussong/scRNA-seq-Analysis-of-Prostate-Cancer-Samples (32) and https://www.ncbi.nlm.nih.gov/geo/query/acc.cgi?acc=GSE264573 (33). These objects were directly imported into R (v.4.0.5) for gene expression and gene signature testing. The scores of the CRPCsig51, SCL, NE, and YAP-TAZ targets signatures were assessed with the Seurat function "AddModuleScore". Gene expression and signature scores were visualized with the Seurat function "FeaturePlot". Heatmaps of gene expression were generated with the Seurat function "DoHeatmat" using the data slot.

Statistical analyses. If not otherwise stated, results were obtained from at least 3 independent experiments. Each independent experiment was performed in technical triplicates. If not otherwise

stated, statistical analyses were performed using Prism 10 (GraphPad Software, RRID:SCR_002798) applying Student's *t*-test, Fisher exact test or one-way ANOVA followed by Tukey's test. $P < 0.05$ was set as the threshold for statistical significance.

Data availability. All data regarding proteomic analysis and quantification were deposited at the ProteomeXchange Consortium via the PRIDE partner repository with the dataset identifier PXD027625 as indicated in the paragraph above. The genomics data analyzed in this study were obtained from public databases or requested to paper authors, as indicated below. Bulk-RNAseq data from Jachetti E. et al., *Cancer Res,* 2015, were obtained from Gene Expression Omnibus (GEO) at GSE65502; Bulk-RNAseq data from Beltran et al., *Nat Med,* 2016 were obtained from dbGap at phs000909.v.p1. Single-cell RNA-seq data from Cheng et al., *Eur. Urol.*, 2022 was obtained by asking the paper authors; Single-cell RNA-seq data from Song et al., *Nat Comm,* 2022 and Zaidi et al., *PNAS*, 2024 were obtained from Gene Expression Omnibus (GEO) at GSE176031 and GSE264573, respectively.

RESULTS

In the absence of male hormones, surviving exocrine PC cells and the tumor-associated ECM promote α2β1 upregulation in NEPC cells and their survival

To identify novel interactions between tumor cells and the tumor microenvironment promoting NEPC in the context of androgen withdrawal, we used PC cell lines obtained by *in vitro* culture of TRAMP prostate specimens in serum-free medium (17). This culture condition allows *in vitro* stabilization of PC lines composed of an heterogenous population of cells at different stages of differentiation. Thus, these cell lines maintain plasticity, and fulfil the criteria of unlimited self-renewal, multilineage differentiation and tumorigenic potential (17). PAC cells [formerly 11wT-Ep; ref. (17)] were obtained from lesions of high-grade prostate intra-epithelial neoplasia (mPIN) that invariably progress to adenocarcinoma. PNE cells [formerly T-NE; ref. (17)] were isolated from poorly differentiated, synaptophysin (Syn)-positive NEPC lesions. Gene expression analyses revealed the two cell types reflect the stages of human PC progression. Additionally, the CRPCsig51 signature characterizing pre-existing CRPC-like cells identified by Cheng et al. (6) clearly segregated PNE from PAC cells (Fig. S1A) as well as human NEPC from CRPC (Fig. S1B). This finding suggests that poorly differentiated cells also exist in human PC specimens before castration.

To test our hypothesis that castration favors novel interactions among androgen-independent exocrine and neuroendocrine PC cells and the ECM, we cultured PNE with PAC cells or more differentiated TRAMP-C2 (19) or RM-1 cells (22) in serum-free medium (androgen-free; Fig. 1A) (17). Both TRAMP-C2 and RM-1 cells inhibited proliferation of PNE cells in a dose-dependent manner (Fig. 1B-D), whereas proliferation of PAC (Fig. S2A) and TRAMP-C2 cells (Fig. S2B) was not affected. Co-culture with PAC cells induced upregulation of integrin α2 (Fig. 1E-F) but not of CD29, CD166, CD133, Sca-1 and CD44 (Fig. S2C-E) in PNE cells. This effect did not occur when PNE cells were co-cultured with TRAMP-C2 (Fig. 1E-F) or RM-1 cells (Fig. S2F). Co-culture with PNE cells did not impact α2 expression in PAC cells (Fig. S2G).

Next, we explored the influence of androgens on α2 upregulation and PNE proliferation. While PNE expressed the AR (17), DHT neither induced upregulation of known AR-target genes in PNE cells (Fig. S2H-I) nor further PNE cell differentiation (Fig. S2J-K). DHT also did not prevent upregulation of α2 in PNE cells co-cultured with PAC cells (Fig. S2L) and did not affect PNE proliferation (Fig. S2M). Thus, PNE cells are insensitive to DHT.

To assess the potential role of the ECM on NEPC, we cultured cells on ECMs from the dorsal prostate lobe (i.e., one of the first site of tumorigenesis) collected from TRAMP mice and wild-type (WT) littermates at 12–13 weeks of age, when TRAMP mice begin to develop PC (19). Only TRAMP lobes fully supported the survival of PNE cells (Fig. 1G) and induced α2 upregulation (Fig. 1H). α2 upregulation by PNE cells was further amplified when they were seeded together with PAC cells on TRAMP dorsal lobe ECM (Fig. 1I), thus demonstrating that the effects of PAC cells and cancer-associated ECM on PNE cells are additive.

Collectively, these data support a model in which more differentiated PC cells prevent less-differentiated NEPC cell proliferation and α2 upregulation. Under androgen ablation, androgen-independent exocrine PC cells and the ECM unleash the proliferative capacity and α2 upregulation in NE cells favoring their migration potential.

α2 upregulation in PNE cells requires cell-to-cell contact and NF-κB signaling

To identify pathways responsible for α2 upregulation, we cultured PNE cells in PAC-conditioned medium (Sup-PAC; Fig. S3A). PNE expression of neither α2 (Fig. S3B) nor CD44 (Fig. S3C) was modulated by PAC-conditioned medium. Similar results were obtained when the two cell populations were physically separated by a porous membrane (Fig. S3D-E), suggesting that cell-to-cell contact is required to induce α2 in PNE cells.

Interactions of RANK with RANKL induce α2 upregulation by cancer cells *via* the NF-κB signaling pathway (36). Interestingly, both PNE and PAC cells expressed RANK and RANKL (Fig. 2A-D).

Inhibition of RANK/RANKL interaction by knocking out RANK in PNE cells (Fig. 2E) or by adding osteoprotegerin (OPG) (Fig. 2F), a natural decoy receptor for RANKL (37), prevented α2 upregulation on PNE cells without affecting their viability (Fig. S3F). Co-culture of PNE and PAC in the presence of a non-cytotoxic concentration of the NF-κB inhibitors sulfasalazine (Fig. S3G) or SC75 (Fig. S3H) also prevented α2 upregulation in PNE cells (Fig. 2G). Interestingly, both OPG (Fig. 2H) and sulfasalazine (Fig. 2I) inhibited α2 upregulation in PNE cells cultured on TRAMP ECM, thus suggesting a common mechanism for α2 upregulation in these cells. All together, these data demonstrate that the interaction of RANK with RANKL and the activation of NF-κB induce α2 upregulation in PNE cells (Fig. 2J).

The ECM from the TRAMP prostate differs structurally and chemically from that of WT mice

We then explored the structure and composition of the prostate ECM. Scanning electron microscopy (SEM) showed that the ECM from TRAMP mice was more linearized and organized than that derived from age-matched WT prostate (Fig. 3A), resulting in higher anisotropy (Fig. 3A, B). We confirmed this finding with polarized light on H&E sections of the whole dorsal lobes (Fig. 3C). Furthermore, atomic force microscopy (AFM) demonstrated that the ECM from TRAMP dorsal lobes was stiffer than the WT ECM (Fig. 3D). These structural features are characteristics of a pro-metastatic ECM (9).

Data obtained in the TRAMP model prompted us to investigate the structure of the human prostate ECM. Polarized light microscopy showed increased anisotropy in H&E sections from PC tissues when compared with perilesional area (Fig. 3E and Fig. S4A). These findings highlight similarities between human and mouse prostate ECM.

Proteomic analysis of ECM from TRAMP and WT prostates identified 484 proteins upregulated and 215 downregulated in TRAMP ECM (Fig. S5A and Supplementary Table S2). Gene ontology (GO) analysis uncovered that these proteins regulate interactions between cells and ECM (Fig. S5B);

512 therefore, we focused our analysis on ECM-specific proteins. Serpine2, Clec2d, Annexin13, Host cell
513 factor 1, Serpin B11, Adam10, Cathepsin F and Plexin-B2 were all upregulated in TRAMP-derived
514 ECMs, whereas Prolargin, Decorin, Laminin subunits α3 and β3, Periostin, Fibrinogen-like protein
515 1, Von Willebrand factor, Transforming growth factor-beta-induced protein, Dermatopontin and
516 Collagen α chains were downregulated (Fig. 3F). The Enrichr algorithm (38) identified ECM-
517 receptor, focal adhesion and PI3K/AKT pathways as the most downregulated pathways in TRAMP-
518 derived ECMs (Fig. 3G). These data suggest that in the early stage of tumorigenesis, the ECM
519 undergoes structural, physical, and chemical rearrangements that may influence behavior of poorly
520 differentiated PC cells. When we analyzed transcriptomic data of PAC and PNE cells (17), we found
521 that while several NEPC-specific pathways were upregulated in latter (Fig. S5C), ECM-receptor
522 interaction, PI3K/AKT signaling, and focal adhesion pathways were downregulated (Fig. S5D) as in
523 the TRAMP-derived ECM (Fig. 3G).
524 To find correlates of these pathways in human NEPC specimens, we compared the transcriptome of
525 34 CRPC-Adeno and 13 CRPC-NE samples (4). As shown in Figure S6A, "ECM organization"
526 pathway of the Kyoto Encyclopedia of Genes and Genomes (KEGG) differentiated human CRPC-
527 NE and CRPC-Adeno. ECM-receptor interaction, focal adhesion and the PI3K/AKT signaling
528 pathway again ranked among the top 10 downregulated transcripts (Fig. S6B). Thus, pathways
529 involved in ECM/cell interactions are downregulated in the tumor-modified ECM and in mouse and
530 human NEPC, but whether this supports, hinders or does not affect metastasis is unclear.
531
532 **α2 upregulation endows PNE cells with invasive ability**
533 To investigate if α2 promoted the metastatic behavior of PNE cells, these cells were cultured alone
534 or together with PAC cells on a collagen I gel substrate. The invasive capacity of PNE cells increased
535 dramatically when the cells were co-cultured with PAC cells (Fig. S7A-B). TC-I 15, a synthetic
536 inhibitor of integrin α2β1 (39), and knocking out α2 in PNE (PNE $\alpha2^{KO}$) significantly reduced their
537 invasion ability (Fig. S7C-D). Thus, α2 upregulation endows PNE cells with more invasive ability.

538

539 **YAP is activated in PNE cells co-cultured with PAC cells**

540 Because interactions between α2, which only forms dimers with β1 subunit (40), and collagen in the
541 ECM trigger YAP/TAZ signaling (41), we investigated YAP in PNE cells. We used
542 immunofluorescence (IF) to quantify cytoplasmic (inactive) and nuclear (active) YAP. Human PC3
543 cells were used as positive control (Fig. S8A). Co-culture induced nuclear translocation of YAP in
544 PNE cells as demonstrated by confocal microscopy (Figs. 4A-B and S8B-C), suggesting its activated
545 status. Indeed, YAP inhibition by CA-3 (42) impaired the invasive ability of PNE cells (Fig. 4C)
546 without affecting cell viability (Fig. S8D). Knocking out YAP in PNE cells (PNE YAP^{KO}) also
547 reduced their invasiveness (Fig. 4D). To provide a molecular link between α2 activation and nuclear
548 translocation of YAP, we pharmacologically intercepted focal adhesion kinase (FAK) and src kinase,
549 integrin downstream key molecules (41). Both PF57 (FAK inhibitor) and Dasatinib (src inhibitor)
550 reduced PNE cell invasion (Fig 4E), supporting the α2-YAP connection (Fig. 4F). Thus, PAC cells
551 induce YAP activation in PNE cells and enhance their invasive capacity.

552

553 **Cells like PNE exist in human PC**

554 To provide an additional link between our data in mice and human PC, we looked for YAP expression
555 in untreated primary PC in Cheng et al. dataset (6). According to the original hypothesis (6), we
556 identified 18 clusters (Fig S9A) discriminating basal, luminal (PSA-low), luminal (PSA-high), small
557 cell NE cancer (SCNC), CRPC (AR-high), mCRPC (PSA-high) and non-epithelial cells (Fig. 5A),
558 YAP was expressed in luminal cancer cells and low/absent in SCNC cells (Fig. 5B). Strikingly, CRPC
559 (AR-high) cluster, which contains CR primary tumor cells (6), showed high expression of YAP (Fig.
560 5B) and a few of these cells co-expressed the NE marker SYP (Fig. 5C). A few cells co-expressing
561 YAP and SYP were also found in luminal (PSA-low) clusters from primary PC that contained cells
562 with stem-cell features (Fig. 5B-C).

To corroborate these findings, we looked for co-expression of YAP and NE markers in additional datasets of single cell RNA sequencing of PC samples from Zaidi et al. (33), and Song et al. (32) (Figs. 5D-G and S9). Zaidi et al. analyzed untreated PC (castration-naïve), castration sensitive PC (CSPC), CRPC and castration resistant NEPC prostate tissues (33). We found cells co-expressing YAP and SYP in all the three clusters independently of their lineage (Fig. 5D-F). Consistently, a minority of cells were YAP positive in the NEPC cluster (Fig. 5E). Song et al. analyzed primary localized treatment-naïve PC samples (32). As expected, a few cells expressed SYP in the primary PC (Fig. S9B), suggesting that even if rare, clones with neuroendocrine features already exist in primary lesions in treatment-naïve patients. To look for human cells with characteristics like our PNE and expressing YAP, we applied the CRPCsig51 signature (6) to the dataset from Cheng et al. (6), Zaidi et al. (33) and Song et al. (32). We found preexisting NE/CRPC-like cells in all datasets. Moreover, these cells were particularly enriched in the NEPC clusters (Fig. S9C and E). As shown in Figure S9C-E, some preexisting NE/CRPC-like cells also express stem cell-like (SCL) signature (34), NE signatures and YAP/TAZ target genes. To identify cells with NE features and potentially expressing YAP, we used cells that scored high in the CRPCsig51 signature (6). We found YAP positive cells among those that expressed SYP, EZH1, EZH2 and NDRG1 (Fig. S9F-H). These data demonstrate that while full-blown NEPC are negative for YAP, preexisting poorly differentiated CRPC cells with NE features can express YAP and its target genes, suggesting YAP is active in these cells. Furthermore, we identified a small population of cells co-expressing YAP and ITGA2 (Fig. 5 G-J). These data also reinforce our original hypothesis that α2 signaling is mediated by the transcriptional activity of YAP.

YAP inhibition abolishes PC aggressiveness *in vivo*

To assess the efficacy of YAP inhibition *in vivo*, and to avoid the potentially confounding effect of the immune response (43), we injected PNE cells into male NSG mice. At tumor onset, we treated the mice with CA-3 or vehicle until surgical removal of the primary tumor (44), the mice were

589 monitored thereafter for LN metastasis (Fig. 6A). CA-3 treatment significantly delayed tumor
590 formation (Figs. 6B and S10A), and when the last control mouse underwent surgery to remove the
591 primary lesion, more than 60% of CA-3-treated mice were still surgery naïve (Fig. 6C). In this
592 neoadjuvant setting, CA-3 treatment significantly reduced the frequency of metastasis (Fig. 6D) and
593 delayed metastasis appearance (Fig. 6E). Because CA-3 did not impact tumor growth in mice
594 challenged with PNE YAP^{KO} cells (Fig. S10B-C), we conclude that YAP was the main target of CA-
595 3 *in vivo*. Interestingly, knocking out YAP in PNE cells impacted the *in vivo* metastatic potential (Fig.
596 6E), further supporting a role of YAP in establishing NEPC metastasis.
597 To investigate the therapeutic effect of CA-3 during the development of castration resistance, we used
598 castrated TRAMP mice (Fig. 6F) (45). NEPC (Fig. 6G) developed in approximately 20% of the intact
599 TRAMP mice aged >30 weeks, and the proportion doubled after surgical castration (Fig. S10D). As
600 shown in Supplementary Table 3, CA-3 administration did not augment the quality and quantity of
601 adverse events in the treated cohort compared to vehicle-treated animals. While 47% of castrated
602 vehicle-treated TRAMP mice (i.e., 9/19) developed neuroendocrine tumors starting at 53 days post-
603 surgery, only 11% (i.e., 2/19) CA-3 treated mice developed NEPC (Fig. 6H). Metastases were
604 observed in four out of nine mice with NEPC in the vehicle group and in one CA-3-treated mouse.
605 To evaluate the sensitivity of more differentiated PC cells to CA-3, we treated mice bearing palpable
606 mouse TRAMP-C2 or human PC-3 tumors with CA-3. Despite YAP expression in both TRAMP-C2
607 and PC-3 cells, the resulting tumors were resistant to CA-3 administration (Fig. S10E-F). Similarly,
608 CA-3 did not prevent the development of CRPC-Adeno in TRAMP mice (Fig. S10G) and its
609 metastases (i.e. 100% in both groups). Thus, YAP inhibition suppresses the development of NEPC
610 and metastasis in castration-naïve mice and CRPC-NE in TRAMP mice.
611
612 **Inhibition of YAP blocks the growth of human NEPC organoids**
613 To evaluate the relevance of our therapeutic approach in human PC, we assessed sensitivity of patient-
614 derived three-dimensional (3D) organoids (24) to the YAP inhibitors CA-3 and the clinical-grade

verteporfin. The existence of poorly differentiated cells in organoids is intrinsic to their *in vitro* regenerative capacity. All four organoids derived from metastatic CRPC-NE (i.e., PM154, PM155, PM1078 and PM1262), the MSKPCA3 organoid from CRPC-Adeno and the CRPC cell line 22Rv1, as well as other prostate cell lines (i.e., VCaP, LNCaP, PC3 and RWPE1) but not NCIH660 cells expressed YAP (Fig. 7A-B) and TAZ (Fig. 7A-C). MSK-PCA3 stained positive for AR-signaling (e.g., AR and NKX3.1) and negative for the NE marker SYP. CRPC-NE organoids stained negative for AR-signaling and positive for SYP (Fig. 7A) indicating that the organoids retained the features of the tissue of origin (24). In 3D culture conditions, both YAP inhibitors impaired growth of all organoids (Fig. 7D-E), with PM1078 and PM1262 being the most sensitive. Additionally, CYR61 and CTGF, genes downstream of YAP (12), were significantly inhibited upon CA-3 treatment in PM1078 and PM1262 organoids (Fig. 7F-G). Hence, therapeutic doses of the YAP inhibitors are effective against human CRPC organoids.

We also generated organoids from TRAMP NEPC and wild type prostate. While constraining the growth of mouse NEPC organoids at doses therapeutically effective *in vivo* (Fig. S11A-B), YAP inhibitors did not alter the growth of prostate organoids from wild type mice (Fig. S11C-D).

All together, these data suggest that both humans and mouse poorly differentiated PC cells are sensitive to the therapeutic effects of YAP inhibition.

DISCUSSION

Here, we aimed to elucidate the mechanism by which NEPC cells nested either in the primary or in the metastatic tumor are suppressed in the presence of androgens, whereas this suppression can be relieved under conditions of androgen-deprivation. To this aim, we took advantage of poorly differentiated PC cells with either neuroendocrine or exocrine characteristics. Based on our findings, we propose a model by which more differentiated PC cells primarily limit the proliferation of NEPC precursors. Without androgens, exocrine PC cells surviving ADT and the ECM activate the α2/YAP signaling axis in NEPC precursors endowing them with aggressive and pro-metastatic behaviors. Therefore, the use of small molecules targeting α2 and/or YAP, especially in the context of androgen insufficiency, might block the surge of NEPC in patients.

This model is supported by experimental evidence obtained in this study. First, we found that α2 upregulation by PNE cells *in vitro* was selectively induced by androgen-independent exocrine PC cells. Conversely, while unable to modulate α2 expression in PNE cells, more differentiated exocrine PC cells diminished PNE cell proliferation. Thus, androgens maintain control of NEPC by supporting the survival of differentiated PC cells that block the proliferation of neuroendocrine clones. Further evidence is needed to confirm this finding in the human disease.

In human and xenograft PC models, primary adenocarcinomas are weakly α2-positive, whereas metastases are strongly positive for this marker, suggesting that the metastatic process selects for $\alpha2^{+}$ clones with greater migratory potential. Development of resistance to ADT by LNCaP and LAPC9 tumors is also associated with α2 upregulation (46). We demonstrated that also poorly differentiated NEPC cells upregulated α2 to augment their invasive ability. However, the ability of α2 to support homing of the migrated tumor cells to metastatic sites, or detachment from the primary tumor remains to be determined.

Our work also provides a mechanistic explanation to the pro-metastatic characteristics of the tumor ECM. Rather early in the development of cancer in TRAMP mice, the ECM from the prostate acquired the capacity to induce α2 upregulation in PNE cells. This phenomenon was further enhanced

by the presence of PAC cells. The structural modification of the tumor ECM correlates with aggressive disease by supporting the invasion of the surrounding tissue (18), and limiting infiltration by cancer-specific immune cells, eventually reducing the efficacy of anti-PD-1 immunotherapy (47). These concepts explain, at least in part, the poor infiltration of PC by T lymphocytes (48).

A stiff matrix also promotes YAP activation, which induces proliferation and migration of transformed cells. We found that co-culture of PNE and PAC cells in a matrix composed of collagen I and Matrigel efficiently induced the nuclear localization of YAP in PNE cells, and its inhibition reduced the invasive capability of PNE cells both *in vitro* and *in vivo*. Thus, our data suggest that the stiff prostate-derived ECM supports the metastatic phenotype of NEPC cells by inducing α2 expression and YAP activation. These data are consistent with a previous study demonstrating that, in the context of androgen deprivation, YAP associates with the AR, and migrates into the nucleus, where it activates the transcription of AR target genes (49). We showed that YAP is also active in AR-positive and androgen-insensitive PC, suggesting that YAP can be triggered both by tumor cell intrinsic and environmental cues. Increased anisotropy of the ECM in human PC suggests that also in humans affected by PC, the tumor ECM is modified by the disease and might favor metastasis likely through a mechanism analogous to the TRAMP model. We propose that the tumor-associated ECM favors tumor aggressiveness in at least two ways; by protecting tumor cells infiltration and attack by T lymphocytes and by promoting their invasiveness. Therefore, targeting synthesis of the ECM may be a promising therapeutic strategy in cancer.

We and others found that YAP is downregulated in full-blown human NEPC and ectopic expression of YAP in YAP-deficient tumors induces adhesion/ECM genes (16). These analyses used NEPC tumors mostly composed of fully differentiated cells. In contrast, PNE cells are heterogenous and much less differentiated than those tumors. Indeed, PNE cells are close to the CRPC-like cells with neuroendocrine features found in human PC well before androgen deprivation therapy (6). Thus, we have been in a unique position to investigate the early phase of NEPC development. By targeting YAP, we greatly reduced NEPC development in mice bearing PNE tumors and in castrated TRAMP

684 mice. Interestingly, while PC3 cells are YAP-positive, they are resistant to CA3 and verteporfin *in*
685 *vivo (14).* We also extended the anti-cancer activity of YAP inhibitors to 3D cultures of human CRPC
686 organoids. All together, these findings support the concept that transient YAP expression in PC cell
687 precursors is required for progression to NEPC and that YAP inhibitors are particularly effective
688 against YAP-positive poorly differentiated PC cells.
689 Tang and colleagues (34) recently identified in CRPC patients a recurrent AR-negative/low PC
690 subtype enriched in stem cell-like features (CRPC-SCL) that relies on YAP/AP-1 signaling for
691 growth. Indeed, YAP inhibition prevented expansion of CRPC organoids from CRPC-SCL patients
692 without affecting AR-dependent PC subtypes. These findings recapitulate the behavior of our CRPC
693 PC organoids and PNE cells. Moreover, the evidence of preexisting CRPC cells in primary PC
694 (6,32,33) that share neuroendocrine features and express YAP, reinforce the idea that YAP inhibitors
695 can serve as complementary treatment for PC patients.
696 One limitation of our study is that we cannot specifically distinguish between *de novo* NEPC and
697 treatment-related NEPC. We did not conduct lineage tracing, and our experiments were not designed
698 to investigate the origin of NEPC. Because the SV40-driven genetic inactivation of Trp53 and Rb1
699 tumor suppressors does not mimic the early events of human PC, the TRAMP model is not well suited
700 to address this biological problem. A distinction between the two has been attempted in the past (50),
701 which however has not been validated yet. Indeed, our and their experiments were performed in
702 castrated TRAMP mice that, by definition, develop CRPC-NE and not *de novo* NEPC. Conversely,
703 because the inactivation of *Trp53* and *Rb1* is a characteristic of both *de novo* NEPC and advanced
704 CRPC-NE (5), the TRAMP model is well suited to investigate the surge of NEPC in condition of
705 androgen deprivation. Moreover, we do not know if PNE cells originated from a transdifferentiated
706 exocrine cancer cell or were the product of *de n*ovo NEPC. Semiquantitative RT-PCR (17) showed
707 that PNE cells also express AR as well as markers of exocrine prostate (e.g., CK5, CK8), which might
708 suggest trans-differentiation. Similarities between our PNE cells and human NEPC identified by
709 Cheng and colleagues (6) and reported herein strongly suggest that cells like PNE exist in human PC

tissues. Another limitation of our study is the difficulty in identifying a human homolog of PNE cells. While analysis of human PC dataset (6,32,33) identified few cells expressing YAP and SYP in primary tumors, these cells cannot be identified by immunohistochemistry. Nonetheless, the efficacy of YAP inhibitors in restraining growth of human CRPC organoids supports the hypothesis that these cells also exist in human PC and are targetable by YAP inhibitors.

In conclusion, we demonstrated that the interaction between exocrine cells, neuroendocrine cells and the tumor ECM promote the aggressiveness and metastasis of NEPC and provide the basis for investigating strategies aimed at preventing dissemination of NEPC. Our findings indicate the therapeutic value of integrin α2 and/or YAP inhibitors during ADT in PC patients. This combined approach could also be investigated in neoadjuvant settings to prevent the spread of NEPC cells before radical prostatectomy or tomotherapy.

Acknowledgements. The authors are thankful to Dr. Irene Locatelli for the help in the generation of the extracellular matrices used in this work. We thank Dr. Cesare Covino and Dr. Desirèe Zambroni from ALEMBIC, an advanced microscopy laboratory (IRCCS Ospedale San Raffaele and Università Vita-Salute San Raffaele). We thank Dr. Amleto Fiocchi from the Animal Histopathology facility (IRCCS Ospedale San Raffaele and Università Vita-Salute San Raffaele). A. Brevi conducted this study in partial fulfillment of her Ph.D. at San Raffaele University. This work was supported by Associazione Italiana per la Ricerca sul Cancro (AIRC; Grant No. #IG16807 to M.B) and the Italian Ministry for Universities and Research (MUR), Dipartimenti di Eccellenza 2023-2027 (l. 232/2016, art. 1, commi 314–337). A. Brevi was supported by a fellowship from the Fondazione Italiana per la Ricerca sul Cancro/AIRC (Grants #22316 to A.B.). The work is dedicated to the memory of Andrea Spataro.

Author contributions. A. Brevi: Conceptualization, data curation, formal analysis, investigation, methodology, validation, visualization, writing – original draft, writing – review and editing. **M. Lorenzoni**: Formal analysis, data curation, investigation, methodology, validation, writing – review and editing. **S. Caputo**: Formal analysis, investigation, methodology, writing – review and editing. **Y. Yamada**: Formal analysis, data curation, investigation, methodology, validation, visualization, writing – review and editing. **M. Grioni**: Investigation, resources, review and editing. **L.L. Cogrossi**: Formal analysis, investigation, methodology, review and editing. **L.M. Vidal**: Formal analysis, investigation, methodology, validation, review and editing. **V. Cassina**: Formal analysis, investigation, methodology, validation, review and editing. **D. Cipria**: Methodology, investigation, review and editing. **C. Venegoni**: Formal analysis, data curation, investigation, methodology, validation, visualization, writing – review and editing. **P. Zordan**: Formal analysis, investigation, methodology, validation, review and editing. **V. Matafora**: Investigation, data curation, formal analysis, software, validation, visualization, review and editing. **A.S. Tascini**: Data curation, formal analysis, software, validation, visualization, writing – review and editing. **N. Tenace**: Data curation, resources, supervision, validation, writing – review and editing. **R. Campanile**: Investigation, review

and editing. **V. Cucchiara**: Resources, writing – review and editing. **V. Pinna**: Investigation, review and editing. **E. Jachetti:** Resources, supervision, validation, review and editing. **R. Galli**: Methodology, supervision, review and editing. **A. Bachi**: Supervision, methodology, review and editing. **M. Colecchia**: Resources, supervision, validation, review and editing. **A. Briganti**: Resources, supervision, review and editing. **M. Freschi**: Resources, supervision, validation, review and editing. **F. Mantegazza**: Supervision, validation, writing – review and editing. **A. Lombardo**: Supervision, validation, writing – review and editing. **F. Demichelis**: Resources, supervision, writing – review and editing. **H. Beltran**: Resources, supervision, writing – review and editing. **M. Alfano**: Resources, supervision, validation, writing – review and editing. **M. Bellone**: Conceptualization, formal analysis, funding acquisition, project administration, supervision, validation, visualization, writing – original draft, writing – review and editing.

REFERENCES

1. Beltran H, Tagawa ST, Park K, MacDonald T, Milowsky MI, Mosquera JM*, et al.* Challenges in recognizing treatment-related neuroendocrine prostate cancer. J Clin Oncol **2012**;30:e386-9
2. Krauss DJ, Amin M, Stone B, Ye H, Hayek S, Cotant M*, et al.* Chromogranin A staining as a prognostic variable in newly diagnosed Gleason score 7-10 prostate cancer treated with definitive radiotherapy. Prostate **2014**;74:520-7
3. Aggarwal R, Huang J, Alumkal JJ, Zhang L, Feng FY, Thomas GV*, et al.* Clinical and Genomic Characterization of Treatment-Emergent Small-Cell Neuroendocrine Prostate Cancer: A Multi-institutional Prospective Study. J Clin Oncol **2018**;36:2492-503
4. Beltran H, Prandi D, Mosquera JM, Benelli M, Puca L, Cyrta J*, et al.* Divergent clonal evolution of castration-resistant neuroendocrine prostate cancer. Nat Med **2016**;22:298-305
5. Chedgy EC, Vandekerkhove G, Herberts C, Annala M, Donoghue AJ, Sigouros M*, et al.* Biallelic tumour suppressor loss and DNA repair defects in de novo small-cell prostate carcinoma. J Pathol **2018**;246:244-53
6. Cheng Q, Butler W, Zhou Y, Zhang H, Tang L, Perkinson K*, et al.* Pre-existing Castration-resistant Prostate Cancer-like Cells in Primary Prostate Cancer Promote Resistance to Hormonal Therapy. Eur Urol **2022**;81:446-55
7. Ku SY, Rosario S, Wang Y, Mu P, Seshadri M, Goodrich ZW*, et al.* Rb1 and Trp53 cooperate to suppress prostate cancer lineage plasticity, metastasis, and antiandrogen resistance. Science **2017**;355:78-83
8. Mu P, Zhang Z, Benelli M, Karthaus WR, Hoover E, Chen CC*, et al.* SOX2 promotes lineage plasticity and antiandrogen resistance in TP53- and RB1-deficient prostate cancer. Science **2017**;355:84-8
9. Lampi MC, Reinhart-King CA. Targeting extracellular matrix stiffness to attenuate disease: From molecular mechanisms to clinical trials. Sci Transl Med **2018**;10

10. Tan Y, Tajik A, Chen J, Jia Q, Chowdhury F, Wang L*, et al.* Matrix softness regulates plasticity of tumour-repopulating cells via H3K9 demethylation and Sox2 expression. Nat Commun **2014**;5:4619
11. Sottnik JL, Daignault-Newton S, Zhang X, Morrissey C, Hussain MH, Keller ET*, et al.* Integrin alpha2beta 1 (alpha2beta1) promotes prostate cancer skeletal metastasis. Clin Exp Metastasis **2013**;30:569-78
12. Franklin JM, Wu Z, Guan KL. Insights into recent findings and clinical application of YAP and TAZ in cancer. Nat Rev Cancer **2023**;23:512-25
13. Ma S, Meng Z, Chen R, Guan KL. The Hippo Pathway: Biology and Pathophysiology. Annu Rev Biochem **2019**;88:577-604
14. Nguyen LT, Tretiakova MS, Silvis MR, Lucas J, Klezovitch O, Coleman I*, et al.* ERG Activates the YAP1 Transcriptional Program and Induces the Development of Age-Related Prostate Tumors. Cancer Cell **2015**;27:797-808
15. Cheng S, Prieto-Dominguez N, Yang S, Connelly ZM, StPierre S, Rushing B*, et al.* The expression of YAP1 is increased in high-grade prostatic adenocarcinoma but is reduced in neuroendocrine prostate cancer. Prostate Cancer Prostatic Dis **2020**;23:661-9
16. Asrani K, Torres AF, Woo J, Vidotto T, Tsai HK, Luo J*, et al.* Reciprocal YAP1 loss and INSM1 expression in neuroendocrine prostate cancer. J Pathol **2021**;255:425-37
17. Mazzoleni S, Jachetti E, Morosini S, Grioni M, Piras IS, Pala M*, et al.* Gene signatures distinguish stage-specific prostate cancer stem cells isolated from transgenic adenocarcinoma of the mouse prostate lesions and predict the malignancy of human tumors. Stem Cells Transl Med **2013**;2:678-89
18. Cazzaniga W, Nebuloni M, Longhi E, Locatelli I, Allevi R, Luciano R*, et al.* Human Prostate Tissue-derived Extracellular Matrix as a Model of Prostate Microenvironment. Eur Urol Focus **2016**;2:400-8

19. Greenberg NM, DeMayo F, Finegold MJ, Medina D, Tilley WD, Aspinall JO*, et al.* Prostate cancer in a transgenic mouse. Proc Natl Acad Sci U S A **1995**;92:3439-43

20. Degl'Innocenti E, Grioni M, Boni A, Camporeale A, Bertilaccio MT, Freschi M*, et al.* Peripheral T cell tolerance occurs early during spontaneous prostate cancer development and can be rescued by dendritic cell immunization. Eur J Immunol **2005**;35:66-75

21. Foster BA, Gingrich JR, Kwon ED, Madias C, Greenberg NM. Characterization of prostatic epithelial cell lines derived from transgenic adenocarcinoma of the mouse prostate (TRAMP) model. Cancer Res **1997**;57:3325-30

22. Baley PA, Yoshida K, Qian W, Sehgal I, Thompson TC. Progression to androgen insensitivity in a novel in vitro mouse model for prostate cancer. J Steroid Biochem Mol Biol **1995**;52:403-13

23. Drost J, Karthaus WR, Gao D, Driehuis E, Sawyers CL, Chen Y*, et al.* Organoid culture systems for prostate epithelial and cancer tissue. Nat Protoc **2016**;11:347-58

24. Puca L, Bareja R, Prandi D, Shaw R, Benelli M, Karthaus WR*, et al.* Patient derived organoids to model rare prostate cancer phenotypes. Nat Commun **2018**;9:2404

25. Bakht MK, Yamada Y, Ku SY, Venkadakrishnan VB, Korsen JA, Kalidindi TM*, et al.* Landscape of prostate-specific membrane antigen heterogeneity and regulation in AR-positive and AR-negative metastatic prostate cancer. Nat Cancer **2023**;4:699-715

26. Alfano M, Tascini AS, Pederzoli F, Locatelli I, Nebuloni M, Giannese F*, et al.* Aging, inflammation and DNA damage in the somatic testicular niche with idiopathic germ cell aplasia. Nat Commun **2021**;12:5205

27. Boudaoud A, Burian A, Borowska-Wykret D, Uyttewaal M, Wrzalik R, Kwiatkowska D*, et al.* FibrilTool, an ImageJ plug-in to quantify fibrillar structures in raw microscopy images. Nat Protoc **2014**;9:457-63

28. Di Stefano V, Torsello B, Bianchi C, Cifola I, Mangano E, Bovo G*, et al.* Major Action of Endogenous Lysyl Oxidase in Clear Cell Renal Cell Carcinoma Progression and Collagen Stiffness Revealed by Primary Cell Cultures. Am J Pathol **2016**;186:2473-85

29. Hutter JLB, J. Calibration of atomic-force microscope tips. Rev Sci Instrum **1993**;64:1868-73

30. Dokukin MES, I. On the measurements of rigidity modulus of soft materials in nanoindentation experiments at small depth. Macromolecules **2012**;45:4277-88

31. Matafora V, Cuccurullo M, Beneduci A, Petrazzuolo O, Simeone A, Anastasio P*, et al.* Early markers of Fabry disease revealed by proteomics. Mol Biosyst **2015**;11:1543-51

32. Song H, Weinstein HNW, Allegakoen P, Wadsworth MH, 2nd, Xie J, Yang H*, et al.* Single-cell analysis of human primary prostate cancer reveals the heterogeneity of tumor-associated epithelial cell states. Nat Commun **2022**;13:141

33. Zaidi S, Park J, Chan JM, Roudier MP, Zhao JL, Gopalan A*, et al.* Single-cell analysis of treatment-resistant prostate cancer: Implications of cell state changes for cell surface antigen-targeted therapies. Proc Natl Acad Sci U S A **2024**;121:e2322203121

34. Tang F, Xu D, Wang S, Wong CK, Martinez-Fundichely A, Lee CJ*, et al.* Chromatin profiles classify castration-resistant prostate cancers suggesting therapeutic targets. Science **2022**;376:eabe1505

35. Wang Y, Xu X, Maglic D, Dill MT, Mojumdar K, Ng PK*, et al.* Comprehensive Molecular Characterization of the Hippo Signaling Pathway in Cancer. Cell Rep **2018**;25:1304-17 e5

36. Yamada T, Tsuda M, Wagatsuma T, Fujioka Y, Fujioka M, Satoh AO*, et al.* Receptor activator of NF-kappaB ligand induces cell adhesion and integrin alpha2 expression via NF-kappaB in head and neck cancers. Sci Rep **2016**;6:23545

37. Simonet WS, Lacey DL, Dunstan CR, Kelley M, Chang MS, Luthy R*, et al.* Osteoprotegerin: a novel secreted protein involved in the regulation of bone density. Cell **1997**;89:309-19

38. Chen EY, Tan CM, Kou Y, Duan Q, Wang Z, Meirelles GV*, et al.* Enrichr: interactive and collaborative HTML5 gene list enrichment analysis tool. BMC Bioinformatics **2013**;14:128
39. Miller MW, Basra S, Kulp DW, Billings PC, Choi S, Beavers MP*, et al.* Small-molecule inhibitors of integrin alpha2beta1 that prevent pathological thrombus formation via an allosteric mechanism. Proc Natl Acad Sci U S A **2009**;106:719-24
40. Adorno-Cruz V, Liu H. Regulation and functions of integrin alpha2 in cell adhesion and disease. Genes Dis **2019**;6:16-24
41. Yui S, Azzolin L, Maimets M, Pedersen MT, Fordham RP, Hansen SL*, et al.* YAP/TAZ-Dependent Reprogramming of Colonic Epithelium Links ECM Remodeling to Tissue Regeneration. Cell Stem Cell **2018**;22:35-49 e7
42. Song S, Xie M, Scott AW, Jin J, Ma L, Dong X*, et al.* A Novel YAP1 Inhibitor Targets CSC-Enriched Radiation-Resistant Cells and Exerts Strong Antitumor Activity in Esophageal Adenocarcinoma. Mol Cancer Ther **2018**;17:443-54
43. Jachetti E, Mazzoleni S, Grioni M, Ricupito A, Brambillasca C, Generoso L*, et al.* Prostate cancer stem cells are targets of both innate and adaptive immunity and elicit tumor-specific immune responses. Oncoimmunology **2013**;2:e24520
44. Caputo S, Grioni M, Brambillasca CS, Monno A, Brevi A, Freschi M*, et al.* Galectin-3 in Prostate Cancer Stem-Like Cells Is Immunosuppressive and Drives Early Metastasis. Front Immunol **2020**;11:1820
45. Gingrich JR, Barrios RJ, Kattan MW, Nahm HS, Finegold MJ, Greenberg NM. Androgen-independent prostate cancer progression in the TRAMP model. Cancer Res **1997**;57:4687-91
46. Li Q, Deng Q, Chao HP, Liu X, Lu Y, Lin K*, et al.* Linking prostate cancer cell AR heterogeneity to distinct castration and enzalutamide responses. Nat Commun **2018**;9:3600

47. Sharma NS, Gupta VK, Garrido VT, Hadad R, Durden BC, Kesh K*, et al.* Targeting tumor-intrinsic hexosamine biosynthesis sensitizes pancreatic cancer to anti-PD1 therapy. J Clin Invest **2020**;130:451-65

48. Petitprez F, Fossati N, Vano Y, Freschi M, Becht E, Luciano R*, et al.* PD-L1 Expression and CD8(+) T-cell Infiltrate are Associated with Clinical Progression in Patients with Node-positive Prostate Cancer. Eur Urol Focus **2019**;5:192-6

49. Kuser-Abali G, Alptekin A, Lewis M, Garraway IP, Cinar B. YAP1 and AR interactions contribute to the switch from androgen-dependent to castration-resistant growth in prostate cancer. Nat Commun **2015**;6:8126

50. Enriquez C, Cancila V, Ferri R, Sulsenti R, Fischetti I, Milani M*, et al.* Castration-Induced Downregulation of SPARC in Stromal Cells Drives Neuroendocrine Differentiation of Prostate Cancer. Cancer Res **2021**;81:4257-74

FIGURES

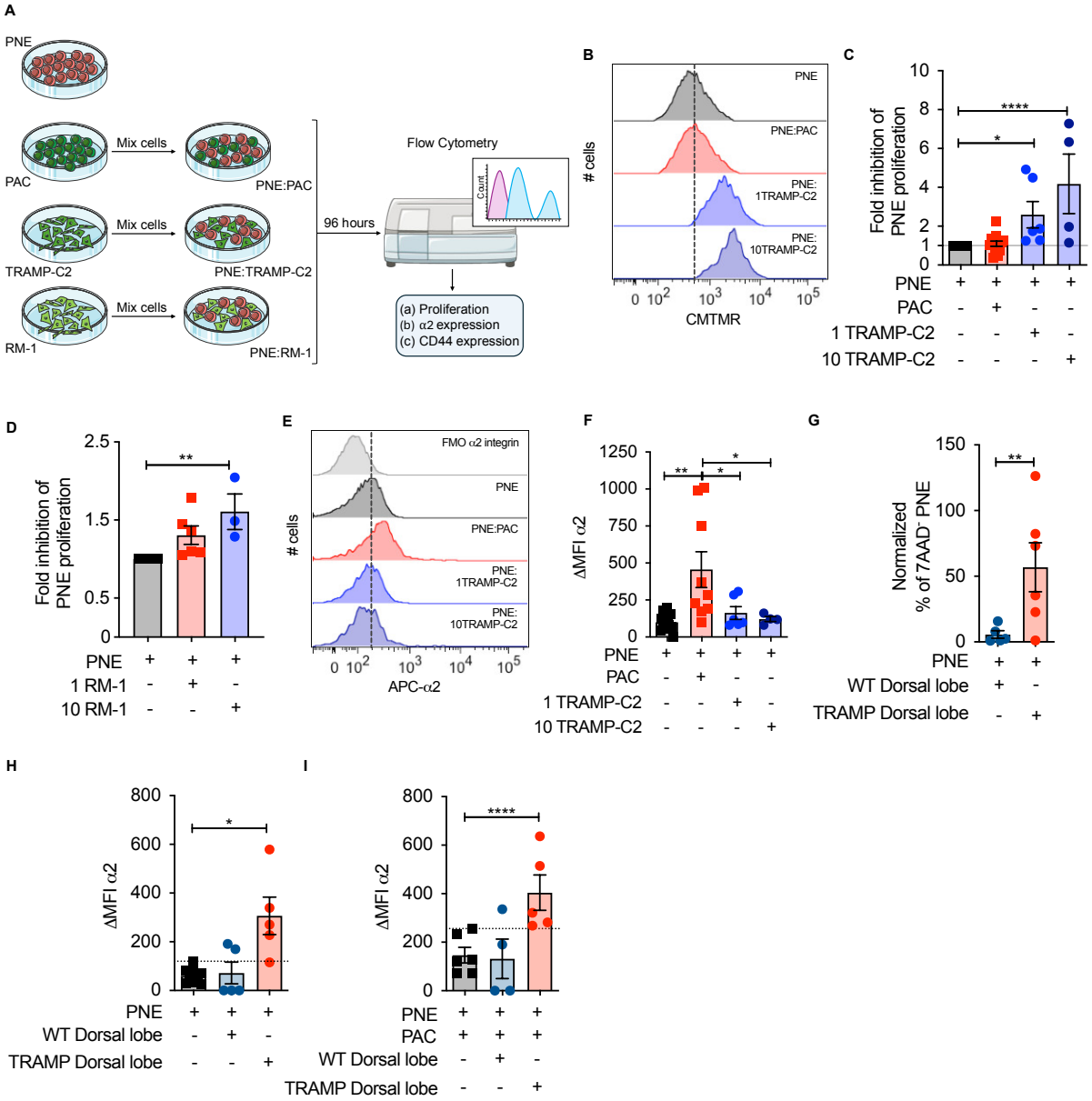

Figure 1. **Lack of male hormones promotes α2 upregulation in PNE cells. A.** Schematic representation of the co-culture experiments. **B**. Representative plot of CMTMR dye dilution in PNE cells cultured with PAC or TRAMP-C2 cells. **C**. Fold-inhibition of proliferation of PNE cells cultured with either PAC or TRAMP-C2 cells. One-way ANOVA. **D** Fold-inhibition of proliferation of PNE cells cultured with RM-1 cells. One-way ANOVA. **E** Representative plot of α2 expression in PNE cells stimulated with PAC or TRAMP-C2 cells. **F** Mean fluorescence intensity (MFI) subtracted of the fluorescence minus one (FMO) (ΔMFI) of α2 in PNE cells. One-way ANOVA. **G.** Percentage of

live PNE cells cultured in the presence of dorsal lobe ECM from either TRAMP (red) or WT (blue) littermate prostates. Values are normalized to the PNE cells alone. One-way ANOVA. **H.** ΔMFI of α2 in PNE cells cultured either alone or in the presence of the dorsal lobe ECMs of TRAMP and WT littermates. One-way ANOVA. **I.** ΔMFI of α2 in PNE cells cultured with PAC cells in the presence of the listed ECMs, as in H. One-way ANOVA. If not otherwise stated, data represent the mean ± SEM of at least 3 independent experiments. Each dot represents the mean of technical triplicates from independent experiments. *P < 0.05, **P < 0.01, ***P < 0.001, ****P < 0.0001. The artwork used in this figure was adapted from Servier Medical Art (http://https://smart.servier.com/). Servier Medical Art by Servier is licensed under CC BY 4.0.

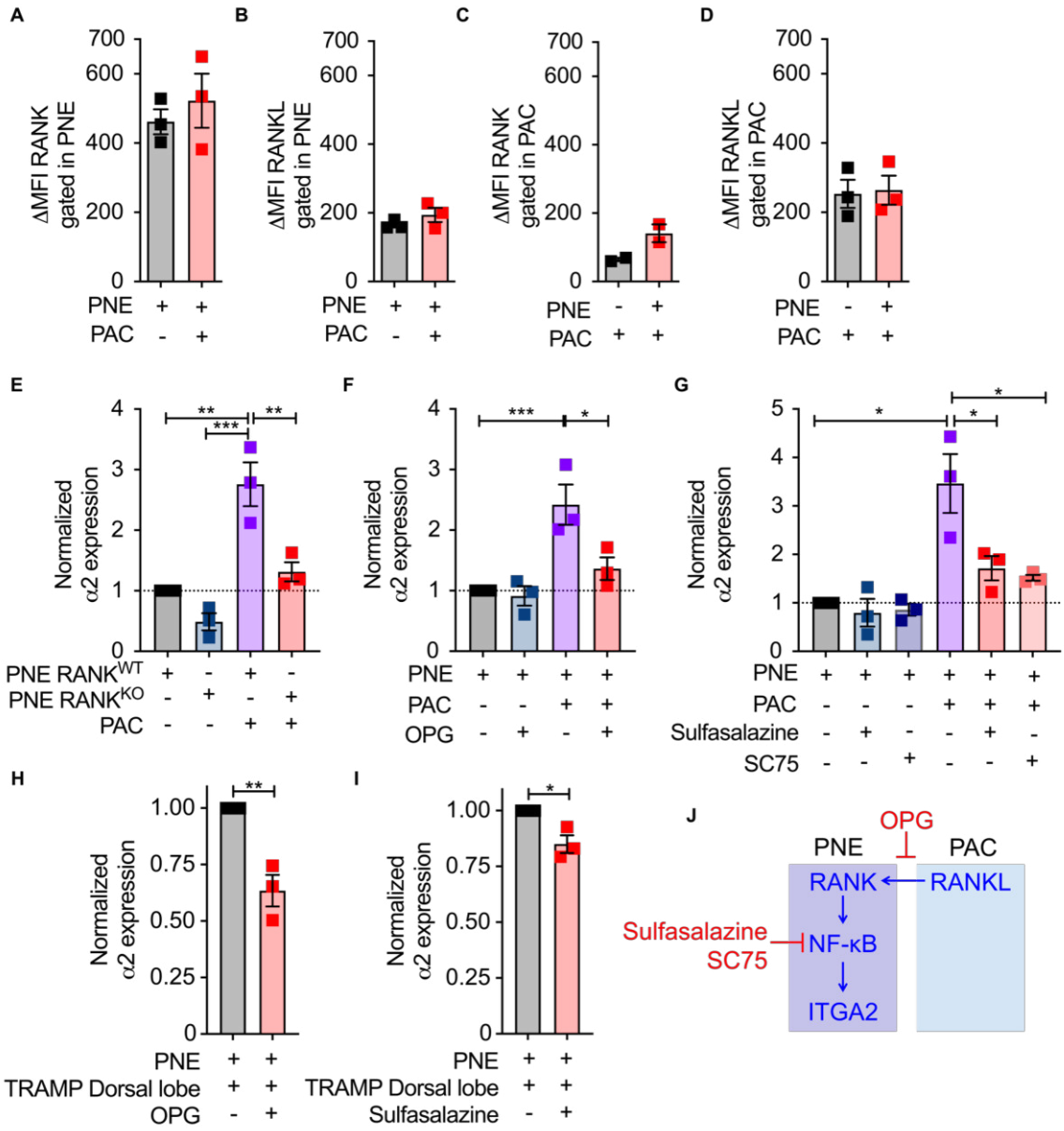

916

917 **Figure 2. α2 upregulation requires RANK/RANKL and NF-κB signaling. A-B**. ΔMFI of RANK
918 (**A**) and RANKL (**B**) expression in PNE cells cultured alone or in the presence of PAC cells. Student's
919 t-test. **C-D.** ΔMFI of RANK (**C**) and RANKL (**D**) in PAC cells cultured alone or in the presence of
920 PNE cells. Student's t-test. **E.** Normalized α2 expression in either PNE $RANK^{WT}$ or PNE $RANK^{KO}$
921 cells cultured with PAC cells. Data are normalized to PNE $RANK^{WT}$ cells only. One-way ANOVA.
922 **F.** Normalized α2 expression in PNE cells cultured either alone or with PAC cells in the presence or
923 absence of OPG. Data normalized to PNE cells only. One-way ANOVA. **G.** Normalized α2
924 expression in PNE cells cultured either alone or with PAC cells in the presence or absence of the NF-

κB inhibitors sulfasalazine or SC75. Data normalized to PNE cells only. One-way ANOVA. **H-I.** Normalized α2 expression in PNE cells cultured in the presence of dorsal lobe ECMs and either treated or not with OPG (**H**) or sulfasalazine (**I**). Data normalized to PNE cells + ECM. Student's t-test. **J**. Schematic summary of the findings described in Figure 2. Blue: RANK/RANKL/ NF-κB/ITAG2 pathway. Red: RANK/RANKL and NF-κB inhibitors. If not otherwise stated, data represent the mean ± SEM of at least 3 independent experiments. Each dot represents the mean of technical triplicates from independent experiments. *P < 0.05, **P < 0.01, ***P < 0.001.

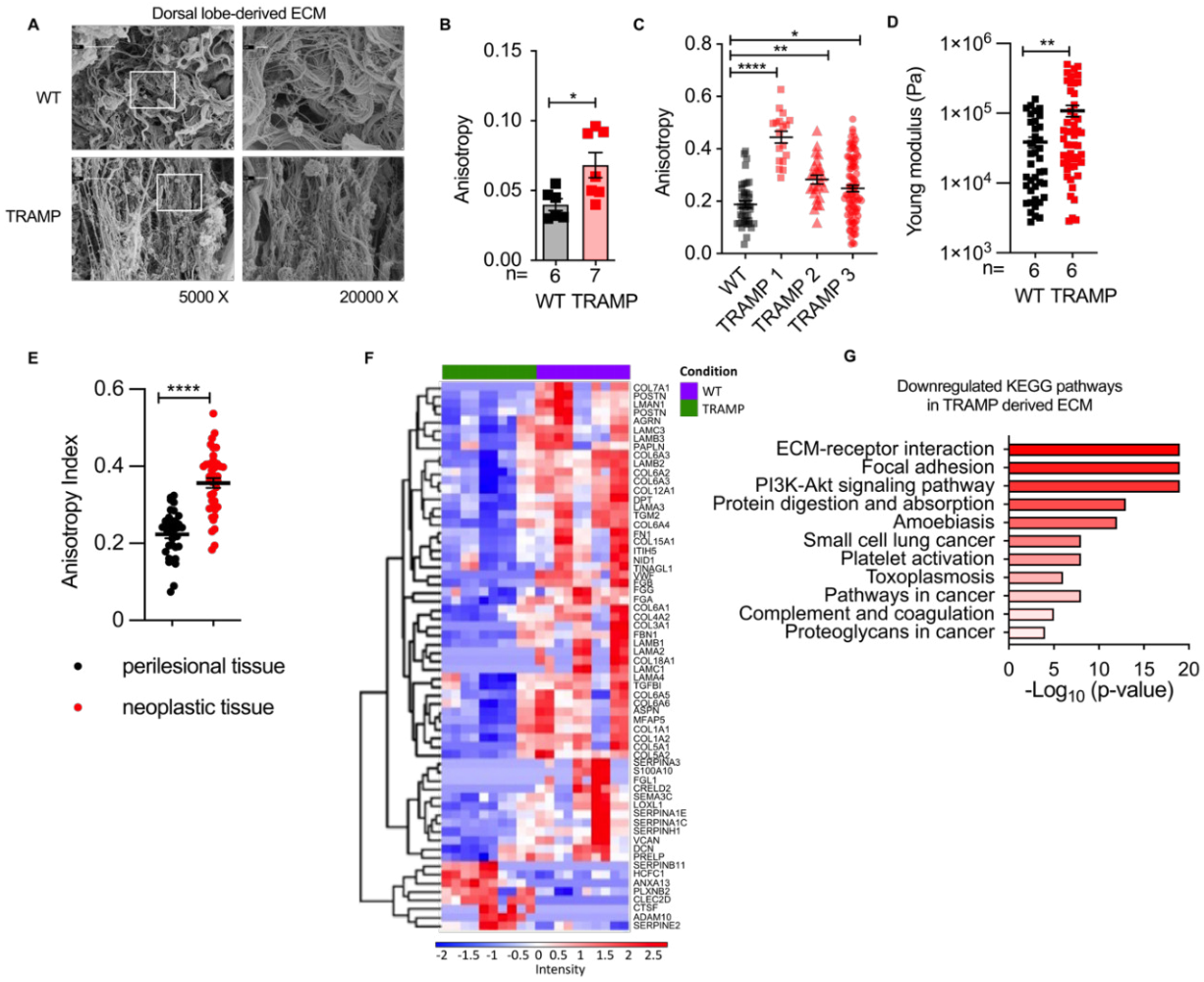

933

934 **Figure 3. The PC ECM differs structurally and chemically from the normal prostate tissue.**
935 **A.** Representative scanning electron microscopy images of decellularized ECM derived from the
936 dorsal lobe of the prostate of TRAMP mice (aged 12–13 weeks) and age-matched WT littermates.
937 Magnification: 5000x (left) and 20000x (right). **B.** Quantification of anisotropy in the dorsal lobe
938 ECM. Student's t-test. Data represent the mean ± SEM. Each dot represents an individual ECM. **C.**
939 Anisotropy quantified with polarized light on H&E-stained dorsal lobes. Each dot represents a single
940 measurement (WT, n=1; TRAMP mice, n=3). One-way ANOVA. **D.** Stiffness measured with AFM
941 in decellularized ECMs from the dorsal lobe of the prostate of TRAMP mice at 12–13 weeks (n=6)
942 and age-matched WT littermates (n=6). For each sample, a minimum of 4 independent grids were
943 analyzed. Each dot is the median value of a single grid. Student's t-test. **E.** Anisotropy quantified
944 with polarized light on H&E-stained human PC samples (Gleason 4+4, n=20; Gleason 4+5, n=20).
945 Each dot represents mean anisotropy value of a single sample. Multiple areas were measured from

each sample as indicated in Materials and Methods section (see also Fig. S4). One-way ANOVA. **F.** Heatmap of differentially expressed proteins ($P < 0.05$) in TRAMP and WT ECMs. Data represent duplicates of five samples for each experimental group. Upregulated and downregulated proteins are shown in red and blue, respectively. **G.** Summary of the top 11 KEGG pathways downregulated in TRAMP-derived ECM. **$P < 0.05$, **$P < 0.01$, ****$P < 0.0001$.

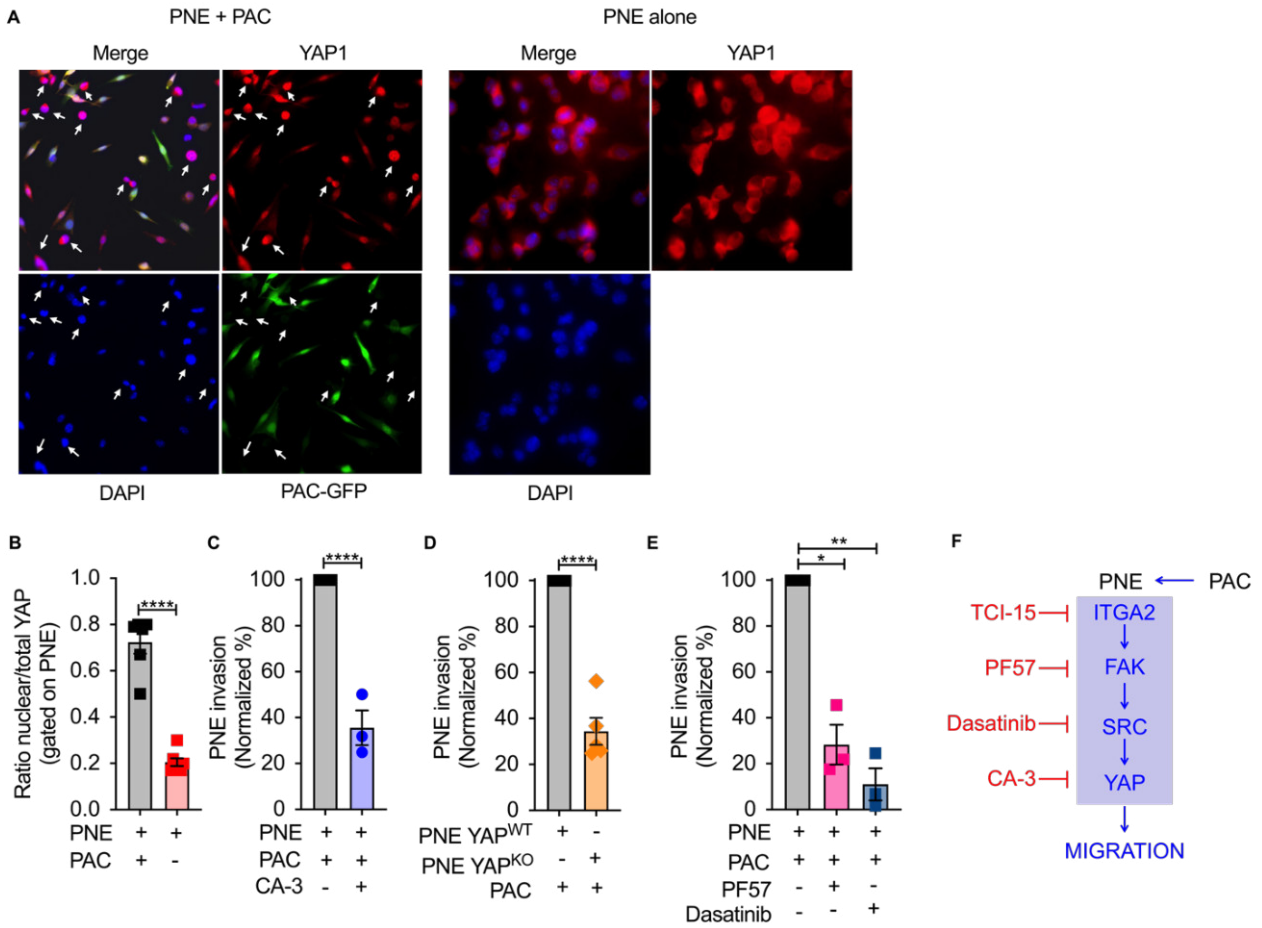

Figure 4. YAP1 is activated in PNE cells co-cultured with PAC cells. A. Representative confocal images of YAP1 expression in PNE cells cultured for 4 days alone (PNE alone) or in the presence of GFP-expressing PAC cells (PNE + PAC) in artificial matrix composed of Matrigel™ and collagen I (Red, YAP1; green, PAC; blue, DAPI stained nuclei). White arrows in the coculture condition indicate PNE cells. **B.** Ratio of PNE with nuclear YAP over total YAP^{+} PNE cells calculated in PNE cells from A. Student's t-test. **C.** Invasion of PNE cells stimulated by PAC cells in the presence or absence of CA-3. Data normalized to the PNE + PAC cells group. Student's t-test. **D.** Invasion of either PNE YAP^{WT} or PNE YAP^{KO} cells stimulated by PAC cells. Data normalized to PNE YAP^{WT} cells only. Student's t-test. **E.** Invasion of PNE cells stimulated by PAC cells in the presence or absence of PF57 (FAK inhibitor, magenta) or dasatinib (src inhibitor, blue). Data normalized to the PNE + PAC group. Student's t-test. **F**. Schematic representation of the pathway connecting ITGA2 to YAP with inhibitors (red). Data represent the mean ± SEM of at least 3 independent experiments.

965 Each dot represents the mean of technical triplicates from independent experiments. *P < 0.05,
966 **P < 0.01, ****P < 0.0001.
967

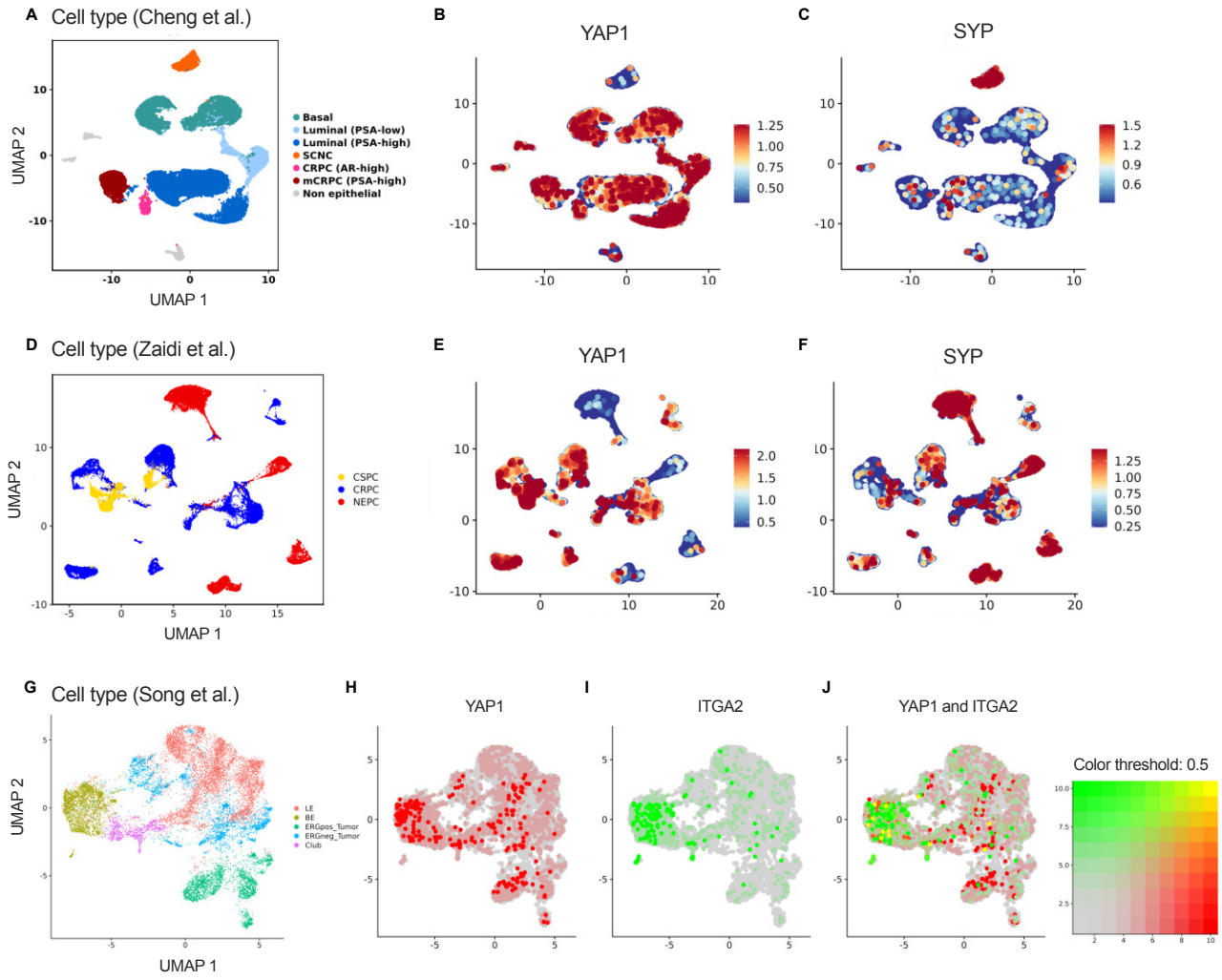

968

969 **Figure 5. Cells with characteristics of PNE exist in human prostate tumors. A.** UMAP plot of
970 primary PC and CRPC/SCNC samples from Cheng et al. (6). Dots represent single cells, colored by
971 lineage subtype. **B-C**. UMAP plot showing gene expression profiles of YAP1 (**B**) and SYP (**C**) in
972 cells from A. **D**. UMAP plot of untreated PC (castration-naïve), castration sensitive PC
973 (CSPC), castration resistant adenocarcinoma (CRPC) and castration resistant NEPC samples from
974 Zaidi et al. (33). Dots represent single cells, colored by tumor category. **E-F**. UMAP plot showing
975 the expression profiles of YAP1 (**E**) and SYP (**F**) in cells from D. **G**. UMAP plot of epithelial cell
976 clusters in primary localized treatment-naïve PC samples from Song et al. (32). LE: luminal
977 epithelial; BE: basal epithelial; ERGpos_Tumor cells; ERGneg_Tumor cells; Club: Club cells
978 expressing *PIGR, MMP7, CP,* and *LTF*. **H-J**. UMAP plot showing the expression of YAP1 in red

(**H**), ITGA2 in green (**I**), and overlay with color threshold plot of YAP1 and ITGA2 (yellow) (**J**) in cells from G.

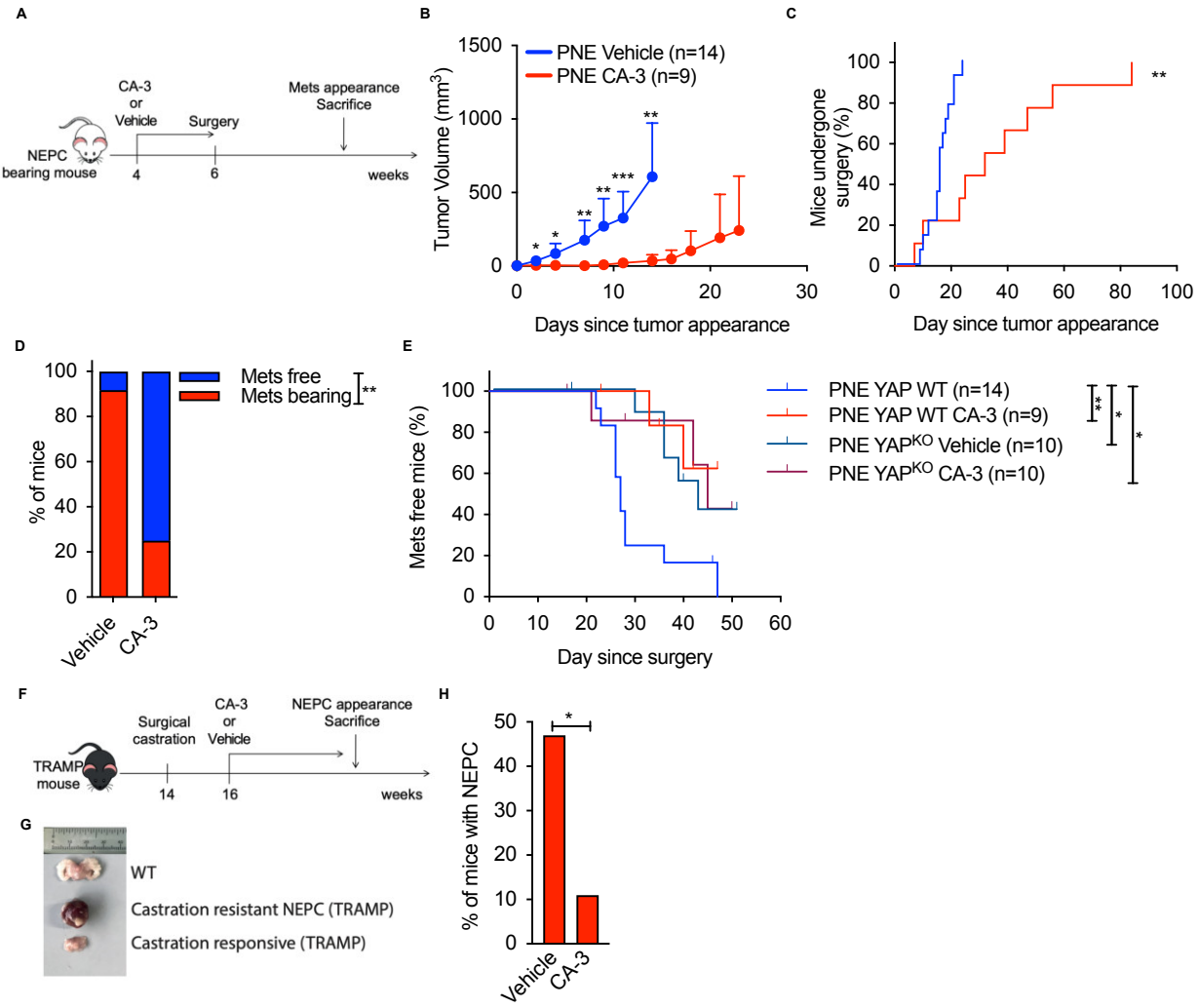

982

983 **Figure 6. YAP inhibition abolishes PC aggressiveness in vivo. A.** Schematic diagram of the
984 experimental protocol for NEPC-bearing mice treated with the YAP1 inhibitor CA-3 or vehicle. **B.**
985 Growth curves of pooled NEPC in NSG mice treated as in A. Two-way ANOVA. **C.** Kaplan–Meier
986 plot of mice undergoing surgical excision of primary NEPC. Log-rank (Mantel–Cox) test. **D.**
987 Metastasis frequency in mice from C. Fisher's exact test. **E.** Kaplan–Meier plot of mice belonging to
988 the indicated group and free from metastasis after excision of the primary NEPC. Log-rank (Mantel–
989 Cox) test. **F.** Schematic diagram of the experimental protocol for castrated TRAMP mice treated with
990 CA-3 or vehicle. **G.** Representative images of the urogenital apparatus of castrated TRAMP mice
991 compared to WT controls. **H.** Frequency of NEPC in castrated TRAMP mice treated with either CA-
992 3 or vehicle. Fisher's exact test. *P < 0.05, ** P < 0.01, *** P < 0.001.

993

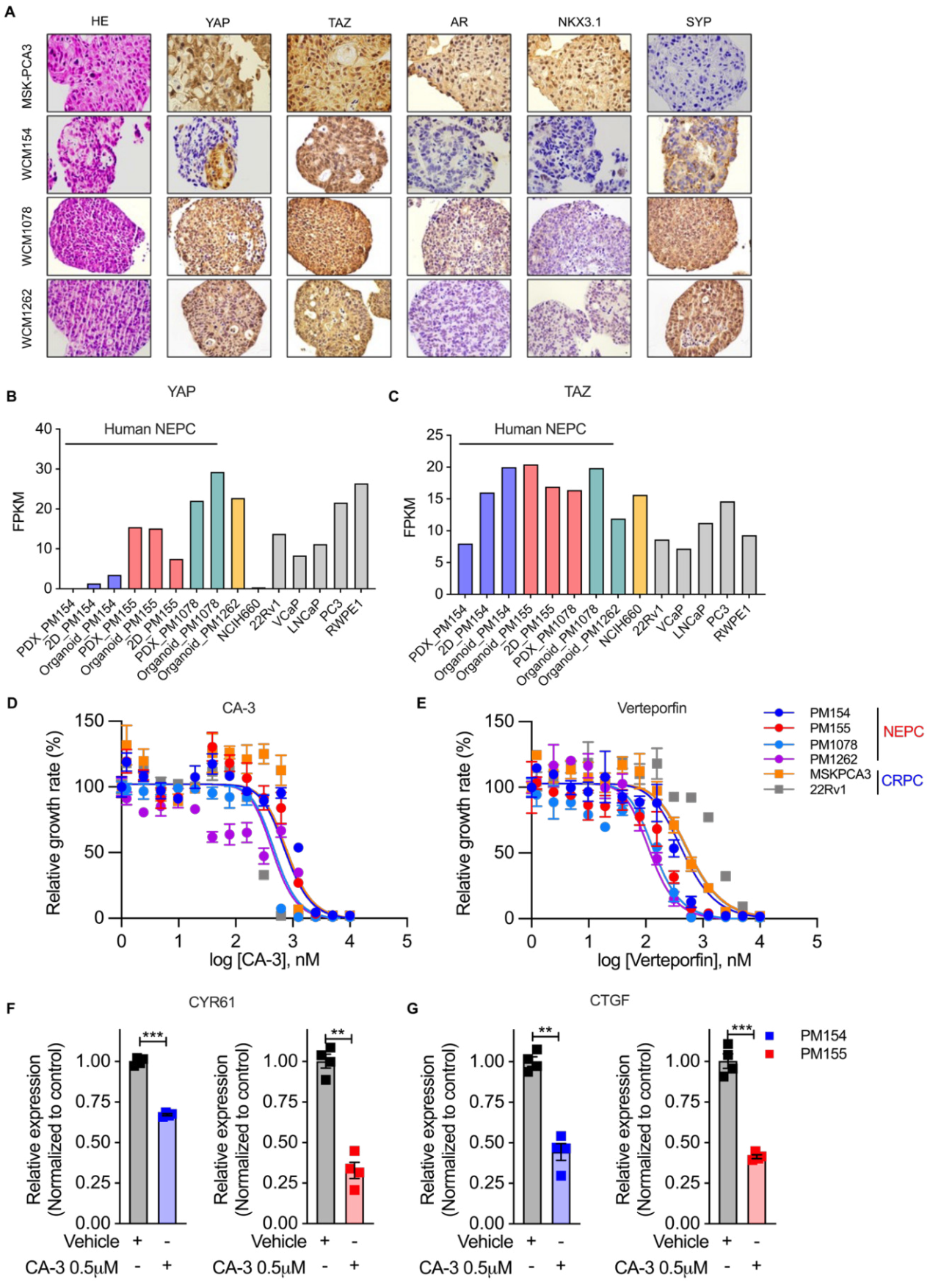
A
HE
YAP
TAZ
AR
NKX3.1
SYP
MSK-PCA3
WCM154
WCM1078
WCM1262
B
YAP
Human NEPC
FPKM
PDX_PM154
2D_PM154
Organoid_PM154
PDX_PM155
2D_PM155
Organoid_PM155
PDX_PM1078
Organoid_PM1078
Organoid_PM1262
NCIH660
22Rv1
VCaP
LNCaP
PC3
RWPE1
C
TAZ
Human NEPC
FPKM
D
CA-3
Relative growth rate (%)
log [CA-3], nM
E
Verteporfin
Relative growth rate (%)
log [Verteporfin], nM
PM154
PM155
PM1078
PM1262
MSKPCA3
22Rv1
NEPC
CRPC
F
CYR61
Relative expression (Normalized to control)
Vehicle
CA-3 0.5μM
G
CTGF
PM154
PM155

994

Figure 7. Inhibition of YAP blocks the growth of human NEPC organoids. A. Representative IHC pictures of H&E, YAP, TAZ, AR, NKX3.1 and SYP staining in human NEPC (WCM154, 1078 and 1262) and CRPC-Adeno (MSK-PCA3) organoids. **B-C.** Expression of YAP **(B)** and TAZ **(C)** in patients' derived xenografts (PDX), organoids and 2D cultures generated from human NEPC specimens and human prostate cancer cell lines. **D-E.** Cell viability assay (Cell-Title Glo) of human NEPC organoids (PM154, PM155, PM1078, PM1262), human CRPC organoids (MSK-PCA3) and human CRPC cells (22Rv1) treated with the indicated doses of CA-3 **(D)** or Verteporfin **(E)**. **F-G.** Expression of CYR61 **(F)** and CTGF **(G)** in human NEPC organoids either treated with CA-3 or vehicle. Data normalized to untreated control. Student's t-test. Data represent the mean ± SEM of 4 independent experiments. Each dot represents the mean of technical triplicates from independent experiments. **P< 0.01, ***P < 0.001.

Parsed Citations

1. Beltran H, Tagawa ST, Park K, MacDonald T, Milowsky MI, Mosquera JM, et al. Challenges in recognizing treatment-related neuroendocrine prostate cancer. J Clin Oncol 2012;30:e386-9

Pubmed: Author and Title
CrossRef: Author and Title
Google Scholar: Google Scholar Search

2. Krauss DJ, Amin M, Stone B, Ye H, Hayek S, Cotant M, et al. Chromogranin A staining as a prognostic variable in newly diagnosed Gleason score 7-10 prostate cancer treated with definitive radiotherapy. Prostate 2014;74:520-7

Pubmed: Author and Title
CrossRef: Author and Title
Google Scholar: Google Scholar Search

3. Aggarwal R, Huang J, Alumkal JJ, Zhang L, Feng FY, Thomas GV, et al. Clinical and Genomic Characterization of Treatment-Emergent Small-Cell Neuroendocrine Prostate Cancer: A Multi-institutional Prospective Study. J Clin Oncol 2018;36:2492-503

Pubmed: Author and Title
CrossRef: Author and Title
Google Scholar: Google Scholar Search

4. Beltran H, Prandi D, Mosquera JM, Benelli M, Puca L, Cyrta J, et al. Divergent clonal evolution of castration-resistant neuroendocrine prostate cancer. Nat Med 2016;22:298-305

Pubmed: Author and Title
CrossRef: Author and Title
Google Scholar: Google Scholar Search

5. Chedgy EC, Vandekerkhove G, Herberts C, Annala M, Donoghue AJ, Sigouros M, et al. Biallelic tumour suppressor loss and DNA repair defects in de novo small-cell prostate carcinoma. J Pathol 2018;246:244-53

Pubmed: Author and Title
CrossRef: Author and Title
Google Scholar: Google Scholar Search

6. Cheng Q, Butler W, Zhou Y, Zhang H, Tang L, Perkinson K, et al. Pre-existing Castration- resistant Prostate Cancer-like Cells in Primary Prostate Cancer Promote Resistance to Hormonal Therapy. Eur Urol 2022;81:446-55

Pubmed: Author and Title
CrossRef: Author and Title
Google Scholar: Google Scholar Search

7. Ku SY, Rosario S, Wang Y, Mu P, Seshadri M, Goodrich ZW, et al. Rb1 and Trp53 cooperate to suppress prostate cancer lineage plasticity, metastasis, and antiandrogen resistance. Science 2017;355:78-83

Pubmed: Author and Title
CrossRef: Author and Title
Google Scholar: Google Scholar Search

8. Mu P, Zhang Z, Benelli M, Karthaus WR, Hoover E, Chen CC, et al. SOX2 promotes lineage plasticity and antiandrogen resistance in TP53- and RB1-deficient prostate cancer. Science 2017;355:84-8

Pubmed: Author and Title
CrossRef: Author and Title
Google Scholar: Google Scholar Search

9. Lampi MC, Reinhart-King CA. Targeting extracellular matrix stiffness to attenuate disease: From molecular mechanisms to clinical trials. Sci Transl Med 2018;10

10. Tan Y, Tajik A, Chen J, Jia Q, Chowdhury F, Wang L, et al. Matrix softness regulates plasticity of tumour-repopulating cells via H3K9 demethylation and Sox2 expression. Nat Commun 2014;5:4619

Pubmed: Author and Title
CrossRef: Author and Title
Google Scholar: Google Scholar Search

11. Sottnik JL, Daignault-Newton S, Zhang X, Morrissey C, Hussain MH, Keller ET, et al. Integrin alpha2beta 1 (alpha2beta1) promotes prostate cancer skeletal metastasis. Clin Exp Metastasis 2013;30:569-78
Pubmed: Author and Title
CrossRef: Author and Title
Google Scholar: Google Scholar Search

12. Franklin JM, Wu Z, Guan KL. Insights into recent findings and clinical application of YAP and TAZ in cancer. Nat Rev Cancer 2023;23:512-25
Pubmed: Author and Title
CrossRef: Author and Title
Google Scholar: Google Scholar Search

13. Ma S, Meng Z, Chen R, Guan KL. The Hippo Pathway: Biology and Pathophysiology. Annu Rev Biochem 2019;88:577-604
Pubmed: Author and Title
CrossRef: Author and Title
Google Scholar: Google Scholar Search

14. Nguyen LT, Tretiakova MS, Silvis MR, Lucas J, Klezovitch O, Coleman I, et al. ERG Activates the YAP1 Transcriptional Program and Induces the Development of Age-Related Prostate Tumors. Cancer Cell 2015;27:797-808
Pubmed: Author and Title
CrossRef: Author and Title
Google Scholar: Google Scholar Search

15. Cheng S, Prieto-Dominguez N, Yang S, Connelly ZM, StPierre S, Rushing B, et al. The expression of YAP1 is increased in high-grade prostatic adenocarcinoma but is reduced in neuroendocrine prostate cancer. Prostate Cancer Prostatic Dis 2020;23:661-9
Pubmed: Author and Title
CrossRef: Author and Title
Google Scholar: Google Scholar Search

16. Asrani K, Torres AF, Woo J, Vidotto T, Tsai HK, Luo J, et al. Reciprocal YAP1 loss and INSM1 expression in neuroendocrine prostate cancer. J Pathol 2021;255:425-37
Pubmed: Author and Title
CrossRef: Author and Title
Google Scholar: Google Scholar Search

17. Mazzoleni S, Jachetti E, Morosini S, Grioni M, Piras IS, Pala M, et al. Gene signatures distinguish stage-specific prostate cancer stem cells isolated from transgenic adenocarcinoma of the mouse prostate lesions and predict the malignancy of human tumors. Stem Cells Transl Med 2013;2:678-89
Pubmed: Author and Title
CrossRef: Author and Title
Google Scholar: Google Scholar Search

18. Cazzaniga W, Nebuloni M, Longhi E, Locatelli I, Allevi R, Luciano R, et al. Human Prostate Tissue-derived Extracellular Matrix as a Model of Prostate Microenvironment. Eur Urol Focus 2016;2:400-8
Pubmed: Author and Title
CrossRef: Author and Title
Google Scholar: Google Scholar Search

19. Greenberg NM, DeMayo F, Finegold MJ, Medina D, Tilley WD, Aspinall JO, et al. Prostate cancer in a transgenic mouse. Proc Natl Acad Sci U S A 1995;92:3439-43
Pubmed: Author and Title
CrossRef: Author and Title
Google Scholar: Google Scholar Search

20. Degl'Innocenti E, Grioni M, Boni A, Camporeale A, Bertilaccio MT, Freschi M, et al. Peripheral T cell tolerance occurs early during spontaneous prostate cancer development and can be rescued by dendritic cell immunization. Eur J Immunol 2005;35:66-75
Pubmed: Author and Title
CrossRef: Author and Title
Google Scholar: Google Scholar Search

21. Foster BA, Gingrich JR, Kwon ED, Madias C, Greenberg NM. Characterization of prostatic epithelial cell lines derived from transgenic adenocarcinoma of the mouse prostate (TRAMP) model. Cancer Res 1997;57:3325-30
Pubmed: Author and Title
CrossRef: Author and Title
Google Scholar: Google Scholar Search

22. Baley PA, Yoshida K, Qian W, Sehgal I, Thompson TC. Progression to androgen insensitivity in a novel in vitro mouse model for prostate cancer. J Steroid Biochem Mol Biol 1995;52:403-13
Pubmed: Author and Title
CrossRef: Author and Title
Google Scholar: Google Scholar Search

23. Drost J, Karthaus WR, Gao D, Driehuis E, Sawyers CL, Chen Y, et al. Organoid culture systems for prostate epithelial and cancer tissue. Nat Protoc 2016;11:347-58
Pubmed: Author and Title
CrossRef: Author and Title
Google Scholar: Google Scholar Search

24. Puca L, Bareja R, Prandi D, Shaw R, Benelli M, Karthaus WR, et al. Patient derived organoids to model rare prostate cancer phenotypes. Nat Commun 2018;9:2404
Pubmed: Author and Title
CrossRef: Author and Title
Google Scholar: Google Scholar Search

25. Bakht MK, Yamada Y, Ku SY, Venkadakrishnan VB, Korsen JA, Kalidindi TM, et al. Landscape of prostate-specific membrane antigen heterogeneity and regulation in AR- positive and AR-negative metastatic prostate cancer. Nat Cancer 2023;4:699-715
Pubmed: Author and Title
CrossRef: Author and Title
Google Scholar: Google Scholar Search

26. Alfano M, Tascini AS, Pederzoli F, Locatelli I, Nebuloni M, Giannese F, et al. Aging, inflammation and DNA damage in the somatic testicular niche with idiopathic germ cell aplasia. Nat Commun 2021;12:5205
Pubmed: Author and Title
CrossRef: Author and Title
Google Scholar: Google Scholar Search

27. Boudaoud A, Burian A, Borowska-Wykret D, Uyttewaal M, Wrzalik R, Kwiatkowska D, et al. FibrilTool, an ImageJ plug-in to quantify fibrillar structures in raw microscopy images. Nat Protoc 2014;9:457-63
Pubmed: Author and Title
CrossRef: Author and Title
Google Scholar: Google Scholar Search

28. Di Stefano V, Torsello B, Bianchi C, Cifola I, Mangano E, Bovo G, et al. Major Action of Endogenous Lysyl Oxidase in Clear Cell Renal Cell Carcinoma Progression and Collagen Stiffness Revealed by Primary Cell Cultures. Am J Pathol 2016;186:2473-85
Pubmed: Author and Title
CrossRef: Author and Title
Google Scholar: Google Scholar Search

29. Hutter JLB, J. Calibration of atomic-force microscope tips. Rev Sci Instrum 1993;64:1868-
Pubmed: Author and Title
CrossRef: Author and Title

Google Scholar: Google Scholar Search

30. Dokukin MES, I. On the measurements of rigidity modulus of soft materials in nanoindentation experiments at small depth. Macromolecules 2012;45:4277-88
Pubmed: Author and Title
CrossRef: Author and Title
Google Scholar: Google Scholar Search

31. Matafora V, Cuccurullo M, Beneduci A, Petrazzuolo O, Simeone A, Anastasio P, et al. Early markers of Fabry disease revealed by proteomics. Mol Biosyst 2015;11:1543-51
Pubmed: Author and Title
CrossRef: Author and Title
Google Scholar: Google Scholar Search

32. Song H, Weinstein HNW, Allegakoen P, Wadsworth MH, 2nd, Xie J, Yang H, et al. Single- cell analysis of human primary prostate cancer reveals the heterogeneity of tumor-associated epithelial cell states. Nat Commun 2022;13:141

33. Zaidi S, Park J, Chan JM, Roudier MP, Zhao JL, Gopalan A, et al. Single-cell analysis of treatment-resistant prostate cancer: Implications of cell state changes for cell surface antigen-targeted therapies. Proc Natl Acad Sci U S A 2024;121:e2322203121
Pubmed: Author and Title
CrossRef: Author and Title
Google Scholar: Google Scholar Search

34. Tang F, Xu D, Wang S, Wong CK, Martinez-Fundichely A, Lee CJ, et al. Chromatin profiles classify castration-resistant prostate cancers suggesting therapeutic targets. Science 2022;376:eabe1505
Pubmed: Author and Title
CrossRef: Author and Title
Google Scholar: Google Scholar Search

35. Wang Y, Xu X, Maglic D, Dill MT, Mojumdar K, Ng PK, et al. Comprehensive Molecular Characterization of the Hippo Signaling Pathway in Cancer. Cell Rep 2018;25:1304-17 e5
Pubmed: Author and Title
CrossRef: Author and Title
Google Scholar: Google Scholar Search

36. Yamada T, Tsuda M, Wagatsuma T, Fujioka Y, Fujioka M, Satoh AO, et al. Receptor activator of NF-kappaB ligand induces cell adhesion and integrin alpha2 expression via NF- kappaB in head and neck cancers. Sci Rep 2016;6:23545
Pubmed: Author and Title
CrossRef: Author and Title
Google Scholar: Google Scholar Search

37. Simonet WS, Lacey DL, Dunstan CR, Kelley M, Chang MS, Luthy R, et al. Osteoprotegerin: a novel secreted protein involved in the regulation of bone density. Cell 1997;89:309-19
Pubmed: Author and Title
CrossRef: Author and Title
Google Scholar: Google Scholar Search

38. Chen EY, Tan CM, Kou Y, Duan Q, Wang Z, Meirelles GV, et al. Enrichr: interactive and collaborative HTML5 gene list enrichment analysis tool. BMC Bioinformatics 2013;14:128

39. Miller MW, Basra S, Kulp DW, Billings PC, Choi S, Beavers MP, et al. Small-molecule inhibitors of integrin alpha2beta1 that prevent pathological thrombus formation via an allosteric mechanism. Proc Natl Acad Sci U S A 2009;106:719-24
Pubmed: Author and Title
CrossRef: Author and Title
Google Scholar: Google Scholar Search

40. Adorno-Cruz V, Liu H. Regulation and functions of integrin alpha2 in cell adhesion and disease. Genes Dis 2019;6:16-24

Pubmed: Author and Title
CrossRef: Author and Title
Google Scholar: Google Scholar Search

41. Yui S, Azzolin L, Maimets M, Pedersen MT, Fordham RP, Hansen SL, et al. YAP/TAZ- Dependent Reprogramming of Colonic Epithelium Links ECM Remodeling to Tissue Regeneration. Cell Stem Cell 2018;22:35-49 e7
Pubmed: Author and Title
CrossRef: Author and Title
Google Scholar: Google Scholar Search

42. Song S, Xie M, Scott AW, Jin J, Ma L, Dong X, et al. A Novel YAP1 Inhibitor Targets CSC-Enriched Radiation-Resistant Cells and Exerts Strong Antitumor Activity in Esophageal Adenocarcinoma. Mol Cancer Ther 2018;17:443-54
Pubmed: Author and Title
CrossRef: Author and Title
Google Scholar: Google Scholar Search

43. Jachetti E, Mazzoleni S, Grioni M, Ricupito A, Brambillasca C, Generoso L, et al. Prostate cancer stem cells are targets of both innate and adaptive immunity and elicit tumor-specific immune responses. Oncoimmunology 2013;2:e24520
Pubmed: Author and Title
CrossRef: Author and Title
Google Scholar: Google Scholar Search

44. Caputo S, Grioni M, Brambillasca CS, Monno A, Brevi A, Freschi M, et al. Galectin-3 in Prostate Cancer Stem-Like Cells Is Immunosuppressive and Drives Early Metastasis. Front Immunol 2020;11:1820
Pubmed: Author and Title
CrossRef: Author and Title
Google Scholar: Google Scholar Search

45. Gingrich JR, Barrios RJ, Kattan MW, Nahm HS, Finegold MJ, Greenberg NM. Androgen- independent prostate cancer progression in the TRAMP model. Cancer Res 1997;57:4687-
Pubmed: Author and Title
CrossRef: Author and Title
Google Scholar: Google Scholar Search

46. Li Q, Deng Q, Chao HP, Liu X, Lu Y, Lin K, et al. Linking prostate cancer cell AR heterogeneity to distinct castration and enzalutamide responses. Nat Commun 2018;9:3600
Pubmed: Author and Title
CrossRef: Author and Title
Google Scholar: Google Scholar Search

47. Sharma NS, Gupta VK, Garrido VT, Hadad R, Durden BC, Kesh K, et al. Targeting tumor- intrinsic hexosamine biosynthesis sensitizes pancreatic cancer to anti-PD1 therapy. J Clin Invest 2020;130:451-65
Pubmed: Author and Title
CrossRef: Author and Title
Google Scholar: Google Scholar Search

48. Petitprez F, Fossati N, Vano Y, Freschi M, Becht E, Luciano R, et al. PD-L1 Expression and CD8(+) T-cell Infiltrate are Associated with Clinical Progression in Patients with Node- positive Prostate Cancer. Eur Urol Focus 2019;5:192-6
Pubmed: Author and Title
CrossRef: Author and Title
Google Scholar: Google Scholar Search

49. Kuser-Abali G, Alptekin A, Lewis M, Garraway IP, Cinar B. YAP1 and AR interactions contribute to the switch from androgen-dependent to castration-resistant growth in prostate cancer. Nat Commun 2015;6:8126

Pubmed: Author and Title
CrossRef: Author and Title
Google Scholar: Google Scholar Search

50. Enriquez C, Cancila V, Ferri R, Sulsenti R, Fischetti I, Milani M, et al. Castration-Induced Downregulation of SPARC in Stromal Cells Drives Neuroendocrine Differentiation of Prostate Cancer. Cancer Res 2021;81:4257-74

Pubmed: Author and Title
CrossRef: Author and Title
Google Scholar: Google Scholar Search

Intercepting Yes-associated protein 1 in prostate cancer blocks neuroendocrine progression

Arianna Brevi[1,#], Marco Lorenzoni[1,#], Sara Caputo[1], Yasutaka Yamada[2], Matteo Grioni[1], Laura Lucia Cogrossi[1,3], Laura Martinez Vidal[4], Valeria Cassina[5], Deborah Cipria[6], Chiara Venegoni[4], Paola Zordan[1], Vittoria Matafora[7], Anna Sofia Tascini[8], Nazario Pio Tenace[9], Riccardo Campanile[5], Vito Cucchiara[4], Valeria Pinna,[10] Elena Jachetti,[10] Rossella Galli[11], Angela Bachi[7], Maurizio Colecchia[3,9], Alberto Briganti[3,4], Massimo Freschi[9], Francesco Mantegazza[5], Angelo Lombardo[3,6], Francesca Demichelis[12], Himisha Beltran[2], Massimo Alfano[4], Matteo Bellone[1,12]

[1]Cellular Immunology Unit, Division of Immunology, Transplantation and Infectious Diseases, IRCCS Ospedale San Raffaele, Milan, Italy; [2]Department of Medical Oncology, Dana Farber Cancer Institute, Harvard Medical School, Boston, MA, USA; [3]Vita-Salute San Raffaele University, Milan, Italy; [4]Division of Experimental Oncology/Unit of Urology, URI, IRCCS Ospedale San Raffaele, Milan, Italy; [5]School of Medicine and Surgery, BioNanoMedicine Center NANOMIB, Università di Milano-Bicocca, Vedano al Lambro (MB), Italy; [6]San Raffaele Telethon Institute for Gene Therapy, IRCCS Ospedale San Raffaele, Milan, Italy; [7]Proteomics Unit, IFOM-FIRC Institute of Molecular Oncology, Milan, Italy; [8]Center for Omics Sciences, IRCCS Ospedale San Raffaele, Milan, Italy; [9]Unità Operativa Anatomia Patologica, IRCCS Ospedale San Raffaele, Milan, Italy; [10]Molecular Immunology Unit, Department of Experimental Oncology, Fondazione IRCCS Istituto Nazionale dei Tumori di Milano, Milan, Italy; [11]Division of Neuroscience, IRCCS Ospedale San Raffaele, Milan, Italy; [12]Cellular, Computational and Integrative Biology (CIBIO), University of Trento, Trento, Italy; [12]Lead Contact.
[#]These authors equally contributed to the work.

SUPPLEMENTAL INFORMATION

Figure S1

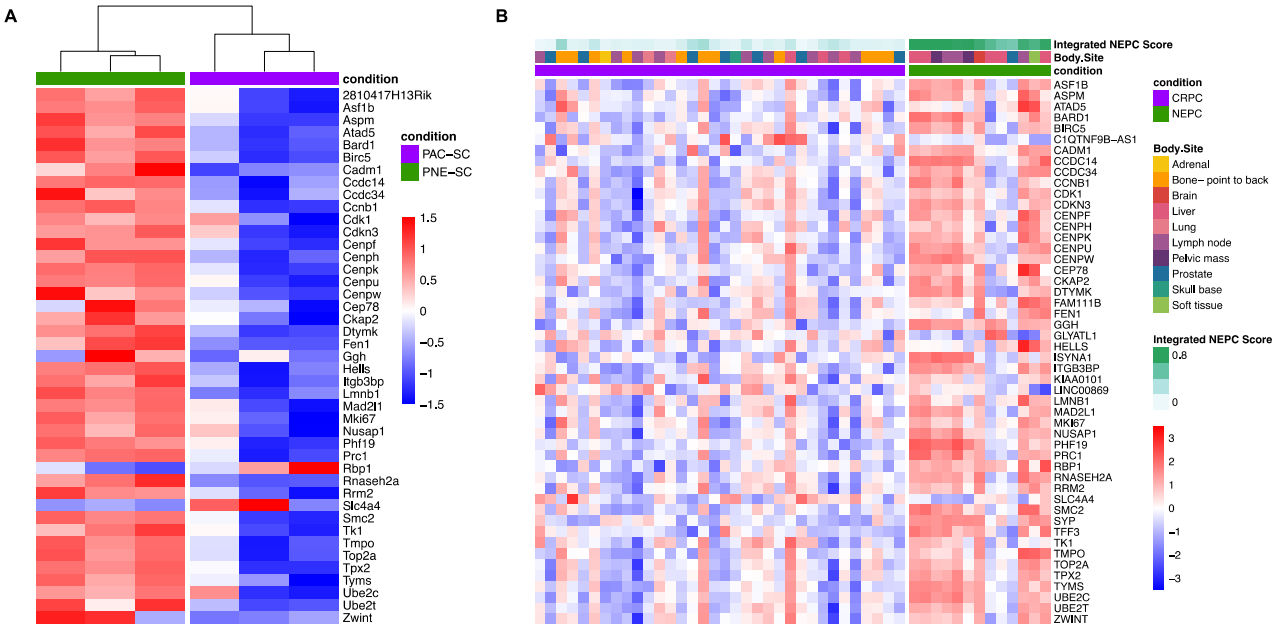

Figure S1. Signature of pre-existing CRPC-like cells segregates NEPC from adenocarcinoma in mice and humans. Heatmaps representative of differentially expressed genes ($P < 0.05$) that belong to the signature CRPCsig51 (Cheng Q. et al., 2022) in PNE and PAC cells **(A)** and in human NEPC and CRPC cells **(B)**. Upregulated and downregulated genes are shown in red and blue, respectively.

Figure S2

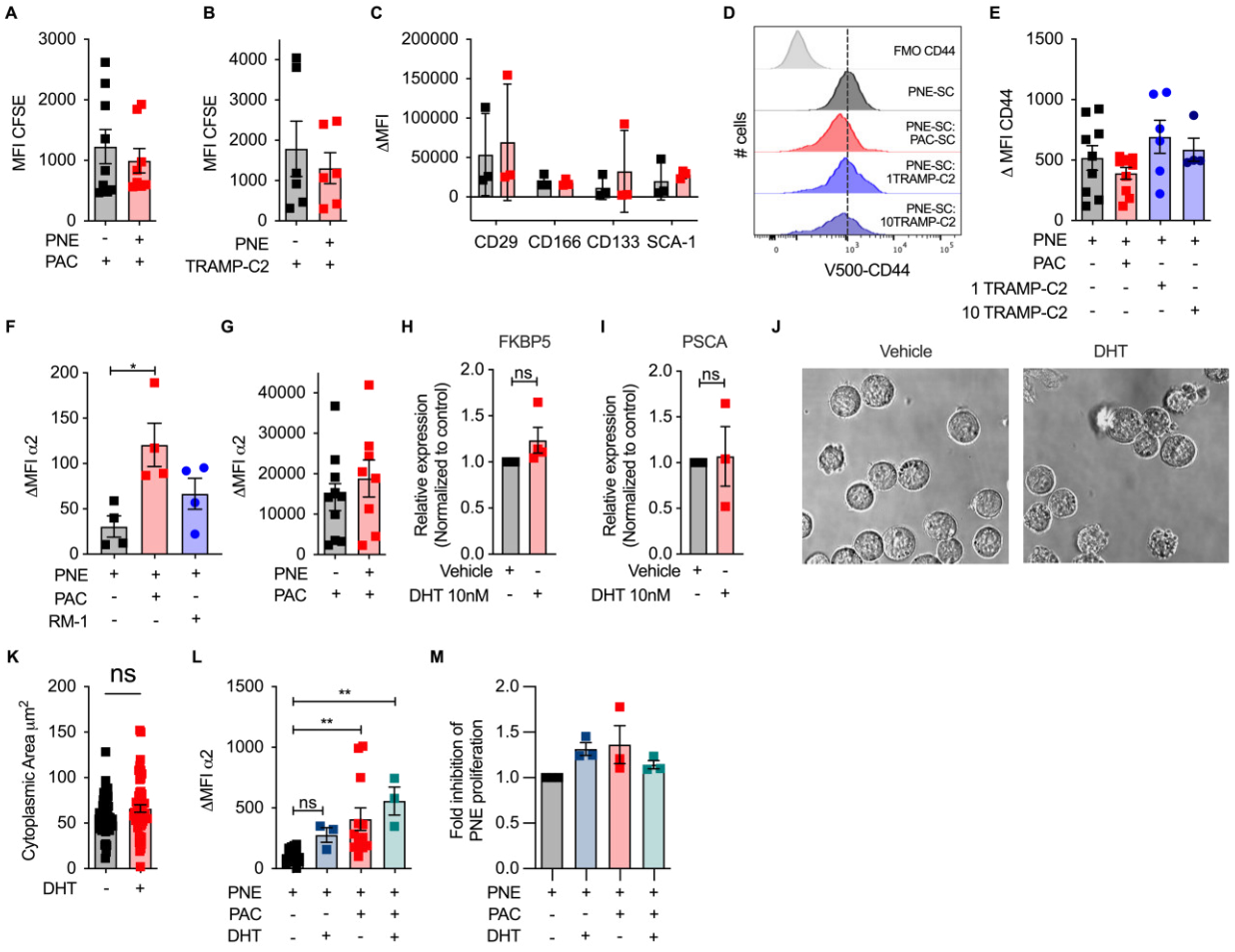

Figure S2. Upregulation of integrin α2 is characteristic of PNE and not PAC cells. A. **B.** Mean fluorescence intensity (MFI) of CFSE in PAC cells **(A)** or TRAMP-C2 cells **(B)** cultured with PNE cells. **C.** MFI subtracted from the fluorescence minus one (MFO; i.e., ΔMFI) of the listed markers in PNE cells cultured with (red squares) or without (black squares) PAC cells. One-way ANOVA. **D.** Representative plot of CD44 expression in PNE cells stimulated with PAC or TRAMP-C2 cells. **E.** ΔMFI of CD44 in PNE cells in the listed conditions. **F.** ΔMFI of α2 in PNE cells cultured with PAC or RM-1 cells. One-way ANOVA. **G.** ΔMFI of α2 in PAC cells cultured with PNE cells. **H-I.** Relative expression of mouse *Fkbp5* and *Psca* genes in PNE cells treated with DHT or vehicle. Data normalized to untreated control. Student's t-test. Data represent the mean ± SEM of 3 independent experiments. Each dot represents the mean of technical triplicates from independent experiments. **J.** Representative pictures of PNE cells treated for 4 days with either DHT or vehicle. **K.** Quantification of cytoplasmic area of PNE cells in J. Quantification indicates the difference between total cell area and nuclear area measured by DAPI staining (not shown). Each dot represents a single cell, data obtained from 3-6 images, respectively. Student's t-test. **L.** ΔMFI of α2 in PNE cells cultured with or without PAC cells and treated with either DHT or

vehicle. One-way ANOVA. **M.** Fold-inhibition of proliferation of PNE cells cultured with or without PAC and treated with either DHT or vehicle. One-way ANOVA. *P < 0.05, **P < 0.01.

Figure S3

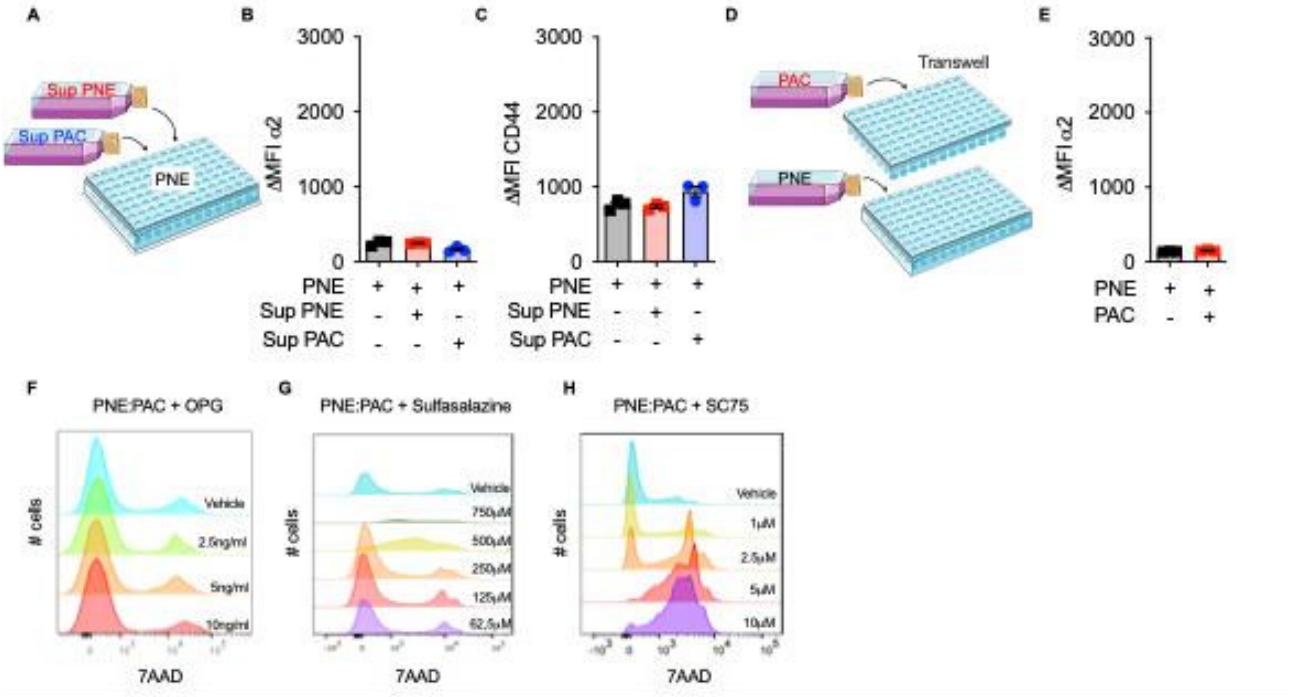

Figure S3. α2 upregulation requires cell-to-cell contact and NF-κB signaling. A. Schematic representation of the experimental setup used for B. **B.** ΔMFI of integrin α2 in PNE cells cultured alone or in the presence of PAC-conditioned medium (Sup PAC); PNE-conditioned medium was used as a control (Sup PNE). One-way ANOVA. **C.** ΔMFI of CD44 in cells described in B. One-way ANOVA. **D.** Schematic representation of the experimental setup used for E. **E.** ΔMFI of α2 in PNE cells cultured in the lower Transwell chamber alone or in the presence of PAC cells in the upper chamber. Data represent the mean ± standard deviation (n = 2 experiments). Student's *t*-test. Representative plots of 7-AAD-stained PNE cells cultured with PAC cells in the presence of the listed concentration of OPG (**F**), Sulfasalazine (**G**) or SC75 (**H**). I f not otherwise stated, data represent the mean ± SEM of at least 3 independent experiments. Each dot represents the mean of technical triplicates from independent experiments. The artwork used in this figure was adapted from Servier Medical Art (http://https://smart.servier.com/). Servier Medical Art by Servier is licensed under CC BY 4.0.

Figure S4

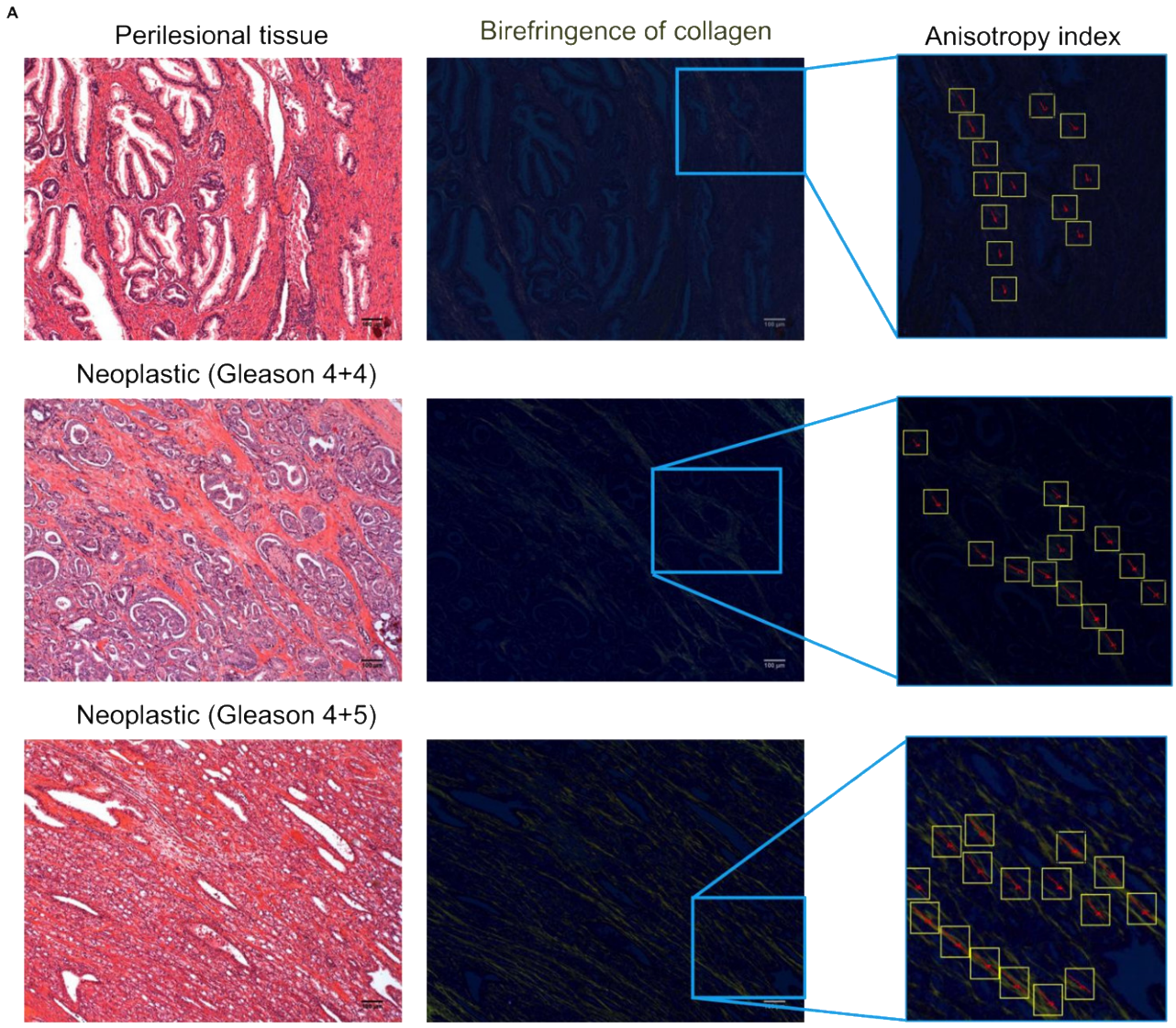

Figure S4. Polarized light analysis of ECM linearization in human prostate cancer specimen. A. Representative H&E images (left) and Birefringence of collagen (central) of Perilesional, Neoplastic (Gleason 4+4) and Neoplastic (Gleason 4+5) tissue. Representative image from each group. The inset (right) shows higher magnification with fiber alignment measurement. Each yellow square indicates a measure.

Figure S5

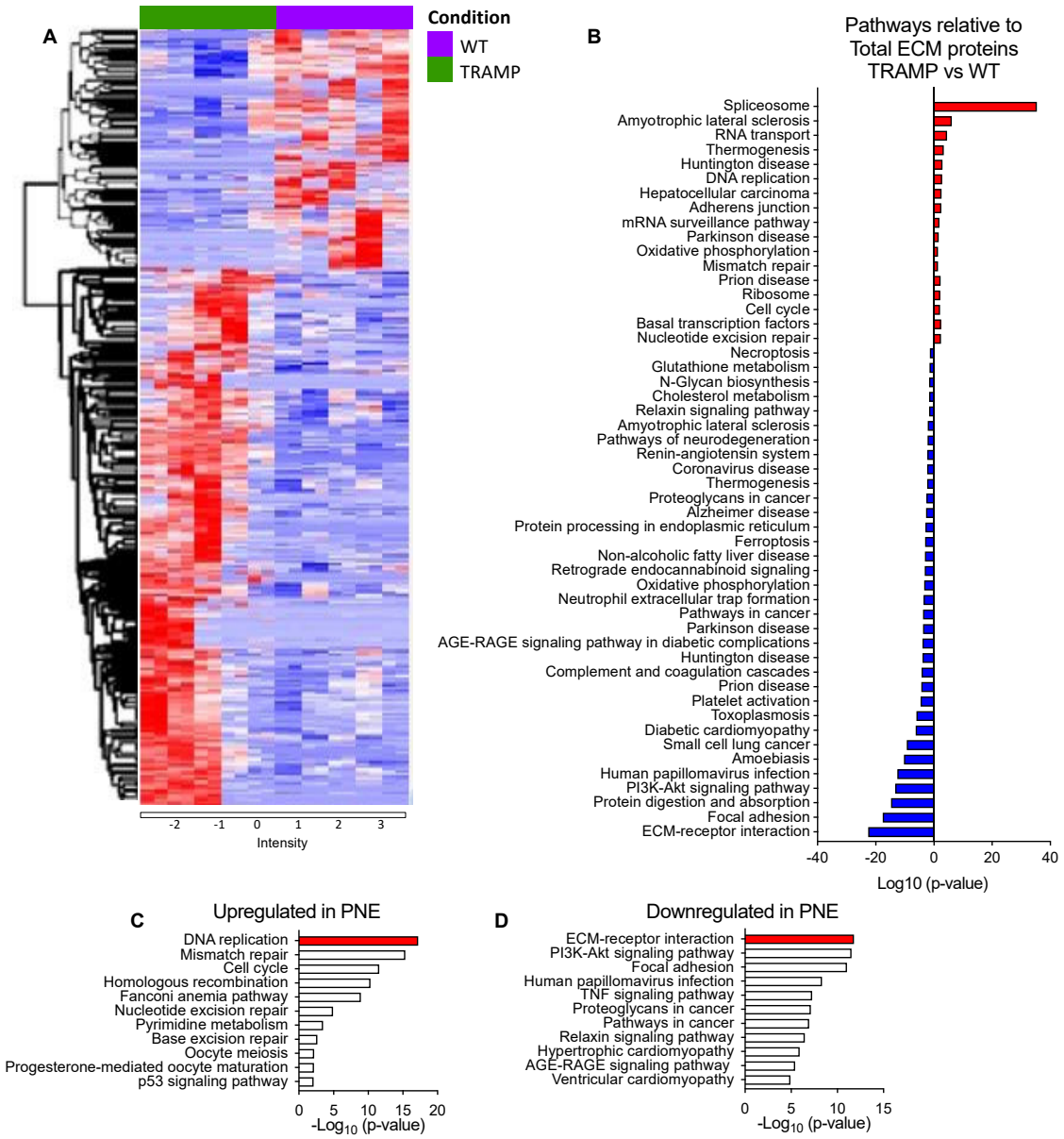

Figure S5. Divergence of the proteomes of ECMs obtained from TRAMP and WT prostates. A. Heatmap representative of the differentially expressed proteins ($P < 0.05$) in the ECM obtained from the prostate dorsal lobe of TRAMP and WT mice. Data represent duplicates of five samples for each experimental group. Upregulated and downregulated proteins are shown in red and blue, respectively. **B.** Summary of upregulated (red) and downregulated (blue) pathways in the ECM described in A. C. Upregulated KEGG pathways from microarray analysis of PNE vs. PAC cells. **D.** Downregulated KEGG pathways from microarray analysis of PNE vs. PAC cells.

Figure S6

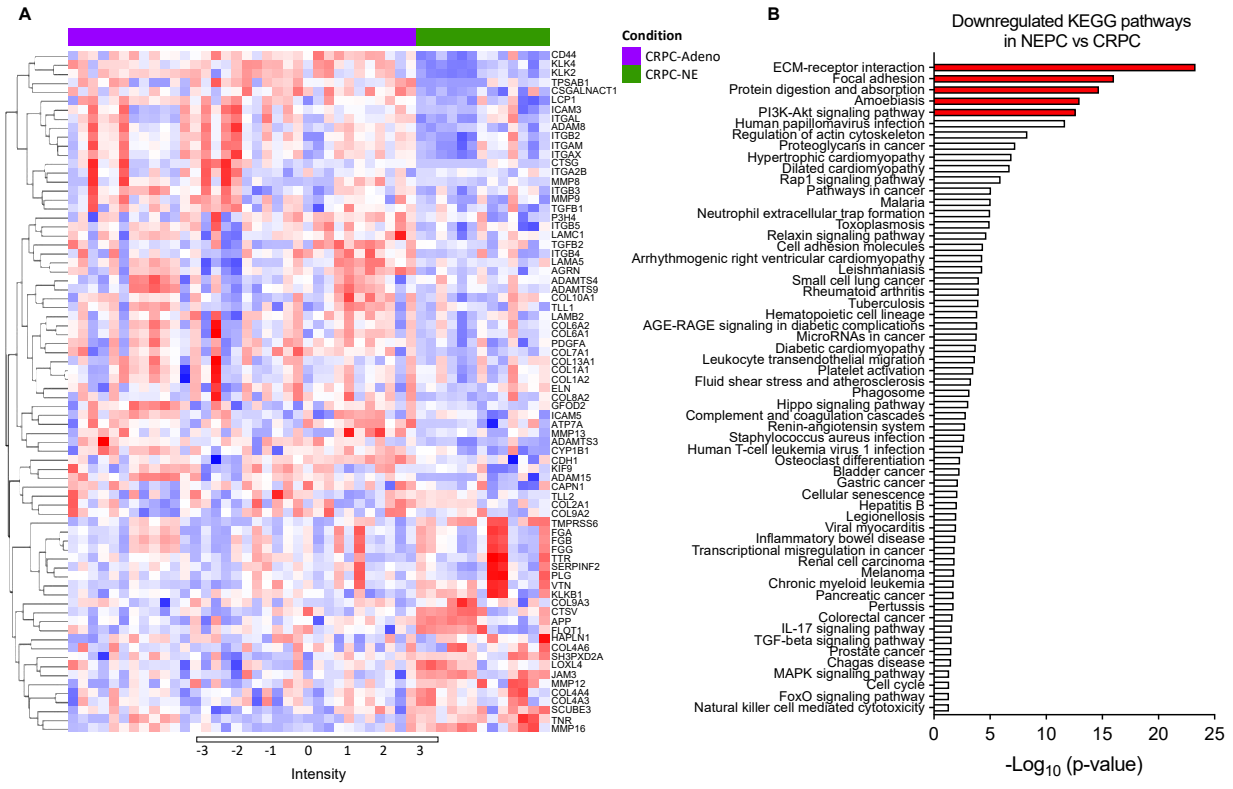

Figure S6. Differentially expressed matrisome genes discriminate human NEPC and CRPC-Adeno. **A.** Heatmap of differentially modulated transcripts enriched in the "extracellular matrix organization" KEGG pathway categories in CRPC-NE (n = 13) vs. CRPC-Adeno (n = 34) samples (Beltran H. et al. Nat Med 2016). Differentially expressed genes ($P < 0.05$): upregulated and downregulated genes are shown in red and blue, respectively. **B.** Summary of KEGG pathways downregulated in CRPC-NE (n = 13) vs. CRPC-Adeno (n = 34) from E.

Figure S7

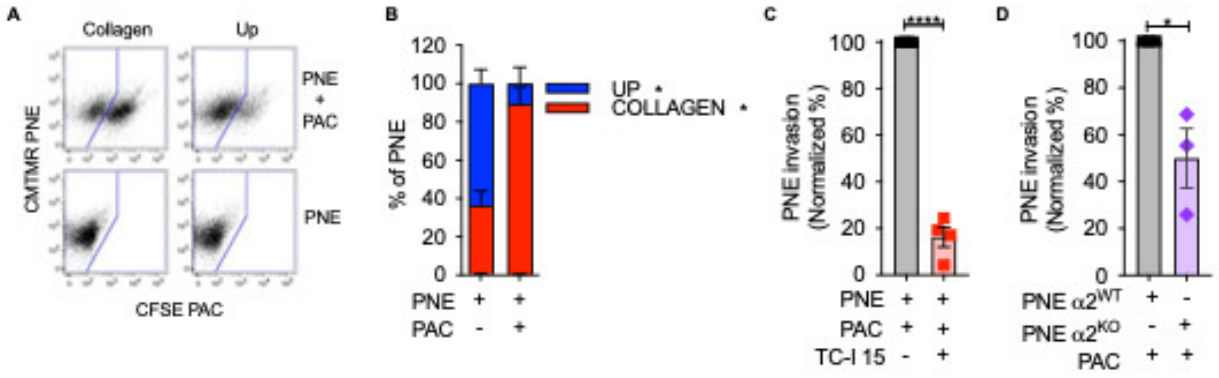

Figure S7. Inhibition of α2 reduces invasiveness of PNE and PAC cells. A-B. Representative plots **(A)** and quantification **(B)** of PNE cells migrated into collagen gel (red) or blocked in the upper (blue) Transwell chamber. Student's *t*-test. **C.** Invasion of PNE cells stimulated by PAC cells in the presence or absence of the α2 inhibitor TC-I 15. Data are normalized to the group without inhibitor. Student's *t*-test. **D.** Invasion of either PNE $\alpha2^{WT}$ or PNE $\alpha2^{KO}$ stimulated by PAC cells. Data normalized to PNE $\alpha2^{WT}$ only. Student's *t*-test. Data represent the mean ± SEM of at least 3 independent experiments. Each dot represents the mean of technical triplicates from independent experiments. *P < 0.05, ****P < 0.0001.

Figure S8

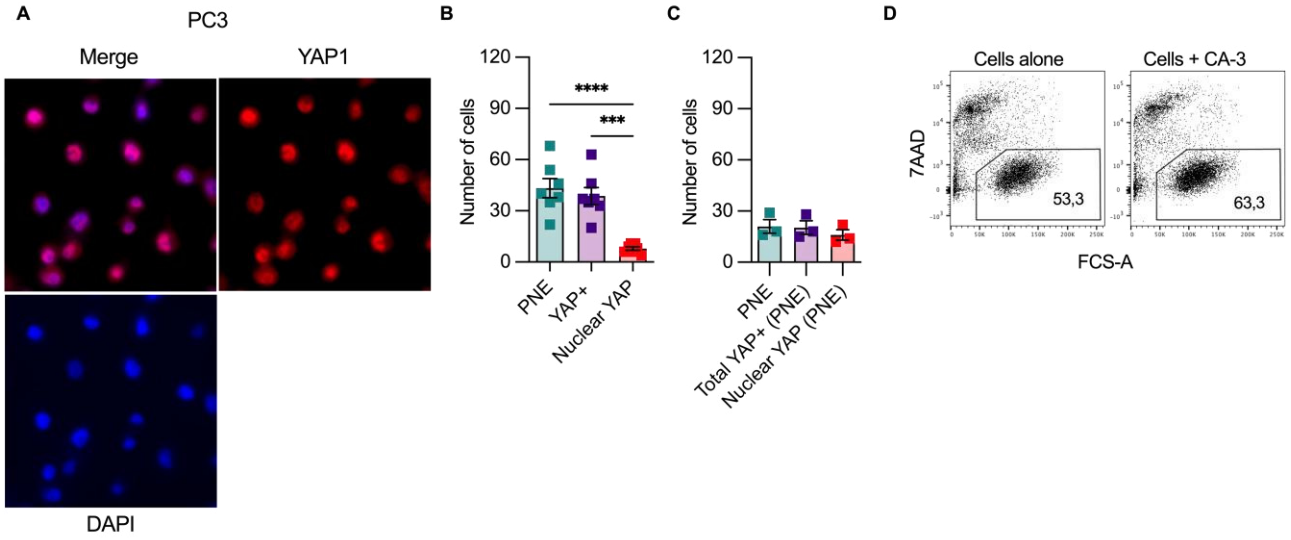

Figure S8. PNE cells translocate YAP into the nucleus when cocultured with PAC cells. A. Representative IF pictures of YAP expression in PC-3 cells. Cells labeled as in Fig. 4A (Red, YAP1; blue, DAPI stained nuclei). **B-C.** Quantification of cells positive for the indicated feature (PNE cells, YAP^+ PNE cells and Nuclear YAP^+ PNE cells) in PNE alone (**B**) or PNE cocultured with PAC (**C**). Data represent quantification of images as showed in Fig. 4A. Each dot represents a different image and quantifies the number of positive cells in that image. One-way ANOVA. **D.** Representative flow cytometry plots of live PNE/PAC cells alone or in the presence of CA-3. ***P < 0.001, ****P < 0.0001.

Figure S9

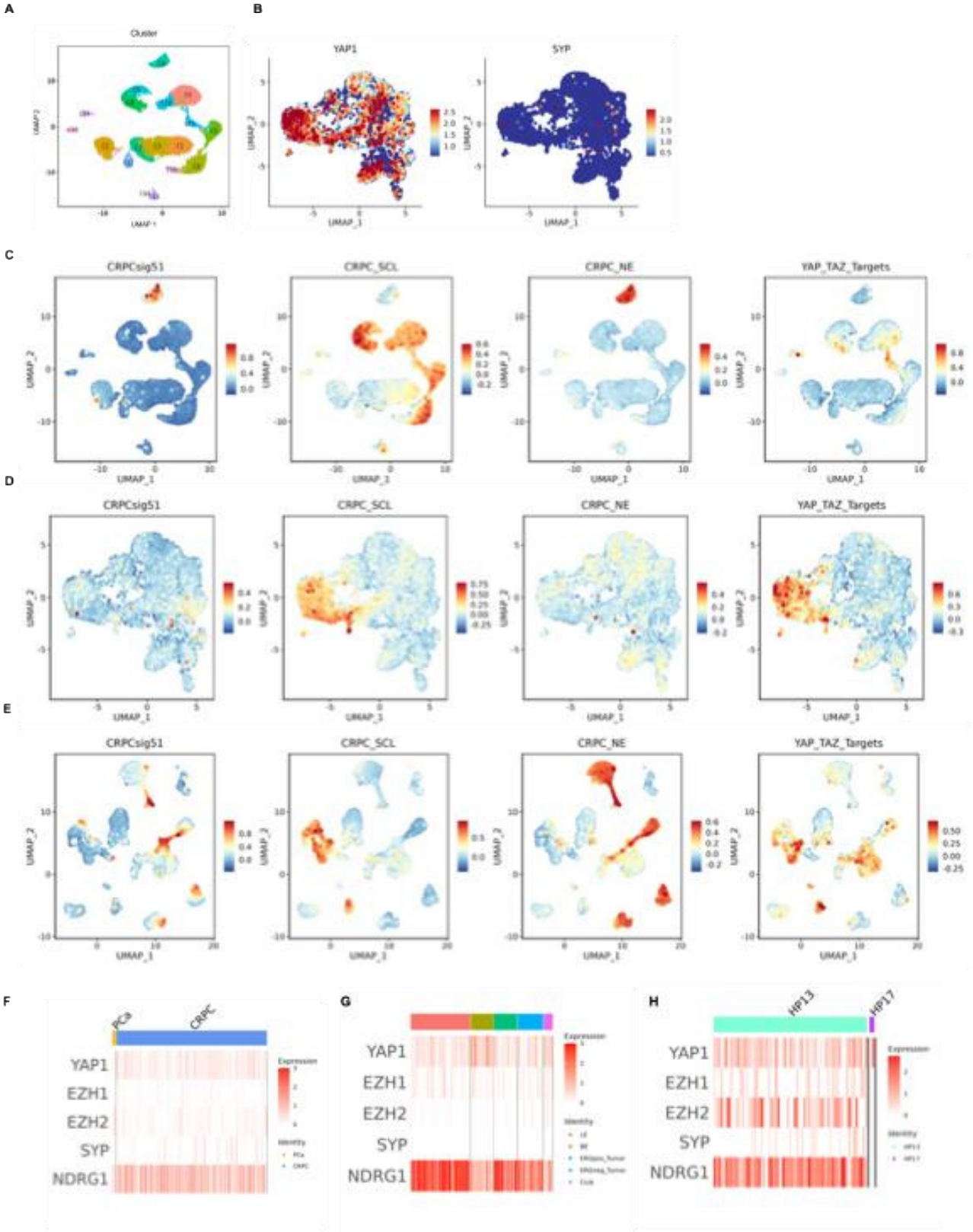

Figure S9. CRPC (AR-high) and luminal (PSA-low) co-express YAP1 and NE markers. A. UMAP showing the clusters of primary prostate tumors from Cheng Q. *et al.* Eur Urol 2022. **B.** UMAP plot showing the expression profiles of YAP1 (left) and SYP (right) of prostate tumors from Song H. *et al.* Nat

Commun 2022. **C-E.** Umap plots showing the expression of CRPCsig51, CRPC_SCL, CRPC_NE signatures, and YAP_TAZ_Target genes in human prostate cancer cells from Cheng et al. (**C**), Song et al. (**D**) and Zaidi S. *et al.* (**E**). **F-H.** Heatmap plots showing the expression of YAP1 and NEPC markers (EZH1, EZH2, SYP, and NDRG1) in selected cells of the previously described datasets, specifically cluster 12 from Cheng et al. (**F**), epithelial cells from Song et al. (**G**), and CRPC cells showing NEPC similar transcriptomic features from Zaidi et al. (**H**).

Figure S10

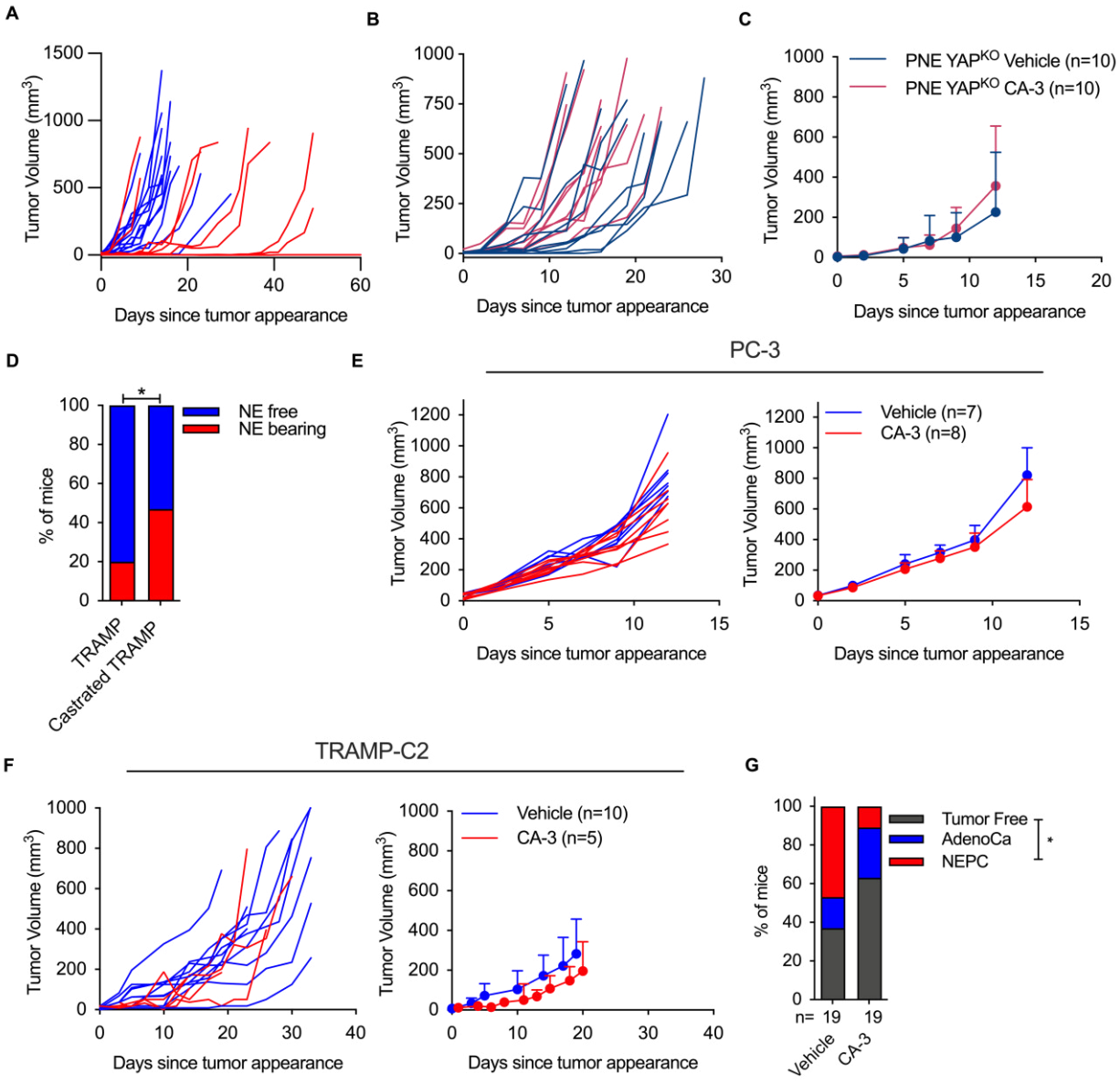

Figure S10. Efficacy of CA-3 treatment in mouse models of PC. A. Growth curves of individual PNE tumors in NSG mice receiving CA-3 (n=9; red) or vehicle (n=14; blue). **B-C.** Growth curves of individual **(B)** and pooled **(C)** PNE YAP^{KO} tumors in NSG mice receiving CA-3 or vehicle (n=10/group). **D.** Frequency of NEPC in castrated or naïve TRAMP mice. Fisher's exact test. (TRAMP, n = 25/113; 22,12% vs Castrated TRAMP n= 8/17; 47,06%). **E.** Growth curves of individual (left) and pooled (right) PC-3 tumors in NSG mice receiving CA-3 or vehicle. Two-way ANOVA. **F.** Growth curves of individual (left) and pooled (right) TRAMP-C2 tumors in C57BL-6N mice receiving CA-3 or vehicle. Two-way ANOVA. **G.** Frequency of NEPC, adenocarcinoma (AdenoCa) and tumor-free castrated TRAMP mice treated with CA-3 or vehicle. Fisher's exact test. If not otherwise stated, data represent the mean ± SD. *P < 0.05, **P < 0.01.

Figure S11

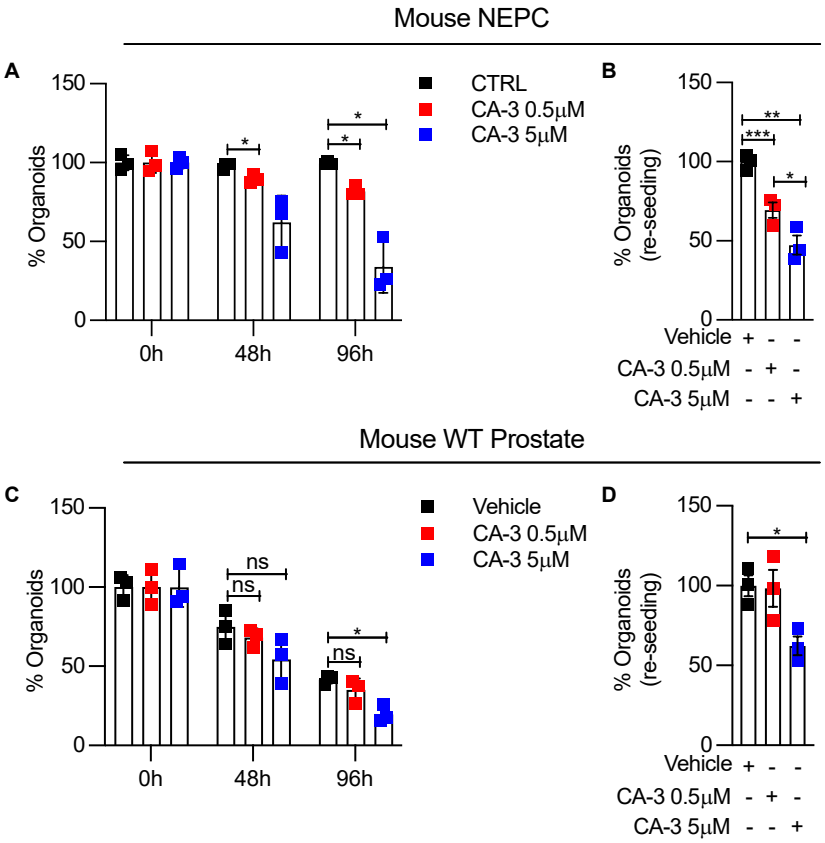

Figure S11. CA-3 inhibits NEPC and not WT organoids. A. and C. Overtime frequency of mouse NEPC **(A)** and WT **(C)** organoids treated with two concentrations of CA-3 or vehicle. Two-way ANOVA. **B and D.** Frequency of NEPC **(B)** and WT **(D)** organoids generated after reseeding cells from A and C. One-way ANOVA. *$P < 0.05$, ** $P < 0.01$, *** $P < 0.001$. Data represent the mean ± SEM of at least 3 independent experiments.

Table S1

See Table S1 document

Table S2

See Table S2 document.

Table S3

Adverse event	Castrated Vehicle	Castrated CA-3 1mg/kg
Weight loss	4/12 (33%)	1/9 (11,11%)
Lethargy	1/12 (8,33%)	1/9 (11,11%)
Preputial gland infection	0/12 (0%)	1/9 (11,11%)
Salivary gland tumor	0/12 (0%)	1/9 (11,11%)
Seminal vesicle tumor	0/12 (0%)	0/9 (0%)
Death	1/12 (8,33%)	0/9 (0%)
Total	6/12 (50%)	4/9 (44,44%)

Table S3. Adverse events. Number of mice affected by the indicated pathology/total number of mice (% of mice affected).

ADVANCED FUNCTIONAL MATERIALS
www.afm-journal.de

Endothelial Cells Angiogenesis in Sulfated Glycosaminoglycan (GAG) Hydrogels Enhanced by Bioactive Glass-Released Ions

Marco Piazzoni, Ilaria Borghi, Francesca Cadamuro, Sophia Dalfino, Riccardo Campanile, Sofia Nizzolo, Valeria Cassina, Francesca Tallia, Julian R. Jones, Francesco Mantegazza, Sabrina Bertini, Lorenzo Moroni, Francesco Nicotra, and Laura Russo**

The successful clinical translation of large-scale tissue-engineered constructs is significantly hindered by the lack of functional vascularization, which is crucial for delivering oxygen and nutrients to cells. Current in vitro angiogenesis models often rely on murine tumor-derived extracellular matrix (ECM) materials, which suffer from non-defined composition and batch-to-batch variability, and on the delivery of growth factors at non-physiological concentrations. Hydrogels offer a superior alternative for the rational design of biomimetic ECM environments, because of their versatility in tuning biochemical and mechanical properties. This study presents a novel growth factor-free hydrogel composed of gelatin, chondroitin sulfate, and laminin, designed to promote endothelial cell (EC) angiogenesis in vitro. The hydrogel's mechanical properties are precisely controlled by varying its crosslinking degree, attesting that a softer substrate (Young's modulus ≈80 Pa) significantly boosts ECs tube formation. Furthermore, the angiogenic process is enhanced by several hours with ions released by bioactive glass 58S (BG58S), specifically calcium and silicon. Finally, the expression of angiogenesis-related genes and the production of matrix remodeling enzymes is augmented in the presence of BG58S-conditioned medium. It is believed that this bioinstructive sulfate GAG based hydrogel represents a promising solution for vascularizing 3D cellular constructs, marking a significant step toward the clinical application of tissue engineering products.

1. Introduction

Vascularization of biological substitutes represents a real issue for the clinical translation of tissue engineering products. [1,2] As a matter of fact, the development of 3D cellular constructs with a clinically relevant size (>1 cm^3)[3–5] is currently hampered by the inability to establish a functional vasculature able to sustain oxygen and nutrients delivery to growing tissues.[6–8]

The human body can generate new blood vessels from preexisting ones through the process of angiogenesis.[9] The best effort to recapitulate this morphogenic process in vitro was achieved with the employment of biomaterials able to mimic the extracellular matrix (ECM),[10–12] and in particular, the basement membrane (BM), so to instruct endothelial cells (EC) to activate the angiogenic molecular pathways.[13] In vitro tests are usually done with commercial ECM-based materials derived from murine sarcoma tumor extracts (i.e., Matrigel). Nonetheless, the unknown exact

M. Piazzoni, I. Borghi, F. Cadamuro, R. Campanile, V. Cassina, F. Mantegazza, F. Nicotra, L. Russo
School of Medicine and Surgery
Università degli Studi Milano-Bicocca
Vedano al Lambro (MB), Italy
E-mail: marco.piazzoni@unimib.it; laura.russo@unimib.it

S. Dalfino, L. Moroni
Complex Tissue Regeneration
MERLN Institute for Technology-Inspired Regenerative Medicine
Maastricht University
Maastricht 6229 ER, the Netherlands

The ORCID identification number(s) for the author(s) of this article can be found under https://doi.org/10.1002/adfm.202519933

DOI: 10.1002/adfm.202519933

S. Dalfino
Department of Biomedical Sciences for Health
Università degli Studi di Milano
Milano, Italy

S. Dalfino
Department of Biomedical
Surgical and Dental Sciences
Università degli Studi di Milano
Milano, Italy

S. Nizzolo, S. Bertini
Istituto di Ricerche Chimiche e Biochimiche "G. Ronzoni"
Milano, Italy

F. Tallia, J. R. Jones
Department of Materials
Imperial College London
South Kensington Campus, London SW7 2AZ, UK

L. Russo
Fondazione IRCCS San Gerardo dei Tintori
Monza, Italy

composition, batch-to-batch variability, and the impossibility of adjusting material types and quantities make them an obsolete option in tissue engineering.[14,15] Within this context, hydrogels represent the most valuable candidates to engineer ECM mimics with a bottom-up approach, due to the possibility of finely tuning their biochemical composition and mechanical properties.[16,17]

The BM is primarily made of collagen IV, laminins (LM), nidogen/entactin, and heparan sulfate proteoglycans (HSPG), each of which is involved in specific functions during angiogenesis.[18] For such reason, efforts have been made to design hydrogel systems incorporating these macromolecules either as complete structures or via the integration of specific functional domains only. The most used strategies to generate synthetic BM consist of covalently linking to a hydrogel peptide sequences of LM (e.g., SIKVAV and YIGSR)[19] or of collagen (e.g., RGD)[20] to ensure ECs attachment to the substrate. However, to ensure functional BM, sulfated glycosaminoglycans (GAG) proved also to be needed. Thanks to their negatively charged sulfate groups, GAGs have the ability to selectively interact with positively charged molecules, like the vascular endothelial growth factor (VEGF), the fibroblast growth factor (FGF), and other chemokines, favoring their stabilization and angiogenetic activity.[21] Both heparan sulfate (HS)[22,23] and chondroitin sulfate (CS)[24] -based hydrogels were indeed reported as extremely effective biomaterials, considering that they have similar charge density and sulfation patterns.[25]

Furthermore, since material stiffness was proven to have a great impact on ECs ability to organize in tubule-like structures, hydrogels with tunable mechanical properties were developed.[26]

Despite these promising results, the majority of hydrogels required VEGF administration at concentrations (μg mL^{-1} range) far superior to what is normally found in vivo (pg mL^{-1} range) in order to effectively induce tube formation,[27] thus limiting their therapeutic use in advanced engineering methods.[28] A valid alternative to growth factors administration are inorganic ions. Within this context, bioactive glasses (BG) not only can stimulate new bone growth, but can also act as angiogenic promoter through their dissolution products.[29–31] Upon contact with physiological solutions (e.g., simulated body fluid (SBF), culture media) BG releases ions (e.g., Si, Ca) that can induce lots of different biological activities.[32,33] Several works have indeed demonstrated the ability of BG to increase ECs proliferation and migration ability, key initial steps of angiogenesis.[24,34]

Here we report a hydrogel made of gelatin (GEL), CS, and LM to promote ECs angiogenesis in vitro without the addition of external growth factors. Moreover, the morphogenic process proved to be kinetically enhanced by medium conditioned with bioactive glass 58S (BG58S). CS and GEL were functionalized with a methyl-furan moiety to undergo a Diels Alder cycloaddition with 4arm-PEG10k-Maleimide, enabling precise control of hydrogel crosslinking density. This fine-tuning allowed modulation of the material Young's modulus (E) at the micro-nanoscale as demonstrated through Atomic Force Microscopy (AFM) measurements, greatly enhancing ECs migration ability and mesh organization on softer substrates (E ≈80 Pa). Medium conditioned with BG58S improved ECs viability and accelerated tube formation by several hours through the release of calcium and silicon. Moreover, upregulation of angiogenesis-related genes and increased secretion of matrix remodeling enzymes suggested that Ca and Si participate at multiple levels to regulate the molecular pathway, that leads to the establishment of cell-cell junctions and ECM degradation. We believe that this growth factor-free GAG-based hydrogel might be a suitable solution to vascularize 3D cellular constructs in vitro, making a step forward the clinical translation of tissue engineering products.

2. Results and Discussion

2.1. Hydrogel Rational Design and Characterization

ECs are in contact with a thin but highly specialized ECM layer: the basal membrane. Hydrogels were designed to bear fundamental biomolecules normally found in this structure in order to recapitulate the complex molecular machinery that leads to angiogenesis in vivo. In particular, gelatin (being the hydrolyzed form of collagen) was introduced to support cell adhesion through the RGD domains[18]; whereas CS, being a sulfated GAG, was used for its capacity to interact with pro-angiogenic growth factors bearing positive charges (e.g., VEGF, FGF), leading to their stabilization and localization in the hydrogel.[18,21]

In particular, in this study, a CS with an average molecular weight (Mw) of 30 kDa and a polydispersity index of 1.3 was used (Table S1, Supporting Information). The sulfate (SO_{3-}) to carboxyl (COO^-) group ratio was found to be ≈1.07 and the 4-sulfate to 6-sulfate (4S/6S) ratio was equal to 2.55, as determined respectively by conductometric titration (Supporting Information) and HSQC experiments (Figure S3, Supporting Information). Both the sulfate-to-carboxyl ratio and the 4S/6S sulfation pattern were thus coherent with the CS molecular structure characteristics that are known to support ECs angiogenesis.[35,36]

GEL and CS were first functionalized with 5-methylfuran (5MF) groups. In detail, the amine groups on lysine residues of gelatin were functionalized via reductive amination with 5-methylfurfural. In contrast, CS was functionalized with 5-methylfurfurylamine through a carbodiimide-mediated coupling reaction involving its carboxylic acid groups. The DoF, determined by ^{1}H NMR spectroscopy, resulted to be around 100 % of the lysine moieties for GEL-5MF and 13 % for CS-5MF (Figures S1,S2, Supporting information).

Functionalized polymers were then crosslinked together with a 4arm-PEG10k-Maleimide through Diels-Alder (DA) reaction (**Figure 1A**). This cycloaddition is a click chemistry reaction, which proceeds with high chemoselectivity between the diene groups on the polymers and the dienophile on the linker, yielding covalent crosslinks.

Varying hydrogel GEL-5MF:CS-5MF % w/w ratios and crosslinking degree (γ) proved to efficiently change the material storage modulus (Figure 1B) of nearly two orders of magnitude (from 58 to 1450 Pa), attesting extreme mechanical tunability.

Hydrogels with GEL-5MF:CS-5MF % w/w ratios of 2:1 and a crosslinking degree of 100 (H-1) and 50 (H-0.5) were proven to be superior in inducing EC morphogenesis compared to

L. Russo
CURAM Research Ireland Centre for Medical Devices
University of Galway
Ireland

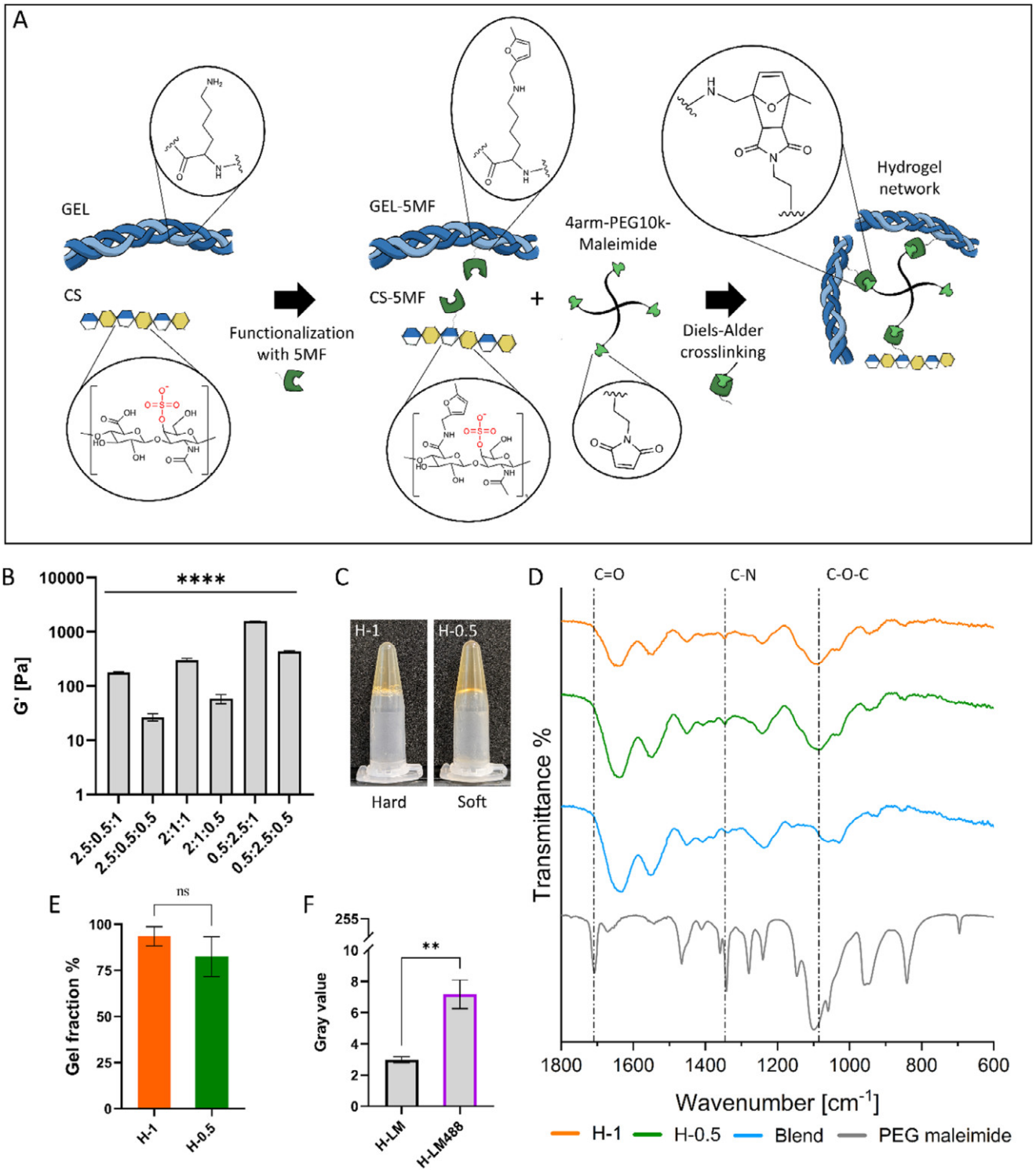

Figure 1. A) Illustration of the materials functionalization with 5MF and crosslinking with 4arm-PEG10k-Maleimide. B) Storage modulus of hydrogels changing GEL-5MF:CS-5MF % w/w ratios (i.e., 2.5:0.5, 2:1, 0.5:2.5). C) A representative picture of crosslinked hydrogel formulations H-1 (left) and H-0.5 (right). D) FT-IR spectra of crosslinked H-1 and H-0.5 hydrogel formulations, 4arm-PEG10k-Maleimide (PEG maleimide) and of a mixed GEL-5MF and CS-5MF (Blend). Dashed lines indicate: C═O stretching (1709 cm^{-1}), C—N stretching (1345 cm^{-1}), C—O—C bending (1080 cm^{-1}). E) Gel fraction % of hydrogel formulations. F) Grayscale values of images taken at the fluorescence microscope for a hydrogel coated with LM (H-LM) and a hydrogel coated with LM-DyLight 488 (H-LM488). Data (n = 3) are presented as mean ± SD. Non-significant (ns), $p > 0.05$, $^{**}p \leq 0.01$, $^{****}p \leq 0.0001$.

other formulations (Figure S4, Supporting Information), therefore further experiments were conducted only on these hydrogels (Figure 1C).

The presence of the DA adduct was confirmed by FT-IR spectroscopy (Figure 1D). The characteristic bands of symmetric C—O—C stretching (1080 cm^{-1}) and C—N stretching (1345 cm^{-1}) were indeed present in crosslinked hydrogel formulations (H-1 and H-0.5) but not in the mixed GEL-5MF and CS-5MF (Blend).[37] Notably, the C═O stretching (1709 cm^{-1}) assigned to the maleimide groups also disappeared after hydrogel crosslinking, supporting the involvement of the maleimide moiety in the cycloaddition reaction.[38] Gel fraction experiments also attested a crosslinking efficiency of 94 ± 5 % for H-1 and 82 ± 11 % for H-0.5. (Figure 1E)

LM was also optionally introduced in the hydrogel system as a surface coating, since this glycoprotein is abundantly found in endothelial cell BM.[18] The LM coating onto the hydrogel surface was confirmed by conjugating LM with a fluorophore (NHS-DyLight 488) (Figure 1F, Supporting Information).

2.2. Endothelial Cells' Tube Formation Assay Onto Hydrogels

ECs were seeded onto the hydrogels to evaluate tube formation in vitro under several different testing conditions (**Figure 2**A). Figure 2B,C illustrates ECs' ability to perform tube formation after 6 and 24 hours from seeding onto hydrogels with different crosslinking degree (H-1 and H-0.5), the addition of LM and VEGF (H-LM, H-LM-VEGF), and on Matrigel (Figure 2D). After 6 h (Figure 2B) on pristine hydrogels (H) ECs had a rounder shape, whereas on LM-coated samples (H-LM) and VEGF-supplied medium (H-LM-VEGF) they already appeared to be sprouting. Subtle but still notable differences can be appreciated between H-1 and H-0.5 hydrogels at this timepoint, with H-0.5 inducing more cellular organization. On the contrary, after 24 h (Figure 2C) differences in terms of ECs morphogenesis clearly emerged between H-1 and H-0.5 hydrogels. On H-0.5 hydrogels cells were indeed clustered in macroscopic tubule-like structures with a mean tube length of few hundred micrometers (300–400 µm) (Figure 2E) and a mean tube width of nearly 15 µm (Figure 2F), whereas on H-1 samples morphogenesis was a much more contained (tube length in the order of 100 µm and a tube width of 5 µm). As observed at the previous timepoint, on pristine hydrogels cells were still more circular in shape when compared to the H-LM and H-LM-VEGF counterparts (Figure 2G).

Nonetheless, on each condition, tubular structures proved to be stable for a longer time (>24 h) compared to commercially available materials (i.e., Matrigel) (Figure S4, Supporting Information) as demonstrated with live-dead staining (Figure 2H,I).

Finer details on ECs morphology could be assessed with DAPI and phalloidin fluorescent staining. From images (Figure 2L,M) it was evident that on H-0.5 samples cells had migrated toward each other to form big cell aggregates, a situation which is not induced on H-1 samples, where cells remained instead rounded and less organized. Despite that, with the addition of LM differences between H-1 and H-0.5 became less pronounced. As a matter of fact, adjacent cells were more elongated and protruding to form cell-cell interactions on both conditions, suggesting the importance of LM in sustaining ECs proliferation and network formation during angiogenesis through integrin binding.[39] Interestingly, conditions with medium supplemented with VEGF (100 ng mL^{-1}) gave different cellular responses depending on the hydrogels' crosslinking degree[19,26] Indeed, on H-1 samples ECs became flattened and proliferated all over the hydrogel surface, whereas on H-0.5 network branching was mildly improved.

Taken together, these results indicate that the ECs ability to perform tube formation was mainly determined by their interaction with the components of the hydrogel macromolecular backbone (i.e., gelatin and chondroitin sulfate) and not by the free VEGF added in the medium. These findings make the GEL-5MF:CS-5MF % w/w ratios, the crosslinking degree and the LM coating, the pivotal parameters to control for the rational design of hydrogels mimicking the BM.

2.3. Studies of Hydrogel Viscoelastic Behavior at the Macro and Microscale

Since the hydrogel crosslinking degree was a key factor in determining ECs phenotype during the tube formation assay, further experiments were performed to deeply investigate how hydrogels' mechanical properties could be modulated. Rheological characterization of H-1 and H-0.5 hydrogels was conducted using both macroscale (rheometer) and micro/nanoscale (AFM) approaches to comprehensively assess their viscoelastic behavior.

Measurements performed by AFM revealed the hydrogels' spatially localized mechanical properties as well as frequency-dependent viscoelastic behavior up to 500 Hz. For both hydrogel formulations (H-1 and H-0.5) and across both timepoints (0 and 24 h), AFM frequency sweeps (**Figure 3**A,B) confirmed a dominant elastic component (G′), although G″ progressively approached and surpassed G′ at high frequency. Specifically, the crossover point (i.e., where G″ exceeded G′) was observed at 220 Hz for H-0.5 and at 100 Hz for H-1, suggesting that both hydrogels made a transition toward a more viscous behavior.[40]

In Figure 3C,D are reported the Young's moduli evaluated from the approaching curve before the application of the corresponding frequency. Young's moduli were found to be rather consistent across the samples in the entire frequency range tested, both before and after swelling in the medium, attesting no aging effect upon mechanical perturbation. As expected, the Young's modulus of H-0.5 samples was found to be lower than H-1 due to lower crosslinking degree. This softening effect was also reflected in the hydrogel network morphology, as H-0.5 hydrogels had a much more porous structure than H-1 (Figure 3L,M).

AFM-based measurements further highlighted time-dependent softening of hydrogels in culture conditions. For H-1, G′ decreased from 2920 ± 990 Pa at 0 h to 320 ± 150 Pa after 24 h (Figure 3E), while Young's modulus (E) dropped from 3830 ± 310 to 510 ± 10 Pa (Figure 3F) over the same time period. Similarly, H-0.5 showed a reduction in G′ from 530 ± 240 to 37 ± 21 Pa and in E from 750 ± 53 to 81 ± 4 Pa. This marked reduction in mechanical parameters is likely due to progressive hydration and/or weight loss of the hydrogel network in cell culture medium during the 24 h of incubation (Figure 3G).[41,42]

Frequency sweeps (Figure 3H) performed with the rheometer confirmed that both hydrogels exhibit a predominant elastic response also in the macroscopic length scale over the tested

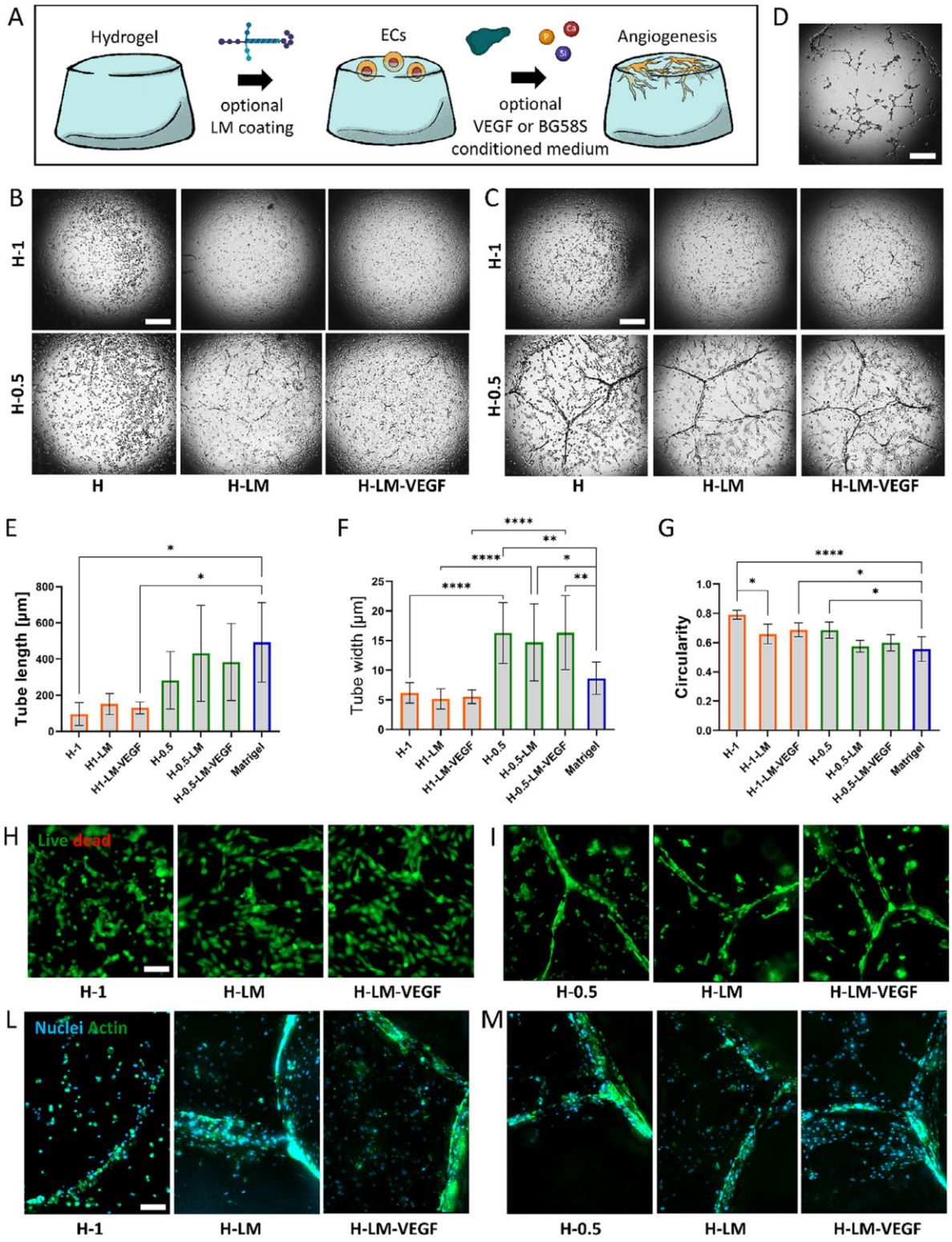

Figure 2. A) Illustration of tube formation assay on hydrogels. ECs tube formation assay after 6 h B) and 24 h C) from seeding onto H-1 and H-0.5 hydrogels. The pristine hydrogels (H) (left), with surface laminin coating (H-LM) (center), and with both surface laminin coating and medium supplemented with 100 ng of VEGF (H-LM-VEGF) (right). D) ECs tube formation assay after 6 h on Matrigel. ECs network analysis at 24 h: tube length E), tube width F), and cells' circularity G). A circularity value of 1.0 indicates a perfect circle. Live-dead staining of ECs tube formation assay after 24 h from seeding onto H-1 H) and H-0.5 I) for different conditions (H, H-LM, H-LM-VEGF). DAPI and Phalloidin-FITC staining of H-1 L) and H-0.5 M) hydrogels formulations at 24 h from seeding for different conditions (H, H-LM, H-LM-VEGF). Scale bar is 500 µm B,C,D), 200 µm H,I) and 100 µm L,M). Data ($n = 3$) are presented as mean ± SD. Non-significant (ns), $p > 0.05$, *$p \leq 0.05$, **$p \leq 0.01$, ****$p \leq 0.0001$.

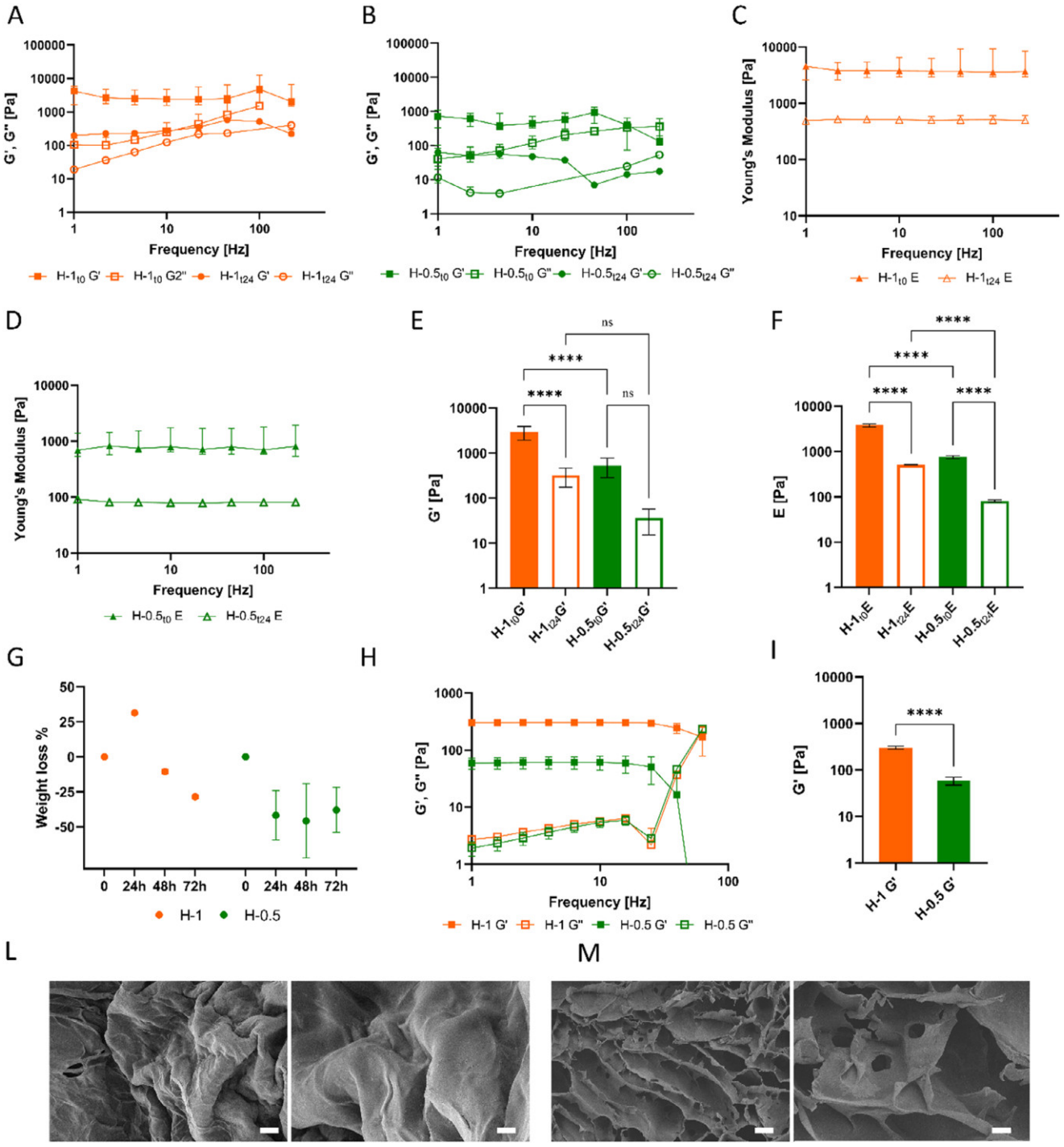

Figure 3. Frequency sweeps curves obtained with AFM of H-0.5 A) and H-1 B) hydrogels before and after 24 h of swelling in the medium. Young's modulus as a function of frequency calculated with AFM for H-1 C) and H-0.5 D), before and after swelling in the medium. G′ values E) and E values F) of both hydrogel formulations before (t0) and after (t24) swelling in the medium. G) Weight loss % of hydrogel formulations when imbibed in PBS (37 °C, 5% CO_2, humidity 100%). H) Frequency sweeps curve of H-0.5 and H-1 hydrogels obtained with the rheometer and associated G′ values I). SEM images of H-1 L) and H-0.5 M) samples at two different magnifications. Scale bar is 100 µm (left) and 20 µm (right). Data ($n = 3$) are presented as mean ± SD. Non-significant (ns), $p > 0.05$, **** $p \leq 0.0001$.

frequency range (<100 Hz), with a mean storage modulus (G′) value of 300 ± 3 Pa for H-1 and 58 ± 2 Pa for H-0.5 (Figure 3I).

Collectively, these findings support the notion that H-1 and H-0.5 hydrogels possess a predominantly elastic character, with a viscous dissipation becoming relevant only at high-frequency regimes, at both length scales. Nonetheless, AFM-derived G′ are substantially higher than those measured via rheometer. This discrepancy between AFM and rheometer-derived values of G′ is attributed to the different length scales at which the two techniques operate. Indeed, the micro/nanoscale probing of AFM may result in higher substrate stiffness values due to microstructural features or inhomogeneities not captured in bulk measurements across the entire sample.[43] It is worth highlighting that the cellular length scale is similar to that one at which AFM operates, making AFM-derived stiffness measures more relevant than those performed with traditional rheology.[44]

These results can explain the different behavior displayed by ECs on the hydrogel during angiogenesis, making it plausible that a substrate with an elastic modulus in the order of ≈80 Pa (H-0.5) can promote a more efficient tube formation due to enhanced cellular mobility.[26]

Since the H-0.5 hydrogel was superior in inducing ECs to form a pseudo-capillary network in vitro, it was used for further experiments.

2.4. Bioactive Glass 58S Characterization After Exposure to Endothelial Cells' Culture Medium

Bioactive glasses can act as an angiogenic promoter capable of boosting vascularization of 3D constructs through ions (e.g., Ca, Si) release.[30,32] Experiments were thus performed aiming at characterizing BG58S bioactivity after exposure to ECs culture medium. We decided to test bioactivity by exposing BG58S directly to cell culture medium instead of simulated body fluid (SBF), since the glass degradation process is tightly dependent on the solution composition. To this purpose, ECGM was conditioned with different concentrations (i.e., 0.5, 1, 2.5, 5, 10 mg mL^{-1}) of BG58S for 2 or 24 h. Afterwards, we studied both the formation of hydroxycarbonate apatite (HCA) on the glass surface and, most importantly, the ions' (i.e., Ca, Si, P) release profiles in the culture medium.

The surface of the unreacted BG58S has an intrinsic porous texture (**Figure 4A**). However, from SEM images it can be appreciated that already after 2 h from immersion in culture medium, the glass surface appeared completely covered by very small precipitates of crystalline HCA layer for both 1 and 5 mg mL^{-1} concentrations (Figure 4B,C).[45]

Surface changes attesting bioactivity were further confirmed by FT-IR spectra (Figure 4D,E). A characteristic band at 875 cm^{-1} started developing at 1 mg mL^{-1} and increased in intensity as glass concentration increased, which has been assigned to C—O stretching from CO_3^{-2} being incorporated into the calcium-phosphate film to form HCA. Also, the bending vibrations of phosphate groups (P—O) in the crystalline phase of the HCA were clearly found at 571 and 603 cm^{-1} for glass concentrations between 0.5 and 10 mg mL^{-1}.[46]

When placed in solution, ions were released from the glass network, with cations exchanging with H^+ ions from the medium. Deposition of HCA at the bioactive glass surface follows the cation exchange. Dissolution was confirmed by ICP analysis, which quantifies elemental concentration in solution, showing that both Ca and Si generally increased in the media as initial glass content increased (Figure 4F,G). Si release is expected to be in the form of SiO_4^{4-}. Ca concentration (Ca^{2+}) rose from a basal level of 58.8 ± 0.7 μg mL^{-1} to almost 200 μg mL^{-1} for the highest BG58S initial concentrations (5 and 10 mg mL^{-1}) and conditioning times (24 h); Si content in the media increased from 0.4 ± 0.1 μg mL^{-1} to a maximum of nearly 50 μg mL^{-1} (BG58S 10 mg mL^{-1}, 24 h). Consistently with the SEM observation, P displayed the opposite behavior since it precipitated from the solution to form the calcium-phosphate layer onto the glass surface (Figure 4H), dropping from 19.9 ± 0.5 to 0.4 ± 0.1 μg mL^{-1}.

The pH also showed a positive correlation with initial glass content due to increased cations (Ca^{2+}) exchange with protons (H^+/H_3O^+) present in solution (Figure S5, Supporting Information).

Despite the extended surface area of BG58S powder, which conferred a high reactivity to the glass when immersed in physiological solutions,[47] it was possible to attest that there were significant differences in terms of ion concentrations between media conditioned for 2 and 24 h for almost all conditions.

2.5. Effect of BG58S-Conditioned Medium on Endothelial Cells Angiogenesis

To explore the biological effects of Ca and Si released from the bioactive glass on ECs, culture medium was conditioned with BG58S powder and biochemical assays were performed.

Viability was first analyzed via AlamarBlue. Medium conditioned for 2 h with BG58S at 1, 2.5, and 5 mg mL^{-1} concentrations resulted in an ECs' viability increase (>1.5-fold change), whereas 10 mg mL^{-1} was found to decrease it (0.6-fold change) (**Figure 5A**). Interestingly, when the medium was conditioned with BG58S for longer time (24 h) (Figure 5B) all conditions resulted instead in a decreased viability (1 mg mL^{-1} = 0.9-fold change; 2.5 mg mL^{-1} = 0.9-fold change; 5 mg mL^{-1} = 0.4-fold change; 10 mg mL^{-1} = 0.1-fold change) except for the lowest BG58S concentration, where no variation in viability was observed (0.5 mg mL^{-1} = 1.0-fold change). The beneficial effect on ECs viability of 2 h conditioning with BG58S can be ascribed to Si and Ca ions released in the medium, which were reported to effectively promote the angiogenic behavior of ECs by increasing their proliferation.[28] Nonetheless, the reversed biological effect observed at 24 h reflected the release profiles recorded through ICP analysis, suggesting that the ion levels became toxic for ECs survival, which is common in in vitro studies.

Given the fact that culture medium conditioned with 1 to 5 mg mL^{-1} of BG58S powder for 2 h gave the best viability increment within the shortest window of time, 5 mg mL^{-1} was chosen as the glass concentration for further experiments.

Tube formation kinetics on H-0.5 hydrogels increased as ECs managed to complete mesh formation more rapidly in the presence of BG58S-conditioned medium (H-BG) than the control condition (H). As shown in Figure 5C,D, in H-BG samples capillary morphogenesis was completed after just 18 h from seeding, as at 24 h there was no further improvement in terms of mesh

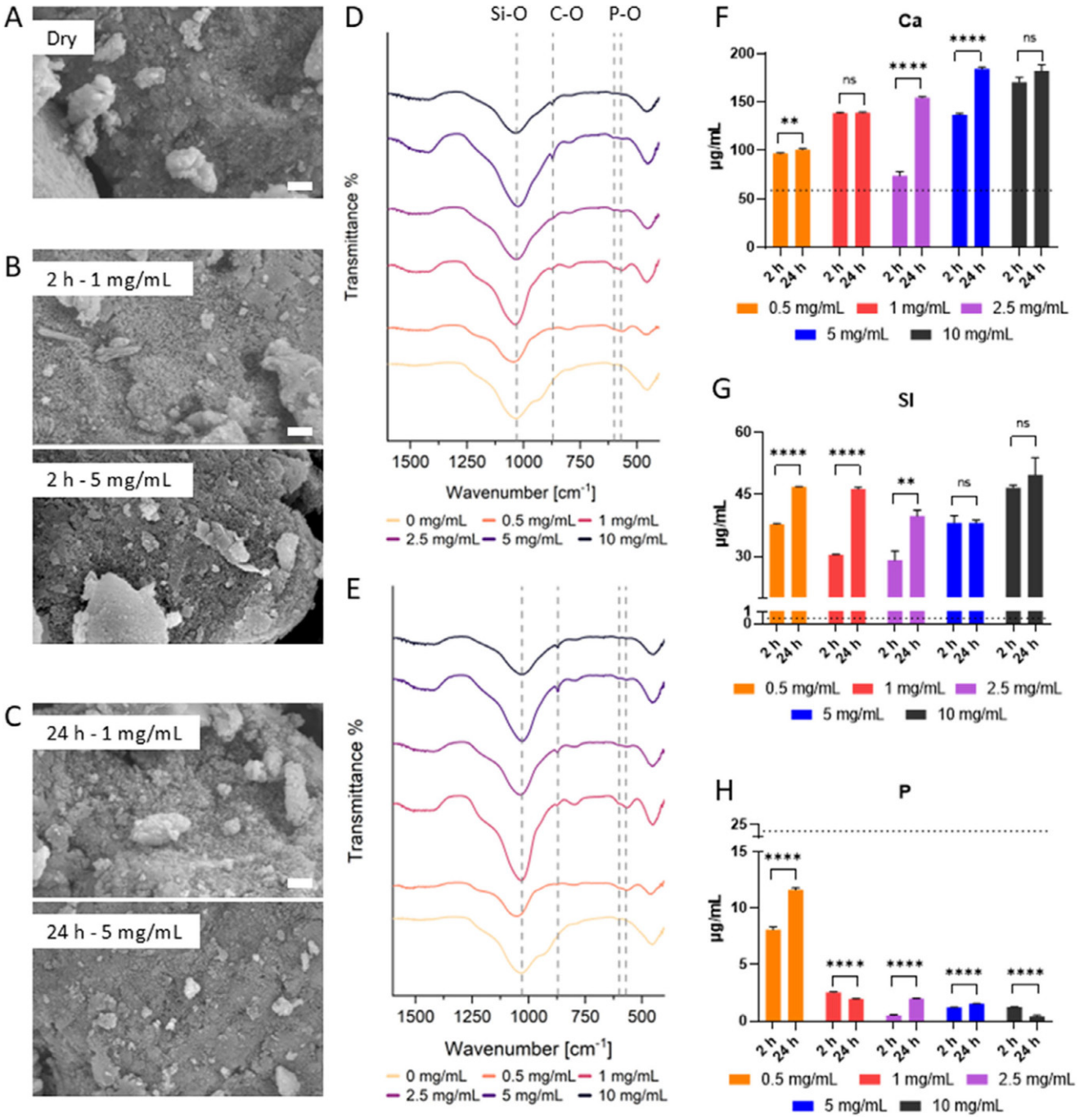

Figure 4. SEM images of dry BG58S A) and after exposure to cell culture medium for 2 h B) and 24 h C) at a concentration of 1 (top) and 5 mg mL^{-1} (bottom). Scale bar is 200 nm. FT-IR spectra of BG58S powder after exposure to cell culture medium for 2 D) and 24 E) h at different concentrations (0.5, 1, 2.5, 5, 10 mg mL^{-1}). Dashed lines indicate: P—O bend at 571 and 603 cm^{-1}, C—O stretch at 870 cm^{-1}, Si—O stretch at 1030 cm^{-1}. ICP analysis of cell culture medium conditioned with 0.5, 1, 2.5, 5, and 10 mg mL^{-1} of BG58S for 2 and 24 h for calcium F), silicon G) and phosphorus H). The dashed lines represent the basal ion concentrations in the ECGM. Data ($n = 3$) are presented as mean ± SD. Non-significant (ns), $p > 0.05$, ** $p \leq 0.01$, **** $p \leq 0.0001$.

organization, whereas on control samples (H) angiogenesis was completed only after 24 h.

We then hypothesized that this enhanced tube formation performance might again be attributable to Ca ions and Si species present in the conditioned medium via the preferential activation of genes involved in the process, especially those mediating cell adhesion, interaction, migration, and ECM remodeling.[34,48,49] Gene expression of platelet endothelial cell adhesion molecule (CD31), vascular endothelial cadherin (VE-Cadherin), vascular endothelial growth factor receptor 2 (VEGFR-2), and matrix

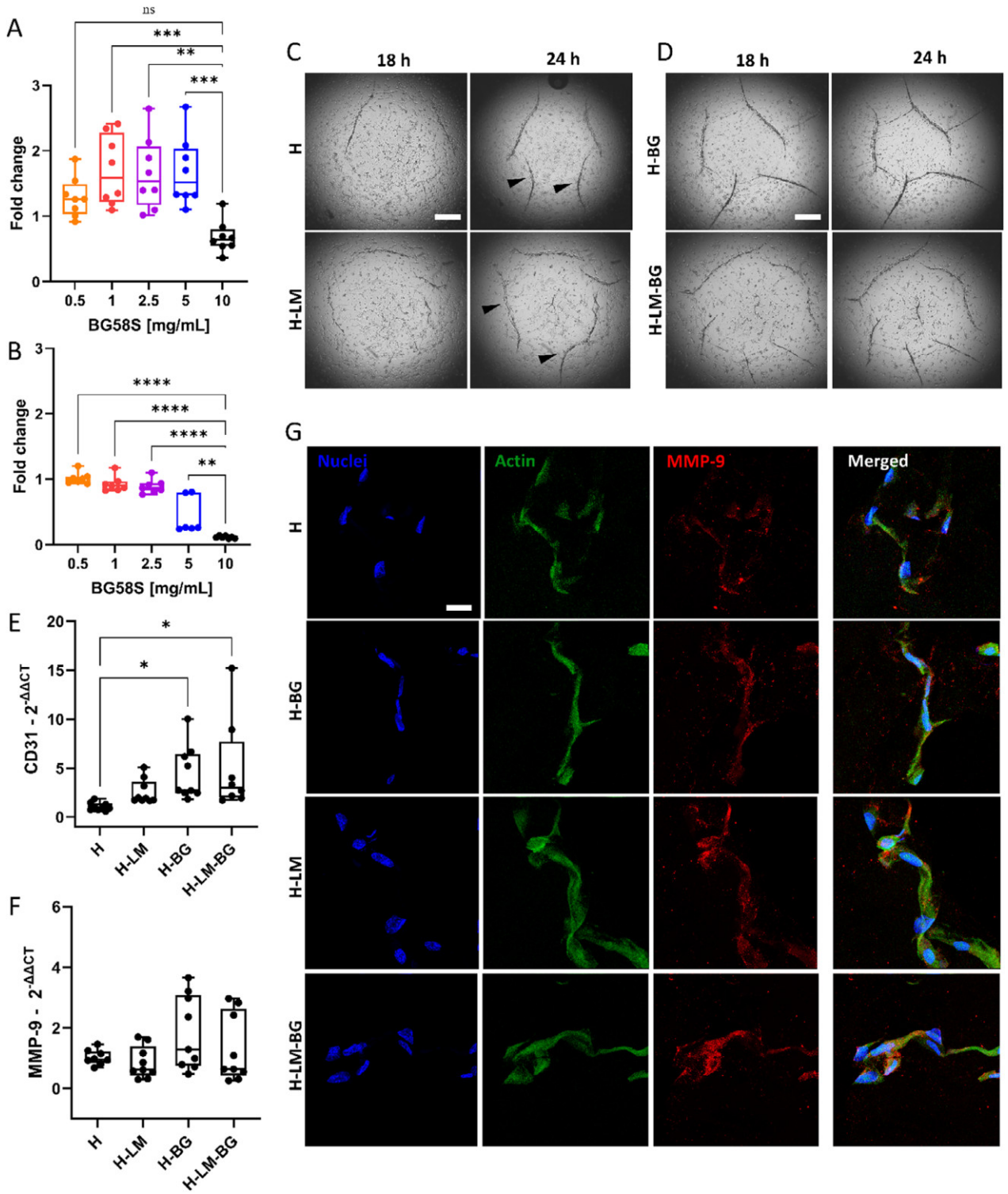

Figure 5. Effect on ECs viability with medium conditioned with increasing concentrations (from 0.5 to 10 mg mL^{-1}) of BG58S for 2 h A) and 24 h B). BG58S effect on ECs angiogenesis onto H-0.5 hydrogels. C) Phase contrast images of ECs tube formation assay on pristine hydrogel (H) (top) and with laminin coating (H-LM) (bottom) after 18 (left) and 24 (right) hours from seeding, and D) with the addition of culture medium conditioned for 2 h with 5 mg mL^{-1} of BG58S. Black arrows indicate new tubule morphogenesis. Gene expression analysis of CD31 E) and MMP-9 F) obtained through qPCR after 24 h from seeding. Data are presented as fold change relative to H calculated with the $2^{-\Delta\Delta CT}$ method. G) Immunofluorescence staining of MMP-9 at 24 h from seeding for H, H-BG, H-LM, and H-LM-BG samples. Counterstain with DAPI (nuclei) and phalloidin-FITC (actin). Scale bar is 500 µm in C and D and 20 µm in G. In the box plots the median is shown as a black line; boxes represent the 25th to 75th percentiles and whiskers extend from the minimum to the maximum values. Data (n = 3) are presented as individual values. Non-significant (ns), $p > 0.05$, * $p \leq 0.05$, ** $p \leq 0.01$, *** $p \leq 0.001$, **** $p \leq 0.0001$.

metalloproteinases 9 (MMP-9) was thus analyzed with qPCR (Figure 5E,F; Figure S6, Supporting Information).[50–52] Interestingly, CD31 turned out to be upregulated (5-fold change) in H-BG and H-LM-BG, as well as VE-Cadherin (2.5-fold change in H-BG). VEGFR-2 was also upregulated in H-LM-BG (2-fold change). Finally, MMP-9 expression levels had a nearly 2-fold increase in the H-BG conditions.

ECs production of MMP-9 could also be visualized through immunofluorescence. These enzymes are in fact engaged in matrix remodeling in order to ECs to sprout and generate new capillaries.[18] Figure 5G shows MMP-9 both on the cell membrane and in the nearby extracellular space, attesting that the molecular machinery for ECM degradation was active in all conditions. However, a burst in MMP-9 signal (red channel) (Figure S7, Supporting Information) was observed when ECs were cultivated in the presence of BG58S-conditioned medium and/or the LM coating, suggesting a further post-transcriptional control of MMP-9 expression.

Taken together, these results attested the ability of BG58S to boost tube formation morphogenesis by triggering multiple signal transduction pathways, in particular by promoting the expression of endothelial junction-associated molecules and the secretion of matrix remodeling enzymes. The use of inorganic agents in GAG-based instructive biomaterials for angiogenesis could therefore bypass some drawbacks related to growth factors delivery (e.g., short half-life and high concentration), leading to a faster approval from the FDA and therefore, a smoother clinical translation.[31]

3. Conclusion

In this study, we successfully developed and characterized a novel, growth factor-free hydrogel system composed of adhesive proteins (GEL and LM) and negatively charged GAGs (CS) capable of interacting with charged species (VEGF and cations), demonstrating its significant potential to promote in vitro angiogenesis.

By precisely tuning the material Young's Modulus by changing the hydrogel crosslinking degree, it was observed a marked enhancement in ECs attachment and migration ability on softer substrates (H-0.5) (γ = 50 %; E ≈80 Pa), which is a critical early step of the blood vessel formation mechanism. Furthermore, tube formation assay on H-0.5 formulation outperformed commercial ECM extracts (e.g., Matrigel) in terms of ECs tubes' size and stability over time.

Crucially, we demonstrated that the released species of BG58S, specifically of Ca and Si ions, could act as potent angiogenic promoters. Indeed, the incorporation of these inorganic ions into the culture medium not only improved ECs viability but also significantly accelerated the kinetics of tube formation onto hydrogels, achieving results comparable to those typically requiring exogenous growth factor supplementation (i.e., VEGF) above physiological concentrations.

Last, qPCR experiments attested an upregulation of genes encoding for endothelial-specific adhesion molecules (CD31 and VE-Cadherin), cell proliferation, survival and migration (VEGFR-2), and ECM remodeling (MMP-9), while immunofluorescence staining proved an increased localization of MMP-9 on both the ECs membrane and in the nearby extracellular space when culture medium was conditioned with BG58S and/or the hydrogel's surface was covered with LM.

The proposed strategy involving the dual use of sulfated GAG-based hydrogels and BG58S dissolution products to boost angiogenesis represents a substantial advancement in the field of tissue engineering. We believe that this innovative approach offers a highly promising and valuable strategy to overcome the persistent challenge of vascularizing 3D cellular constructs in vitro, paving the way for the successful clinical translation of engineered tissues and organs.

4. Experimental Section

Materials: CS (Mw 30000; Purity >90%; Biosynth), gelatin type A (GEL), 4arm-polyethileneglycole-maleimide (4arm-PEG10k-Maleimide) (Mn 10000), 5-methylfurfural, 5-methylfurfurylamine (TCI), sodium cyanoborohydride ($NaBH_3CN$), mouse LM, VEGF, BG58S powder (60 mol % SiO_2, 36 mol % CaO, 4 mol % P_2O_5; particle size ≤10 µm), Ca (19 051), P (38 338), Si (0 8729) standards for ICP. All reagents were purchased from Merck unless otherwise specified.

Materials Functionalization: GEL and CS were functionalized with 5-methylfurfural and 5-methylfurfurylamine, respectively as previously reported.[53–56] In brief, 100 eq (3.4 mL) of 5-methylfurfural were added to a solution of GEL (1 g in 15 mL of PBS pH 5.5). After 30 min 50 eq (1.2 g) of $NaBH_3CN$ were added, and the mixture was stirred at 40 °C for 24 h. Equivalents were calculated on the total amount of lysine (5–7 % w/w) present in the GEL. To a solution of CS (1 g in 15 mL of MES buffer pH 5.5), 1 eq of EDC and 1 eq of NHS (0.4 and 0.2 g) were added in this order. After 30 min 1.5 eq (0.3 mL) of 5-methylfurfurilammine were added drop by drop and stirred overnight at 40 °C. Equivalents were calculated on the total amount of COOH groups present in CS.

Solutions were dialyzed against a NaCl solution (0.1 M) for 1 day, followed by distilled water for 4 days, using 14 and 1 kDa dialysis membranes for functionalized GEL and CS, respectively. The dialyzed solutions were freeze-dried and kept under vacuum at −20 °C until usage.

The degree of functionalization (DoF) was calculated with ^{1}H NMR spectroscopy using the software MNova (Mestrelab research).

Hydrogels Crosslinking: GEL-5MF, CS-5MF, and 4arm-PEG10k-Maleimide were dissolved in PBS (pH 7.4) separately at a concentration of 100 mg mL^{-1} and were kept at the thermomixer (37 °C, 1200 rpm) until complete dissolution. Materials were then diluted and mixed to generate hydrogels with different GEL-5MF:CS-5MF % w/w ratios (i.e., 2.5:0.5, 2:1, 0.5:2.5) and crosslinking degrees (i.e., 100% and 50%). γ % was calculated considering the DoF of GEL-5MF and CS-5MF. Hydrogels were always kept overnight in incubator (37 °C, 5 % CO_2, 100 % humidity) to allow full crosslinking.

Rheological Analysis: A 2 mL of hydrogel formulations were crosslinked in Eppendorf. Rheological measurements were performed with a rheometer (MCR 92e, Anton Paar), using a parallel-plate geometry with a diameter of 50 mm and gap height of 1 mm. Frequency sweeps analysis (frequency from 0.1 to 100 Hz; shear strain = 1 %; T = 37 °C) were used to evaluate G′ and G″.

Hydrogels Physicochemical Characterization: GEL-5MF and CS-5MF were diluted to 20 and 10 mg mL^{-1}, respectively (GEL-5MF:CS-5MF w/w % ratio 2:1), whereas 4arm-PEG10k-Maleimide was diluted either to 22 or 11 mg mL^{-1} in order to obtain a crosslinking degree (γ of 100 (H-1) and 50 % (H-0.5).

H-1 and H-0.5 hydrogels were prepared in cylindrical molds (height = 10 mm; diameter = 5 mm).

Hydrogels were lyophilized for analysis at scanning electron microscopy (SEM) and Fourier transform infrared (FT-IR) spectroscopy. SEM images were taken at 5 kV and prior graphite sputtering (ZEISS Gemini 500 field emission HR-SEM). FT-IR spectra were recorded in attenuated total reflection (ATR) mode from 4000 to 550 cm^{-1} (4 cm^{-1} resolution, 32 scans) (PerkinElmer Spectrum 100).

Hydrogels employed for calculating weight loss (W %) measurements were imbibed in PBS (pH 7.4) in cell culture conditions (37 °C, 5 % CO_2, 100 % humidity). W % was calculated as follows:

$$W\,\% = \frac{Wf - Wi}{Wi} \cdot 100 \quad (1)$$

where W_f is the weight of the hydrogel at desired timepoint and W_i is the weight of the hydrogel post synthesis.

Hydrogels employed for calculating gel fraction % were dried in the oven at 40 °C for 4 h and then imbibed in PBS (pH 7.4) in cell culture conditions overnight. Gel fraction % was calculated as follows:

$$\text{Gel fraction}\,\% = \frac{Ws}{Wd} \cdot 100 \quad (2)$$

where *Ws* is the weight of the dried hydrogel after swelling and *Wd* is the weight of the dried hydrogel post-synthesis.

Cell Culture: Human umbilical vein endothelial cells (HUVEC) (PromoCell) were cultivated in endothelial cell growth medium (ECGM) (PromoCell) supplemented with Supplementpack aliquots (PromoCell). Penicillin-streptomycin (1 % v/v) (Euroclone) and Amphotericin B (1 % v/v) (Euroclone) were also added to the medium. Cells were maintained at 80–90% confluency. HUVEC were used between passage 5 and 8 for all experiments as recommended.[14]

Tube Formation Assay on Hydrogels: Materials were weighed and sterilized for 30 minutes under UV light. Then, 50 µL of H-1 and H-0.5 hydrogels were prepared into 96-well plates and were then left in incubator overnight.

Different conditions were tested, namely: H-1, H-0.5, hydrogels coated with LM (H-LM), and with the addition in the medium of 100 ng mL^{-1} of VEGF (H-LM-VEGF).

H-LM hydrogels were coated with 50 µL of a LM solution to reach a final coverage of 5 µg cm^{-2}. After 1.5 h, LM solution was removed. LM coating was confirmed by labelling LM with a fluorescent NHS tag (DyLight 488 NHS Ester, Thermo Fisher Scientific).

HUVEC were seeded onto hydrogels (45000 cells cm^{-2}) in a total volume of 100 µL. After 2 h from seeding, another 100 µL of medium was added to the culture.

Images were taken at different timepoints (6 h and 24 h from seeding) by phase contrast and fluorescence microscopy. For fluorescence microscopy, cells were either stained directly in the culture for 30 min with 100 µL of live-dead solution (Calcein-AM 2 µM; Propidium iodide 4 µM) (Thermo Fisher Scientific) or fixed with a paraformaldehyde solution (4 % v/v), permeabilized with Triton X-100 (0.1 % v/v), and stained with 25 µL of DAPI and 25 µL of phalloidin-FITC solutions. Phase contrast images were used to quantify tube length, tube width and cell circularity with the software ImageJ. Region of interest (ROI) of 322 x 322 µm were used.

AFM Measurements: H-1 and H-0.5 hydrogels were prepared in cylindrical molds (height = 3 mm; diameter = 3 mm). After demolding, samples were transferred into petri dishes for AFM analysis. Measurements were performed in liquid (ECGM) using an atomic force microscope (Nanowizard 4XP, Bruker) equipped with a pyramidal square-based tip (MLCT-BIO Tip E, Bruker Probes). The AFM tip was brought into contact with the hydrogel surface and indented until a force setpoint of 0.75 nN was reached. The tip position was then held constant for 8 s to allow for stress relaxation, followed by a frequency sweep in a logarithmic scale from 1 to 500 Hz. Each frequency point consisted of 20 sinusoidal cycles with an amplitude of 50 nm. Force data were used to estimate the storage (G′) and the loss (G″) moduli. Additionally, the Young's modulus was extrapolated by fitting the force–distance approach curves with the Hertz–Sneddon model.[57] Analysis was performed in at time 0 and after 24 h of swelling in cell culture medium.

BG58S Characterization After Exposure to Cell Culture Medium: BG58S was added to ECGM to reach the final concentrations of 0.5, 1, 2.5, 5, and 10 mg mL^{-1} and was left shaking at RT. pH was monitored within the first 24 h using a bench pH meter.

At desired timepoints (2 h and 24 h), conditioned medium was centrifuged, filtered (0.45 µm) and diluted by a factor of 10 with 2 M HNO_3 for analysis at inductively coupled plasma-optical emission spectrometry (ICP-OES) (iCAP 6300 Duo, Thermo Scientific). Mixed standards of Ca, Si and P (0, 0.1, 0.2, 0.4, 0.8, 1, 5, 10, and 20 µg mL^{-1}) were prepared in 2 M HNO_3 for the calibration curve and ECGM was used as reference. P was measured in the axial direction of the plasma flame, whereas Ca and Si were measured in the radial direction.

BG58S exposed to culture medium was instead washed with MilliQ water for 1 h on a shaking plate. Then, it was centrifuged to eliminate unbound impurities and dried at 60 °C in the oven for 4 hours before SEM and FT-IR spectroscopy.

For SEM analysis, BG58S powder was previously fixed with conductive adhesive on aluminum supports and coated with graphite. Images were then taken at 5 kV. FT-IR spectra were recorded in attenuated total reflection (ATR) mode from 1600 to 400 cm^{-1} (2 cm^{-1} resolution, 32 scans).

Cell Viability Assessment: Culture medium was conditioned by adding BG58S at different concentrations (1, 2, 5, 10, and 20 mg mL^{-1}) for 2 or 24 h. Medium was then centrifuged (1000 rpm; 5 min) and filtered (0.22 µm). HUVEC were seeded in 96-well plates at a seeding density of 5000 cells/cm^2 in 100 µL of medium. After 4 hours from seeding 100 µL of BG58S-conditioned medium was added to each condition to the following final dilution (0.5, 1, 2.5, 5, and 10 mg mL^{-1}).

After 24 h viability was assessed using AlamarBlue (Invitrogen). To this purpose, medium was removed from wells and AlamarBlue was diluted in fresh medium (1:10) and 200 µL were added to the culture. Cells were left in the incubator for 2 h. Afterwards, 100 µL of medium were transferred to empty wells and absorbance was read at 570 and 600 nm.

Resazurin reduction percentage (r %) was calculated as reported in the datasheet using as negative control the cell culture medium with the diluted (1:10) AlamarBlue reagent but without cells. Viability was reported as a fold change of r % compared to the positive control (HUVEC cultured in medium without BG58S).

BG58S Effects on Angiogenesis: ECGM medium was conditioned with BG58S (10 mg mL^{-1}) for 2 h. Tube formation was performed on H-0.5 samples, with and without LM coating. After 2 h from seeding 100 µL of BG58S-conditioned medium were optionally added to the culture (H-BG and H-LM-BG) to reach a final concentration of 5 mg mL^{-1}. Tube formation was evaluated at 18 and 24 h with phase contrast microscopy, and at 24 h with immunofluorescence and quantitative gene expression analysis.

Immunofluorescence Staining: Cells were fixed with a paraformaldehyde solution (4 % v/v), included in OCT and frozen at -20 °C for cutting at the cryostat. Slices were permeabilized with Triton X-100 (0.1 % v/v), and a bovine serum albumin (BSA) solution (3% w/v) was used for blocking. An anti-MMP-9 primary antibody (SAB5300247, Sigma-Aldrich) (final dilution 0.001 mg mL^{-1}) was left for 2 h at room temperature (RT) and after a secondary antibody (Anti-Mouse CF 568, Sigma-Aldrich) (1:1000 dilution) for 1 h at RT. 100 µL of a 1:1 solution made of DAPI and phalloidin-FITC was used as a counterstain. Finally, a water-soluble mounting medium (Fluoromount-G Mounting Medium) was used to mount stained hydrogels on glass slides.

MMP-9 area coverage % was calculated with the software ImageJ.

Real-Time Polymerase Chain Reaction (qPCR): Hydrogels were minced and transferred in Eppendorf. 1 mL of TRIzol (Invitrogen) was added and samples were stored at −80 °C. After three steps of freeze-thawing, samples were centrifuged (12000 rpm; 5 min; 4 °C) to remove hydrogel fragments. The supernatant was transferred into new Eppendorf, mixed with 200 mL of chloroform, and centrifuged (12000 rpm; 15 min; 4 °C). The aqueous phase was then collected, mixed with 500 mL of isopropanol and left at −20 °C. The day after, samples were centrifuged (12000 rpm; 15 min; 4 °C), the supernatant was discarded, and the precipitated RNA was resuspended in RNase-free water. The RNA concentration and the 260/280 and 260/230 values were measured using a microvolume spectrophotometer (NanoDrop, Thermo Fisher Scientific).

cDNA was synthesized from 200 ng of RNA, using iScript cDNA Synthesis Kit (Bio-Rad), following the manufacturer's protocol. The obtained cDNA was diluted in RNase-free water to a concentration of 2 ng μL^{-1}.

10 µL composed of 2 µL of cDNA (4 ng), 5 µL of Luna Universal qPCR Master Mix (New England Biolabs), and 3 µL of reverse and forward primer

mix (1.25 µM) (Table S2, Supporting Information) were prepared in 96-well reaction plate of 0.1 mL (Applied Biosystems). Finally, qPCR was conducted using a 7900HT system (Thermo Fisher Scientific) with a thermal cycle of 95 °C for 15 s, 55 °C for 15 s, and 60 °C for 30 s. The $2^{-\Delta\Delta Ct}$ method was employed to calculate the relative gene expression, using B2M as the housekeeping gene and H samples as the control group for normalization.

Statistical Analysis: Data were always presented as mean ± standard deviation. Values were averaged from at least three repeated measurements (n = 3). To determine statistical difference between two groups unpaired two-tailed *t*-test was used, whilst comparing three or more groups was done with one-way ANOVA using Tukey's multiple-comparison test. Statistical significance of the data was calculated at 95% ($P < 0.05$) confidence intervals. Non-significant (ns), $p > 0.05$, * $p \leq 0.05$, ** $p \leq 0.01$, *** $p \leq 0.001$, **** $p \leq 0.0001$.

Supporting Information

Supporting Information is available from the Wiley Online Library or from the author.

Acknowledgements

The authors thank Sara Curatolo for assistance with the preparation of the illustrations in Figures 1A and 2A. Ministero dell'Università e della Ricerca (MUR) PNC0000003 CUP BICOCCA B53C22006670001. Ministero della Salute RF-2021-12371959. Ministero dell'Università e della Ricerca (MUR) 2022MY7AZT. Fondazione Cariplo 2024-NAZ-0094 CUP BICOCCA H45E24000440007. Ministero dell'Università e della Ricerca (MUR) 2023-2027 - l. 232/2016, art. 1, commi 314–337. National Institute for Health and Care Research (NIHR) NIHR133314.

Conflict of Interest

The authors declare no conflict of interest.

Data Availability Statement

The data that support the findings of this study are openly available in Zenodo at [https://doi.org/10.5281/zenodo.17777638], reference number 17777637.

Keywords

angiogenesis, bioactive glass, ECM mimics, hydrogel, sulfated glycosaminoglycans, tissue engineering

Received: August 1, 2025
Revised: December 1, 2025
Published online:

[1] T. Hoffman, A. Khademhosseini, R. Langer, *Tissue Eng., Part A* **2019**, *25*, 679.
[2] M. J. Webber, O. F. Khan, S. A. Sydlik, B. C. Tang, R. Langer, *Ann. Biomed. Eng.* **2015**, *43*, 641.
[3] D. Gholobova, L. Terrie, M. Gerard, H. Declercq, L. Thorrez, *Biomaterials* **2020**, *235*, 119708.
[4] D. S. Sparks, S. Saifzadeh, F. M. Savi, C. E. Dlaska, A. Berner, J. Henkel, J. C. Reichert, M. Wullschleger, J. Ren, A. Cipitria, J. A. McGovern, R. Steck, M. Wagels, M. A. Woodruff, M. A. Schuetz, D. W. Hutmacher, *Nat. Protoc.* **2020**, *15*, 877.
[5] S. Dalfino, E. Olaret, M. Piazzoni, P. Savadori, I. Stancu, G. Tartaglia, C. Dolci, L. Moroni, *Tissue Eng., Part A* **2025**, *31*, 13.
[6] B. O. Palsson, S. N. Bhatia, *Tissue Eng.* **2004**, 208.
[7] T. L. Place, F. E. Domann, A. J. Case, *Free Radical Biol. Med.* **2017**, *113*, 311.
[8] F. Iberite, M. Piazzoni, D. Guarnera, F. Iacoponi, S. Locarno, L. Vannozzi, G. Bolchi, F. Boselli, I. Gerges, C. Lenardi, L. Ricotti, *ACS Appl. Bio Mater.* **2023**, *6*, 2712.
[9] S. P. Herbert, D. Y. R. Stainier, *Nat. Rev. Mol. Cell Biol.* **2011**, *12*, 551.
[10] F. Cadamuro, F. Nicotra, L. Russo, *J. Controlled Release* **2023**, *354*, 726.
[11] J. Nicolas, S. Magli, L. Rabbachin, S. Sampaolesi, F. Nicotra, L. Russo, *Biomacromolecules* **2020**, *21*, 1968.
[12] F. Iberite, I. Gerges, L. Vannozzi, A. Marino, M. Piazzoni, T. Santaniello, C. Lenardi, L. Ricotti, *Ann. Biomed. Eng.* **2020**, *48*, 734.
[13] P. S. Briquez, L. E. Clegg, M. M. Martino, F. Mac Gabhann, J. A. Hubbell, *Nat. Rev. Mater.* **2016**, *1*, 15006.
[14] I. Arnaoutova, H. K. Kleinman, *Nat. Protoc.* **2010**, *5*, 628.
[15] S. Yang, J. Graham, J. W. Kahn, E. A. Schwartz, M. E. Gerritsen, *Am. J. Pathol.* **1999**, *155*, 887.
[16] P. Lu, D. Ruan, M. Huang, M.i Tian, K. Zhu, Z. Gan, Z. Xiao, *Signal Transduction Targeted Ther.* **2024**, *9*, 166.
[17] F. Cadamuro, M. Piazzoni, E. Gamba, B. Sonzogni, F. Previdi, F. Nicotra, A. Ferramosca, L. Russo, *Biomater. Adv.* **2025**, *175*, 214323.
[18] R. Kalluri, *Nat. Rev. Cancer* **2003**, *3*, 422.
[19] M. V. Tsurkan, K. Chwalek, S. Prokoph, A. Zieris, K. R. Levental, U. Freudenberg, C. Werner, *Adv. Mater.* **2013**, *25*, 2606.
[20] K. Chwalek, M. V. Tsurkan, U. Freudenberg, C. Werner, *Sci. Rep.* **2014**, *4*, 4.
[21] Y. D. P. Limasale, M. Fusenig, M. Samulowitz, P. Atallah, J. Sievers, N. Dennison, U. Freudenberg, J. Friedrichs, C. Werner, *Adv. Funct. Mater.* **2024**, *34*, 2411475.
[22] Y. D. P. Limasale, P. Atallah, C. Werner, U. Freudenberg, R. Zimmermann, *Adv. Funct. Mater.* **2020**, *30*, 2000068.
[23] S. Kühn, V. Magno, R. Zimmermann, Y. D. P. Limasale, P. Atallah, A. Stoppa, M. J. Männel, J. Thiele, J. Friedrichs, U. Freudenberg, C. Werner, *Adv. Mater.* **2025**, *37*, 2409731.
[24] E. Quinlan, S. Partap, M. M. Azevedo, G. Jell, M. M. Stevens, F. J. O'Brien, *Biomaterials* **2015**, *52*, 358.
[25] S. L. Jan, M. Hayashi, Z. Kasza, I. Eriksson, J. R. Bishop, I. Weibrecht, J. Heldin, K. Holmborn, L. Jakobsson, O. Söderberg, D. Spillmann, J. D. Esko, L. Claesson-Welsh, L. Kjellén, J. Kreuger, *Arterioscler., Thromb., Vasc. Biol.* **2012**, *32*, 1255.
[26] U. Freudenberg, J.-U. Sommer, K. R. Levental, P. B. Welzel, A. Zieris, K. Chwalek, K. Schneider, S. Prokoph, M. Prewitz, R. Dockhorn, C. Werner, *Adv. Funct. Mater.* **2012**, *22*, 1391.
[27] C. Kut, F. Mac Gabhann, A. S. Popel, *Br. J. Cancer* **2007**, *97*, 978.
[28] M. Šalandová, I. A. J. van Hengel, I. Apachitei, A. A. Zadpoor, B. C. J. van der Eerden, L. E. Fratila-Apachitei, *Adv. Healthcare Mater.* **2021**, *10*, 2002254.
[29] L. L. Hench, *J. Mater. Sci.: Mater. Med.* **2006**, *17*, 967.
[30] J. R. Jones, *Acta Biomater.* **2013**, *9*, 4457.
[31] S. Dalfino, P. Savadori, M. Piazzoni, S. T. Connelly, A. B. Giannì, M. Del Fabbro, G. M. Tartaglia, L. Moroni, *Adv. Healthcare Mater.* **2023**, *12*, 2300128.
[32] A. A. Gorustovich, J. A. Roether, A. R. Boccaccini, *Tissue Eng., Part B, Rev.* **2010**, *16*, 199.
[33] J. H. Lee, P. Parthiban, G. Z. Jin, J. C. Knowles, H. W. Kim, *Prog. Mater. Sci.* **2021**, *117*, 100732.
[34] C. Mao, X. Chen, G. Miao, C. Lin, *Biomed. Mater. (Bristol)* **2015**, *10*, 025005.
[35] P. Kastana, E. Choleva, E. Poimenidi, N. Karamanos, K. Sugahara, E. Papadimitriou, *FEBS J.* **2019**, *286*, 2921.
[36] D. Li, C. C. Clark, J. C. Myers, *J. Biol. Chem.* **2000**, *275*, 22339.

[37] F. Orozco, J. Li, U. Ezekiel, Z. Niyazov, L. Floyd, G. M. R. Lima, J. G. M. Winkelman, I. Moreno-Villoslada, F. Picchioni, R. K. Bose, *Eur. Polym. J.* **2020**, *135*, 109882.
[38] C. Nakason, K. Sasdipan, A. Kaesaman, *Iran. Polym. Journal (English Edition)* **2014**, *23*, 1.
[39] I. Arnaoutova, J. George, H. K. Kleinman, G. Benton, *Angiogenesis* **2009**, *12*, 267.
[40] J. Alcaraz, L. Buscemi, M. Grabulosa, X. Trepat, B. Fabry, R. Farré, D. Navajas, *Biophys. J.* **2003**, *84*, 2071.
[41] Y. Lai, Y. Hu, *Soft Matter* **2018**, *14*, 2619.
[42] R. Subramani, A. Izquierdo-Alvarez, P. Bhattacharya, M. Meerts, P. Moldenaers, H. Ramon, H. Van Oosterwyck, *Front. Mater.* **2020**, *7*, 212.
[43] C. F. Guimarães, L. Gasperini, A. P. Marques, R. L. Reis, *Nat. Rev. Mater.* **2020**, *5*, 351.
[44] M. D. A. Norman, S. A. Ferreira, G. M. Jowett, L. Bozec, E. Gentleman, *Nat. Protoc.* **2021**, *16*, 2418.
[45] P. Sepulveda, J. R. Jones, L. L. Hench, *J. Biomed. Mater. Res.* **2002**, *61*, 301.
[46] J. R. Jones, P. Sepulveda, L. L. Hench, *J. Biomed. Mater. Res.* **2001**, *58*, 720.
[47] D. M. M. dos Santos, G. L. de Oliveira, D. C. F. Soares, M. V. Maia, F. Tallia, A. Heyraud, J. Jones, M. Houmard, E. H. M. Nunes, *Mater. Chem. Phys.* **2025**, *332*, 130308.
[48] F. Monte, T. Cebe, D. Ripperger, F. Ighani, H. V. Kojouharov, B. M. Chen, H. K. W. Kim, P. B. Aswath, V. G. Varanasi, *J. Tissue Eng. Regener. Med.* **2018**, *12*, 2203.
[49] Y. Zhu, X. Zhang, G. Chang, S. Deng, H. F. Chan, *Adv. Mater.* **2025**, *37*, 2312964.
[50] H. M. DeLisser, M. Christofidou-Solomidou, R. M. Strieter, M. D. Burdick, C. S. Robinson, R. S. Wexler, J. S. Kerr, C. Garlanda, J. R. Merwin, J. A. Madri, S. M. Albelda, *Am. J. Pathol.* **1997**, *151*, 671.
[51] C. Lee, M. J. Kim, A. Kumar, H. W. Lee, Y. Yang, Y. Kim, *Signal Transduction Targeted Ther.* **2025**, *10*, 170.
[52] T. L. Haas, J. A. Madri, *Trends Cardiovasc. Med.* **1999**, *9*, 70.
[53] S. Magli, G. B. Rossi, G. Risi, S. Bertini, C. Cosentino, L. Crippa, E. Ballarini, G. Cavaletti, L. Piazza, E. Masseroni, F. Nicotra, L. Russo, *Front. Chem.* **2020**, *8*, 524.
[54] L. Rossi, C. Pignatelli, K. Kerekes, F. Cadamuro, A. Dinnyés, F. Lindheimer, J. Seissler, M. Lindner, S. Ziegler, P. Bartenstein, Y. Qiu, J. Kovács-Kocsi, Z. Körhegyi, M. Bodnár, E. Fazekas, E. Prépost, F. Nicotra, L. Russo, *Carbohydr. Polym. Technol. Appl.* **2024**, *8*, 100610.
[55] F. Cadamuro, L. Russo, F. Nicotra, *Eur. J. Org. Chem.* **2021**, *2021*, 374.
[56] S. Magli, L. Rossi, C. Consentino, S. Bertini, F. Nicotra, L. Russo, *Biomolecules* **2021**, *11*, 683.
[57] M. Sampietro, V. Cassina, D. Salerno, F. Barbaglio, E. Buglione, C. A. Marrano, R. Campanile, L. Scarfò, D. Biedenweg, B. Fregin, M. Zamai, A. Díaz Torres, V. Labrador Cantarero, P. Ghia, O. Otto, F. Mantegazza, V. R. Caiolfa, C. Scielzo, *HemaSphere* **2023**, *7*, 931.

Supporting Information

Endothelial Cells Angiogenesis in Sulfated Glycosaminoglycan (GAG) Hydrogels Enhanced by Bioactive Glass-Released Ions

Authors:

Marco Piazzoni[1], Ilaria Borghi[1], Francesca Cadamuro[1], Sophia Dalfino[2,3,4], Riccardo Campanile[5], Sofia Nizzolo[6], Valeria Cassina[5], Francesca Tallia[7], Julian R. Jones[7], Francesco Mantegazza[5], Sabrina Bertini[6], Lorenzo Moroni[2], Francesco Nicotra[1], Laura Russo[1,8].

1) ^{1}H NMR spectra of functionalized gelatin and chondroitin sulphate

^{1}H NMR were performed using a Varian Mercury 400 M Hz with a pulse angle of 90°C and a relaxion delay of 2 sec. Sample were dissolved at a concentration of 6 mg/mL in D_2O with 0.05 % (w/w %) TMSP standard.

The spectra were elaborated with MNova (Mestrelab research) software. The moles of the linked moiety (5-methylfuran - 5MF) were calculated by integration of the furan protons using TMSP as reference. The degree of functionalization (DoF) was then calculated as follows:

$$\frac{nX}{nP} \cdot 100$$

where nX are the moles of 5MF and nP are the moles of the repeating units of chondroitin sulfate (MW 480.35 g/mol) or of the lysine of gelatin (MW 146.19).

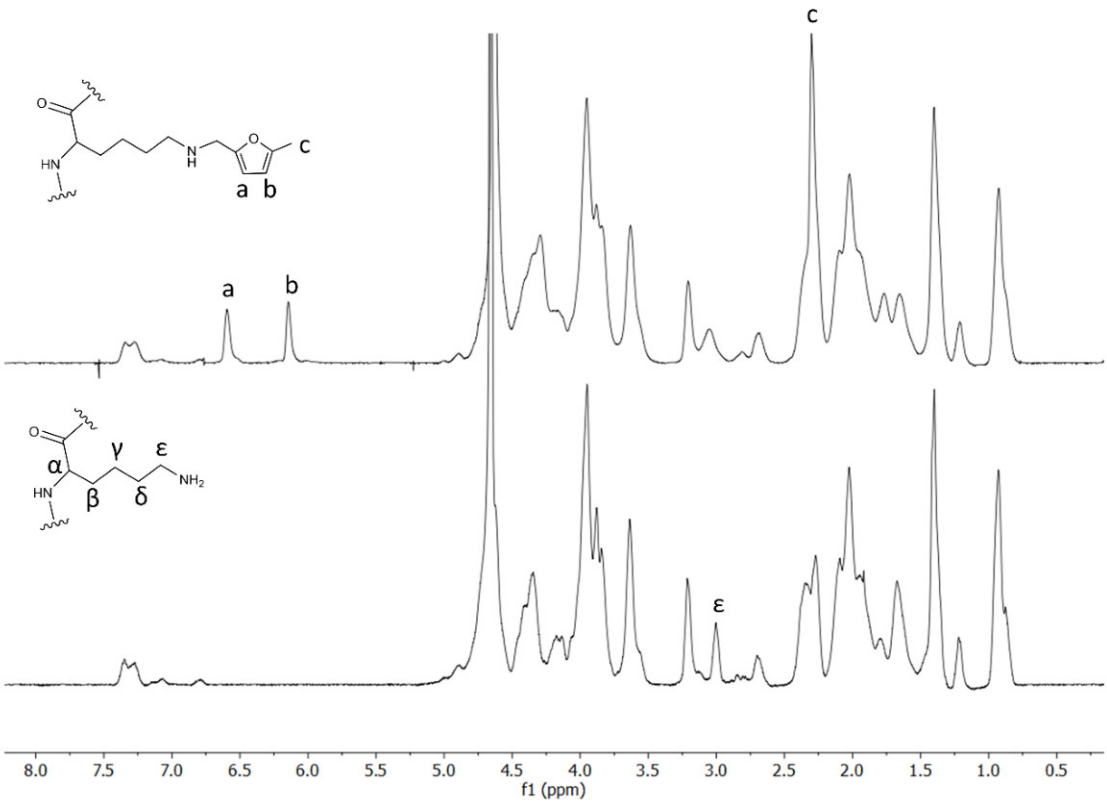

Figure S1: The ^{1}H NMR spectra of gelatin (bottom) and its derivative functionalized with 5-methylfurfural (top). The successful functionalization is evidenced by the appearance of new signals at 6.2 and 6.5 ppm in the top spectrum, corresponding to the furan ring protons (Ha and Hb) of the 5-methylfurfural moiety. Additionally, a notable decrease in the signal at 3.0 ppm—assigned to the ε-CH_2 protons of lysine residue—and the new signal at 2.4 ppm, attributed to the methyl group protons (Hc), further confirm the modification. Integration of the Ha and Hb peaks suggests complete (100%) functionalization of the lysine residues.

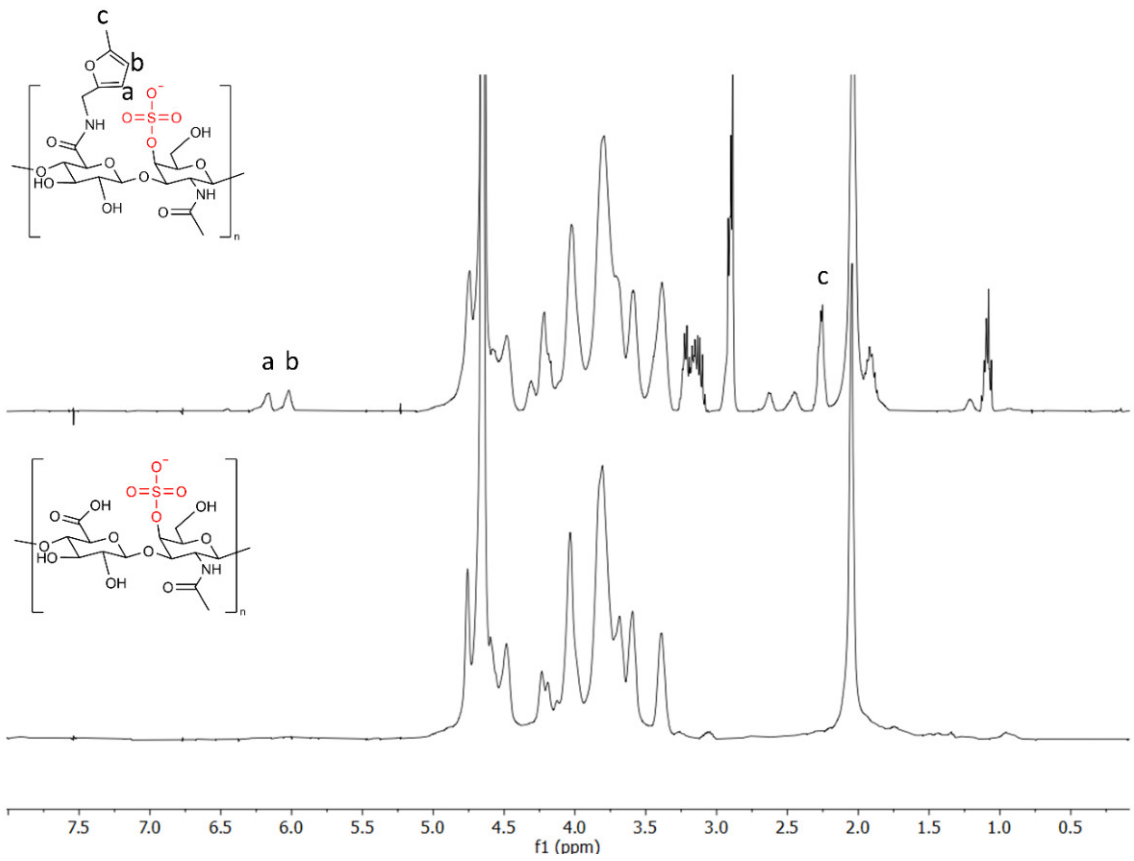

Figure S2: The ^{1}H NMR spectra of chondroitin sulfate (bottom) and its derivative functionalized with 5-methylfurfurylamine (top). The presence of characteristic signals at 6.0 and 6.2 ppm in the top spectrum, corresponding to the furan ring protons (Ha and Hb), along with the signal at 2.2 ppm attributed to the methyl group protons (Hc), confirms the successful functionalization. The DoF was determined to be ~ 13%, based on the integration of the Ha and Hb signals compared to the signal at 1.9–2.0 ppm, which corresponds to the methyl protons of the N-acetyl groups naturally present in chondroitin sulfate.

2) Determination of the molecular weight with High Performance Size Exclusion Chromatography with Triple Detector Array (HP-SEC/TDA)

The molecular weight (Mw) of CS was determined using a HP-SEC/TDA Viscotek system (model TDA305, Malvern Panalytical) equipped with refractive index (RI), right-angle light scattering (RALS), and differential pressure (DP) viscometer detectors. Measurement was performed at 40 °C with a flow rate of 0.6 mL/min, using two TSK-GMPWXL columns (13 µm, 7 mm ID × 30 cm L, Tosoh Bioscience) connected in series. The system was calibrated with certified Pullulan standards (PolyCAL-PullulanSTD, Malvern Panalytical). CS and CS-5MF were dissolved in the mobile phase (0.1 M $NaNO_3$ and 0.05 % NaN_3) at a concentration of 10 mg/mL and 5 mg/mL, respectively and injected in duplicate. Chromatograms were analyzed using OmniSEC software (version 4.6.2), applying an experimentally determined refractive index increment (dn/dc) of 0.125.

For the determination of molecular weight (Mw), the main peak corresponding to CS was integrated. Based on the refractive index (RI) area, the CS content was found to be between 86 % and 95 % for the functionalized and non-functionalized samples, respectively. The functionalization led to an increase in Mw, intrinsic viscosity (η) and hydrodynamic radius (Rh), which consists of a larger, more extended macromolecular structure. Additionally, the polydispersity index (Mw/Mn) also increased. A significant decrease in the Mark–Houwink α parameter was observed, indicating a transition from a rigid rod-like structure to a flexible random coil.

Table S1: Average results from HP-SEC/TDA:

Sample	Mw (kDa)	Mn (kDa)	Mw/Mn	η (dL/g)	Rh (nm)	a	logK	Recovery %
CS	30.8	24.1	1.3	0.50	6.03	1.09	-5.19	95.5
CS-5MF	53.4	35.2	1.5	0.55	7.34	0.81	-4.08	86.4

Mw, weight-average molecular weight; Mn: number-average molecular weight; Mn/Mw: molecular-weight dispersity; Rh: hydrodynamic radius; η: viscosity; *a* and logK: Mark–Houwink costant; Recovery: The percentage of the sample recovered after chromatography, calculated by comparing the refractive index (RI) area of the eluted sample to that of the injected sample.

3) Determining degree of sulfation using conductometric titration

The analysis was carried out using an automated titrator (Titrando 888, Metrohm) coupled with a Metrohm 801 magnetic stirrer and a Metrohm 712 Conductometer equipped with a conductivity cell with a cell constant of 0.76. An aqueous solution of CS (80 mg in 80 mL), previously treated with Amberlite IR-120 (H^+) resin, was titrated by adding point by point 0.15 µL of 0.1 M NaOH. The conductivity value was recorded after 160 s-200 s of every aliquot addition to reach the solution equilibrium. The obtained titration curves were mathematically processed as described by Casu and Gennaro. [1]

4) Heteronuclear single quantum coherence (HSQC)

The 4-sulfate to 6-sulfate (4S/6S) ratio, determined using HSQC experiment and the method reported by Mauri et al. [2] HSQC experiment was performed at 303 K using a Bruker AVANCE NEO spectrometer operating at a proton frequency of 500 MHz, equipped with a 5 mm TCI cryoprobe. HSQC spectra were acquired using the Bruker hsqcetgpsisp2.2 pulse sequence, with the following acquisition parameters: 32 scans, 2 s of relaxation delay, 1k of time domain, and a spectral width of 10 ppm (F2) and 80 ppm (F1) with the transmitter offset at 4.7 ppm (F2) and 80 ppm (F1). The 4S/6S sulfation patter was determined as the ratio of HSQC between the cross-peaks area of the anomeric proton of 4-O- sulfated glucuronic acid (U1 4S) and the anomeric proton of 6-O- sulfated glucuronic acid (U1 6S), as reported in the following formula:

$$4S/6S = \frac{\text{Signal intensity (U1 4S)}}{\text{Signal intensity (U1 6S)}}$$

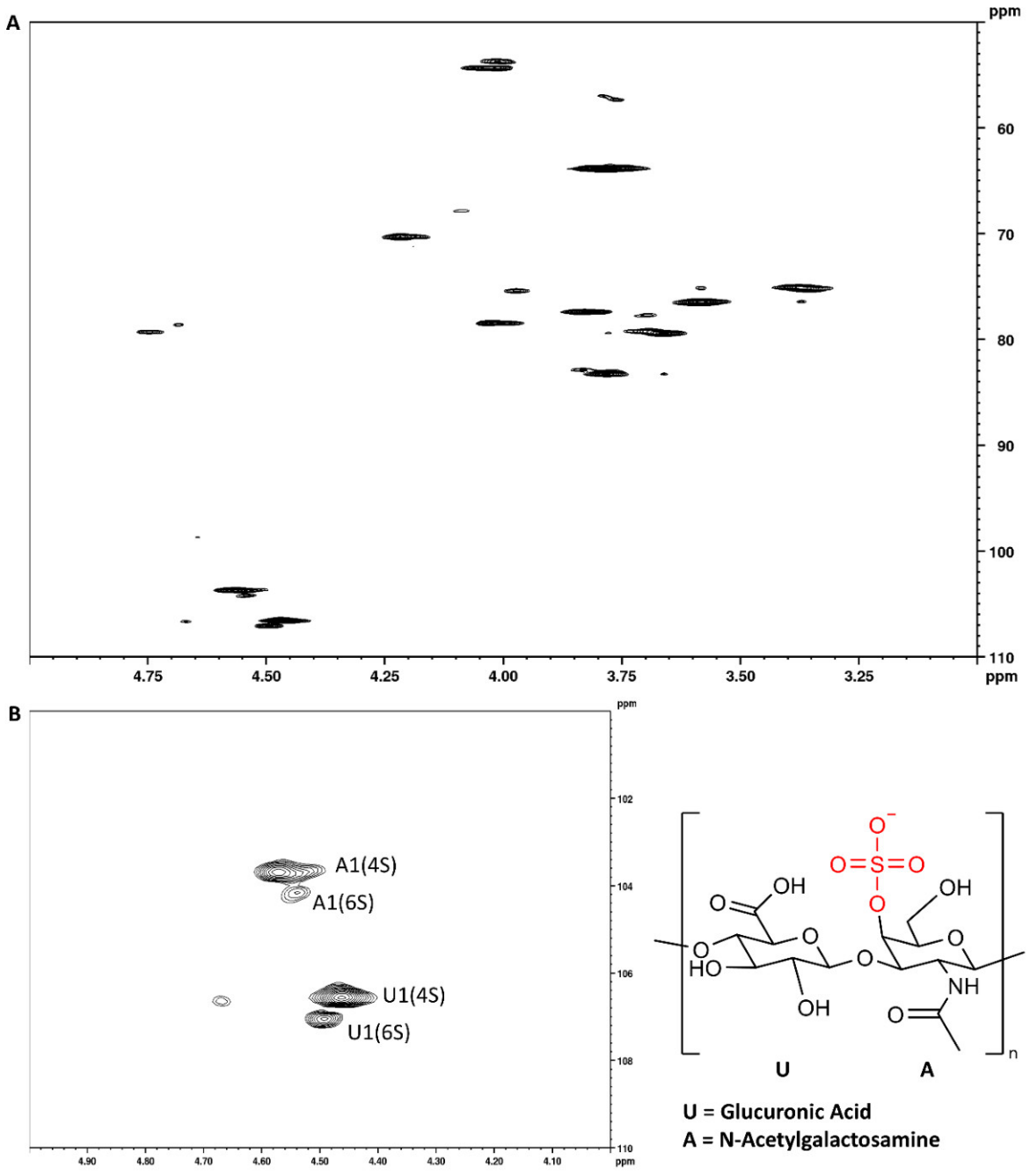

Figure S3: A) ^{1}H -^{13}C HSQC spectrum of CS. The signals in the region between 110- 50 and 5.0-3.0 ppm are in agreement with data reported by Mucci et al. B) ^{1}H -^{13}C HSQC anomeric region of the CS, highlighting the signals used for calculation of the 4S/6S sulfation ratio.

5**) Labelling laminin with NHS-dylight488**

100 µL of LM (1.6 mg/mL) were added to Vivaspin (cutoff 30 kDa) and were centrifuged (15' at 4,000 rpm) to eliminate tris-HCl buffer trace. LM was then resuspended in 100 µL of PBS (pH 7.4). Afterwards, 4 uL of NHS-DyLight 488 (a 40 times molar excess) were added and left reacting with amino groups present on LM for 1 h (RT, in the dark). Finally, LM conjugated with DyLight 488 (LM488) was centrifuged (15'at 4,000 rpm) 3 times and was resuspended in 100 µL of PBS (pH 7.4). 50 µL of H-1 and H0.5 hydrogels were prepared in 96-well plate and fluorescent LM were cast on top of samples (H-LM488) and were left in incubator for 1.5 h. Afterwards unbound LM was aspirated and samples were washed with PBS 3 times. Images were taken at the fluorescence microscope. ImageJ software was used to calculate the gray value compared to the control.

6) Screening of hydrogel formulations for HUVEC tube formation

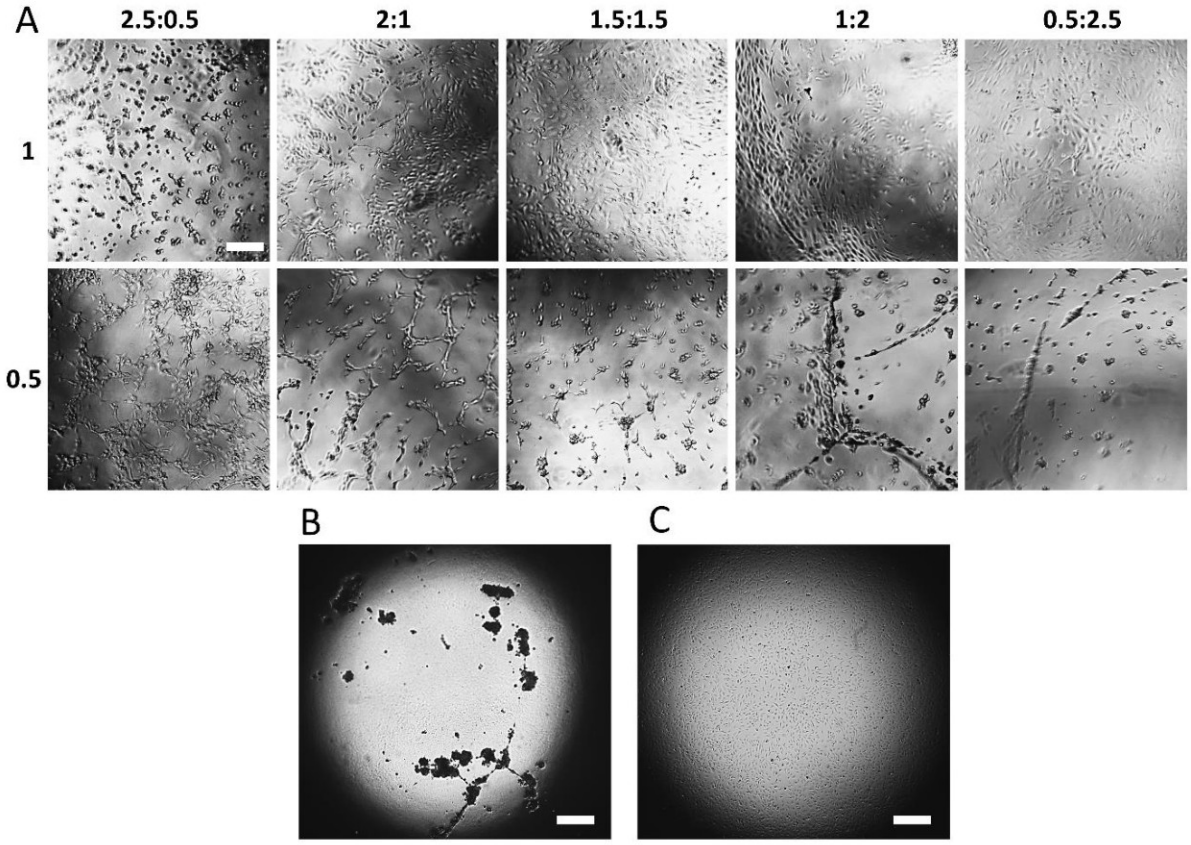

Figure S4: A) Screening of hydrogel formulations. From left to right is changed the % w/w ratios of GEL-5MF to CS-5MF (2.5:0.5, 2:1, 1.5:1.5, 1:2, 0.5:2.5), whereas from top to bottom the crosslinking degree (γ) obtained with 4arm-PEG10k-Maleimide (1 and 0.5). B) HUVEC tube formation assay on Matrigel after and 24 h from seeding. C) HUVEC on empty 96-weel plate. Scale bar is 200 μm in A and 500 μm in B and C.

7) pH of cell culture medium after exposure to BG58S

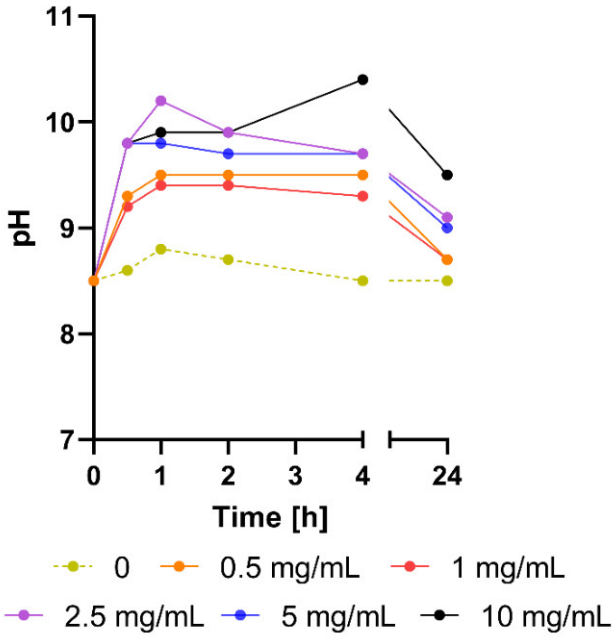

Figure S5: pH measurements of cell culture medium conditioned with 0.5, 1, 2.5, 5 and 10 mg/mL of BG58S over a period of 24 h.

8) Gene expression analysis of VE-Cadherin and VEGFR-2

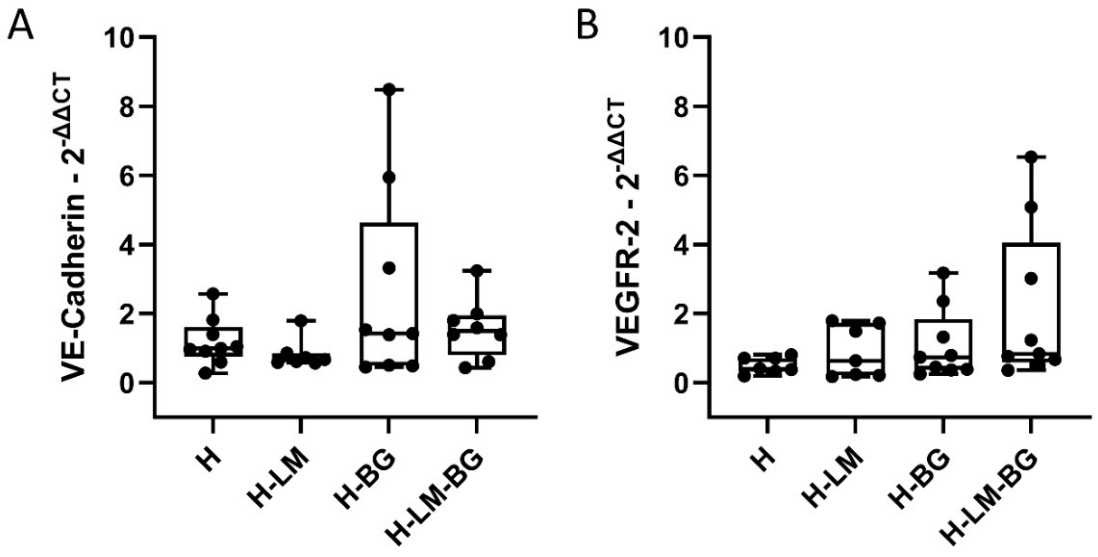

Figure S6: $2^{-\Delta\Delta CT}$ values of vascular endothelial cadherin (VE-Cadherin) (A) and vascular endothelial growth factor receptor 2 (VEGFR-2) (B) at 24 h.

Table S2: forward and reverse primers' sequences used for qPCR.

Gene	Forward	Reverse
B2M	ACAAAGTCACATGGTTCACA	GACTTGTCTTTCAGCAAGGA
MMP9	GGGACGCAGACATCGTCATC	TCGTCATCGTCGAAATGGGC
CD31	GAAAGCCAAGGCCAAGCAGATG	TTTCCACGGCATCAGGGACAG
VECAD	TCATGTATCGGAGGTCGATGGT	GGCATCATCAAGCCCATGAA
KDR	CCCTACAAGACCAAAGGGGCAC	GCGATGCCAAGAACTCCATGC

9) Area coverage % of MMP-9

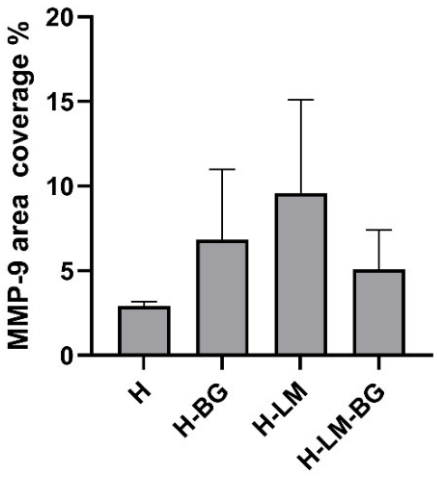

Figure S7: Area coverage % of MMP-9 calculated with ImageJ from immunofluorescence images at 24 h from seeding.

References

[1] B. Casu, U. Gennaro, *Carbohydr. Res.* **1975**, *39*, 168.

[2] L. Mauri, M. Marinozzi, G. Mazzini, R. E. Kolinski, M. Karfunkle, D. A. Keire, M. Guerrini, *Molecules* **2017**, *22*.

Methods 236 (2025) 1–9

Contents lists available at ScienceDirect

Methods

journal homepage: www.elsevier.com/locate/ymeth

Production of AFM wedged cantilevers for stress-relaxation experiments: Uniaxial loading of soft, spherical cells

Riccardo Campanile [a], Jonne Helenius [b], Cristina Scielzo [c], Lydia Scarfò [d,e], Domenico Salerno [a], Mario Bossi [a], Marta Falappi [a], Alessia Saponara [a], Daniel J. Müller [b], Francesco Mantegazza [a], Valeria Cassina [a,*]

[a] School of Medicine and Surgery, BioNanoMedicine Center NANOMIB, Università di Milano-Bicocca, Vedano al Lambro, Italy
[b] Department of Biosystems Science and Engineering, ETH Zurich, Basel, Switzerland
[c] Division of Experimental Oncology, Malignant B cells biology and 3D modelling Unit, IRCCS Ospedale San Raffaele Milano, Italy
[d] School of Medicine, Università Vita-Salute San Raffaele, Milano, Italy
[e] Division of Experimental oncology, B-cell neoplasia Unit and Strategic Research Program on CLL, IRCCS Ospedale San Raffaele, Milano, Italy

ARTICLE INFO

Keywords:
AFM
Cantilever
Cantilever modification
Cell shape
Cell mechanics
Confinement
Stress-relaxation
Spherical cell
Leukemia

ABSTRACT

The fabrication of wedge-shaped cantilevers for Atomic Force Microscopy (AFM) remains a critical yet challenging task, particularly when precision and efficiency are required. In this study, we present a streamlined protocol for producing these wedges using NOA63 UV-curing polymer, which simplifies the process and eliminates the need for dedicated equipment. Our method reduces preparation time while maintaining the mechanical properties of the cantilevers, in line with the manufacturer's specifications. We demonstrate the effectiveness of our wedged cantilevers in stress-relaxation experiments performed by means of AFM and confocal microscopy on primary Chronic Lymphocytic Leukemia cells and the MEC1 cell line. These experiments highlight the effectiveness of using modified cantilevers to consistently apply precise uniaxial loading to soft, spherical cells. This technique offers a marked improvement in fabrication speed and operational ease compared to traditional methods, without compromising the accuracy or performance of the measurements. This protocol is not only time-saving, but also adaptable for use in a wide range of biological applications, making it a valuable tool for AFM-based research in cellular mechanics.

1. Introduction

The ability of living cells to maintain specific mechanical properties is essential for their function. The measurement of these properties and their correlation with various pathological and physiological conditions is of significant interest in medical research [1,2]. Among the various available techniques, Atomic Force Microscopy (AFM) is particularly noteworthy for its suitability to investigate the mechanical characteristics of biological samples under conditions that mimic their natural environments [3,4]. Indeed, AFM is versatile and applicable to a wide range of samples, including tissues, cells, membranes, protein complexes, and even individual proteins and nucleic acids [5–8]. The critical component of an AFM system is the flexible spring-like cantilever, whose movement is monitored by a laser-based optical lever system [9]. This setup enables the precise detection of minute cantilever deflections and forces ranging from piconewtons to micronewtons, allowing for detailed mechanical characterization.

Using an AFM facility, a variety of experiments can be performed, enabling the extraction of different mechanical parameters. Indentation experiments, for example, can provide insights into cellular stiffness by measuring Young's Modulus [10,11]. Furthermore, creep and stress-relaxation experiments yield information on the viscoelastic properties of cells over longer timescales [12], while recent advances in AFM-based microrheology have enabled researchers to investigate rapid changes in the cytoskeleton and short-timescale viscoelastic phenomena [13]. However, the feasibility of these experiments is heavily dependent

Abbreviations: AFM, Atomic Force Microscopy; PDMS, Polydimethylsilane; SEM, Scanning Electron Microscopy; PBS, Phosphate-Buffer Saline; CLL, Chronic Lymphocytic Leukemia; FBS, Fetal Bovine Serum; RPMI, Roswell Park Memorial Institute; PB, Push-Back; FIB, Focused Ion Beam.

* Corresponding author.
E-mail address: valeria.cassina@unimib.it (V. Cassina).

https://doi.org/10.1016/j.ymeth.2025.02.004
Received 13 November 2024; Received in revised form 30 January 2025; Accepted 13 February 2025
Available online 17 February 2025

on the nature of the sample and, more importantly, the geometry of the cantilever. Traditional AFM experiments typically use square-based pyramidal tips or colloidal probes, which are particularly effective for measuring nanoscale morphology and characterizing the stiffness of biological samples [14,15]. However, these geometries are not suitable for experiments on small, soft, and round cells, such as leukocytes. Indentation with a sharp tip can lead to cell rupture, while using a colloidal probe is likely to cause the sample to slide under the applied pressure. Additionally, the standard positioning of the AFM tipless cantilever at an 8–12° angle relative to the sample surface complicates the achievement of uniaxial loading.

Given these limitations, a more suitable approach for the mechanical characterization of rounded samples is the use of parallel microplates. This method allows for the application of uniaxial loading, enabling the compression, confinement, and micromanipulation of biological samples [16–19].

Inspired by the work of *M.P. Stewart et al.* [20], we present a simplified method for the fabrication of wedged cantilevers for AFM without the need for a 3D-printed micrometer gauge, and we demonstrate their application in stress-relaxation experiments performed on primary cells from patients with chronic lymphocytic leukemia.

2. Materials and methods

Among the various polymers presented by *M.P. Stewart et al.* [20], we focused our study on a UV-curing adhesive. This polymer offers several advantages over other materials, such as two-component epoxy glue or PDMS. Specifically, the UV-curing adhesive NOA63 (Norland Optical Adhesive) simplifies the preparation process by eliminating the need for mica foils or cantilever surface pretreatment with a plasma cleaner before the wedging process. Furthermore, NOA63 has a shorter curing time, which enables faster and more efficient production of wedged cantilevers.

The key steps of the fabrication process can be summarized as follows: initial deposition of glue on the cantilever, seeding of glue droplets, second deposition for proper wedge formation, UV curing, and finally detachment of the wedge.

To perform the described process, an AFM coupled with an optical microscope is required to monitor the cantilever positioning relative to the deposited glue droplets. Additionally, precise fabrication of the wedge requires the possibility to realize micromovements of either the tip or the sample.

In the setup used, the AFM (a Nanowizard 4 XP BioAfm JPK) is mounted above an inverted optical microscope (Axio Zeiss), connected to either a LED light source (Colibri, Carl Zeiss system was adopted) or a mercury lamp (HXP 120, Zeiss), capable of exciting the sample at a wavelength of 365 nm in order to cure the polymer.

2.1. Fabrication of wedged AFM cantilevers

The fabrication process begins with mounting the cantilever, whether tipless or tipped, onto the AFM glass block, which is then positioned on the AFM head. Subsequently, a small amount of glue was deposited onto a standard glass surface. Using a syringe or a plastic tip from a laboratory pipette, we gently touched the glue and transferred a smaller droplet onto a siliconized cover glass (22 mm, square, Hampton Research Corp). This siliconized material is particularly effective for detaching the modified cantilevers at the end of the process. The cover glass was then placed under the inverted optical microscope in the sample holder position, ensuring the mounted tip remains safely above the bottom surface. Using a camera (Xic, Ximea), we located the glue droplet and carefully lowered the cantilever near the edge of the droplet, but not directly above it (Fig. 1A). Once the cantilever was positioned close to the droplet edge, it was moved horizontally forward and backward by a few micrometers to gently dip into the glue, allowing some adhesive to coat the part of the cantilever where the tip is placed. It is crucial during this step not

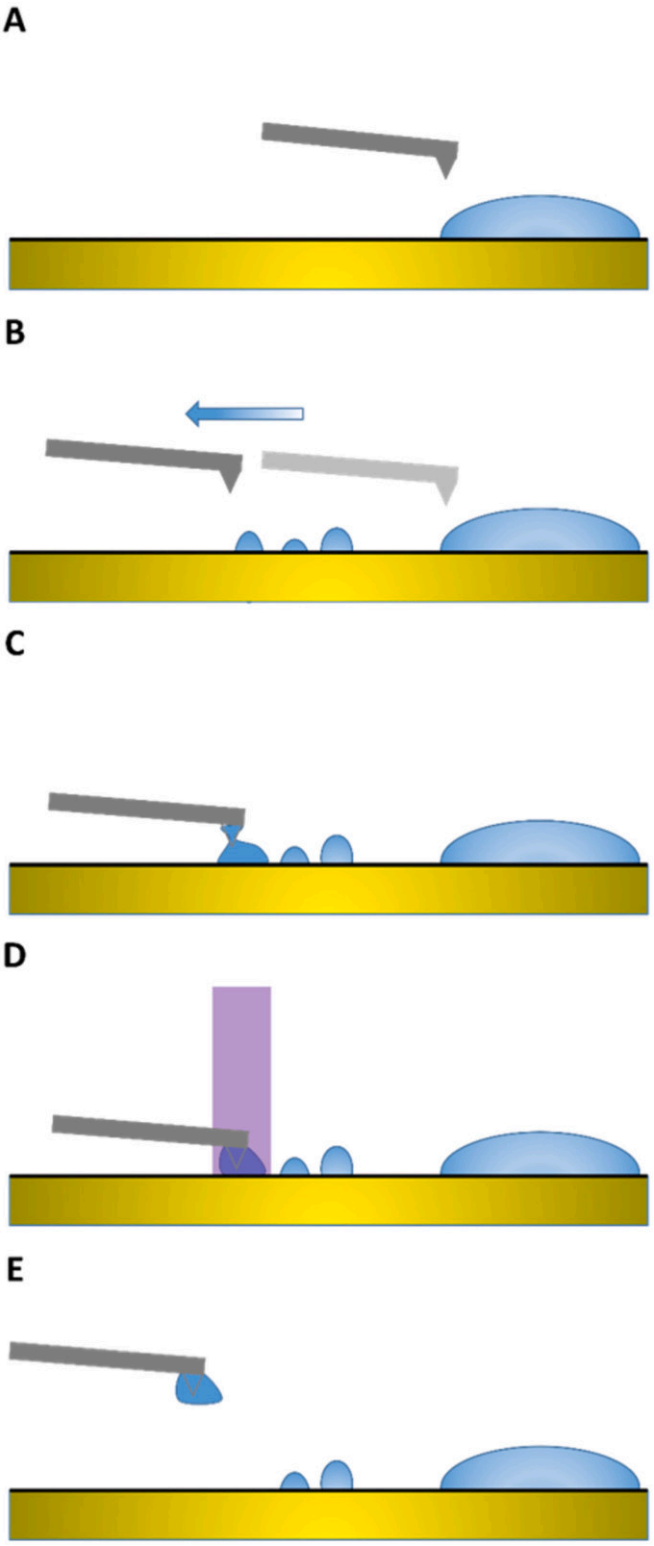

Fig. 1. Key steps in wedge fabrication. Schematic representation (not in scale) showing (**A**) initial approach of the cantilever (gray) to the larger adhesive droplet (blue) deposited on the siliconized cover glass (yellow); (**B**) seeding of multiple smaller glue droplets and the subsequent approach of the cantilever to one of them (the size of the droplets during seeding depends on the retraction speed of the cantilever from the original large droplet); (**C**) deposition of a small droplet on the cantilever; (**D**) UV-light curing process; (**E**) formation of the wedge at the cantilever end after the polymer has cured. These steps are shown for a tipped cantilever, however the same process applies for a tipless one. (For interpretation of the colors in the figure(s), the reader is referred to the web version of this article.)

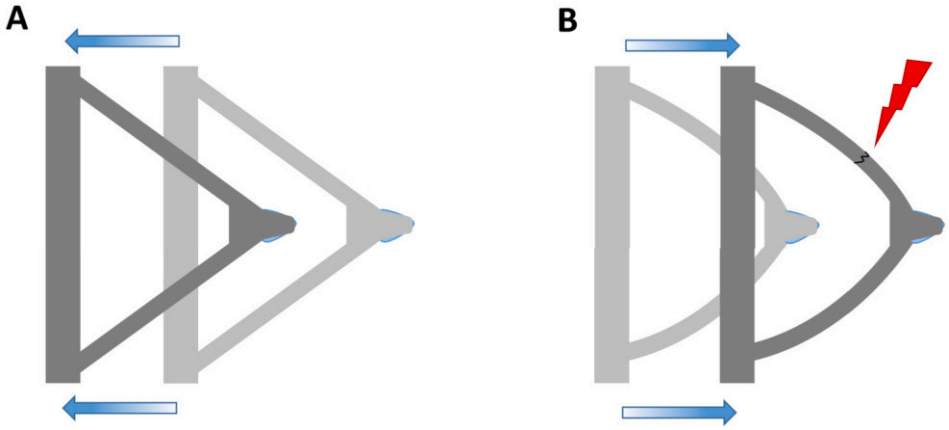

Fig. 2. Procedure for wedge detachment. Schematic representation illustrating (**A**) the proper horizontal movement of the cantilever (gray) required to facilitate the detachment of the wedge without damaging the cured polymer (blue, barely visible in the figure below the cantilever tip), and (**B**) the incorrect horizontal movement direction of the cantilever, which is likely to cause excessive bending of the cantilever arms, potentially leading to fractures or breakage (indicated by red lightning). This procedure is applicable to both triangular and rectangular cantilevers.

Table 1
List of all the cantilever wedged with the process described in the text with their nominal spring constant k by manufacturer.

Cantilever	Manufacturer	Tipped	Geometry	k [N/m]	n wedge obtained
MLCT-BIO, C	Bruker	Yes	Triangular	0.01	2
MLCT-BIO, D	Bruker	Yes	Triangular	0.03	2
MLCT-BIO, E	Bruker	Yes	Triangular	0.1	3
MLCT-BIO, F	Bruker	Yes	Triangular	0.6	1
MLCT-O10, C	Bruker	No	Triangular	0.01	5
MLCT-O10, D	Bruker	No	Triangular	0.03	5
MLCT-O10, E	Bruker	No	Triangular	0.1	4
MLCT-O10, F	Bruker	No	Triangular	0.6	3
CSC38, A	MikroMasch©	No	Rectangular	0.09	8
CSC38, B	MikroMasch©	No	Rectangular	0.03	12
CSC38, C	MikroMasch©	No	Rectangular	0.05	1

to immerse the cantilever too deeply into the glue. The adhesive should not reach the cantilever arms, particularly for triangular cantilevers, and the same precaution applies to rectangular cantilevers. Indeed, having a small amount of glue on these parts will preclude the detachment of the tip at the end of the curing process.

While the cantilever was still in contact with the glue, it was moved horizontally backward to deposit several smaller polymer droplets ($\sim 20-30$ μm diameter). Simultaneously, the vertical step motor was adjusted to gradually lift the cantilever away from the surface until its detachment (Fig. 1B). This step helps prevent an excess of glue on the cantilever, which could lead to larger wedge formation, altering the cantilever spring constant, and causing complications during detachment after curing. The stability over time of the deposited glue droplets is shown in Fig. S1.

At this stage, we placed the cantilever above one of the droplets and we progressively lowered it in steps of 1 μm until it contacted the top of the droplet (Fig. 1C). This step ensures the proper formation of the wedge, which compensates for the standard tilt angle of the tipless cantilever. Typically, a glue droplet with a diameter of 30 μm is sufficient to produce a satisfactory wedge. However, depending on the intended application of the modified cantilever, a slightly larger wedge may be required. In this case, after contacting one droplet, it is necessary to simply move the tip to a second or third droplet until the uncured wedge reaches the desired size. Nevertheless, it is important to notice that larger wedge will lead to larger value of added mass to the cantilever and this can in principle affect the reliability of spring constant determination if thermal noise method is applied [15].

At this point, we used a LED light source (or a mercury lamp) of 365 nm to expose the cantilever for $20-30$ minutes at maximum power (Fig. 1D).

To detach the wedged cantilever at the end of the process, we initially lifted it by $2-5$ μm and gently moved the sample holder to ensure that the traction force on the cantilever was directed toward the chip (Fig. 2A). During this movement, the vertical step motor applied upward steps of 1 μm to aid in detachment. We continued applying these steps until the cantilever bending, caused by the glue on the surface, became sufficient to release the wedged from the siliconized glass (Fig. 1E).
It is crucial to note that overbending the cantilever or moving it in the wrong direction can cause it to break, making it unsuitable for further experiments (Fig. 2B). For soft cantilevers with a spring constant of approximately $k \simeq 0.1-0.01\ N/m$ detachment typically occurs when the cantilever is $40-50$ μm away from the surface, while breaking tends to occur at a distance of $80-100$ μm. Generally, the stiffer the cantilever, the shorter the distance required for detachment, making the wedging process easier.

The procedure outlined in the previous sections is particularly well suited for modifying and wedging various types of cantilevers (Table 1), including both tipless (CSC38, MikroMasch©, and MLCT-O10, Bruker AFM Probes) and tipped (MLCT-BIO, Bruker AFM Probes). In the case of tipped cantilevers, it is crucial to ensure complete coverage of the tip, which typically measures $2.5-4.5$ μm in length. Additionally, this procedure can be applied to previously used wedge cantilevers. Indeed, the polymer will cover any residual cells or tissues present on the cantilever end. Nevertheless, we immersed the cantilever in trypsin (0.25% trypsin in 1x EDTA solution, MedChemExpress) for at least 5 minutes, followed by rinsing with MilliQ water and allowing it to dry before trying the wedging process. This step helps to removing larger biological residues also on wedged tips without altering the modification of the cantilever. In doing so, the longevity of the wedged tip is significantly enhanced.

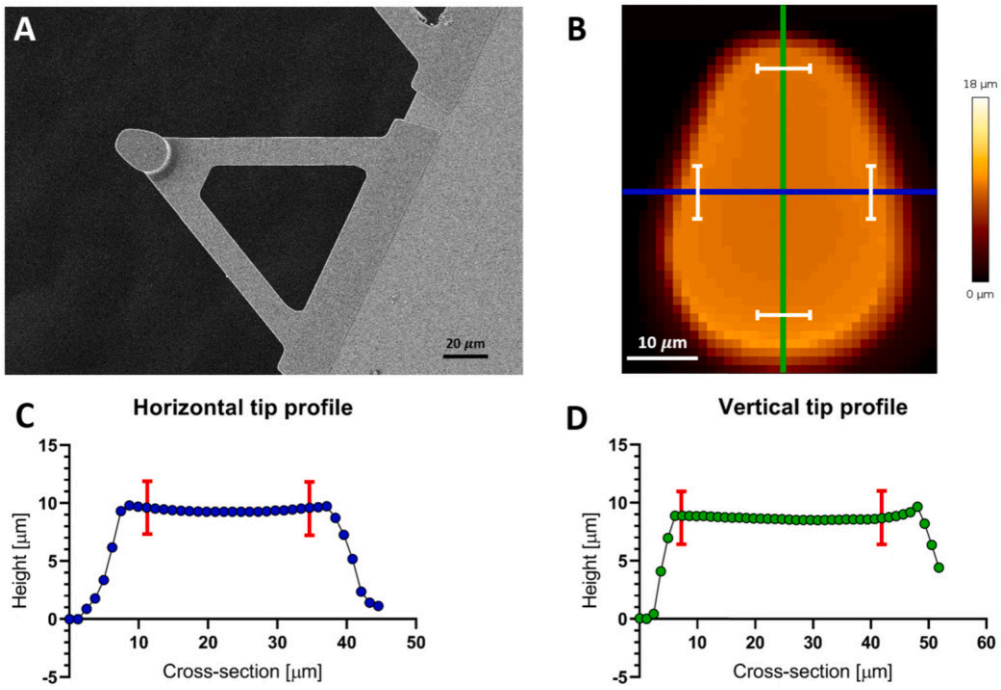

Fig. 3. Characterization of the wedge. (**A**) SEM image and (**B**) AFM topography map of a tipped cantilever acquired with the reverse imaging technique described previously in the text. (**C**), **(D)** Cross-sections of the wedge cantilever along the horizontal (blue) and vertical (green) probe profile. To characterize the wedge, the mean and standard deviation of the height profile were calculated for the points located between the segments, highlighted in white in panel **(B)** and in red in panels **(C, D)**. The average height profile along the horizontal axis (blue) is 9.36 ± 0.12 μm (coefficient of variation is equal to 1.2%), while along the vertical axis (green), it is 8.65 ± 0.11 μm (coefficient of variation is equal to 1.3%). The little variations found along the two profiles are small enough to correct the standard 8-12° tilt.

2.2. Characterization of wedge cantilevers

2.2.1. Probe topography and morphology

After completion of the wedging process, each wedge cantilever was imaged by scanning electron microscopy (SEM) (FEI Nova Nano SEM 230). Before imaging, each cantilever was sputtered (for 15 seconds, 18 mA) with a gold layer to ensure conductivity. SEM images were obtained using an acceleration voltage of 5 kV, in secondary electron mode. In Fig. 3A, SEM image of a well-fabricated wedge cantilever is shown. As clearly visible, the selected polymer was particularly effective in producing a smooth and well-defined wedge structure.

Subsequently, topographic images of the wedge cantilevers were acquired using reverse force mapping with AFM (Fig. 3B). A tipped cantilever (RTESP, Bruker AFM Probes) was mounted tip pointing upward on the bottom of a Petri dish (TPP) using super glue (Loctite) and then placed on the microscope stage. The wedged cantilever was mounted on the AFM system and used to image the tipped cantilever, realizing the conditions for accurate reverse imaging of the wedge, as shown in Fig. 3B. Each map was acquired in liquid (PBS) with the following settings: force set-point of 30 nN, vertical range of 8 μm, scan velocity of 150 μm/s, sampling rate of 4096 Hz, with z-closed loop control and baseline adjustment before each approach. A wedge was deemed satisfactory if the coefficient of variation (standard deviation/mean) in the height difference was less than 3% (Fig. 3C, D). 3D reconstruction of the modified cantilever can be found in Fig. S2. Unsatisfactory wedges were dissolved in piranha solution and reprocessed using the wedging procedure.

2.2.2. Spring constant

Once the modified cantilevers were deemed satisfactory, their spring constant was measured to assess whether the presence of the polymer wedge, and the tip when present, affected the modified cantilever mechanical properties. Calibration of the cantilevers was performed using integrated capabilities of the AFM system. A contact-based method was employed to determine the deflection sensitivity, followed by the thermal noise method to assess the spring constant of the cantilever [21]. The thermal noise method was adopted due to its ease of implementation in biological AFM setups and it is widely accepted for its precision [22]. In this method, a force-distance curve is first acquired by pressing the cantilever against a rigid substrate, such as glass or plastic, to determine the deflection sensitivity. This allows conversion of the laser deflection signal (in Volts) to the actual tip deflection (in nanometers) [23]. To estimate the deflection sensitivity, force curves were acquired on a standard rigid glass slide substrate in MilliQ water at room temperature. Representative force curves obtained before and after the wedging procedure can be found in Fig. S3. While the wedge geometry could introduce minor perturbations in the vertical deflection profile, these perturbations did not significantly affect the linear portion of the approach curve used to determine the sensitivity.

Since we were able to acquire the force-curve with modified wedge cantilevers and estimate the deflection sensitivity, we could proceed to determine the spring constant with thermal noise method. To assess changes within the frequency spectrum of the normal oscillation modes of the cantilever, such profiles were measured for the adopted tipped and tipless cantilevers before and after the wedging process (Fig. S4). The addition of mass due to the polymer forming the wedge resulted in a reduction in the resonance peak intensity, accompanied by a negligible variation in the measured spring constant compared to those of their unmodified counterparts.

Specifically, the spring constant of various cantilevers, both tipless and tipped, was measured before and after the wedging procedure, and the ratio between the two constants was calculated as follows:

$$k_{ratio} = \frac{k_m}{k_w} \tag{1}$$

where k_m is the spring constant of the cantilever in its original manufacturing conditions, before wedging, and k_w is the spring constant of the same cantilever after the wedge was applied. For tipless cantilevers, we found a ratio of $k_{ratio} = 1.03 \pm 0.06$ (mean ± std, n = 38), while for tipped cantilevers, the ratio was $k_{ratio} = 1.11 \pm 0.15$ (mean ± std, n = 8).

We found that the addition of NOA63 polymer did not significantly alter the spring constant of the cantilevers. For tipless cantilevers, the change due to polymer is less than 5%, with a variation of 3% in the values of the spring constant between the unmodified and modified cantilevers. In contrast, tipped cantilevers exhibit a more pronounced alteration, with a 11% increase in the spring constant. These results validate the proposed calibration method and the suitability of the modified cantilevers for the described procedure. However, it is important to note that for a larger wedge, when required for specific needs, these variations can increase and severely affect the reliability of thermal noise methods. According to the work of *Chighizola et al.* [15], it is important to estimate the contribution of the added mass to the cantilever to consider whether or not it is necessary to take into account a correction factor during the calibration of the spring constant. The calculation for CSC38 rectangular tipless cantilever (see Supplementary Materials, Fig. S5 for details) led us to a reduced mass of $\tilde{m} = 0.62$ and a reduced gyration radius of $\tilde{r} = 0.067$ for which the variation due to the added mass is less than 10%, so it can be considered negligible (see Table 3 of [15]).

Lastly, standard cantilever cleaning typically involves plasma cleaning, which is highly effective in removing biological residues and, unfortunately, polymer wedges [24]. In our case, we treated each cantilever with trypsin for 5 minutes at the end of the experiment, followed by a rinse with MilliQ water. In addition, dish detergent can be used for cleaning. These simple and cost-effective procedures allowed us to reuse the same cantilever multiple times without compromising the integrity of the wedge, enabling consistent measurements over several weeks.

2.2.3. Success rate and challenges in wedged cantilever fabrication

The procedure described for fabricating wedged cantilevers is straightforward and does not require specialized skills in handling the AFM setup. However, some care must be taken, since some issues may arise during the wedged protocol. The primary challenge lies in the detachment process after UV light cure (Fig. 1D, E), which can occasionally result in cantilever breakage due to incomplete separation from the siliconized cover-glass. After having defined the protocol, we observed a 92% success rate for wedge fabrication. Specifically, of the 50 cantilevers subjected to the procedure, 46 were successfully modified. One tipped cantilever required reprocessing after its first initial wedge due to incomplete coverage of the tip (Fig. S6), therefore it was dissolved in piranha solution and again subjected to the wedging protocol; 3 cantilevers (2 tipless and 1 tipped) broke during the detachment process due to incomplete separation of the cantilever from the cover glass.

Another potential challenge arises in measuring the deflection sensitivity of wedged cantilevers given the unique geometry of the probe and possible non-ideality during contact. First, acquiring force curves in air could be difficult because of the strong adhesion forces attributed to the polymer used and the larger contact area, which affects the ability of the probe to reach the substrate and acquire force curves, as well as its capability to detach during withdrawal. However, these issues are resolved when the measurements are performed in liquid (Fig. S3). Nevertheless, residual deformability can occur after the glue curing process, particularly if the UV light exposure time is less than 20 minutes. To ensure that the added polymer does not affect the determination of the deflection sensitivity, it is essential to acquire force curves against a hard substrate, typically glass or plastic, to assess the presence of multiple slopes in the force-curve profile. Multiple slopes are usually indicative of residual deformability in the polymer. In such cases, it is recommended to dissolve the wedge in piranha solution and repeat the wedging process extending the UV-light exposure time to at least 30 minutes. In contrast, if the added polymer does not exhibit residual deformability, the presence of the wedge can be identified by a more gradual increase after the contact point compared to an unmodified cantilever, while the force-curve profile exhibits a single slope (Fig. S3). Lastly, to ensure consistency, it is recommended to measure the sensitivity and estimate the spring constant before each experiment.

2.2.4. Primary cells purification

Primary Chronic Lymphocytic Leukemia (CLL) cells were negatively selected from fresh peripheral blood from CLL patients using the RosetteSep B-lymphocyte enrichment kit (StemCell Technologies). The purity of all preparations was always higher than 99%, and cells co-expressed CD19 and CD5 on their surface as assayed by flow cytometry (Navios, Beckman Coulter); preparations were virtually devoid of natural killer cells, T lymphocytes, and monocytes. After purification, cells were immediately frozen for further measurements. For the experiments described, cells were thawed in the morning in cell culture medium (RPMI-1640 with red phenol, Euroclone, Pero, Italy), supplemented with 10% (v/v) Fetal Bovine Serum (FBS) and 15 mg/ml Gentamicin, centrifuged at 1500 rpm for 5 minutes, and resuspended in fresh culture medium and then kept at 37 °C and 5% CO_2.

2.2.5. Cell culture

MEC1 cell line [25] was obtained from Deutsche Sammlung von Mikroorganismen und Zellkulturen GmbH (DSMZ, Braunschweig, Germany) and was recently genotyped as follows: 10 ng of MEC1 cell DNA was purified with the QiAmp DNA Mini Kit (Qiagen, Düsseldorf, Germany) and amplified by PCR with GenePrint ®10 System (Qiagen, Düsseldorf, Germany) and sold Eurofins Genomics Standard FLA Service to perform genotyping. Data were analyzed with DSMZ Online STR Analysis. We confirmed the identity of the cell line analyzed. MEC1 cells were cultured in RPMI-1640 with red phenol (Euroclone, Pero, Italy), supplemented with 10% (v/v) FBS and 15 mg/ml Gentamicin at 37 °C and 5% CO_2.

2.2.6. Human ethics statement

CLL Patients were diagnosed according to the updated National Cancer Institute Working Group (NCIWG) guidelines. Peripheral blood samples were obtained after informed consent from patients who were untreated or off treatment for at least 6 months. The study was approved by the Ospedale San Raffaele (OSR) ethics committee under the protocol CLL-BIO.

3. Application of wedge cantilevers on soft round cells

To demonstrate the compressive capability of the wedge cantilever, we conducted stress-relaxation experiments on primary Chronic Lymphocytic Leukemia (CLL) cells and the MEC1 cell line, a widely used leukemia model. CLL is the most prevalent leukemia in Western countries, with an incidence of five new cases per 100,000 individuals per year [26,27]. The disease is marked by clonal expansion of mature CD5+ B lymphocytes, which accumulate in peripheral blood, bone marrow, and secondary lymphoid organs. These sites provide a supportive microenvironment that promotes cell proliferation and disease progression. Additionally, CLL cells exhibit significant trafficking between peripheral blood and lymphoid tissues [28], a dynamic migration that requires cytoskeletal remodeling, making these cells suitable for AFM-based investigation.

Traditional AFM approaches, typically using tipped cantilevers, are most effective for probing the cell cortex, where the actomyosin network primarily resides [29]. In previous work, AFM force-spectroscopy measurements were used to determine cortical stiffness, facilitating comparisons between primary CLL cells and healthy B cells (HD-B) [29]. The results indicated that CLL cells exhibit lower cortical stiffness than HD-B cells, in line with research linking cellular mechanical properties with disease progression [29]. However, when assessing the mechanical properties of deeper regions, such as the nucleus, or evaluating responses to prolonged stimuli, standard cantilevers often require higher applied forces, raising the risk of cellular rupture. To address this, we employed a wedge-shaped cantilever, enabling controlled uniaxial loading along a single axis while minimizing cellular damage performing experiment of stress-relaxation.

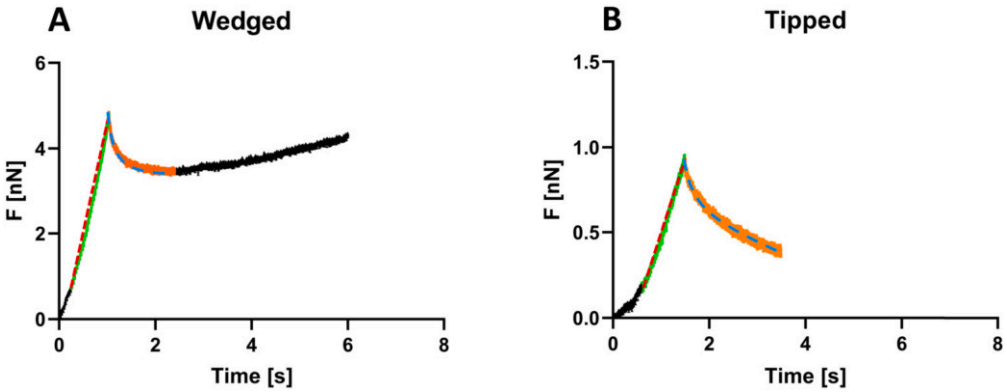

Fig. 4. Cellular response during stress-relaxation experiments. Representative data collected during stress-relaxation experiments performed on CLL cells with (**A**) wedged cantilevers and (**B**) tipped cantilevers. Notably, the cellular response varies depending on the geometry of the probe: in (**A**), cells exhibit an initial relaxation lasting approximately 1 s followed by a push-back against the probe, while in (**B**), cells exhibit pure relaxation behavior. Raw data are reported in black, green and orange, to differentiate diverse portions of the curves, while the fitting curves are reported with dashed line in red (linear fit) and blue (exponential decay fit).

Stress-relaxation experiments were conducted on live primary cells plated on Poly-L-Ornithine (Sigma)-coated Petri dishes. The coating was prepared by diluting Poly-L-Ornithine 1 : 10 in PBS, incubating for 30 minutes at 37 °C, and washing with PBS before cell seeding. During the experiments, cells were maintained in cell culture medium (RPMI-1640 with red phenol, Euroclone, Pero, Italy), supplemented with 10% (v/v) FBS, 15 mg/ml Gentamicin, and 10% HEPES (Gibco, N-2-hydroxyethylpiperazine-N-2-ethane sulfonic acid).

The experimental setup depended significantly on the tip geometry. For tipped cantilevers, the maximum waiting time was approximately 2 seconds, since cells, due to their low adhesion, tended to detach and migrate away from the tip, making the data unreliable beyond this point. In contrast, the wedge cantilever allowed for extended waiting times of several seconds, ensuring greater stability during measurements. However, restricting the waiting time to 5 seconds was sufficient to detect differences in the nanomechanical behavior of cells when probed with the two types of cantilevers. Similarly, the applied force varied according to the geometry of the tip: for tipped cantilevers, a force of 1 nN was used, while for wedge cantilevers, the applied force ranged from 2.5 to 5 nN. This variation is related to the shape of the probe: exceeding the force threshold for sharp tips would lead to cell rupture. Regardless of the geometry of the tip, the sampling frequency was set to 4096 Hz, the z-closed loop control was maintained throughout the experiments, and the approaching and retracting speed was set to 1 μm/s.

The collected data were analyzed by separating two distinct portions of the force curve: the initial segment (Fig. 4, green), corresponding to the tip-sample contact until the maximum applied force was reached, and the relaxation phase (Fig. 4, orange). For the initial segment, a linear fit was applied to estimate the slope of compression (Fig. 4, red dashed line), which serves as an indicator of cell rigidity and can be considered a proxy of cell stiffness. The relaxation phase was fitted by using a single exponential decay model to determine the relaxation time (Fig. 4, blue dashed line). Stress-relaxation experiments performed adopting wedge cantilevers suggest that leukemic cells generate mechanical push-back forces when completely confined (Fig. 4A), and this can be part of their invasive strategy. Likely, this response reflects a dynamic interplay between cytoskeletal reorganization and cellular rigidity, allowing leukemic cells to occupy and overcome structural constraints. Conversely, stress-relaxation experiments performed using tipped cantilevers suggest that leukemic cells redistribute internal stresses over time (Fig. 4B), when indented with a sharp tip, primarily through cytoskeletal reorganization. This behavior not only highlights the dynamic interplay between elastic and viscous components, but also underscores the importance of mechanical adaptation in preserving cellular integrity under mechanical perturbations.

The fitting results are presented in Fig. 5. The cell response varies depending on the applied compression. Specifically, when stress-relaxation experiments are conducted adopting standard tipped cantilevers, which apply a localized stimulus to the cell, the response is softer under compression (Fig. 5A), and cells tend to relax gradually after the initial probe interaction (Fig. 5B, C). This behavior reflects a mechanical response likely driven by the intrinsic viscoelastic properties of the cell. Indeed, when subjected to localized compression, leukemic cells redistribute internal stresses by reorganizing their cytoskeleton and cytoplasm, leading to a time-dependent reduction in force. This behavior is characteristic of the viscoelastic nature of cells, which balances elastic deformation with viscous flow [30,31]. Furthermore, the relaxation response is predominantly governed by the dynamics of actin filaments, microtubules, and intermediate filaments, which adapt to mechanical stresses by remodeling or dissipating tension. This mechanical adaptation is particularly relevant in maintaining cellular integrity during mechanical perturbations [32,33].

In contrast, when wedge cantilevers are used, the entire cell can be probed because of the stronger confinement, which allows for a more uniform and extended applied pressure, without causing cell rupture. Under these conditions, cells exhibit a steeper compression slope, indicating greater resistance to the compressing probe (Fig. 5A). Furthermore, because the applied stimulus is more global, the relaxation time decreases as the entire cell adapts more rapidly to the confined state (Fig. 5B). Additionally, the distinct probe geometry leads the cells to push-back against the sensor in an attempt to counteract the imposed confinement. The push-back phenomenon occurs in the vast majority of cells, as indicated in Fig. 5C (blue columns) which specify the percentage of push-back (PB) and standard relaxation (Relax) occurrence. This behavior may be attributed both to the nucleus, which plays a regulatory role in cellular responses to spatial constraints [34], and to the geometry of the cantilever. Moreover, this behavior can be associated with a significant role in cell migration and invasiveness, particularly within three-dimensional environments. Leukemic tumor cells frequently encounter physical barriers in tissues, necessitating active mechanical responses to travel across and invade these obstacles. Push-back may represent the ability of these cells to counteract external compression by reorganizing their cytoskeletal structures, such as actin filaments and microtubules, to produce opposing forces [30]. Furthermore, the ability to generate a push-back might indicate a capacity for dynamic cellular rigidity, allowing cells to fine-tune their mechanical properties and adapt to diverse microenvironmental challenges. This adaptability could improve the tumor cell invasiveness by facilitating their passage through confined spaces or enabling them to overcome physical constraints [35].

Lastly, to ensure uniaxial loading of the cell during compression with the wedge cantilever, the MEC1 cell line was used, with cells

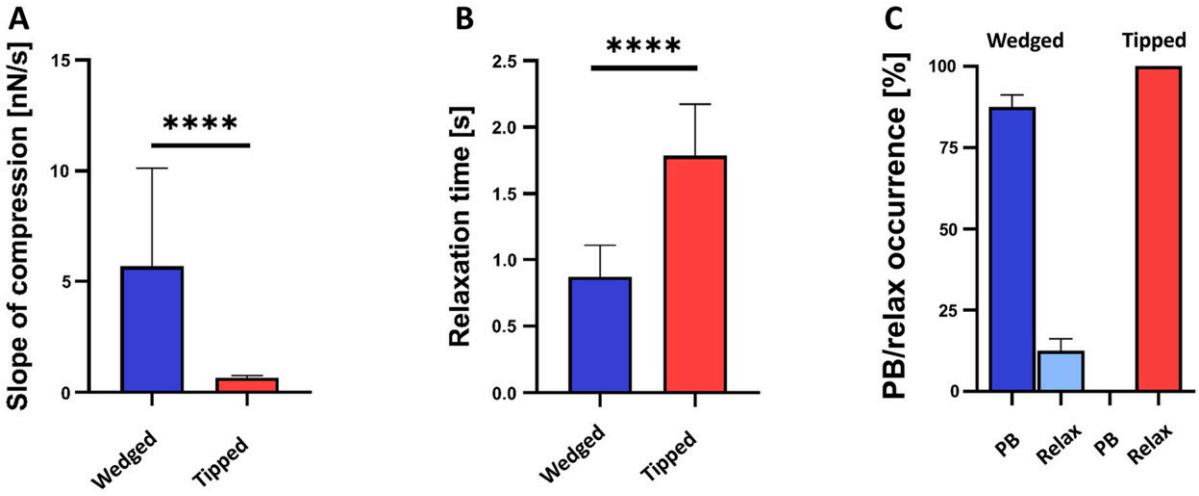

Fig. 5. Fitting analysis of experimental data. Bar graphs representing median values of (**A**) slope of compression of force vs time data, and (**B**) different relaxation time of exponentially decay estimated in experiment performed with wedge (blue) and standard tipped (red) cantilevers on primary CLL cells. Error bars give the standard deviation, for each experiment $n = 16$, $p < 0.0001$ estimated with Mann-Whitney test. (**C**) Percentage of push-back (PB) and relaxation (Relax) occurrence exhibited by cells during confined time for experiment performed with wedge (blue) and standard tipped (red) cantilevers.

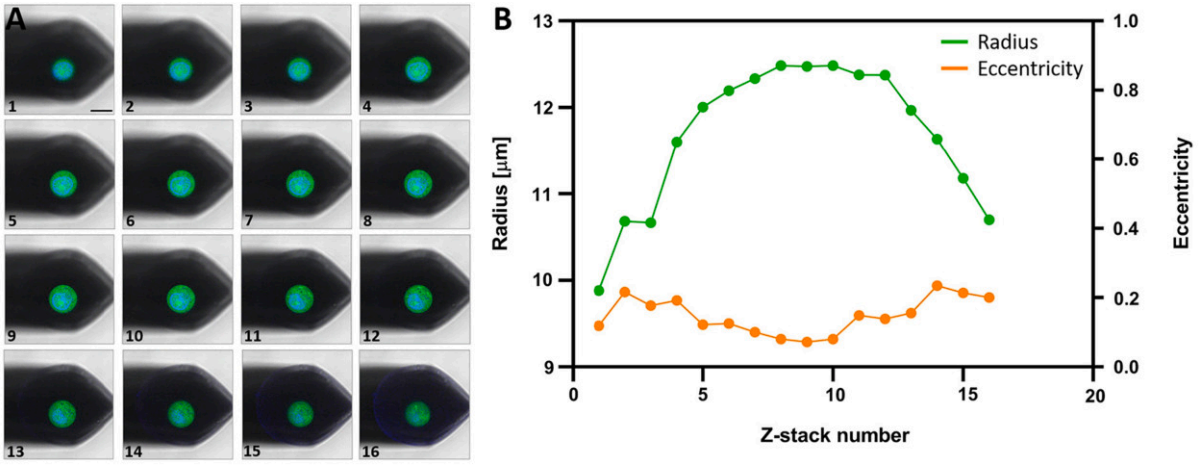

Fig. 6. Z-stack images analysis of MEC1 cell during stress-relaxation experiment. (A) Different z-planes of a MEC1 cell during a stress-relaxation experiment conducted with a wedge cantilever. The cell is labeled with CMFDA (green) and Hoechst (blue), with a scale bar of 10 μm. The total acquisition time for the z-stack was 120 seconds. **(B)** For each z-plane, the cell radius and its eccentricity were calculated (Eq. (2)). Cell radius initially increases, peaks, and then decreases under compression (green), indicating uniaxial loading. Eccentricity remains within 0.07–0.23 (orange), confirming axis-restricted, uniform compression.

labeled with fluorescent markers (CellTracker CMFDA and Hoechst 34580, ThermoFisher). This allowed us to visualize cell expansion under compression using a confocal microscope integrated into the AFM setup (objective 20x, Plan-Apochromat 20x/0.8 M27, Zeiss). The z-stack of fluorescent images was captured at full excitation with an exposure time of 250 ms in both the DAPI and Alexa488 channels (Fig. 6A). The MEC1 cell line was chosen because of its ease of biological manipulation. The stack consists of 16 images from which the cell radius and eccentricity were extracted. The eccentricity, defined as

$$e = \sqrt{1 - \frac{b^2}{a^2}} \tag{2}$$

where a, b are the major and minor semiaxis of an ellipse fitting the cell cross-section, is a particularly effective parameter to assess directional confinement. Specifically, eccentricity equals 0 when the ellipse becomes to a circumference and 1 when it degenerates into a straight line. As compression progresses, the radius initially increases, reaching a peak before decreasing (Fig. 6B, green). This behavior supports the hypothesis of uniaxial loading, as the initial expansion followed by compression along the same axis is consistent with the wedge applying force perpendicularly to the cell surface. Furthermore, the absence of significant lateral expansion, as indicated by the eccentricity (Fig. 6B, orange) remaining within a narrow range (0.07 to 0.23), further confirms that the wedge confines the deformation to a single axis, ensuring uniform compression throughout the process.

4. Discussion

In this work, we have introduced a simplified and efficient protocol for fabricating wedge-shaped cantilevers, which resulted in sufficient simplicity for an AFM users, but nevertheless it addresses the limitations of existing methods.

Among the existing methods for producing flat cantilevers, the Focused Ion Beam (FIB) technique is also employed, primarily in industrial settings, for the fabrication of AFM tips. However, the FIB ablation process for modifying AFM cantilevers presents several challenges [36]. Thinning the cantilever to 2–3 μm introduces structural fragility, increasing the probability of damage during use. Additionally, the high-energy ion beam (30 kV) can cause localized contamination or damage to the cantilever, potentially altering its mechanical response, compromising the reproducibility between samples, and potentially the force

calibration, which is essential for precise AFM measurements. Finally, the process is time-consuming and costly, potentially limiting its practicality for experiments that require multiple modified cantilevers.

Compared to traditional approaches, our protocol streamlines the wedging process by eliminating the need for additional instruments, such as 3D-printed micrometer gauges, and significantly reduces the time required for cantilever preparation. The use of the NOA63 UV-curing polymer not only improves the fabrication efficiency but also ensures the formation of high-quality wedges, without the need for surface pretreatment or complex materials such as mica foils. Our results show that the mechanical properties of the wedged cantilevers remain consistent with the original manufacturer's specifications, confirming that the rapid fabrication process does not compromise performance.

Moreover, the comparison between wedged and tipped cantilevers highlights an improved performance of wedged cantilevers in experiments aimed at performing a comprehensive mechanical characterization. Tipped cantilevers are suitable for providing localized information; however, their limited force application and the increased risk of inducing cell rupture limit their use in the field of mechanobiology. Indeed, the necessity of exploring a deeper part of the cell, such as the nucleus, requires the possibility of increasing the applied force on the cells and the indentation depth, without damaging the sample or extending the time of contact between tip and sample, likely resulting in lateral displacement and sliding of the cells [37]. In this context, wedged cantilevers facilitate uniaxial compression and allow for prolonged measurement durations, offering a more comprehensive perspective on cell mechanics [38]. Furthermore, the deeper part of the cell can be probed due to the possibility of reaching a deeper indentation with respect to the tipped cantilevers (Fig. S7). This capability makes wedge cantilevers particularly valuable for studies involving stress-relaxation, confinement, and push-back phenomena in soft, low adhering, spherical cells.

In conclusion, the proposed protocol offers a practical and time-saving solution for producing wedged cantilevers, making it an appealing option for researchers working in cellular mechanics on soft, round and low-adherent cells.

CRediT authorship contribution statement

RC and JH developed the protocol. RC wrote the article. RC, AS and VC performed the experiments. RC, AS, FM and VC analyzed the data. JH, DS, DM, FS and VC supervised the activity. CS and LS provided patients and clinical information, as well as cell line. MB provided SEM images. RC, JH, CS, DS, MF, DM, FM and VC revised the article.

Declaration of competing interest

The authors declare that they have no known competing financial interests or personal relationships that could have appeared to influence the work reported in this paper.

Acknowledgements

FM and DS project is supported by grant from Ministero dell'Università e della Ricerca-NextGenerationEU (PNRR M4.C2.I1.1- Avviso 104/2022, CUP H53D23000860006). CS project is supported by Associazione Italiana per la Ricerca sul Cancro AIRC under IG2023 Project ID:28750.

Appendix A. Supplementary material

Supplementary material related to this article can be found online at https://doi.org/10.1016/j.ymeth.2025.02.004.

Data availability

Data will be made available on request.

References

[1] C.T. Mierke, The fundamental role of mechanical properties in the progression of cancer disease and inflammation, Rep. Prog. Phys. 77 (7) (2014) 076602.
[2] M.N. Starodubtseva, Mechanical properties of cells and ageing, Ageing Res. Rev. 10 (1) (2011) 16–25.
[3] Y.F. Dufrêne, T. Ando, R. Garcia, D. Alsteens, D. Martinez-Martin, A. Engel, C. Gerber, D.J. Müller, Imaging modes of atomic force microscopy for application in molecular and cell biology, Nat. Nanotechnol. 12 (4) (2017) 295–307.
[4] D.J. Müller, Y.F. Dufrene, Atomic force microscopy as a multifunctional molecular toolbox in nanobiotechnology, Nat. Nanotechnol. 3 (5) (2008) 261–269.
[5] M. Lekka, D. Gil, K. Pogoda, J. Dulińska-Litewka, R. Jach, J. Gostek, O. Klymenko, S. Prauzner-Bechcicki, Z. Stachura, J. Wiltowska-Zuber, et al., Cancer cell detection in tissue sections using afm, Arch. Biochem. Biophys. 518 (2) (2012) 151–156.
[6] A. Stylianou, M. Lekka, T. Stylianopoulos, Afm assessing of nanomechanical fingerprints for cancer early diagnosis and classification: from single cell to tissue level, Nanoscale 10 (45) (2018) 20930–20945.
[7] Y.L. Lyubchenko, L.S. Shlyakhtenko, Afm for analysis of structure and dynamics of dna and protein–dna complexes, Methods 47 (3) (2009) 206–213.
[8] Y.L. Lyubchenko, L.S. Shlyakhtenko, T. Ando, Imaging of nucleic acids with atomic force microscopy, Methods 54 (2) (2011) 274–283.
[9] G. Meyer, N.M. Amer, Novel optical approach to atomic force microscopy, Appl. Phys. Lett. 53 (12) (1988) 1045–1047.
[10] E.C. Faria, N. Ma, E. Gazi, P. Gardner, M. Brown, N.W. Clarke, R.D. Snook, Measurement of elastic properties of prostate cancer cells using afm, Analyst 133 (11) (2008) 1498–1500.
[11] M. Radmacher, Measuring the elastic properties of biological samples with the afm, IEEE Eng. Med. Biol. Mag. 16 (2) (1997) 47–57.
[12] E.M. Darling, S. Zauscher, J.A. Block, F. Guilak, A thin-layer model for viscoelastic, stress-relaxation testing of cells using atomic force microscopy: do cell properties reflect metastatic potential?, Biophys. J. 92 (5) (2007) 1784–1791.
[13] A. Rigato, A. Miyagi, S. Scheuring, F. Rico, High-frequency microrheology reveals cytoskeleton dynamics in living cells, Nat. Phys. 13 (8) (2017) 771–775.
[14] I. Sokolov, M.E. Dokukin, N.V. Guz, Method for quantitative measurements of the elastic modulus of biological cells in afm indentation experiments, Methods 60 (2) (2013) 202–213.
[15] M. Chighizola, L. Puricelli, L. Bellon, A. Podestà, Large colloidal probes for atomic force microscopy: fabrication and calibration issues, J. Mol. Recognit. 34 (1) (2021) e2879.
[16] G.W. Brodland, J. Yang, J. Sweny, Cellular interfacial and surface tensions determined from aggregate compression tests using a finite element model, HFSP J. 3 (4) (2009) 273–281.
[17] A. Mgharbel, H. Delanoë-Ayari, J.-P. Rieu, Measuring accurately liquid and tissue surface tension with a compression plate tensiometer, HFSP J. 3 (3) (2009) 213–221.
[18] M. Yoneda, Tension at the surface of sea-urchin egg: a critical examination of Cole's experiment, J. Exp. Biol. 41 (4) (1964) 893–906.
[19] M. Schmidt, H. Löwen, Phase diagram of hard spheres confined between two parallel plates, Phys. Rev. E 55 (6) (1997) 7228.
[20] M.P. Stewart, A.W. Hodel, A. Spielhofer, C.J. Cattin, D.J. Müller, J. Helenius, Wedged afm-cantilevers for parallel plate cell mechanics, Methods 60 (2) (2013) 186–194.
[21] H.-J. Butt, M. Jaschke, Calculation of thermal noise in atomic force microscopy, Nanotechnology 6 (1) (1995) 1.
[22] J.L. Hutter, J. Bechhoefer, Calibration of atomic force microscope tips, Rev. Sci. Instrum. 64 (7) (1993) 1868–1873.
[23] H.-J. Butt, B. Cappella, M. Kappl, Force measurements with the atomic force microscope: technique, interpretation and applications, Surf. Sci. Rep. 59 (1–6) (2005) 1–152.
[24] L. Sirghi, Plasma cleaning of silicon surface of atomic force microscopy probes, Rom. J. Phys. 56 (2011) 144.
[25] A. Stacchini, M. Aragno, A. Vallario, A. Alfarano, P. Circosta, D. Gottardi, A. Faldella, G. Rege-Cambrin, U. Thunberg, K. Nilsson, et al., Mec1 and mec2: two new cell lines derived from b-chronic lymphocytic leukaemia in prolymphocytoid transformation, Leuk. Res. 23 (2) (1999) 127–136.
[26] P. Tolar, Cytoskeletal control of b cell responses to antigens, Nat. Rev. Immunol. 17 (10) (2017) 621–634.
[27] L. Scarfò, A.J. Ferreri, P. Ghia, Chronic lymphocytic leukaemia, Crit. Rev. Oncol./Hematol. 104 (2016) 169–182.
[28] F. Caligaris-Cappio, M.T. Bertilaccio, C. Scielzo, How the microenvironment wires the natural history of chronic lymphocytic leukemia, Semin. Cancer Biol. 24 (2014) 43–48.
[29] M. Sampietro, V. Cassina, D. Salerno, F. Barbaglio, E. Buglione, C.A. Marrano, R. Campanile, L. Scarfò, D. Biedenweg, B. Fregin, et al., The nanomechanical properties of cll cells are linked to the actin cytoskeleton and are a potential target of btk inhibitors, Hemasphere 7 (8) (2023) e931.
[30] D.A. Fletcher, R.D. Mullins, Cell mechanics and the cytoskeleton, Nature 463 (7280) (2010) 485–492.
[31] E. Moeendarbary, A.R. Harris, Cell mechanics: principles, practices, and prospects, Wiley Interdiscip. Rev., Syst. Biol. Med. 6 (5) (2014) 371–388.
[32] D.E. Discher, P. Janmey, Y.-l. Wang, Tissue cells feel and respond to the stiffness of their substrate, Science 310 (5751) (2005) 1139–1143.

[33] D.E. Ingber, Cellular mechanotransduction: putting all the pieces together again, FASEB J. 20 (7) (2006) 811–827.
[34] A. Lomakin, C. Cattin, D. Cuvelier, Z. Alraies, M. Molina, G. Nader, N. Srivastava, P. Sáez, J. Garcia-Arcos, I. Zhitnyak, et al., The nucleus acts as a ruler tailoring cell responses to spatial constraints, Science 370 (6514) (2020) eaba2894.
[35] V. Swaminathan, K. Mythreye, E.T. O'Brien, A. Berchuck, G.C. Blobe, R. Superfine, Mechanical stiffness grades metastatic potential in patient tumor cells and in cancer cell lines, Cancer Res. 71 (15) (2011) 5075–5080.
[36] C.J. Cattin, M. Düggelin, D. Martinez-Martin, C. Gerber, D.J. Müller, M.P. Stewart, Mechanical control of mitotic progression in single animal cells, Proc. Natl. Acad. Sci. 112 (36) (2015) 11258–11263.
[37] K. Haase, A.E. Pelling, Investigating cell mechanics with atomic force microscopy, J. R. Soc. Interface 12 (104) (2015) 20140970.
[38] M. Zanetti, S.N. Chen, M. Conti, M.R. Taylor, O. Sbaizero, L. Mestroni, M. Lazzarino, Microfabricated cantilevers for parallelized cell-cell adhesion measurements, Eur. Biophys. J. 51 (2) (2022) 1–10.

Supplementary Information:

Production of AFM Wedged Cantilevers for Stress-Relaxation Experiments: Uniaxial Loading of Soft, Spherical Cells

Riccardo Campanile[1], Jonne Helenius[2], Cristina Scielzo[3], Lydia Scarfò[4,5], Domenico Salerno[1], Mario Bossi[1], Marta Falappi[1], Alessia Saponara[1], Daniel J Müller[2], Francesco Mantegazza[1], and Valeria Cassina[1,*]

[1]School of Medicine and Surgery, BioNanoMedicine Center NANOMIB, Università di Milano-Bicocca, Vedano al Lambro, Italy

[2]Department of Biosystems Science and Engineering, ETH Zurich, Basel, Switzerland

[3]Division of Experimental Oncology, Malignant B cells biology and 3D modelling Unit, IRCCS Ospedale San Raffaele Milano, Italy

[4]School of Medicine, Università Vita-Salute San Raffaele, Milano, Italy

[5]Division of Experimental oncology, B-cell neoplasia Unit and Strategic Research Program on CLL, IRCCS Ospedale San Raffaele, Milano, Italy

[*]Corresponding author: valeria.cassina@unimib.it

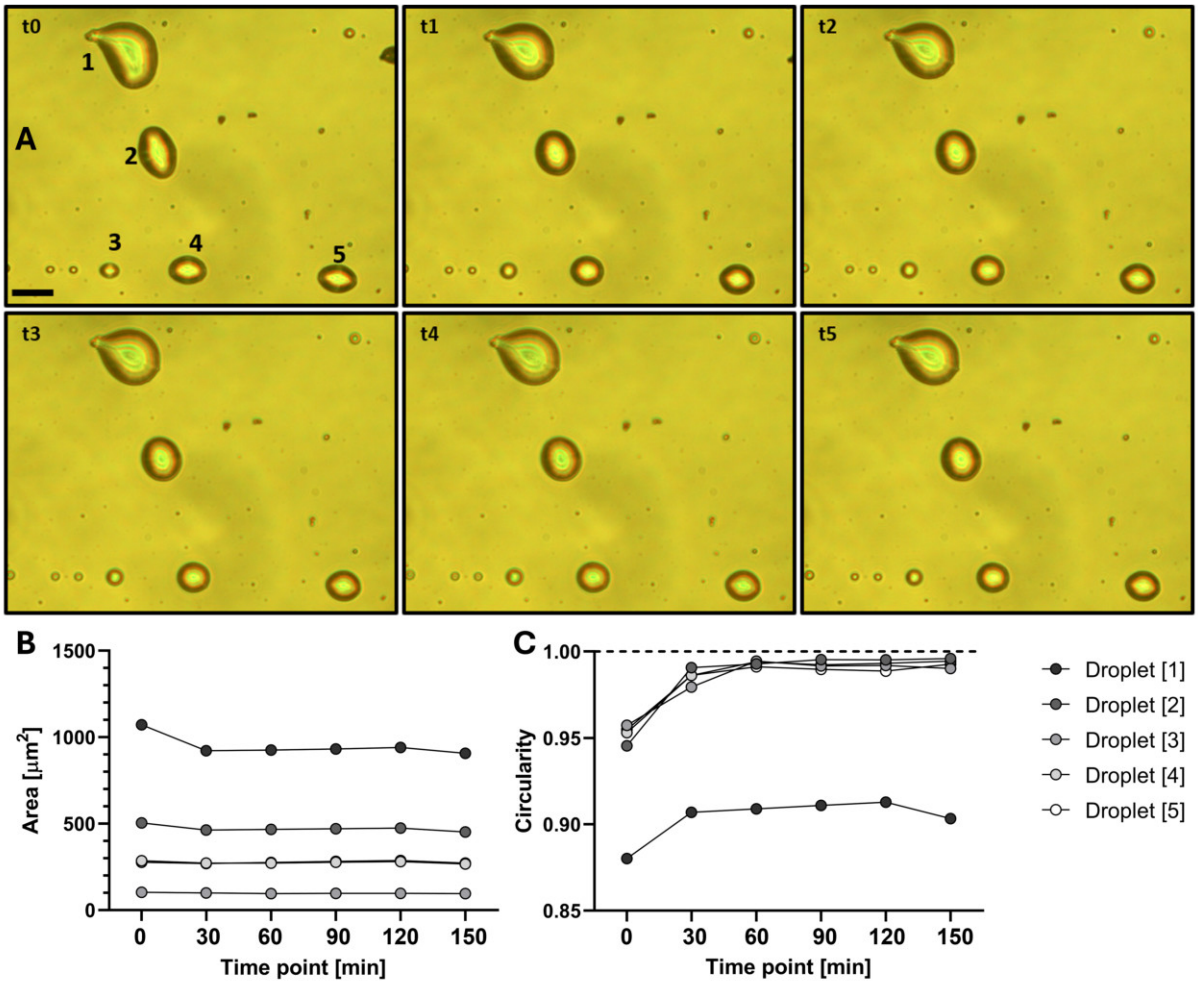

Figure S1: **Stability and morphological analysis of glue droplets seeding process.** **(A)** Bright-field microscopy images of glue droplets acquired at different time points during the seeding process ($t_0 = 0$ min deposition of the glue, $t_1 = 30$ min, $t_2 = 60$ min, $t_3 = 90$ min, $t_4 = 120$ min, $t_5 = 150$ min). Scale bar length is 30 μm. **(B)** Representation of the area and **(C)** circularity of the glue droplets, as numbered in panel **(A)**, over the different acquisition time points.

The area and circularity of the glue droplets were calculated over 150 minutes. The calculated parameters indicate that both the area and the shape of the glue droplets remain stable during the observation time. Changes in droplet area and shape are observed only immediately after seeding, likely due to the traction forces exerted during the deposition of the droplets onto the glass substrate. The circularity was computed as:

$$\text{circularity} = 4\pi \cdot \frac{\text{A}}{\text{P}^2}$$

where A is the area of each glue droplet, while P is the perimeter. The closer the circularity to 1, the rounder the glue droplet.

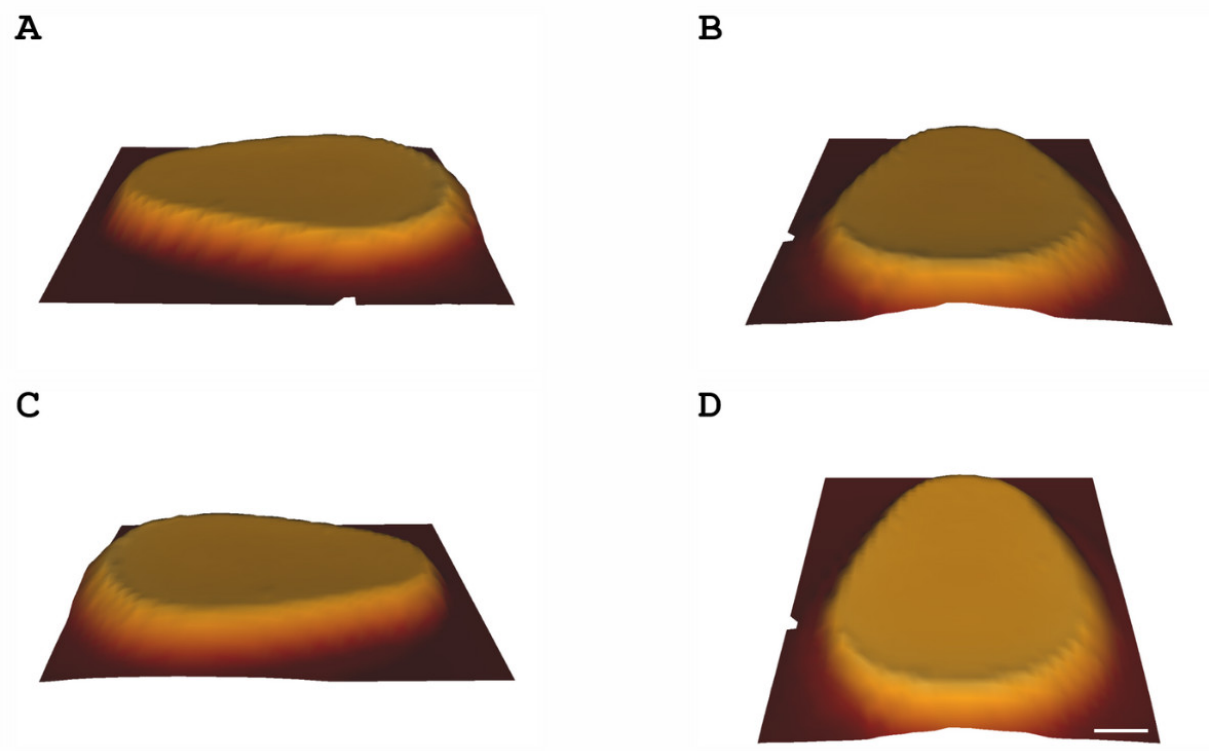

Figure S2: **Modified cantilever 3D reconstruction:** Representation of the different planes of a cantilever properly modified through the wedging process. **(A)** YZ plane ($y > 0$), **(B)** XZ plane, **(C)** YZ plane ($y < 0$), **(D)** XY plane. Scale bar length is 7.5 μm.

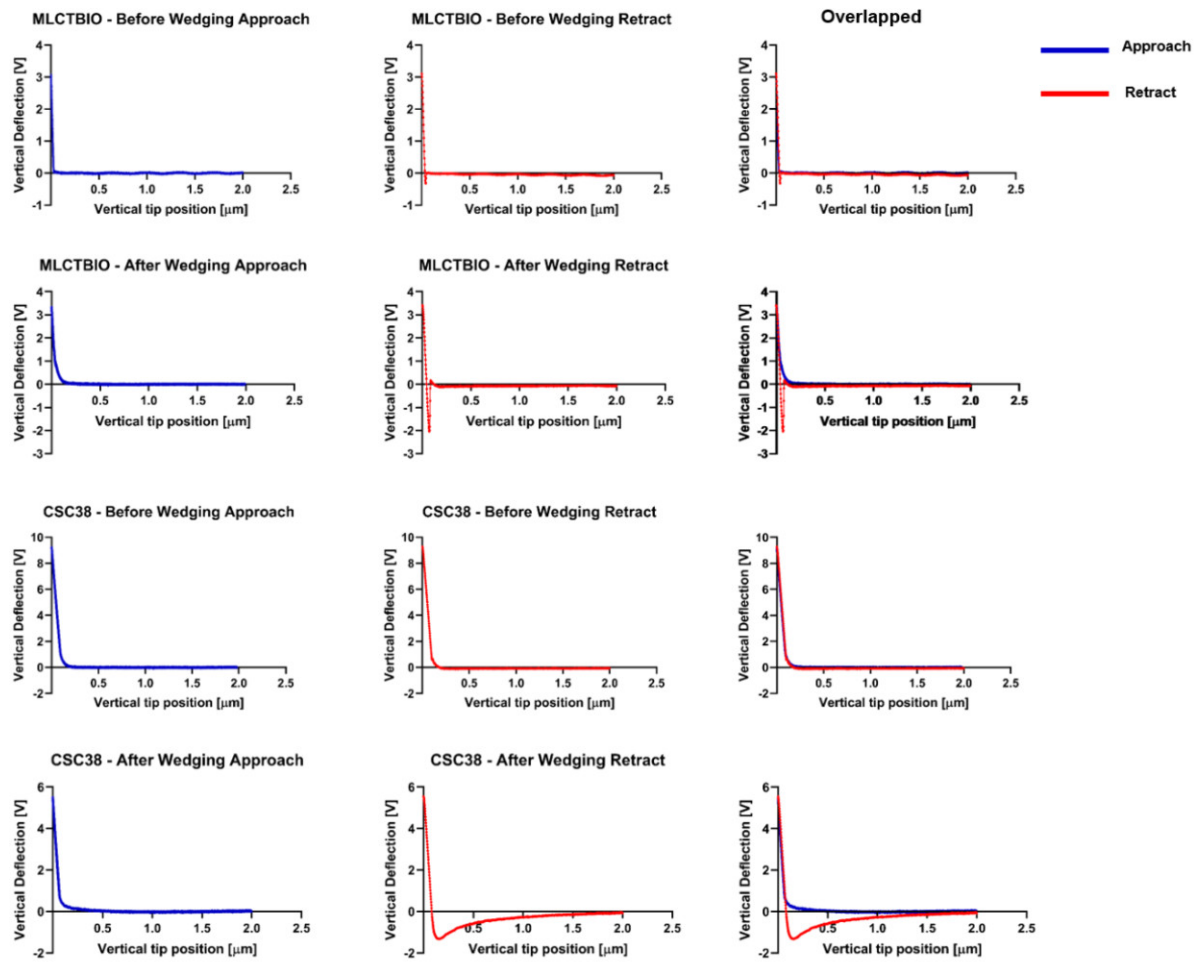

Figure S3: **Sensitivity calibration.** Representation of the averaged force curves acquired to determine the deflection sensitivity of the cantilevers (MLCT-BIO and CSC38) before (first and third row) and after (second and fourth row) the wedging process. The overlap of approach (blue solid line) and retraction (red solid line) curve is shown in the last column.

The deflection sensitivity was calculated by performing a linear fit on 15% of the data from the approach curve, starting from the defined set-point, after acquiring 5 force curves and averaging them. The force curves were recorded on a Petri dish (TPP) in MilliQ water at room temperature. The approach curves (blue solid line), both before and after the wedging process, exhibit classical expected behavior. The difference observed after the wedging process occurs near the contact point, where a more blunt curve is observed and it is associated with the presence of the wedge. Examination of the retraction curves (red solid line) shows that the presence of the wedge on the cantilever increases the tip-substrate adhesion. This increase in adhesion may result in cell attachment to the wedge at the end of a measurement, particularly when analyzing low adhering cells and applying forces exceeding 5 nN. To address this issue, rinsing the cantilever with the buffer adopted during the measurements is sufficient. The deflection sensitivities before the process were: $S_{MLCT-BIO} = 10.23$ nm/V, $S_{CSC38} = 26.22$ nm/V; sensitivities after the process were: $S_{MLCT-BIO} = 14.65$ nm/V, $S_{CSC38} = 22.34$ nm/V.

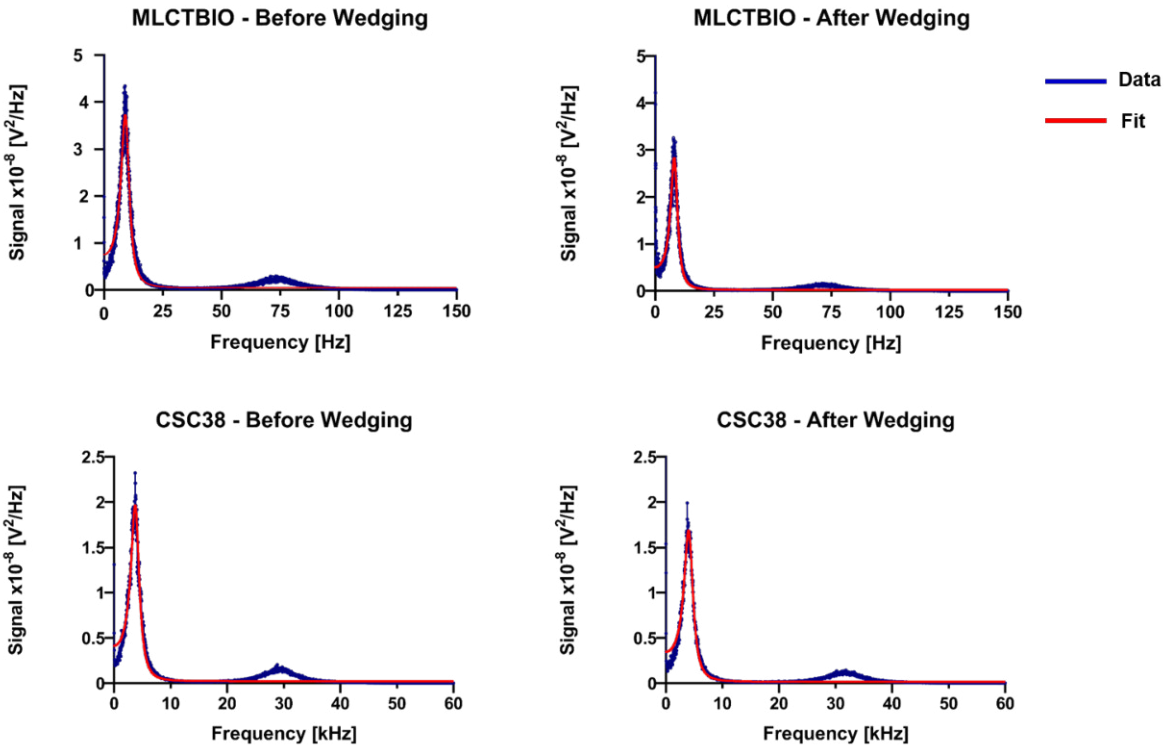

Figure S4: **Thermal noise spectra.** Representation thermal noise spectra, raw data (blue) and Lorentzian fit (red), acquired in MilliQ water at room temperature for different cantilevers (MLCTBIO and CSC38) before (left column) and after (right column) the wedging process.

Modification of the cantilever results in a slight reduction of the first resonance peak in both cases, which could be associated with a change in the determined spring constant. The spring constant values before the process were $k_{MLCT-BIO} = 0.122$ N/m, $k_{CSC38} = 0.136$ N/m; spring constant values after the process were: $k_{MLCT-BIO} = 0.121$ N/m, $k_{CSC38} = 0.140$ N/m.

Impact of the added mass on the cantilever:

According to the work of [15], it is important to estimate the contribution of the added mass to the cantilever to consider whether or not it is necessary to take into account a correction factor during the calibration of the spring constant. To estimate the impact of the added mass, we need to compute the reduced mass $\tilde{m}$ and the reduced gyration radius $\tilde{r}$, defined as

$$\tilde{m} = \frac{m_w}{m_c}, \qquad \tilde{r} = \sqrt{\frac{7}{5}}\frac{R}{L}$$

where m_c is the mass of the cantilever, m_w the mass of the wedge, R the radius of the wedge, and L the nominal length of the cantilever. For a CSC38 rectangular tipless cantilever, the manufacturer's instruction gives: $L = 250\ \mu m$ (length), $w = 32.5\ \mu m$ (width), and $h = 1\ \mu m$ (thick). The density of the cantilever is equal to $\rho_{Si} = 2.32\ g/cm^3$. On the other hand, the wedge attached to the cantilever can be approximated as an ellipse with dimensions of its semi-axis equal to $a = 15\ \mu m$ and $b = 25\ \mu m$ (Fig. S5) with height equal to $h = 10\ \mu m$ (Fig. 3). The density of NOA63 given by the manufacturer is equal to $\rho_{NOA63} \sim 1\ g/cm^3$.

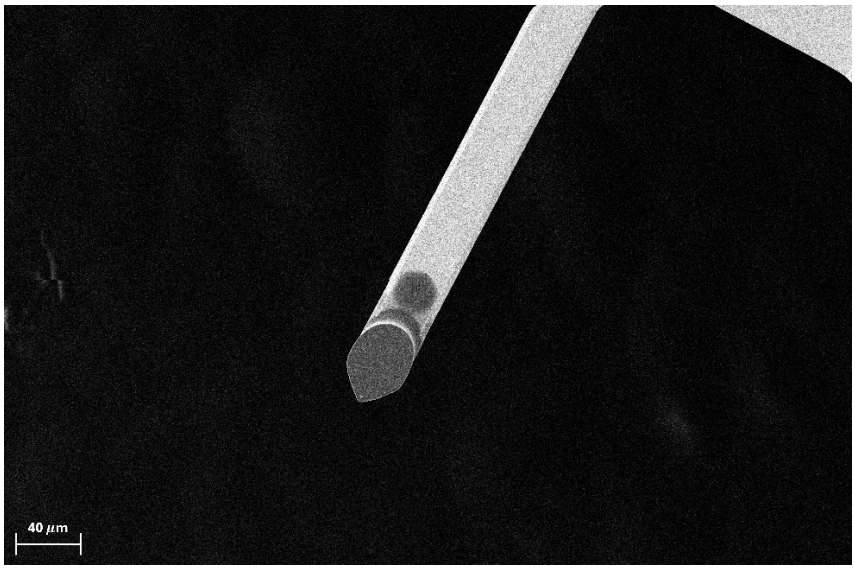

Figure S5: **SEM image of a wedged CSC38 cantilever.**

The reduced mass can be computed as:

$$\tilde{m} = \frac{m_w}{m_c} = 0.62$$

while for the reduced gyration radius we obtained:

$$\tilde{r} = \sqrt{\frac{7}{5}}\frac{R}{L} = 0.067$$

where R was estimated by approximating the wedge to a sphere of volume $V = \frac{4}{3}\pi R^3 = 11780\ \mu m^3$.

Chighizola addresses the issue of the added mass for rectangular cantilevers but does not provide any information for triangular ones. In the absence of a reference for this latter geometry, we decided to use the existing model to consider if the correction factor is needed. We adopted the same procedure described above to calculate $\tilde{m}$ and $\tilde{r}$ for triangular cantilever by starting from the manufacturer's information. We calculated these parameters for the MLCT (BIO and O10)-E cantilever tip (nominal length $L_E = 140\ mum$, nominal width $w_E = 18\ \mu m$), as the F tip is generally less used due to its high spring constant, making it unsuitable for biological investigations. Conversely, the other tip models, D and C, have larger nominal lengths and widths (nominal length $L_D = 225\ \mu m$ and $L_C = 310\ mum$, nominal width $w_D = w_C = 20\ \mu m$), reducing the impact of the added mass compared to the E tip. The calculation led us to $\tilde{m_E} = 1.1$ and $\tilde{r_E} = 0.12$. According to *Chighizola et al.*, since the values $\tilde{m}$ and $\tilde{r}$, for both rectangular and triangular cantilevers give a variation due to the added mass less than 10%, it can be considered negligible (Table 3 of [15]).

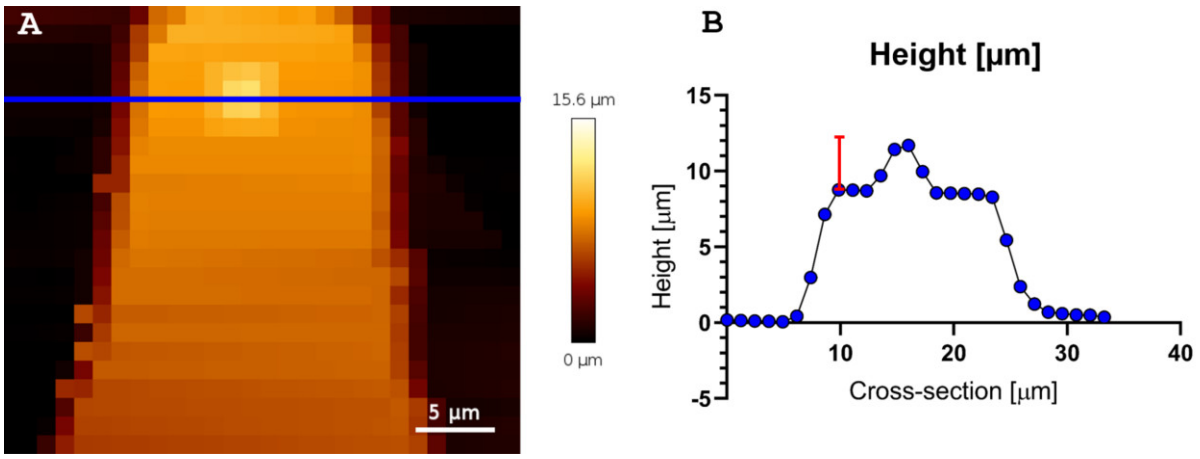

Figure S6: **Failure of the wedging process.** Representation of incomplete coverage of the cantilever tip following the wedging process. **(A)** AFM topography map of a tipped cantilever acquired using the reverse imaging technique. **(B)** Cross-sections of the wedge cantilever along the blue axis. The height profile reconstruction reveals that the tip on the MLCT-BIO cantilever was not fully covered by the polymer added to form the wedge. This failure is attributed to the insufficient size of the glue droplet used during the wedging process. The tip protrudes beyond the wedge by approximately ~ 3 μm (red segment in **(B)**).

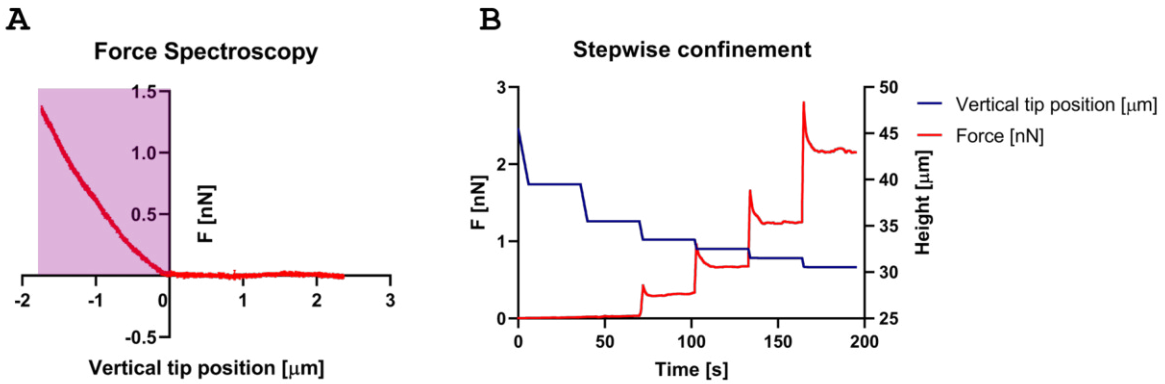

Figure S7: **Comparison of classical force spectroscopy experiments conducted with a sharp tip versus stepwise confinement experiments performed with a wedge tip on the MEC1 cell line.** **(A)** Illustration of a force spectroscopy experiment performed using an MLCT-BIO cantilever. The purple-highlighted region represents the indentation of the tip into the cell, which measures 1.7 μm at the set point force of $\sim$ 1.5 nN. **(B)** Example of a stepwise confinement experiment conducted using a wedge tip. The applied force on the cell (red solid line) and the position of the wedge (blue solid line) are shown.

When comparing the two experiments, it is evident that in force spectroscopy, due to the maximum set-point force $\sim$ 1.5 nN that can be applied with sharp tips without causing cell rupture or damage, the achieved indentation is limited to less than 2 μm. In contrast, during stepwise confinement experiments, where six confinement steps of 6, 4, 2, 1, 1, and 1 μm were applied starting from a height of 20 μm from the bottom of the Petri dish, a greater indentation was achieved. From the contact point, the wedge progressively compressed the cell, resulting in an overall deformation of approximately 5 μm, corresponding to 50% of the dimension of the cell.

Stepwise Confinement Unveils HS1 Contribution to the Mechanical Phenotype of CLL Cells

Riccardo Campanile[a], Jonne Helenius[b], Cristina Scielzo[c], Domenico Salerno[a], Daniel J Müller[b], Francesco Mantegazza[a], and Valeria Cassina[a,*]

[a]School of Medicine and Surgery, BioNanoMedicine Center NANOMIB, Università di Milano-Bicocca, Vedano al Lambro, Italy

[b]Department of Biosystems Science and Engineering, ETH Zurich, Basel, Switzerland

[c]Division of Experimental Oncology, Malignant B cells biology and 3D modelling Unit, IRCCS Ospedale San Raffaele Milano, Italy

[*]Corresponding author: valeria.cassina@unimib.it

Abstract

Chronic Lymphocytic Leukemia (CLL) is characterized by dysregulated cytoskeletal dynamics that influence disease progression. Hematopoietic lineage cell-specific protein 1 (HS1) plays a key role in actin remodeling, yet its mechanobiological impact in CLL remains poorly understood. Here, we investigate the role of HS1 in cellular mechanics using Atomic Force Microscopy-based force spectroscopy and stepwise confinement assays on MEC1 and MEC1-HS1 knock-out cell lines which are two *in vitro* model for human B luekemia. While Young's Modulus measurements showed no significant differences between cell lines, stepwise confinement experiments revealed that HS1 depletion alters cellular viscoelasticity and mechanical properties. Pharmacological treatments with Ibrutinib, Defactinib, Cytochalasin-D and Blebbistatin further highlighted HS1 role in mechanotransduction, with differential responses between MEC1 and KO1 cells. Our findings indicate that HS1 is critical for cytoskeletal integrity and mechanical adaptability, with implications for disease progression and potential mechanotype-based therapeutic strategies.

Abbreviations

AFM, Atomic Force Microscopy; YM, Young's Modulus; HS1, hematopoietic lineage cell-specific protein 1; CLL, Chronic Lymphocytic Leukemia; KO1, MEC1-HS1 knock-out; BCR, B cell receptor; BTK, Bruton's Tyrosine Kinase; PBS, Phosphate-Buffer Saline; RPMI, Roswell Park Memorial Institute; FBS, Fetal Bovine Serum.

Keywords:

1. Chronic Lymphocytic Leukemia;

2. Atomic Force Microscopy;

3. Cell Mechanics;

4. Mechanotransduction;

5. HS1 Protein;

6. Stepwise Confinement.

7. Mechanobiology

1. Introduction

Living cells are highly dynamic systems that continuously interact with their microenvironment, responding to mechanical, chemical, and biological stimuli. These interactions play a fundamental role in key cellular processes, including differentiation, migration, and disease progression [1–3]. From a mechanical perspective, cells exhibit viscoelastic behavior, possessing both solid-like and fluid-like properties that depend on the timescale and magnitude of applied forces [4, 5]. To investigate these biomechanical properties at the single-cell level, several advanced techniques have been developed, including micropipette aspiration [6], optical and magnetic tweezers [7, 8], and Atomic Force Microscopy (AFM) [9, 10].

Among these techniques, AFM has emerged as a powerful and versatile tool for the mechanical characterization of both cells and tissues [11, 12]. In particular, AFM-based force spectroscopy is widely used to determine Young's Modulus (YM), a key parameter describing cellular stiffness. By analyzing the force-indentation response of different cell types and tissues, researchers have established nanomechanical fingerprints that distinguish between physiological and pathological conditions, such as cancerous versus non-cancerous state [13, 14]. This capability is particularly valuable in the study of hematological malignancies, where alterations in cellular mechanics can provide insights into disease detection and progression [15].

In this study, we focus on the role of hematopoietic lineage cell-specific protein 1 (HS1), an actin-binding protein involved in cytoskeletal remodeling, cell adhesion, and migration, in the pathophysiology of Chronic Lymphocytic Leukemia (CLL). CLL is a malignancy characterized by the clonal expansion of mature CD5+ B lymphocytes, which progressively accumulate in the peripheral blood, bone marrow, and secondary lymphoid organs, where they encounter a supportive microenvironment that promotes their accumulation leading to metastasis, and disease progression [16–18]. Elevated HS1 expression in CLL patients has been associated with more aggressive disease phenotypes, with higher levels correlating with accelerated progression and poorer clinical outcomes [19]. Functionally, HS1 is a critical regulator of B cell receptor (BCR) signaling, a key pathway in CLL pathogenesis, and its overexpression has been linked to enhanced leukemic cell survival,

proliferation, and resistance to apoptosis [20]. Additionally, HS1-mediated cytoskeletal remodeling facilitates cellular trafficking between the peripheral blood and lymphoid tissues, a process essential for CLL cell homing and microenvironmental interactions [21].

To elucidate the mechanical role of HS1 in CLL, we employed MEC1 cells, a widely adopted in vitro model of human B leukemia, along with a genetically modified MEC1-HS1 knock-out (KO1) cell line generated using the CRISPR-Cas9 system. This approach allowed us to directly assess how HS1 depletion affects cellular mechanics and viscoelastic properties of the cells.

We initially performed force spectroscopy experiments, by means of AFM, using a square-based pyramidal tip to probe the actomyosin cortex (∼500 nm from external membrane) of both cell lines in basal condition (Fig. S1). Surprisingly, our results revealed no significant differences in YM between MEC1 and KO1 cells (Fig. S1). Given the well-established role of HS1 in regulating actin polymerization and cellular responses to mechanical stimuli, this finding suggested that traditional stiffness measurements might not fully capture the functional impact of HS1 depletion. To gain a more comprehensive understanding of HS1 mechanical contributions, we expanded our investigation by employing a complementary AFM-based approach which exploits a modified wedge tip (Fig. 1**A**) to perform stepwise confinement (Fig. 1**B - F**) on cell lines to study cellular deformation under progressive compression. This approach enabled us to assess diverse mechanical properties of MEC1 and KO1 cells both in basal condition and under various pharmacological treatments, providing deeper insights into the cytoskeletal alterations and cellular response induced by HS1 depletion.

2. Results and Discussion

In this study, to systematically probe cellular mechanics under varying confinement levels, we employed a stepwise AFM-based compression protocol, adopting a modified-wedged tip (Fig. 1**A**) wherein cells were subjected to a series of controlled indentations with progressively increasing deformation (Fig. 1**B**). The procedure enabled the classification of the force response of the cells (Fig. 1**C - F**) into five levels of confinement (<25%, 25–40%, 40–50%, 50–60%, and >60%, respect the original size of the cell), accounting for natural variations in cell size and contact geometry. Furthermore, four pharmacological agents were employed to selectively modulate key signaling pathways involved in cytoskeletal regulation and mechanotransduction in leukemic B cells. Ibrutinib (Fig. 1**D - E**, green data) is a covalent inhibitor of Bruton's Tyrosine Kinase (BTK), a central kinase in B-cell receptor (BCR) signaling that governs adhesion, motility, and cytoskeletal dynamics in CLL cells [22]. Previous studies have shown that Ibrutinib can increase cortical stiffness in leukemic cells, partially restoring their mechanical phenotype toward that of healthy B cells [15, 23]. Defactinib (Fig. 1**D - E**, orange data) is a selective inhibitor of Focal Adhesion Kinase (FAK) and Proline-rich Tyrosine Kinase 2 (PYK2), both of which

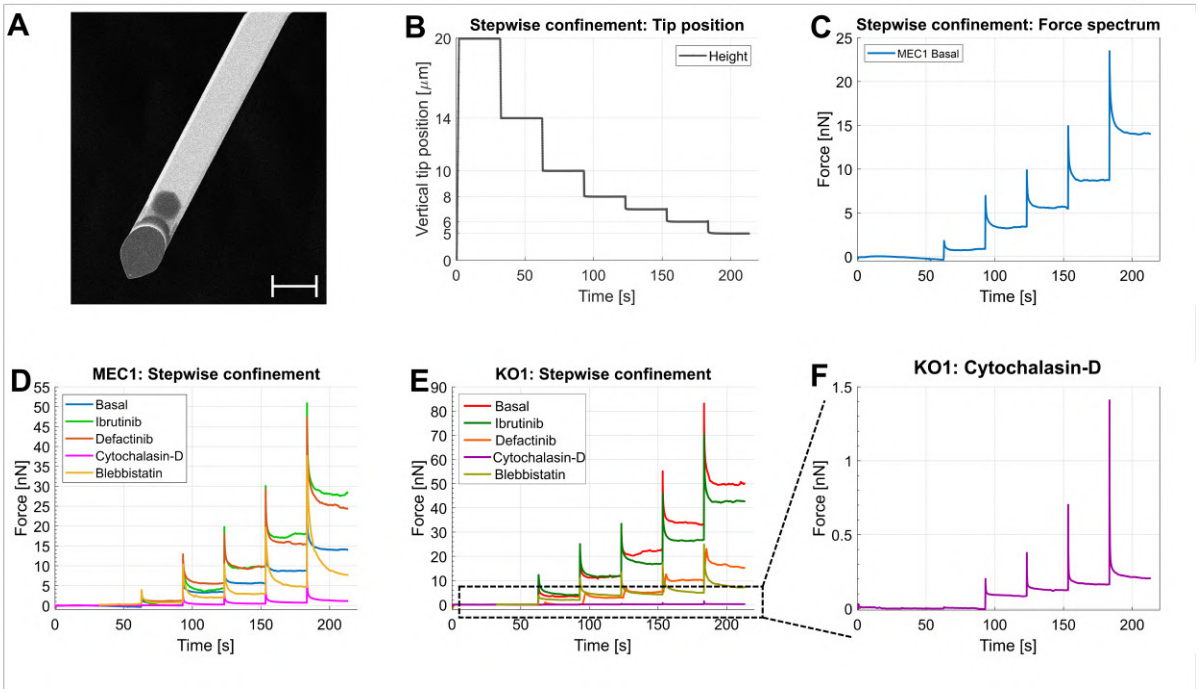

Figure 1: **Stepwise confinement setup and drug-modulated force spectra of MEC1 HS1 cells.** (**A**) scan electron microscopy image of a wedge-shaped modified AFM tip adopted to perform stepwise confinement experiments. Scale bar $40\mu m$. (**B**) Representative plot of the vertical position of the AFM wedged tip during a stepwise confinement experiment, showing six sequential compression steps applied to a single cell. (**C**) Representative force spectrum acquired from untreated MEC1 cell under stepwise confinement, corresponding to the AFM-tip trajectory shown in panel (**B**). (**D, E, F**) Representative force spectra showing the mechanical responses of MEC1 and KO1 cells under different pharmacological treatments during stepwise confinement. Each trace reflects the cell force response profile under sequential compression, with color-coded lines indicating specific drug conditions as detailed in the legend within each plot. The blue trace reported is the same shown in panel (**C**).

coordinate mechanotransduction between the cytoskeleton and the nucleus and are essential for maintaining structural integrity under mechanical stimuli [24, 25]. Cytochalasin-D (Fig. 1**D - F**, purple data) is a potent inhibitor of actin polymerization that binds to the barbed ends of F-actin filaments, preventing elongation and leading to cortical destabilization and mechanical fragility [26, 27]. Finally, Blebbistatin (Fig. 1**D - E**, yellow data) inhibits the ATPase activity of myosin II, disrupting actomyosin contractility, and weakening cortical tension, particularly under high mechanical load [28, 29]. The use of these compounds enabled a systematic evaluation of the role of HS1 in governing cellular mechanical adaptation under compressive stress, revealing significant differences between wild-type MEC1 cells and HS1-deficient, KO1, counterparts.

2.1 Stepwise confinement Reveals Distinct Nanomechanical Response under Basal conditions in MEC1 and KO1 cells

We studied the mechanical parameters illustrated in Fig. 2 **C, F, I, L**. The significancy of the drug effect over these parameters with respect the basal was assessed by Mann-Whitney test and reported. for simplicity of visualization, in Fig. S2. Starting from the basal measurements, mechanical parameters did not differ significantly between MEC1 and KO1 cells during the early stages of confinement (less than 40%) (Fig. S2, tables in first row). However, starting from 40% confinement and beyond, distinct differences emerged, highlighting altered biomechanical behavior associated with HS1 deficiency (Fig. S2, tables in first row).

Specifically, KO1 cells exhibited a significantly lower relaxation time compared to MEC1 at the third ($p = 0.0014$), fourth ($p = 0.0253$), and fifth ($p = 0.0007$) confinement levels (Fig. S2, first row first table). The reduction in relaxation time suggests that KO1 cells have a diminished ability to dissipate mechanical stress over time, indicative of a more solid-like, less viscous cytoskeletal behavior. This behavior likely reflects impaired cytoskeletal remodeling or reduced viscoelastic adaptability in the absence of HS1 [30]. Moreover, the role of HS1 as an actin nucleation-promoting factor that interacts with the Arp2/3 complex underscores its importance in maintaining cytoskeletal remodeling capacity and mechanical flexibility [31].

KO1 cells showed significantly higher loading rates starting from the second confinement ($p = 0.0177$), with increasing significance at the third ($p = 0.0016$) and the highest levels of confinement ($p < 0.0005$). The elevated loading rate indicates that KO1 cells resist deformation more rapidly upon compression, suggesting increased cortical stiffness or altered cytoskeletal tension [15] (Fig. S2 first row second table). This may represent a compensatory response to the loss of HS1, which normally regulates actin branching and remodeling through the Arp2/3 complex [31]. This supports the hypothesis that HS1 loss leads to cytoskeletal rearrangements that manifest as increased mechanical resistance during early deformation [15]. Loading rate was the most sensitive parameter affected by HS1 loss.

Similarly, peak force and resistance to compression were both significantly higher in KO1 cells at the fourth ($p = 0.0028$, $p = 0.0158$, respectively) and fifth ($p = 0.0071$, $p = 0.0294$, respectively) confinement levels (Fig. S2 first row, third and fourth table). These results imply that KO1 cells can generate and sustain greater mechanical loads at higher compression levels, further supporting the notion of increased cellular stiffness or altered force generation mechanisms in the absence of HS1 (Fig. S2 first row, third and fourth table). Increased peak force and mechanical resistance have been linked to cytoskeletal rearrangements that reinforce cell rigidity, particularly through enhanced actin cortex tension and crosslinking [32]. Therefore, these mechanical adaptations may reflect an altered balance between contractile force generation and cytoskeletal remodeling in KO1 cells not detectable with classical force spectroscopy experiment (Fig. S1).

2.2 BTK Inhibition Increases Loading Rate and Cytoskeletal Tension in MEC1 Cells

In MEC1 cells, treatment with Ibrutinib (Fig. 1**D**, green data) did not significantly affect peak force, or resistance to compression during confinement (Fig. 2**G, I, J, L**). However, a clear and statistically significant effect was observed on the loading rate (Fig. 2**D, F**). Specifically, Ibrutinib induced a marked, confinement-dependent increase in loading rate , with statistically significant differences beginning from the first compression level (<25% cell height; $p = 0.0271$) and becoming progressively stronger with deeper compressions ($p = 0.0035$ for the 25–40% confinement, $p = 0.0028$ for the 40–50% confinement, $p = 0.0006$ for 50–60% confinement and $p < 0.0005$ above 60% compression) (Fig. 2**D, F**). These results indicate that Ibrutinib treatment leads to progressive mechanical stiffening of MEC1 cells under compressive stress. This observation aligns with Ibrutinib known mechanism of action. As a covalent inhibitor of BTK, Ibrutinib blocks a central node in BCR signaling, which regulates cell adhesion, motility, and cytoskeletal dynamics in CLL cells [22]. Although its biochemical effects are well-documented, recent studies have also revealed its ability to influence mechanical properties of CLL cells [15]. Notably, Ibrutinib has been shown to increase cortical stiffness (YM) in primary CLL cells, thereby restoring their mechanical phenotype closer to that of healthy B cells [15]. The observed increase in loading rate in MEC1 cells is consistent with these findings, suggesting that BTK inhibition enhances cortical tension and strengthens the cells ability to resist deformation [23]. This mechanical stiffening may arise from BTK inhibition-induced actin cytoskeletal reorganization, enhanced myosin contractility, or increased focal adhesion maturation [15, 33]. In this context, Ibrutinib appears to reinforce mechanical integrity through cytoskeletal remodeling, even in the absence of significant changes in peak force or compressive resistance.

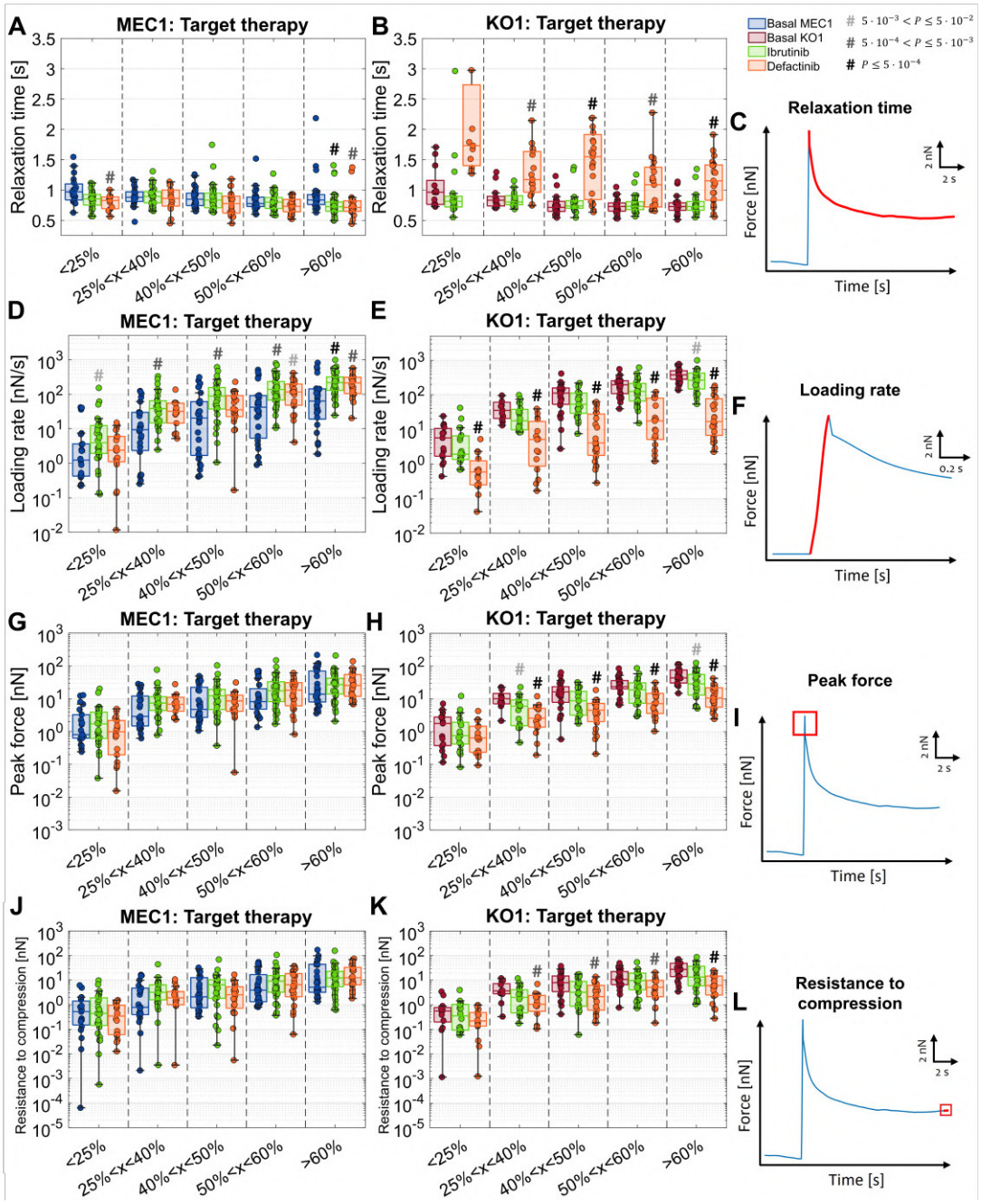

Figure 2: **Mechanical response of MEC1 and KO1 cells to Ibrutinib and Defactinib under stepwise confinement.** (**A, B**) Distribution of relaxation time values across all confinement steps for untreated (basal) and drug treated MEC1 and KO1 cells. Conditions are color-coded as described in the legend. **C, F, I, L**) Insets summarizing the studied mechanical parameters shown in the adjacent left-hand panels: (**C**) relaxation time, (**F**) loading rate, (**I**) peak force, and (**L**) resistance to compression. (**D, E**) Distribution of loading rate values at each confinement level for basal and treated MEC1 and KO1 cells. (**G, H**) Distribution of peak force values measured during each confinement step in basal and treated MEC1 and KO1 cells. (**J, K**) Distribution of resistance to compression measured at the end of each confinement phase for basal and treated MEC1 and KO1 cells. The data represented within each boxplot correspond to 50% of the dataset, central line is the median and the confidence intervals are calculated at the 95% level. Statistical significance of each treatment condition versus the corresponding basal condition at each confinement step, calculated using the Mann–Whitney test.

2.3 HS1 Deficiency Impairs Modification in Mechanical Parameters in KO1 Cells Upon Ibrutinib Treatment

In KO1 cells, Ibrutinib treatment (Fig. 1**E**, green data) did not produce significant changes in any of the measured mechanical parameters, including loading rate (Fig. 2**B, C, E, F, H, I, K, L**). This lack of response contrasts with the progressive increase in loading rate observed in MEC1 cells under the same treatment conditions. These results suggest that HS1 is essential for the mechanical remodeling induced by BTK inhibition. Without HS1, leukemic B cells fail to alter their biomechanical phenotype in response to Ibrutinib. HS1 functions as an actin-regulatory protein linking BCR signaling to cytoskeletal dynamics through its interactions with F-actin and the Arp2/3 complex, facilitating branched actin polymerization and remodeling [31]. Its absence likely restricts the cell capacity to reorganize the cytoskeleton and adapt mechanically to external forces or pharmacological agents [34]. Notably, Ibrutinib inhibits BTK, which under normal conditions phosphorylates HS1 [35]. In KO1 cells, where HS1 is already depleted, the effect of Ibrutinib on cell mechanics appears negligible, as HS1 is not present to mediate downstream cytoskeletal responses. Thus, HS1 emerges as a key mediator of cytoskeletal plasticity that enables mechanical responses to BTK inhibition in CLL cells.

2.4 FAK Inhibition Enhances Cytoskeletal Dynamics and Stiffness in MEC1 Cells

Treatment with Defactinib (Fig. 1**D**, orange data) elicited distinct mechanical responses in MEC1 and KO1 CLL cell lines. In particular, MEC1 cells exhibited a significant increase in loading rate at the fourth ($p = 0.0223$) and fifth ($p = 0.0017$) confinement levels (Fig. 2**D, F**), indicating greater mechanical resistance as compressive depth increased. This increase in loading rate suggests that Defactinib enhances cellular stiffness particularly when internal structures are engaged, likely the nucleus [36]. Such behavior aligns with the recognized role of FAK in maintaining nuclear integrity and coordinating mechanotransduction processes that bridge the cytoskeleton and nucleus [25, 37].

In particular, despite these viscoelastic changes, peak force (Fig. 2**G, I**) and resistance to compression (Fig. 2**J, L**) were not significantly altered, indicating that while cytoskeletal stiffness was enhanced, the cells capability to exert force while being compressed and their resistance to deformation remained unchanged in MEC1 cells [38].

2.5 Defactinib Impairs Mechanical Resilience in HS1-Deficient KO1 Cells

In KO1 cells Defactinib treatment (Fig. 1**E**, orange data) induced deep alterations in mechanical behavior, markedly distinct from those observed in their HS1-expressing counterparts. Relaxation time progressively increased across confinement steps, with signific-

ant differences emerging in every level of confinement starting from the second ($p = 0.0028$, $p < 0.0005$ for the third, $p = 0.0039$ for the fourth and $p < 0.0005$ for the fifth), indicating a decreased capacity to dissipate stress after deformation (Fig. 2**B, C**). This suggests that, in the absence of HS1, FAK inhibition compromises the cytoskeletal ability to adapt to mechanical strain, leading to increased intracellular viscosity and slower mechanical recovery. Such behavior may reflect a weakened physical coupling between the cytoskeleton and the nucleus, reducing the efficiency of nuclear deformation and force redistribution during compression [39].

In parallel, KO1 cells displayed a consistent and highly significant reduction in loading rate across all confinement levels ($p < 0.0005$) (Fig. 2**E, F**), indicating reduced stiffness and mechanical resistance. This was further supported by a significant decrease in peak force at all levels ($p < 0.0005$) except the first (Fig. 2**H, I**), and a reduction in resistance to compression that reached significance in the second ($p = 0.0017$), third ($p = 0.0037$), fourth ($p = 0.0015$) and fifth ($p < 0.0005$) confinement levels (Fig. 2**K, L**). Together, these findings demonstrate that the absence of HS1 severely impairs the structural integrity and mechanical resilience of CLL cells when FAK signaling is inhibited, reinforcing the necessity of HS1 for sustaining force transmission under mechanical stress [40]. Indeed, HS1 likely plays a key role in actin polymerization and cytoskeletal remodeling in response to mechanical stress [41]. Without it, FAK inhibition not only disrupts focal adhesion signaling but also exacerbates cellular vulnerability by destabilizing cytoskeletal tension and weakening cell-matrix adhesions, resulting in an inability to maintain biomechanical resistance under compressive load [30, 42].

2.6 Cytochalasin-D Alters Viscoelastic and Force-Generating Properties of MEC1 Cells

Treatment of MEC1 an KO1 cells with Cytochalasin-D induced marked alterations in their mechanical behavior.

Following Cytochalasin-D treatment (Fig. 1**D**, purple data), MEC1 cells exhibited a significant reduction in relaxation time across all confinement levels, with $p < 0.0005$, except for the second confinement level ($p = 0.0008$) (Fig. 3**A, C**). This decrease suggests a shift toward a more solid-like mechanical behavior, indicating a diminished capacity to dissipate mechanical stress [26, 43]. Such behavior likely reflects compromised cytoskeletal viscoelasticity, due to the inhibition of actin polymerization which lead to and impairment of cell adaptive deformation mechanism under stress [43, 44].

Interestingly, the loading rate (Fig. 3**D, F**) remained unaffected by Cytochalasin-D treatment in MEC1 cells. The preservation of this parameter despite actin disruption suggests that HS1 may play a compensatory role in preserving mechanical resistance since its depletion causes a steeper decrease of the loading rate in KO1 cells (Fig. 3**E, F**). In fact, HS1 binds to both F-actin and the Arp2/3 complex via its coiled-coil and repeat domains promoting actin polymerization and stabilizing branched actin structures [45].

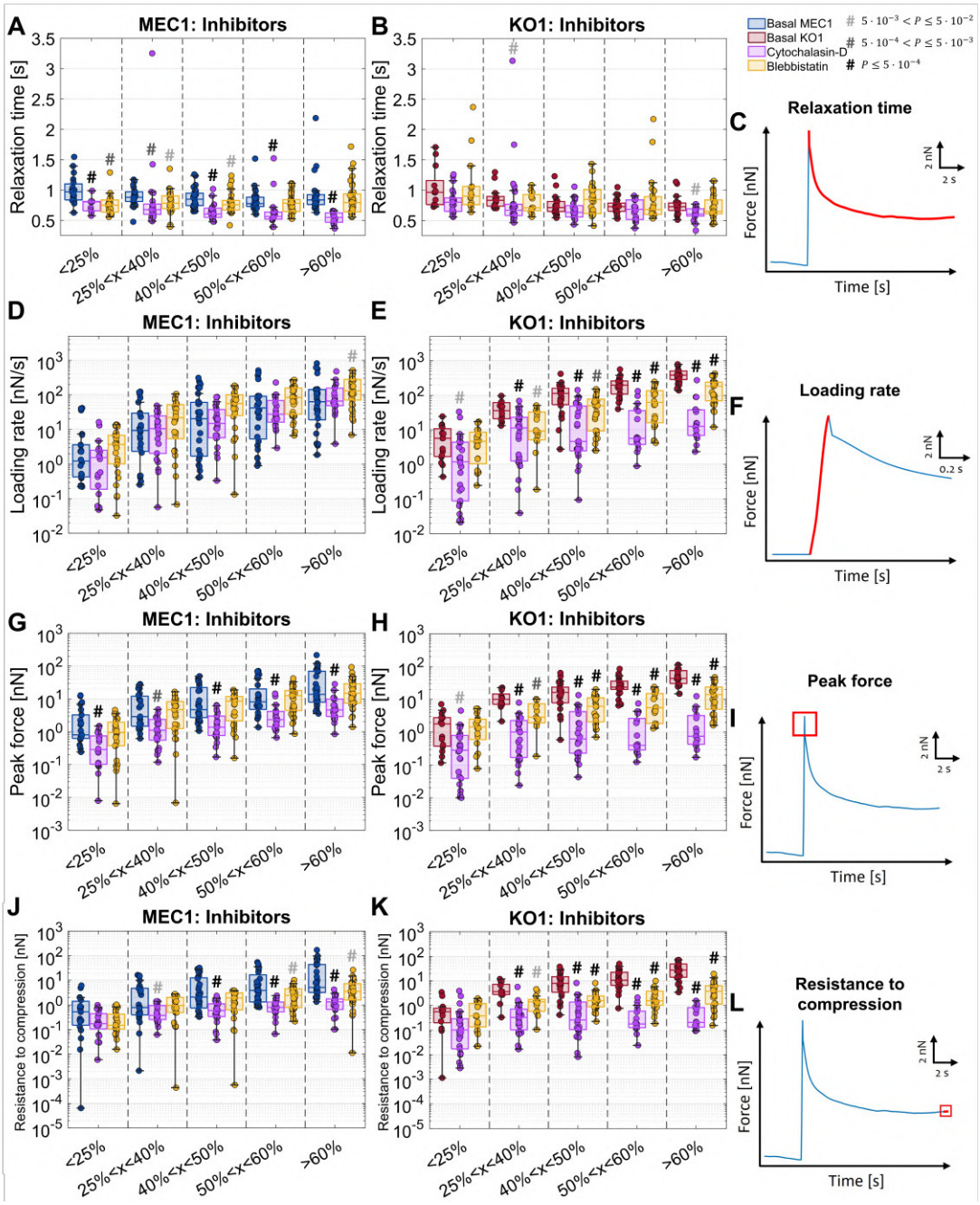

Figure 3: **Mechanical response of MEC1 and KO1 cells to Cytochalasin-D and Blebbistatin under stepwise confinement.** (**A, B**) Distribution of relaxation time values across all confinement steps for untreated (basal) and drug treated MEC1 and KO1 cells. Conditions are color-coded as described in the legend. (**C, F, I, L**) Insets summarizing the studied mechanical parameters shown in the adjacent left-hand panels: (**C**) relaxation time, (**F**) loading rate, (**I**) peak force, and (**L**) resistance to compression. (**D, E**) Distribution of loading rate values at each confinement level for basal and treated MEC1 and KO1 cells. (**G, H**) Distribution of peak force values measured during each confinement step in basal and treated MEC1 and KO1 cells. (**J, K**) Distribution of resistance to compression measured at the end of each confinement phase for basal and treated MEC1 and KO1 cells. The data represented within each boxplot correspond to 50% of the dataset, central line is the median and the confidence intervals are calculated at the 95% level. Statistical significance of each treatment condition versus the corresponding basal condition at each confinement step, calculated using the Mann–Whitney test.

Therefore, the ability of HS1 to stabilize actin structures and promote polymerization may help maintain loading rate values close to those observed under basal conditions, buffering the mechanical impact of Cytochalasin-D [44, 46].

In contrast, both peak force (Fig. 3**G, I**) and resistance to compression (Fig. 3**J, L**) were significantly reduced following treatment, indicating a diminished ability to sustain mechanical load and resist deformation. Specifically, peak force was significantly decreased across all confinement levels with $p < 0.0005$, but for the second in which $p = 0.0008$ (Fig. 3**G, I**). Resistance to compression was also reduced, starting from the second confinement level in which $p = 0.0176$ and becoming even more pronounced in subsequent levels with $p < 0.0005$ (Fig. 3**J, L**). These findings further highlight the essential role of the actin cortex in force generation and mechanical resilience. The loss of structural integrity under increasing compression suggests that MEC1 cells become more compliant and mechanically fragile when actin dynamics are perturbed due to actin depolymerization which compromises cortical stiffness and mechanical stability [27, 47, 48].

2.7 KO1 Cells Exhibit Increased Sensitivity to Actin Disruption

Treatment of KO1 cells with Cytochalasin-D (Fig. 1**E - F**, purple data) led to significant changes in their mechanical behavior. Specifically, a significant reduction in loading rate, peak force, and resistance to compression was observed following Cytochalasin-D treatment (Fig. 3**E, F, H, I, K, L**). The loading rate ($p = 0.0143$) (Fig. 3**E, F**) and peak force ($p = 0.0051$) (Fig. 3**H, I**) were already reduced at the first compression step, while resistance to compression (Fig. 3**K, L**) remained unchanged at that level. From the second confinement onward, all three parameters exhibited highly significant decreases ($p < 0.0005$), suggesting a pronounced impairment in the cells ability to sustain mechanical load and resist deformation. These findings underscore the central role of the actin cytoskeleton in maintaining mechanical integrity in KO1 cells. The pronounced mechanical weakening following actin disruption suggests that, in the absence of HS1, KO1 cells lack the compensatory mechanisms required to preserve biomechanical resilience, further reinforcing the importance of cytoskeletal integrity in force generation and mechanical stability [48–50]. Indeed, HS1 acts as a nucleation-promoting factor, linking signaling pathways to actin remodeling via the Arp2/3 complex [31], its depletion may prevent adequate cytoskeletal compensation during pharmacological perturbation [51]. These results reinforce the idea that actin integrity—along with HS1-mediated cytoskeletal regulation—is essential for maintaining biomechanical strength and stability in leukemic B cells.

2.8 Blebbistatin Modulates MEC1 Mechanics Without Affecting Force Generation

Upon treatment with Blebbistatin (Fig. 1**D**, yellow data), MEC1 cells exhibited significant alterations in their mechanical behavior. A notable reduction in relaxation time was observed at the first ($p = 0.0016$), second ($p = 0.0258$), and third ($p = 0.0257$) compression levels, indicating a shift toward a more solid-like phenotype with diminished capacity to dissipate mechanical stress (Fig. 3**A, C**). This result implies that myosin II contributes to the viscoelastic response of the cell, and its inhibition stiffens shift cell behavior to more solid-like by limiting internal rearrangement [28], as similarly reported with actin-disrupting agents [49, 52].

Surprisingly, no significant changes were detected in peak force across confinement steps (Fig. 3**G, I**), indicating that the ability of MEC1 cells to respond actively during compression remains intact despite myosin II inhibition. This finding contrasts with prior studies [53, 54] showing reduced contractility following myosin II blockade and may be explained by compensatory mechanisms likely involving HS1, promoting linking of F-actin to the Arp2/3 complex, thus leading to the formation of stable branched actin networks [45].

Finally, a significant reduction in resistance to compression was observed only at the final two compression steps ($p = 0.0251$ and $p = 0.0066$) (Fig. 3**J, L**), highlighting the essential role of myosin II in maintaining cellular structural integrity under sustained or high-intensity mechanical stress. These results underscore the contribution of actomyosin dynamics to mechanical resilience and suggest that MEC1 cells can maintain some mechanical functions in the early phases of compression despite impaired contractility [28].

2.9 Decoupling Viscoelastic and Contractile Mechanics in KO1 Cells under Blebbistatin Treatment

Upon inhibition of myosin II with Blebbistatin (Fig. 1**E**, yellow data), KO1 cells displayed a distinctive mechanical profile, indicating selective dependence on actomyosin contractility for specific aspects of mechanical behavior. Notably, relaxation time remained unaffected across all levels of confinement (Fig. 3**B, C**), suggesting that the viscoelastic properties of KO1 cells, in particular their ability to dissipate mechanical stress, are largely independent of myosin II function. This preservation of relaxation dynamics may (Fig. 3**B, C**) reflect cytoskeletal adaptations or a diminished reliance on contractile machinery in the absence of HS1, which could rewire mechanical compensation through alternative pathways.

While relaxation time remained unchanged substantial changes were observed in the cell ability to resist and respond to mechanical stress. Starting from the second confinement step, KO1 cells showed a marked reduction in loading rate ($p = 0.0082$), with

even stronger effects in the third ($p = 0.0018$), fourth, and fifth steps ($p < 0.0005$) (Fig. 3**E, F**). A similar trend was observed in peak force, which decreased significantly from the second confinement onward ($p = 0.0035$; $p < 0.0005$ in subsequent steps) (Fig. 3**H, I**). This progressive decline suggests that myosin II contributes increasingly to resistance against deformation as the mechanical load deepens, particularly when nuclear or perinuclear regions are engaged. Thus reflecting a compromised capacity for generating active contractile force, reinforcing the role of myosin II in sustaining intracellular tension during compression. These findings are consistent with prior studies showing that Blebbistatin-induced myosin II inhibition reduces cytoskeletal contractility and disrupts stress fiber formation, leading to decreased cortical tension and mechanical strength [55, 56].

Likewise, resistance to compression was significantly reduced beginning at the second confinement ($p = 0.0103$), with more pronounced reductions at higher compressive loads ($p < 0.0005$) (Fig. 3**K, L**), suggesting a critical role for myosin II in preserving structural resilience under sustained stress. Additionally, AFM-based studies have confirmed that loss of myosin-generated tension weakens cellular stiffness and limits force generation, particularly under high-load conditions [57].

Furthermore, comparing the effect of Blebbistatin on KO1 cells with MEC1, it becomes clear that the presence of HS1 is not only important for organizing the actin cytoskeleton but also crucial to preserving cellular mechanical integrity. In MEC1 cells, Blebbistatin has a milder effect, selectively impacting the studied mechanical parameters only at high confinement. In contrast, KO1 cells exhibit a broader and more pronounced reduction across all elastic parameters, particularly loading rate, peak force, and resistance to compression—closely resembling the mechanical vulnerability induced by Cytochalasin-D. This suggests that HS1 may provide compensatory cytoskeletal stabilization in response to contractility loss [31, 44] due to myosin II inhibition.

3. Conclusion

Chronic Lymphocytic Leukemia is characterized by disrupted cytoskeletal dynamics that influence the mechanical behavior of malignant B cells and affect their ability to respond to environmental cues. Among the molecular regulators of cytoskeletal organization, the hematopoietic lineage cell-specific protein 1 has been implicated in actin remodeling and B cell receptor signaling, but its mechanobiological role has remained unclear. This study aimed to elucidate the contribution of HS1 to the mechanical properties of leukemic cells by comparing MEC1 cells and their HS1-deficient counterparts under stepwise confinement using atomic force microscopy.

The results demonstrated that although HS1 depletion did not alter basal stiffness measured by Young's Modulus, it significantly impaired the cells ability to adapt mechanically. HS1-deficient cells exhibited shorter relaxation times and reduced resistance to compression, especially under pharmacological perturbation. Ibrutinib, a BTK in-

hibitor, increased the loading rate and reduced relaxation time in MEC1 cells, indicating enhanced cytoskeletal tension and solid-like behavior, but had little effect in KO1 cells, revealing a loss of mechanical responsiveness in the absence of HS1. Similarly, Defactinib, a FAK/PYK2 inhibitor, increased stiffness and reduced relaxation time in MEC1 cells, suggesting a reinforcement of cytoskeletal dynamics, whereas it markedly weakened HS1-deficient cells, leading to increased viscosity and reduced mechanical resistance. Cytochalasin-D, an actin polymerization inhibitor, disrupted viscoelastic and force-generating properties in both cell types but had a more severe impact on KO1 cells, confirming their heightened mechanical fragility. Lastly, Blebbistatin, a myosin II inhibitor, modestly affected MEC1 cells under high compression, but significantly reduced stiffness and force generation in KO1 cells, further underscoring HS1's role in preserving mechanical resilience under stress.

Collectively, these findings reveal that HS1 is a key mediator of leukemic cell mechanics, enabling proper cytoskeletal remodeling and force transmission in response to mechanical stress and pharmacological challenge. The study highlights that stepwise confinement is a sensitive approach to detect dynamic mechanical phenotypes not captured by conventional stiffness measurements. These insights suggest that HS1 may serve not only as a mechanotransductive effector but also as a potential therapeutic target or biomarker for CLL, especially in the context of treatments that rely on altering cell mechanics.

4. Materials and Methods

4.1 Cell culture

MEC1 cell line [58] was obtained from Deutsche Sammlung von Mikroorganismen und Zellkulturen GmbH (DSMZ, Braunschweig, Germany) and was recently genotyped as follows: 10 ng of MEC1 cell DNA was purified with the QiAmp DNA Mini Kit (Qiagen, Düsseldorf, Germany) and amplified by PCR with GenePrint ®10 System (Qiagen, Düsseldorf, Germany) and sold Eurofins Genomics Standard FLA Service to perform genotyping. Data were analyzed with DSMZ Online STR Analysis. We confirmed the identity of the cell line analyzed. MEC1 cells were cultured in RPMI-1640 with red phenol (Euroclone, Pero, Italy), supplemented with 10% (v/v) FBS and 15 mg/ml Gentamicin at 37°C and 5% CO_2.

4.2 Stepwise confinement experiment

Experiments were conducted using an atomic force microscope (Nanowizard IV XP Bruker) operating in force spectroscopy mode, specifically in advanced mode, following a predefined sequence of operations.

Initially, the AFM tip was retracted from the bottom of the plate until a height of 20 μm above the surface was reached, with a retraction velocity of 10 μm/s and an acquisition

frequency of 2048 Hz. Subsequently, six confinement steps were applied sequentially, with step sizes of 6, 4, 2, 1, 1, and 1 μm, respectively. The approach velocity for each step was set to 10 μm/s. After each confinement step, the tip position (height) was kept constant for 30 seconds, allowing the force to evolve freely as the cell underwent relaxation. During the lowering steps of the AFM tip and the confinement phases, the acquisition frequency was set at 4096 Hz. A z-closed loop control was maintained throughout the experiment. At the end of the sixth confinement step, the tip was retracted from the cell until it reached a height of 50 μm above the bottom of the Petri dish. Due to natural variability in cell diameter (ranging from 14 to 18 μm), the six sequential indentations performed by the AFM tip were grouped into five confinement levels, as not all cells were actually confined during the initial lowering of the AFM tip. Different percentages of cell confinement levels (<25%, between 25-40%, between 40-50%, between 50-60% and >60%, respect the original size of the cell) were calculated based on the estimated contact point, and thus on the known cell size.

Stepwise confinement experiments were carried out using a modified wedged AFM tip [59, 60]. Before each experiment, the tip was subjected to a calibration process, during which sensitivity was determined by acquiring a force-distance curve on a standard glass slide [10, 61], while the spring constant was estimated using the thermal noise method [62].

Stepwise experiments were performed on living cell lines, MEC1 and KO1, that were plated on Poly-L-Ornithine (Sigma)-coated Petri dishes (TPP). The coating was prepared by diluting Poly-L-Ornithine 1 : 10 in PBS, incubating for 30 minutes at 37°C at 5% CO_2, and washing with PBS before cell seeding. Seeding procedure was performed by adding the cells directly into the Petri dish and incubating them at 37°C at 5% CO_2 for 2 hours before starting the experiment. During the experiments, cells were maintained in cell culture medium (RPMI-1640 with red phenol, Euroclone, Pero, Italy), supplemented with 10% (v/v) FBS, 15 mg/ml Gentamicin, and 10% HEPES (Sigma, N_2-hydroxyethylpiperazine-N_2-ethane sulfonic acid).

For each cell lines and condition, 15-20 cells were measured and analyzed.

4.3 Pharmacological treatments

In the proposed experiments, four different pharmacological treatments were applied to each cell line.

4.3.1 Ibrutinib treatment

Ibrutinib treatment was performed by adding the drug directly to the cell culture at a final concentration of 10 μM. Cells were incubated at 37°C at 5% CO_2 for 4 hours. After incubation, the drug was removed by centrifuging the suspension at 1500 RPM for 5 minutes. The supernatant was discarded, and the cells were resuspended in fresh culture medium before being plated in a Petri dish previously coated with Poly-L-Ornithine.

4.3.2 Defactinib treatment

Defactinib treatment was performed by adding the drug directly to the cell culture at a final concentration of 4 μM. Cells were incubated at 37°C at 5% CO_2 for 4 hours. After incubation, the drug was removed by centrifuging the suspension at 1500 RPM for 5 minutes. The supernatant was discarded, and the cells were resuspended in fresh culture medium before being plated in a Petri dish previously coated with Poly-L-Ornithine.

4.3.3 Cytochalasin-D treatment

Cytochalasin-D treatment was performed directly adding the drug to plated cells in a coated Petri dish at a dilution of 1:1000 from a stock solution with a concentration of 1 mg/ml. The drug was incubated for 30 minutes at 37°C at 5% CO_2 before starting the AFM measurements. During the measurements, Cytochalasin-D was maintained in the solution containing the cells.

4.3.4 Blebbistatin treatment

Blebbistatin treatment was performed directly adding the drug to plated cells in a coated Petri dish at a final concentration of 25 μM. The drug was incubated for 45 minutes at 37°C at 5% CO_2 before starting the AFM measurements. During the measurements, Blebbistatin was maintained in the solution containing the cells.

4.4 Data analysis

Force curve analysis was performed using custom MATLAB scripts. The mechanical parameters of interest were estimated as follows: the characteristic relaxation time was obtained by fitting the stress-relaxation phase with a single exponential decay function, providing insight into the viscoelastic properties of the sample according to the following equation:

$$f(x) = A\mathrm{e}^{-t/\tau} + B \tag{1}$$

Where τ is the characteristic relaxation time and A, B normalization constant. The loading rate parameter, accounting for cellular stiffness and surface tension, was derived by applying a linear fit to the force vs time curve during the approach phase of each step of the AFM tip. The peak force parameter, representing the cellular response to confinement, was estimated as the force value reached at the end of the vertical indentation step performed by the AFM tip. Furthermore, the resistance of compression was estimated by computing the median of the last ten force values at the end of each confinement phase. All the mechanical parameters were estimated implementing ad hoc MATLAB script.

Lastly, statistical significance between dataset was assessed using the Mann-Whitney test, implemented in a custom MATLAB script.

Highlights:

1. HS1 depletion reduces relaxation time and increases stiffness in MEC1 cells.
2. Stepwise confinement reveals HS1 mechanobiological role beyond Young's Modulus.
3. Drug responses differ in MEC1 and KO1 cells, highlighting HS1 role in mechanotransduction.
4. HS1 supports mechanoadaptation, enabling cells to adjust to mechanical stress.
5. Therapeutic potential: HS1 modulation may impact CLL treatment strategies.

CRediT authorship contribution statement

Riccardo Campanile: Data curation, Methodology development, Software development, Visualization, Investigation, Project administration, Writing - original draft, Writing - review & editing and Conceptualization. Jonne Helenius: Project administration, Writing - review & editing, Supervision. Cristina Scielzo: Writing - review & editing, Resources, Supervision. Domenico Salerno: Writing - review & editing, Resources, Funding acquisition, Supervision. Daniel J Müller: Writing - review & editing, Resources, Supervision. Francesco Mantegazza: Writing - review & editing, Resources, Funding acquisition, Supervision. Valeria Cassina: Writing - review & editing, Resources, Supervision.

Declaration of competing interest

The authors declare that they have no known competing financial interests or personal relationships that could have appeared to influence the work reported in this paper

Acknowledgment

Supported by a grant from Italian Ministry for Universities and Research (MUR), Dipartimenti di Eccellenza 2023-2027 (l. 232/2016, art. 1, commi 314–337).

References

[1] Curtis, A., & Clark, P. (1990). The effects of topographic and mechanical properties of materials on cell behavior. *Critical Reviews in Biocompatibility*, 5(4), 343–362.

[2] Alcaraz, J., Buscemi, L., Grabulosa, M., Trepat, X., Fabry, B., Farré, R., & Navajas, D. (2003). Microrheology of human lung epithelial cells measured by Atomic Force Microscopy. *Biophysical Journal*, 84(3), 2071–2079.

[3] Han, S.-B., Kim, J.-K., Lee, G., & Kim, D.-H. (2020). Mechanical properties of materials for stem cell differentiation. *Advanced Biosystems*, 4(11), 2000247.

[4] Rother, J., Nöding, H., Mey, I., & Janshoff, A. (2014). Atomic Force Microscopy-based microrheology reveals significant differences in the viscoelastic response between malign and benign cell lines. *Open Biology*, 4(5), 140046.

[5] Mahaffy, R., Shih, C., MacKintosh, F., & Käs, J. (2000). Scanning probe-based frequency-dependent microrheology of polymer gels and biological cells. *Physical Review Letters*, 85(4), 880.

[6] Hochmuth, R. M. (2000). Micropipette aspiration of living cells. *Journal of Biomechanics*, 33(1), 15–22.

[7] Zhang, H., & Liu, K.-K. (2008). Optical tweezers for single cells. *Journal of the Royal Society Interface*, 5(24), 671–690.

[8] De Vries, A. H., Krenn, B. E., van Driel, R., & Kanger, J. S. (2005). Micro magnetic tweezers for nanomanipulation inside live cells. *Biophysical Journal*, 88(3), 2137–2144.

[9] Wu, P.-H., Aroush, D. R.-B., Asnacios, A., Chen, W.-C., Dokukin, M. E., Doss, B. L., Durand-Smet, P., Ekpenyong, A., Guck, J., Guz, N. V., et al. (2018). A comparison of methods to assess cell mechanical properties. *Nature Methods*, 15(7), 491–498.

[10] Butt, H.-J., Cappella, B., & Kappl, M. (2005). Force measurements with the Atomic Force Microscope: Technique, interpretation and applications. *Surface Science Reports*, 59(1-6), 1–152.

[11] Lekka, M. (2016). Discrimination between normal and cancerous cells using AFM. *Bionanoscience*, 6, 65–80.

[12] Zemła, J., Danilkiewicz, J., Orzechowska, B., Pabijan, J., Seweryn, S., & Lekka, M. (2018). Atomic Force Microscopy as a tool for assessing the cellular elasticity and adhesiveness to identify cancer cells and tissues. *Seminars in Cell & Developmental Biology*, 73, 115–124.

[13] Lekka, M., Pogoda, K., Gostek, J., Klymenko, O., Prauzner-Bechcicki, S., Wiltowska-Zuber, J., Jaczewska, J., Lekki, J., & Stachura, Z. (2012). Cancer cell recognition–mechanical phenotype. *Micron*, 43(12), 1259–1266.

[14] Hayashi, K., & Iwata, M. (2015). Stiffness of cancer cells measured with an AFM indentation method. *Journal of the Mechanical Behavior of Biomedical Materials*, 49, 105–111.

[15] Sampietro, M., Cassina, V., Salerno, D., Barbaglio, F., Buglione, E., Marrano, C. A., Campanile, R., Scarfò, L., Biedenweg, D., Fregin, B., et al. (2023). The nanomechanical properties of CLL cells are linked to the actin cytoskeleton and are a potential target of BTK inhibitors. *Hemasphere*, 7(8), e931.

[16] Ghia, P., Ferreri, A. J., & Caligaris-Cappio, F. (2007). Chronic lymphocytic leukemia. *Critical Reviews in Oncology/Hematology*, 64(3), 234–246.

[17] Scarfò, L., Ferreri, A. J., & Ghia, P. (2016). Chronic lymphocytic leukaemia. *Critical Reviews in Oncology/Hematology*, 104, 169–182.

[18] Caligaris-Cappio, F., Bertilaccio, M. T., & Scielzo, C. (2014). How the microenvironment wires the natural history of chronic lymphocytic leukemia. *Seminars in Cancer Biology*, 24, 43–48.

[19] Butrym, A., Majewski, M., Dzietczenia, J., Kuliczkowski, K., & Mazur, G. (2012). High expression of hematopoietic cell specific lyn substrate-1 (HS1) predicts poor survival of B-cell chronic lymphocytic leukemia patients. *Leukemia Research*, 36(7), 876–880.

[20] Scielzo, C., Ghia, P., Conti, A., Bachi, A., Guida, G., Geuna, M., Alessio, M., Caligaris-Cappio, F., et al. (2005). HS1 protein is differentially expressed in chronic lymphocytic leukemia patient subsets with good or poor prognoses. *The Journal of Clinical Investigation*, 115(6), 1644–1650.

[21] Koya, Y., Liu, W., Yamakita, Y., Senga, T., Shibata, K., Yamashita, M., Nawa, A., Kikkawa, F., & Kajiyama, H. (2018). Hematopoietic lineage cell-specific protein 1 (HS1), a hidden player in migration, invasion, and tumor formation, is over-expressed in ovarian carcinoma cells. *Oncotarget*, 9(66), 32609.

[22] Ponader, S., Chen, S.-S., Buggy, J. J., Balakrishnan, K., Gandhi, V., Wierda, W. G., Keating, M. J., O'Brien, S., Chiorazzi, N., & Burger, J. A. (2012). The Bruton Tyrosine Kinase inhibitor PCI-32765 thwarts chronic lymphocytic leukemia cell survival and tissue homing in vitro and in vivo. *Blood, The Journal of the American Society of Hematology*, 119(5), 1182–1189.

[23] Herman, S. E., Mustafa, R. Z., Jones, J., Wong, D. H., Farooqui, M., & Wiestner, A. (2015). Treatment with ibrutinib inhibits BTK-and VLA-4–dependent adhesion of chronic lymphocytic leukemia cells in vivo. *Clinical Cancer Research*, 21(20), 4642–4651.

[24] Bergert, M., Erzberger, A., Desai, R. A., Aspalter, I. M., Oates, A. C., Charras, G., Salbreux, G., & Paluch, E. K. (2015). Force transmission during adhesion-independent migration. *Nature Cell Biology*, 17(4), 524–529.

[25] Zebda, N., Dubrovskyi, O., & Birukov, K. G. (2012). Focal adhesion kinase regulation of mechanotransduction and its impact on endothelial cell functions. *Microvascular Research*, 83(1), 71–81.

[26] Mihashi, S., & Watanabe, M. (2024). Effects of cytochalasin D on relaxation process of skinned taenia cecum and carotid artery from guinea pig. *The Journal of Physiological Sciences*, 74(1), 24.

[27] Chugh, P., & Paluch, E. K. (2018). The actin cortex at a glance. *Journal of Cell Science*, 131(14), jcs186254.

[28] Duda, M., Kirkland, N. J., Khalilgharibi, N., Tozluoglu, M., Yuen, A. C., Carpi, N., Bove, A., Piel, M., Charras, G., Baum, B., et al. (2019). Polarization of myosin II refines tissue material properties to buffer mechanical stress. *Developmental Cell*, 48(2), 245–260.

[29] Allen, A., Maddala, R., Eldawy, C., & Rao, P. V. (2022). Mechanical load and piezo1 channel regulated myosin II activity in mouse lenses. *International Journal of Molecular Sciences*, 23(9), 4710.

[30] Fabry, B., Maksym, G. N., Butler, J. P., Glogauer, M., Navajas, D., & Fredberg, J. J. (2001). Scaling the microrheology of living cells. *Physical Review Letters*, 87(14), 148102.

[31] Kumari, S., Curado, S., Mayya, V., & Dustin, M. L. (2014). T cell antigen receptor activation and actin cytoskeleton remodeling. *Biochimica et Biophysica Acta (BBA)-Biomembranes*, 1838(2), 546–556.

[32] Suresh, S. (2007). Biomechanics and biophysics of cancer cells. *Acta Biomaterialia*, 3(4), 413–438.

[33] Rey-Barroso, J., Munaretto, A., Rouquié, N., Mougel, A., Chassan, M., Gadat, S., Dewingle, O., Poincloux, R., Cadot, S., Ysebaert, L., et al. (2023). Lymphocyte migration and retention properties affected by ibrutinib in Chronic Lymphocytic Leukemia. *Haematologica*, 109(3), 809.

[34] Castro-Ochoa, K. F., Guerrero-Fonseca, I. M., & Schnoor, M. (2019). Hematopoietic cell-specific lyn substrate (HCLS1 or HS1): A versatile actin-binding protein in leukocytes. *Journal of Leukocyte Biology*, 105(5), 881–890.

[35] Yamanashi, Y., Okada, M., Semba, T., Yamori, T., Umemori, H., Tsunasawa, S., Toyoshima, K., Kitamura, D., Watanabe, T., & Yamamoto, T. (1993). Identification of HS1 protein as a major substrate of protein-tyrosine kinase(s) upon B-cell antigen receptor-mediated signaling. *Proceedings of the National Academy of Sciences*, 90(8), 3631–3635.

[36] Lomakin, A., Cattin, C., Cuvelier, D., Alraies, Z., Molina, M., Nader, G., Srivastava, N., Sáez, P., Garcia-Arcos, J., Zhitnyak, I., et al. (2020). The nucleus acts as a ruler tailoring cell responses to spatial constraints. *Science*, 370(6514), eaba2894.

[37] Lecuit, T., & Yap, A. S. (2015). E-cadherin junctions as active mechanical integrators in tissue dynamics. *Nature Cell Biology*, 17(5), 533–539.

[38] Tsai, M. A., Waugh, R. E., & Keng, P. C. (1998). Passive mechanical behavior of human neutrophils: Effects of colchicine and paclitaxel. *Biophysical Journal*, 74(6), 3282–3291.

[39] Li, X., Ni, Q., He, X., Kong, J., Lim, S.-M., Papoian, G. A., Trzeciakowski, J. P., Trache, A., & Jiang, Y. (2020). Tensile force-induced cytoskeletal remodeling: Mechanics before chemistry. *PLoS Computational Biology*, 16(6), e1007693.

[40] Huang, H., Kamm, R. D., & Lee, R. T. (2004). Cell mechanics and mechanotransduction: Pathways, probes, and physiology. *American Journal of Physiology-Cell Physiology*, 287(1), C1–C11.

[41] Fabry, B., Klemm, A. H., Kienle, S., Schäffer, T. E., & Goldmann, W. H. (2011). Focal adhesion kinase stabilizes the cytoskeleton. *Biophysical Journal*, 101(9), 2131–2138.

[42] Swaminathan, V., Mythreye, K., O'Brien, E. T., Berchuck, A., Blobe, G. C., & Superfine, R. (2011). Mechanical stiffness grades metastatic potential in patient tumor cells and in cancer cell lines. *Cancer Research*, 71(15), 5075–5080.

[43] Hemmer, J. D., Nagatomi, J., Wood, S. T., Vertegel, A. A., Dean, D., & LaBerge, M. (2009). Role of cytoskeletal components in stress-relaxation behavior of adherent vascular smooth muscle cells. *Journal of Biomechanical Engineering*, 131(4).

[44] Gomez, T. S., McCarney, S. D., Carrizosa, E., Labno, C. M., Comiskey, E. O., Nolz, J. C., Zhu, P., Freedman, B. D., Clark, M. R., Rawlings, D. J., et al. (2006). HS1 functions as an essential actin-regulatory adaptor protein at the immune synapse. *Immunity*, 24(6), 741–752.

[45] Hao, J.-J., Zhu, J., Zhou, K., Smith, N., & Zhan, X. (2005). The coiled-coil domain is required for HS1 to bind to F-actin and activate Arp2/3 complex. *Journal of Biological Chemistry*, 280(45), 37988–37994.

[46] Bendell, A. C., Williamson, E. K., Chen, C. S., Burkhardt, J. K., & Hammer, D. A. (2017). The Arp2/3 complex binding protein HS1 is required for efficient dendritic cell random migration and force generation. *Integrative Biology*, 9(8), 695–708.

[47] Salbreux, G., Charras, G., & Paluch, E. (2012). Actin cortex mechanics and cellular morphogenesis. *Trends in Cell Biology*, 22(10), 536–545.

[48] Rotsch, C., & Radmacher, M. (2000). Drug-induced changes of cytoskeletal structure and mechanics in fibroblasts: An Atomic Force Microscopy study. *Biophysical Journal*, 78(1), 520–535.

[49] Garcia, P. D., Guerrero, C. R., & Garcia, R. (2017). Time-resolved nanomechanics of a single cell under the depolymerization of the cytoskeleton. *Nanoscale*, 9(33), 12051–12059.

[50] Masters, T. A., Sheetz, M. P., & Gauthier, N. C. (2016). F-actin waves, actin cortex disassembly and focal exocytosis driven by actin-phosphoinositide positive feedback. *Cytoskeleton*, 73(4), 180–196.

[51] Uruno, T., Zhang, P., Liu, J., Hao, J.-J., & Zhan, X. (2003). Haematopoietic lineage cell-specific protein 1 (HS1) promotes actin-related protein (Arp)2/3 complex-mediated actin polymerization. *Biochemical Journal*, 371(2), 485–493.

[52] Wang, N., Tytell, J. D., & Ingber, D. E. (2009). Mechanotransduction at a distance: Mechanically coupling the extracellular matrix with the nucleus. *Nature Reviews Molecular Cell Biology*, 10(1), 75–82.

[53] Chan, C. J., Ekpenyong, A. E., Golfier, S., Li, W., Chalut, K. J., Otto, O., Elgeti, J., Guck, J., & Lautenschläger, F. (2015). Myosin II activity softens cells in suspension. *Biophysical Journal*, 108(8), 1856–1869.

[54] Martens, J. C., & Radmacher, M. (2008). Softening of the actin cytoskeleton by inhibition of myosin II. *Pflügers Archiv-European Journal of Physiology*, 456, 95–100.

[55] Tinevez, J.-Y., Schulze, U., Salbreux, G., Roensch, J., Joanny, J.-F., & Paluch, E. (2009). Role of cortical tension in bleb growth. *Proceedings of the National Academy of Sciences*, 106(44), 18581–18586.

[56] Wilson, C. A., Tsuchida, M. A., Allen, G. M., Barnhart, E. L., Applegate, K. T., Yam, P. T., Ji, L., Keren, K., Danuser, G., & Theriot, J. A. (2010). Myosin II contributes to cell-scale actin network treadmilling through network disassembly. *Nature*, 465(7296), 373–377.

[57] Kollmannsberger, P., & Fabry, B. (2011). Linear and nonlinear rheology of living cells. *Annual Review of Materials Research*, 41(1), 75–97.

[58] Stacchini, A., Aragno, M., Vallario, A., Alfarano, A., Circosta, P., Gottardi, D., Faldella, A., Rege-Cambrin, G., Thunberg, U., Nilsson, K., et al. (1999). MEC1 and MEC2: Two new cell lines derived from B-chronic lymphocytic leukaemia in prolymphocytoid transformation. *Leukemia Research*, 23(2), 127–136.

[59] Campanile, R., Helenius, J., Scielzo, C., Scarfò, L., Salerno, D., Bossi, M., Falappi, M., Saponara, A., Müller, D. J., Mantegazza, F., et al. (2025). Production of AFM wedged cantilevers for stress-relaxation experiments: Uniaxial loading of soft, spherical cells. *Methods*, 236, 1–9.

[60] Stewart, M. P., Hodel, A. W., Spielhofer, A., Cattin, C. J., Müller, D. J., & Helenius, J. (2013). Wedged AFM-cantilevers for parallel plate cell mechanics. *Methods*, 60(2), 186–194.

[61] Butt, H.-J., & Jaschke, M. (1995). Calculation of thermal noise in Atomic Force Microscopy. *Nanotechnology*, 6(1), 1.

[62] Hutter, J. L., & Bechhoefer, J. (1993). Calibration of Atomic Force Microscope tips. *Review of Scientific Instruments*, 64(7), 1868–1873.

[63] Jung, W., Li, J., Chaudhuri, O., & Kim, T. (2020). Nonlinear elastic and inelastic properties of cells. *Journal of Biomechanical Engineering*, 142(10), 100806.

[64] Muzio, M., Scielzo, C., Frenquelli, M., Bachi, A., De Palma, M., Alessio, M., Ghia, P., & Caligaris-Cappio, F. (2007). HS1 complexes with cytoskeleton adapters in normal and malignant chronic lymphocytic leukemia B cells. *Leukemia*, 21(9), 2067–2070.

[65] Tissino, E., Pozzo, F., Benedetti, D., Caldana, C., Bittolo, T., Rossi, F. M., Bomben, R., Nanni, P., Chivilò, H., Cattarossi, I., et al. (2020). CD49d promotes disease progression in chronic lymphocytic leukemia: New insights from CD49d bimodal expression. *Blood, The Journal of the American Society of Hematology*, 135(15), 1244–1254.

[66] Isermann, P., & Lammerding, J. (2013). Nuclear mechanics and mechanotransduction in health and disease. *Current Biology*, 23(24), R1113–R1121.

[67] Clark, K., Langeslag, M., Figdor, C. G., & van Leeuwen, F. N. (2007). Myosin II and mechanotransduction: A balancing act. *Trends in Cell Biology*, 17(4), 178–186.

Supplementary Material

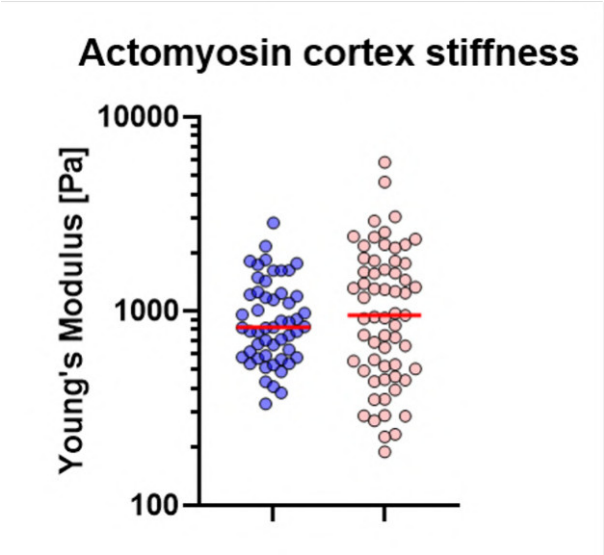

Figure S1: **Scatter plot of Young's Modulus values derived from AFM force spectroscopy measurements on MEC1 (blue) and KO1 (red) cells.** Each dot represents the median value from a single cell for which four different curves were acquired and fitted. The bright red solid line indicates the overall median for each group. No significant difference in cortical stiffness was observed between the two cell lines.

Standard AFM force spectroscopy measurements were performed using a sharp tip (MLCT-BIO, E tip, Bruker Probes) with a setpoint of 1 nN. The acquired force curves were fitted over the first 500 nm using the Hertz–Sneddon model to estimate the YM of the actomyosin cortex in the two cell lines, MEC1 (Fig S1, blue) and KO1 (Fig S1, red). For each cell 4 different curve were acquired with an approaching and retracting velocity of 1 $\mu m/s$, fitted and the median was computed. These experiments did not reveal any significant differences between the two cell lines leading to the necessity of a new approach to characterize the effect of HS1 depletion.

Figure S2 offers a visual summary of how different pharmacological treatments affect cellular mechanical responses across confinement levels. The layout is designed to highlight both the magnitude and direction of changes induced by each drug, facilitating the identification of consistent trends related to increasing confinement. The use of color gradients and symbol intensity provides an intuitive overview of statistical significance and drug effects, without the need to delve into individual p-values. This representation emphasizes how confinement modulates the impact of each treatment, and how such effects may differ between MEC1 and KO1 cells.

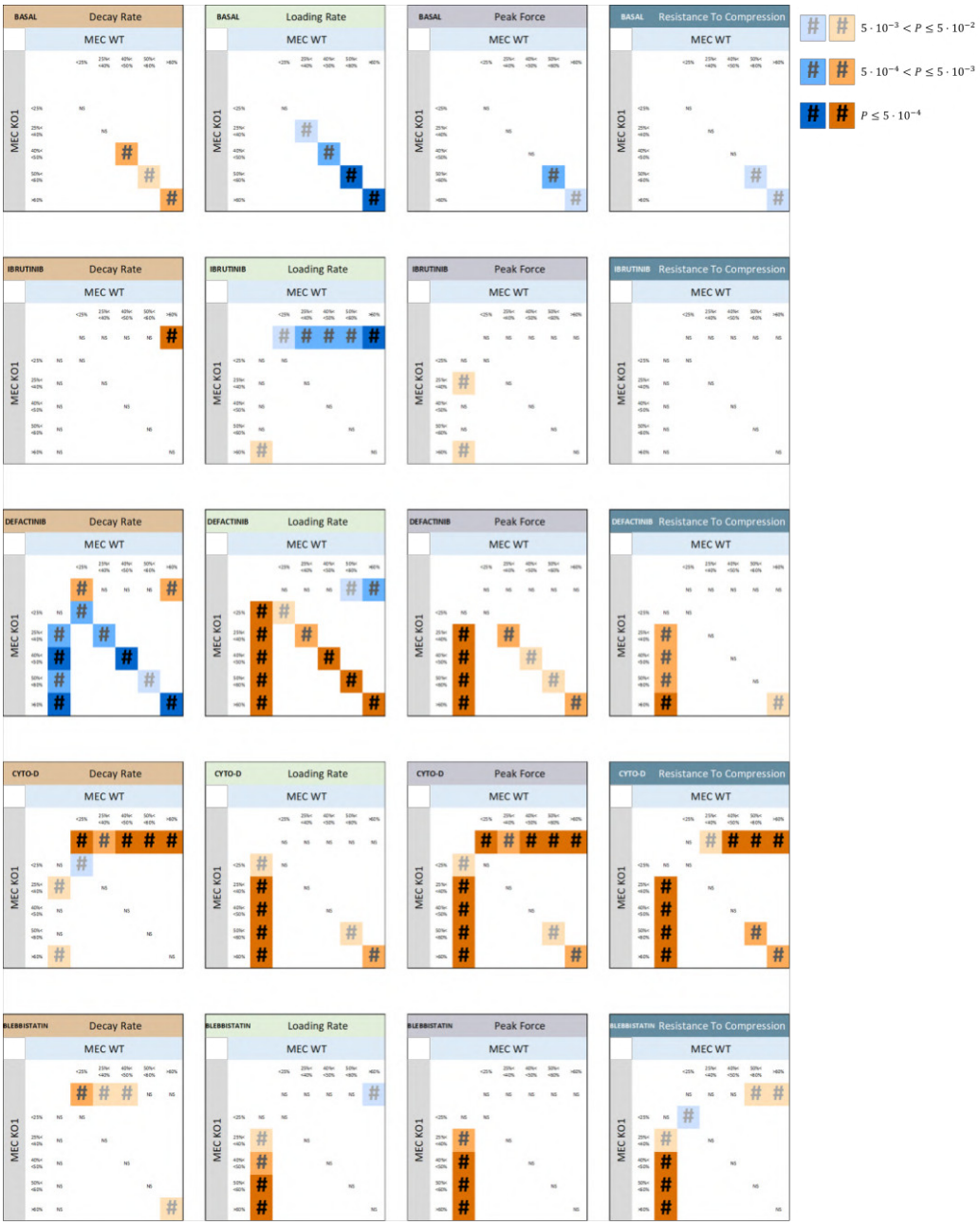

Figure S2: **Summary tables of Mann–Whitney test results for each pharmacological condition: Basal, Ibrutinib, Defactinib, Cytochalasin-D, and Blebbistatin; rows top to bottom).** Each table refers to a mechanical parameter, with conditions labeled at the top. Cell lines (MEC1 and KO1) are shown in the second row and first column, with five confinement levels listed below or beside each. Off-diagonal entries show p-values comparing treated versus basal conditions within each cell line; diagonal entries compare MEC1 vs KO1 under the same condition and confinement level. Color coding follows the legend (top right): darker symbols indicate stronger significance; blue/orange backgrounds indicate increased/decreased values relative to basal (or KO1 vs MEC1 on the diagonal).

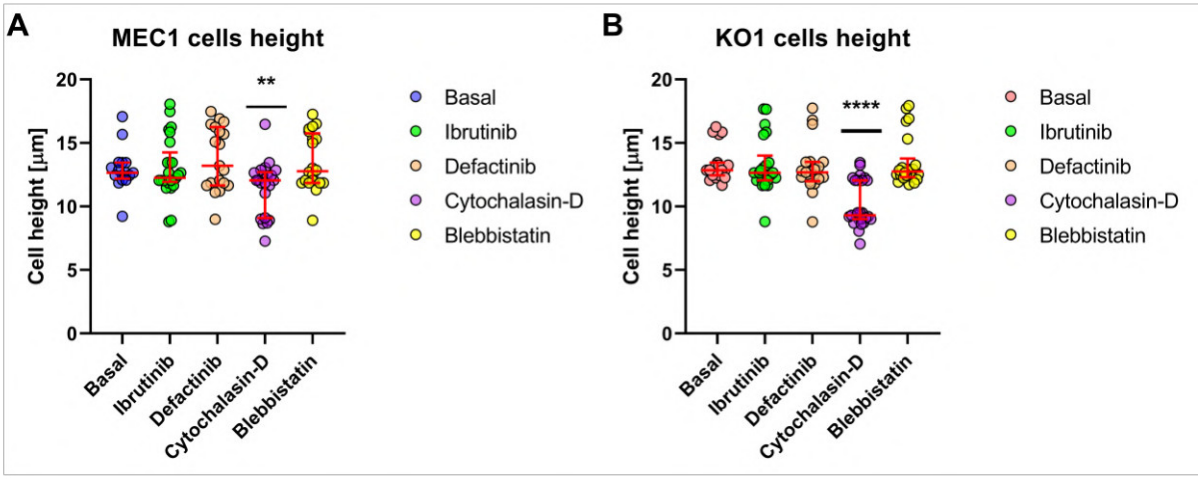

Figure S3: **Cell height measurements reveal differences in vertical dimension between MEC1 and HS1-deficient KO1 cells under various pharmacological treatments.** Quantification of cell height in round-shaped MEC1 (**A**) and KO1 (**B**) cells following treatment with: Ibrutinib (BTK inhibitor, green), Defactinib (FAK inhibitor, orange), Cytochalasin-D (actin depolymerizing agent, purple), and Blebbistatin (myosin II inhibitor, yellow). Dots represent individual cell measurements, and bars indicate median ± interquartile range. MEC1 cells exhibit a modest decrease in height upon Cytochalasin-D treatment compared to other conditions (**$p<0.05$), while KO1 cells show a significant reduction (****, $p<0.0005$) indicating a higher sensitivity to actin disruption.

Cell height measurements revealed differences in vertical dimensions between MEC1 cells and KO1 cells under various pharmacological treatments. The analysis was performed on round-shaped cells and the height was estimated starting from the contact point of the AFM probe. Treatments with different drugs induced changes in cells dimension only when Cytochalasin-D (purple dot) was administered.

A. Further considerations on data

A.1 Addition of Ibrutinib to MEC1

Regarding the addition on Ibrutinib to MEC1 cells, they also exhibited a significant reduction in relaxation time at compressions above 60% following Ibrutinib treatment ($p < 0.0005$) (Fig. 2**A, C**). This reduction further supports the cell stiffening due to the fact that it indicates a diminished capacity to dissipate mechanical stress, suggesting that the cells adopt a more solid-like behavior under extreme compression. Such behavior is typically associated with increased cytoskeletal or nuclear stiffness and may reflect Ibrutinib-induced modulation of viscoelastic properties [15, 63]. Under high confinement, deformation likely involves deeper cellular structures such as the nucleus. Therefore, the reduced relaxation time could signal minor mechanical compliance via nuclear reshaping, a response that contributes to the overall mechanical adaptation of the cell [64, 65].

A.2 Addition of Ibrutinib to KO1

Interestingly, although overall mechanical remodeling was absent, KO1 cells exhibited a slight reduction in loading rate under extreme confinement conditions, specifically above 60% cell compression ($p = 0.0417$; Fig. 2**E, F**). This decrease suggests that when deeper cellular regions, such as the nucleus, are engaged, Ibrutinib may weaken the mechanical integrity of HS1-deficient cells rather than reinforcing it. These findings imply that HS1 is required for confinement-induced mechanical reinforcement, particularly in response to pharmacological perturbation [15].

Further supporting this interpretation, Ibrutinib treatment led to a significant reduction in peak force at the second ($p = 0.0287$) and fifth ($p = 0.0417$) confinement levels (Fig. 2**H, I**). These observations indicate that HS1 is also required to sustain force generation during mechanical loading. In its absence, Ibrutinib may impair mechanotransduction processes that involve actin-driven force production and nuclear–cytoskeletal coupling, both of which are crucial for mounting an effective mechanical response to external stress [66].

A.3 Addition of Defactinib to MEC1

After Defactinib addition, MEC1 cells showed a significantly reduced relaxation time at the first ($p = 0.0031$) and last ($p = 0.0008$) confinement levels (Fig. 2**A, C**), suggesting enhanced cytoskeletal dynamics and reduced intracellular viscosity. These changes reflect

a more efficient dissipation of mechanical stress and an accelerated return to baseline shape following deformation, pointing to an intact and responsive cytoskeletal network [24].

A.4 Addition of Ciytochalasin-D to KO1

After the Cytochalasin-D addition to KO1 cells, the relaxation time (Fig. 3**B, C**) decreased at the second (25–40% confinement; $p = 0.0064$) and final (>60% confinement; $p = 0.009$) compression levels, indicating a shift toward a more solid-like mechanical phenotype. Thus highlighting a diminished ability to dissipate mechanical stress, consistent with a loss of cytoskeletal viscoelasticity resulting in an impaired cell deformability and fluidity under mechanical load [49, 52].

A.5 Addition of Blebbistatin to MEC1

After the addition of Blebbistatin to MEC1 cells, interestingly, the loading rate was significantly reduced only at the final confinement level ($p = 0.0183$) (Fig. 3**D, F**), suggesting that myosin II plays a more prominent role under higher mechanical loads, progressively contributing to resistance against deformation [29]. However, this effect, visible only when cells were subjected to extreme confinement, also implies that the actomyosin contractile apparatus may be less critical for initial passive resistance to compression [67].

Chapter 2

Conclusion

This PhD work demonstrates that Atomic Force Microscopy can serve as a powerful bridge between physics and medicine, transforming nanoscale mechanical analysis into a meaningful biological language. By measuring how cells and tissues deform, relax, and resist external forces, AFM unveils information that complements molecular and biochemical assays, providing an alternative window into cellular physiology and pathology.

The studies presented here show that nanoscale mechanical changes can act as reliable indicators of biological state. In tissues, stiffness alterations mirror extracellular matrix degradation and remodeling, while in hematological cells, cytoskeletal reorganization translates into measurable differences in elasticity and viscoelasticity. These findings support the view that mechanical behavior is not a secondary property but a defining aspect of biological samples that can anticipate or accompany functional transitions, from disease progression to pharmacological response in presence of diverse target therapy.

Beyond its biological insights, this thesis also makes a methodological contribution by extending AFM to samples traditionally considered too fragile or unstable for quantitative testing. The development of wedged-cantilever and stepwise confinement approaches allowed the measurement of mechanical responses in small, round, and not-adherent cells under controlled and reproducible conditions. These innovations broaden the applicability of AFM and open new directions in high-resolution single cell mechanics and microrheology.

To further summarize the main scientific contributions of this thesis, Table 2.1 provides an overview of the published works included in the manuscript, highlighting for each study the AFM methodology employed and the key biological or biomechanical findings obtained.

Table 2.1: Overview of the AFM-based studies included in this PhD thesis. For each work, the AFM modality, the investigated biological system, and the main mechanical or structural findings are reported.

Paper	**AFM technique**	**Sample**	**Key findings**
1. Bracchi et al.	Imaging	Meniscal ECM	Highly heterogeneous nanoscale architecture composed of fibrillar, porous, and amorphous domains, reflecting injury- and degeneration-induced ECM remodeling.
2. Pellegrino et al.	Imaging	Patterned surfaces	Surface wrinkling induces bacterial localization within valleys; physical confinement under shear flow reduces bacterial cell length compared to flat substrates.
3. Sampietro et al.	Force spectroscopy	CLL cells	Leukemic cells are mechanically softer than healthy B cells; BTK inhibition restores physiological stiffness prior to drug resistance onset.
4. Brevi et al.	Force spectroscopy	Prostate ECM	ECM from TRAMP mice exhibits increased stiffness compared to controls, linking matrix mechanics to neuroendocrine prostate cancer progression.

Paper	AFM technique	Sample	Key findings
5. Piazzoni et al.	Microrheology + force spectroscopy	Hydrogels	Frequency-dependent viscoelastic behavior observed; optimal Young's Modulus (∼80 Pa) promotes endothelial cell angiogenesis.
6. Campanile et al.	Wedged cantilever production	CLL cells	Wedged cantilevers enable controlled uniaxial compression of low-adherent cells, revealing nonlinear and time-dependent mechanical responses.
7. Campanile et al.	Stepwise confinement	CLL cells	Stepwise confinement enables comprehensive mechanical phenotyping including stiffness, viscoelasticity, and relaxation dynamics.

Ultimately, this work underscores the potential of AFM as a translational nanomechanical tool, capable of bridging scales from cells to tissues. It highlights that understanding the mechanics of living systems is crucial not only for fundamental biophysics but also for biomedical applications, from early diagnostics to the design of biomaterials and the evaluation of drug efficacy. By connecting nanoscale force measurements to physiological meaning, this research contributes to shaping a more integrated and mechanistically informed vision of modern medicine.

2.1 Future perspectives

The findings presented in this thesis position Atomic Force Microscopy as more than a high-resolution research tool, pointing toward its potential role in future biomedical and clinical applications. A key perspective emerging from this work is the translation of nanomechanical phenotyping into a functional readout for

disease characterization and therapeutic monitoring. Mechanical properties of cells and tissues, when measured with sufficient precision and reproducibility, may evolve into a new class of biophysical biomarkers, capable of capturing aspects of pathology that are not accessible through molecular or imaging techniques alone [22, 45, 47].

From a clinical standpoint, AFM-based biomechanics could contribute to the stratification of patients and the evaluation of treatment efficacy [22, 119]. The sensitivity of mechanical parameters to cytoskeletal remodeling and extracellular matrix alterations suggests that nanomechanical measurements may serve as early indicators of disease progression or response to drug delivery, potentially preceding detectable molecular changes. Future studies involving patient-derived cells and tissues, measured during therapy, could pave the way toward personalized mechanical profiling in precision medicine.

More broadly, this work supports a paradigm shift in which mechanics is recognized as an active regulator of biological function, rather than a secondary consequence of molecular processes that take place in the background. By bridging physics and medicine at the nanoscale, AFM-based mechanobiology has the potential to reshape how diseases are diagnosed, monitored, and treated. Interdisciplinary collaboration, in fact, will be essential to transform nanomechanical insights into clinically actionable tools, ultimately contributing to a more integrated and predictive approach to medicine.

Bibliography

1. Binnig, G., Quate, C. F. & Gerber, C. Atomic force microscope. *Physical review letters* **56,** 930 (1986).
2. Binnig, G. & Rohrer, H. Scanning tunneling microscopy—from birth to adolescence. *Reviews of modern physics* **59,** 615 (1987).
3. Giessibl, F. J. Advances in atomic force microscopy. *Reviews of modern physics* **75,** 949 (2003).
4. Hersam, M. C. & Chung, Y.-W. Detecting elusive surface atoms with atomic force microscopy. *Proceedings of the National Academy of Sciences* **100,** 12531–12532 (2003).
5. Radmacher, M., Tillmann, R., Fritz, M. & Gaub, H. From molecules to cells: imaging soft samples with the atomic force microscope. *Science* **257,** 1900–1905 (1992).
6. Santos, N. C. & Castanho, M. A. An overview of the biophysical applications of atomic force microscopy. *Biophysical chemistry* **107,** 133–149 (2004).
7. Dufrêne, Y. F. *et al.* Imaging modes of atomic force microscopy for application in molecular and cell biology. *Nature nanotechnology* **12,** 295–307 (2017).
8. Gadegaard, N. Atomic force microscopy in biology: technology and techniques. *Biotechnic & Histochemistry* **81,** 87–97 (2006).
9. Ralston, J., Larson, I., Rutland, M. W., Feiler, A. A. & Kleijn, M. Atomic force microscopy and direct surface force measurements (IUPAC Technical Report). *Pure and applied chemistry* **77,** 2149–2170 (2005).

10. Trache, A. & Meininger, G. A. Atomic force microscopy (AFM). *Current protocols in microbiology* **8,** 2C–2 (2008).

11. Wu, P.-H. *et al.* A comparison of methods to assess cell mechanical properties. *Nature Methods* **15,** 491–498 (2018).

12. Butt, H.-J., Cappella, B. & Kappl, M. Force measurements with the Atomic Force Microscope: Technique, interpretation and applications. *Surface Science Reports* **59,** 1–152 (2005).

13. Lekka, M. & Laidler, P. Applicability of AFM in cancer detection. *Nature nanotechnology* **4,** 72–72 (2009).

14. Zemła, J. *et al. Atomic Force Microscopy as a tool for assessing the cellular elasticity and adhesiveness to identify cancer cells and tissues* in *Seminars in Cell & Developmental Biology* **73** (2018), 115–124.

15. Lekka, M. *Cellular analysis by atomic force microscopy* (Jenny Stanford Publishing, 2017).

16. Dufrêne, Y. F. Atomic force microscopy, a powerful tool in microbiology. *Journal of bacteriology* **184,** 5205–5213 (2002).

17. Miranda, A. *et al.* How did correlative atomic force microscopy and super-resolution microscopy evolve in the quest for unravelling enigmas in biology? *Nanoscale* **13,** 2082–2099 (2021).

18. Alessandrini, A. & Facci, P. AFM: a versatile tool in biophysics. *Measurement science and technology* **16,** R65 (2005).

19. Lambert, E. *et al.* Real time and quantitative imaging of lignocellulosic films hydrolysis by atomic force microscopy reveals lignin recalcitrance at nanoscale. *Biomacromolecules* **20,** 515–527 (2018).

20. Kirmizis, D. & Logothetidis, S. Atomic force microscopy probing in the measurement of cell mechanics. *International journal of nanomedicine,* 137–145 (2010).

21. Alsteens, D. Probing living cell dynamics and molecular interactions using atomic force microscopy. *Biophysical Reviews* **16,** 663–677 (2024).

22. Sampietro, M. *et al.* The nanomechanical properties of CLL cells are linked to the actin cytoskeleton and are a potential target of BTK inhibitors. *Hemasphere* **7,** e931 (2023).

23. Alcaraz, J., Otero, J., Jorba, I. & Navajas, D. *Bidirectional mechanobiology between cells and their local extracellular matrix probed by atomic force microscopy* in *Seminars in cell & developmental biology* **73** (2018), 71–81.

24. Cho, D. H., Aguayo, S. & Cartagena-Rivera, A. X. Atomic force microscopy-mediated mechanobiological profiling of complex human tissues. *Biomaterials* **303,** 122389 (2023).

25. Hecht, F. M. *et al.* Imaging viscoelastic properties of live cells by AFM: power-law rheology on the nanoscale. *Soft matter* **11,** 4584–4591 (2015).

26. Krieg, M. *et al.* Atomic force microscopy-based mechanobiology. *Nature Reviews Physics* **1,** 41–57 (2019).

27. Parot, P. *et al.* Past, present and future of atomic force microscopy in life sciences and medicine. *Journal of Molecular Recognition: An Interdisciplinary Journal* **20,** 418–431 (2007).

28. Eaton, P. & West, P. *Atomic force microscopy* (Oxford university press, 2010).

29. Scheuring, S., Sapra, K. T. & Müller, D. J. in *Handbook of Single-Molecule Biophysics* 449–485 (Springer, 2009).

30. Xie, H., Vitard, J., Haliyo, D. S. & Régnier, S. Enhanced accuracy of force application for AFM nanomanipulation using nonlinear calibration of optical levers. *IEEE Sensors Journal* **8,** 1478–1485 (2008).

31. Liu, S. & Wang, Y. Application of AFM in microbiology: a review. *Scanning* **32,** 61–73 (2010).

32. Butt, H.-J. Measuring electrostatic, van der Waals, and hydration forces in electrolyte solutions with an atomic force microscope. *Biophysical journal* **60,** 1438–1444 (1991).

33. Schillers, H. *et al.* Standardized nanomechanical atomic force microscopy procedure (SNAP) for measuring soft and biological samples. *Scientific reports* **7,** 5117 (2017).

34. Sader, J. E., Larson, I., Mulvaney, P. & White, L. R. Method for the calibration of atomic force microscope cantilevers. *Review of Scientific Instruments* **66,** 3789–3798 (1995).

35. Bruker. *AFM Probes, Tips and Cantilevers* `https://www.brukerafmprobes.com/`.

36. Jalili, N. & Laxminarayana, K. A review of atomic force microscopy imaging systems: application to molecular metrology and biological sciences. *Mechatronics* **14,** 907–945 (2004).

37. Martin, Y., Williams, C. C. & Wickramasinghe, H. K. Atomic force microscope–force mapping and profiling on a sub 100-Å scale. *Journal of applied Physics* **61,** 4723–4729 (1987).

38. Zhong, Q., Inniss, D., Kjoller, K. & Elings, V. Fractured polymer/silica fiber surface studied by tapping mode atomic force microscopy. *Surface Science Letters* **290,** L688–L692 (1993).

39. Putman, C. A., Van der Werf, K. O., De Grooth, B. G., Van Hulst, N. F. & Greve, J. Tapping mode atomic force microscopy in liquid. *Applied physics letters* **64,** 2454–2456 (1994).

40. Evans, C. T., Payton, O., Picco, L. & Allen, M. J. Visualisation of microalgal-viral interactions by high-speed atomic force microscopy. *Frontiers in Virology* **3,** 1111335 (2023).

41. Ray, A. *et al.* From viral assembly to host interaction: AFM's contributions to virology. *Journal of Virology* **99,** e00873–24 (2025).

42. Kuznetsov, Y. G. & McPherson, A. Atomic force microscopy in imaging of viruses and virus-infected cells. *Microbiology and molecular biology reviews* **75,** 268–285 (2011).

43. Zeng, C., Vitale-Sullivan, C. & Ma, X. In situ atomic force microscopy studies on nucleation and self-assembly of biogenic and bio-inspired materials. *Minerals* **7,** 158 (2017).

44. Pellegrino, L. *et al.* Reduction of bacterial colonization on buckling-induced wrinkled surfaces under fluid shear. *Nature Communications.* Submitted (2025).

45. Bracchi, M. *et al.* Meniscal extracellular matrix remodelling caused by injuries and degeneration. *Matrix Biology Plus.* Submitted (2025).

46. Piazzoni, M. *et al.* Endothelial cells angiogenesis in sulfated glycosaminoglycan (GAG) hydrogels enhanced by bioactive glass released ions. *Advanced Functional Materials.* Submitted (2025).

47. Brevi, A. *et al.* Intercepting Yes-associated protein 1 in prostate cancer 1 blocks neuroendocrine progression. *Cancer Research.* Submitted (2025).

48. Guzz, N., Dokukin, M., Kalaparthi, V. & Sokolov, I. If Cell Mechanics Can Be Described by Elastic Modulus: Study of Different Models and Probes Used in Indentation Experiments. *Biophysical Journal* **107,** 564 (2014).

49. Chighizola, M., Puricelli, L., Bellon, L. & Podestà, A. Large colloidal probes for atomic force microscopy: Fabrication and calibration issues. *Journal of Molecular Recognition* **34,** 2879 (2021).

50. Heinz, W. F. & Hoh, J. H. Spatially resolved force spectroscopy of biological surfaces using the atomic force microscope. *Trends in biotechnology* **17,** 143–150 (1999).

51. Carvalho, F. A. & Santos, N. C. Atomic force microscopy-based force spectroscopy—biological and biomedical applications. *IUBMB life* **64,** 465–472 (2012).

52. Sokolov, I. Atomic force microscopy in cancer cell research. *Cancer nanotechnology* **1,** 1–17 (2007).

53. Stylianou, A., Lekka, M. & Stylianopoulos, T. AFM assessing of nanomechanical fingerprints for cancer early diagnosis and classification: from single cell to tissue level. *Nanoscale* **10,** 20930–20945 (2018).

54. Moreno-Flores, S., Benitez, R., Vivanco, M. & Toca-Herrera, J. L. Stress relaxation and creep on living cells with the atomic force microscope: a means tocalculate elastic moduli and viscosities of cell components. *Nanotechnology* **44,** 445101 (2010).

55. Li, W., Chen, G. & Yeo, S. Viscoelastic properties of MR fluids. *Smart Materials and Structures* **8,** 460 (1999).

56. Schwarzl, F. Numerical calculation of storage and loss modulus from stress relaxation data for linear viscoelastic materials. *Rheologica acta* **10,** 165–173 (1971).

57. Alcaraz, J. *et al.* Microrheology of human lung epithelial cells measured by Atomic Force Microscopy. *Biophysical Journal* **84,** 2071–2079 (2003).

58. Efremov, Y., Wang, W.-H., Hardy, S. D., Geahlen, R. L. & Raman, A. Measuring nanoscale viscoelastic parameters of cells directly from AFM force-displacement curves. *Scientific Reports* **7,** 1541 (2017).

59. Weihs, D., Mason, T. G. & Teitell, M. A. Bio-microrheology: a frontier in microrheology. *Biophysical journal* **91,** 4296–4305 (2006).

60. Rigato, A., Miyagi, A., Scheuring, S. & Rico, F. High-frequency microrheology reveals cytoskeleton dynamics in living cells. *Nature Physics* **13,** 771 (2107).

61. Sheng, Czajkowsky & Shao. AFM tips: how sharp are they? *Journal of microscopy* **196,** 1–5 (1999).

62. NanoAndMore. *The World of Scanning Probes and More* `https://www.nanoandmore.com/eu/`.

63. Nanosensors. *The World Leader in Scanning Probes* `https://www.nanosensors.com/`.

64. Gavara, N. A beginner's guide to atomic force microscopy probing for cell mechanics. *Microscopy research and technique* **80,** 75–84 (2017).

65. Puricelli, L., Galluzzi, M., Schulte, C., Podestà, A. & Milani, P. Nanomechanical and topographical imaging of living cells by atomic force microscopy with colloidal probes. *Review of Scientific Instruments* **86** (2015).

66. Lacaria, L., Podestà, A., Radmacher, M. & Rico, F. Contact Mechanics. *Biomedical Methods,* 21–64 (2023).

67. Song, J., Tranchida, D. & Vancso, G. J. Contact mechanics of UV/ozone-treated PDMS by AFM and JKR testing: mechanical performance from nano-to micrometer length scales. *Macromolecules* **41,** 6757–6762 (2008).

68. Campanile, R. *et al.* Production of AFM wedged cantilevers for stress-relaxation experiments: Uniaxial loading of soft, spherical cells. *Methods* **236,** 1–9 (2025).

69. Stewart, M. P. *et al.* Wedged AFM-cantilevers for parallel plate cell mechanics. *Methods* **60,** 186–194 (2013).

70. Burnham, N. *et al.* Comparison of calibration methods for AFM cantilevers. *Nanotechnology* **14,** 1 (Dec. 2002).

71. Mullin, N. & Hobbs, J. A non-contact, thermal noise based method for the calibration of lateral deflection sensitivity in atomic force microscopy. *The Review of scientific instruments* **85,** 113703 (Nov. 2014).

72. Butt, H.-J. & Jaschke, M. Calculation of thermal noise in atomic force microscopy. *Nanotechnology* **6,** 1 (1995).

73. Hutter, J. & Bechhoefer, J. Calibration of Atomic-Force Microscope Tips. *Review of Scientific Instruments* **64,** 1868–1873 (Aug. 1993).

74. Gibson, C., Watson, G. & Myhra, S. Scanning force microscopy—calibrative procedures for 'Best Practice'. *Scanning* **19,** 564–581 (Nov. 2006).

75. Cleveland, J., Manne, S., Bocek, D. & Hansma, P. A Nondestructive Method for Determining the Spring Constant of Cantilevers for Scanning Force Microscopy. *Review of Scientific Instruments* **64,** 403–405 (Mar. 1993).

76. Incaviglia, I. *et al.* Tailoring the sensitivity of microcantilevers to monitor the mass of single adherent living cells. *Nano Letters* **23,** 588–596 (2023).

77. Najafi, M., Farhood, B. & Mortezaee, K. Extracellular matrix (ECM) stiffness and degradation as cancer drivers. *Journal of cellular biochemistry* **120,** 2782–2790 (2019).

78. Fujii, Y. *et al.* Spatiotemporal dynamics of single cell stiffness in the early developing ascidian chordate embryo. *Communications biology* **4,** 341 (2021).

79. Evers, T. M., van Weverwijk, A., de Visser, K. E. & Mashaghi, A. Single-cell analysis of innate immune cell mechanics: an application to cancer immunology. *Materials Advances* **5,** 5025–5035 (2024).

80. Wiegand, C. & White, R. Microdeformation in wound healing. *Wound Repair and Regeneration* **21,** 793–799 (2013).

81. Vining, K. H. & Mooney, D. J. Mechanical forces direct stem cell behaviour in development and regeneration. *Nature reviews Molecular cell biology* **18,** 728–742 (2017).

82. Xu, W. *et al.* Cell stiffness is a biomarker of the metastatic potential of ovarian cancer cells. *PLOS one* **7(10),** e46609 (2012).

83. Swaminathan, V. *et al.* Mechanical stiffness grades metastatic potential in patient tumor cells and in cancer cell lines. *Cancer research* **71,** 5075–5080 (2011).

84. Nguyen, A. V. *et al.* Stiffness of pancreatic cancer cells is associated with increased invasive potential. *Integrative biology* **8,** 1232–1245 (2016).

85. Suresh, S. Biomechanics and biophysics of cancer cells. *Acta biomaterialia* **3,** 413–438 (2007).

86. Guck, J. *et al.* Optical deformability as an inherent cell marker for testing malignant transformation and metastatic competence. *Biophysical journal* **88,** 3689–3698 (2005).

87. Plodinec, M. *et al.* The nanomechanical signature of breast cancer. *Nature nanotechnology* **7,** 757–765 (2012).

88. Alibert, C., Goud, B. & Manneville, J.-B. Are cancer cells really softer than normal cells? *Biology of the Cell* **109,** 167–189 (2017).

89. Fuhs, T. *et al.* Rigid tumours contain soft cancer cells. *Nature Physics* **18,** 1510–1519 (2022).

90. Mueller, S. & Sandrin, L. Liver stiffness: a novel parameter for the diagnosis of liver disease. *Hepatic medicine: evidence and research,* 49–67 (2010).

91. Patel, A. K. *et al.* A review on atherosclerotic biology, wall stiffness, physics of elasticity, and its ultrasound-based measurement. *Current atherosclerosis reports* **18,** 83 (2016).

92. Palombo, C. & Kozakova, M. Arterial stiffness, atherosclerosis and cardiovascular risk: Pathophysiologic mechanisms and emerging clinical indications. *Vascular pharmacology* **77,** 1–7 (2016).

93. Jaffar, J. *et al.* Greater cellular stiffness in fibroblasts from patients with idiopathic pulmonary fibrosis. *American Journal of Physiology-Lung Cellular and Molecular Physiology* **315,** L59–L65 (2018).

94. Khan, A. U., Qu, R., Fan, T., Ouyang, J. & Dai, J. A glance on the role of actin in osteogenic and adipogenic differentiation of mesenchymal stem cells. *Stem cell research & therapy* **11,** 283 (2020).

95. Ambriz, X., De Lanerolle, P. & Ambrosio, J. The mechanobiology of the actin cytoskeleton in stem cells during differentiation and interaction with biomaterials. *Stem cells international* **2018,** 2891957 (2018).

96. Trepat, X. *et al.* Universal physical responses to stretch in the living cell. *Nature* **447,** 592–595 (2007).

97. Stamenović, D. Rheological behavior of mammalian cells. *Cellular and molecular life sciences* **65,** 3592–3605 (2008).

98. Fläschner, G., Roman, C. I., Strohmeyer, N., Martinez-Martin, D. & Müller, D. J. Rheology of rounded mammalian cells over continuous high-frequencies. *Nature communications* **12,** 2922 (2021).

99. Guo, M. *et al.* Probing the stochastic, motor-driven properties of the cytoplasm using force spectrum microscopy. *Cell* **158,** 822–832 (2014).

100. Caporizzo, M. A., Chen, C. Y., Salomon, A. K., Margulies, K. B. & Prosser, B. L. Microtubules provide a viscoelastic resistance to myocyte motion. *Biophysical Journal* **115,** 1796–1807 (2018).

101. Efremov, Y. M. *et al.* Distinct impact of targeted actin cytoskeleton reorganization on mechanical properties of normal and malignant cells. *Biochimica et Biophysica Acta (BBA)-Molecular Cell Research* **1853,** 3117–3125 (2015).

102. Bera, K. *et al.* Extracellular fluid viscosity enhances cell migration and cancer dissemination. *Nature* **611,** 365–373 (2022).

103. Ahangar, P., Strudwick, X. L. & Cowin, A. J. Wound healing from an actin cytoskeletal perspective. *Cold Spring Harbor Perspectives in Biology* **14,** a041235 (2022).

104. Molnar, K. & Labouesse, M. The plastic cell: mechanical deformation of cells and tissues. *Open Biology* **11,** 210006 (2021).

105. Villeneuve, C. *et al.* Mechanical forces across compartments coordinate cell shape and fate transitions to generate tissue architecture. *Nature Cell Biology* **26,** 207–218 (2024).

106. Eliahoo, P. *et al.* Viscoelasticity in 3D cell culture and regenerative medicine: measurement techniques and biological relevance. *ACS Materials Au* **4,** 354–384 (2024).

107. Huang, D. *et al.* Viscoelasticity in natural tissues and engineered scaffolds for tissue reconstruction. *Acta biomaterialia* **97,** 74–92 (2019).

108. Mierke, C. T. Viscoelasticity acts as a marker for tumor extracellular matrix characteristics. *Frontiers in Cell and Developmental Biology* **9,** 785138 (2021).

109. Zemła, J. *et al.* Indenting soft samples (hydrogels and cells) with cantilevers possessing various shapes of probing tip. *European Biophysics Journal* **49,** 485–495 (2020).

110. Campanile, R. *et al.* Stepwise Confinement Unveils HS1 Contribution to the Mechanical Phenotype of CLL Cells. *Advanced Science.* Ready to be submitted (2025).

111. Lomakin, A. *et al.* The nucleus acts as a ruler tailoring cell responses to spatial constraints. *Science* **370,** eaba2894 (2020).

112. Lulevich, V., Zink, T., Chen, H.-Y., Liu, F.-T. & Liu, G.-y. Cell mechanics using atomic force microscopy-based single-cell compression. *Langmuir* **22,** 8151–8155 (2006).

113. Schroyen, B., Vlassopoulos, D., Van Puyvelde, P. & Vermant, J. Bulk rheometry at high frequencies: a review of experimental approaches. *Rheologica Acta* **59,** 1–22 (2020).

114. Squires, T. M. Nonlinear microrheology: Bulk stresses versus direct interactions. *Langmuir* **24,** 1147–1159 (2008).

115. Arbore, C., Perego, L., Sergides, M. & Capitanio, M. Probing force in living cells with optical tweezers: from single-molecule mechanics to cell mechanotransduction. *Biophysical reviews* **11,** 765–782 (2019).

116. Bustamante, C. J., Chemla, Y. R., Liu, S. & Wang, M. D. Optical tweezers in single-molecule biophysics. *Nature Reviews Methods Primers* **1,** 25 (2021).

117. Prager, J. *et al.* Stiffness-matched biomaterial implants for cell delivery: clinical, intraoperative ultrasound elastography provides a 'target'stiffness for hydrogel synthesis in spinal cord injury. *Journal of tissue engineering* **11,** 2041731420934806 (2020).

118. Lock, G. *et al.* Contrast-enhanced ultrasound and real-time elastography for the diagnosis of benign Leydig cell tumors of the testis–a single center report on 13 cases. *Ultraschall in der Medizin-European Journal of Ultrasound* **35,** 534–539 (2014).

119. Lekka, M. Discrimination between normal and cancerous cells using AFM. *Bionanoscience* **6,** 65–80 (2016).